LANDSCAPE DEVELOPMENT IN THE SOUTHERN DRAKENSBERG AND LESOTHO HIGHLANDS, SE AFRICA: QUANTIFYING DENUDATION RATES USING *IN SITU*-PRODUCED COSMOGENIC CHLORINE-36 DATA

ALASTAIR FLEMING

Submitted for the degree of Doctor of Philosophy
The University of Edinburgh
2000

DECLARATION OF ORIGINALITY

I declare that the research reported in this thesis has been carried out by me, except where due acknowledgement has been made, that this thesis has been composed entirely by me and that it does not include work submitted for any other degree or professional qualification.

A posse ad esse

TABLE OF CONTENTS

ACKNOWLEDGEMENTS

The financial support of the following bodies is gratefully acknowledged - NERC (grant GR9/01730 and ICP-MS Facility application 135/0698 both to M. Summerfield); the Department of Geography, University of Edinburgh; the Carnegie Trust for the Universities of Scotland; and the University of Edinburgh Development Trust.

Numerous people have provided me with welcome support, motivation and encouragement and thereby played parts in ensuring that this project was completed. Special thanks are due to the following people:-

Mike Summerfield for introducing me to the joys of passive margin morphology and for his constant encouragement, guidance, and support;

John Stone for explaining, both patiently and excellently, the mysteries and intricacies of ^{36}Cl, for guiding me through the laboratory procedures, for providing me with a copy of his ^{36}Cl data reduction program, and for answering many, many, questions!;

Keith Fifield for showing me round the 14-UD pelletron AMS, for running all the ^{36}Cl and total Cl samples and for answering numerous queries;

Richard Cresswell for packing the targets, running AMS analyses and for great field assistance in 1997;

Hermione Cockburn and Ross Purves for excellent assistance with sample collection;

Dodie James and Godfrey Fitton for assistance with the XRF analysis; and

Kym Jarvis, Leon Clarke and Martin McCartney for assistance with the ICP-MS analysis.

My research has been greatly assisted by discussions with / comments from Paul Bishop, Rod Brown, Hermione Cockburn, Geoff Goldrick, Bernard Hallet, Goonie Marsh, Sarah Metcalfe, Malcolm Murray, Bill Phillips, Ross Purves, Michele Seidl, Fin Stuart, Terry Swanson and Peter van der Beek. All are gratefully thanked for their time, interest and input.

Preparation of the samples in the Department of Geography would not have been possible without the construction of the dedicated ^{36}Cl preparation laboratory and the provision of the necessary laboratory equipment. Special thanks are due to David Sugden and Mike Summerfield for their foresight and faith in pursuing this and to Sarah Metcalfe, Andy Dugmore, Bob McCulloch and Malcolm Murray for all their assistance in seeing the construction completed.

Thanks are due to the Research School of Earth Sciences, ANU, for my appointment as a School Visitor during April / May, 1997 and to everyone there who made me feel very welcome, in particular, John Stone, Keith Fifield, Richard Cresswell, Peter van der Beek, Jean Braun and Tim Barrows. I was also fortunate enough to be a visitor at the Quaternary Research Center, University of Washington, in February, 1999 and special thanks are due to John Stone, Bernard Hallet, Steve Porter, Terry Swanson and Sean Willet for providing a very memorable experience.

Fellow postgraduates in the Department of Geography, in particular, Herm, Sarah, Andy, Alastair, Simon, Anthony, Malcolm, Hjalti, Alun, Ian and Nick, are thanked for their empathy and support. Kerry Watt and Anne Pagan provided excellent librarian services and good humour in putting up with, *inter alia*, my numerous inter library loan requests!

And, on a more personal level, thanks are due to family and friends for their unwavering support and encouragement. Special thanks are due to to my wife, Fiona Fleming, to whom I am indebted for her absolute belief in my ability to undertake this project, constant support and for proof reading drafts!!

ABSTRACT

Over geological timescales, the spatial and temporal pattern of denudation is a primary control on the evolution of landscapes. Hence the ability to quantify denudation is fundamentally important to the comprehension and explanation of long-term landscape development. The recently developed technique of *in situ*-produced cosmogenic isotope analysis affords unique insights into the exposure history of the Earth's surface. In particular, in denudational terrains, this technique provides useful new, landform-scale, data on denudation rates applicable to timescales of 10^3 – 10^6 years. By using the analysis of one such *in situ*-produced cosmogenic isotope, chlorine-36 (^{36}Cl), this research quantifies, directly, rates of bedrock summit denudation and free face retreat in the basaltic terrain of the southern Drakensberg escarpment and Lesotho Highlands, both cardinal components of the SE African passive margin landscape.

Cosmogenic ^{36}Cl concentrations in 33 samples collected from flat-lying bedrock summits in the southern Drakensberg and Lesotho Highlands yield a mean denudation rate, integrated over the past ~ 50 ka, of 10.6 ± 1.6 m Ma^{-1}. Individual rates range from 1.2 ± 0.4 m Ma^{-1} to 43.0 ± 6.6 m Ma^{-1}. Possible site-specific sources of this variability are discussed. The mean summit denudation rate is similar to longer term (10^7 – 10^8 a), regional scale, estimates of crustal stripping provided by, for example, zeolite zonation studies and apatite fission track thermochronology (AFTT). Denudation of these summit flats at the measured rates is sufficient to prevent the long-term intact survival of erosion cycle surfaces formed prior to the break-up of Gondwana which were previously inferred for this region.

In total, 44 samples were collected from basalt free faces in the southern Drakensberg and Lesotho Highlands. For these steeply dipping surfaces, backwearing rates are calculated using two models, assuming (i) 'steady-state' denudation (Lal, 1991) and (ii) intermittent shedding of 0.5 m thick blocks. In both models, allowance is made for the impact of the cliff face in obstructing the incident cosmic-ray flux and in reducing the effective cosmic-ray attenuation length perpendicular to the free face. The mean backwearing rates (n = 19) for the main free face of the southern Drakensberg, derived from samples collected at three separate locations spread over ~ 175 km along the escarpment, are 50.9 ± 7.4 m Ma^{-1} (model i) and 87.9 ± 12.9 m Ma^{-1} (model ii), averaged over the past ~ 6 – 7 ka. Although the calculated mean escarpment retreat rate is more than an order of magnitude less than previously suggested, it is consistent with (i) geological evidence and AFTT data which imply similarly slow rates of escarpment retreat during the Cenozoic and (ii) general numerical model predictions of passive margin escarpment development. In combination these suggest that traditional notions about the manner of post-continental-break-up landscape development of the SE African continental margin require some re-appraisal.

Mean backwearing rates (n = 9) for non-escarpment free faces at the same three southern Drakensberg locations, at 29.8 ± 2.7 m Ma^{-1} (model i) and 50.3 ± 4.7 m Ma^{-1} (model ii), are similar to those derived for free faces in various morphological settings in the Lesotho Highlands (n = 16) (35.0 ± 4.8 m Ma^{-1} (model i) and 61.1 ± 7.9 m Ma^{-1} (model ii)). These rates are ~ 40 % lower than escarpment free face retreat rates. The ratio of the ^{36}Cl derived mean summit lowering rate to mean free face backwearing rate is 1 : 6 in the Lesotho Highlands and 1 : 9 in the southern Drakensberg. These total downwearing / backwearing ratios are likely to reduce once the impact of fluvial incision, presently unknown for this area, is included. Therefore, although backwearing is a very important modifier of this part of the SE African landscape, it does not operate exclusively, as was previously proposed.

This research confirms that the analysis of *in situ*-produced cosmogenic ^{36}Cl provides an important new technique for assessing, directly, landscape change at the scale of individual landforms over timescales of 10^3 – 10^5 years. When these data are coupled with longer term, regional scale, estimates of denudation, such as provided by AFTT, and the heuristic predictions of numerical modelling of morphological evolution, they provide new insights into the long-term development of landscapes.

CHAPTER 1: OLD PROBLEM, NEW DIRECTIONS: AN INTRODUCTION TO THE PROJECT

1.1 OVERALL AIM

The overall aim of this project is to use the analysis of *in situ*-produced ^{36}Cl (chlorine-36) to quantify bedrock denudation and free face retreat rates in the southern Drakensberg and Lesotho Highlands, SE Africa. By providing new data on rates of denudation and backwearing of key landscape elements in the study area, this project will further our understanding of the long-term evolution of the SE African landscape and thereby contribute to the more general debate on passive margin landscape development.

1.2 RESEARCH BACKGROUND

The comprehension and explanation of terrestrial (and, increasingly, extraterrestrial) landscapes is the fundamental focus of geomorphology. Although the discipline concentrated, during the first half of the 20th century, on understanding the development of landscapes this progressed within an essentially qualitative framework concerned primarily with evolutionary stage. The well-documented dissatisfaction with this approach (eg Chorley, 1965a; Summerfield, 2000) and the widespread acceptance by practitioners of more 'scientific' quantitative techniques combined to re-focus the discipline, at least in the UK and North America, on small spatial and short temporal resolution process-based studies more applicable to landforms and their constituent parts (Selby, 1985; Summerfield, 1991a). Recently, however, there have been both calls for these reductionist studies to be more integrated with the historical approach and other suggestions that long-term landscape development studies are beginning a renaissance within geomorphology (eg Ahnert, 1996; Bishop, 1998, 1999; Smith *et al*, 1999; Sugden *et al*, 1997; Summerfield, 1996b, 2000).

The proposed renaissance is being driven by various factors – the growing recognition of interactions between Earth systems; the advent of numerical modelling; and the development of new techniques for quantifying landscape development. The Earth sciences community is increasingly appreciative of the existence of complex interactions / feedbacks between macroscale morphological development and other Earth systems, specifically climate and tectonics (eg Molnar and England, 1990; Merritts and Ellis, 1994; Koons, 1995; Sugden *et*

al, 1995; Whipple *et al*, 1999; Kerr *et al*, 2000; Summerfield, 2000; Beaumont *et al*, 2000) (Figure 1.1). Appreciation of these complex relationships is helping to focus attention on the geomorphic processes and rates of landscape change, specifically denudation, which apply at the temporal and spatial scales applicable to long-term landscape development.

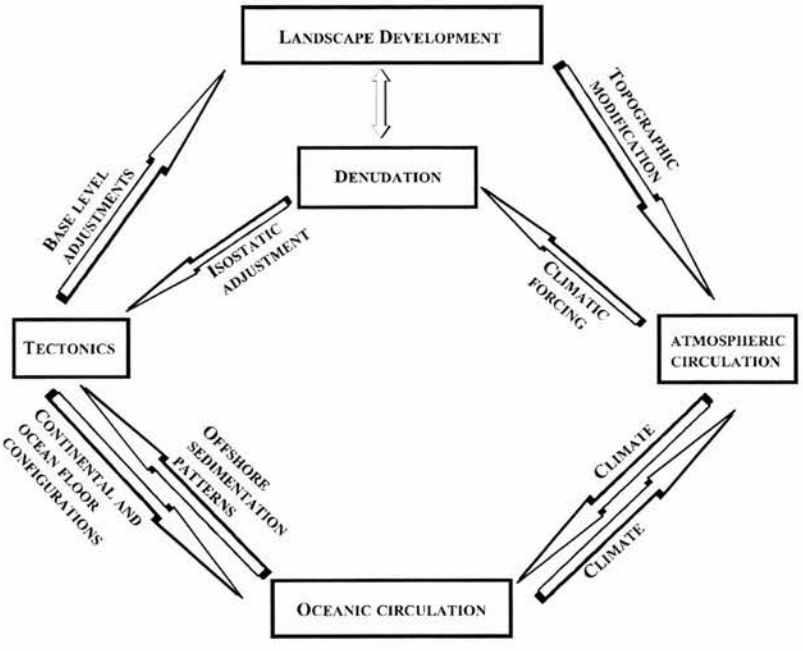

Figure 1.1: Interactions between macroscale morphological development and other Earth systems. Although tectonic processes operate as a first order control on landscape development, the operation of onshore denudational unloading and on- / offshore sediment loading lead to isostatic adjustments which feedback into tectonic processes. On a global scale, crustal tectonics control continental distribution which, in turn, modifies oceanic and atmospheric circulation patterns. These patterns affect climate which partly influences landscape development through denudation. Increases in topographic elevation, induced either by tectonic processes or, perhaps, accelerated denudation caused by climatic change, in turn influence atmospheric circulation and hence climate. After Beaumont *et al*, 2000 and Cockburn, 1998.

The advent of computer modelling has enabled the $10^6 - 10^8$ year development of synthetic, macroscale, landscapes to be simulated (eg Kooi and Beaumont, 1994; van der Beek and Braun, 1999; Beaumont *et al*, 2000). Although these models were based, originally, solely on endogenic mechanisms, they recognise increasingly the role of exogenic processes (Beaumont *et al*, 2000). These models provide a powerful means of demonstrating quantitatively the repercussions of different scenarios of landscape development, however, their main value is heuristic (Oreskes *et al*, 1994; van der Beek and Braun, 1999). They enable the "what if" questions to be explored (Merritts and Ellis, 1994, p12139), within the

limits of the model simplifications and assumptions (Bishop, 1998; Gunnell and Fleitout, 1998; van der Beek and Braun, 1999), and it needs to be borne in mind "that model results are not 'truth' (and can never be so)" (Merritts and Ellis, 1994, p12140). These numerical models have, nevertheless, brought the development of macroscale morphology back into focus and have highlighted the lack of unequivocal quantitative geomorphic data capable of constraining the model parameters and evaluating model predictions (eg Thomas, 1995; van der Beek and Braun, 1999; Kooi and Beaumont, 2000).

Providing incontrovertible quantitative geomorphic data on macroscale morphological evolution is a fundamental problem for long-term landscape development studies. Bishop (1998, p8) has highlighted this by asking the question "[h]ow [do] we handle the methodological question of reconstructing the history of denudational terrains ..... when the central element of this history (denudation) involves destruction of the evidence (the evidence of past landscape forms)? ". Whilst localised morphological reconstruction may be possible in exceptional situations (eg where basalt flows have preserved part of the pre-eruption drainage network - Bishop, 1988; Bishop and Goldrick, 2000), identifying temporal changes in morphology remains problematic in the vast majority of landscapes which do not contain unequivocal evidence of past topographic form (Summerfield, 1996b, 2000). In such denudational terrains it is, however, increasingly possible following the advent of various new techniques, to obtain data on the rates of landscape change, and specifically on denudation.

Denudation, as defined by Jackson (1997), encompasses all processes which result in the wearing down, or progressive lowering, of the Earth's surface, including weathering, erosion, mass wasting and transportation. Since the evolution of landscapes is the direct expression of spatially and temporally differentiated removal and addition of rock material (Ahnert, 1994), denudation, in this broad sense, is clearly a critical factor in landscape change. Hence the ability to measure both depths and rates of denudation is central to understanding long-term morphological development. However, despite the importance of denudation it has proved to be particularly difficult to quantify over the timescales required for landscape evolution.

Many techniques have been employed to quantify denudation. Saunders and Young (1983) list catchment scale denudation rates from 73 short-term studies which were mainly based on river sediment volumes or volumes of reservoir sedimentation. Inherent problems with these approaches include:- the lack of measurements of bed loads; the fact that short-term

monitoring is unlikely to estimate, accurately, the role of high magnitude / low frequency denudational events; non-denudational extraneous material, for example, solutes in precipitation or wind-borne particles, need to be excluded; anthropogenic influences may render modern sediment load atypical of the past; and complications of intra-basin sediment storage, which may introduce a lag between sediment supply and removal from the basin (Trimble, 1977; Saunders and Young, 1983; Summerfield and Hulton, 1994; Goudie, 1995).

Various new techniques have been developed recently which quantify long-term denudation rates – sedimentary basin volume studies; geochronometric techniques and thermochronologic techniques. If adequate chronological controls are available, sediment volumes in on- and offshore sedimentary basins may be used to calculate the timing and rate of denudation which has occurred in the basin's hinterland (eg Bishop, 1985; Brown *et al*, 1990; Rust and Summerfield, 1990; Pazzaglia and Brandon, 1996). Whilst constraining the sediment source area may be possible for small onshore basins during relatively short timescales, problems exist at the spatial and temporal scales relevant to macroscale morphological development (Gallagher and Brown, 1999; Gleadow and Brown, 2000) when even the basin mouth may have shifted dramatically (eg Dingle and Hendey, 1984). In addition such an approach yields very limited information about the spatial distribution of denudation rates within the basin (Pazzaglia and Brandon, 1996).

Geochronometric techniques rely on the ability to date by, for example, K – Ar and $^{40}Ar - ^{39}Ar$ dating, landforming material and to derive denudation estimates from post-formation depths of incision. Dating of basalts has been extensively employed in east Australia to derive well-constrained data on long-term landscape development, including plateau denudation rates and escarpment, gorge head and valley side wall retreat rates (summarised in Bishop and Goldrick, 2000). The application of these increasingly accurate dating techniques, whilst clearly capable of providing very useful denudation data, is limited by their reliance both on the availability of suitable material for dating and that material's position within the landscape.

By far the most widely applied and valued of the new techniques for deriving denudational data is thermochronology which involves the quantitative study of the thermal histories of rocks through the use of temperature-sensitive radiometric dating methods (Gleadow and Brown, 2000). A variety of methods is available, but the most relevant to macroscale landscape development are apatite fission track thermochronology (AFTT) (eg Summerfield, 1996b; Gallagher and Brown, 1999; Gleadow and Brown, 2000), and potentially, radiogenic

helium from uranium and thorium decay in apatite (U-Th/He) (eg Wolf *et al*, 1997). Essentially the thermal history of the rock reflects the progress of the sample from a given depth within the rock column to outcrop. If the geothermal gradient is known, or can be modelled, the thermal history can be interpreted to reflect a depth of crustal stripping and rate of denudation. AFTT provides $10^7 - 10^8$ a timescale denudation data and, although the spatial resolution is high when compared to offshore sediment volume studies (Gleadow and Brown, 2000), it cannot yield data at a spatial resolution finer than regional scale.

Given the factors outlined above it is clear that the drive for this re-awakening of interest in macroscale landscape development has been provided more by other Earth science sub-disciplines rather than by geomorphologists. This implies that future studies of landscape development should not involve a return to the traditional methodology of the denudation chronologists, particularly since unequivocal identification of temporal morphological change remains problematic in the vast majority of landscapes (Summerfield, 1996b; Bishop, 1998). Rather, the tackling of long-term landscape issues should be undertaken within a new, interdisciplinary, framework. This framework requires that the improved understanding of long-term landscape development will only be achieved by the assembly of disparate information from geomorphology and other Earth science sub-disciplines (Merritts and Ellis, 1994; Summerfield, 1996b, 2000; Bishop, 1998; Smith *et al*, 1999; Beaumont *et al*, 2000).

The numerical models, which, increasingly, involve the coupling of exogenic process modelling with tectonic / geophysical models (eg Beaumont *et al*, 2000), provide the best means of integrating this diverse information. However the output of these models remains synthetic and poorly constrained by the limited availability of empirical data on long-term rates of denudation and landscape change (eg Thomas, 1995; van der Beek and Braun, 1998, 1999). Although the new techniques for quantifying landscape change outlined above, and AFTT in particular, have gone some way to addressing this problem, they do not provide data at the landform-scale necessary to constrain surface process models of landscape evolution. An exception to this is the geochronometric techniques but, as already mentioned, their application is limited spatially by the availability of suitable substrates. However, a relatively new technique, involving the analysis of *in situ*-produced cosmogenic isotopes, is capable of quantifying rates of geomorphic modification at the resolution of landforms and, importantly, is less substrate dependent and, hence, more universally applicable.

1.3 *IN SITU*-PRODUCED COSMOGENIC ISOTOPE ANALYSIS

The ability to detect rare isotopes produced by the interaction of highly energetic cosmic-ray derived particles with terrestrial minerals affords unique, quantitative, insights into the exposure history of the Earth's surface (eg Bierman, 1994; Cerling and Craig, 1994a). The accumulation of these *in situ*-produced cosmogenic isotopes begins when target materials, including rock, are exposed to cosmic radiation within the cosmic-ray attenuation zone which extends, typically, 1 – 2 m metres below the ground surface. The abundance of cosmogenic radionuclides within a target sample is then determined by the rate of isotope production, the rate of radioactive decay and the dwell time of the target both within the attenuation zone and at the Earth's surface. The yields of *in situ*-produced cosmogenic isotopes from terrestrial samples are typically very small and their analysis has only become possible because of recent advances in both conventional and accelerator mass spectrometry (Elmore and Phillips, 1987; Fifield, 1999). Once measured, the *in situ*-produced cosmogenic isotope abundance is generally interpreted either as a surface exposure age or a denudation rate (eg Lal, 1991).

This interpretation is critically dependent on the geomorphological setting of the target sample. If the sampled surface can be inferred to be freshly exposed, perhaps through deglaciation or rockfall, and to have experienced insignificant denudation at the surface, evidenced by, for example, striations, then the isotopic yield reflects the exposure age of the surface (eg Nishiizumi *et al*, 1991, Zreda *et al*, 1999). In erosional environments the isotopic concentration is a measure of the rate of denudation, which controls the time spent by the target material passing through the 1 – 2 m cosmic-ray attenuation zone as it is gradually exposed (eg Lal, 1991; Nishiizumi *et al*, 1991).

By quantifying rates of denudation over timescales of $10^3 - 10^6$ a this new technique "neatly fills the gap between present-day and historical denudation rate data, and the long-term estimates provided by thermochronology and offshore sediment volumes" (Summerfield, 1996b, p214). The availability of denudation data at this temporal scale, if considered within the interdisciplinary framework outlined above, provides another independent source of evidence both for testing existing hypotheses of macroscale morphological development and formulating new reconstructions of long-term landscape history (Bishop, 1998). In addition, by providing site-specific denudation rates at the finer spatial resolution of landforms and their constituent parts, over timescales relevant to landscape development, the technique may

also offer the, as yet unrealised, possibility of addressing, at least in part, the problem expressed by Bishop (1998) of reconstructing morphology in denudational terrains.

A small number of previous studies have demonstrated the capability of the technique to yield denudation data in a variety of geomorphic situations (Table 2.5). Generally these studies have relied on a small (< 10) number of samples and the denudation data have been unconstrained by, independent, estimates of denudation. This study uses considerably more samples (77) and is able to compare results with existing longer term, regional scale, estimates of denudation. By coupling the shorter term, site-specific, *in situ*-produced cosmogenic isotope analysis results with longer term, AFTT data, an assessment can be made of certain aspects of existing qualitative models of landscape development in the study area.

1.4 Choice of study area

The southern Drakensberg and Lesotho Highlands in southeast Africa were chosen as the study area for four main reasons.

- The SE African landscape has played a key role in the development of qualitative geomorphic theories of macroscale morphological development having provided the inspiration for King's parallel retreat model of landscape evolution (eg 1944, 1953, 1982). The morphological development of this region has also been the subject of several other schemes (reviewed in Chapter 5). These have provided certain strong qualitative assertions which are capable of being testing by analysis of *in situ*-produced cosmogenic isotopes. Firstly, King (eg 1944, 1982) asserted that remnants of an erosion surface formed before the break-up of Gondwana were preserved at the highest elevations in the Drakensberg and Lesotho Highlands. Although this idea has been doubted (eg De Swardt and Bennet, 1974), the ability of *in situ*-produced cosmogenic isotope analysis to determine denudation rates directly from these surfaces, will enable King's assertion to be subjected to quantitative assessment. Secondly, the Great Escarpment of southern Africa (Rogers, 1920), which lies *circa* 100 – 200 km inland of the southern African coast, is the key geomorphic feature of this region. Despite the erosional nature of the escarpment having been known for some time (Suess, 1904), and its retreat being central to all existing explanations of the development of the regional morphology, available estimates of its backwearing rate are crude and based on indirect evidence (King, 1953; Mathews and Maud, 1988). Analysis of *in situ*-produced

cosmogenic isotopes from samples collected from the main free face of the southern Drakensberg provides the ability to quantify backwearing retreat rates directly from part of the Great Escarpment.

- Southeast Africa is a high-elevation passive margin formed during the fragmentation of Gondwana. These type of margins, comprising elevated terrain flanked by ocean-facing escarpments, are cardinal morphological features on a global scale, and their evolution reflects the long-term interaction of tectonic and surface geomorphic processes following supercontinent break-up (Gilchrist and Summerfield, 1994). Appreciation of the significance of passive margin landscapes to the comprehension of continental fragmentation processes has recently instigated a number of attempts to model numerically their morphological development (eg Gilchrist *et al*, 1994; van der Beek and Braun, 1999). Quantitative models have specifically addressed the issue of passive margin escarpment evolution (Kooi and Beaumont, 1994; Tucker and Slingerland, 1994). These models have suggested that escarpments are only likely to retreat where the escarpment summit coincides with the continental drainage divide, and even when these conditions are met the escarpment will only retreat at a slow rate. Such numerical modelling, however, is poorly constrained by data on passive margin escarpment retreat rates. The Drakensberg is widely regarded as the 'type' high elevation passive margin escarpment (Fleming *et al*, 1999) and provides an example of an escarpment summit which, generally, coincides with the continental drainage divide. Backwearing rates for the main free face of the southern Drakensberg, derived using the analysis of *in situ*-produced cosmogenic isotopes, will therefore provide quantitative field data with which to assess the output of these models. In addition it is proposed that the data will provide a constraint on the parameters of a future numerical model of the development of the southeast African landscape (P. van der Beek, pers. comm.).

- Independent, longer term, quantitative assessments of denudation exist for the study area. The shorter term, site-specific, data derived from the analysis of *in situ*-produced cosmogenic isotopes can be usefully compared with this other denudation data. Recent and ongoing studies of onshore drill core and outcrop samples in southern Africa have created a large AFTT database (Brown, 1992; Brown *et al*, 1990, 1994; Brown and Summerfield, in prep.). Zeolite zonation studies also provide an independent measure of the depth of denudation in the Lesotho Highlands.

- The Lesotho Highlands correspond to the largest sub-aerial outcrop of the 183 ± 1 Ma old Drakensberg Group basalts (Duncan *et al*, 1997) (Figure 5.4). This outcrop is the main denudational remnant of the Central Area of the very extensive Karoo Igneous Province (Eales *et al*, 1984; Cox, 1988). The southern Drakensberg forms the south-eastern (oceanward) erosional boundary of this outcrop. Basalt is the ideal substrate for the analysis of the *in situ*-produced cosmogenic isotope chlorine-36 (^{36}Cl). This is because of the comparatively high production rates of ^{36}Cl in reactions involving two major elements (calcium (Ca) and potassium (K)) and one minor isotope (chlorine-35 (^{35}Cl) which are ubiquitously present in this lithology (Zreda *et al*, 1991; Stone *et al*, 1996a, 1998a). In addition, the spatially extensive nature of the Drakensberg Group basalts (Figure 5.4) and their remarkably uniform strength characteristics (Moon and Selby, 1983), suggested that results could be compared and grouped without concern for the impact of lithological variability between sample sites.

1.5 Specific objectives of the research

The specific objectives of the study are:

- To establish at what rate denudation has been occurring on the bedrock summits of the southern Drakensberg and Lesotho Highlands;

- To quantify the rate at which the main free face of the southern Drakensberg escarpment has been retreating;

- To determine the rate at which free faces in high local relief settings within the Lesotho Highlands have been backwearing and to compare these to the retreat rate established above; and

- To compare the rates determined by the analysis of *in situ*-produced ^{36}Cl to existing, longer term, regional scale denudation data for southeast Africa.

1.6 Structure of the thesis

Following this introductory chapter there are eight chapters. The first three chapters focus on the technique. Because of the relative novelty of the technique, particularly when used to establish denudation rates, Chapter 2 provides a general review of *in situ*-produced cosmogenic isotopes and their application within geomorphology. The nature of the basaltic

lithology in the study area meant that only one cosmogenic isotope, ^{36}Cl, could be used in this study. Of the cosmogenic isotopes commonly used to date, ^{36}Cl has the most complex production pathways, an understanding of which is critical to the interpretation of measured abundances of this isotope as denudation rate estimates. For this reason Chapter 3 explores the production systematics and the interpretation of ^{36}Cl yields, particularly from steeply sloping surfaces. In Chapter 4 the field and analytical procedures are described. These were included in the body of the thesis, rather than as an appendix, because of the somewhat unfamiliar nature of the procedures. The remaining chapters focus on the application of the technique to long-term landscape development in SE Africa. Chapter 5 describes the physical setting of the study area and then reviews the current understanding of both the development of passive margin landscapes in general and the existing ideas about the long-term landscape evolution of southeast Africa. Chapter 6 provides the field descriptions and the ^{36}Cl derived denudation rates for the samples collected from the flat-lying summits of the southern Drakensberg and Lesotho Highlands. Similarly, Chapter 7 presents the field descriptions and results for the samples collected from free faces within the Lesotho Highlands and along the southern Drakensberg. The significance of the results from both the flat-lying and free face sites for the development of the southeast African landscape are discussed in Chapter 8. Finally, Chapter 9 summarises the main conclusions of the study and suggests possible areas of further research. Supplementary information, including, photographs of the sample settings, the major and trace element results for the individual samples, the results of the isotope dilution curve fitting procedure, and a copy of the *Mathematica* ® program used to calculate the denudation rates are contained in various appendices. An offprint of the published Fleming *et al* (1999) paper, which reported the results of the six initial samples used in this project, is included as Appendix 9.

CHAPTER 2: *IN SITU*-PRODUCED COSMOGENIC ISOTOPES: 'TOOLS' FOR GEOMORPHOLOGY

2.1 INTRODUCTION

Nishiizumi *et al* (1993, p423) referred to *in situ*-produced cosmogenic isotope analysis as a "set of tools" which could be used to explore geomorphic surfaces. This chapter represents a handbook for that toolkit as it explains the fundamental aspects of the analysis of *in situ*-produced cosmogenic isotope and reviews the use of the technique in geomorphology. In essence the method enables the measured concentration of cosmogenic isotopes which accumulate when a surface is subject to cosmic radiation, to be used to interpret the exposure history of that surface, usually as a surface exposure age or a denudation rate. It is the ability of the technique to provide a range of interpretations (the 'set of tools'), governed by geomorphic and modelling constraints, which has led the technique to be applied increasingly to a diverse range of geomorphological problems over the past few years (Table 2.1). The majority of studies to date have analysed samples collected from bedrock and intact boulders and, although the technique has also been applied to sedimentary deposits such as ice (eg Lal *et al*, 1990), soils (eg Phillips *et al*, 1998) and fluvial sediments (eg Brown *et al*, 1998b), this chapter concentrates on cosmogenic isotope production *in situ* within bedrock.

The potential application of the technique to geomorphology was advocated in the seminal work of Davis and Schaeffer (1955) who first suggested the possibility of dating Quaternary glacial events using cosmogenic ^{36}Cl. As a result of the difficulties of measuring the small abundances of *in situ*-produced cosmogenic isotopes found at the Earth's surface, studies thereafter focused on using atmospherically produced cosmogenic isotopes as tracers (eg Lal and Peters, 1967). Advances in mass spectrometry in the late 1970's made it possible to measure these small yields and *in situ*-produced cosmogenic isotope studies started to appear in the mid-1980's (eg Kurz, 1986a; Klein *et al*, 1986; Nishiizumi *et al*, 1986; Phillips *et al*, 1986). Initial studies mainly concentrated on systematics (eg Nishiizumi *et al*, 1989, 1990; Zreda *et al*, 1991), but a number of review articles (eg Nishiizumi *et al*, 1993; Bierman, 1994; Cerling and Craig, 1994a) have helped to focus interest on potential geomorphological applications. To date five cosmogenic isotopes, ^{3}He, ^{10}Be, ^{21}Ne, ^{26}Al and ^{36}Cl, have been

routinely measured and some of their properties are listed in Table 2.2. Also listed is ^{14}C which, along with ^{41}Ca, is in the early stages of development (Henning *et al*, 1987; Cerling and Craig, 1994a; Handwerger *et al*, 1999).

Table 2.1: Published examples from the past three years of geomorphological situations in which *in situ*-produced cosmogenic isotope analysis has been applied.

Application	Isotope	Surface sampled	Reference
glacial chronology	^{3}He, ^{21}Ne	boulders, bedrock	Bruno *et al*, 1997
	^{36}Cl	boulders	Jackson *et al*, 1997
	^{36}Cl, ^{10}Be	boulders	Phillips *et al*, 1997
	^{10}Be, ^{26}Al	boulders, bedrock	Steig *et al*, 1998
	^{36}Cl	boulders, bedrock	Zreda *et al*, 1999
	^{10}Be, ^{26}Al	bedrock	Bierman *et al*, 1999
glacial denudation rates	^{36}Cl	bedrock	Briner and Swanson, 1998
river terrace chronology	^{10}Be, ^{26}Al	clasts	Repka *et al*, 1997
	^{10}Be, ^{26}Al	bedrock	Leland *et al*, 1998
	^{10}Be, ^{26}Al	clasts	Hancock *et al*, 1999
dating depositional landforms	^{10}Be	boulders	Siame *et al*, 1997
	^{10}Be	clasts	Brown *et al*, 1998a
	^{3}He	clasts	Cerling *et al*, 1999
dating landslides / fault scarps / perched boulders	^{36}Cl	boulders	Ballantyne *et al*, 1998
	^{36}Cl	boulders	Bell *et al*, 1998
	^{36}Cl	bedrock	Zreda and Noller, 1998
soil / regolith studies	^{10}Be, ^{26}Al	soil covered bedrock	Heimsath *et al*, 1997, 1999
	^{21}Ne	soil, regolith	Phillips *et al*, 1998
	^{10}Be, ^{26}Al	regolith, bedrock	Small *et al*, 1999
duricrust dynamics	^{10}Be	bedrock	Braucher *et al*, 1998a, 1998b, 1999
periglacial weathering limits	^{10}Be, ^{26}Al, ^{36}Cl	bedrock	Stone *et al*, 1998b
fluvial incision rates	^{10}Be, ^{26}Al	alluvium	Granger *et al*, 1997
river long profile development	^{10}Be, ^{26}Al, ^{36}Cl, ^{3}He, ^{21}Ne	boulders	Seidl *et al*, 1997
landscape denudation studies	^{10}Be, ^{26}Al	bedrock	Small *et al*, 1997
	^{10}Be	alluvium	Brown *et al*, 1998b
	^{10}Be, ^{26}Al	bedrock	Cockburn *et al*, 1999
	^{36}Cl	bedrock	Fleming *et al*, 1999
	^{21}Ne	bedrock	Summerfield *et al*, 1999a & 1999b

This chapter is split into two sections, the first of which focuses on terrestrial cosmogenic isotope production. The following section discusses how to derive geomorphological data and provides examples of recent geomorphological applications. The following two chapters focus exclusively on the cosmogenic isotope used in this study, ^{36}Cl, Chapter 3 dealing with isotope systematics and Chapter 4 detailing experimental procedures.

2.2 COSMOGENIC ISOTOPES AND THEIR TERRESTRIAL PRODUCTION

2.2.1 COSMIC RADIATION

In common with matter throughout the universe, the Earth is subject to the constant bombardment of cosmic radiation which originates in the solar system (eg from solar flares) and the galaxy (the source is not well known, but has been suggested to be *inter alia* supernovae explosions). Outwith the Earth's atmosphere the high-energy particles that comprise this radiation are mainly protons (~ 87 – 90 %), ~ 10 – 12 % α-particles and ~ 1 % heavier atomic nuclei (Honda and Arnold, 1967; Reedy *et al*, 1983a, 1983b; Raisbeck and Yiou, 1989; Masarik and Reedy, 1995). Solar cosmic-rays (SCRs) have energies within the 1-100 MeV (10^6 electron volt nucleon^{-1}) range and a flux ranging from ~ 1 – 100 particles cm^{-2} s^{-1}. Galactic cosmic-rays (GCRs) have higher energies, typically ranging from 100 MeV to 3 GeV (10^9 electron volt nucleon^{-1}) (they can reach 100 GeV, Cerling and Craig, 1994a), but a lower flux of between 0.03 and 3 particles cm^{-2} s^{-1} (Lal and Peters, 1967; Reedy *et al*, 1983b).

When the cosmic radiation enters the atmosphere the high-energy particles interact with atomic nuclei. The exact interaction process is determined by the particles' energy, mass and charge and the chemistry of the target nuclei. The low energy SCRs tend to be stopped by ionization energy loss within the topmost part of the atmosphere whilst the higher energy GCRs lose energy by inducing nuclear reactions with the target nuclei. In these reactions a cascade of secondary particles, mainly neutrons, pions and γ-rays, are produced. Many of these secondaries are produced before the GCRs are stopped and it is these secondary particles, especially the neutrons, but also muons (the decay products of the pions) which are responsible for terrestrial cosmogenic isotope production. SCRs induce few secondary particles and are thus relatively unimportant. The nature of the GCRs produced cascade is well known from theoretical calculations, bombardments of targets with accelerated particles and studies of cosmogenic nuclides in extraterrestrial objects (eg moon, meteorites) (Reedy *et al*, 1983b).

Within the atmosphere, these secondary particles interact with nuclei to produce new cosmogenic isotopes (atmospheric, meteoric or 'garden variety' cosmogenic isotopes – Nishiizumi *et al*, 1986). For example, fast secondary neutrons are involved in spallation reactions with the nuclei of N, O and Ar producing, respectively, cosmogenic ^{3}He, ^{10}Be, and ^{36}Cl. These atmospherically produced cosmogenic isotopes are oxidised (except the noble gases) and become attached to aerosols which collect on condensation droplets and are transferred from the atmosphere to the Earth's surface during wet and dry precipitation (Lal and Peters, 1967). These atmospheric isotopes have been used extensively in the Earth sciences to study, for example, subsurface hydrology (eg Phillips, 1995; Lyons *et al*, 1998; Sueker *et al*, 1999) and soil production and transport rates (eg McKean *et al*, 1993).

Atmospheric production reduces the cosmic-ray flux exponentially and therefore, at the Earth's surface, the flux is only ~ 0.1 % of that at the top of the atmosphere (Brown *et al*, 1992). This explains the relatively small concentrations of *in situ*-produced cosmogenic nuclides encountered in geomorphic samples. This chapter is only concerned with cosmogenic isotopes that have actually been produced *in situ* at the surface, and not with those which accumulate at the surface through precipitation. Indeed pre-treatment procedures, outlined in Chapter 4, are used to remove any potential atmospheric component from rock samples. Atmospherically produced cosmogenic isotopes will not be considered further.

2.2.2 *In situ* cosmogenic isotope production: mechanisms

Cosmogenic isotopes are produced *in situ* during nuclear reactions involving cosmic-ray produced secondary particles and the nuclei of target elements. These new isotopes are generated by three principal reactions:– high-energy spallation; thermal neutron capture and muon reactions. In the case of ^{36}Cl production in whole rock samples all three reactions are significant and therefore, as these mechanisms are considered in detail in the following chapter, what follows is a very brief overview.

2.2.2.1 *Spallation*

When a high-energy secondary particle, such as a neutron, collides with a target nucleus the latter may fragment creating new product nuclei (cosmogenic isotopes) and particles. This reaction, called spallation, is only possible if the incident particle is sufficiently energetic to overcome the average nucleon binding force (~ 8 MeV, Fabryka-Martin, 1988). Secondary

cosmic-rays tend to have such energies and as a result spallation is the most important production mechanism for the majority of cosmogenic isotopes produced *in situ* in the topmost metre or so of the Earth's surface.

2.2.2.2 THERMAL NEUTRON ACTIVATION

Thermal neutrons (energy ≤ 0.5 MeV, Fabryka-Martin, 1988; Cerling and Craig, 1994a) are produced within the Earth's surface from a variety of sources – spallation, muon capture reactions, photodisintegration reactions induced by fast muons, uranium fission, and (α, n) reactions (see Chapter 3 for a discussion of these). Once thermalized (the kinetic energy is reduced by elastic collisions between neutrons and nuclei, Fabryka-Martin, 1988) these neutrons are captured by nuclei with large neutron capture cross-sections to produce new isotopes. The cross-section is the probability of the reaction occurring, expressed as the target area presented by the target nucleus to the bombarding particle (Fabryka-Martin, 1988).

2.2.2.3 MUON REACTIONS

Muons, the decay products of the secondary cosmic-ray pions, are low mass (~ 200 times the mass of an electron) unstable sub-atomic particles with an extremely short mean life of ~ 2.2×10^{-6} s and a wide energy spectrum, ranging from ~ 27 MeV to > 100 GeV (Lal and Peters, 1967; Fabryka-Martin, 1988; Stone *et al*, 1998a). Fast muons contribute to thermal neutron production, while those with lower energies are stopped by ionization and then either decay radioactively, or, in the case of negative muons, are captured by positively charged nuclei to form cosmogenic isotopes (Charalambus, 1971; Fabryka-Martin, 1988; Stone *et al*, 1998a).

The relative contribution of the particular mechanism varies from isotope to isotope and depends on the chemical composition of the target. Table 2.2 highlights the main production mechanisms, the principal production targets and the common sample materials for each of the five most frequently used isotopes. It is clear that for the majority of commonly used *in situ*-produced isotopes spallation is the main but, normally, not the sole mechanism.

Table 2.2:Some properties of *in situ*-produced cosmogenic isotopes commonly used in geomorphology (source Bierman, 1994; Cerling and Craig, 1994a).

Property	***In situ*-produced isotope**					
	^{3}He	^{10}Be	^{14}C	^{21}Ne	^{26}Al	^{36}Cl
Half-life (a)	stable	1.5×10^{6}	5730	stable	7.16×10^{5}	3.01×10^{5}
Decay constant (a^{-1})	-	4.62×10^{-7}	1.21×10^{-4}	-	9.68×10^{-7}	2.30×10^{-6}
Main production mechanism	spallation; muon capture	spallation; muon capture	spallation	spallation	spallation; muon capture	spallation; thermal neutron capture; muon capture
Principal production targets	O, Mg, Si, Fe	O, Mg, Si, Fe	O	Na, Mg, Al, Si, Ca	Al, Si	^{35}Cl, K, Ca
Common sample material	olivine, pyroxene	quartz, olivine	quartz, calcite	quartz, olivine, pyroxene	quartz	whole rock
Measurement technique	MS*	AMS**	AMS**	MS*	AMS**	AMS**
Measurement target compound	He	BeO	C	Ne	Al_2O_3	AgCl

* Mass spectrometry. ** Accelerator mass spectrometry.

The stable isotope ^{3}He is produced mainly by spallation reactions between fast neutrons and the major elements in rock (eg O, Si, Fe) with a significantly lesser contribution from thermal neutron activation of ^{6}Li or ^{10}B (Kurz, 1986a, 1986b, 1987; Lal, 1987b). Muon reactions become important from ~ 300 g cm^{-2} (~ 1m) below the surface (Lal, 1987a, 1987b) and therefore can be significant in situations where denudation rates are rapid (Kurz, 1986b). Common sampling materials for ^{3}He studies are olivine and pyroxenes (eg Kurz, 1986a, 1986b; Anthony and Poths, 1992; Bruno *et al*, 1997; Cerling *et al*, 1999). Due to potential post-production diffusive loss of ^{3}He controlled by temperature and grain size, quartz, plagioclase and whole rock samples are avoided (Cerling, 1990; Trull *et al*, 1991; Brook and Kurz, 1993; Trull *et al*, 1995; Bruno *et al*, 1997; Summerfield *et al*, 1999a).

The other stable isotope, ^{21}Ne, produced by spallation of Na, Mg, Al, Si, and Ca, has been studied in quartz, olivine, pyroxene, and plagioclase (Marti and Craig, 1987; Graf *et al*,

1991; Poreda and Cerling, 1992; Niedermann *et al*, 1993 and 1994; Bruno *et al*, 1997; Phillips *et al*, 1998; Summerfield *et al*, 1999a). Muon production has not been assessed, but may be important at depth and therefore may affect samples from sites of rapid denudation (Cerling and Craig, 1994a).

Beryllium-10 is produced predominantly by spallation of O, but with some contribution from spallation of Si, Mg and Fe (Klein *et al*, 1986; Nishiizumi *et al*, 1986, 1990). Muon induced reactions have been suggested to account for 1 – 3 % of ^{10}Be production in quartz at the Earth's surface, with a linear relationship with increasing denudation rates and exposure times (Brown *et al*, 1995a; Braucher *et al*, 1998a, 1998b). Quartz is the common sample material for ^{10}Be for various reasons: the tight crystal lattice minimizes meteoric ^{10}Be contamination; it is ubiquitous in nature; it has a simple chemistry and relatively simple separation procedure; and the production rate of ^{10}Be in quartz is well studied (Lal and Arnold, 1985; Nishiizumi *et al*, 1986, 1989; Kohl and Nishiizumi, 1992; Clark *et al*, 1995). ^{10}Be has also been measured in olivine (Nishiizumi *et al*, 1990; Shepard *et al*, 1995).

Often paired with ^{10}Be, ^{26}Al, is produced by spallation of Si and Al (Nishiizumi *et al*, 1986; Klein *et al*, 1986). Negative muon capture reactions involving Si have also been reported for depths over ~3 m below the ground surface and would be important in situations of rapid denudation (Strack *et al*, 1994). Quartz and olivine are the preferred sample materials as both have low natural Al content which is essential for measurements of ^{26}Al (Nishiizumi *et al*, 1990).

In situ-produced cosmogenic ^{14}C is produced in rocks primarily by spallation of O (Jull *et al*, 1992). Production has been reported from quartz and limestone samples (Donahue *et al*, 1990; Handwerger *et al*, 1999). The production of ^{36}Cl, which can involve all three of the production mechanisms, is discussed extensively in the next chapter.

One complication in cosmogenic isotope analysis arises from the possibility that the same isotope can be produced either by a non-cosmogenic mechanism, or by non *in situ*-production. Inclusion of such isotopes would produce errors in interpretation and hence these isotopes have to be distinguished from the *in situ*-produced cosmogenic component.

Two non-cosmogenic sources are important. For the noble gases in olivine and pyroxene phenocrysts in basalt, a non-cosmogenic component can be inherited from, for example, the mantle. Primordial ^{3}He is released from fluid inclusions by crushing *in vacuo* and stepwise heating (Kurz, 1986a; Kurz *et al*, 1990), while inherited ^{21}Ne is distinguished by its isotopic

ratio (Niedermann *et al*, 1994). Nucleogenic (non-cosmogenic) neutrons, produced by (α, n) reactions involving U- and Th- decay series and by spontaneous fission of ^{238}U, may interact, for example, with lithium to produce ^{3}He via the reaction ^{6}Li (n, α) T $\rightarrow$ ^{3}He, or with magnesium producing ^{21}Ne through the reaction ^{24}Mg (n, α) ^{21}Ne, or with chlorine-35 to produce ^{36}Cl (see Chapter 3) (Lal, 1987a; Niedermann *et al*, 1993). The nucleogenic contribution can be evaluated using the U and Th content, the nucleogenic neutron yield and the reaction cross-section of the isotope (Fabryka-Martin, 1988; Stone *et al*, 1998a).

Atmospherically produced cosmogenic isotopes can be introduced to sample sites by precipitation, as outlined earlier. These non *in situ*-produced isotopes are only problematic for ^{10}Be and ^{36}Cl (Lal and Peters, 1967; Bentley *et al*, 1982). Preliminary acid leaching of samples is sufficient to remove this component (Kohl and Nishiizumi, 1992; Stone *et al*, 1996a).

2.2.3 *In situ* COSMOGENIC ISOTOPE PRODUCTION: SPATIAL INFLUENCES

Three spatial factors influence *in situ*-production of cosmogenic isotopes: altitude and latitude; depth below the ground surface and topographic shielding.

2.2.3.1 *Altitude and latitude*

The primary cosmic radiation (PCR) is predominantly comprised of protons which, being positively charged, are subject to modulation by the Earth's magnetic field (Lal and Peters, 1967). The ability of each PCR proton to penetrate the geomagnetic field is dependent on both its momentum ('rigidity') and its angle of incidence to the field. For each angle of incidence there is a critical rigidity below which the incoming PCR particle will be deflected from entering the atmosphere (the 'cutoff rigidity') (O'Brien, 1979; Masarik and Reedy, 1995). The vertical cutoff rigidity ranges from 0 at high latitudes to ~ 17.5 GV near the equator (Masarik and Reedy, 1995).

The geomagnetic field is thought to be well represented as an eccentric dipole with the field paralleling the surface at the equator and being perpendicular at the poles (Quenby and Webber, 1959). Cutoff rigidities are therefore highest at equatorial and low latitudes and decrease towards the poles. More PCR particles therefore penetrate the atmosphere at high latitudes leading to increasing cosmogenic isotope production rates from low to high latitudes (Lal and Peters, 1967). Above 60° latitude the production rate flattens as the additional primary protons that do penetrate the atmosphere have lower energies and are

therefore brought to rest by ionization energy loss rather than nuclear interactions (Lal and Peters, 1967).

Once the PCR particles have penetrated the geomagnetic field they interact with nuclei in the atmosphere to produce the nuclear cascade mentioned earlier (Section 2.2.1). At any given latitude the energy spectrum of secondary nucleons remains invariant at atmospheric depths[1] exceeding 200 g cm^{-2} (~ 12 km asl), and the production rate of cosmogenic isotopes is proportional to the nuclear disintegration rate caused by the PCR in the atmosphere (the 'star' production rate) (Lal and Peters, 1967). The secondary cosmic-ray neutrons decrease in abundance due to absorption and scattering as they pass through matter, including the atmosphere (Lal and Peters, 1967; Fabryka-Martin, 1988). The neutron attenuation length in the atmosphere, that is the distance over which the secondary cosmic-ray neutrons is reduced by a factor of 1/e, varies with latitude from ~200 g cm^{-2} at low latitudes to ~ 160 g cm^{-2} for > 60° latitude (Lingenfelter, 1963, quoted in Cerling and Craig, 1994a). Lal (1991) give values of between 140 and 160 g cm^{-2} for fast neutrons between sea level and 5 km, although a value of 160 g cm^{-2} is often quoted (eg Brown *et al*, 1992). This reduction in neutrons with increasing atmospheric depth means that with increasing altitude above sea level (equivalent to decreasing the atmospheric overburden) the number of secondary cosmic neutrons will increase and thus so will *in situ* cosmogenic isotope production.

Lal (1991) has produced scaling factors for neutrons, based on Lal and Peter's work (1967), which can be used to adjust production rates calculated at one site to be applicable to any altitude or latitude on the Earth's surface. Other schema have been proposed (eg Lingenfelter, 1963, quoted in Cerling and Craig, 1994a; Yokoyama *et al*, 1977; O'Brien, 1979, and, very recently, Dunai, 2000), but Lal's third order polynomial (the nuclear disintegration rate (g^{-1} a^{-1}) = $a + (b * y) + (c * y^2) + (d * y^3)$, where y is the altitude in km and a, b, c and d have the values ascribed in Table 2.3) is most frequently used and has been applied in this study. For samples that have been exposed to cosmic radiation for in excess of 2000 a, the geographic latitude may be used as the geomagnetic pole averages the position of the geographic pole over such periods (Cerling and Craig, 1994a).

---

[1] For cosmogenic reactions depths are commonly expressed in mass shielding depths (g cm^{-2}) as the rates of nuclear reactions induced by cosmic radiation are functions of the total mass of material traversed by the cosmogenic particle (Fabryka-Martin, 1988, Liu *et al*, 1994a). The mass shielding depth is thus independent of density of the matter (air, water, rock etc.) being traversed, and the depth in centimetres can be calculated by dividing the mass shielding depth by the relevant density (g cm^{-3}).

Table 2.3: Altitude and latitude scaling factors which relate production due to fast neutrons at sea level and high latitudes (> 60°) to any altitude or latitude on Earth. Scaling factors for latitudes not shown may be calculated by linear interpolation (based on Lal, 1991).

Geomagnetic latitude (°)	a	b	c	d
0	0.587	0.454	0.175	0.036
10	0.600	0.447	0.197	0.037
20	0.678	0.483	0.235	0.044
30	0.833	0.700	0.174	0.084
40	0.933	0.897	0.252	0.104
50	1.014	1.044	0.303	0.135
60-90	1	1.104	0.315	0.140

Muons are also attenuated in the atmosphere, but with an e-folding length of 247 g cm^{-2} (Lal, 1988; Conversi, 1950, quoted by Stone *et al*, 1998a). The latitude dependence is less well known, and is generally assumed to be similar to that of star production at sea level (Lal, 1991; Stone *et al*, 1998a). For isotopes produced by a combination of neutron and muon reactions, such as ^{36}Cl in whole rock targets, the slow muon stopping rate (and hence muon production) must be scaled separately (Lal, 1988; Stone *et al*, 1998a). The following equation can be used to derive the scaling factor for muon production at altitude y (km) and > 60°, $SF_{m,>60°}$ (Lal, 1988; Nishiizumi *et al*, 1989; Lal, 1991):

$$SF_{m,>60^\circ} = e^{\left(\left(1033-\left(1032.92-\left(121.95*y\right)+\left(5.657*y^2\right)-\left(0.1095*y^3\right)\right)\right)/\Lambda_m\right)} \qquad \text{Equation 2.1}$$

Λ_m, is the attenuation length for muons in the atmosphere, 247 g cm^{-2}. Scaling factors for 50° to 0°, can be obtained by multiplying $SF_{m,>60°}$ by 1.014, 0.933, 0.833, 0.678, 0.600 and 0.587, respectively (Lal, 1991; Stone *et al*, 1996a, 1998a). Figure 2.1 provides a comparison of the altitude scaling factors for muons and fast neutrons for high latitude. An accurate knowledge of the contribution of fast neutrons and muon capture reactions to the total production of an isotope is therefore required for accurate production rate estimates, particularly at high altitudes (Stone *et al*, 1998a).

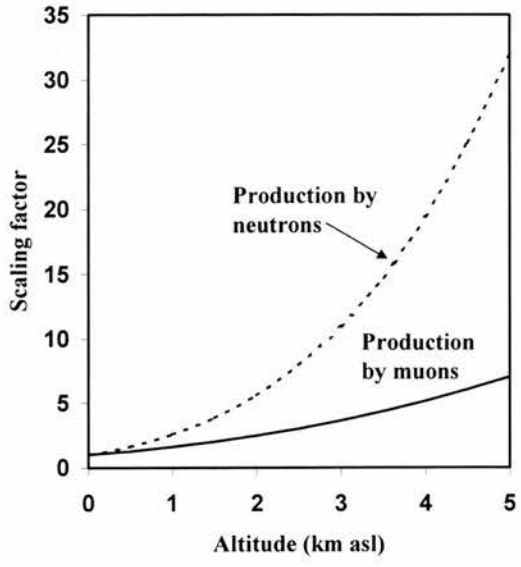

Figure 2.1: Comparison of altitude scaling factors for high latitude (> 60°) for *in situ*-production by fast neutrons and muons (based on Lal, 1991 and Stone *et al*, 1998a respectively).

2.2.3.2 *Depth below ground surface*

The decline in the secondary cosmogenic particle flux in the atmosphere is mirrored by a reduction in the topmost few metres of the Earth's surface. This reduction in the cosmic-ray energy and flux as it traverses rock is due to nuclear interactions and ionization losses (Lal, 1991), and results in a corresponding reduction in the production rate of *in situ*-produced cosmogenic isotopes. This aspect is fundamental to the ability of the technique to be used to derive denudation rate data (Nishiizumi *et al*, 1989, 1991). Several empirical studies, based on the variation of the concentration of a particular isotopes with depth below the Earth's surface, have confirmed this reduction (Kurz, 1986a; Brown *et al*, 1992; Sarda *et al*, 1993; Braucher *et al*, 1998a, 1998b; Stone *et al*, 1998a) (Figure 2.2). The attenuation length for production of ^{3}He, ^{21}Ne, ^{10}Be, and ^{26}Al has been both estimated (Lal and Peters, 1967; Lal, 1991; Masarik and Reedy, 1995) and calculated from studies of terrestrial drill core results (Kurz, 1986a; Brown *et al*, 1992; Sarda *et al*, 1993). These studies produced attenuation lengths of ~ 165 g cm^{-2} for ^{3}He and ^{21}Ne, for sites with latitude ~ 20°, and 145 – 156 g cm^{-2} for ^{10}Be and ^{26}Al for high latitude Antarctic sites. This is in line with the expected latitudinal variation due to the effect of the geomagnetic shield (Lal, 1991; Cerling and Craig, 1994a).

In the case of spallation produced isotopes, the production rate, P (atoms g^{-1} a^{-1}), varies with depth, z (g cm^{-2}) below the ground surface as follows (eg Lal, 1991):

$$P_{sp}(z) = P_{sp}(0)e^{-z/\Lambda_{sp}} \qquad \text{Equation 2.2}$$

where $P_{sp}(0)$ is the spallogenic production rate of the isotope at the ground surface and Λ_{sp} is the effective attenuation length for spallogenic production (assumed in this thesis to be 160 g cm^{-2}). For depths in cm, z can be replaced by x (cm) multiplied by the density of the material, ρ, (g cm^{-3}). Where the cosmogenic isotope is produced by thermal neutron activation or muon capture reactions as for example, ^{36}Cl, the variation in production with depth is more complex (see Chapter 3).

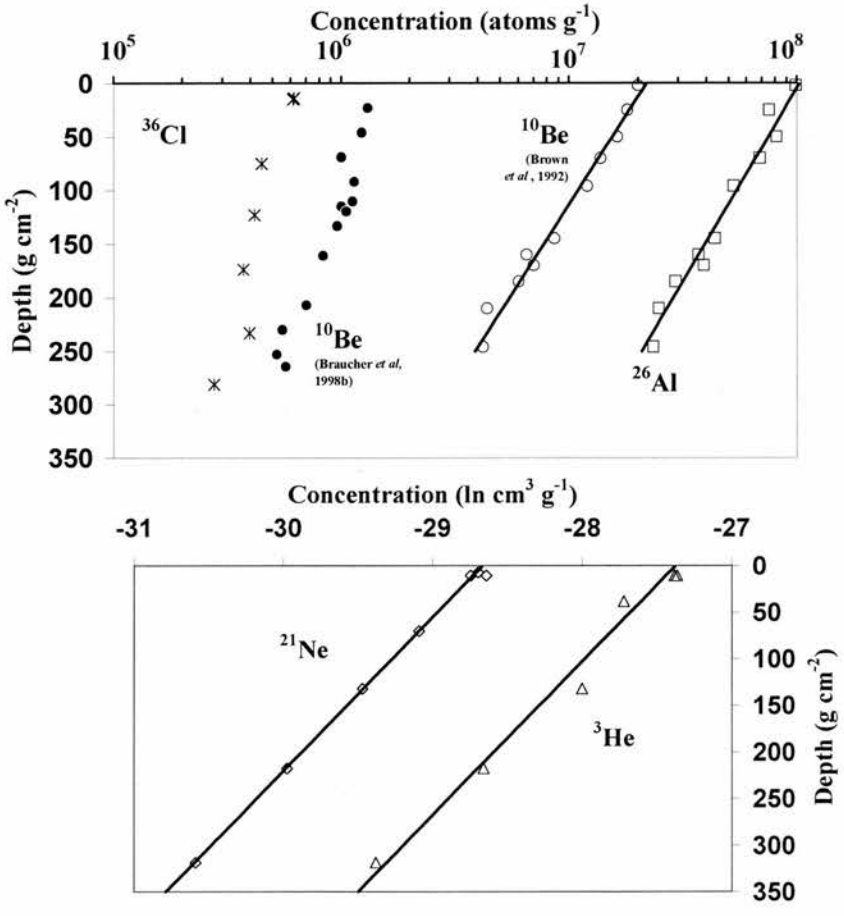

Figure 2.2: Variation in the concentration of *in situ*-produced ^{36}Cl, ^{10}Be, ^{26}Al, ^{3}He, and ^{21}Ne as measured by Stone *et al* (1998a), Braucher *et al* (1998b), Brown *et al* (1992) and Sarda *et al* (1993), respectively. Similar results for ^{10}Be, reported by Braucher *et al* (1998a), highlight a muon contribution of ~ 1.5 % to total ^{10}Be production. The straight lines represent the depth-dependent production based on suggested attenuation lengths.

2.2.3.3 TOPOGRAPHIC SHIELDING

On the Earth's surface, cosmogenic isotope production is greatest on a horizontal plane with an uninterrupted 360°, or 2π, horizon as it will receive the maximum flux of cosmic radiation (Nishiizumi *et al*, 1989; Dunne *et al*, 1999). If a portion of the 2π horizon is obscured by an object that has sufficient mass (> a few metres) to block out the incoming radiation, the flux will be decreased and the production rate correspondingly lowered (Dunne *et al*, 1999). This can be corrected by applying a topographic shielding factor, S, which is the ratio of the remaining flux to the maximum flux (Dunne *et al,* 1999):

$$S = 1 - \frac{1}{360^\circ} \sum_{i=1}^{n} \Delta\phi_i \sin^{m+1} \theta_i \qquad \text{Equation 2.3}$$

where, $\Delta\phi_i$ is the azimuth angle of the obstructing object as viewed by the sample, θ_i is the inclination (zenith) angle measured from the horizon to the top of the obstruction, and n is the number of obstructions. The value of m is assumed to be 2.3 in most studies (Nishiizumi *et al*, 1989; Cerling and Craig, 1994a; Dunne *et al*, 1999). Equation 2.3 is based on rectangular obstructions and Dunne *et al* (1999) provide a polynomial for converting a triangular obstruction zenith angle to an equivalent 'rectangular' inclination angle. The effective attenuation length will also be affected (reduced), although the correction is minimal unless θ_i is $> \sim 20°$ and $\Delta\phi_i$ is $> \sim 90°$ (Dunne *et al*, 1999, figures 2 and 3). Shielding by the surrounding topography is not normally a significant factor unless samples are being collected in high relief valleys.

If the sampling surface is sloped, rather than horizontal, allowance has to made for the obstruction of the incident cosmic-ray flux by the sloping surface and for the reduction of the effective cosmic-ray attenuation length perpendicular to the slope (Dunne *et al*, 1999; Fleming *et al*, 1999). Production on inclined surfaces is discussed extensively in Section 3.3.

2.2.4 *In situ* COSMOGENIC ISOTOPE PRODUCTION: TEMPORAL INFLUENCES

2.2.4.1 *Variations in primary cosmic radiation*

Any temporal variation in the primary cosmic-ray flux reaching the Earth may influence the *in situ*-production rate. Although changes in the sources, modes of acceleration and interstellar modulation of the GCRs can lead to temporary changes in their fluxes in the solar system, solar modulation is the dominant source of recorded variations in the GCRs (Reedy *et al*, 1983a). Although changes over time in solar activity also affect SCRs, as their flux is unimportant for *in situ*-production such variations in the SCRs can be ignored. Solar modulation is caused by the interaction of incoming GCRs with dynamic magnetic fields associated with solar-wind plasma and solar-flare particles which results in modulation of the GCRs due to scattering, diffusion and energy losses (Lal and Peters, 1967; Reedy *et al*, 1983a; Raisbeck and Yiou, 1989). The overall result is a reduction in GCRs during periods of increased solar activity, with high latitudes and high altitudes experiencing the most pronounced reductions as the low-energy ($E < 1GeV$ nucleon^{-1}) part of the spectrum is most affected (Reedy *et al*, 1983a). Given that high-energy GCRs particles are not influenced much by solar activity (Reedy *et al*, 1983a) and that these particles are responsible for *in situ*-production, solar modulation averaged over time has little influence on this type of cosmogenic isotope production (Lal and Peters, 1967; Lal, 1991).

2.2.4.2 *Temporal variations in the geomagnetic field*

Temporal variations in the Earth's magnetic field strength have been documented from palaeointensity studies of well dated volcanic rocks, lacustrine and marine sediments. A synthetic curve for the modulations of the past 800 ka has recently been presented (Guyodo and Valet, 1999). Increases in the field strength reduce the abundance of cosmic-rays penetrating the atmosphere thus lowering *in situ*-production rates. Decreases in the field intensity similarly increase production. Studies of both atmospheric and *in situ*-production have shown temporal variations which appear to be related to changes in the dipole moment (eg Kurz *et al*, 1990; Cerling and Craig, 1994b; Plummer *et al*, 1997; Baumgartner *et al*, 1998).

If it can be assumed that a temporal change in the geomagnetic field strength is equivalent to a spatial (latitude) change in the present day geomagnetic field (eg a stronger geomagnetic field in the past at a particular site is equivalent to the present day field experienced by a site with a lower latitude), then the formulation presented by Nishiizumi *et al* (1989, equation 5)

can be used to quantify the effect of past field strength variations (Nishiizumi *et al*, 1989; Lal, 1991). This approach relies on the accuracy of the palaeointensity record which is not well constrained (Raisbeck *et al*, 1994; Gosse *et al*, 1996). Production rates calibration studies have, however, been made using this method (eg Clark *et al*, 1995; Stone *et al*, 1996a).

Changes in the geomagnetic field strength have greatest impact at low latitudes and high altitudes (Kurz *et al*, 1990; Lal, 1991; Clark *et al*; 1995). At latitudes > 60°, the geometric configuration of the geomagnetic field is such that the shielding effect of the field is minimal and thus varying the intensity has little, if any, impact. At sea level, production is derived from high-energy primaries (>> 13 GeV) which are unaffected by the magnetic field (Kurz *et al*, 1990). Although the measured and calculated variations appear high (eg Clark *et al* (1995) calculated a maximum variation of 22 % between time specific production rates compared over the past 137 ka for a site at 30 °), the production rate experienced by a sample is integrated over the entire exposure history of the sample which leads to temporal variations in the geomagnetic field being attenuated with time (Clark *et al*, 1995; Cerling and Craig, 1994a). Such variations are therefore most critical in very young samples, exposure age dating studies and production rate calibration projects.

2.2.4.3 OTHER TEMPORAL INFLUENCES ON PRODUCTION

Given that *in situ*-production varies with altitude, any significant surface uplift or subsidence of the sampling site during cosmic-ray exposure of the sample will affect the production rate. This issue will only be of relevance to samples which have experienced very long exposures (and are therefore only likely to be encountered by studies employing the stable isotopes or ^{10}Be (eg Sarda *et al*, 1993; Bruno *et al*, 1997)) and which are in areas of rapid tectonic deformation or isostatic uplift / subsidence.

Temporary shielding, in the form of soil, snow, ash, water, sand, rock debris, vegetation, etc., which has in the past, perhaps episodically, covered the sampling site will have affected the constancy of the production rate. Accumulations, which have occurred while the sample was within the cosmic-ray attenuation zone, will have acted to increase the depth of the overburden and thereby affected, temporarily, the *in situ*-production rate for the duration of the cover. The exact impact will depend on the mass of the deposit (ie both the depth and density). The shielding by mixed deciduous and evergreen forest cover was calculated by Cerling and Craig (1994b) to be 6 g cm^{-2} and clearly other low density material, such as

vegetation and snow, would require considerable depths to impact significantly on production. Nishiizumi *et al* (1996) provide a formula for correction by temporary shielding. In the field, careful consideration should be taken to avoid sites where there is geomorphic evidence of past burial. The use of two 'paired' isotopes, the production ratio of which is well known, can be useful in highlighting samples with complex exposure and burial histories (Lal, 1991; Gillespie and Bierman, 1995; Bierman *et al*, 1999).

2.2.5 QUANTIFYING *IN SITU* COSMOGENIC ISOTOPE PRODUCTION

Any geomorphologically meaningful interpretation of *in situ*-produced cosmogenic isotope abundance depends, critically, on having precise knowledge of the production rate. The foregoing analysis of the spatial and temporal factors which influence *in situ*-production has shown that each sample will have its own, unique, site-specific production rate. Each site's production rate may be derived either theoretically or be estimated from a calibrated empirically derived rate. Both approaches have problems and the accurate determination of production rates remains the most significant problem facing the technique (Reedy *et al*, 1994; Clark *et al*, 1995; Gosse *et al*, 1996; Santa Fe Workshop Abstracts, 1996).

Accurate theoretical calculation of the production rate for each individual sample is complicated by uncertainties in the fluxes of cosmic-ray particles in the terrestrial surface and a lack of high-energy neutron cross-section data (Lal, 1991; Masarik and Reedy, 1995; Nishiizumi *et al*, 1996; Gosse *et al*, 1996). Despite these problems, several studies have produced theoretical estimates (eg Lal and Peters, 1967; Yokoyama *et al*, 1977; Lal and Arnold, 1985; Masarik and Reedy, 1995). Unlike the preceding theoretical modelling studies, Masarik and Reedy (1995) used a series of numerical simulations previously tested on extraterrestrial production in meteorites and lunar samples to estimate production rates in the atmosphere and spallogenic production rates at the Earth's surface. This approach avoided some of the uncertainties in terrestrial cosmic-ray fluxes and produced spallogenic rates that agree reasonably well with empirically derived rates (Table 2.4).

Table 2.4: Comparison of *in situ*-production rates for various isotopes and target materials all scaled to sea level and high latitude. The list is not exhaustive.

Isotope	Target material	Length of exposure (ka)	Production rate (0 m asl, >60°) atoms g^{-1} a^{-1}	Reference
^{3}**He**	olivine {$(Mg, Fe)_2[SiO_4]$}	7-10	127	Kurz *et al*, 1990
	olivine	18	109	Poreda & Cerling, 1992
	olivine	2 – 18	115	Cerling & Craig, 1994b
	olivine	2 – 7	116	Licciandi *et al*, 1999
^{10}**Be**	quartz {SiO_2}	11	6.0 (5.09 nucleons; 0.94 muons)	Nishiizumi *et al*, 1989
	quartz	2500	6.4	Brown *et al*, 1991
	quartz	21.5	4.74 - 5.10	Clark *et al*, 1995
	quartz	theoretical	5.97 (spallation)	Masarik & Reedy, 1995
	quartz	present	6.0	Nishiizumi *et al*, 1996
	quartz	10	5.75	Kubik *et al*, 1998
	quartz	11.5	4.62	Stone *et al*, 1998a
^{14}**C**	basalt	???	20	Donahue *et al*, 1990
	quartz	???	18	Lal *et al* 1990
	quartz	theoretical	18.6 (spallation)	Masarik & Reedy, 1995
	limestone {$CaCO_3$}	17.5	18	Handwerger *et al*, 1999
^{21}**Ne**	olivine	20	45	Poreda & Cerling, 1992
	quartz	11	21	Niedermann *et al*, 1994.
^{26}**Al**	quartz	11	36.8	Nishiizumi *et al*, 1989
	quartz	2500	41.7	Brown *et al*, 1991
	quartz	21.5	28.9 - 31.1	Clark *et al*, 1995
	quartz	theoretical	36.1 (spallation)	Masarik & Reedy, 1995
	quartz	10	37.4	Kubik *et al*, 1998
^{36}**Cl**	calcium {Ca}	theoretical	64.6 (spallation)	Masarik & Reedy, 1995
	calcium	2-55	73.3 (spallation)	Phillips *et al*, 1996a
	calcium	17.3	48.8 (spallation)	Stone *et al*, 1996a
		17.3	5.3 (muon capture)	Stone *et al*, 1998a
	calcium	15.5	87.2 (combines spallation and muon production)	Swanson & Caffee *in prep*
	potassium {K}	2-55	154 (spallation)	Phillips *et al*, 1996a
	potassium	13	171 (spallation)	Evans *et al*, 1997
			9 (muon capture*)	Evans *et al*, 1997
	potassium	15.5	218 (combines spallation and muon production)	Swanson & Caffee *in prep*
	^{35}Cl	-	composition dependant	Liu *et al*, 1994a, 1995 Phillips *et al*, 1996a

* value assumed by Evans *et al*, 1997.

To avoid the difficulties associated with theoretical calculations, production rates have been derived empirically from the abundance of the particular isotope measured in a substrate that has been irradiated for a known length of time. The exposure of artificial targets, ranging from acids, water baths / beds to aluminium television masts and aeroplane wreckage have yielded rates for an assortment of cosmogenic isotopes (eg Lal *et al*, 1960; Yokoyama *et al*, 1977; Nishiizumi *et al*, 1996). This type of approach suffers from the limited duration of the experimental exposure that, in practice, can extend for a few years only. Such present day rates are atypical and need to be adjusted to reflect the impact of the temporal variations in production outlined above, the exact duration and magnitude of which are not known with sufficient accuracy.

Long-term (~ few ka) natural irradiation sites are therefore regularly used to calculate *in situ*-production rates which are integrated over a specific time interval. These rates will tend to attenuate the temporal variations depending on the length of exposure of the site (Cerling and Craig, 1994a; Kubik *et al*, 1998). Sites chosen for this type of natural calibration study must be accurately and independently dated, normally by radiocarbon or $^{40}Ar - {}^{39}Ar$ dating. Radiocarbon dates must be converted to absolute years (eg Nishiizumi *et al*, 1989; Stone *et al*, 1998a). The site should have a simple history involving instantaneous exposure to radiation to preclude any inherited *in situ* component, no burial by soil, snow etc., and no denudation since exposure (Clark *et al*, 1995). These criteria have meant that glacially polished bedrock and 'young' basalt flows have been preferred as sites for calibration studies (eg Nishiizumi *et al*, 1989; Kurz *et al*, 1990; Brown *et al*, 1991; Phillips *et al*, 1996a; Stone *et al*, 1996a; Evans *et al*, 1997; Licciandi *et al*, 1999), although a landslide has also been used (Kubik *et al*, 1998). The preservation of striations is usually regarded as sufficient evidence of no denudation, but care needs to be exercised with regard to the quality of the independent dating (Clark *et al*, 1995), and the possibility of an *in situ*-produced yield which accumulated prior to the dated exposure event ('inheritance') (Briner and Swanson, 1998; Stone *et al*, 1998b).

Table 2.4 lists some recent estimates of *in situ*-production rates in various target materials, scaled to sea level and high latitude (> 60°) for comparison purposes. The majority of these have been derived from natural sites with varying lengths of exposure. The evident variability is accounted for by the factors that are considered relevant to the site (eg including / excluding possible temporary burial by snow; influence of geomagnetic variations; interpretation of the geomorphology; using mineral separates, etc.), which,

inevitably, entail subjective decisions. With the increasing application of the technique in geomorphology extreme care needs to be taken to understand the criteria used to determine a particular rate and to consider both explicit and implicit uncertainties (Clark *et al*, 1995). The production rate accuracy will improve with more detailed studies in the future (Gosse *et al*, 1996).

2.2.6 Measuring isotopic yields: (accelerator) mass spectrometry

The isotopic yields for both stable isotopes and radioisotopes are determined by mass spectrometry. This analytical technique uses the unique mass-to-charge ratios that each atomic and many molecular species have to separate and measure the relative abundance of the isotopes of an element (Elmore and Phillips, 1987; Finkel and Suter, 1993; Fifield, 1999). The noble gases, ^{3}He and ^{21}Ne, are measured using conventional mass spectrometry (MS) (eg Dickin, 1995). This involves the formation of a positively charged ion from a prepared sample that is then accelerated through an electrostatic potential of a few kV. The ions are separated on the basis of their mass-to-charge ratio and the number of relevant ions is measured in a detector.

Conventional MS is insufficiently sensitive to enable detection of the *in situ*-produced long-lived radioisotopes listed in Table 2.2 which occur at low radioactive : stable abundance ratios of $10^{-10} - 10^{-16}$ (Finkel and Suter, 1993). In addition, isobaric interference (isotopes with the same number of nucleons, but different atomic numbers) is dealt with in conventional MS by reducing the width of the ion beam by closing the slits. This reduces the level of efficiency below that which is essential for the successful measurement of the low abundances of radioisotopes (Elmore and Phillips, 1987; Finkel and Suter, 1993; Fifield, 1999). Counting, which uses only the small number of atoms that decay during the measurement, is not suitable for long-lived radioisotopes, although it was used in the initial study by Davis and Schaeffer (1955) of *in situ*-produced ^{36}Cl from large > 25 g samples of silver chloride.

The development of accelerator mass spectrometry (AMS) (Muller, 1977) not only reduced sample sizes by several orders of magnitude but has meant that long-lived radioisotopes can today be measured routinely with very high levels of accuracy in over 45 AMS facilities world-wide (Fifield, 1999). The underlying principle is the same as conventional MS except negative ions are produced and are accelerated to higher energies (several MV) (Elmore and

Phillips (1987), Finkel and Suter (1993) and Fifield, 1999 provide detailed reviews of AMS). Figure 2.3 provides a schematic representation of a typical accelerator mass spectrometer.

The relevant purified target (see Table 2.2) is loaded into the ion source and bombarded with a beam of Cs^+ ions to produce a negative ion beam from the target (eg Cl^-, BeO^-, etc.). The negative ions are pre-accelerated to 30 – 200 keV after which the mass of interest is selected by the mass analysis magnet. The mass-analysed negative ion beam is then injected into the acceleration tank where it is accelerated towards the positive potential high voltage terminal (2.5 – 20 MV, Kutschera, 1997). A gas or foil electron stripper at the terminal causes electrons to be stripped leaving the ions in a positive multiple-charge state. The now positively charged ions are accelerated back to ground potential with the ions of interest being selected by magnetic analysis. Further selectivity is achieved by the use of an electrostatic analyser or velocity filter which removes any background ions which may have the correct energy to follow the same path as the isotope of interest (Fifield, 1999).

Following this filtration, the relevant isotope is then counted in an ion detector. Isobaric interference is dealt with by a combination of pre-measurement chemical purification of the sample, the stripping procedure, and the use of an ionization chamber for ion detection. Ionization chambers enable the rate of an ion's energy loss, as it slows, to be detected and, since ions with different atomic numbers lose energy at different rates, isobars, such as ^{36}S in the case of ^{36}Cl, can be separated (Finkel and Suter, 1993, Fifield, 1999). The isotopic ratio is obtained by measuring both the more abundant stable isotopes in a Faraday cup and the rare radioisotope in the ion detector. Standards of known isotopic ratios are regularly run for normalization of the AMS and blanks are run to determine the background level of the radioisotope. The isotopic ratios are converted mathematically to an absolute concentration in the sample material (atoms g^{-1}) after subtracting the background component.

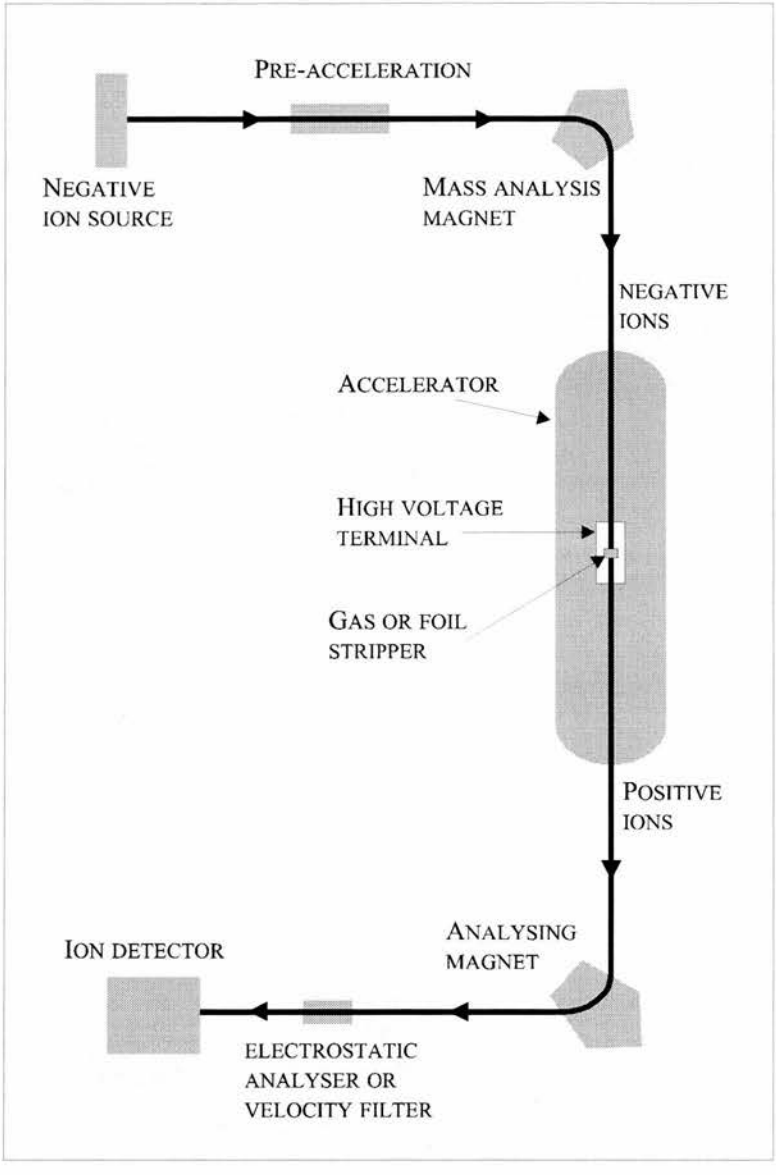

Figure 2.3: Schematic representation of the central components of an accelerator mass spectrometer. After Fifield, 1999.

2.3 Deriving geomorphic data: interpreting cosmogenic isotope abundances

2.3.1 Exposure history: general principles

Material, including rock, accumulates *in situ*-produced cosmogenic isotopes during the time that the sample is exposed to cosmic radiation both at the Earth's surface and in the zone

immediately below the surface that is penetrated by cosmic-rays. The measured abundance of such isotopes, of itself, reveals nothing about the geomorphic history of the samples. Interpretation of this measured abundance into geomorphologically useful information relies on modelling. If the underlying assumptions of the mathematical models do not fit the field evidence, or are shown to be otherwise invalid, any interpretation relying on the model is likely to be flawed. Therefore a thorough understanding of the modelling limitations is critical to the sound use of the technique in geomorphology.

In the case of spallogenic production, where the production rate declines exponentially (Equation 2.2), the concentration of a radionuclide in a sample, N (atoms g^{-1}), is a function of the production rate, the radioactive decay rate, the rate of passage through the attenuation zone and time and is described by the following equation:

$$N = \frac{P_{sp}}{\lambda + \varepsilon\rho/\Lambda_{sp}}\left[1 - \exp^{-\left(\lambda+\varepsilon\rho/\Lambda_{sp}\right)t}\right] \qquad \text{Equation 2.4}$$

where P_{sp} is the spallogenic production rate at the ground surface (atoms g^{-1} a^{-1}), λ is the decay constant of the radioisotope (a^{-1}), ε is the denudation rate (which controls the rate of passage through the attenuation zone) (cm a^{-1}), ρ is the density of the material (g cm^{-3}), Λ_{sp} is the attenuation length for spallogenic production in the material (g cm^{-2}), and t is the period of exposure to cosmic radiation (a). For stable isotopes this equation is simplified by the removal of the decay constant term, λ. Equations similar to 2.4 exist for production by thermal neutron activation and negative muon capture and will be discussed in Chapter 3.

Equation 2.4 is derived assuming that: the spallogenic production rate remains constant throughout t; at the start of the irradiation, t = 0, there were no *in situ*-produced cosmogenic nuclides present in the material; production declines exponentially within the material, with a known attenuation length; the denudation rate, ε, is constant and involves the removal of material in steps with a depth less than the equivalent of one attenuation length (~ 0.5 m of rock, assuming Λ_{sp} = 160 g cm^{-2} in rock) (Nishiizumi *et al*, 1991) and the isotope is produced in a closed system with no loss or contamination during irradiation.

From a geomorphological perspective, Equation 2.4, contains two important terms, t and ε. The determination of t, the period of time during which the material has been irradiated, can, given certain circumstances, yield an 'age' for a landform and therefore this technique provides a new dating method. However, the possibility also exists of using the technique to

yield a denudation rate based on solving Equation 2.4 for ε. Such a value would represent a direct measurement of denudation in comparison to existing, indirect, methods. In the cosmogenic literature, the term ε is usually referred to as the erosion rate, but without definition. This thesis concentrates on *in situ*-production within bedrock and, in this situation, the term ε quantifies the movement of the target through the attenuation zone towards the bedrock surface. Because this movement is caused by the removal of any overburden, without reference to the processes responsible for that removal, the broader definition of denudation rate, provided by Jackson (1997) (Section 1.2) is preferred for the term ε.

2.3.1 EXPOSURE AGE CALCULATIONS

Equation 2.4 can be rearranged to solve for t as follows:

$$t = -\frac{1}{\lambda + \rho\varepsilon/\Lambda_{sp}} \ln\left(1 - \left(\lambda + \rho\varepsilon/\Lambda_{sp}\right)\frac{N}{P_{sp}}\right) \qquad \text{Equation 2.5}$$

This equation may be used to determine a surface exposure age if the denudation rate, ε, can be independently determined, which is only possible in exceptional circumstances. If the denudation rate can be assumed to be zero, then Equations 2.4 and 2.5 simplify respectively to:

$$N = \frac{P_{sp}}{\lambda}\left(1 - \exp^{-\lambda t}\right) \qquad \text{Equation 2.6}$$

$$t = -\frac{1}{\lambda}\ln\left(1 - N\lambda/P_{sp}\right) \qquad \text{Equation 2.7}$$

It is important to stress that t is the length of time that the sample material has been exposed to cosmic radiation and hence is an 'exposure' or 'event' age (Lal, 1995). The limiting assumption that there has been no prior accumulation of *in situ*-produced isotopes, means that such exposure event dating is limited to geomorphological situations where a surface, previously shielded from cosmic radiation, becomes 'instantaneously' exposed to radiation by an event. Landslides, lava flows and glacially polished bedrock (cf. Briner and Swanson, 1998) have each been regarded as constituting such an event (eg Kurz *et al*, 1990; Kubik *et al*, 1998; Zreda *et al*, 1999) as well as being situations in which, in most cases, post-exposure denudation can be adjudged insignificant. Exposure ages are best regarded as minimum ages unless there is incontrovertible evidence of zero surface denudation and compelling evidence

for the surface having been exposed for less than the time required for secular equilibrium (see below) to be achieved.

In Equation 2.7, t is determined from the measured concentration of the radioisotope, the site-specific production rate and the decay constant. The half-life of the cosmogenic isotope therefore provides a constraint on the maximum period of exposure that can be determined. This is illustrated in Figure 2.4.

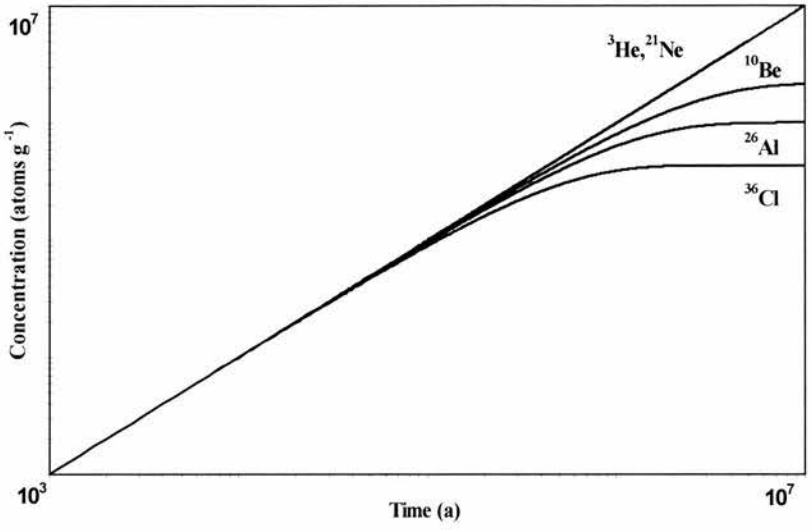

Figure 2.4: Accumulation of spallogenic produced ^{3}He, ^{21}Ne, ^{10}Be, ^{26}Al and ^{36}Cl, assuming, for the purpose of comparison, a unit production rate of 1 atom g^{-1} for all five, and no denudation. Stable isotopes accumulate in a linear fashion while the radioisotopes approach a saturated concentration (secular equilibrium) related to their half-life. Secular equilibrium is usually reached after approximately four half-lives, which represents the maximum age that can be determined by each radioisotope. Stable isotopes, in theory, have no upper limit, but in practice quantitative loss from within the target may provide a limit.

2.3.2 Denudation rate calculations

It is possible to derive the denudation rate, ε, using Equation 2.4 if the age of the surface can be established independently. In practice this is likely to be extremely problematic in denudational environments since many dating techniques, such as radiocarbon, rely on the preservation of a depositional sequence. Figure 2.4 shows that given sufficient time the concentration of a radioisotope reaches secular equilibrium, when the rate of nuclei production is balanced by the rate of radioactive decay (Honda and Arnold, 1967). Denudation is another way in which nuclei can be lost and therefore when a surface denudes at a constant rate secular equilibrium is achieved earlier, as shown in Figure 2.5.

The time required to achieve secular equilibrium depends on both the rate of decay of the isotope and the rate of denudation, with the period being shorter for higher, constant, denudation rates. Lal (1986, 1991, 1995) defined this time, which he termed the apparent surface exposure age (T_{eff}), as being $>> 1 / \lambda + (\varepsilon\rho/\Lambda_{sp})$. Where a surface has been exposed for such a sufficient period of time and the rate of denudation during that period has been in 'steady-state' (meaning, in this context, the continuous removal of thickness' smaller than Λ_{sp} / ρ, Nishiizumi *et al*, 1991), the denudation rate can be derived as follows:

$$\varepsilon = \frac{\Lambda_{sp}}{\rho}\left(\frac{P_{sp}}{N} - \lambda\right) \qquad \text{Equation 2.8}$$

It is important to realise that the denudation rate derived from this equation is a modelled rate and therefore the model assumptions, specifically the achievement of secular equilibrium and a 'steady-state' denudation rate have to be applicable to the sampling site. In the case of studies using a single isotope, secular equilibrium has to be assumed. The assumption of secular equilibrium may be tested by using two or more radionuclides of different half-lives. If secular equilibrium has been achieved, the value in parenthesis in Equation 2.8 should be invariant for the different isotopes (Lal, 1991).

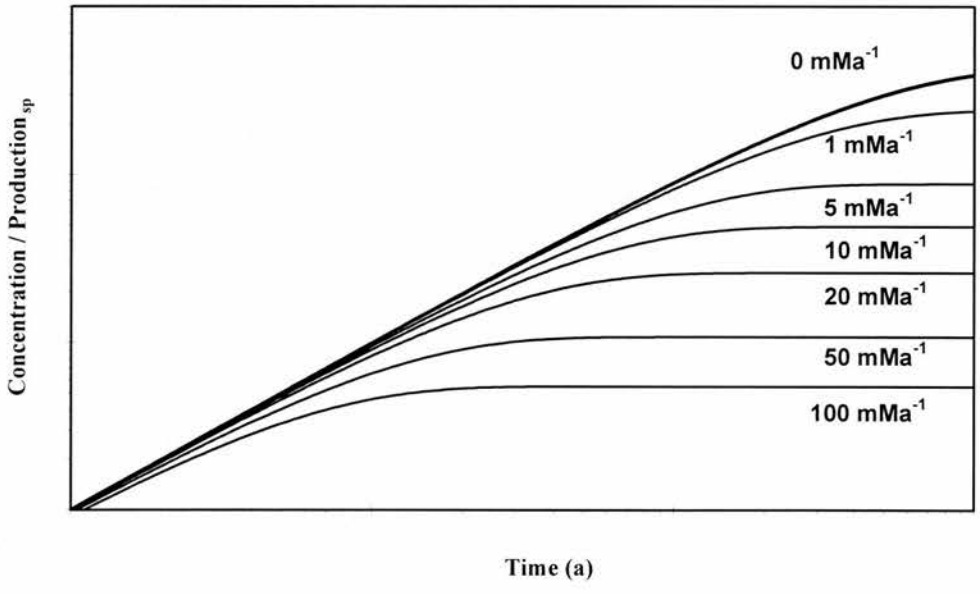

Figure 2.5: The general effect of different denudation rates on the time required to achieve secular equilibrium for a radioisotope produced by spallation. As stable isotopes do not decay, without denudation they do not achieve an equilibrium. When denudation is introduced, stable isotopes also reach a saturation concentration that is determined by the denudation rate. The absolute values on the abscissa and ordinate axes are isotope dependent.

If 'steady-state' denudation is thought to have been ongoing at the site, the modelled denudation rate is regarded as the mean denudation rate applicable over the minimum time, T_{eff}. No maximum period for the rate is imposed by the model equation. However, in practice, denudation is more likely to have been discontinuous and at a non-uniform rate of less than the attenuation length, in which case the modelled rate represents an upper limit on the average rate applicable over at least T_{eff} (Lal, 1991). Lal (1991) proposed that, in this situation, the lower limit would be determined by assuming the removal of 0.5 m of rock one mean life ($1 / \lambda$) ago, corresponding to a time averaged lower limit of ~ 0.2 m Ma^{-1}, ~ 0.5 m Ma^{-1}, and ~ 1.1 m Ma^{-1}, for studies using solely ^{10}Be, ^{26}Al or ^{36}Cl, respectively. Lal's view has been challenged by Small *et al* (1997), who modelled the impact of various episodic denudation events with thickness' of $< \Lambda / \rho$ on the isotopic concentration. They concluded that the modelled denudation rate may be either a maximum, or a minimum, depending on when the episodic event occurs, and that for episodic removal of depths $\geq$ ~ 0.25 m variability around the actual mean denudation rate is > 20 %. Small *et al* (1997) have proposed that a more accurate measure of the actual mean denudation rate, in situations of episodic denudation, is arrived at by taking the mean value of several measured steady-state denudation rates from an area. Averaging effectively takes account of the likelihood that episodic events are non-synchronous between sampling sites, thereby reducing the error. If the denudation involves removal of blocks $> \Lambda / \rho$, the model in Equation 2.8 is inapplicable and the data should be interpreted as a modelled surface exposure age (Fleming *et al*, 1999).

Where the substrate permits, studies involving two 'paired' isotopes (eg ^{10}Be and ^{26}Al (Nishiizumi *et al*, 1989); ^{10}Be and ^{36}Cl (Phillips *et al*, 1997) or ^{21}Ne and ^{10}Be (Cockburn, 1998)) may enable the assumption of a 'steady-state' denudation rate to be tested (Klein *et al*, 1986; Nishiizumi *et al*, 1989, 1991; Lal, 1991; Gillespie and Bierman, 1995). Plotting the log of the concentration of one nuclide against its ratio with another nuclide with a different half-life for various constant denudation rates produces a steady-state denudation island. If denudation is indeed in a 'steady-state' all measurements will fall within the island. Points plotting below the island disclose that the sample has experienced a more complex irradiation history suggesting at least one phase of burial and re-exposure. Mathematical modelling may be capable of distinguishing between the different likely geomorphic scenarios that may explain this irradiation history. Small *et al*, (1997) have shown that for modelled rates of denudation > 1 m Ma^{-1}, the 'steady-state' denudation assumption cannot be tested using paired isotopes as samples which have experienced episodic denudation (removal of blocks of thickness $\approx \Lambda / \rho$) still plot within the island. Stone *et al* (1998a) have

suggested that the assumption of steady-state denudation and complex irradiation may be checked by comparing surface and deeper samples containing isotopes, such as ^{36}Cl, which are produced by both spallation and muon reactions which exhibit differences in sensitivity to denudation.

The use of paired spallogenic isotopes of different half-lives has been suggested as a means of determining both the exposure age and denudation rate for an eroding surface (Nishiizumi *et al*, 1986; Lal 1991; Gillespie and Bierman, 1995). This, however, requires very precise isotopic analyses to detect the small change in the production ratio due to denudation (Gillespie and Bierman, 1995). Using a single isotope that is produced by different production mechanisms with different depth-dependent profiles, and comparing concentrations in surface and subsurface samples, has also been put forward as a means of determining both an exposure age and denudation rate (Dep *et al*, 1994a; Liu *et al*, 1994a; Stone *et al*, 1998a).

2.3.3 Examples of geomorphic applications

The usefulness of the cosmogenic isotope 'tool set' depends on our ability to interpret the measured abundance correctly in terms of the geomorphic history of the sampling site. Some examples of the diverse range of geomorphic situations in which the 'tool set' has been employed over the past 3 years are highlighted in Table 2.1. In these and earlier studies, the interpretation of the isotopic yield from bedrock samples has been based on the surface exposure and denudation rate models outlined above (for different type of model for sediments see, for example, Bierman and Steig, 1996 or Phillips *et al*, 1998). Despite the intrinsic limitation of the surface exposure model, Equation 2.7, that the denudation rate has to be independently determined, surface exposure dating has been the main application of the technique. Although many other dating techniques exist, including cosmic-ray derived radiocarbon dating, the allure of this new technique is its ability to date rock surfaces directly, which has proved particularly useful in glacial geomorphology.

2.3.3.1 Glacial geomorphology

Glacial chronology studies have used samples collected from glacially polished bedrock, boulders on moraines and glacial erratics (eg Nishiizumi *et al*, 1989; Brown *et al*, 1991; Brook *et al*, 1993, 1995a, 1995b; Gosse *et al*, 1995a, 1995b; Ivy-Ochs *et al*, 1995; Duk-Rodkin *et al*, 1996; Phillips *et al*, 1996b; Bruno *et al*, 1997; Jackson *et al*, 1997; Phillips *et*

al, 1997; Steig *et al*, 1998; Bierman *et al*, 1999; Zreda *et al*, 1999). Given the dominant view of the magnitude of the erosive power of glaciation, glacially scoured bedrock has been regarded as an instantaneously exposed surface that has no prior accumulation of *in situ*-produced isotopes. Caution is required, however, following the study by Briner and Swanson (1998) which identified previously accumulated cosmogenic isotopes on the stoss side of glacially smoothed bedrock implying insufficient removal of bedrock to reset the concentration, N, to zero at $t = 0$. The presence of striations, chattermarks, etc. have been regarded as evidence for minimal post-exposure surface denudation (eg Nishiizumi *et al*, 1989; Brook *et al*, 1995a, 1995b; Gosse *et al*, 1995b), and, although these erosive features can be preserved for considerable periods (eg > 550 ka, Bierman *et al*, 1999) such preservation does not preclude the possibility of post-exposure burial and subsequent re-exposure (Bierman, 1994; Bierman *et al*, 1999).

Studies using samples collected from boulders, whether as glacial erratics (eg Jackson *et al*, 1997; Zreda *et al*, 1999) or from moraines (eg Ivy-Ochs *et al*, 1995; Brook *et al*, 1995a, 1995b; Phillips *et al*, 1997) have faced additional difficulties. Each boulder will have its own emplacement history, which includes its exposure prior to detachment from the parent bedrock, possible burial and re-exposure prior to transportation, exposure during transportation, and post-depositional burial and / or surface denudation. Such histories have to be de-ciphered from the field evidence and accounted for in the subsequent interpretation of the measured abundance. Similar problems have been encountered in studies of boulders and smaller clasts in fluvial settings (eg Cerling *et al*, 1994; Liu *et al*, 1996; Seidl *et al*, 1997; Repka *et al*, 1997; Hancock *et al*, 1999).

Following the study by Phillips *et al* (1990), great care has to be taken when sampling from moraines. The cosmogenic isotope ages derived by Phillips *et al* (1990) were in disagreement with prior age estimates based on morphological and stratigraphical evidence. Bierman and Gillespie (1991), Hallet and Putkonen (1994) and Zreda *et al* (1994) have demonstrated that post-depositional denudational processes, involving both the degradation of the moraine surface and denudation of the boulders thereon, would lead to boulders yielding ages different to the age of formation of the moraine. Such work highlights the need to use multiple samples from individual deposits (Brook *et al*, 1993).

Vertical sampling patterns have enabled cosmogenic isotope yields to be used to differentiate between glaciations and to establish periglacial weathering limits. Brook *et al* (1996), using samples from a vertical transect established a significant difference in ages between summit

and valley samples and used this as corroboration of an existing trimline and support for the presence of nunataks during the last glaciation in western Norway. Similar circumstances are thought to have prevailed in northwest Scotland (Stone *et al*, 1998b). Bierman *et al* (1999) have shown that studies using paired isotopes can highlight the long-lived nature of summit top tors in glaciated regions which may survive burial beneath cold-based ice and subsequent re-exposure.

2.3.3.2 *Fluvial geomorphology*

Studies applying cosmogenic isotope analysis to fluvial geomorphology have also, to date, used the surface exposure dating model. Samples collected from exposed fluvially scoured bedrock have been used to date Quaternary mega-floods (Cerling, 1990; Cerling *et al*, 1994), and to determine fluvial incision rates in the northwest Himalayas (Burbank *et al*, 1996; Leland *et al*, 1998). Burbank *et al* (1996) and Leland *et al* (1998) used ^{10}Be and ^{26}Al in samples to date abandoned strath terraces of the Indus and combined these ages with the elevation of the terraces above the present river channel to estimate incision rates of 9 – 12 km Ma^{-1}. The Burbank *et al* (1996) study also demonstrated how cosmogenic isotope analysis can be usefully coupled with other data, in this case regional scale denudation date from fission track analysis and a digital elevation model, to interpret landscape evolution.

Most studies of fluvial landforms have used samples collected from boulders (eg Cerling *et al*, 1994) or smaller clasts (eg Repka *et al*, 1997; Phillips *et al*, 1997; Hancock *et al*, 1999). Of the studies using boulders, Cerling *et al* (1994) attributed discrepancies between boulder and bedrock derived ages as being due to pre-emplacement inherited exposure of the boulders, while Phillips *et al* (1997) derived similar ages for flood derived boulders as for moraines and ruled out inheritance. Seidl *et al* (1997), using multiple isotopes in a combination of boulder and bedrock samples to investigate river long profile development and knickpoint migration, ruled out inheritance from prior exposure and transportation on morphological grounds, although this might have partly explained the inconsitencies in their results.

The smaller the material the greater the problem of inheritance from prior exposure at the source, during transportation and subsequent re-working. This issue of inheritance has to be considered very carefully when dating alluvial surfaces. Liu *et al* (1996) used radiocarbon dates to determine the proportion of ^{36}Cl inherited from repeated cycles of alluviation, re-working of higher level surfaces, incision and deposition on a piedmont surface. Repka *et al*

(1997) and Hancock *et al* (1999) used modified versions of an amalgamation technique, first suggested by Anderson *et al* (1996), to explicitly determine the inherited component of clasts in alluvium and enable river terraces to be dated. Phillips *et al* (1998), also expanding on the work of Anderson *et al* (1996), showed that post-depositional burial and bioturbation processes create distinct cosmogenic nuclide depth profiles and that mathematical models of these profiles can assist in interpreting more accurate surface exposure ages for alluvial surfaces. Granger *et al* (1997) avoided the problems of re-working by using a model based on the differential decay rates of cosmogenic ^{10}Be and ^{26}Al in samples buried deeper than the radionuclide production zone in abandoned river caves to constrain fluvial incision rates.

2.3.3.3 *Environmental hazards*

Ritz *et al* (1995), Siame *et al* (1995) and Brown *et al* (1998a) used ^{10}Be exposure ages for small boulders on offset alluvial fans and the measured amount of offset to derive slip rates ranging from 1 – 2 mm a^{-1} for faults in Central Asia and South America. Again, sampling from boulders was problematic, with Ritz *et al* (1995) attributing unexpected consistency in exposure ages to (unmeasured) post-emplacement denudation of boulder surfaces, which given ages of ~ 80 ka, would require 'steady-state' denudation of > 10 m Ma^{-1}. Brown *et al* (1998a) measured concentration in samples collected from present day stream beds to quantify accumulations due to inheritance from source exposure and subsequent transportation. The amalgamation technique suggested by Anderson *et al* (1996) was rejected on the basis that prior exposure scatter had been measured and that the remaining scatter must be due to post-depositional processes (burial, denudation, etc.), which unlike pre-depositional processes, would tend to decrease isotopic accumulations. Using mean values would therefore, in this situation, underestimate surface exposure ages.

Earthquake recurrence intervals have been estimated from isotopic abundances measured in samples collected from boulders in debris flow deposits (Bierman *et al*, 1995), perched boulders in seismically active terrains (Bell *et al*, 1998) and bedrock fault scarps (Zreda and Noller, 1998). Holocene age landslides (Ballantyne *et al*, 1998) and debris flows (Cerling *et al*, 1999) have also been successfully measured. The Bierman *et al* (1995), Zreda and Noller (1998) and Cerling *et al*, (1999) studies have all shown that, given a site with a sufficiently high production rate, late Holocene surfaces exposure ages may be derived.

2.3.3.4 LANDFORM AND LANDSCAPE EVOLUTION

The technique has been applied to the evolution of specific landforms in a limited number of studies. Stone *et al* (1996b) calculated the surface exposure age of the main rock platform in western Scotland which, when combined with isostatic modelling, suggested that formation had occurred during the Loch Lomond Stadial. Bedrock channel long profile evolution and knickpoint migration were investigated by Seidl *et al* (1997). Sub-tropical and equatorial surface armouring provided by desert pavements and duricrusts have been investigated. Wells *et al* (1995) and Shepard *et al* (1995) independently measured exposure ages of desert pavement clasts to assess competing theories of desert pavement development. Both found that the clast ages were indistinguishable from exposure ages of parent bedrock and concluded that the clasts forming the pavement had been continuously exposed, supporting the accretionary theory. Liu *et al* (1994b) used ^{36}Cl to investigate soil carbonate ages in calcrete, while laterite dynamics, and specifically the origin of sub-surface cobbles (stone-lines), were studied by Braucher *et al* (1998a, 1998b, 1999). These cobbles were shown by analysis of *in situ*-produced ^{10}Be to be emplaced by slope and fluvial processes as well as sub-surface lateral creep from intact quartz veins (calculated displacement rates of 53 – 89 m Ma^{-1}).

Despite early suggestions (Lal, 1986; Nishiizumi *et al*, 1986; Kurz,1986b, Nishiizumi *et al*, 1991), the potential for deriving denudation rates, and thus quantifying an important aspect of landscape development, is only just beginning to be fulfilled. Several studies have derived denudation rates by using the 'steady-state' model to interpret measured concentrations from bedrock surfaces, but as can be seen from Table 2.5, the majority has relied on ≤ 10 samples. Whilst these studies clearly demonstrate that denudation data may be obtained using this technique, little useful information on landscape development may be had from single samples, particularly given the site-specific nature of the data. Where multiple samples have been collected, several of the studies have provided thoughtful consideration of the implications of the modelled rates for landscape development. Stone *et al* (1994) considered how their modelled rates for karst landscapes related to climatic settings. Bierman and Turner (1995) and Cockburn *et al* (1999) discussed the implications of modelled rates of lowering of bornhardt surfaces for the preservation of ancient landsurfaces. Small *et al*, (1997) and Bierman *et al* (1999) discussed the development of summit-top tors in previously glaciated terrain. Fleming *et al* (1999) and Summerfield *et al* (1999a, 1999b) explored the significance of modelled denudation rates for the long-term development of passive margin landscapes, the latter study contributing to the debate on ice-sheet stability in Antarctica.

These studies have illustrated that, with a good sampling strategy and sufficient samples, meaningful modelled denudation rates may be used to tackle long-standing issues in landscape development.

Table 2.5: Published denudation estimates derived from *in situ*-produced cosmogenic isotope analysis of exposed bedrock surfaces.

Study	Field Location	Lithology	Number of samples used to determine denudation rate	Denudation rate (m Ma^{-1})
Nishiizumi *et al*, 1991	Antarctica	sandstone	21	< 0.1 – 2.53
Nishiizumi *et al*, 1993	Himalayas	granodiorite	2	14.0 – 56.0
	Wyoming	granodiorite	1	48.0
	Colorado	granite	1	8.2
Albrecht *et al*, 1993	New Mexico	volcanic tuff	6	0.5 – 11.0
Stone *et al*, 1994	Australia	limestone	8	4.5 – 29.0
	Papua New Guinea	limestone	1	184.0
Bierman & Turner, 1995	Australia	granite	6	0.6 – 4.9
Brown et al, 1995b	Puerto Rico	quartz	1	25.0
Shepard *et al*, 1995	Nevada	basalt	1	3.5
Liu *et al*, 1996	Arizona	volcanic	1	20.0
Small *et al*, 1997	Western USA	granite / gneiss / schist	19	2.1 – 18.6
Braucher *et al*, 1998b	Brazil	quartz	2	2.5 – 9.0
Bierman *et al*, 1999	Baffin Island	gneiss	7	0.5 – 1.1
Cockburn *et al*, 1999	Namibia	granite	6	2.7 – 8.0
Heimsath *et al*, 1999	California	chert / greenstone / greywacke	3	15.0 – 39.0
Fleming *et al*, 1999	SE Africa	basalt	6	1.4 – 62.3
Summerfield *et al*, 1999a, 1999b	Antarctica	sandstone / granite	8	< 1.0

Applying the denudation model to bedrock buried beneath a soil horizon, Heimsath *et al* (1997, 1999) have determined soil production rates which they found to decrease exponentially with increasing soil depth. This they have applied to study morphological equilibrium in small river catchments. The mean denudation rate of such catchments has been suggested to be quantifiable from the measurable concentration of *in situ*-produced isotopes in river sediment (Brown *et al*, 1995b; Bierman and Steig, 1996; Bierman *et al*, 1998). The pilot study by Brown *et al* (1995b) has been followed by two further studies (Granger *et al*, 1996; Brown *et al*, 1998b) which have derived mean denudation rates from the models suggested by the earlier authors. Such models are, at present, limited to higher order catchments by virtue of their limiting conditions (eg uniformity of sampling material within basin, short transportation and storage periods, etc.).

2.4 CONCLUSIONS

This chapter has introduced the 'set of tools' provided by the *in situ*-produced cosmogenic isotope analysis technique. The usefulness of the toolkit to geomorphology depends on our ability to interpret correctly the measured concentration of particular isotopes in terms of the irradiation experienced by the sample in the zone, on and immediately below the Earth's surface, that is penetrated by cosmic radiation. This ability is currently limited by technical issues, particularly those related to quantifying time-averaged production rates, and by the underlying assumptions of the interpretive models, which require studies to be constrained by the geomorphic evidence. This, in turn, limits the geomorphological problems that can be tackled. Despite these limitations, studies to date have shown the potential of the technique to derive quantitative measurements from bedrock surfaces over timescales of $10^3 - 10^6$ a which have not hitherto been possible. In particular, as Bierman (1994) and Bierman and Gillespie (1995) pointed out, modelled denudation rates are geomorphically useful, despite the uncertainties in production rate estimates, as there are relatively few determinations of bedrock denudation rates, and no alternative means of obtaining such data. In time production rates will become further refined (eg Gosse *et al*, 1996) and advances in the interpretive models will further address the challenge presented to geomorphologists by Nishiizumi *et al* (1993, p424) "to rethink and create innovative tests of some long-held assumptions about how landscapes evolve".

CHAPTER 3: *IN SITU-PRODUCED* CHLORINE-36: PRODUCTION SYSTEMATICS AND INTERPRETATION OF MEASURED ABUNDANCES

3.1 INTRODUCTION

Chlorine-36 (^{36}Cl), produced both in the atmosphere and within the topmost few metres of the Earth's surface, is one of the most commonly utilised cosmogenic isotopes in the Earth and environmental sciences. Applications, to date, (Table 3.1), include the study of groundwater evolution, dating of sedimentary deposits and rock, and estimating denudation rates in karst landscapes (Phillips *et al*, 1995; Phillips *et al*, 1997; Zreda *et al*, 1999; Stone *et al*, 1994). Davis and Schaeffer (1955) highlighted the potential applicability of atmospherically produced ^{36}Cl to geoscientific problems, and the early studies used this meteoric ^{36}Cl to study, mainly, groundwater evolution. With the advent in the late 1970's of AMS (Elmore and Phillips, 1987; Finkel and Suter, 1993), detection limits were reduced by several orders of magnitude allowing quantification of the relatively small yields found in surface samples. This enabled *in situ*-produced cosmogenic ^{36}Cl to be applied, almost exclusively as a surface exposure dating tool, to a wide range of geomorphological problems (Table 3.1). This thesis is concerned with the application of such *in situ*-production in whole rock basalt to study denudation rates.

Although many of the comments in the preceding chapter relating to the production and application of *in situ* cosmogenic isotopes apply equally to *in situ*-produced ^{36}Cl, the multiple production pathways of ^{36}Cl make the determination of modelled denudation rates considerably more complex than for isotopes produced solely by spallation. The first section of this chapter therefore looks at the different mechanisms responsible for the *in situ*-production of ^{36}Cl in basalt, the rates of such production, and the influence of depth within the rock column on production. The second section considers the impact of sloping surfaces on ^{36}Cl production, particularly important for the samples used in this project that were collected from free face settings. The final section discusses the interpretation of the measured abundance of ^{36}Cl as a modelled denudation rate. Analytical procedures, including the measurement of ^{36}Cl, are covered in the following chapter.

Table 3.1: Examples of the application of terrestrially produced cosmogenic ^{36}Cl to Earth science problems. Extra-terrestrially produced ^{36}Cl has been used, for example, in the study of meteorites and lunar samples (eg. Nishiizumi *et al*, 1984).

Project type	**^{36}Cl production site**	**Application**	**Material sampled**	**Example reference**
Surface exposure dating	Surface	Dating meteor impact crater	boulders	Phillips *et al*, 1991.
	Surface	Dating basalt flows	bedrock	Zreda *et al*, 1993.
	Surface	Glacial chronology	boulders	Zreda & Phillips, 1995.
	Surface	Pediment chronology	boulders / gravel / bedrock	Liu *et al*, 1996.
	Surface	Dating shoreline formation	bedrock	Stone *et al*, 1996b.
	Surface	Glacial erratics chronology	boulders	Jackson *et al*, 1997.
	Surface	Landslide chronology	bedrock	Ballantyne *et al*, 1998.
	Surface	Dating glacial / fluvial deposits	sediment	Phillips *et al*, 1997.
	Surface	Dating periglacial weathering limits	bedrock	Stone *et al*, 1998b.
	Surface	Glacial chronology	boulders / bedrock	Zreda *et al*, 1999
Sediment accumulation rates	Surface	Soil carbonate accumulation	soil	Liu *et al*, 1994b.
Denudation rate	Surface	Karst landscapes	Bedrock	Stone *et al*, 1994.
	Surface	Glacial denudation	Bedrock	Briner & Swanson, 1998.
	Surface	Passive margin landscape denudation rates	Bedrock	Fleming *et al*, 1999.
Hydrogeological	Atmospheric	Dating groundwater	Groundwater	Phillips *et al*, 1995.
	Atmospheric	Tracing groundwater	groundwater	Fabryka-Martin, *et al*, 1987.
Dating saline lakes	Atmospheric	Saline lake chronology	water	Jannick *et al*, 1991.
Dating palaeontological samples	Atmospheric	Dating teeth and bones	teeth, bones	Cornett *et al*, 1997.

3.2 MECHANISMS AND RATES OF *IN SITU*-PRODUCTION OF ^{36}Cl

Chlorine-36 is produced *in situ* at the Earth's surface by various nuclear reactions (Table 3.2). In whole rock, including basalt, the vast majority of ^{36}Cl is produced *in situ* by three principal reactions - nuclide spallation, neutron activation and negative muon capture – involving Ca, K and ^{35}Cl as the targets (Bentley *et al*, 1986; Fabryka-Martin, 1988; Bierman, 1993; Stone *et al*, 1996a, 1998a). Although the mechanisms listed in the second half of Table 3.2 are thermodynamically possible, they contribute insignificantly to the total *in situ* cosmogenic ^{36}Cl production and are therefore not considered further (Fabryka-Martin, 1988). The range of target elements has meant that studies using ^{36}Cl have tended to make use of whole rock samples in preference to mineral separates, although quartz and Ca - / K - feldspar separates have been used in production rate calibration studies (Dep *et al*, 1994a; Stone *et al*, 1996a, 1998a; Evans *et al*, 1997).

3.2.2 NUCLIDE SPALLATION

Spallation reactions, involving the collision of high-energy secondary cosmic-rays with Ca and K isotopes (^{40}Ca and ^{39}K), account for ~ 85 - 95 % of the total *in situ* ^{36}Cl production in the basalts used in this study. This is due to the combination of the abundance of these two elements (Appendix 3) and their relatively high surface production rates.

Several studies have empirically derived surface production rates for spallation of ^{40}Ca and ^{39}K (Table 2.4). Masarik and Reedy (1995) adopted a theoretical approach and, using numerical simulations, calculated a spallation production rate for Ca of 46.2 atoms $(g\ CaO)^{-1}$ a^{-1} with an estimated uncertainty of ~ 20 %, for sea level and no geomagnetic cutoff (ie high latitude). This converts to 64.6 atoms $(g\ Ca)^{-1}$ a^{-1} for sea level and > 60° latitude. Stone *et al* (1996a), adopting an empirical methodology, and using Ca-feldspar mineral separates, calculated a Ca spallation rate of 48.8 ± 3.4 atoms $(g\ Ca)^{-1}$ a^{-1} for sea level and high latitude. Another field based calibration study (Phillips *et al*, 1996a) calculated a rate of 73.3 ± 4.9 atoms $(g\ Ca)^{-1}$ a^{-1} for Ca spallation also for sea level and high latitude. This rate supersedes that group's earlier rate given in Zreda *et al* (1991). Yet another empirical study, Swanson and Caffee (in prep.), yields an even higher rate of 87.2 ± 6.8 atoms $(g\ Ca)^{-1}$ a^{-1} for combined spallation and muon production from Ca. If the muon contribution is taken to be 5.3 atoms $(g\ Ca)^{-1}$ (per Stone *et al*, 1998a), the Swanson and Caffee (in prep.) figure converts to a Ca spallation rate of 81.9 atoms $(g\ Ca)^{-1}$ a^{-1} for sea level and high latitude.

Table 3.2: *In situ*-production mechanisms for ^{36}Cl up to 2m below the Earth's surface. Compiled from information in Fabryka-Martin, 1988 and Zreda *et al*, 1991.

Relative importance in surface and near (< -2m) surface environment	**Reaction type**	**Target element(s)**	**Reaction notation #**
Major Production Mechanisms	Spallation	Ca, K,	^{40}Ca (n, 2n3p) ^{36}Cl; ^{39}K (n, 2n2p) ^{36}Cl
	Thermal neutron capture	^{35}Cl, ^{39}K	^{35}Cl (n, γ) ^{36}Cl; ^{39}K (n, α) ^{36}Cl
	Negative muon capture	^{40}Ca, ^{39}K	^{40}Ca (μ^-, α) ^{36}Cl; ^{40}Ca (μ^-,2p2n) ^{36}Cl; ^{39}K (μ^-, p2n) ^{36}Cl
Negligible Production Mechanisms*	Spallation	Fe, Ti	-
	Alpha capture	^{33}S	^{33}S (α, p) ^{36}Cl
	Photonuclear reaction	^{37}Cl	^{37}Cl (γ, n) ^{36}Cl
	Negative muon capture	^{40}K, ^{36}Ar, ^{38}Ar, ^{40}Ar	^{40}K (μ^-, p3n) ^{36}Cl; ^{36}Ar (μ^-, ν_μ) ^{36}Cl; ^{38}Ar (μ^-, 2n) ^{36}Cl; ^{40}Ar (μ^-, 4n) ^{36}Cl
	Thermal neutron capture	^{36}Ar	^{36}Ar (n, p) ^{36}Cl

These are written in the standard nuclear reaction terminology shorthand in the form X (a b) Y, where X and Y are, respectively, the target and product nuclei, and a and b are, respectively, the incident and emitted particles (α = alpha particle; γ = gamma ray; μ- = negative muon; ν_μ = neutrino; n = neutron, and p = proton) (Fabryka-Martin, 1988).

* Although thermodynamically possible, these reactions have either not yet been evaluated, in the case of spallation of Fe and Ti, or are thought to contribute significantly less than 5% of total production in common rock types (Fabryka-Martin, 1988; Zreda *et al*, 1990, 1991).

The reasons for the discrepancies in the field based calibrated rates of Stone *et al* (1996a), Phillips *et al* (1996a) and Swanson and Caffee (in prep.) are unclear. Various factors may, however, play a part. Firstly, the calibrated rate determined using whole rock samples (Phillips *et al,* 1996a) may not be as accurate as that derived from mineral separates (Stone *et al* 1996a). The use of mineral separates enables ^{36}Cl production by Ca spallation to be more readily isolated. Stone *et al* (1996a) used Ca-feldspars which had Ca / K and Ca / Cl ratios 4 and 40 times higher, respectively, than they were in the parent whole rock. This means that the Ca spallation calibration using these separates was insensitive to the other ^{36}Cl production mechanisms involving K and ^{35}Cl (Table 3.2). If whole rock samples are used for calibration, then erroneously underestimating the contribution from one production mechanism will, correspondingly, over emphasise another mechanism's contribution. For

example, Stone *et al* (1996a) were able to show that the re-calibration of the K spallation rate (increase of ~ 77 %) in the whole rock samples used by Zreda *et al* (1991) led to an automatic corresponding reduction in the Ca spallation contribution of ~ 12 – 16 %. Secondly, as the field based calibration cannot be more reliable that the chronology upon which it is based, errors in the independent age constraints may be partly responsible. Both the Stone *et al* (1996a) and Swanson and Caffee (in prep.) calibration studies rely on samples from single locations which appear to have very sound independent dating controls. The Phillips *et al* (1996a) study used samples from 8 locations and, although it is less sensitive to erroneous ages at one site, it may, perhaps, be more likely to have encountered sites with erroneous dates. Thirdly, the use of multiple locations (Phillips *et al*, 1996a) requires the application of the altitude / latitude scaling factors in the calibration calculation. Therefore any uncertainties in these scaling factors are also likely to affect the calibrated figure. Lastly, although the exact details of the materials used and the underlying measurements / calculations applied in the Swanson and Caffee (in prep.) study are not yet available to the author, that calibration is based on samples from a site at sea level. At sea level ^{36}Cl production from muon reactions with Ca is more significant that at higher altitudes (Figure 2.1) and, hence, more of the measured ^{36}Cl abundance in those samples may be attributable to muons than is thought, which would reduce the calibrated Ca spallation rate. Stone *et al* (1996a) chose a high altitude site (~ 1500 m) to reduce the impact of muon reactions involving ^{40}Ca on their Ca spallation calibration.

The comments in the foregoing paragraph are only suggestive of possible reasons for the differences in the calibrated rates produced by these studies. Until the exact reasons for the differences become clear and are resolved, most probably by further calibration studies, each application of the analysis of *in situ*-produced cosmogenic ^{36}Cl has to adopt the Ca spallation rate which it regards as most suitable. In this project the rate adopted is that of Stone *et al* (1996a), suitably scaled for the sample locations in southern Africa. This calibrated rate is preferred because:- (1) the use by Stone *et al* (1996a) of mineral separates may, for the reasons outlined above, make this calibration more reliable; (2) both the Stone *et al* (1996a) calibration site and the sites in this study are mid-latitude, which reduces the impact of any potential scaling factor error; and (3) similar laboratory and measurement procedures were used for the calibration study and this project. Use of the higher rates of Phillips *et al* (1996a) or Swanson and Caffee (in prep.) would systematically increase the modelled denudation rates by ~ 25 – 35 %, and ~ 30 – 50 % respectively (the exact impact being dependent on both the Ca content and the ratio of Ca / K in the particular sample). Appendix

2 provides a comparison of denudation rates derived for a few of this study's samples (with various Ca and K contents) using the different calibrated Ca spallation rates of Stone *et al* (1996a), Phillips *et al* (1996a) and Swanson and Caffee (in prep.). Whilst such large, potential, increases may cause problems for surface exposure dating studies using *in situ*-produced cosmogenic ^{36}Cl, they have little impact on the overall geomorphic conclusions of this project.

Although no theoretical calculations have been made of the ^{36}Cl production rate due to spallation of K, three empirical studies have calibrated this rate. Phillips *et al* (1996a) calculated a sea level and high latitude rate of 154 ± 10 atoms $(g\ K)^{-1}\ a^{-1}$. Evans *et al* (1997), using K-feldspar mineral separates with low chloride content, derived a rate of 171 ± 15 atoms $(g\ K)^{-1}\ a^{-1}$ for sea level and high latitude, based on samples from sites in the Sierra Nevada, California and Scotland. This calibrated spallation rate was based on an assumed negative muon capture contribution of 9 ± 2 atoms $(g\ K)^{-1}\ a^{-1}$. Swanson and Caffee (in prep.) determined a higher rate of 209 ± 23 atoms $(g\ K)^{-1}\ a^{-1}$ for sea level and high latitude based on samples from Washington State. The reasons for the discrepancies between these calibrated rates are again unclear and will require further data to resolve. For the reasons outlined above, the rate of Evans *et al* (1997) has been preferred for this thesis. Use of the Phillips *et al* (1996a) rate would lower the modelled denudation rates by ~ 1 – 5 %, while calculations based on the Swanson and Caffee (in prep.) rate, would increase the denudation rates by ~ 2 – 10 %. Again the impact is systematic, the exact percentage change depending on the K content and the K / Ca ratio of the sample. Appendix 2 contains examples of the effect of using these different calibrated K spallation rates for samples with different K and Ca contents.

These rates of ^{36}Cl production by spallation from Ca and K apply to the ground surface. As with other spallogenic isotopes, the depth dependence of ^{36}Cl production due to spallation is given by Equation 2.2, which describes an exponentially decline in the rate with increasing depth below the ground surface.

3.2.3 NEUTRON ACTIVATION (CAPTURE)

Whilst spallation involves predominantly high-energy cosmic-ray neutrons, lower energy cosmic-ray neutrons also produce ^{36}Cl *in situ* through neutron capture reactions involving the isotopes ^{35}Cl and ^{39}K (Table 3.2). At the surface, and within a depth of a few metres, these lower energy neutrons have various sources:– spallation, muon capture reactions, photodisintegration reactions initiated by fast muons, uranium fission and (α, n) reactions. The contribution of the neutrons from each source to the total neutron activation production rate is dependent on the Cl and K concentrations and chemical composition of the samples. Hence there is no calibrated production rate for neutron activation and this rate has to be uniquely determined for every sample based on the contribution from each neutron source. The neutron yield from these sources therefore needs to be considered before discussing the neutron activation production rate calculation. A detailed discussion of this topic is presented by Fabryka-Martin (1988), Bierman (1993), Liu *et al* (1994a), and Stone *et al* (1998a), and what follows is a summary based on these papers.

3.2.3.1 NEUTRON PRODUCTION SOURCES: SPALLOGENIC SECONDARY NEUTRONS

Within the topmost metre of the Earth's surface, bombardment of target nuclei by high-energy cosmic-rays produces neutrons with mean energies of ~ 1 MeV which, once thermalized (kinetic energy reduced), may be captured by ^{35}Cl to produce ^{36}Cl (Yamashita *et al*, 1966; O'Brien *et al*, 1978). Spallogenic secondary neutrons ('knock-on' and 'evaporation') are disintegration products of the spallation reaction and are produced in two ways. High-energy neutrons are emitted following cosmic-ray initiated hadron – nucleus interactions. These neutrons lose energy mainly by inelastic scattering and are called 'knock-on' neutrons (Dep *et al*, 1994b). During spallation a two stage nuclear reaction occurs, the first involving the formation of a compound nucleus resulting from the incident particle being absorbed by the target nucleus, and the second stage involving the de-excitation of the compound nucleus by the emission of one or more 'evaporation' neutrons (Fabryka-Martin, 1988; Dep *et al*, 1994b). Spallogenic secondary neutrons comprise the dominant component of the total neutron flux in the upper ~ 2 m of the Earth's surface (Fabryka-Martin, 1988; Stone *et al*, 1998a; Figure 3.1).

3.2.3.1 NEUTRON PRODUCTION SOURCES: NEUTRON EMISSION FOLLOWING MUON CAPTURE

The negative muon capture reaction is discussed in more detail later, but a consequence of the capture of a slow negative muon is de-excitation by neutron emission (Charalambus, 1971; Fabryka-Martin, 1988; Stone *et al*, 1998a). The capture by the Ca nucleus' Coulomb (electric) field of a slow negative muon creates a new product nucleus that is excited:

$$\mu^- + {}^{40}_{20}Ca \rightarrow {}^{40}_{19}K^* + \nu_\mu \qquad \text{Equation 3.1}$$

where, μ^- is a negative muon, ν_μ is a neutrino and * indicates that the product nucleus is excited. The excitation can be dissipated by evaporation of *inter alia*, one or more neutrons, for example:

$${}^{40}_{19}K^* \rightarrow {}^{36}_{17}Cl + 2n + 2p \qquad \text{Equation 3.2}$$

De-excitation by emission of protons and α-particles occurs, on average, less frequently than emission of neutrons (Stone *et al*, 1998a). Once emitted most neutrons are slowed to thermal energies before capture by isotopes in the rock.

The neutron yield attributable to this mechanism is controlled by the number and distribution of muon captures by the relevant target nuclei and the average neutron yield per muon capture. Each element constituting the rock has a set of probabilities for muon capture to the 1s orbital (a spherical region around an atom), the proportion of these which lead to nuclear capture and the relative probability of the emission of 1-, 2-, 3- ... neutrons following excitation (Bierman, 1993, Stone *et al*, 1998a). Stone *et al* (1998a) provide an equation for calculating the neutron yield per stopped negative muon at depth z:

$$P_s(z) = \psi_\mu - (z)\left(f_{c,i} f_{d,i}\left(P_{1n,i} + 2P_{2n,i} + 3P_{3n,i} + ...\right)\right)$$

$$P_s(z) = \psi_{\mu^-}(z) Y_s \qquad \text{Equation 3.3}$$

where, ψ_μ-(z) is the intensity of negative muons stopping at depth z ((stopped μ^-) g^{-1} a^{-1}), $f_{c,i}$ is fraction of stopped negative muons captured by element i, $f_{d,i}$ is the fraction of nuclear captures from 1s muonic level by element i, and $P_{1n,i}$ is the probability of 1 neutron emission following muon capture by element i. Y_s is equal to the bracketed part of the equation and is the average neutron yield from negative muon capture in the target compound (neutron (stopped μ^-)$^{-1}$). For the purpose of Equation 3.36, the value of Y_s was determined for the

sample basalts using negative muon capture ratios ($f_{c,i}$) from von Egidy and Hartmann (1982), nuclear capture probabilities ($f_{d,i}$) from J. Stone (pers. comm.) and average neutron emission probabilities (P) from Charalambus (1971) and J. Stone (pers. comm.).

3.2.3.2 Neutron production sources: Photoneutrons initiated by fast muons

The electric field of a nucleus can deflect the path of a fast charged particle leading to deceleration and emission of electromagnetic radiation. Such braking radiation is known as bremsstrahlung and gamma radiation is often the emitted product. The deceleration of fast muons can be a source of gamma radiation through bremsstrahlung leading to the production of cosmogenic neutrons in photonuclear (γ, n) disintegration reactions. The processes involved are discussed in detail in Fabryka-Martin (1988). An equation to calculate the production rate of photoneutrons is given by Fabryka-Martin, (1988 equation 3-9) and Stone *et al* (1998a, equation 7):

$$P_f = N_{tot} Y_n \int_0^{E_{max}} (\sigma_{abs}\, dE / E) E_g\, j_\gamma (> E_g)\, \phi_{\mu\pm}(z) \qquad \text{Equation 3.4}$$

where, N_{tot} is the atomic density of rock (atoms g^{-1}). Y_n is the average neutron yield per photodisintegration, which has a conventional value of 1 neutron (disintegration)$^{-1}$ (Stone *et al*, 1998a, p438). $\int^{Emax}_0(\sigma_{abs}\, dE/E)$ is the absorption cross-section per nucleus, averaged over the bremsstrahlung energy spectrum (cm^2); E_g is the average γ-ray energy (MeV) at which the photonuclear cross-section is at a maximum for a (γ,n) reaction in the medium; $j_\gamma(>E_g)$ is the intensity of μ-associated γ-rays with an energy greater than E_g (γ cm^{-2} a^{-1}); and $\phi_{\mu\pm}(z)$ is the fast muon flux at depth z (muon cm^{-2} a^{-1}). This final term was added by Stone *et al* (1998a) and may be calculated from the 5th order polynomial provided in the appendix to that paper.

3.2.3.3 Neutron production sources: Nucleogenic neutrons from U-fission and (α, n) reactions

Two nucleogenic (and hence non-cosmogenic) sources of neutrons are (α, n) reactions on light nuclei, where the alpha particles are emitted in the uranium and thorium alpha decay series, and neutrons produced directly by spontaneous fission of ^{238}U (Feige *et al*, 1968, Fabryka-Martin, 1988). The production rate of these nucleogenic neutrons is dependant on the elemental composition of the target material. Although the highest neutron yields are produced by α-bombardment of Be, B, F and Li (265, 62, 31 and 21 n g^{-1} a^{-1} per ppm U,

respectively), the trace concentrations of these elements make them less significant targets for (α, n) reactions in basalts than the light elements, O, Na, Mg, Al, and Si (Feige *et al*, 1968; Fabryka-Martin, 1988, table C-3).

To determine the background ^{36}Cl produced by these reactions, the major element, U, Th and absorbing trace element concentrations were measured in each sample (Appendices 3 & 4) and the neutron yields calculated as follows. The neutron yield from the spontaneous fission of ^{238}U, P_{sf} (neutron g^{-1} a^{-1}), depends on the concentration of uranium in the target and the neutron yield per fission reaction and was calculated per Fabryka-Martin, (1988, equation 3-16):

$$P_{sf} = N_{238}\lambda_{sf}\nu \qquad \text{Equation 3.5}$$

where, N_{238} is the atomic concentration of ^{238}U, λ_{sf} is the decay constant for spontaneous fission of ^{238}U (8.45×10^{-17} a^{-1}, based on the decay constant, 1.5513×10^{-10} a^{-1}, and branching ratio for ^{238}U fission, 5.45×10^{-7}, quoted in Stone *et al*, 1998a), and ν is the neutron yield per fission (2.00 ± 0.08 neutrons per fission, Vandenbosch and Huizenga, 1973, quoted by Stone *et al*, 1998a).

The neutron yield from (α, n) reactions, $P_{(\alpha,n)}$ (neutrons g^{-1} a^{-1}), may be determined using the following equations (Fabryka-Martin, 1988):

$$P_{(\alpha,n)} = a[U] + b[Th] \qquad \text{Equation 3.6}$$

$$a = \sum S_i F_i Y_n^U / \sum S_i F_i$$

$$b = \sum S_i F_i Y_n^{Th} / \sum S_i F_i \qquad \text{Equation 3.7}$$

where, [U] and [Th] are the measured U and Th content (ppm). S_i is the cross-section of element i for α-particles of a given energy (MeV g^{-1} cm^2), but for the purpose of this thesis the α-particle cross-sections were averaged over the U- and Th-series decay energies spectrum (Feige *et al*, 1968). F_i is the fractional abundance of element i and $Y^U{}_n$ and $Y^{Th}{}_n$ are, respectively, the neutron yield of element i per ppm U and Th.

3.2.3.4 Relative production rates of neutrons

The relative production rate of neutrons from these four sources at the ground surface and with depth below the ground surface is shown in Figure 3.1 for basalt of typical composition.

Down to a depth of a metre or so below the surface, spallogenic secondary neutrons account for the vast majority of lower energy neutrons. At depths over ~ 2 m, the two muon induced mechanisms make increasingly larger contributions to the total. The two nucleogenic mechanisms are solely dependent on the chemical composition of the medium, and hence their production remains constant with depth, assuming chemical homogeneity.

Spallogenic secondary neutrons and the two muon induced neutrons are created with a range of energies, but are quickly slowed to thermal energies (≤ 0.5eV) below the air / ground surface interface due to elastic collisions with light nuclei and are ultimately captured in nuclear reactions (Fabryka-Martin, 1988). This attenuation happens at different rates for the cosmogenic neutron production pathways as reflected in Figure 3.1, and means that, for typical rock surfaces, at depths below 33 – 60 m neutron production by (α, n) and U-fission is wholly dominant (Fabryka-Martin, 1988, Liu *et al*, 1994a).

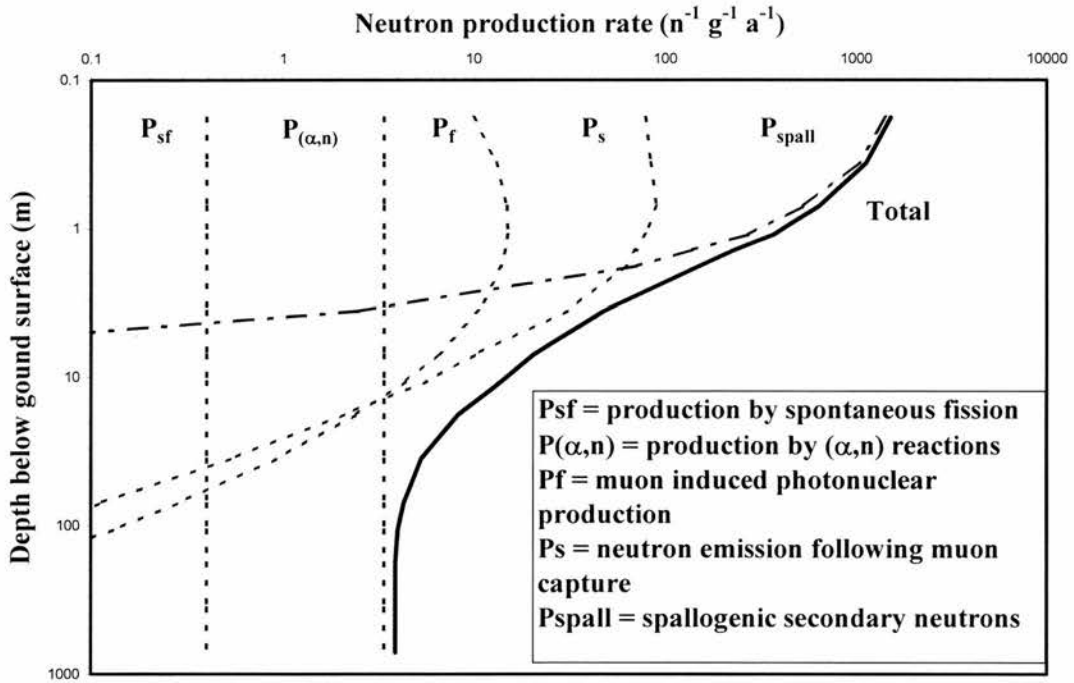

Figure 3.1: Relative production rates of neutrons in basalt as a function of depth below the ground surface for sea level and high latitude. The absolute rates vary with the chemical composition of the basalt sample. P_{spall} is based on a rate of 2000 n g^{-1} a^{-1} for surface production at sea level and high latitude. Note that both the depth and neutron production rate are log 10 values. Based on data in Fabryka-Martin (1988, table D-2b).

For the purpose of calculating the thermal neutron activation production rates and the modelled denudation rates derived in this thesis, it has not been necessary to calculate the low-energy neutron production rates from spallogenic secondary neutrons, neutrons emitted

following muon capture and photoneutrons initiated by fast muons. Phillips *et al* (1996a) empirically derived a value of 586 ± 40 neutrons $(g\ air)^{-1}\ a^{-1}$ for the total cosmogenic secondary neutron production at the surface at sea level and high latitude and this figure, scaled as appropriate, has been used in this thesis. This rate includes both the spallogenic and muogenic contributions, and scaling was based on 90 % due to spallation and 10 % due to muons, which corresponds to the ratio of ^{36}Cl production due to spallation and negative muon capture by Ca at sea level and high latitude (Stone *et al*, 1996a, 1998a).

Swanson and Caffee (in prep.) have calculated a total secondary neutron production rate of 871 ± 50 neutrons $(g\ air)^{-1}\ a^{-1}$. Reasons for the large discrepancy between this and the Phillips *et al* (1996a) rate are, again, unclear. However, due to the low chloride content of the basalts in this study (Appendix 4), the impact of using the higher figure would be to increase the modelled denudation rates by a maximum of ~ 3 – 5 % only.

3.2.3.5 SUB-SURFACE THERMAL NEUTRON FLUX

Calculation of the neutron activation production rate requires consideration of both the rate at which the neutrons are produced (see above) and the rate at which these neutrons are then slowed for capture within the rock. Neutrons produced by the mechanisms outlined above have high initial energy levels (see Fabryka-Martin, 1988, section 3.2.2 for a summary) and, before they can be captured to produce ^{36}Cl, the neutrons have to be slowed to thermal (≤ 0.5 eV) or epithermal (0.5 eV→ 0.1MeV) energies. This thermalization results, primarily, from elastic scattering of fast neutrons with O, H and Si in the rock (Fabryka-Martin, 1988).

In the metre or so below the ground surface, the neutron production rate and the thermal and epithermal neutron fluxes are not proportional (Fabryka-Martin, 1988). In Figure 3.1 the total neutron production rate decreases continuously with increasing depth below the ground surface. However, it has been established (Yamashita *et al*, 1966, O'Brien *et al*, 1978, Dep *et al*, 1994a, Liu *et al*, 1994a) that the low-energy neutron fluxes increase significantly below the air / ground interface to a depth of ~ 50 $g\ cm^{-2}$ (~ 0.18 m) before decreasing with increasing depth (Figure 3.2). This increase is due to backscattering and neutron leakage whereby a proportion of the neutrons produced in the upper few centimetres diffuse into the atmosphere and are captured there, rather than being absorbed by elements in the rock (Fabryka-Martin, 1988, Liu *et al*, 1994a, Dep *et al*, 1994a). The water content of the target medium is important as hydrogen is the most effective neutron energy moderator (Liu *et al*, 1994a). A higher water content results in a more rapid thermalization of the fast neutrons. A

lower water content permits more neutrons to be captured at epithermal energies, thereby reducing the thermal neutron flux and nuclide production by thermal neutrons (Fabryka-Martin, 1988, Liu *et al*, 1994a, Dep *et al*, 1994a).

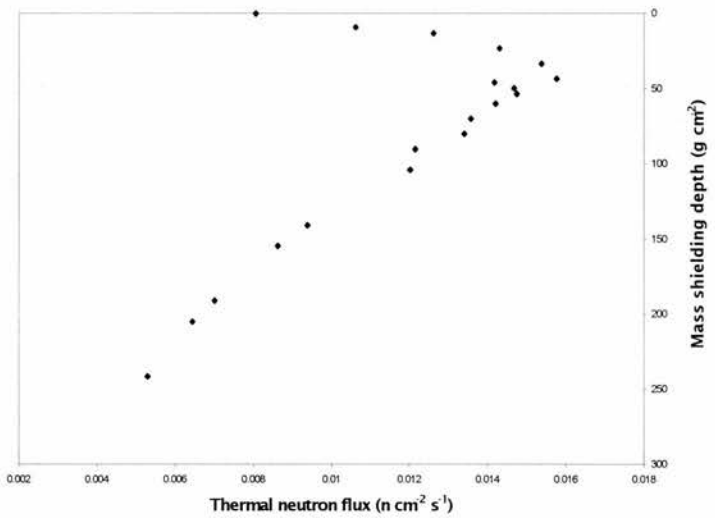

Figure 3.2: Measured thermal neutron flux in a concrete block plotted as a function of cumulative mass shielding depth (based on data in Liu *et al*, 1994a, table 2. Similar results have been reported in a natural sample by Dep *et al*, 1994a).

This thermal neutron flux distribution has been successfully modelled (Lal and Peters, 1967; O'Brien *et al*, 1978; Dep *et al*, 1994b; Liu *et al*, 1994a). However, as pointed out by Liu *et al* (1994a, p3119), the results of these previous studies are too complex to be readily useable in analytical equations for cosmogenic nuclide production. Although the Liu *et al* (1994a) model is based on the assumption that all thermal neutrons are derived from spallation reactions, it has been used in this study due to the model's ease of use, the altitude of the present study's sample sites (which reduces the muogenic contribution) and the fact that other low-energy neutron sources are negligible in the topmost metre of the Earth's surface (Figure 3.1).

The thermal neutron flux, Φ_{ss}, in the subsurface is given by (Liu *et al*, 1994a, equation 13):

$$\Phi_{ss} = \Phi^*_{ss} e^{\left(-z/\Lambda_{sp}\right)} + F\Delta\Phi^* e^{\left(-z/L_{ss}\right)} \qquad \text{Equation 3.8}$$

where, Φ_{ss}^* is the thermal neutron flux that would be observed at the air land interface if there was no neutron leakage, z is the cumulative mass shielding depth (g cm^{-2}), Λ_{sp} is the effective attenuation length for fast neutrons (g cm^{-2}), F is a weighting factor, $\Delta\Phi^*$ is the difference between the thermal neutron fluxes in the air and the ground in the absence of the air / ground interface, and L_{ss} is the characteristic thermal neutron diffusion length in the subsurface (g cm^{-2}). Values for Φ_{ss}^*, F, and $\Delta\Phi^*$ are determined as follows (Liu *et al*, 1994a, equations 14, 15, 16 and Liu *et al*, 1995, equations 3 and 4):

$$\Phi^*_{ss} = p\left(E_{th}\right)_a P_f\left(0\right) R\Lambda_{th,ss} \qquad \text{Equation 3.9}$$

where, $p(E_{th})_a$ is the unitless probability that a neutron will reach thermal energies (≤ 0.5eV) without capture in the atmosphere (the resonance escape probability – a calculation for this is provided in Fabryka-Martin , 1988, equation 3.18, and Liu *et al*, 1994a, equation 4). $P_f(0)$ is the production rate of neutrons in air at ground level, 586 ± 40 neutrons (g air)$^{-1}$ a^{-1}, as determined by Phillips *et al* (1996a), scaled for the altitude and latitude of the sample site. R is the ratio of neutron production and attenuation to thermal energies in the subsurface to that in the atmosphere, and varies with the elemental composition of the rock surface (see Liu *et al* (1994a) equation 9). $\Lambda_{th,\,ss}$ is the effective thermal neutron attenuation length in the subsurface (g cm^{-2}), and is the reciprocal of $\Sigma_{th,i}$, the thermal neutron macroscopic absorption cross-section (= the total cross-section for thermal neutron absorption in the rock). It is not necessary to undertake a complete elemental analysis of the rock to determine this as fourteen elements (B, Na, Mg, Al, Si, P, Cl, K, Ca, Ti, Mn, Fe, Sm, Gd) absorb 98 % of the thermal neutrons (Andrews *et al*, 1986; Leavy 1987). In this study Li and Cr were included (Appendices 3 & 4).

$$F = \frac{(D_a / D_{ss})L_a^{-1} + \Lambda_{sp}^{-1}}{(D_a / D_{ss})L_a^{-1} + L_{ss}^{-1}} \qquad \text{Equation 3.10}$$

where, D is the thermal neutron diffusion coefficient (g cm^{-2}) in the $_a$ atmosphere and $_{ss}$ subsurface (Liu *et al* (1994a) provide a basis for calculation). L and Λ_{sp} are as in Equation 3.8.

$$\Delta\Phi^* = p(E_{th})_a P_f(0)(\Lambda_{th,a} - R\Lambda_{th,ss}) \qquad \text{Equation 3.11}$$

where the symbols are per Equation 3.9, except $\Lambda_{th,a}$ which is the effective thermal neutron attenuation length in air (g cm^{-2}).

3.2.3.6 ^{36}Cl PRODUCTION DUE TO NEUTRON CAPTURE

The *in situ*-production rate of ^{36}Cl due to thermal neutron activation was calculated using the thermal neutron flux model of Liu *et al* (1994a) and the total cosmogenic secondary neutron production rate of Phillips *et al* (1996a). Unlike spallation, where the production rate is at a maximum at the surface and decreases exponentially, production due to thermal neutrons is maximised at the depth at which the thermal neutron flux is maximised.

In the uppermost zone of the Earth's surface there are two reactions involving low-energy neutron capture which produce ^{36}Cl, ^{35}Cl (n, γ) ^{36}Cl and ^{39}K (n, α) ^{36}Cl (Table 3.2). The reaction involving the stable isotope ^{35}Cl was the basis for the pioneering study by Davis and Schaeffer (1955). The production rate is derived from the thermal neutron flux and the fraction of the stopped neutrons that are then captured by ^{35}Cl (Dep *et al*, 1994b; Liu *et al*, 1994a; Phillips *et al*, 1996a; Stone *et al*, 1996a; 1998a). This can be represented as follows:

$$P_{n,35}(z) = \frac{f_{35}}{\Lambda_{th,ss}}(\Phi_{ss}) \qquad \text{Equation 3.12}$$

where, $P_{n,35}(z)$ is the ^{36}Cl production rate from capture of thermalized neutrons by ^{35}Cl at depth z (g cm^{-2}). $\Lambda_{th,ss}$ is the effective thermal neutron attenuation length in the rock (g cm^{-2}), which is the reciprocal of the thermal neutron macroscopic absorption cross-section (Liu *et al*, 1994a), Φ_{ss} is the thermal neutron flux in the subsurface derived using Equation 3.8 and f_{35} is the fraction of the stopped neutrons captured by ^{35}Cl, which depends on the chemical composition of the sample.

This fraction is derived as follows (Davis and Schaeffer, 1955):

$$f_{35} = \frac{\sigma_{35} N_{35}}{\sum \sigma_i N_i} \qquad \text{Equation 3.13}$$

where, σ_{35} is the ^{35}Cl neutron capture cross-section, (43.6b = 43.6 x 10^{-24} cm^2 (Lide, 1995)), N_{35} is the atomic concentration of ^{35}Cl, σ_i is the neutron capture cross-section for all elements in the sample material, and N_i is the abundance of all elements in the sample. $\Sigma\sigma_i N_i$ in this equation is the same as $\Sigma_{th,i}$ in Liu *et al* (1994a) equation 19, the thermal neutron macroscopic absorption cross-section.

Equations 3.12 and 3.13 can be used to determine the thermal neutron capture production rate for the ^{39}K (n, α) ^{36}Cl reaction ($P_{n,39}$ (z)) by substituting f_{39} for f_{35}, and σ_{39} for σ_{35}. The value of σ_{39}, the ^{39}K cross-section for the ^{39}K (n, α) ^{36}Cl reaction, is 0.0043x10^{-24} cm^2 (Lide, 1995).

In the topmost few metres of the Earth's surface, not all neutrons will be thermalized before capture (Fabryka-Martin, 1988). A proportion will be captured at epithermal energy (0.5ev $\rightarrow$ 1MeV), and the production of ^{36}Cl due to epithermal neutrons can be calculated as follows :

$$P_{n,epi} = \left(1 - p(E_{th})_a\right) P_f(0) R_{epi} \frac{N_{35}}{I_{eff}} 0.6 \qquad \text{Equation 3.14}$$

where, R_{epi} is the epithermal neutron capture ratio, derived using equation 9 of Liu *et al* (1994a) and substituting (1- $p(E_{th})_{ss}$) for $p(E_{th})_{ss}$. I_{eff} is the effective resonance integral of the rock for absorption of epithermal neutrons, which is the sum of the dilute resonance integrals for all the elements in the rock. This is equivalent to the macroscopic cross-section for thermal neutrons ($\Sigma\sigma_i N_i$). Fabryka-Martin (1998, p19) explains that, normally, reaction cross-sections are smooth functions of energy, however, in the epithermal energy range, the cross-section may increase by several orders of magnitude at certain energies ('resonance energies'). The resonance integral is the reaction cross-section where the most important resonances occur. The term 'dilute' refers to the fact that the resonance integral is only applicable to a situation in which the medium through which the neutrons travel does not significantly modify the neutron energy spectrum (Fabryka-Martin, 1988). The constant, 0.6,

is equal to 1 minus the fractional reduction in the epithermal flux at the air-ground interface (J. Stone, pers. comm.).

3.2.4 NEGATIVE MUON CAPTURE

In situ ^{36}Cl is also produced by reactions involving negative muons. Muon reactions are dealt with in detail in Charalambus (1971), Fabryka-Martin (1988), Bilokon *et al* (1989) and Stone *et al* (1998a), and what follows is a summary based on these sources.

High-energy cosmogenic protons react with atmospheric nuclei to produce charged pions ($\pi^{\pm}$) and $K^{\pm}$ mesons that can decay to muons ($\mu^{\pm}$). Muons are unstable subatomic particles with an extremely short mean life of ~ 2.2 x 10^{-6} s, (Fabryka-Martin, 1988, Stone *et al*, 1998a). The muon flux has a wide energy spectrum ranging from ~ 27 MeV to > 100 GeV (Lal and Peters, 1967; Stone *et al*, 1998a) and, for the purposes of ^{36}Cl production, this flux can be split into slow (≤ 50 GeV) and fast components. The slowing of the fast muon component can produce γ-radiation by bremsstrahlung leading to photoneutron production as mentioned above.

Slow muons lose energy mainly (95-99%) by ionization in air and rock (Hayakawa, 1969 quoted in Stone *et al*, 1998a). Positive muons are repelled by nuclei and therefore, on stopping, decay radioactively as follows:

$$\mu^{+} \rightarrow e^{+} + \nu_{\in} + \bar{\nu}_{\mu} \qquad \text{Equation 3.15}$$

In contrast, negative muons when stopped have two alternatives. They may radioactively decay,

$$\mu^{-} \rightarrow e^{-} + \bar{\nu}_{\in} + \nu_{\mu} \qquad \text{Equation 3.16}$$

or, they may be captured by positively charged nuclei (Charalambus, 1971, Fabryka-Martin, 1988, Stone *et al*, 1998a). The production of ^{36}Cl by negative muon capture by the nuclei of

various isotopes is possible, however, ^{40}Ca and ^{39}K are the only significant producers in the immediate subsurface (Table 3.2).

Charalambus (1971) outlines the stages involved in negative muon capture reactions. An illustration of this reaction, involving the excitation of a calcium nucleus and subsequent neutron emission, can be found in Section 3.2.3.1. The production rate of a nuclide due to negative muon capture reactions, P_{μ^-} (atoms g^{-1} a^{-1}), as a function of depth, z, is controlled by five factors, represented as follows (Charalambus, 1971, Dockhorn *et al*, 1991, Stone *et al*, 1998a):

$$P_{\mu^-}(z) = \psi_{\mu^-}(z) f_{c,i} f_i f_d P_\alpha$$

$$P_{\mu^-}(z) = \psi_{\mu^-}(z) Y_i$$

Equation 3.17

where, ψ_{μ}-(z) is the intensity of negative muons stopping at depth z ((stopped μ^-) g^{-1} a^{-1}); $f_{c,i}$ is the fraction of stopped negative muons captured by the target nucleus of element i, where the target is one of the constituents of a compound; f_i is the isotopic abundance of the target isotope; f_d is the fraction of muons captured by the target nucleus from the 1s muonic level before radioactive decay; and P_α is the probability of the de-excitation of the product nucleus by emission of neutrons, protons or alpha particles. Y_i is the ^{36}Cl yield from negative muon capture by element i in the target compound, equal to $f_{c,i} f_i f_d P_\alpha$, and is measured in atoms (stopped μ^-)$^{-1}$. For the purpose of Equation 3.36, the values of Y_{Ca} and Y_K, are the ^{36}Cl yield from negative muon capture by ^{40}Ca and ^{39}K, respectively. These were derived from values for $f_{c,i}$ from von Egidy and Hartmann (1982) and values for $f_{d,Ca} = 0.85$, $f_{d,K} = 0.82$, $P_{\alpha,Ca} = 0.043$ and $P_{\alpha,K} = 0.043$ from J. Stone (pers. comm.).

The negative muon stopping rate at sea level and high latitude is assumed to be 175 ± 10 μ^- g^{-1} a^{-1}, for sea level and high latitude (Stone *et al*, 1998a, p 444 and references quoted therein). Stone *et al* (1998a) present a 5th order polynomial (Equation 3.18) which may be used to calculate the sub-surface rate at depths ranging from 100 g cm^{-2} to 5500 g cm^{-2} (~ 30cm to 20m) (Figure 3.3):

$$\log_{10}\left(\psi_{\mu-(z)}\right) = a + b\log_{10}(z) + c[\log_{10}(z)]^2 + d[\log_{10}(z)]^3 + e[\log_{10}(z)]^4 + f[\log_{10}(z)]^5$$

Equation 3.18

where, $\psi_{\mu^-}(z)$ is the negative muon stopping rate ($\mu^- g^{-1} a^{-1}$) at depth z (g cm^{-2}). The letters a, b, c, d, e and f are, respectively, 1.586, 1.709, -1.817, 0.9642, -0.2384, and 0.01955 at sea level and high latitude (Stone *et al*, 1998a).

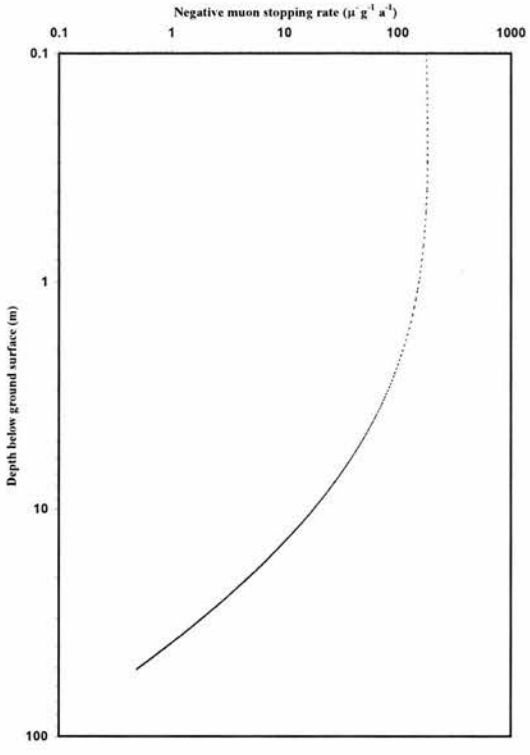

Figure 3.3: Depth-dependent total negative muon stopping rate based on a surface rate for sea level and high latitude of 175 ± 10 $\mu^- g^{-1} a^{-1}$, and the 5th order polynomial of Stone *et al* (1998a).

Using natural samples from a well constrained field site, Stone *et al* (1998a) calculated a ^{36}Cl yield from negative muon capture by ^{40}Ca in pure calcite of 0.012 ± 0.002 atoms ^{36}Cl per stopped negative muon. This, when combined with the negative muon stopping rate for sea level and high latitude, yields a ^{36}Cl production rate, P_{μ^-}, of 5.3 ± 1.0 atom $(g\ Ca)^{-1} a^{-1}$ (Stone *et al*, 1998a). This rate, scaled for altitude and latitude per Stone *et al* (1998a), has been used in this study.

The negative muon capture reaction involving the potassium isotope, ^{39}K (μ^-,p2n) ^{36}Cl, has not been independently calibrated. For the purpose of this thesis the rate has been taken to be 9 ± 2 atoms $(g\ K)^{-1} a^{-1}$ at sea level and high latitude, the value assumed by Evans *et al*, 1997. This value corresponds to 5% of the ^{36}Cl spallogenic production rate from potassium at sea level and high latitude.

3.2.5 COMPARISON OF THE ^{36}Cl PRODUCTION PATHWAYS

Figure 3.4 illustrates the breakdown of *in situ*-production of cosmogenic ^{36}Cl over a depth of 0 – 2800 g cm^{-2} (~ 0 – 10 m, assuming ρ = 2.9 g cm^{-3}) in a basalt composed of 9.30 wt % CaO, 0.88 wt % K_2O and 15 ppm Cl, located at sea level and high latitude. This figure shows the depth-dependent production rates for the major production mechanisms, namely, Ca and K spallation ($P_{sp, Ca}$ and $P_{sp, K}$, respectively), thermal neutron activation reactions involving ^{35}Cl and ^{39}K ($P_{n, 35}$ and $P_{n, 39}$, respectively), negative muon capture by Ca and K ($P_{\mu-, Ca}$ and $P_{\mu-, K}$ respectively) and the total production rate (P_{total}). These production profiles were calculated using the following equations: 2.2 - spallation; 3.8, 3.12 and 3.13 - thermal neutron activation; 3.17 and 3.18 - muon capture. The relative importance of each of the production mechanisms at different depths below the surface is highlighted in this figure. At the surface the two spallation reactions account for ~ 87 % of the production total, but at ~ 2m below the surface this has dropped to ~ 30 %, and the contribution by negative muon capture has risen to ~ 66 %.

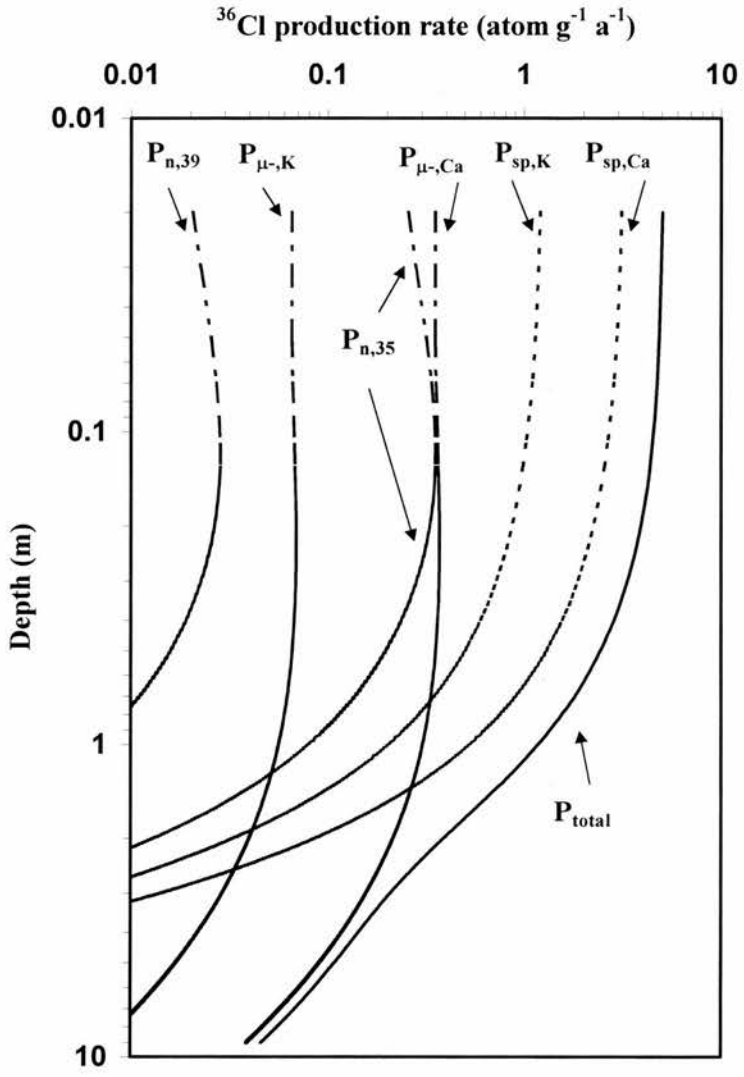

Figure 3.4: Production rates of *in situ*-produced cosmogenic ^{36}Cl in a basalt (with composition of 9.30 %wt CaO, 0.88 % wt K_2O and 15 ppm chloride) at sea level and high latitude, as a function of depth below the ground surface. $P_{n,35}$ and $P_{n,39}$ calculated assuming all thermal neutrons produced are spallogenic secondary neutrons, and ignoring muon-induced thermal neutrons. Increasing, or reducing, the chloride and potassium content would have the effect of moving the $P_{n,35}$ and $P_{n,39}$ curves to the right and left, respectively. The value of Pf(0) was taken as 586 ± 40 n (g air)$^{-1}$ a^{-1} (Phillips *et al*, 1996a). Sub-surface production by muon capture involving ^{39}K ($P_{\mu-,K}$) calculated using the surface production rate of 9 ± 2 atoms (g K)$^{-1}$ a^{-1} assumed by Evans *et al* (1997) and an assumed ^{36}Cl yield per stopped negative muon of 0.051 atom (stopped μ^-)$^{-1}$ at sea level and high latitude. The surface production rates for spallation and muon reactions used are from Stone *et al* (1996a, 1998a) and Evans *et al* (1997).

3.3 CHLORINE-36 PRODUCTION ON INCLINED SURFACES

The foregoing discussion on production has assumed that samples were collected from flat-lying, horizontal (± 20°) surfaces. In Chapter 2 mention was made of the impact of spatial factors on production including obstruction of the incident cosmic-ray flux by a sloping surface. The incident cosmic radiation responsible for spallogenic production is assumed to have a $\cos^{2.3}(\theta)$ zenith angle distribution (Nishiizumi *et al*, 1989), which means that most of the flux is received from vertical or near vertical angles. A more complex distribution exists for the slow muon component (Stone *et al*, 1998a). Given this type of distribution, the surface of a vertical cliff face will receive only 50 % of the flux received by a horizontal surface, (assuming no other topographic obstructions) and the effective attenuation length perpendicular to the surface of the cliff face will be reduced (Dunne *et al*, 1999; Fleming *et al*, 1999).

Samples used in this thesis to constrain backwearing denudation rates were collected from free face sites with dip angles of ~ 70 – 90 °, and modifications have to be made to some of the parameters in the standard production equations to account of the reduction in the 1/e absorption length and the obstruction of the incident flux by the cliff face. Each adjustment is unique for the particular dip angle of the slope and the computation of the adjustments is described in this section.

Production on and beneath surfaces with dip angles > 20 ° is complicated by the sloping surface itself obstructing part of the incident cosmic-ray flux. This type of shielding, whilst similar to topographic shielding (Chapter 2), has to be treated separately as the angle of shielding (α^i) is determined by the azimuth angle (ϕ). This is best illustrated by an example. Assume that a free face is oriented north (ϕ = 0 °) / south (ϕ = 180 °) and has an average dip (α) of 80 °. Treating this free face as topographic shielding would result in the horizon being assumed shielded to 80 ° over 180 °. However this is an oversimplification, as the maximum angle of shielding (α^i = 80 °) only occurs at azimuth angle ϕ = 90 ° (ie east, at right angles to the orientation of the face). At all other azimuth angles which coincide with the free face (ie azimuth angles between 0 ° (N) and 180 ° (S)) the shielding angle (α^i), is given by the inverse trigonometric function, $\arctan(\tan(\alpha)\sin(\phi))$ (Dunne *et al*, 1999). Using the same example, at azimuth angle 45 ° (NE) the shielding angle, α^i, is 76 °, whilst at azimuth angle 22.5 ° (NNE) α^i = 65 ° and so on. On the free face, the area below α^i is infinitely shielded, assuming that the distance between the target and the surface above the free face prevents

penetration of cosmic-rays incident upon the latter surface (ie below two attenuation lengths for spallation). Calculation of the production rate applicable in such situations therefore requires account to be taken of both the shielding imposed by any topography in the azimuth angles not affected by the free face and the shielding imposed by the slope. In addition shielding of the slope leads to a consequent reduction in the cosmic-ray attenuation length perpendicular to the free face, which receives most of the incoming radiation at grazing angles. This section, which draws extensively from discussions with Dr John Stone, describes how these points were addressed for the free face samples described in Chapter 7.

3.3.1 SPALLOGENIC PRODUCTION

To calculate both the shielding imposed by the slope and the reduction in the effective attenuation length for spallogenic production (Λ_{sp}, assumed in this thesis to be 160 g cm^{-2}), it is necessary to determine the attenuation length of unidirectional, collimated, cosmic-rays responsible for spallation reactions (λ g cm^{-2}). This collimated radiation is attenuated exponentially as it travels through matter such that the intensity of the flux at a perpendicular distance (d) below the surface is given by the following equation (Lal, 1991; Dunne *et al*, 1999):

$$I(d) = I(0)e^{-d/\lambda} \qquad \text{Equation 3.19}$$

where *I(d)* is the intensity of the flux at depth d (g cm^{-2}), *I(0)* is the unattenuated flux and λ is the attenuation length (g cm^{-2}). The total flux, F, that a target on a flat, level, unobstructed horizon surface receives is given by (Dunne *et al*, 1999):

$$F = \int_{\phi=0}^{2\pi} \int_{\theta=0}^{\pi/2} I(\theta,\phi)\cos\theta d\theta d\phi \qquad \text{Equation 3.20}$$

where I(θ, ϕ) is the intensity of the flux for the inclination angle (θ) measured from the horizontal with azimuthal angle (ϕ).

This intensity is generally regarded as being of the form:

$$I(\theta,\phi) = I(0)\sin^{2.3}(\theta) \qquad \text{Equation 3.21}$$

assuming that the radiation responsible for spallogenic production has a $\cos^{2.3}(\theta)$ zenith angle distribution (Nishiizumi *et al*, 1989).

Substituting Equations 3.19 and 3.21 into Equation 3.20 and replacing the perpendicular distance, d, by the distance travelled by a ray having an angle of inclination θ (d/sinθ) produces the following equation:

$$F = \int_{\phi=0}^{2\pi}\int_{\theta=0}^{\pi/2} I(0)\sin^{2.3}\theta\cos\theta\exp^{-d/\lambda\sin\theta}\, d\theta d\phi \qquad \text{Equation 3.22}$$

Assuming a value of one for *I(0)* and solving this integration iteratively for a value of λ which best reproduced the observed value for Λ_{sp}, the attenuation length for the decrease in the rate in spallogenic production with depth (160 g cm^{-2}), yielded a value for λ of ~ 210 g cm^{-2}. Figure 3.5 shows both Equation 3.22, derived using the value of 210 g cm^{-2}, and Equation 2.2 (the reduction in spallogenic production with depth), using a value of 160 g cm^{-2} for Λ_{sp}, for perpendicular depths down to 360 g cm^{-2} (~ 1.2 m in basalt). For comparison purposes the x values in both cases are the natural logarithm of the reduction in the surface value (flux intensity and surface production rate respectively). Although not a perfect match, the value of λ = 210 g cm^{-2} derived from Equation 3.22 is similar to that derived by Dunne *et al* (1999) ($\lambda = 1.3\ \Lambda_{sp}$) using a least-squares fitting procedure.

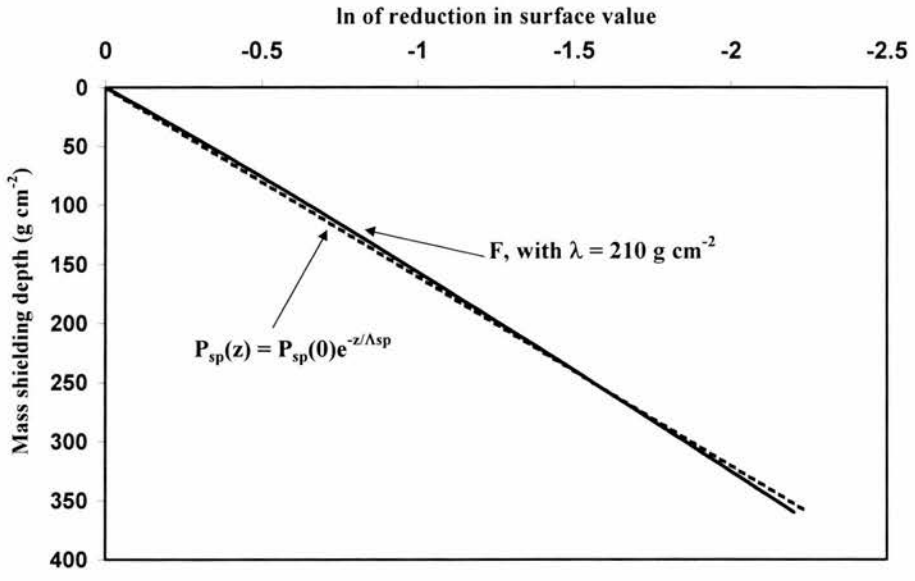

Figure 3.5: Comparison of the reduction in the surface value, plotted as a natural logarithm, for the function given in Equation 3.22, using a value for λ of 210 g cm^{-2}, and the function which describes the reduction in the spallogenic production rate with depth (Equation 2.2), which uses Λ_{sp} = 160 g cm^{-2}. The total mass shielding depth is ~ 1.4 m in basalt.

Using 210 g cm^{-2} as the 1/e absorption length and assuming that the radiation responsible for the spallogenic production has a $\cos^{2.3}(\theta)$ zenith angle distribution a variation of Equation 3.22 was then used to determine the fractional reduction in the total flux caused by the dipping surface.

To illustrate the problem and the approach adopted here a cross-section through a free face is shown in Figure 3.6 A. This free face is assumed to be oriented north / south and has a dip angle of α degrees in the direction of $\phi = 90°$. To reach a target located at depth p, measured perpendicular to the dipping surface, the thickness of rock through which the incident radiation has to pass is dependent on the inclination angle of the ray, θ, measured from the horizontal. This thickness of rock between the surface of the free face and the target varies with both θ, the angle of incidence, and, given what was said above, ϕ, the azimuth angle.

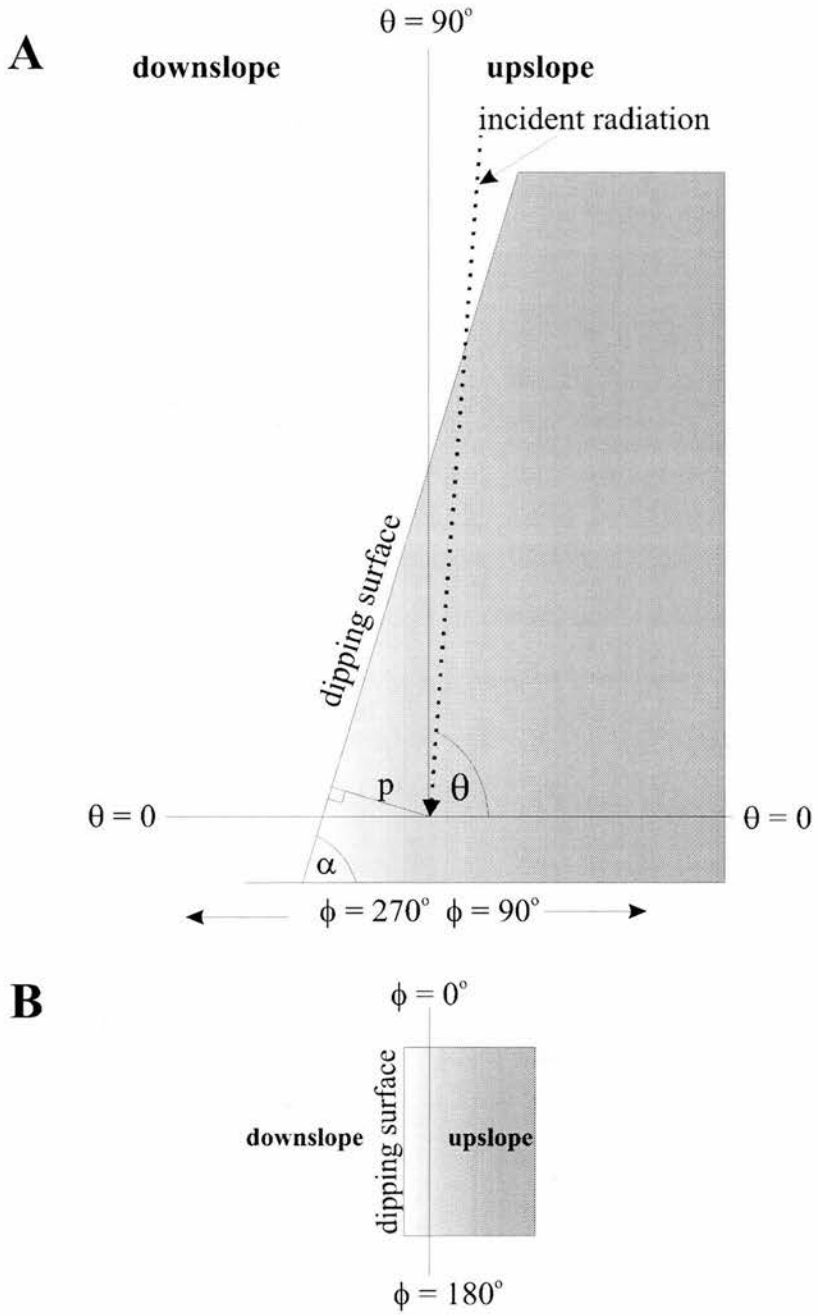

Figure 3.6: A: Cross-section through a surface with a dip angle of α degrees in the direction of azimuth angle ϕ = 90 °, assuming that the face is oriented north / south. In order to reach a target located at a perpendicular distance, p, from the dipping surface, the incident radiation will have to travel through the rock, the exact distance being related to the angle of incidence, θ, of the radiation. Determination of this distance, or more correctly mass shielding depth, depends on whether the incident radiation is in the upslope or downslope section (see text). B: Plan view of the same free face, showing the upslope and downslope sections used for calculation purposes. Upslope section here from ϕ = 0 ° (north) to ϕ = 180 ° (south), and the downslope section, from south to north.

For ease of calculation the cross-section is split in two, an upslope section, which deals with incident radiation from inclination angle θ from $\alpha^{i} = \arctan(\tan(\alpha)\sin(\phi))$ to θ = 90 ° in the direction of azimuth angle ϕ = 90 °. The area below α^{i} is infinitely shielded. The shielding distance in this upslope section, S_D (g cm^{-2}), is given by:

$$S_D = p/\cos(\alpha)\sin(\theta) - \sin(\alpha)\cos(\theta)\sin(\phi) \qquad \text{Equation 3.23}$$

In the downslope section, which deals with incident radiation from inclination angles θ = 0 ° to θ = 90 ° in the direction of azimuth angle ϕ = 270 °, the shielding distance is also given by Equation 3.23. However, for the purpose of calculating Equation 3.23 in the downslope section, the dip angle of the surface, α, is assumed to be equal to that of α at the upslope azimuth angle = downslope azimuth angle – 180 °. For example, for a target at p = 50 g cm^{-2} beneath a free face dipping at α = 80 ° in azimuth direction ϕ = 90 °, the shielding distance for incident radiation (θ = 85 °, ϕ = 90 ° (upslope section)) is 574 g cm^{-2}. For incident radiation (θ = 85 °, ϕ = 270 ° (downslope section)) the distance is 193 g cm^{-2}.

The total flux seen by a target at depth p, perpendicular to a surface sloping at angle α can be determined by integrating over all angles of incidence and all azimuth angles. Combining Equations 3.22 and 3.23 for the upslope and downslope sections, respectively, gives this total flux, F:

$$F = \int_{\phi=0}^{\pi}\int_{\theta=\alpha^{i}}^{\pi/2} I(0)\sin^{2.3}(\theta)\cos(\theta)\exp^{(-S_D/\lambda)} + \int_{\phi=\pi}^{2\pi}\int_{\theta=0}^{\pi/2} I(0)\sin^{2.3}(\theta)\cos(\theta)\exp^{(-S_D/\lambda)}$$

Equation 3.24

Assuming a value of I(0) = 1 and solving Equation 3.24 for a flat, level, surface, a maximum value of F, F_{max}, was derived ($F_{max} = 2\pi/3.3$). By normalising values of F for slope angles, α, from 0 ° to 90 ° (in intervals of 10 °), to F_{max} for targets at the surface of such slopes the following function was derived to determine the shielding factor for spallogenic production on dipping slopes:

$$SF_{dip,>20^{o}} = 1 + 0.002034\alpha - 0.000083706(\alpha^{2}) \qquad \text{Equation 3.25}$$

The surface spallation production rate for each free face site is derived by multiplying the calibrated rate, scaled for altitude and latitude as before, by $SF_{dip,>20°}$ and also by any scaling

factor which is necessary to account for topographic shielding (Equation 2.3). In determining the topographic shielding the azimuth sector corresponding to the free face is ignored (inclination angle set at zero) so as to avoid making a double correction.

The effect of slope angle on the attenuation length was addressed in a similar matter. This time Equation 3.24 was solved for various depths p from the surface to 300 g cm^{-2} in 50 g cm^{-2} intervals for a particular slope angle. These values were fitted with a curve in the form $\exp^{(-p/\Lambda sp,\alpha)}$, where $\Lambda_{sp,\alpha}$ is the effective attenuation length for spallogenic production for a slope of dip α. By combining the calculated values of $\Lambda_{sp,\alpha}$ over slopes of dip angles 0 ° to 90 ° (using 10 ° intervals) the following function was derived to determine the effective attenuation length for spallogenic production for a slope of dip α:

$$\Lambda_{sp,\alpha} = 161.8 - 0.302406\alpha - 0.00506263(\alpha^2) \quad \text{Equation 3.26}$$

This new attenuation length, $\Lambda_{sp,\alpha}$ is substituted for Λ_{sp} when calculating the decline in spallogenic production with depth beneath a dipping surface (Equation 2.2) and in the denudation rate calculations (Equation 3.36).

3.3.2 Neutron activation

A dipping surface will also affect the neutron capture production rate as this is largely dependent on spallogenic secondary neutrons (Figure 3.1). The production rate of neutrons in the air at ground level ($P_f(0)$, Section 3.2.3.5) has to be scaled to account for the shielding of the free face. This was done by multiplying $P_f(0)$ by the appropriate value of $SF_{dip,>20°}$. In addition the new attenuation length, $\Lambda_{sp,\alpha}$, has to be substituted for Λ_{sp} in the calculation of the thermal neutron flux in the subsurface (Φ_{ss}, Equation 3.8), the weighting factor (F, Equation 3.10) and in the denudation rate calculations (Equation 3.36). Figure 3.7 shows the impact of a dipping surface (selected angles) on the subsurface ^{36}Cl production rate from the capture of thermalized neutrons by ^{35}Cl ($P_{(n)35}(z)$, Equation 3.12) at depths, perpendicular to the sloping surface, down to 200 g cm^{-2}. In the Liu *et al* (1994a) model used for these calculations, a greater proportion of neutrons are lost by diffusion as the dip angle increases which is reflected by the decline in the difference of $P_{(n)35}$ at the surface ($z = 0$) and when $P_{(n)35}(z)$ is greatest. This is thought to reflect what would happen in reality (J. Stone, pers. comm.). When the surface is flat and level this difference is 1.86 x $P_{(n)35}$ ($z = 0$) and for an 80 ° slope the difference is 1.72 x $P_{(n)35}$ ($z = 0$). In addition the depth of the maximum

production rate is brought slightly nearer to the surface as the slope increases (for $\alpha = 0$ °, ~ 40 g cm^{-2}, for $\alpha = 80$ °, ~ 35 g cm^{-2}) due to the reduction in the attenuation length.

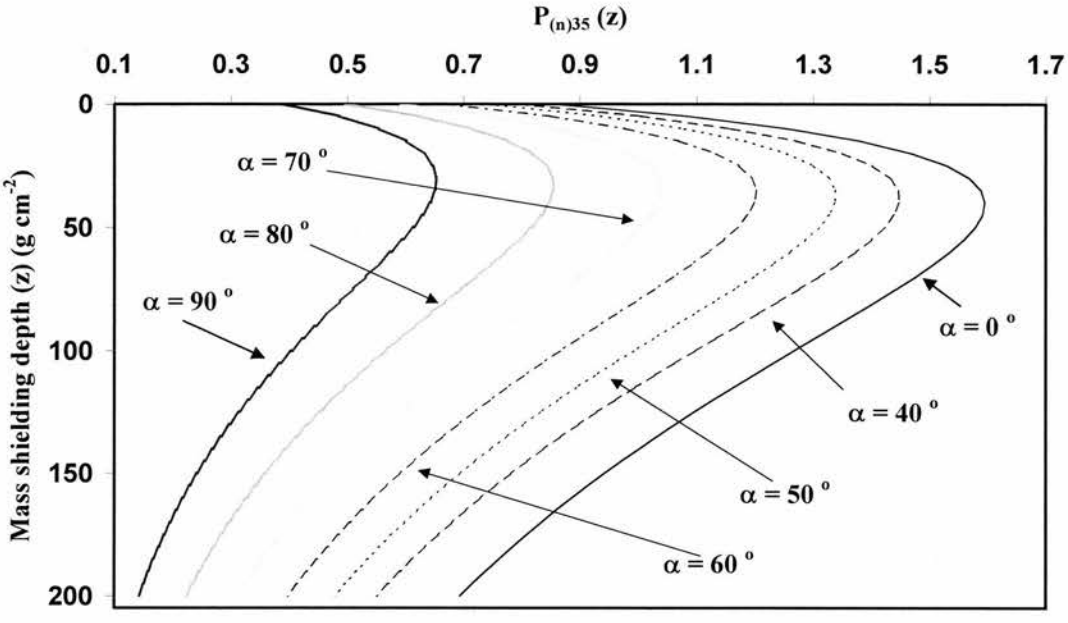

Figure 3.7: Plot of the variation in ^{36}Cl production rate from the capture of thermalized neutrons by ^{35}Cl determined using the Liu *et al* (1994a) model (Section 3.2.3.5) with mass shielding depth for sloping surfaces of various dip angles (α °). The actual values for $P_{(n)\,35}$ z (determined for a hypothetical sample with a total Cl content of 5.7 ppm) are unimportant. The plot illustrates the relative overall drop in the production rate, both at the surface and at depth, caused by the dipping surface.

3.3.3 NEGATIVE MUON CAPTURE

Sloping surfaces present the same problems for production by negative muon capture as they do for spallogenic production (ie both a reduction in the negative muon stopping rate due to the shielding of the cliff face and a change in the rate of attenuation of the negative muon stopping rate with depth). As a consequence, these problems were addressed in a similar manner to that outlined above. Muons were treated as outlined in Stone *et al*, (1998a), modified as necessary. The vertically incident negative muon stopping rate was integrated over the appropriate zenith angle distribution, taking account of the shielding imposed by the dipping surface, for depths down to 10000 g cm^{-2} (~ 35 m). Normalising the results for the surface of the dipping slope to that for a flat, level, surface with an unobstructed horizon, yielded a function which provides the correction for the shielding of the face. Fitting the results for depth to 10000 g cm^{-2} (~ 35 m) produced a polynomial for the muon stopping rate for the relevant slope angle.

Various measurements and models of the vertically incident negative muon stopping rate exist in the literature (eg Charalambus, 1971; Allkofer and Jokisch, 1973; Bilokon *et al*, 1989). However, these have tended to cover depths greater than those of interest in geomorphological studies and tend not to be in an easily manipulatable form (Stone *et al*, 1998a). Stone *et al* (1998a) have addressed these problems by modelling the stopping rate for vertically incident negative muon, $\psi_{\mu^-,vert}$, (μ^- g^{-1} a^{-1} sr^{-1}) for sea level and high latitude to a depth of 5500g cm^{-2} (at depths < 20 g cm^{-2} this model becomes inaccurate). This modelled rate is given by the following polynomial (Stone *et al*, 1998a; J. Stone, pers. comm.):

$$\log_{10}(\psi_{\mu^-,vert}(z)) = 7.062952 - 8.8491046[\log_{10}(z)] + 5.3646455[\log_{10}(z)]^2 - 1.3137036[\log_{10}(z)]^3 + 0.10315814[\log_{10}(z)]^4$$

Equation 3.27

Although this polynomial is based on the stopping rate beneath a limestone surface, Stone *et al* (1998a) indicate that its use for other rock types, including basalts, should be accurate to within 1 – 2 %.

The depth that a muon will penetrate beneath a surface is governed by the muon's momentum (quoted in GeV/c because of the very small mass of muons). This depth is regarded as the range, h, of muons with a particular momentum and trajectory, so, for example, vertical muons with a momentum of ~ 0.35 GeV/c have a range of 140 g cm^{-2}, those with a momentum of ~ 10 GeV/c have a range of 6000 g cm^{-2} (~ 21 m), and those with a momentum of 80 GeV/c have a range of 35000 g cm^{-2} (~ 121 m) (Bilokon *et al*, 1989; Stone *et al*, 1998a). Vertically incident muons are responsible for only ~ 50 % of the total muon-induced isotope production, and therefore it is necessary, in a determination of the omnidirectional stopping rate at any depth, z, to take account of the stopping rate of muons arriving on inclined trajectories (Stone *et al*, 1998a). This zenith-integrated negative muon stopping rate is most accurately derived by calculating the vertical range spectrum of the total incident flux (Stone *et al*, 1998a). This is achieved by summing all the muons with the same vertical range, $z = h \cos \theta$, where θ is the muon's angle of trajectory measured from the zenith and h is the range in the angle of inclination (Stone *et al*, 1998a). For example, for a depth, z = 5000 g cm^{-2}, perpendicular to a flat, level, surface, this would include vertical muons with a range of 5000 g cm^{-2}, and inclined muons on a trajectory of, say, $\theta = 45$ °, with a range of ~ 7070 g cm^{-2} and so on.

This zenith integration is complicated because the angular distribution of the sub-surface muon flux, for inclination angle θ, measured from the zenith, is of the form $\cos^n(\theta)$ where the exponent, n, is muon momentum dependent (Allkofer and Jokisch, 1973; Stone *et al*, 1998a and references therein). The value of the exponent varies from $n \approx 3$ for low momenta muons (strongly collimated near vertical flux), to $n \approx 0$ for muons with momentum ~ 25 GeV/c (an isotropic flux) and $n \approx -1$ for high (> ~ 50 GeV/c, Smith and Duller, 1959) momenta muons (near horizontal flux) (Stone *et al*, 1998a and references therein). This variation in the angular distribution is caused by the trajectory of a pion controlling the likely probability of that pion decaying to an energetic muon. Pions travelling vertically penetrate the more dense regions of the atmosphere and are more likely to interact with atmospheric nuclei than to decay to energetic muons, whilst pions travelling on an inclined angle of trajectory in the low density upper atmosphere are more likely to decay to energetic muons (Smith and Duller, 1959; Stone *et al*, 1998a).

For the purpose of calculations in this thesis, the cosine exponent, n, was taken to be the same as that used by Stone *et al* (1998a) which avoids the complications of specifying the range of very high energy (≥ 50 GeV/c) momenta. Limiting ranges to $< 2.3 \times 10^4$ g cm^{-2} and running the integration to a depth, z, of 10^4 g cm^{-2} means that muons arriving on trajectories flatter than $\theta = 64°$ are excluded. This exclusion underestimates the stopping rate at depths approaching 10^4 g cm^{-2} by 2 – 3 % (Stone *et al*, 1998a). The cosine exponent, n, as a function of range $< 2.4 \times 10^4$ g cm^{-2} is given by (J. Stone, pers. comm.):

$$n_{range} = 3.1x \exp[-(10^{([\log_{10}(range)]-3.7)}] \qquad \text{Equation 3.28}$$

For a flat, level, horizon, this equation returns values for the cosine exponent of n = 3.01 for a range of 140 g cm^{-2} (muon momentum = 0.35 GeV/c), n = 0.94 for a range of 6000 g cm^{-2} (~ 10 GeV/c momentum) and n = 0.03 for a range of 23000 g cm^{-2} (< 50 GeV/c momentum).

The zenith-integrated negative muon stopping rate, $\psi_{\mu^-}(z)$, (stopped $\mu^- g^{-1} a^{-1}$) beneath a flat, level, surface is given by an equation in a form similar to Equation 3.22 (J. Stone, pers. comm.):

$$\psi_{\mu^-}(z) = \int_{\phi=0}^{2\pi} \int_{\theta=\pi/18}^{\pi/2} \psi_{\mu^-,vert}(range) \sin^{n_{range}}(\theta) \cos(\theta) d\theta d\phi \qquad \text{Equation 3.29}$$

where the range, h, is given by z / sin θ, with θ in this function and the rest of the equation being measured from the horizontal. Given the angular boundary on the range, θ was started at 10 ° above the horizontal.

The procedure for calculating the zenith-integrated negative muon stopping rate beneath a surface dipping with angle, α, is similar to that for spallogenic production (see Figure 3.6). To reach a target at depth, p, measured perpendicular to the dipping surface, the negative muon will need sufficient momentum to penetrate the rock overburden, the thickness of which is dependent on the inclination angle, θ, measured from the horizontal, of the particle. This thickness, or shielding distance, S_D, varies with both this angle of incidence and, ϕ, the azimuth angle, and is given by Equation 3.23 for both the upslope and downslope sections. For the purpose of establishing the negative muon stopping rate for dipping surface, this shielding distance defines the range for the upslope and downslope sections. In calculating the range in the downslope section using Equation 3.23, the dip angle of the surface, α, is assumed to be equal to that of α at the upslope azimuth angle = downslope azimuth angle – 180 °. For example, for a target at depth p = 100 g cm^{-2}, measured perpendicular to a slope of dip angle α = 80 °, the range in the upslope section (azimuth direction ϕ = 90 °) is 1147 g cm^{-2} for a muon on an inclined trajectory of θ = 85 ° (measured from the horizontal), and for a muon on the same trajectory in the downslope section (azimuth direction ϕ = 270 °) the range is 386 g cm^{-2}. Substituting Equation 3.23 into Equation 3.29 provides the zenith-integrated negative muon stopping rate (stopped $\mu^- g^{-1} a^{-1}$) for a perpendicular distance, z, beneath a surface sloping at an angle of α for both upslope and downslope sections as follows:

$$\psi_{\mu-,dip=\alpha}(z) = \int_{\phi=0}^{\pi} \int_{\theta=\alpha^i}^{\pi/2} \psi_{\mu-,vert}(S_D) \sin^{n_{S_D}}(\theta) \cos(\theta) + \int_{\phi=\pi}^{2\pi} \int_{\theta=\pi/18}^{\pi/2} \psi_{\mu-,vert}(S_D) \sin^{n_{S_D}}(\theta) \cos(\theta)$$

Equation 3.30

Note that θ in the upslope section runs from α^i, the shielding angle given by arctan $(\tan(\alpha)\sin(\phi))$, as beneath this angle the target is infinitely shielded, and from $\theta = 10°$ in the downslope section, for reasons discussed above.

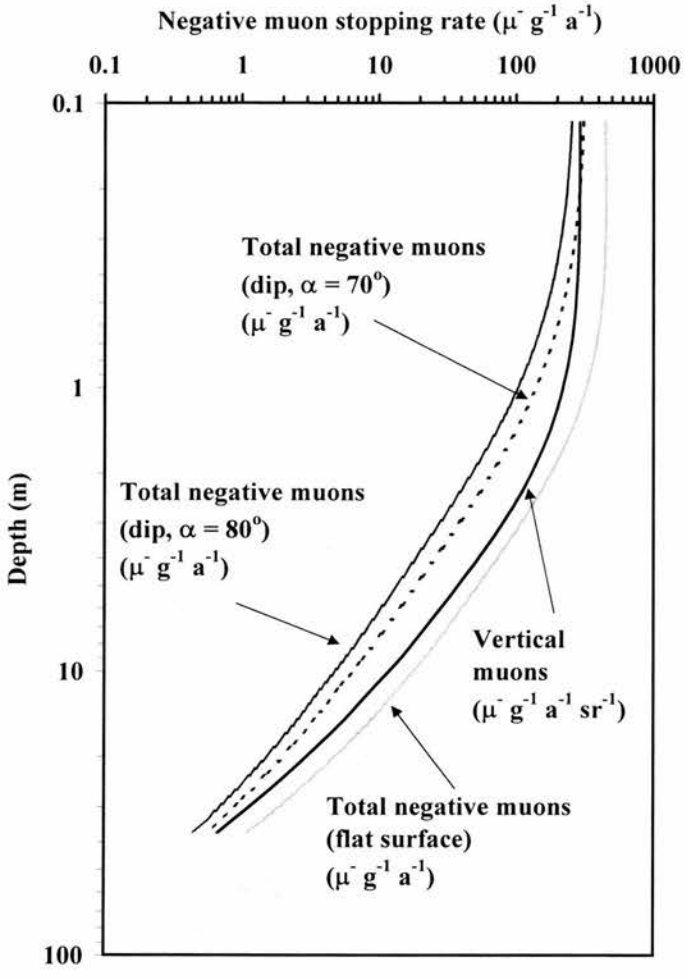

Figure 3.8: Calculated stopping rates for vertically incident negative muons (Equation 3.27), total zenith-integrated negative muons for flat, level, surface (Equation 3.29) and for total zenith-integrated negative muons for surfaces with dip angles 70 ° and 80 ° (Equation 3.30). All calculations have been scaled for an altitude of 3000 m at 30 ° S. The calculations are to a mass shielding depth of 10^4 g cm^{-2} perpendicular to the surface.

Figure 3.8 provides a comparison of the depth-dependent nature of the negative muon stopping rate based on Equations 3.27 (vertically incident negative muons), 3.29 (total, zenith-integrated, negative muon stopping rate for a flat, level, surface) and 3.30 (total, zenith-integrated, negative muon stopping rate for dipping surfaces). This figure shows the effect of the dipping surface which is to attenuate the stopping rate, with the attenuation increasing with increasing slope angle.

Prior to determining the shielding factor and the impact of the slope on the attenuation of the negative muon stopping rate with depth beneath the sloping surface, the issue of correction for the altitude and latitude of the target sites has to be considered. As Equations 3.29 and 3.30 refer to the vertically incident muon stopping rate, $\psi_{\mu^-, vert}(z)$, it is this rate which needs to be scaled, prior to solving Equations 3.29 and 3.30. Scaling of this is more complicated than simply applying Equation 2.1, which is applicable to the surface muon production rate. The incident spectrum is affected by latitude, being lower at the equator than high latitude, but only in relation to muons with a momenta < 4 GeV/c and reaching a peak at ~70 % less for a momentum of 0.5 GeV/c (Allkofer and Jokisch, 1973; Bilokon *et al*, 1989). In addition the muon ranges increase with increasing altitude (Stone *et al*, 1998a). Dr John Stone provided the author with a function which accounts for these affects. This function is of the form $1 + 2.5 \text{ Exp}^{(-z / 500)}$, where z is the range in g cm^{-2}, which scales $\psi_{\mu^-, vert}(z)$ for a site at 3000 m and 30 ° latitude. To simplify the subsequent calculation of the effect of sloping surfaces on the negative muon stopping rate, this function was assumed to apply to all the sample sites, even although they range in altitude from 2500 m to 3275 m and in latitude from 28 ° 45` S to 30 ° 47 ` S. At the altitude of the sample sites, the production of ^{36}Cl is dominated by spallation reactions and the contribution from negative muon capture is only ~ 3 – 5 % (Tables 6.8 and 7.9). This simplification therefore has very little impact on the calculated denudation rate. For sites at lower altitude or lower elevation, this simplification overestimates the ^{36}Cl production rate from negative muon capture and the denudation estimate, while for sites at higher latitude or altitude the effect is the opposite. An under- or overestimate in the negative muon capture rate of 20 % creates an under- or overestimate in the calculated denudation rate of only 3 %. To account for any potential impact of this simplification, negative muon capture rates calculated using the subsequent procedure were assigned an error of 20 % which was propagated through the subsequent calculations, including that of the estimated denudation rate.

To determine the shielding factor for negative muon production on dipping slopes, Equation 3.29 was solved to provide a zenith-integrated stopping rate for a flat, level, surface. Equation 3.30 was then solved to provide zenith-integrated stopping rates for surfaces dipping from 10 ° - 90 ° in 10 ° intervals. These equations cannot be applied to depths of less than 20 – 30 g cm^{-2} (Stone *et al*, 1998a). Therefore, to estimate the shielding factor, the stopping rate at a perpendicular depth of 30 g cm^{-2} was calculated for each of the slopes and normalised to the rate for a flat surface, all calculations being scaled to 3000 m elevation and

latitude 30 °. The following function was then derived to determine the shielding factor, $SF_{\mu^-, dip > 20°}$, for negative muon production on dipping slopes:

$$SF_{\mu^-,dip>20^o} = 0.977927 + 0.002059\alpha - 0.00008184\alpha^2 \quad \text{Equation 3.30}$$

where, α is the slope angle, > 20 °. The surface negative muon capture rate for each free face site is derived by multiplying the calibrated rate, scaled for altitude and latitude using Equation 2.1, by this shielding factor and any necessary correction for other topographic shielding (as for spallation production). A small error, expected to be of the order of ± 2 %, will be introduced by the inability of the equations to model the stopping rate at the surface.

The zenith-integrated negative muon stopping rate for perpendicular depths to 10000 g cm^{-2} below sloping surfaces located at 3000 m altitude and 30 ° latitude were calculated using Equation 3.30. For manipulation within the denudation calculation (Equation 3.36) the stopping rate profiles were then fitted with a 5th order polynomial of the form:

$$\psi_{\mu-,dip=\alpha}(z) = 10\hat{}(a + b[\ln(z)] + c[\ln(z)]^2 + d[\ln(z)]^3 + e[\ln(z)]^4 + f[\ln(z)]^5)$$

Equation 3.31

The coefficients, $a - f$, vary with slope angle. The coefficients for the polynomial for selected slopes applicable at 3000 m and 30 ° latitude are given in Table 3.3. Plots of the stopping rates produced by the polynomials for slopes of 70 ° and 80 °, together with the stopping rate calculated using Equation 3.30, are shown in Figure 3.9. The fit of the polynomial to the calculated values is better than ± 5 % over the depth from 30 to 10000 g cm^{-2}.

Table 3.3: Coefficients for the polynomial describing the negative muon stopping rate for selected sloping surfaces at 3000 m and 30 ° latitude.

Slope (°)	***a***	***b***	***c***	***d***	***e***	***f***
76	2.5025	-0.05219	0.01603	0.005335	-0.002463	0.0001495
78	2.4870	-0.05671	0.02080	0.003624	-0.002245	0.0001404
80	2.4707	-0.06123	0.02555	0.001901	-0.002023	0.0001311
82	2.4538	-0.06573	0.03025	0.0001747	-0.001798	0.0001216
84	2.4364	-0.07026	0.03486	-0.001540	-0.001572	0.0001119
86	2.4189	-0.07494	0.03938	-0.003232	-0.001348	0.0001022
88	2.4015	-0.07996	0.04366	-0.004829	-0.001135	0.00009305

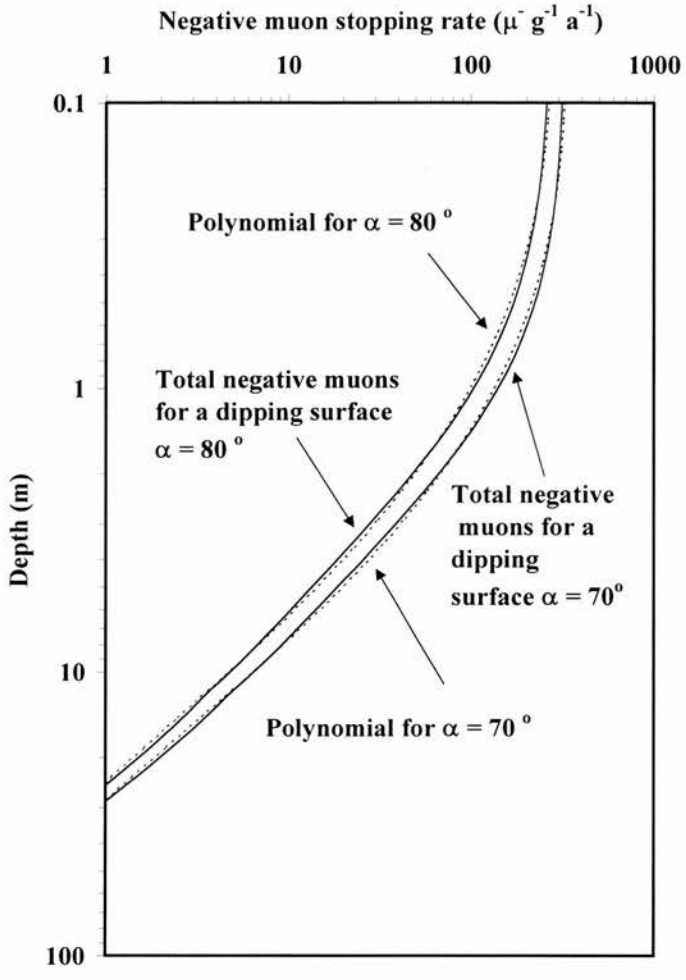

Figure 3.9: Calculated values for the total, zenith-integrated, negative muon stopping rate, using Equation 3.30, for slopes with dip angles of 70 ° and 80 ° at 3000 m altitude and 30 ° S (solid lines). The respective polynomial fits given by Equation 3.31 are also shown (shaded lines). These were used for manipulation within the denudation rate calculation (Equation 3.36). The fit is better than ± 5 %.

The treatment above addresses the impact of sloping surfaces on the negative muon stopping rate which affects production of ^{36}Cl by both negative muon capture (Equation 3.17) and neutron activation where the source of the neutron is emission following negative muon capture (Equation 3.3). Chlorine-36 can also be produced following the capture by ^{35}Cl of photoneutrons initiated by fast muons (Equation 3.4). For various reasons no correction has been made to account for the impact of the sloping surface on this production mechanism. Firstly, specifying the range of very high-energy (fast) muons has many complications (Stone *et al*, 1998a). Secondly, at sea level neutrons initiated by fast muons are produced at a rate that is an order of magnitude less than neutrons emitted following negative muon capture and two orders of magnitude less than spallogenic secondary neutron production

(Figure 3.1). This differential increases with altitude as muon reactions increase less rapidly than spallogenic reactions (Figure 2.1) and by the elevation of the sample sites (~ 3000 m), spallogenic neutron production is three orders of magnitude greater. Finally the low total Cl content of the samples means that capture by ^{35}Cl of thermal neutrons from all sources, including fast muons, contributes 2 – 5 % only to the total production rate. Ignoring the impact of the sloping face on fast neutrons will lead to an underestimate in the total number of neutrons available for capture and consequent underestimates of the total ^{36}Cl production rate and calculated denudation rate. This impact is expected to be minimal, as a 50 % increase in available neutrons leads to increases of < 1 – 5 % in both the total ^{36}Cl production rate and estimated denudation rate in these Cl-poor basalts.

3.4 INTERPRETING ^{36}Cl ABUNDANCES AS DENUDATION RATES

The abundance of *in situ*-produced ^{36}Cl is determined by AMS analysis using AgCl target pellets. AgCl is the preferred material as it readily precipitates out of solution and provides high and steady beam currents, essential for AMS (Conrad *et al*, 1986; Zreda *et al*, 1990; Stone *et al*, 1996a). The targets used in this project were produced from the whole rock basalt samples following the analytical procedures outlined in Chapter 4, and the ^{36}Cl / Cl ratios were measured by the 14-UD pelletron accelerator at ANU (Chapter 4). The AMS measures the ratio of ^{36}Cl to stable Cl and this has to be converted to an abundance of ^{36}Cl. Part of the measured ^{36}Cl abundance will be attributable to neutron capture of thermal neutrons produced by non-cosmogenic nucleogenic production involving U-fission and (α, n) reactions and this background component needs to be deducted to determine the cosmogenic ^{36}Cl concentration. This calculated concentration is then interpreted in terms of a model to yield geomorphic data.

3.4.1 DETERMINING THE ^{36}Cl CONCENTRATION FROM THE MEASURED AMS RATIO

The measured isotopic ratios were converted to an absolute concentration of ^{36}Cl in the sample material (atoms g^{-1}) by multiplying the ratios by the atomic concentration of Cl. The sample chloride concentration was determined using isotope dilution (Chapter 4). The ^{36}Cl content of analytical blanks, measured with each batch of five samples, was deducted.

3.4.2 BACKGROUND ^{36}Cl

The ^{36}Cl concentration derived above includes both a cosmogenic component and a 'background' non-cosmogenic component attributable to $P_{(\alpha, n)}$ and P_{sf}, the exact proportion of which is dependent on the U and Th concentrations in the sample. Some studies (eg Zreda *et al*, 1991) have assumed that nucleogenic ^{36}Cl is negligible. Whilst this might be a safe assumption for samples with low abundances of U and Th which have large concentrations of cosmogenic ^{36}Cl (due to a long irradiation history as might be encountered in samples with low denudation rates), it, nevertheless, introduces a further source of potential error. Failure to correct for this contribution would lead to an underestimation of the denudation rates.

The background ^{36}Cl of the samples in this study was determined from measured U and Th concentrations (Appendix 4) and derived from the following equation:

$$^{36}Cl_{background} = \frac{(P_{sf} + P_{(\alpha,n),U} + P_{(\alpha,n),Th}) * f_{35}}{\lambda} \qquad \text{Equation 3.32}$$

P_{sf} and $P_{(\alpha, n)}$ were calculated using Equations 3.5 and 3.6. The total ^{36}Cl contribution derived from capture of such nucleogenic neutrons is shown in Tables 6.6 and 7.6. In all samples there are very low background levels of ^{36}Cl, less than 0.1% of the cosmogenic ^{36}Cl even in the samples with the highest denudation rates (and thus lowest total ^{36}Cl content).

3.4.3 PRODUCTION RATES

Site-specific surface production rates were determined, in the case of spallation and negative muon capture reactions, from the measured concentration of the relevant target nuclei and the calibrated rates of Stone *et al* (1996a, 1998a) and Evans *et al* (1997), scaled for altitude, latitude and sloping surface, as appropriate. Surface production by thermal neutron activation was calculated from the measured elemental composition of the sample. The overall ^{36}Cl production rate in the basalts used for this study is given by the sum of the reactions discussed in Section 3.2. Based on the depth-dependence of each of the production mechanisms (Equations 2.2, 3.12, and 3.17) the following expression is derived for the total ^{36}Cl production rate at a depth z beneath a flat-lying surface:

$$P_{total}(z) = P_{sp}(0)[Ca]e^{-z/\Lambda_{sp}} + P_{sp}(0)[K]e^{-z/\Lambda_{sp}} + \frac{f_{35}}{\Lambda_{th,ss}}(\Phi_{ss})$$

$$+ \frac{f_{39}}{\Lambda_{th,ss}}(\Phi_{ss}) + Y_{Ca}\psi_{\mu^-}(z) + Y_K\psi_{\mu^-}(z) \qquad \text{Equation 3.33}$$

All symbols are as defined in previous Equations (2.2, 3.12 and 3.17). Figure 3.10 shows the ^{36}Cl production rate profile, based on Equation 3.33, for a flat-lying Drakensberg Group basalt as a function of depth (0- 2800 g cm^{-2}). Whilst Figure 3.4 highlighted the depth-dependent production profiles for sea level and high latitude, the basalt samples used in this project have higher ^{36}Cl production rates attributable to the high altitude of the samples (~ 2500 – 3300 m asl). For Figure 3.10 the production rates have been scaled to reflect an

altitude of 3000 m asl and a latitude of 30° south (roughly similar to Sani Pass), using the scaling procedure for spallation and muon production outlined in Chapter 2. Scaling for neutron activation production assumes that 90 % of the thermal neutrons have a spallogenic origin and 10 % are due to muon induced reactions. Due to the 3000 m altitude of the site there has been an overall enhancement of the production rate when compared to Figure 3.4, however, $P_{\mu\text{-},Ca}$ and $P_{\mu\text{-},K}$ contribute less to the P_{total} in Figure 3.10. This is because muon production diminishes relative to production by fast nucleons with increasing altitude (Stone *et al*, 1996a; Figure 2.1).

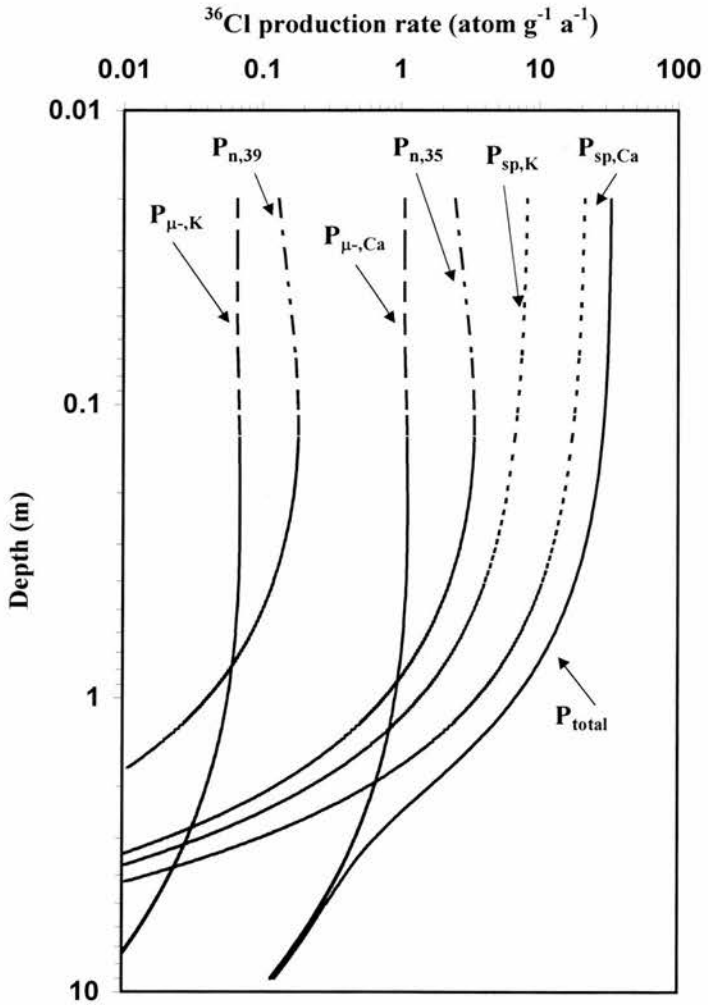

Figure 3.10: ^{36}Cl production with depth for a flat-lying Drakensberg Group basalt (9.30 wt % CaO; 0.88 wt % K_2O; 15 ppm Cl) scaled for Sani Pass (3000 m, 30° S) using the scaling procedures of Lal (1991) and Equation 2.1. $P_{n,35}$ and $P_{n,39}$ scaled assuming 90 % spallogenic secondary neutrons and 10 % muon-induced neutrons. Note that the muon reactions account for only 3% of the total surface production rate as compared to 8% in Figure 3.4. This is due to the longer attenuation length of muons in the atmosphere (Lal, 1991).

3.4.4 MODELLED DENUDATION RATES

Like the other *in situ*-produced cosmogenic isotopes, the measured abundances of cosmogenic ^{36}Cl have been interpreted, to date, as either modelled surface exposure ages or denudation rates (Table 3.1). Calculation of a modelled denudation rate is complicated by the multiple production pathways for ^{36}Cl which mean the denudation rate model outlined in Chapter 2 is too simplistic. The modelled denudation calculation in Equation 2.8 is based on the sub-surface exponential production profile for spallation, but, as discussed in this chapter, ^{36}Cl is in part produced by neutron and muon capture reactions which have non-exponential sub-surface production profiles (Figures 3.2, 3.3). Ignoring neutron activation and muon production lead to large errors in denudation rate estimates (Liu *et al*, 1994a; Stone *et al*, 1998a). Modelled denudation rate calculations for ^{36}Cl abundances, therefore, have to include these non-exponential production profiles.

Where a surface has been exposed for a sufficient period of time for secular equilibrium to have been achieved (Figure 2.5), the abundance of *in situ*-produced cosmogenic ^{36}Cl is a complex function of the depth-dependent rate of production by each mechanism (Figure 3.10), the rate of radioactive decay and the 'steady-state' rate of denudation. The steady-state ^{36}Cl concentration at a depth, z (g cm^{-2}), beneath a surface which is denuding at a rate, ε, is given by (Stone *et al*, 1998a, equation 11):

$$N_{total}(z,\varepsilon) = \int_0^\infty P(z+\rho\varepsilon t)e^{-\lambda t}\,dt \qquad \text{Equation 3.33}$$

where P is the production rate, ρ is the density, t is time and λ is the decay constant, all as before.

The production rate, $P(z + \rho \varepsilon t)$ can be divided into its constituent reactions for ^{36}Cl production (Equation 3.33, Figure 3.10) and each integrated to provide a steady-state contribution to the concentration at depth z:

$$N_{total}(z,\varepsilon) = \frac{\left(P_{sp}(0)[Ca] + P_{sp}(0)[K]\right)e^{-z/\Lambda_{sp}}}{\left(\lambda + \rho\varepsilon/\Lambda_{sp}\right)}$$
$$+ \frac{f_{35}}{\Lambda_{th,ss}}\left(\frac{\Phi^*_{ss}e^{-z/\Lambda_{sp}}}{\left(\lambda + \rho\varepsilon/\Lambda_{sp}\right)} + \frac{F\Delta\Phi^* e^{-z/L_{ss}}}{\left(\lambda + \rho\varepsilon/L_{ss}\right)}\right) \qquad \text{Equation 3.35}$$
$$+ \frac{f_{39}}{\Lambda_{th,ss}}\left(\frac{\Phi^*_{ss}e^{-z/\Lambda_{sp}}}{\left(\lambda + \rho\varepsilon/\Lambda_{sp}\right)} + \frac{F\Delta\Phi^* e^{-z/L_{ss}}}{\left(\lambda + \rho\varepsilon/L_{ss}\right)}\right)$$
$$+ \left(Y_{Ca} + Y_K + \left(Y_s f_{35}\right)\right)\int_0^\infty \psi_{\mu^-}(z + \rho\varepsilon t)e^{-\lambda t}\,dt$$

Equation 3.35 simplifies in the case of the concentration at the surface, N_{36} to the following:

$$N_{36} = \frac{P_{sp,Ca} + P_{sp,K}}{\left(\lambda + \rho\varepsilon/\Lambda_{sp}\right)} + \frac{f_{35}}{\Lambda_{th,ss}}\left(\frac{\Phi^*_{ss}}{\left(\lambda + \rho\varepsilon/\Lambda_{sp}\right)} + \frac{F\Delta\Phi^*}{\left(\lambda + \rho\varepsilon/L_{ss}\right)}\right)$$
$$+ \frac{f_{39}}{\Lambda_{th,ss}}\left(\frac{\Phi^*_{ss}}{\left(\lambda + \rho\varepsilon/\Lambda_{sp}\right)} + \frac{F\Delta\Phi^*}{\left(\lambda + \rho\varepsilon/L_{ss}\right)}\right)$$
$$+ \left(Y_{Ca} + Y_K + \left(Y_s f_{35}\right)\right)\int_0^\infty \psi_{\mu^-}(z + \rho\varepsilon t)e^{-\lambda t}\,dt \qquad \text{Equation 3.36}$$

The first part of Equation 3.36 is the same as Equation 2.8, rearranged for N. The second and third parts relate to thermal neutron production involving capture by ^{35}Cl and ^{39}K and are in similar terms to that derived by Liu *et al* (1994a, equation 26) for neutron capture by ^{35}Cl only. The final part relates to negative muon capture and is similar to part of Stone *et al*'s (1998a) equation 12.

If there is no denudation then, for a typical flat-lying surface formed of Drakensberg Group basalts (Figure 3.10), the contribution from muon reactions is only ~ 3 % of the total surface production rate. However, with denudation the relative muon contribution increases as a result of the longer attenuation length for muons in the subsurface compared with both spallogenic and thermal neutron reactions (Figure 3.10). This longer attenuation length

effectively decreases the sensitivity of negative muon reaction produced ^{36}Cl to denudation. This decreased sensitivity results in higher surface concentrations, N_{36}, for a given denudation rate than would result from spallation and / or thermal neutron capture alone and therefore if muon production was ignored, interpretation of a given N_{36} value would underestimate the denudation rate (Stone *et al*, 1998a). Hence the contribution from muon production, P_{μ}-, to N_{36} is a function of the denudation rate, such that the higher the denudation rate, the greater the contribution derived from muon reactions. In this project this was dealt with by calculating the denudation rate in two stages. Firstly, an estimate of the denudation rate was derived by solving Equation 3.36, less the final part relating to muon production, for ε. This first estimate of the denudation rate was then used to fix the limits of integration for the muon flux received by the sample, such that the final term in Equation 3.36 was integrated over sufficient time to allow ~ 30 m of denudation to occur. The whole of Equation 3.36, was then solved iteratively, with the new value of ε being taken as the final denudation rate.

The denudation rate derived using Equation 3.36 is for a 'steady-state' denudation rate, which, as defined by Nishiizumi *et al*, (1991), means the continuous removal of rock of thickness' smaller than Λ_{sp} / ρ. The premiss' which underpin Lal's model (1991) (Equation 2.8) apply equally to the model presented in Equation 3.36. The applicability of these assumptions to the denudation rates calculated in this thesis is discussed in Chapter 8.

Due to the complex nature of the production pathways and the modelled denudation rate calculation for abundances of ^{36}Cl in whole rock samples, computations are best made using a computer program. The computations in this thesis were made using a program written in *Mathematica* ® originally by Dr John Stone, University of Washington, Seattle and subsequently modifed by this author to reflect the particular circumstances (eg free face settings) of the samples used for this thesis (other programs exist eg 'CHLOE', Phillips and Plummer, 1996). This program covers all the production mechanisms outlined in this Chapter and calculates denudation rates using Equation 3.36. A paper copy of the *Mathematica* ® program used for determining the 'steady-state' denudation rate for samples from free face surfaces forms Appendix 8.

3.5 Conclusions

In situ cosmogenic ^{36}Cl is produced in three types of reaction - spallation, neutron activation and negative muon capture - each of which has a different depth-dependent production

profile. In whole rock basalt, the contribution of each mechanism to the total production rate depends on the relative concentrations of the target nuclei, Ca, K and Cl, and is therefore unique for each sample. Production by neutron activation and muons must be taken into account to derive accurate denudation estimates from measured ^{36}Cl abundances (Liu *et al*, 1994a; Stone *et al*, 1998a). Production on and beneath sloping surfaces is more complex and allowance has to be made for obstruction by the inclined surface and a reduction of the effective cosmic ray attenuation length perpendicular to the steep face. Corrections have been suggested for spallation, neutron activation and muon capture. The existence of these multiple production pathways mean estimated denudation rates have to be derived using a model that is more complex than Equation 2.8. The model presented in Equation 3.36 takes account of spallogenic production that declines exponentially with depth as well as the non-exponential production profiles of neutron and muon reactions.

CHAPTER 4: *IN SITU*-PRODUCED CHLORINE-36: EXPERIMENTAL PROCEDURES

4.1 INTRODUCTION

This research involves the determination of denudation rates based on the analysis of *in situ*-produced cosmogenic ^{36}Cl in whole rock basalt. Various experimental procedures were used and these are outlined in this chapter. The first section considers aspects of field sampling. These considerations are not exclusive to this project and would apply equally to a study using any of the other commonly employed cosmogenic isotopes (see Table 2.2). Once collected each sample was subject to various procedures leading to the chemical extraction and eventual measurement of ^{36}Cl. These steps are discussed in the second section, analytical procedures. Unlike other cosmogenic isotopes, such as ^{10}Be and ^{26}Al, the interpretation of ^{36}Cl abundances requires various additional measurements which are considered under ancillary chemical analyses.

In all four separate procedures involving six measurements techniques were required to both measure and interpret the ^{36}Cl yield of the whole rock basalt samples used in this study (Table 4.1). Isotopic ratios were measured using accelerator mass spectrometry (AMS). Total chlorine (Cl) content was determined by isotope dilution (ID) and mass spectrometry (MS). Major element concentrations were obtained by X-ray fluorescence spectrometry (XRF). The concentration of the thermal neutron capture competitors, lithium (Li), chromium (Cr), gadolinium (Gd) and samarium (Sm), together with the thorium (Th) and uranium (U) concentrations (necessary for calculation of the radiogenic ^{36}Cl component), were determined by inductively coupled plasma mass spectrometry (ICP-MS). The content of another thermal neutron capture competitor, boron (B), was determined using both inductively coupled plasma atomic emission spectrometry (ICP-AES) and prompt gamma neutron activation analysis (prompt gamma NAA).

4.2 FIELD PROCEDURES

The site-specific nature of the production rate and the corresponding uniqueness of each sample make the identification and collection of appropriate samples in the field perhaps the most important issue in cosmogenic isotope analysis. Each sample has therefore to be chosen

with care bearing in mind the nature of the geomorphic problem being addressed and the need for the sample to characterise the relevant event or process (Cerling and Craig, 1994a). Sample collection should, ideally, target the key landscape elements from which broader inferences can be drawn (Fleming *et al*, 1999). The exact strategy and the number of samples are determined by the nature of the project, the availability of appropriate (*sensu* technique) samples, and analytical costs.

Table 4.1: Measurements required for interpretation of ^{36}Cl in whole rock samples.

Element	Measurement technique	Instrument location
^{36}Cl	AMS	14-UD pelletron accelerator, ANU.
whole rock Cl	MS	14-UD pelletron accelerator, ANU.
major elements	XRF	Geology and Geophysics, Edinburgh.
Li, Cr, Sm, Gd, U and Th	ICP-MS	NERC Facility, Imperial College.
B	ICP-AES and prompt gamma NAA	XRAL Laboratories, Ontario.

The sampling strategy for this project had to overcome the inherent problem of constraining the denudation and retreat rate for a large morphological feature. To achieve this certain key areas along the southern section of the Drakensberg – Naudesnek, Ongeluk's Nek and Sani Pass – and the Lesotho Highlands (Figure 6.1) were targeted, and in each area samples were taken from the most representative geomorphological features. In total over 80 samples were collected from exposed, intact, bedrock at geomorphologically well constrained sites which appeared to have simple exposure histories, to have been undergoing prolonged, continuous, denudation, and which were unlikely to have been subject to protracted burial by soil, snow or falling detritus. Detailed descriptions of the individual sites can be found in Chapters 6 and 7. Once selected, samples of between 5 and 10 cm thickness were removed using a hammer and chisel. Sample size varied from site to site according to the likely isotopic concentration (higher denudation rates reduce this yield) with on average ~2 kg being removed at each location.

To calculate the site-specific production rate, and to interpret the measured ^{36}Cl yield as a denudation rate estimate, various field data were recorded at each site:

Geographical position	Fixed using a combination of digital GPS readings and co-ordinates from 1:50 000 scale maps.
Altitude	Measured using a digital altimeter, calibrated each day at a site of known elevation determined from 1: 50 000 scale maps.
Sample surface dip and orientation	Determined using a compass and Abney level.
Local topographic shielding	Assessed using a compass (to determine sector width) and an Abney level (to measure angle to local horizon).
Geomorphological situation	Recorded using a combination of notes, sketches and photographs.

4.3 ANALYTICAL PROCEDURES

Chlorine-36 may be analysed using either a mineral separate such as calcite (eg Stone *et al*, 1994) or in whole rock samples (eg Zreda *et al*, 1999). This is in contrast to other commonly used cosmogenic isotopes, such as ^{10}Be and ^{26}Al, which are analysed using a mono-minerallic separate, eg quartz (Kohl and Nishiizumi, 1992). The nature of the Drakensberg and Lesotho Highlands basalt meant that only whole rock ^{36}Cl analysis would be appropriate for this project. Stone *et al* (1996a) present a method, developed from Conrad *et al* (1986) for the extraction of ^{36}Cl from silicate rocks in the form of silver chloride (AgCl), and this method has been used here. The various stages of the sample preparation are shown in Figure 4.1.

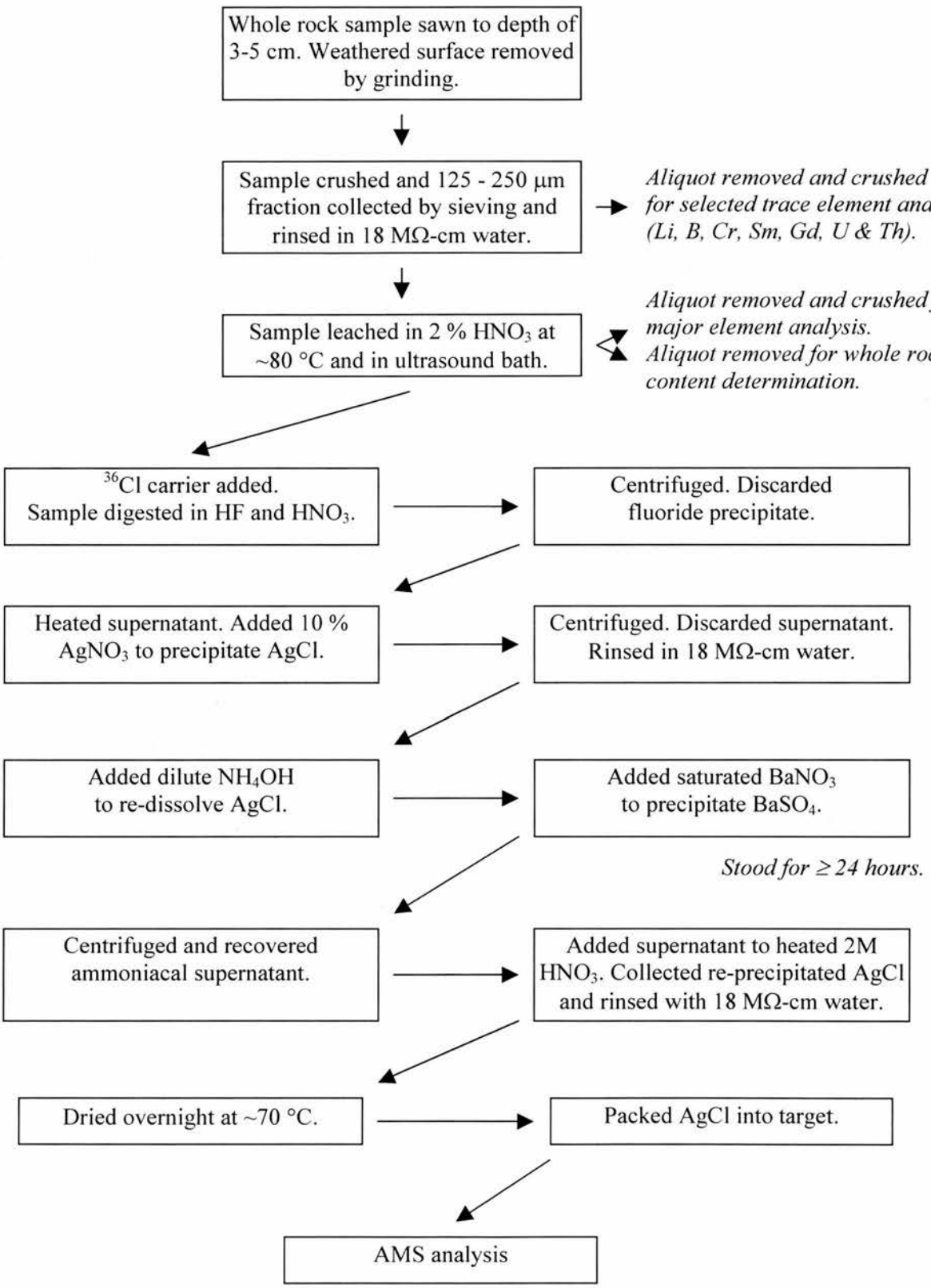

Figure 4.1: Flow chart highlighting the stages involved in the extraction and recovery of ^{36}Cl from whole silicate rock samples used in this project.

4.3.1 SAMPLE PRE-TREATMENT

4.3.1.1 SAWING

Given the depth-dependent nature of cosmogenic isotope production (see Chapter 2 and 3 on mechanisms of production), it is important to know the depth of the sample below the surface to within ~ 10 mm. This was determined by removing part of the underside of the sample by sawing and measuring the resultant thickness of the sample. In addition any weathering rinds and other surface contaminants (eg lichen and other organic material) were removed by grinding, noting the depth removed. This weathering zone acts to trap atmospherically produced ^{36}Cl, introduced to the surface by precipitation. In addition, during the weathering processes, minerals within this zone, which may have produced ^{36}Cl, may have been altered leading to the production of 'open system chlorine' (J. Stone, pers. comm.). Inclusion of this 'open system' component would produce an erroneous *in situ*-produced ^{36}Cl yield.

4.3.1.2 CRUSHING

The sawn samples were dried overnight in an oven at ~ 70 °C and then crushed to yield 250 - 125 μm size material which was collected by hand sieving. This size fraction eliminates composite grains in fine-grained basalts (mean grain size < 1 mm) and ensures that individual grains are exposed for subsequent acid leaching. Fragments > 250 μm were re-crushed until at least 100 g was collected. Cross-contamination between samples was avoided by thoroughly cleaning and washing the crushing equipment and sieve sets between each sample. The 250 - 125 μm size fraction was rinsed in ultra-pure water (resistivity = 18.2 MΩ-cm) to remove fines and oven dried in open beakers at < 70 °C. A 20 g aliquot of the 250 - 125 μm size fraction, used to prepare samples for determination of the Li, B, Cr, Sm, Gd, U and Th content, was ground to fine powder using a gyro-mill. Again, to avoid contamination, the grinding barrels were thoroughly washed before using and between samples.

4.3.1.3 LEACHING

The atmospheric production of ^{36}Cl is at least an order of magnitude higher than terrestrial production (atmosphere: $3.5 - 6.5 \times 10^4$ atoms ^{36}Cl cm^{-2} a^{-1}, Lal and Peters, 1967; Roth, 1989; *in situ*-production in calcite: 48.8 atoms (g Ca)$^{-1}$ a^{-1}, Stone *et al*, 1996a). This atmospherically produced ^{36}Cl, together with stable chloride in the atmosphere, accumulates

at the ground surface due to precipitation and settling of airborne particles. Inclusion of this meteoric component would produce an erroneous *in situ*-produced ^{36}Cl yield and correspondingly inaccurate denudation rate. If the meteoric component is ^{36}Cl rich, a lower denudation rate would be calculated. If the atmospheric contamination increased the apparent chloride content of the rock erroneously high denudation rates would result. The hydrophilic nature of chloride, coupled with the extensive use of ^{36}Cl as a groundwater tracer suggests that the atmospheric ^{36}Cl and chloride are likely to be easily removed from grain surfaces (Stone *et al*, 1996a).

The meteoric component (which generally adheres to any weathering pits and cracks on the grain's surface) was removed by etching the surface of each grain in a weak (2%) nitric acid solution. Each sample was leached a minimum of three times. The first two involved leaching ~ 80 g of sample in hot (80 – 90 °C) 2 % HNO_3 for 4 – 6 hours. After each leach, the sample was thoroughly rinsed in ultra-pure water, oven dried at ~ 70°C and weighed to calculate the loss on leaching. Due to the weathered nature of the samples (reflecting the length of exposure), the third leach involved placing a beaker containing the sample and HNO_3 in an ultrasound bath for 2 hours at ~ 70 °C. The impact of this leaching step was assessed by determining the loss on ignition (an indication of the level of weathering and hence possibility of trapping meteoric Cl) before and after this leaching stage for 12 samples. The average percentage difference before and after the ultrasound leach was 33 %, indicating that the ultrasound leach was more efficient at etching the grain surface. If after the third leach a large quantity of fine material was still being produced by the sample a fourth ultrasound leach was carried out. Typical yields for successive stages in the leaching process are shown in Figure 4.2.

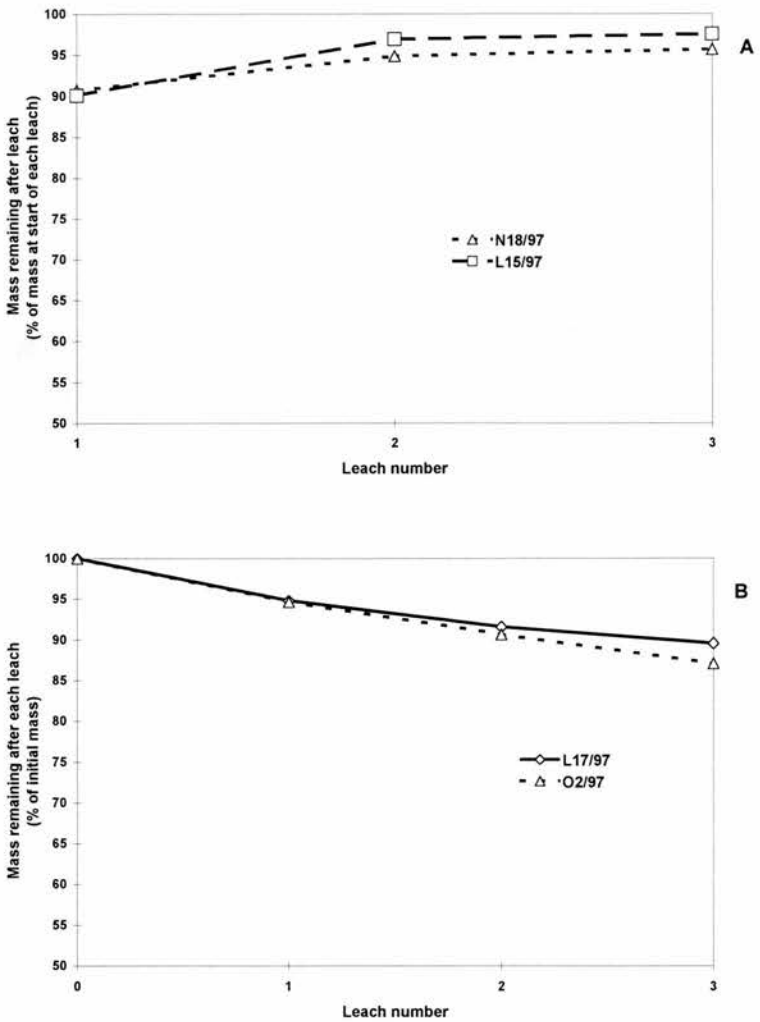

Figure 4.2: Mass remaining after each successive leach for typical samples expressed as a percentage of (A) the mass at the start of the respective leach and (B) the initial sample mass.

4.3.2 CHLORIDE EXTRACTION

4.3.2.1 CONTAMINATION

Four sources of Cl contamination need to be considered when extracting Cl - meteoric; laboratory; analytical reagents; and anthropogenic. Atmospheric Cl may be introduced following its attachment to airborne particles in the laboratory and the subsequent settling of those particles into uncovered samples. Cl produced by other laboratory preparations which regularly use HCl, such as ^{10}Be and ^{26}Al preparation, can, due to the solubility of Cl, contaminate exposed wet samples. To limit these sources of contamination, all of the samples collected during the 1997 field season were prepared in the new dedicated ^{36}Cl clean room laboratory in the Department of Geography. This laboratory is positively pressured

with HEPA filtered air which reduces airborne particulate matter. The air is drawn from another part of the building, away from laboratory sources of Cl. Overshoes and protective clothing reduce the ingress of contamination with the analyst. The reagents used in the wet chemistry potentially introduce trace concentration of Cl. To limit this source, reagents were chosen which contained only very low ppm concentrations of Cl and only ultra-pure water was used. To avoid anthropogenic Cl (bodily fluids typically have a ^{36}Cl / Cl ratio of ~ 50 x 10^{-15}, R. Cresswell, pers. comm.) gloves were always worn and care taken to avoid coughing or sneezing near samples.

To monitor the level of Cl introduced during the chemical procedure, a complete procedural blank was run alongside each batch of 5 samples. The Cl content of the blank was deducted in the data reduction program. Eighteen blanks were run during this project, producing an average $2.22 \pm 0.35 \times 10^4$ atoms ^{36}Cl and ranging from $4.87 \pm 7.30 \times 10^3$ to $5.65 \pm 1.72 \times 10^4$ atoms. The uncertainties in the blank measurements are high as the ^{36}Cl / Cl blank ratios were very close to the lowest limit of detection of the ANU AMS (~1 x 10^{-15}, K. Fifield, pers. comm.) when counting statistics dominate the measurement uncertainty (Stone *et al*, 1996a).

4.3.2.2 SAMPLE DIGESTION

The mass of whole rock dissolved during the extraction process depended on the anticipated ^{36}Cl concentration. Samples exposed for long periods, indicating low denudation rates, will yield a higher ^{36}Cl concentration than those from sites of higher denudation rates. Typically 10 – 12 g of the leached 250 - 125 μm size material was used for samples from sites used to assess the rate of downwearing, while 15 – 19 g was used for free face sites (Tables 6.5, 7.5).

Weighed samples were loaded into 500 ml FEP Teflon® bottles. To increase the final silver chloride (Ag Cl) precipitation and to decrease the propagation of the whole rock Cl concentration measurement errors into the calculation of ^{36}Cl concentrations, ~ 1 mg of ^{36}Cl-free chloride carrier was added (Stone *et al*, 1994, 1996a; Evans *et al*, 1997). The accuracy of the whole rock Cl measurement affects both the ^{36}Cl estimate and the estimate of the ^{36}Cl production rate (because of the existence of the ^{35}Cl (n, γ) ^{36}Cl reaction).

For example, underestimating the whole rock Cl concentration leads to the ^{36}Cl abundance being underestimated (Section 3.4.1), but this is partly compensated in the denudation rate calculation by a corresponding reduction in the contribution of the ^{36}Cl production rate due to the ^{35}Cl reaction to total ^{36}Cl production (Equation 3.36). To reduce such error completely, sufficient carrier would need to be added such that:

$$ratio\left(\frac{Cl_{carrier}}{Cl_{rock}}\right) = ratio\left(\frac{P_{Ca,K}}{P_{Cl-35}}\right) \qquad \text{Equation 4.1}$$

where, $Cl_{carrier}$ and Cl_{rock} are, respectively, the Cl content of the carrier and the whole rock. $P_{Ca,K}$ and P_{Cl-35} are the production rates due to Ca, K and ^{35}Cl respectively. In this situation compensation for the error in the whole rock Cl is exact as the rock Cl measurement error propagates equally into the calculation of the ^{36}Cl concentration and the ^{36}Cl production rate. Generally the quantity of carrier required to achieve this ratio would suppress the ^{36}Cl / Cl ratio too much for AMS measurement. The addition of ~ 1.5 mg to ~ 10 – 19 g of rock reduces the error sufficiently without suppressing the ^{36}Cl / Cl ratio (Stone *et al*, 1996a; J. Stone pers. comm.).

Hydrofluoric acid is the only acid that will readily dissolve silicate material, however, as some salts (eg those of calcium and potassium) do not have high solubilities in this acid it is commonly mixed with nitric acid (Potts, 1987). The basalt samples in this study were therefore digested in a mineral acid mix comprising 6 ml 2M HNO_3 and 3.5 ml conc. HF for each gram of sample. Dissolution was achieved in 2 – 3 days at ~ 70 - 80 °C, with the samples being swirled periodically to prevent the fluorides from caking together and coating undissolved sample grains. Digestion was complete when no grains were visible in the solution or fluoride paste. Occasionally a very small number (<< 1 %) of black coloured grains were present. These were assumed to be iron / titanium oxides such as rutile (TiO_2), ilmenite ($FeTiO_3$), chromite ($FeCr_2O_4$) and magnetite (Fe_3O_4) which are particularly resistant to acid attack (Potts, 1987; J. Stone pers. comm.).

4.3.2.3 Chloride recovery

Chloride was recovered from the sample solutions as AgCl. The supernatant was separated from the fluoride precipitate by centrifuging in 50 ml batches. After dissolution and homogenization with the Cl carrier it was assumed that the isotopic ratio of the Cl in the sample and the Cl carrier was fixed and that no mass fractionation occurred throughout the

remainder of the chemical procedures. Failure to achieve 100 % recovery of the chloride therefore did not affect the final ratio measured by the AMS. The acidic supernatant was heated in 250 ml PFA Teflon® beakers before the addition of ~1 ml of 10 % $AgNO_3$ solution. The beakers were left on the hotplate for a further hour to enable the AgCl to fully flocculate before being cooled and left overnight to allow the AgCl precipitate to settle. Recovery of the precipitate was undertaken in subdued lighting and involved centrifuging with several rinses of ultra-pure water to remove all trace of the acidic solution.

Ag_2SO_4 co-precipitated with the AgCl. Removal of sulphur is essential due to the interference of isobaric ^{36}S with ^{36}Cl in AMS measurements (Stone *et al*, 1996a, Fifield, 1999). The AgCl was re-dissolved in dilute NH_4OH and transferred to a 50 ml borosilicate glass centrifuge tube. Some (~1 ml) of saturated barium nitrate solution was added and the sample solution left for at least 24 hours, normally 2 to 4 days. The $BaSO_4$ precipitated as translucent to white fine crystals on the wall of the tube. After centrifuging to concentrate this precipitate, the supernatant was withdrawn from beneath the meniscus and the AgCl re-precipitated by adding this ammoniacal supernatant to a hot acidic solution. Approximately 2 - 3 ml of solution was left to avoid disturbing the precipitate and thereby carrying the $BaSO_4$ into the final AgCl precipitate. Due to the use of the Cl Carrier, sacrificing ~ 5 - 10 % of the sample chloride in this way did not affect the AMS measured ratio.

The final AgCl was recovered in the same manner as the initial AgCl precipitate. The AgCl pellet was centrifuged and rinsed in ultra-pure water twice. The pellet was then dried overnight at 60 - 70 °C. To avoid photolytic decomposition of AgCl, the tube containing the dried sample was wrapped in aluminium foil and stored in a dark cupboard until posted to ANU for measurement. Typical yields for AMS analysis ranged from 2 - 4 mg AgCl.

4.3.3 Isotopic analysis

All samples were packed into targets and measured, by K. Fifield and R. Cresswell, using the 14-UD pelletron accelerator at ANU (Fifield *et al*, 1990, 1994). Measurements were made on ~ 1 – 2 mg of AgCl which was embedded under pressure in a substrate of high-purity, low sulphur, AgBr. This lining reduces the ^{36}S count by preventing the caesium (Cs) beam of the sputter source from striking the copper sample holders (Fifield *et al*, 1990, 1994; Fifield, 1999). Great care was taken to avoid contamination during the loading phase by cleaning all packing equipment (tweezers, spatulas, pliers etc.) in ethanol (R. Cresswell, pers. comm.).

The AMS technique is explained in Section 2.2.6. The ANU accelerator uses a Cs sputter source, MC-SNICS (multi-cathode source of negative ions by Cs sputtering), to bombard the target material and create a beam of Cl^- ions. Typical negative ion beam currents are 20 μA for Cl^- (K. Fifield, pers. comm.). Chlorine-36 is transmitted at a terminal voltage of 14 MV, and detected at 154 MeV in the 10^+ charge state. Counting times for the samples were 10 - 20 minutes depending on the ratio. Background ratios for ^{36}Cl are, currently, typically below 1×10^{-15} (K. Fifield, pers. comm.). Measurement of the ^{36}Cl / Cl ratio at ANU is possible without reference to a standard due to the ability to transport the stable ^{35}Cl and ^{37}Cl beams to a Faraday cup immediately in front of the ^{36}Cl detector (Fifield *et al* , 1990, 1994). Isotopic ratios are therefore calculated directly from ion counts and integration of the stable isotope currents without re-course to normalisation, although a working standard is run in every 32 sample wheel batch.

4.3.4 WHOLE ROCK CHLORIDE CONCENTRATION

To determine both the ^{36}Cl concentration and the production rate from reactions involving ^{35}Cl it is necessary to know the total Cl content. Various methods for estimating the chloride concentration in silicates including ion-selective electrodes, pyrohydrolysis, and ion chromatography (Potts, 1987) have been employed in past ^{36}Cl studies (eg Zreda *et al*, 1990; Ivy-Ochs, 1996; Stone *et al*, 1996a). These standard methods tend to be complex, time consuming or lack adequate levels of selectivity and sensitivity (Potts, 1987) and, for these reasons, a higher precision isotope dilution (ID) method has been developed which involves the addition of a spike which has been artificially enriched in ^{37}Cl (J. Stone, pers. comm.).

ID is widely recognised as one of the most precise and sensitive analytical methods for accurate concentration determinations (Faure, 1986; Potts, 1987; Dickin, 1995). ID has been widely used, for example, in determining the Rb content for the Rb – Sr dating method, but can be applied to all elements which have two or more naturally occurring isotopes. The underlying principle of the technique is straight-forward and involves mixing a known weight of rock sample with a spike consisting of a precisely known amount of the element artificially enriched in one of those naturally occurring isotopes.

Following dissolution and homogenization the element of interest is chemically separated and the isotopic composition of the isolated element is analysed by mass spectrometry. The measured ratio of the spiked mass peak and an unspiked, naturally occurring, isotope is then used to calculate the concentration of the element in the sample using an equation in the following form (Faure, 1986; Potts, 1987; Dickin, 1995):

$$\frac{{}^{A}E/{}_{B}E_{meas.} - {}^{A}E/{}_{B}E_{spike}}{{}^{A}E/{}_{B}E_{natural} - {}^{A}E/{}_{B}E_{meas.}} = \frac{W_{sample} \times {}^{B}E_{sample}}{W_{spike} \times {}^{B}E_{spike}} \qquad \text{Equation 4.2}$$

where, ${}^{A}E$ and ${}^{B}E$ are, respectively, the isotopes A and B of element E. ${}^{A}E/{}^{B}E_{meas.}$ is the measured ratio of the two isotopes in the analysed sample, ${}^{A}E/{}^{B}E_{spike}$ is the pre-calibrated ratio of these isotopes in the spike and ${}^{A}E/{}^{B}E_{natural}$ is the known natural ratio of these isotopes. W_{sample} and W_{spike} are, respectively, the weights of the analysed sample and the spike added thereto. The equation is rearranged to determine ${}^{B}E_{sample}$ and then converted, using the known natural ratio of the two isotopes, into the concentration (ppm) of element E in the sample. Critical to this determination is the need to calculate, independently, the concentration and isotopic composition of the spike solution and ensure complete homogenization between the spike and the natural element.

For this project a spike solution containing 57.517 µg/g Cl (6.16 % ^{35}Cl : 93.84 % ^{37}Cl) was made up using ^{37}Cl isotopically enriched NaCl (obtained from Oak Ridge National Laboratories, USA) and ultra-pure water. The Cl concentration in the spike solution was initially calculated gravimetrically, and then, more accurately determined by isotope dilution using the natural ^{35}Cl / ^{37}Cl ratio (75.77 / 24.23) in the Weeks Island halite solution used as the carrier in the ^{36}Cl chemistry. The isotopically enriched NaCl was certified as having a ratio of 6.34 % ^{35}Cl : 93.66 % ^{37}Cl, but this was assessed independently using mass spectrometry as being 6.16 % ^{35}Cl : 93.84 % ^{37}Cl. This latter ratio was used in preference to the certified ratio.

For optimum analysis the ratio of ^{35}Cl / ^{37}Cl in the sample / spike mixture should be close to unity. If the ratio deviates from this by a factor of 10 or more errors in analytical measurement are magnified (Faure, 1986; Potts, 1987). When dealing with low Cl content samples such as those found in this study it is difficult to achieve unity without using large (>1 g) samples which create dissolution and recovery problems (J. Stone, pers. comm.).

Given that the importance of accurate Cl determination reduces with decreasing Cl concentration and that error propagation is less severe for over spiked samples (ie where the ^{35}Cl / ^{37}Cl ratio in the mixture is < 1) (J. Stone, pers. comm.), approximately 0.5 ml of spike solution was added to ~1 g aliquots of sample. These aliquots were taken from the same leached material as used for the ^{36}Cl determination (leaching procedures remove atmospheric Cl contamination which would affect the Cl measurements - Stone *et al*, 1996a). To bulk up the final precipitate for mass spectrometry, ~ 0.25 ml of NaBr solution (2.0093 mg/g Br) was also added at this stage.

The subsamples were dissolved in a mixture of ~ 0.5 ml 2M HNO_3 and ~ 5.5 ml conc. HF in a capped 14 ml Teflon® jar at a temperature of ~ 60 °C. After complete digestion the fluoride residue was separated from the solution by centrifuging at ~ 2500 rpm for ~ 10 minutes. The supernatant was heated before ~ 0.5 ml 10% $AgNO_3$ solution was added to precipitate AgCl and AgBr. The vials were cooled before being capped and left overnight. The silver halide precipitate was collected by centrifuging and rinsed twice with ultra-pure water before being dried overnight in an oven at ~ 60-70 °C. When dry the centrifuge tube containing each sample was capped and wrapped in aluminium foil to prevent photolytic decomposition of AgCl. Typical yields ranged from 0.2 - 0.9 mg Ag halide.

The ^{35}Cl / ^{37}Cl ratio of the AgCl pellet was measured, by K. Fifield and R. Cresswell, using the ion source and the mass analysing magnet of the 14-UD pelletron accelerator at ANU. The currents of the two isotopes were measured in a Faraday cup above the accelerator (ie without the ion beam being injected into the actual accelerator) (K. Fifield, pers. comm.). Use of the 'front end' of the accelerator as a normal mass spectrometer was easier than running the analyses in a conventional mass spectrometer as Cl prefers to make negative ions and the ANU AMS ion source produces these prolifically (K. Fifield, pers. comm.).

Typically the ^{35}Cl / ^{37}Cl ratio of a sample was measured 10 times producing a scatter of ratios as illustrated in Figure 4.3A. This scatter should be random and within ± 1 % of the mean ratio. This was the case for about 50 % of the samples and here the mean of the measured ratios was used to calculate the total Cl content. In the remaining 50 % a distinct downward trend in the measured ^{35}Cl / ^{37}Cl ratios was identified (Figure 4.2B). This is thought to be attributable to a combination of the small size of the Ag halide pellets produced by these samples and the degreasing agent used to clean the target holders for the ANU AMS (K. Fifield, pers. comm.). When the Ag halide pellet is small (~ < 0.5 mg) it cannot cover the whole of the ~ 1mm diameter circle in the holder which forms the target for

the AMS Cs sputter source. This means that the surface of the holder is exposed to the Cs ion beam. Prior to use the AMS target holders have to be degreased to remove contaminants. Chloromethane was used for this purpose and even although the holders were subsequently washed in distilled water and ethanol small amounts of chloride may have been left on the surface of the holders. Bromoethane is now used as the degreasing agent (K.Fifield, pers. comm.). Where the bare copper surface of holders was exposed to the Cs sputter source any chloride contamination from the degreasing procedure would influence the results. This extraneous chloride would evaporate from the surface during the bombardment of the target holder and therefore the impact would reduce during the course of the analysis. This would be reflected in a downward trend in the ratios, with the ratios eventually flattening out when the contamination disappears. This is illustrated in Figure 4.3C for sample N14/97. Here the ratio was measured 20 times and flattens after the 8^{th} measurement.

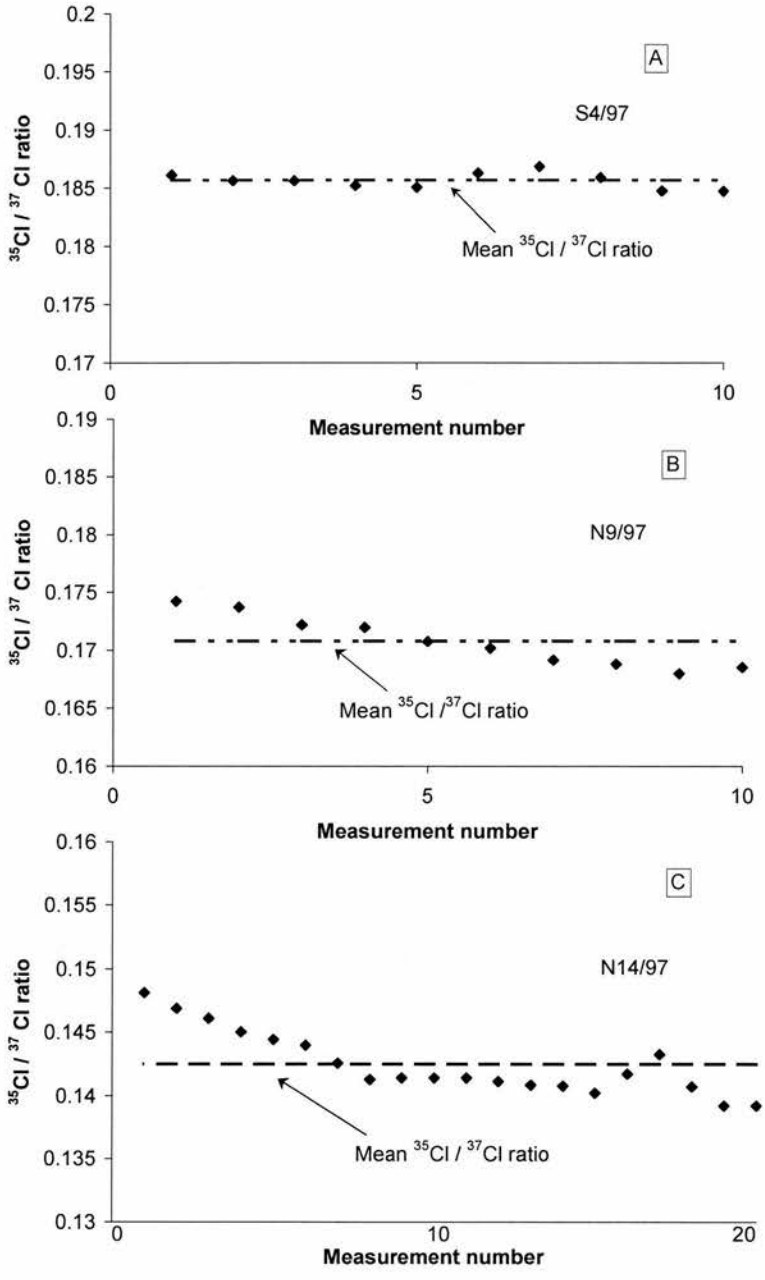

Figure 4.3: [A] shows the ^{35}Cl / ^{37}Cl ratios for sample S4/97. The ratio was measured 10 times and these values plot to within ± 1 % of the mean value. This plot is typical of samples that have not experienced any contamination during mass spectrometry. [B] plots the ^{35}Cl / ^{37}Cl ratios for sample N9/97. The ratios show a distinct downward trend from the first to the last measurement. The mean has been plotted to more clearly show this trend. This is typical of a sample that has experienced some contamination during mass spectrometry. [C] shows the ^{35}Cl / ^{37}Cl ratios for sample N14/97. Here 20 measurements of the ratio have been made and these show an initial downward trend, indicative of contamination, followed by a more level trend from measurement eight onwards. This latter trend is thought to reflect more accurately the ratio of the actual sample. The mean ratio, based on all 20 measurements, is shown and it is clear that using this value would overestimate the ratio leading to a higher, erroneous, estimate of the Cl content of the sample.

Samples thought to have been affected by this contamination should, ideally, have been re-analysed using new Ag halide pellets. This was not undertaken for various reasons. Firstly, all the samples used for this research have a low-Cl content (almost all << 10 ppm) and therefore any error in this measurement will have little impact in the final denudation rate estimate. This is illustrated in Table 4.2. Secondly, as mentioned in Section 4.3.2.2, preparation of the samples for ^{36}Cl analysis involved the addition of a ^{36}Cl-free carrier which acts to reduce the impact of whole rock Cl measurement errors in the final denudation rate calculation. Thirdly, measuring the ^{35}Cl / ^{37}Cl ratio using the AMS is expensive, with each sample requiring at least 10 minutes of machine time (K. Fifield, pers. comm.). Lastly, the clear levelling off shown in Figure 4.3C suggested that an asymptotic value may be estimated for the ^{35}Cl / ^{37}Cl ratio. An asymptote is a straight line that becomes tangent to a graph at infinity (Jeffrey, 1996) and an illustration is provided in Figure 4.4. The estimated asymptotic value of the ^{35}Cl / ^{37}Cl ratio can be used in place of the mean value to determine the Cl content.

Table 4.2: The impact of increasing the Cl content on denudation rate estimates. Results are shown for two samples, N1/97 and S3/97. In both cases, for Cl contents below 10 ppm there is little, if any, difference in the calculated denudation rate.

	N1/97		S3/97	
Cl content (ppm)	**Denudation rate (m Ma^{-1})**	**Increase on initial rate (%)**	**Denudation rate (m Ma^{-1})**	**Increase on initial rate (%)**
1.0	1.5	-	22.1	-
1.5	1.5	0	22.2	< 1
3.0	1.5	0	22.4	< 1
5.0	1.6	7	22.6	2
10.0	1.6	7	23.0	4
15.0	1.7	12	23.5	6
30.0	1.9	20	24.8	12
50.0	2.1	40	26.1	18
100.0	2.5	67	28.3	28
200.0	3.0	100	30.5	38
500.0	3.3	120	32.4	47

Estimates of the asymptotic ^{35}Cl / ^{37}Cl ratio were made by fitting a curve to the measured ratios using the least-squares method (Taylor, 1997). The ratios for sample N14/97 (Figure 4.3C) were used to establish the general form of the curve as $y = a + b\ x^{0.01}$. A curve in this form was then applied to all the samples that displayed the downward trend. The curve was established on the basis of the 10 measured ratios and then extended to cover 20 measurements in all (Figure 4.4). The results of this, together with the correlation

coefficients, are given in Appendix 5. The asymptotic ratio was estimated from a straight line, parallel to the x-axis, that passed through each curve at between estimated measurements 19 and 20 (as illustrated in Figure 4.4). The intercept of this line with the y-axis provided the asymptotic ^{35}Cl / ^{37}Cl ratio.

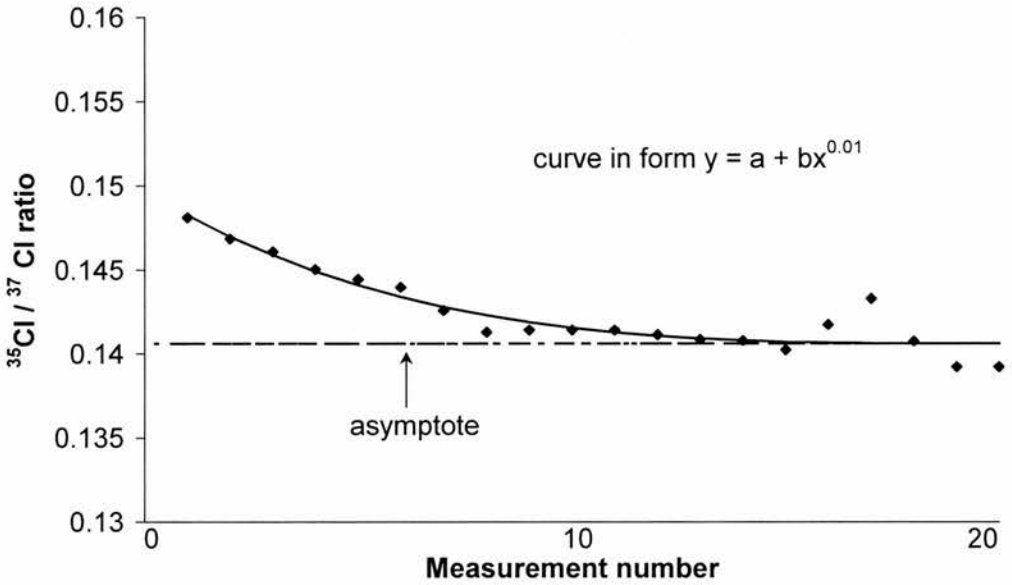

Figure 4.4: A curve in the form y = a + b x$^{0.01}$ together with the measured ratios for sample N14/97 are shown. The asymptote is a line which is tangent to a graph at infinity and here the asymptote has been shown as being parallel to the x-axis at measurements 19 and 20. The intercept of the asymptote with the y-axis was used as the estimated 'asymptotic' ^{35}Cl / ^{37}Cl ratio.

The total Cl content (ppm), Cl_{sample}, for each sample was calculated using either the mean of the measured ratios, or if the measured ratios illustrated the downward trend, the asymptotic ratio, using the following equation (based on Equation 4.2 above):

$$Cl_{sample} = \frac{AW_{Cl} \times 10^6}{F_{37} \times N_A} \times {}^{37}Cl_{spike} \times \frac{W_{spike}}{W_{sample}} \times \left(\frac{{}^{35}Cl/{}^{37}Cl_{spike} - {}^{35}Cl/{}^{37}Cl_{meas.}}{{}^{35}Cl/{}^{37}Cl_{meas.} - {}^{35}Cl/{}^{37}Cl_{natural}} \right) \qquad \text{Equation 4.3}$$

where, AW_{Cl} is the atomic weight of Cl; F_{37} is the fraction of ^{37}Cl present in natural Cl (= 0.2423); N_A is the Avogadro constant ; ${}^{37}Cl_{spike}$ is the calibrated concentration of ^{37}Cl in the spike solution (9.1687 ± 0.0598 x 10^{17} atoms ^{37}Cl g^{-1}). ${}^{35}Cl/{}^{37}Cl_{meas.}$ is either the mean measured ratio or, if appropriate, the asymptotic ratio. Background ^{37}Cl from the reagents

and sample handling was calculated from procedural blanks as $6.98 \pm 1.01 \times 10^{15}$ atoms (^{37}Cl) g^{-1} (< ~ 1.5 ppm Cl) and was deducted during the calculation. The results are given in Appendix 4, with the values derived using the asymptotic ratio being shown by '$^{\chi}$'. Where an asymptotic ratio was used to determine the Cl content, the uncertainty in the Cl content is given as ± 25 %. For comparison purposes, Table 4.3 shows how the Cl content values for each sample with the downward trend vary depending on whether the highest measured ^{35}Cl / ^{37}Cl ratio, the mean ratio or the asymptotic ratio is used.

Four replicates, chosen at random, were prepared and analysed to check the reproduction capabilities of this technique. The results for the samples and their replicates are shown in Table 4.4. Fortuitously, three of the samples, S1/97, S4/97 and L18/97, provide a check on the use of the asymptotic ratios as the measured ratios for one of each of these samples showed the downward trend. An asymptotic ratio was therefore estimated for these while the other sample had no such trend and the mean measured ratio could be used. Despite this, all the replicate results are within error which suggests that the Cl content estimated using the asymptotic ^{35}Cl / ^{37}Cl ratios are reliable, particularly given the ± 25 % error.

Table 4.4: Chloride content of samples and replicates

Sample	Chloride content (ppm)
O4/97	$7.1 \pm 1.8^{\chi}$
O4/97 replicate	$6.8 \pm 1.7^{\chi}$
S1/97	$1.9 \pm 0.5^{\chi}$
S1/97 replicate	1.7 ± 0.3
S4/97	3.2 ± 0.3
S4/97 replicate	$3.5 \pm 0.9^{\chi}$
L18/98	2.4 ± 0.3
L18/97 replicate	$2.3 \pm 0.6^{\chi}$

χ Estimated from asymptotic ^{35}Cl / ^{37}Cl ratio.

Table 4.3: Comparison of the Cl content derived using the highest measured ratio, the mean measured ratio and the estimated asymptotic ratio for samples showing a downward trend in the measured ratios.

Sample	Cl content determined using the alternative ratios (ppm)		
	Highest measured ^{35}Cl / ^{37}Cl ratio	Mean measured ^{35}Cl / ^{37}Cl ratio	Asymptotic ^{35}Cl / ^{37}Cl ratio
N1/97	2.4 ± 0.2	1.9 ± 0.3	1.7 ± 0.4
N3/97	4.8 ± 0.2	4.4 ± 0.3	4.0 ± 1.0
N6/97	3.8 ± 0.2	3.7 ± 0.2	3.6 ± 0.9
N8/97	3.6 ± 0.2	3.4 ± 0.2	3.3 ± 0.8
N9/97	4.1 ± 0.2	3.9 ± 0.3	3.7 ± 0.9
N10/97	3.1 ± 0.2	2.9 ± 0.3	2.8 ± 0.7
N11/97	5.9 ± 0.2	4.5 ± 0.8	3.3 ± 0.8
N12/97	3.8 ± 0.2	2.8 ± 0.5	2.1 ±0.5
N13/97	7.5 ± 0.3	6.5 ± 0.6	5.8 ± 1.4
N14/97	1.5 ± 0.3	1.2 ± 0.3	1.2 ± 0.3
N17/97	2.6 ± 0.3	2.2 ± 0.3	2.0 ± 0.5
N18/97	5.2 ± 0.2	4.9 ± 0.3	4.5 ± 1.1
O1/97	3.6 ± 0.2	3.6 ± 0.3	3.4 ± 0.9
O3/97	7.3 ± 0.3	6.6 ± 0.5	6.1 ± 1.5
O4/97	8.3 ± 0.3	7.7 ± 0.5	7.1 ± 1.8
O5/97	3.5 ± 0.3	2.8 ± 0.5	2.3 ± 0.6
O8/97	3.2 ± 0.3	2.9 ± 0.3	2.7 ± 0.7
O9/97	2.6 ± 0.3	2.1 ± 0.4	1.6 ± 0.4
O10/97	7.2 ± 0.3	6.2 ± 0.9	4.9 ± 1.2
O11/97	1.6 ± 0.3	1.3 ± 0.3	1.0 ± 0.3
S1/97	2.2 ± 0.3	2.0 ± 0.3	1.9 ± 0.5
S2/97	3.7 ± 0.3	3.5 ± 0.3	3.3 ± 0.8
S3/97	5.9 ± 0.3	5.3 ± 0.4	4.9 ± 1.2
S7/97	5.6 ± 0.3	5.4 ± 0.3	5.1 ± 1.3
S9/97	2.6 ± 0.3	2.4 ± 0.3	2.2 ± 0.6
S10/97	6.5 ± 0.2	5.7 ± 0.5	5.1 ± 1.3
S12/97	5.0 ± 0.3	4.5 ± 0.4	4.2 ± 1.1
L1/97	3.1 ± 0.3	2.8 ± 0.3	2.6 ± 0.7
L6/97	4.7 ± 0.3	4.3 ± 0.3	3.9 ± 1.0
L10/97	4.1 ± 0.3	3.8 ± 0.3	3.5 ± 0.9
L11/97	2.9 ± 0.3	2.5 ± 0.3	2.2 ± 0.6
L13/97	1.7 ± 0.3	1.4 ± 0.3	1.2 ± 0.3
L22/97	2.5 ± 0.2	2.4 ± 0.3	2.2 ± 0.6
L24/97	2.5 ± 0.2	2.3 ± 0.3	2.2 ± 0.6
L25/97	2.2 ± 0.3	1.9 ± 0.3	1.5 ± 0.4
L27/97	4.3 ± 0.3	3.9 ± 0.4	3.5 ± 0.9

4.4 ANCILLARY CHEMICAL ANALYSES

4.4.1 MAJOR ELEMENT MEASUREMENTS

X-ray fluorescence spectrometry is one of the most widely used routine instrumental methods of analysing the major element content of bulk samples (Potts, 1987). This analysis was used, principally, to establish the Ca and K content of the whole rock samples, however other major elements also influence the thermal neutron capture reactions involving ^{35}Cl and ^{39}K. For example, although the thermal neutron absorption cross-section of Fe is 2.56×10^{-24} cm^2 (Lide, 1995), compared to 48800×10^{-24} cm^2 for Gd (Lide, 1995), the higher concentration of Fe meant that it was the major thermal neutron absorber in all samples.

The fragile weathering products removed by the leaching procedure, might contain Ca and K but be unable to retain *in situ*-produced cosmogenic ^{36}Cl (J. Stone pers. comm.). Therefore XRF using pre-leached material may yield a higher concentration of Ca and K than was actually involved in the production of the measured ^{36}Cl content. For this reason the major element analysis was made using an aliquot of the leached sample.

Major element analysis was carried out on fused glass discs prepared by a method based on that of Norrish and Hutton (1969) and Fitton *et al* (1998). A 5 g aliquot of each leached sample was ground in a tungsten carbide tema mill for 2 minutes to a flour-like consistency. The grinding barrels were thoroughly washed and dried between each sample to prevent cross-contamination. The samples were dried overnight at ~ 110 °C before removal of ~ 1 g to a platinum crucible. This 1 g sub-sample was ignited at ~ 1100 °C for 20 minutes to determine the loss on ignition. The ignited sample was mixed with a flux containing 47 % lithium tetraborate ($Li_2B_4O_7$), 37 % lithium oxide (Li_2O) and 16 % lanthanum oxide (La_2O_3) (Spectroflux® 105) in a sample : flux ratio of 1: 5 and fused at ~ 1100 °C for 20 minutes. The molten mixture was swirled several times during fusion to ensure complete dissolution and sample homogeneity. Each sample was cast and annealed at ~ 220 °C to produce clear glass discs.

The fused discs were analysed, by D. James, using the Phillips PW1480 wavelength-dispersive automatic X-ray fluorescence spectrometer fitted with a rhodium anode X-ray tube located in the Department of Geology and Geophysics, University of Edinburgh. The spectrometer was calibrated using USGS and CRPG standards. The results are provided in

Appendix 3. The relative uncertainties are better than ± 1 % (D. James, pers. comm.). The sum of the oxides plus the loss on ignition (LOI) total is quoted within the range 99.4 -100.4 allowing for trace element concentration and reproduction errors in the measurements (D. James, pers. comm.). Samples with totals lying outside this range were re-analysed using new glass discs.

Oven drying of the powdered sample at ~ 110 °C is a widely recognised method of removing water absorbed onto the powder (H_2O –). Water present within the crystal lattice, structural water (H_2O +), is not removed in this manner. In ^{36}Cl analysis, the H_2O + content can be important for thermal neutron capture reactions, as the greater the structural water content the more rapid the thermalization of fast neutrons (Section 3.2.3.5). The H_2O + content of silicate rocks can be estimated very crudely from LOI or can be determined more accurately using, for example, the Penfield method or Karl Fischer titrations (Potts, 1987). LOI only provides a very rough indication of the H_2O + content as this value is the sum of the loss of H_2O +, CO_2, loss by volatilization of alkali metals, fluorine and oxides of sulphur and some gain on ignition due to oxidation of ferrous iron (Potts, 1987). Given the low-Cl content of the basalts used in this study the H_2O + content was not measured and instead was estimated as being 75 % of LOI.

4.4.2 Trace element measurements (excluding boron)

The abundance of the competing thermal neutron absorbing trace elements - Li, Cr, Sm and Gd - and the concentration of elements responsible for the non-cosmogenic ^{36}Cl production, U and Th, was measured using ICP-MS. The measurement of B was dealt with separately. ICP-MS was used as it offers the twin advantages of fast, high precision, results and the ability to determine the concentrations of selected elements from the same solution (Jarvis *et al*, 1992). In ICP-MS charged atoms are generated from each sample in an electrical plasma at ~ 8000 °C at atmospheric pressure and drawn into the mass spectrometer where the selected elements are detected by their characteristic signals under vacuum conditions (Jarvis *et al*, 1992; Montaser, 1998). The samples collected during the 1995 field season were prepared and analysed, by M. McCartney, at Scottish Universities Environmental Research Centre, East Kilbride. The 1997 season samples were prepared, by the author, in the main Physical Geography Laboratory, Geography Department and analysed, with the assistance of K. Jarvis and L. Clarke, at the NERC ICP-MS facility based at Imperial College, Ascot.

Preparation of samples followed closely the standard rock digestion procedure method employed by the NERC ICP-MS facility. Approximately 5 g of the ground aliquot produced during the crushing stage was dried overnight at ~ 110 °C to drive off H_2O –, and from this ~ 0.50 g was subjected to acid attack by a mixture of ~10 ml conc. HF and ~ 4 ml conc. $HClO_4$. Perchloric acid was used as it substantially increases the boiling point of the mixture (~ 200 °C for $HClO_4$ as compared to ~ 112 °C for HF alone, Potts, 1987) which results in the removal of silicon and fluorine by evaporation as volatile silicon tetrafluoride. The mixture was heated to ~ 200 °C in a 60 ml Teflon® beaker until near dryness. To dissolve the sample fully it was necessary to repeat the acid digestion a second time. After dissolution each sample was fumed to near dryness once with ~ 4 ml conc. $HClO_4$ to eliminate any remaining fluorides and residual HF. The samples were then re-dissolved by heating gently in ~10 ml 5M HNO_3. After cooling the sample solution was made up to 50 ml with ultra-pure water and stored in clean HDPE bottles.

In addition to the samples, a full procedural blank was prepared with each batch of samples to monitor background levels. Four USGS reference material samples, W-2, BCR-2, GSP-2 and AGV-2, were prepared using the above procedure and these were used, together with standard solutions to establish the accuracy of the ICP-MS analysis. Five replicate samples (N2/97, O7/97, O10/97, S11/97 and L14/97) were also prepared to test the reproduceability of the preparation procedure. Concentrations were determined using an F1 Elemental PlasmaQuad instrument with a 60 s count time and machine repeatability was assessed by analysing each sample three times. Procedural blank and machine drift corrected concentrations (ppm) for the samples, reference materials and replicates, are given in Appendix 4.

4.4.3 Boron measurement

Due to its high cross-section for thermal neutron reactions (765 x 10^{-24} cm^2, Lide, 1995)), boron is another competing neutron absorbing element which is known to occur in trace quantities in silicate material. Nakamura *et al* (1992) detail the problems involved in the separation and measurement of B in rock samples. To reduce the total number of measurement techniques employed in this project it was initially decided to use ICP-MS to measure B, particularly given the experience of the NERC ICP-MS facility in the measurement of boron (eg Porteous *et al*, 1995; K. Jarvis pers. comm.). A different preparation procedure to the mineral acid digestion outlined above was required because of the ease with which B is volatilized as BF_3 in the presence of HF. Ishikawa and Nakamura

(1990) have shown that volatilization can be suppressed by the addition of mannitol to HF solutions prior to dissolution of silicate material and that a high level of analytical precision can be achieved (Nakamura *et al*, 1992). The method of Nakamura *et al* (1992) has been modified to make it suitable for ICP-MS analysis (J. Stone, pers. comm.). This procedure, which involves an HF-only dissolution, is unsuitable for preparing the samples for measurement of the other relevant trace elements as not all the elements are guaranteed to go into solution (J. Stone, pers. comm.).

As a trial four standard reference materials with known concentrations of B were prepared (W-2, NIST-688, AC-E and GSD-1). The rock powder was dried overnight at ~ 110 °C before ~ 0.50 g was pre-wet with ~ 0.3 ml of a 1 % mannitol in 0.1 M HF solution. The mannitol forms a very stable, involatile complex with B keeping it in solution during dissolution (Nakamura *et al*, 1992). 10 ml of conc. HF was added to the sample and the 60 ml Savillex Teflon® jar was then capped. The sample was left to decompose in a fume cupboard at room temperature. After two days the lid was removed and the jar heated at < 80 °C until near dryness. To dissolve the sample fully it was necessary to repeat the acid digestion a second time. The samples were then re-dissolved by heating gently in ~10 ml 5M HNO_3. After cooling the sample solution was made up to 50 ml with ultra-pure water and stored in clean HDPE bottles. The B content of these solutions was then measured by K. Jarvis at the NERC ICP-MS facility. The results are shown in Table 4.5.

All four samples show a very high recovery, well in excess of the expected values, and very similar mean values despite the range in expected concentrations. This suggests that contamination has occurred either during the sample preparation or during the measurement. The procedural blank yielded a very low background count suggesting that the preparation was not the source. B is difficult to flush from the surface of the ICP-MS glassware (Jarvis *et al*, 1992), however measurements of other samples run at the same time indicated that machine contamination was not an issue (K. Jarvis, pers. comm.). Further sample preparation and measurements would be required to resolve this problem, but, unfortunately, the NERC ICP-MS facility at Imperial College closed prior to resolution of this issue.

Table 4.5: Boron concentrations of standard reference material samples determined by ICP-MS compared to expected B concentrations. Measured data corrected for blank and other external calibrations.

Sample		B (ppm)
W-2 #1		79.4
W-2 #2		86.6
W-3 #3		86.0
	Mean	84.0
	Expected	12
	% Recovery	700
NIST-688 #1		81.9
NIST-688 #2		89.4
NIST-688 #3		87.3
	Mean	86.2
	Expected	1.4
	% Recovery	6157
AC-E #1		61.3
AC-E #2		58.1
AC-E #3		58.1
	Mean	59.2
	Expected	21
	% Recovery	282
GSD-1 #1		71.6
GSD-1 #2		72.1
GSD-1 #3		68.8
	Mean	70.8
	Expected	4.6
	% Recovery	1540

Given the problems with the determination of B by ICP-MS it was decided to send aliquots of the samples to XRAL laboratories, Ontario where the B content was measured using a combination of sodium fusion ICP-AES and prompt gamma NAA. The results are given in Appendix 4. When values are reported as < 10 ppm, less than the detection limit of the ICP-AES, and < 0.1 ppm, less than the detection limit of the prompt gamma NAA, values of 5 ± 5 ppm and 0.05 ± 0.05 ppm respectively were used in the calculation of the ^{36}Cl derived denudation rates. The low Cl content of the samples meant that the final denudation rate was insensitive to such large errors in B concentration.

CHAPTER 5: EVOLVING IDEAS ABOUT THE LANDSCAPES OF PASSIVE MARGINS AND SOUTHEAST AFRICA

5.1 INTRODUCTION

Before considering the results of the analysis of *in situ*-produced ^{36}Cl in samples from bedrock summits and free faces in the southern Drakensberg and Lesotho Highlands, it is necessary to provide both an outline of the physical setting of southeast Africa (morphology, regional geology, tectonic setting and climate) (Section 5.2) and a review of the theories about how this landscape has developed (Section 5.4). The southeast African landscape is one of the best examples of a high-elevation passive margin (attaining > 3000 m within ~ 200 km of the coast) and, because of this, it has played a key role in the formation of conceptual ideas about the long-term development of passive margin landscapes. This chapter therefore also reviews ideas about the development of passive margin morphology in general (Section 5.3)

5.2 SOUTHEAST AFRICA: PHYSICAL SETTING

5.2.1 MORPHOLOGY

The macroscale morphology of southeast Africa (Figures 5.1, 5.2 & 5.3) is typical of a high-elevation passive margin (Section 5.3.1) as it comprises three major regions – a high-relief coastal zone, a high-elevation hinterland and, separating these two regions, a distinctive oceanward facing erosional escarpment. The coastal zone rises from sea level to ~ 1800 m in altitude and extends, laterally, for 150 – 220 km from the sea to the escarpment. This zone has high local relief (Figure 5.2) and is drained by rivers flowing to the Indian Ocean. The hinterland is plateau-like only northwest of an approximate line running from 27° 30' S, 29° 30' E to 31° 30' S, 26° E (Figure 5.1). This area is generally one of low local relief sloping to the northwest from an elevation of ~ 2100 m at the escarpment rim to ~ 1400 m in the northwesternmost part of Figure 5.1. The remaining part of the hinterland, lying on the southeast side of the foregoing line, is one of both high-elevation, reaching 3482 m at Thabana-Ntlenyana, the highest summit in southern Africa, and high local relief (Figure 5.2). The whole of the hinterland is drained by the headwaters of the westward flowing Orange River system which empties into the Atlantic Ocean some 1200 km to the west.

The major topographic feature of southeast Africa is the erosional escarpment. First named the 'Great Escarpment' by Rogers (1920), this name is commonly used (eg King, 1951; Wellington, 1955; Ollier and Marker, 1985) along with 'Main Escarpment' (eg Moon and Selby, 1983) and 'Große Randstufe' (eg Obst and Kayser, 1949) to describe the extensive escarpment that roughly parallels the coast of southern Africa from the Limpopo river in the east to Angola in the west. The Great Escarpment displays appreciable variation throughout its length, which is thought to reflect the impact of variable lithology, structure and drainage (Rogers, 1920; King, 1951; Wellington, 1955; Ollier and Marker, 1985), but in general it coincides with the continental drainage divide (a drainage divide escarpment, Seidl *et al*, 1996). In southeast Africa, the Great Escarpment is known as the Drakensberg ('Dragon Mountain'), or Natal Drakensberg to avoid confusion with the Transvaal Drakensberg which is another section of the Great Escarpment located close to the Limpopo river.

For most of its length the Drakensberg is formed in the mid-Jurassic Drakensberg Group basalts and indeed it forms the oceanward erosional boundary of the largest sub-aerial outcrop of these basalts. The Drakensberg is the most spectacular section of the Great Escarpment forming a generally abrupt steep cliff-like free face which can extend for up to 1000 m from the foot of the face to the crest (eg The Amphitheatre, 28° 45' S, 28° 55' E, Figure 5.1). Below the free face there is usually a steeply sloping ($\leq \sim 35 - 40°$), well vegetated, rectilinear slope. In planform (Figure 5.1), the Drakensberg is sinuous which is assumed to reflect the interaction of headward fluvial erosion and lithological characteristics (Ollier and Marker, 1985). The sharp ($\sim 90°$) change in direction at 28° 45' S, 29° E and again at 29° 20' S, 29° 30' E is suggested to be due to structural control (Ollier and Marker, 1985), but this has not been subject to any analysis. Interestingly this change in direction roughly coincides with the northernmost magnetic anomaly, M12 located in the Indian Ocean, which marks the beginning of the break-up of South America and Africa (see below – Figure 5.5).

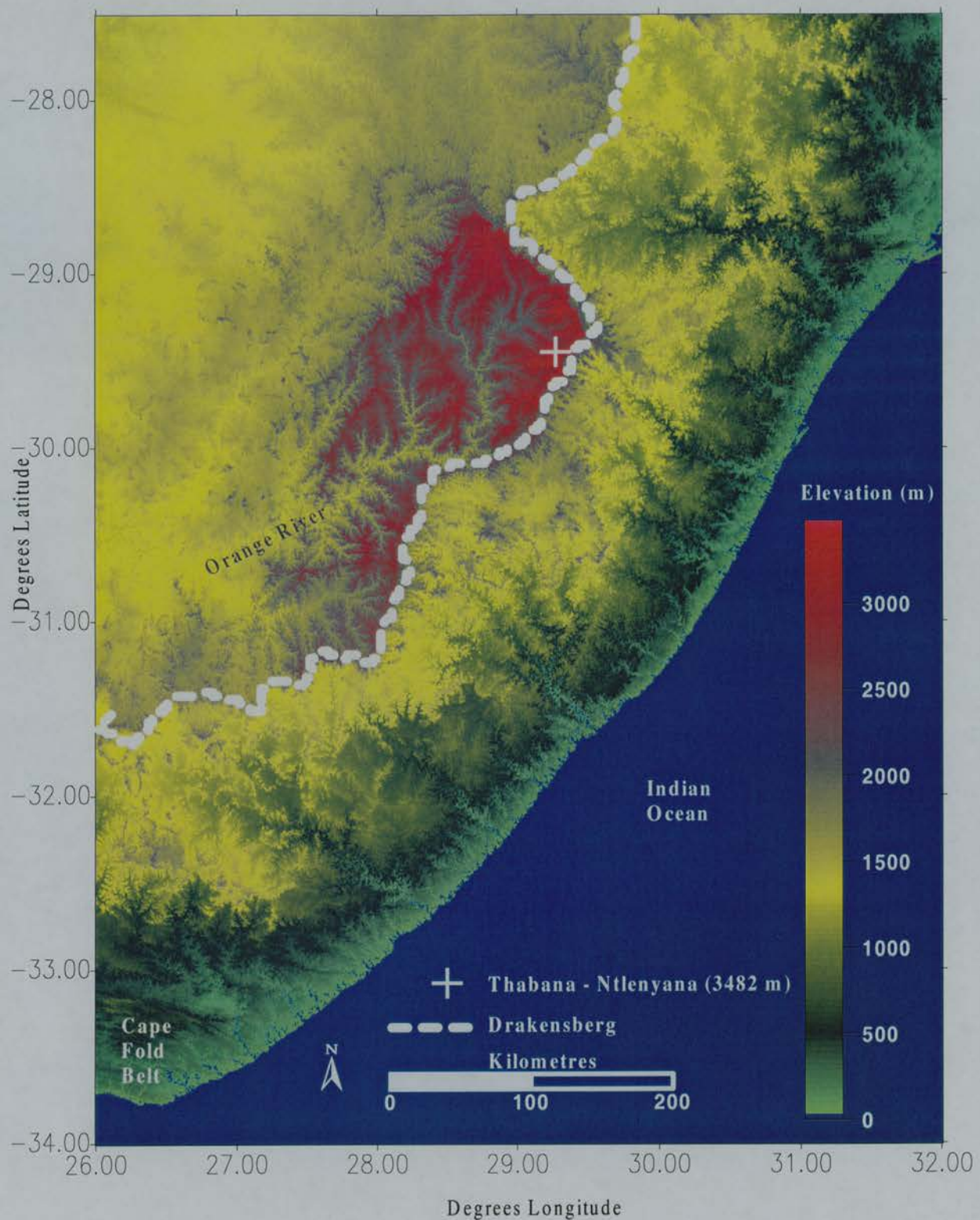

Figure 5.1: The macro-scale morphology of southeast Africa. The position of the Drakensberg and the highest point in southern Africa, Thabana-Ntlenyana (3482 m) are shown. The Lesotho Highlands comprise the area exceeding 2500 m that lies inland of the Drakensberg. The dual nature of the drainage in this area is highlighted. Short rivers drain to the Indian Ocean, whilst the Orange River, whose headwaters have deeply incised the Lesotho Highlands, flows to the Atlantic Ocean. Based on US Geological Survey 1 km topographic data.

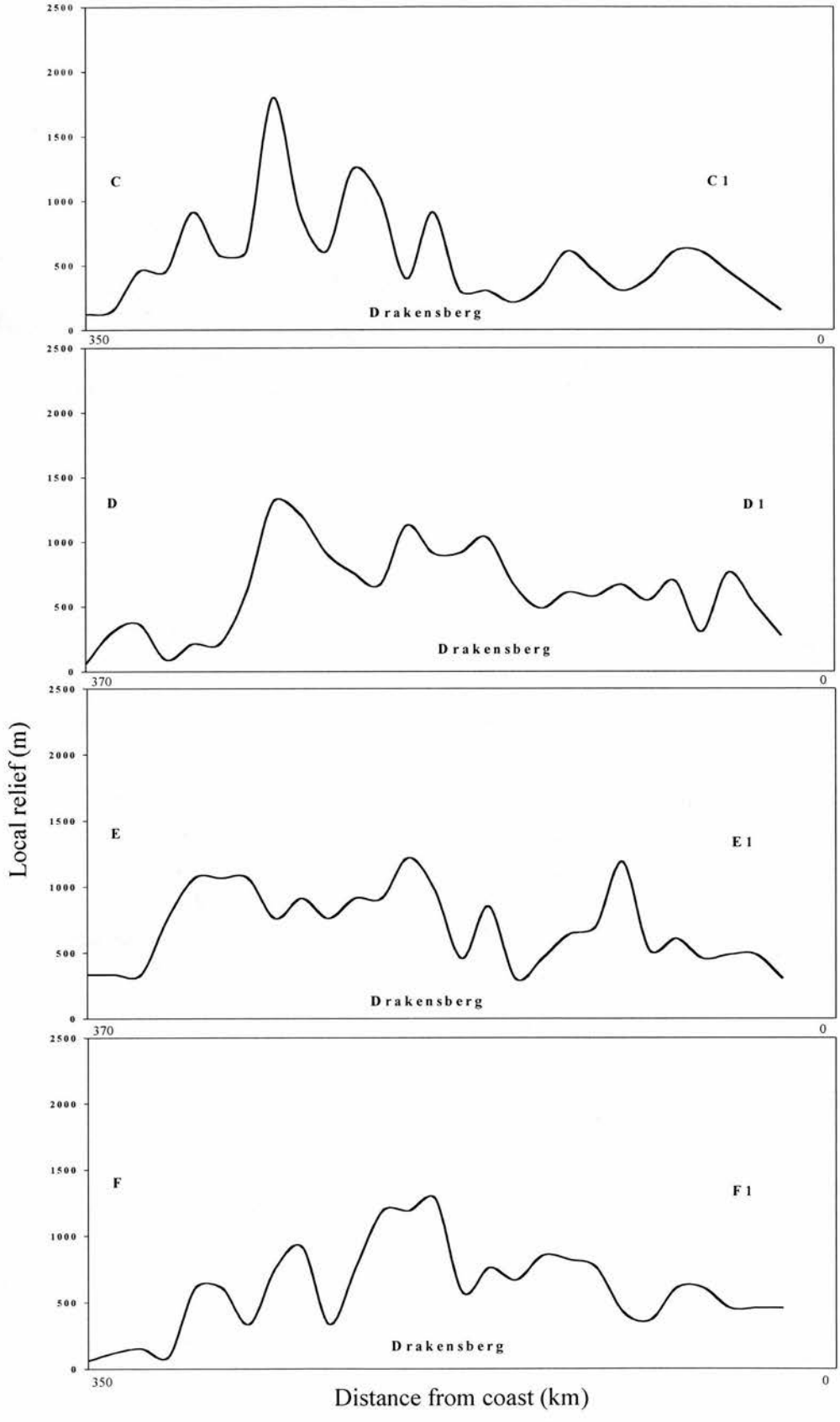

Figure 5.2: Local relief (maximum relief within an ~ 16 x 18 km region) for four representative cross-sections of SE Africa which include the Lesotho Highlands. The approximate position of the Drakensberg is indicated. Locations of the cross-sections are provided in Figure 5.3(i). Local relief values calculated from 10-minute resolution NGDC database provided by M. Summerfield.

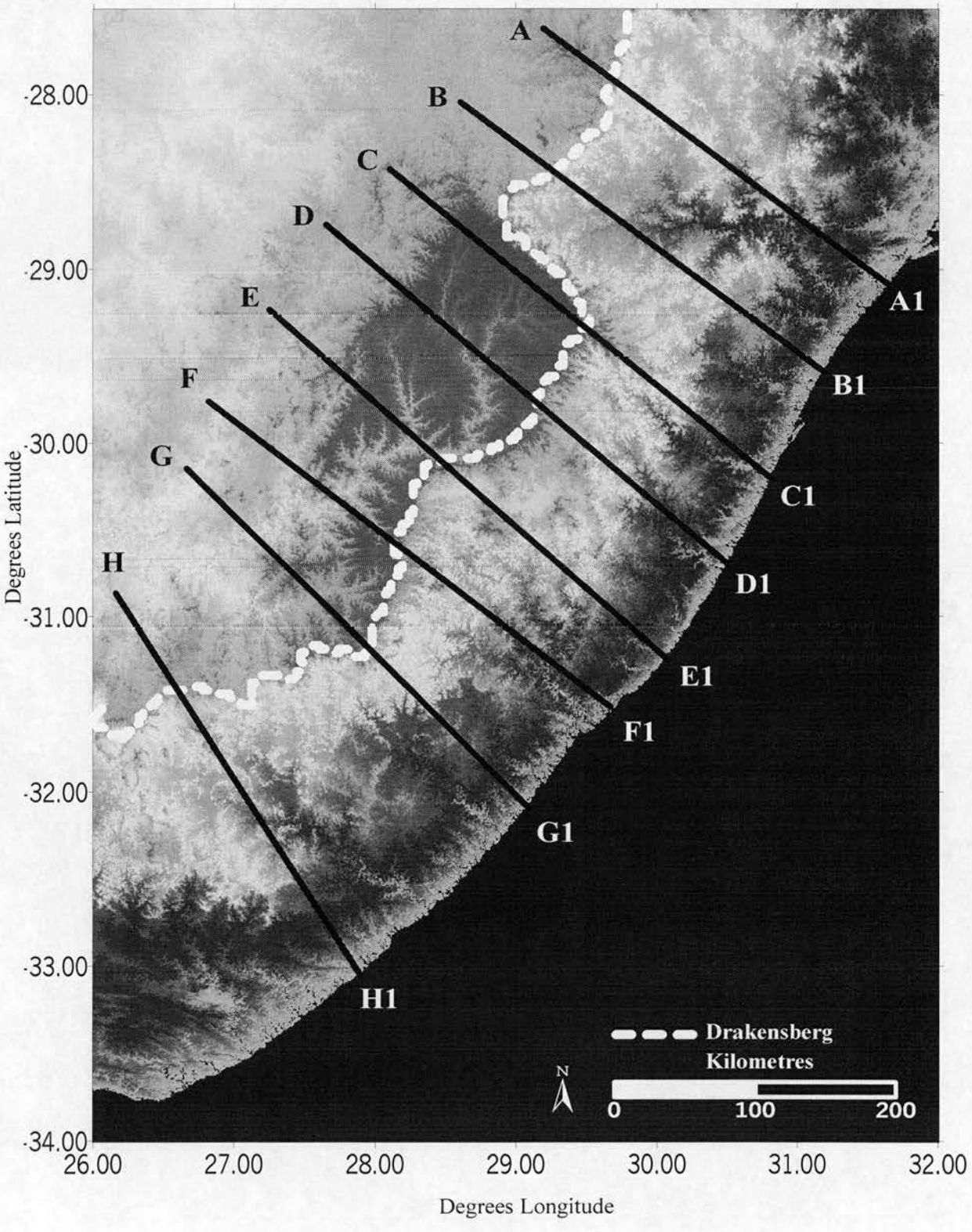

Figure 5.3(i): Locations of local relief cross-sections shown in Figure 5.2 and topographic profiles shown in Figure 5.3(ii). Note that the base map is taken from Figure 5.1.

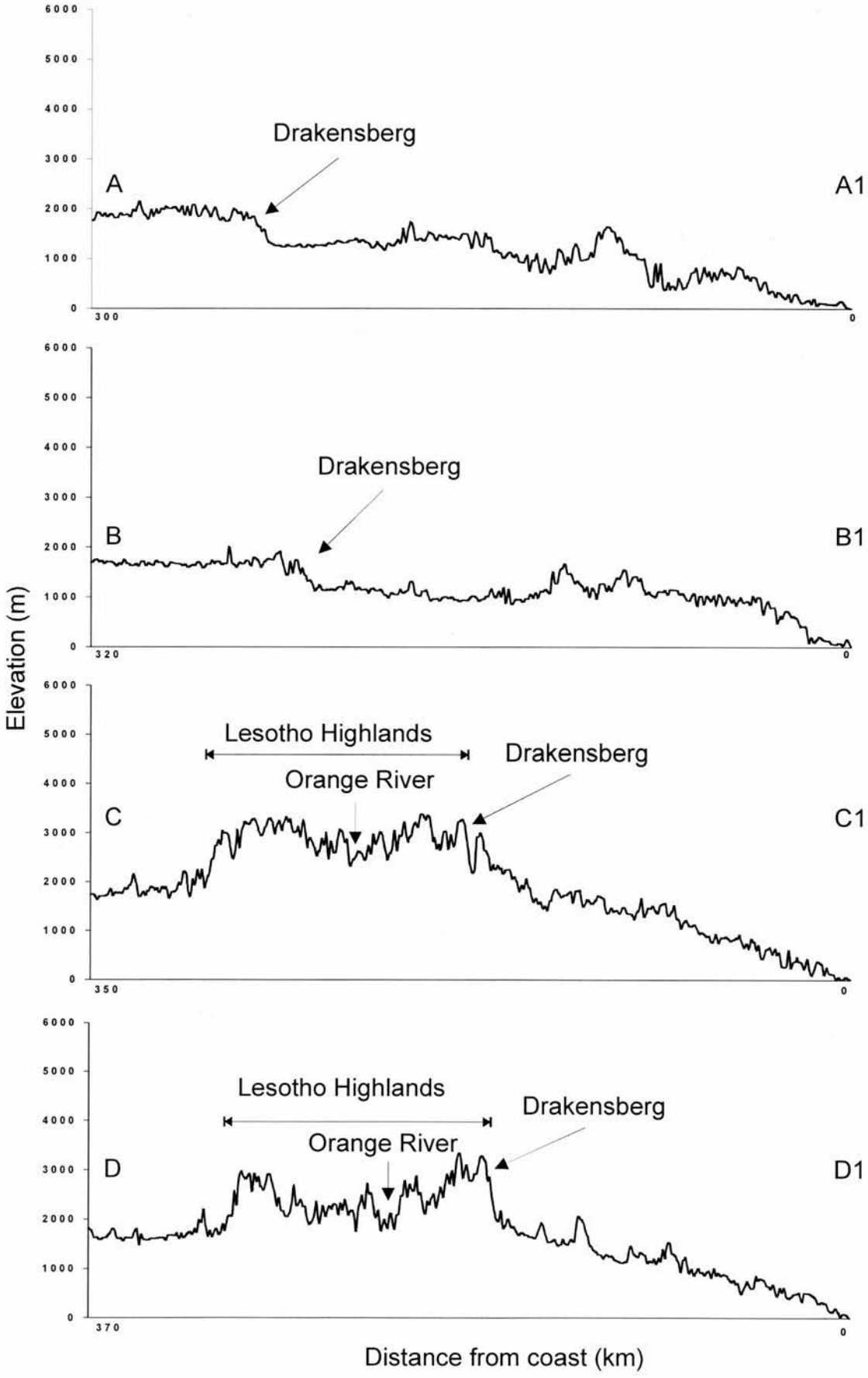
Elevation (m)
6000
5000
4000
3000
2000
1000
0
Drakensberg
A
A1
300
0
Drakensberg
B
B1
320
0
Lesotho Highlands
Drakensberg
Orange River
C
C1
350
0
Lesotho Highlands
Drakensberg
Orange River
D
D1
370
0
Distance from coast (km)

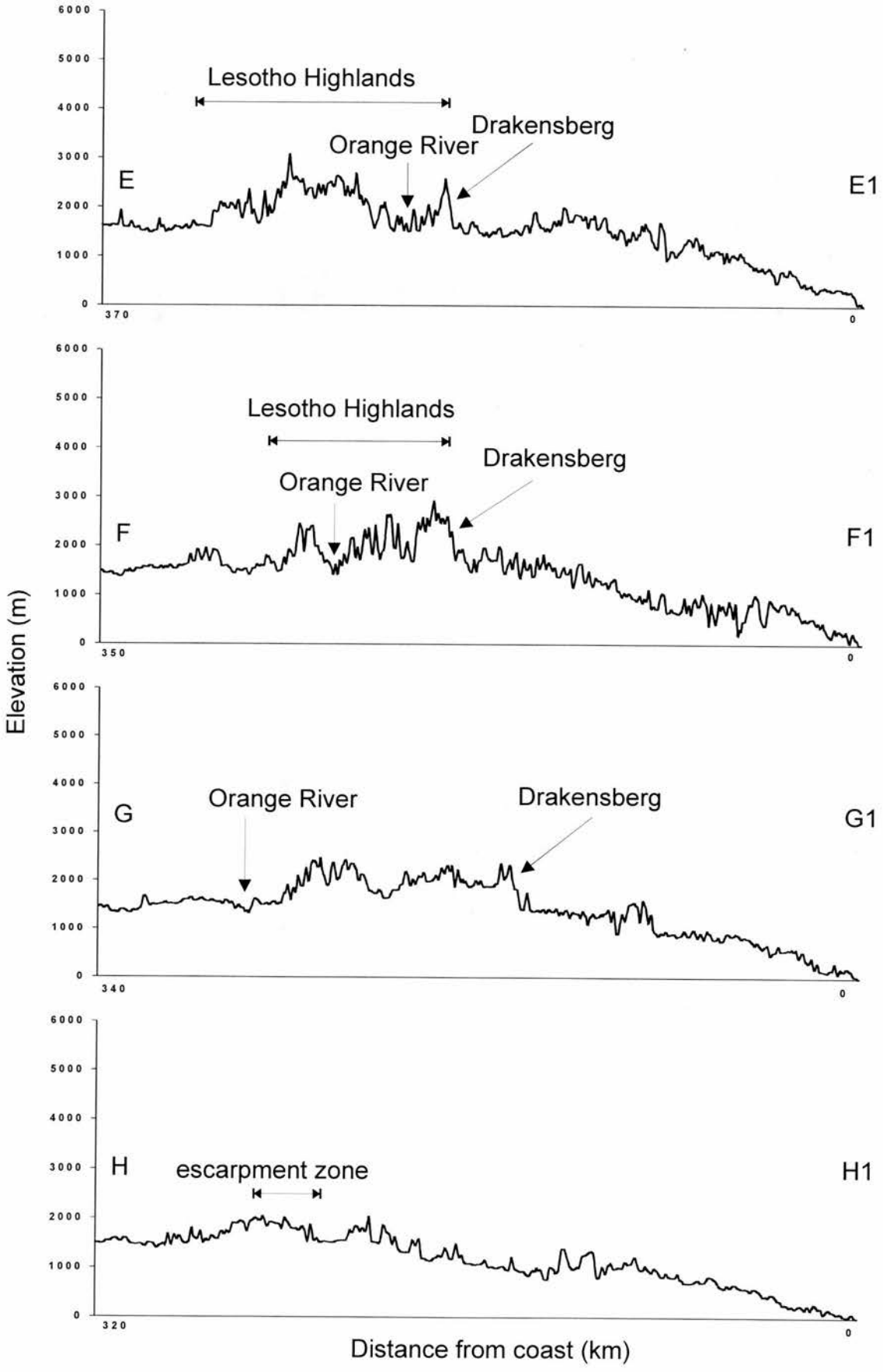
Elevation (m)
6000
5000
4000
3000
2000
1000
0
Lesotho Highlands
Drakensberg
Orange River
E
E1
370
0
Lesotho Highlands
Drakensberg
Orange River
F
F1
350
0
Orange River
Drakensberg
G
G1
340
0
escarpment zone
H
H1
320
0
Distance from coast (km)

5.2.1 REGIONAL GEOLOGY

At a regional level, the geology of southeast Africa can be viewed as comprising four major elements: the basement, the Karoo sedimentary sequence, the Drakensberg Group basalts and the kimberlitic intrusives (Figure 5.4). The basement, which underlies the sedimentary sequence and the basalts, comprises the Archean age (2.8 – 3.7 Ga, Thomas *et al*, 1993) Kaapvaal Craton and, south of ~ 30° S, the mid-Proterozoic (~ 1.2 Ga, Tankard *et al*, 1982; Thomas *et al*, 1993) Namaqua-Natal orogenic / metamorphic province. In the coastal zone, from 28° S to just south of 31° S, the generally flat-lying depositional Natal Group (SACS, 1980) sandstones crop out. This ~ 490 Ma age sedimentary sequence rests uncomformably on the basement granitoid gneisses and is thought to be derived from erosion of a Pan-African mountain chain (Thomas *et al*, 1993; Marshall, 1994).

The basement is overlain by the mostly flat-lying continental sediments of the Permo-Carboniferous to early Jurassic age Karoo Sequence or Supergroup (Tankard *et al*, 1982: Dingle *et al*, 1983; Cole, 1992; Smith *et al*, 1993; Catuneanu *et al*, 1998). The SACS (1980) definition of Karoo Sequence includes the Drakensberg Group basalts (known as the Lesotho Formation in Lesotho – Schmitz and Rooyani, 1987) but, for the purposes of this discussion, the basalts will be treated separately and the remaining lithostratigraphic units will be referred to as the Karoo sedimentary sequence. The Karoo sedimentary sequence accumulated in the intracratonic retroarc foreland Karoo Basin, the formation of which has been linked to the ending of the Permo-Carboniferous glaciation and the start of subduction along the paleao-Pacific ocean plate margin of Gondwana (Cole, 1992; Thomas *et al*, 1993; Catuneanu *et al*, 1998). The maximum preserved thickness of the Karoo sedimentary sequence, ~ 6 km (Smith *et al*, 1993; Catuneanu *et al*, 1998), is found at around 33° S, immediately to the north of the Permo-Triassic age Cape Fold Belt (CFB) which was part of the larger Gondwanide orogen that can traced into South America, Antarctica and eastern Australia (Thomas *et al*, 1993).

Figure 5.3(ii): (on two preceding pages) Eight (A-A1 to H-H1) representative topographic cross-sections of the morphology of southeast Africa. Locations are shown in Figure 5.3(i). The Drakensberg forms a distinctive 'step' in the landscape in all profiles except H-H1. In profile H-H1 the escarpment is indistinct and is best considered as a zone. Note that the horizontal distance of each profile is different varying from 300 km to 370 km from the coast. The vertical exaggeration is x 20. Profiles constructed from US Geological Survey 1 km topographic data and from the 1 : 250 000 scale map series produced by the Surveys and Land Information Department of the South African Government.

The Karoo Basin has been mainly viewed as a single subsiding basin with a main depocentre in front of the CFB (Tankard *et al*, 1982; Dingle *et al*, 1983). Catuneanu *et al* (1998) have demonstrated, however, that the depocentre migrated due to the subsidence and uplift induced by the flexural behaviour of the basin as it responded to the orogenic loading and unloading of the CFB.

The Karoo sedimentary sequence (Table 5.1) contains a basal unit of late Carboniferous – early Permian glacial sediments. This is overlain by a sedimentary succession of marine, deltaic and terrestrial deposits which culminate in early Jurassic age aeolian facies (Dingle *et al*, 1983; Cole, 1992; Smith *et al*, 1993). The major provenance of the post-Dwyka sediments is the CFB, but studies of the Stormberg Group indicate that the lower Karoo sedimentary sequence provided the source, suggesting that the deposition of the Stormberg Group was coeval with denudation of the older Karoo strata (Catuneanu *et al*, 1998).

Table 5.1: Lithostratigraphy of the Karoo sedimentary sequence. Ages from Catuneanu *et al* (1998) for sites north of 31°S.

Geological time	**Age (~ Ma BP)**	**Group**	**Formation**	**Sedimentary environment**
early Jurassic – middle Jurassic	200 – 183		Clarens	Ephemeral stream, sheetflood, playa, aeolian sand
late Triassic – early Jurassic	215 – 200	Stormberg	Elliot	Fine grained fluvial
late Triassic	225 - 215		Molteno	Coarse grained fluvial
middle Triassic – late Triassic	240 – 225	stratigraphic gap		
late Permian – early / Middle Triassic	250 – 240	Beaufort		Terrestrial – river / floodplain
early Permian – late Permian	265 – 250	Ecca		Marine - continental slope, deltaic, lacustrine
late Carboniferous – early Permian	300 – 265	Dwyka		Marine and continental glaciation

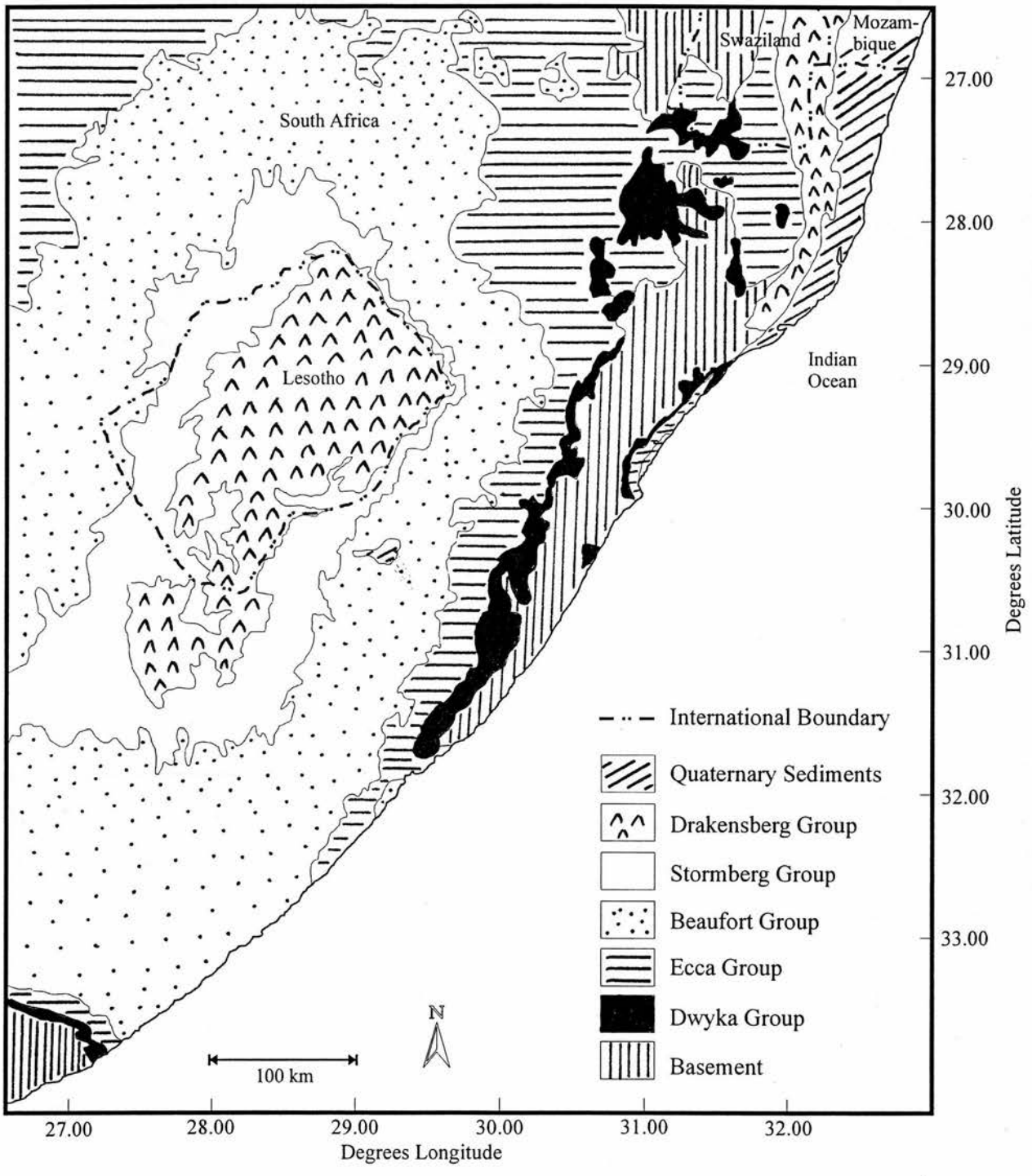

Figure 5.4: Simplified geological map of southeast Africa. For clarity the extensive Karoo Igneous Province doleritic dykes and sills and the kimberlite pipes have not been shown. Based on the 1: 4000000 scale map produced by the Geological Society of South Africa, 1985.

Karoo Basin sedimentation was terminated by the magmatic emplacement of the Karoo Igneous Province, a term that refers to all volcanic and intrusive rocks in southern Africa, south of 14°S (Eales *et al*, 1984; Cox, 1988). This Province has been divided on the basis of volcanic rock composition and age (Marsh and Eales, 1984; Cox, 1988; Duncan *et al*, 1997; Marsh *et al*, 1997). The Central Area, extending from about 25°S to 31°S, but excluding the basalts of the Lebombo Mountains (~ 32°E), is distinguished on the basis that the intrusive and extrusive volcanic rocks are tholeiitic basalts emplaced in a stable cratonic setting 183 ± 1 Ma BP (Marsh and Eales 1984; Marsh *et al*, 1997; Duncan *et al*, 1997). This Central Area includes the Drakensberg Group basalts, and the associated dykes and sills of intrusive dolerites, gabbros and their derivatives that occur throughout southern Africa, north of 33°S (Dingle *et al*, 1983; Eales *et al*, 1984; Marsh *et al*, 1997). The present day denudational remnant of Drakensberg Group basalts, centred on Lesotho, has a thickness of ~ 1.4 km and an estimated volume of ~ 2.6 x 10^4 km^3. The cumulative thickness of sills within the Karoo Basin alone is ~ 1 – 1.5 km, suggesting that 1 – 2 x 10^6 km^3 of basaltic magma may have been emplaced in the Central Area (Marsh and Eales, 1984; Rehacek, 1995; Marsh *et al*, 1997).

Drakensberg Group basalts lie conformably on the Clarens Formation, although intercalations of basalt and sandstone are common in the lower part of the volcanic sequence exposed in the Barkly East area (31°S, 27° 30'E) and in parts of Lesotho indicating an overlap between volcanic activity and the latter stages of deposition of the Stormberg Group (Du Toit, 1954; Lock *et al*, 1974; Eales *et al*, 1984; Schmitz and Rooyani, 1987). Recent step heating $^{40}Ar - ^{39}Ar$ dating, coupled with the widespread recognition of a single palaeomagnetic reversal and the lack of weathering horizons within the basalts, have shown that the Drakensberg Group and the Karoo Basin intrusives were emplaced over a ~ 0.5 Ma period at 183 ± 1 Ma BP (Duncan *et al*, 1997; Marsh *et al*, 1997). This timing corresponds well with the date established for Ferrar dolerites from Antarctica leading to suggestions that emplacement was synchronous and related to one Gondwana-wide causal event (Encarnacion *et al*, 1996; Duncan *et al*, 1997).

Following the cessation of magmatic emplacement in the Central Area, the Karoo Basin switched from being a predominantly depositional to a dominantly denudational environment. Voluminously limited igneous activity continued until ~ 65 Ma BP in the form of emplacement of kimberlites and related intrusive rocks which have a widespread temporal and spatial distribution in southern Africa (Dingle *et al*, 1983; Dawson, 1989; Shee *et al*,

1989). Kimberlites have been emplaced during distinct phases – 1600 Ma, 1200 Ma, 500 Ma, 200 – 110 Ma and 100 – 65 Ma (Smith *et al*, 1985; Shee *et al*, 1989; Skinner *et al*, 1992). Those older than 110 Ma are restricted to the Kaapvaal craton region. The distinctive morphology of the kimberlite pipes has been used to provide a very general estimate of post emplacement denudation (Hawthorne, 1975; Chapter 8).

5.2.3 TECTONIC SETTING

The plate tectonic setting of southeast Africa is complicated and is shown in Figure 5.5. The complication arises from the continental margin being the product of two continental break-up events, the separation of East (Africa, South America) and West (Antarctica, Australia and India) Gondwana (~ 170 – 156 Ma BP) and the later rifting of South America from Africa (~ 133 Ma BP).

Initial rifting between East and West Gondwana began during the mid-Jurassic and is related to the emplacement of the basalts of the Karoo Igneous Province (eg White and McKenzie, 1989, 1995; Cox, 1992; Storey, 1995; White, 1997; Storey and Kyle, 1997; Duncan *et al*, 1997). The association of flood basalts with continental rifting in a global context is now widely accepted (White and McKenzie, 1995; Courtillot *et al*, 1999). The 183 Ma basalts pre-date the oldest known magnetic anomaly identified in the Mozambique Basin, southwest Indian Ocean (Figure 5.5), M22 (~ 156 Ma, Storey, 1995) by ~ 26 Ma. This is thought to be a maximum age difference because of the uncertainties in magnetic anomaly ages (White and McKenzie, 1995) and the presence of ~ 300 km between the identified anomalies and the continental margins. This 300 km gap indicates that sea floor spreading may have started at ~ 170 Ma (Lawver *et al*, 1991). An interval of ~ 10 Ma between flood basalt emplacement and the oldest evidence of sea floor spreading is typical for flood basalt provinces (White and McKenzie, 1995; White, 1997). The nature and position of the mantle plume(s) / 'megaplume' responsible for the Karoo Igneous Province, the relationship of plume activity and lithospheric thinning in continental break-up, and the possible involvement of plate boundary forces induced by subduction are all subject to debate (White and McKenzie, 1989; 1995; Campbell and Griffiths, 1990; Antoine and Moyes, 1992; Cox, 1992; Storey, 1995; Duncan *et al*, 1997; Storey and Kyle, 1997; White, 1997; Coutillot *et al*, 1999).

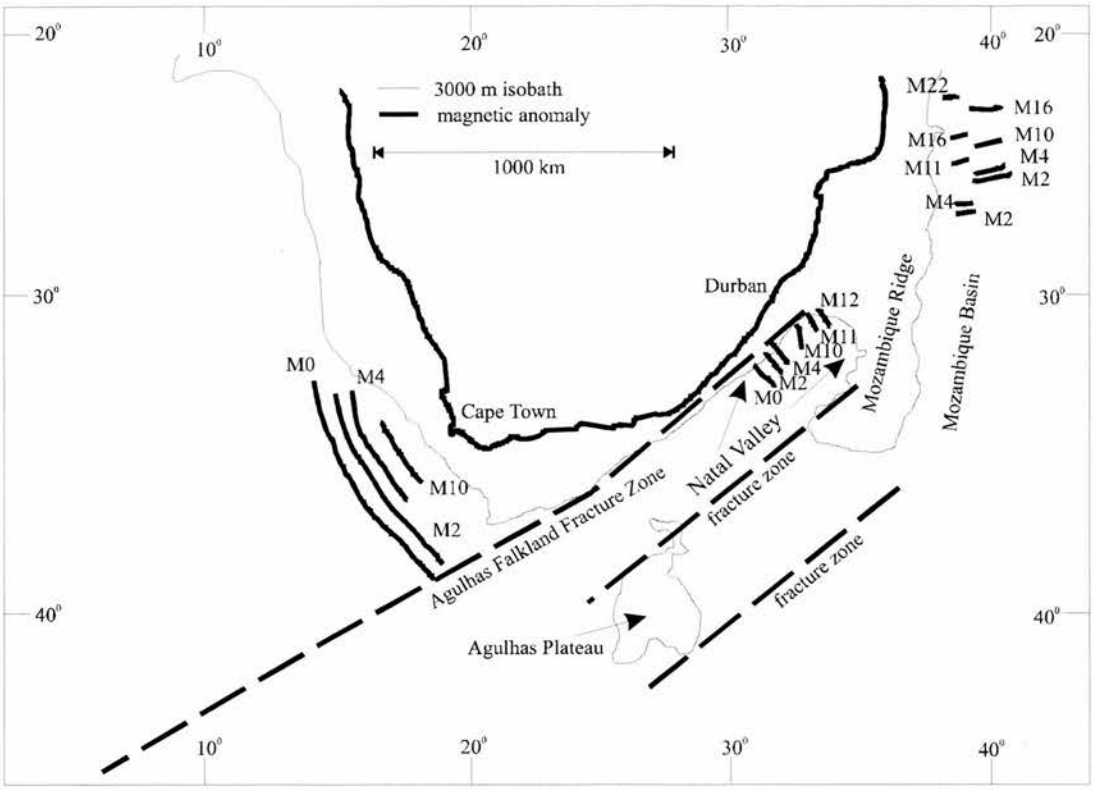

Figure 5.5: Plate tectonic setting of southern Africa. The Mozambique Basin was formed during the break-up of East and West Gondwana. The separation of South America and Africa led to the formation of the Natal Valley, the former position of the Falkland Plateau, and the south Atlantic. After Dingle *et al*, 1983.

Rifting of South America and Africa, related to the mantle plume presently situated under Tristan da Cunha (White and McKenzie, 1989), resulted in the opening of the south Atlantic in the early Cretaceous. The earliest evidence for sea-floor spreading is given by magnetic anomalies found in both the south Atlantic, off the Agulhas Bank, and off the east coast of South Africa, south of ~ 30 °S, in the Natal Valley (Figure 5.5). The Natal Valley was the site, prior to break-up, of the Falkland Plateau which is regarded either as part of the South American plate (Dingle *et al*, 1983; Martin and Hartnady, 1986) or part of a separate microplate system (Cole, 1992; Ben-Avraham *et al*, 1993; Marshall, 1994; Storey and Kyle, 1997; Storey *et al*, 1999). Although the exact fit of the Falkland Islands and the associated plateau are subject to some debate (eg Ben-Avraham *et al*, 1993; Marshall, 1994; Storey *et al*, 1999), the rifting of South America and Africa caused the Falkland Plateau to shear southeast from Africa along the Agulhas Falkland Fracture Zone (Figure 5.5). Onshore, this is evidenced by a series of faults between 28° 30' to 31° S and 30° to 32° E, the nature and

orientation of which are consistent with the dextral strike-slip shearing of the Falkland Plateau (Martin, 1983; von Veh and Anderson, 1990).

Goodlad *et al* (1982) and Martin and Hartnady (1986) suggest that a rift opened along the southern face of the northeastern edge of the Natal Valley (Figure 5.5) and the northern extremity of the Falkland Plateau at M11 – M12. A spreading centre which created oceanic crust progressively from north to south in the Natal Valley, developed by M10 (~ 133 Ma, Storey, 1995). This corresponds with the oldest magnetic anomaly identified in the south Atlantic (Dingle *et al*, 1983). The continental margin has remained a passive feature since this time, although there have been some recent suggestions of on- and offshore neotectonic activity of a minor nature (Hartnady, 1985; Ben-Avraham, 1995; Ben-Avraham *et al*, 1995).

Cox (1992), based on the nature of the Karoo Igneous Province basalts, suggested that this area would have experienced considerable underplating. This view is supported by the gravity anomaly pattern that suggests an unusually thickened crust (Birot, 1982, cited by Gunnell and Fleitout, 1998). Isostatic compensation, induced by the underplating, is likely to have increased the pre-break-up elevation of this area. Tectonic modelling of sheared margins (eg Gadd and Scrutton, 1997) would suggest that some, transient, thermally induced uplift may have occurred during the passage of the ocean spreading centre reported by Martin and Hartnady (1986).

5.2.4 CLIMATE

5.2.4.1 PRESENT CLIMATE

At present southeast Africa encompasses three main climatic zones: a subtropical coastal zone; an inland temperate plateau area and a zone that connects the two. The subtropical zone extends along the coastal areas of KwaZulu-Natal and Eastern Cape provinces and is characterised by humid wet summers and warm dry winters. The temperate plateau runs inland from the escarpment and experiences cool wet summers and cold dry winters. The zone between these two areas has warm wet summers and cool dry winters.

Southeast Africa receives > 80 – 85 % of annual rainfall during the summer months of October to March with a pronounced dry season during June and July (Schulze, 1972; Tyson, 1986; Schmitz and Rooyani, 1987). Most summer rain is of a convective origin with thunder occurring on average 40 days per year at the coast, rising to > 80 days at the escarpment and the Lesotho Highlands before falling to 70 inland of Lesotho (Tyson, 1986;

Sene *et al*, 1998). Light orographic rain also occurs on the escarpment (Sene *et al*, 1998). The mean annual precipitation (MAP) rises from 1000 mm at the coast to 1250 – 1500 mm at and just above the escarpment (Tyson, 1986; Schmitz and Rooyani, 1987; Schulze, 1997; Sene *et al*, 1998). There is a marked rainshadow effect in the central portion of the Lesotho Highlands, with MAP dropping to 500 mm in lower-lying regions of Lesotho and further inland (Schmitz and Rooyani, 1987; Hanvey and Marker, 1992; Sene *et al*, 1998). The highest regions of the Lesotho Highlands and the Drakensberg experience snow falls on 5 – 9 occasions per year (Schulze, 1972; Tyson, 1986). These are light, having a water equivalent annual total depth of < 10 % of MAP, and snowmelt is usually complete within a few days (Schulze, 1997; Sene *et al*, 1998).

Mean annual temperatures (MAT) usually exceed 20 °C along the coast but fall, as altitude increases, to 11 – 12 °C along the escarpment and over the Lesotho Highlands before rising again to 14 – 16 °C inland (Tyson, 1986: Schulze, 1997). The escarpment and Lesotho Highlands experience mean daily maximum summer temperatures of < 22 °C and mean daily minimum winter temperatures of < 0 °C (Schulze, 1997). Frost (air temperature < 3 °C) occurs on ~ 180 days in the highest areas of the Drakensberg and Lesotho (Schulze, 1972; Sene *et al*, 1998).

5.2.4.2 PALAEOCLIMATE

The denudational nature of the southeast African landscape severely limits the number of depositional sites that have the potential to yield temporally constrained palaeoenvironmental data. What data that do exist concentrate on the late Quaternary and Holocene. The longest continuous record is that provided by the lacustrine sediment of the Pretoria Saltpan (~ 25 ° 30 'S, 28 °E). Data from this site (Partridge *et al*, 1993, 1997) records that MAP declined during previously colder phases in the summer rainfall area of southern Africa. Evidence from various sites, including the Pretoria Saltpan, indicates that during the last glacial maximum (~ 24 – 16 ka BP) southeast Africa would have been cooler by ~ 5 – 8 °C and drier by up to 50 % (Butzer, 1984; Deacon and Lancaster, 1988; Mitchell, 1996; Partridge, 1990, 1997a; Partridge *et al*, 1990, 1993, 1997, 1999; Scott, 1984).

Palaeoclimatic information for the Drakensberg and Lesotho Highlands is almost exclusively derived from geomorphic evidence. Despite several attempts to invoke some limited Quaternary glaciation of the Lesotho Highlands (eg Dyer and Marker, 1979; Marker, 1991, 1995a, 1995b; Hanvey and Marker, 1994) no unequivocal evidence of past glaciations has

been identified and the view is widely held that this area has experienced no Pleistocene glaciation (eg Tyson, 1986; Deacon and Lancaster, 1988; Hall, 1992; Boelhouwers, 1994; Sumner, 1995; Grab and Hall, 1996; Goudie, 1996; Grab, 1998a). That cooler conditions prevailed in the Lesotho Highlands at some point in the past is well supported by the identification of relict periglacial features (Table 5.2). These features are not well constrained temporally, the oldest reported radiocarbon data for any site in the Lesotho Highlands being ~ 13500 a BP for a peat deposit recovered from the base of 'nivation' hollow (Marker, 1998). The presence of periglacial features at the lower elevations of the Eastern Cape may reflect the expansion of the winter rainfall regime, presently confined to the south of ~ 32 °S, during colder periods which it is thought may have extended northwards to 30 °S (Tyson, 1986). Currently active frost-related processes result in the seasonal appearance of needle ice, patterned ground, and thufur above 2800 – 3000 m (Hastenrath and Wilkinson, 1973; Grab, 1994, 1997a, 1997b, 1998a, 1998b; Hanvey and Marker, 1992; Lewis, 1988a, 1988b; van Zinderen Bakker and Werger, 1974).

Table 5.2: Some relict periglacial features reported from southeast Africa.

Feature	Altitude (m asl)	Location	Authors
'Nivation' hollows	2900-3100	Lesotho	Hastenrath & Wilkinson 1973
	3000	Lesotho	Dyer & Marker 1979, Marker 1991
	>2650	Lesotho	Marker 1995a
Protalus rampart	2000	Eastern Cape	Lewis 1994
Rock glacier	1800-2000	Eastern Cape	Lewis & Hanvey 1993
Solifluction / head	2700+	Lesotho	Hastenrath & Wilkinson 1973
deposits /	1980	Eastern Cape	Lewis & Darbis 1985
sedimentary	2900	Lesotho	Marker 1994
sequences	1800	Eastern Cape	Lewis & Hanvey 1988
	2000	Eastern Cape	Hanvey & Lewis 1991
	1920	Eastern Cape	Lewis & Hanvey 1991
	3275	Lesotho	Hanvey & Marker 1994
	2900-3000	Lesotho	Marker 1994, 1995a, 1995b
	3140-3300	Drakensberg	Boelhowers 1994
Blockstreams/	2700-3200	Lesotho	Hastenrath & Wilkinson 1973
blockfields/debris	3140-3300	Drakensberg	Boelhouwers 1994
deposits	3200	Drakensberg	Grab, 1996
	>3300	Lesotho	Grab, 1999
Cryoturbation	1980	Eastern Cape	Lewis & Darbis 1985
Ice-wedge casts	1980	Eastern Cape	Lewis & Darbis 1985
Compacted soils	2500-3050	Lesotho	Fitzpatrick 1978

5.3 EVOLVING IDEAS ABOUT PASSIVE MARGIN LANDSCAPES

5.3.1 INTRODUCTION

The advent and widespread acceptance of a coherent plate tectonic theory has provided a new framework within which to study the impact of endogenic processes on landscape evolution. The plate tectonics model, developed in the 1960's, permits a basic distinction to be drawn between active continental margins and passive continental margins (Kearey and Vine, 1996; Summerfield, 1991a). Passive margins exhibit a range of gross morphologies (Figure 5.6). Gilchrist and Summerfield (1990) identified two end members of passive margin morphology, low-elevation and high-elevation margins. Low-elevation margins, such as southern Australia and Argentina, have a broad continental shelf, a low-elevation, low-relief, coastal plain which rises gently to a relatively low-elevation interior. In contrast, high-elevation passive margins, such as southeastern Australia, southwest Africa, and Arabia, are characterised by a narrow continental shelf, an extensively dissected coastal zone which is separated by a major coastal-facing escarpment from a generally high-elevation, low-relief, interior. Seidl *et al* (1996) sub-divided high-elevation margins into those in which the drainage divide coincided with the top of the escarpment (drainage divide escarpments) and those which have rivers flowing seaward across the escarpment (gorge-like escarpments).

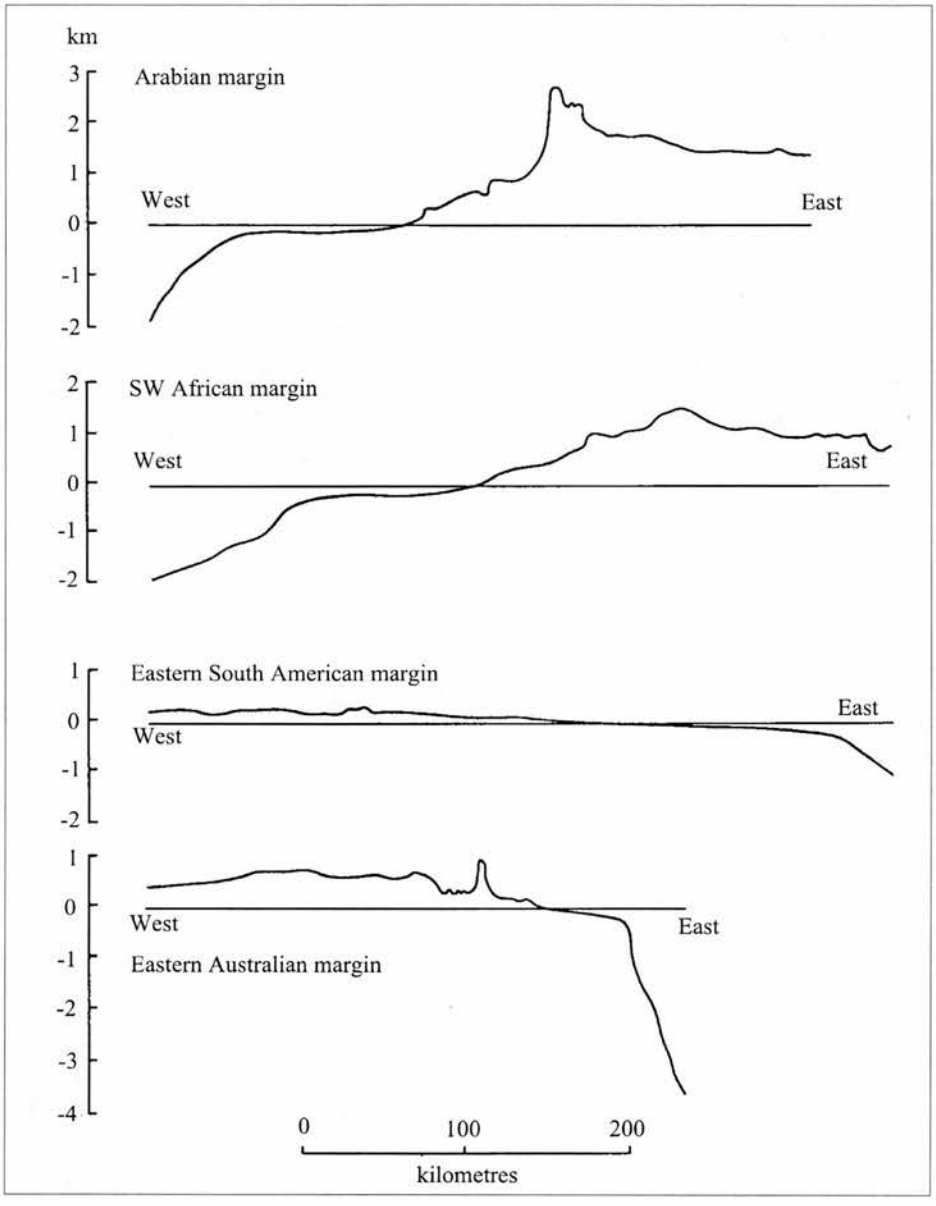

Figure 5.6: Representative cross-sections of passive margin morphology. Onshore irregularities attributable, primarily, to major fluvial incision. (After Gilchrist and Summerfield, 1994).

5.3.2 CLASSIC CONCEPTUAL MODELS

Various conceptual models have been proposed to explain long-term, macroscale, landscape development some of which, although formulated prior to the advent of plate tectonic theory, are applicable to passive margin landscapes. The formulation of these ideas and their application to the great variety of global landscapes was the central tenet of geomorphology

for over sixty years ending in the 1960's with a major shift in emphasis towards quantitative surface process studies at short temporal and small spatial scales of investigation. The most influential scheme was the 'geographical cycle' or 'cycle of erosion' of W.M. Davis (Davis, 1899; 1954). Davis viewed time as a neglected geographical element and pushed landscape evolution to the forefront of geomorphology. His cycle (Figure 5.7) assumes a rapid single uplift, or deformation event, and envisages a prolonged period of downwearing that reduces the uplifted mass to a 'featureless lowland' or peneplain.

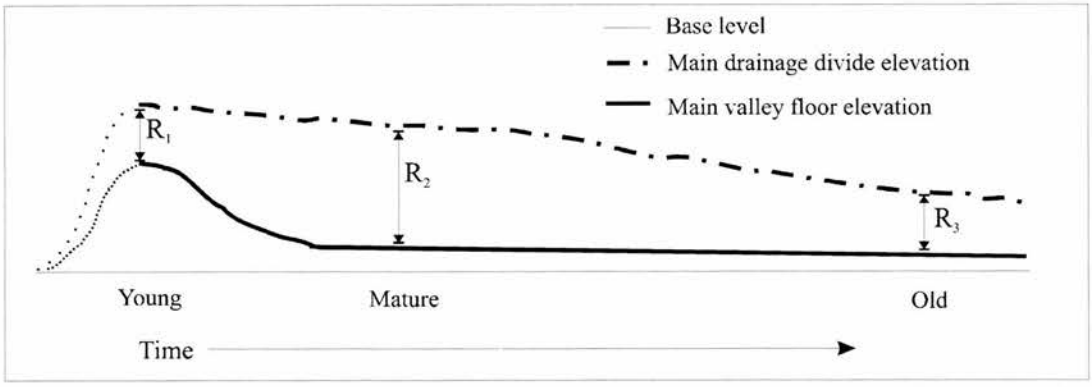

Figure 5.7: Davis' ideal geographical cycle. A short period of uplift leads to a relatively small maximum relief (R_1) between the drainage divide and the main valley floor (a ' young' landscape). With time, fluvial processes reduce the valley floor altitude quicker than the divides leading to increased relief (R_2), diagnostic of a 'mature' landscape. After maturity, relief (R_3) reduces as the interfluves lower more quickly than the valley floors creating an 'old' landscape of low subdued relief, the 'peneplain'. (After Davis, 1899).

This cycle was based on the importance of weathering and fluvial processes and subsequent modifications were made to account for arid and glacial processes, endogenic interruptions and climatic change (Davis, 1954). Polycyclic landscapes, produced by changing climates, tectonic rejuvenations or lithological differences, in which 'youthful' features were overprinted on older forms, were quickly recognised as being commonplace. These landscapes were interpreted in terms of stages of evolution with base level adjustments, attributable to tectonic or eustatic interruptions, punctuating relatively prolonged periods of exogenic downwearing. This Davisian approach was applied to explain the development of landscapes in, for example, the North American Atlantic passive margin and southeast Australian passive margin.

W. Penck (1953) questioned the Davisian cycle's assumption of a single rapid uplift and proposed, instead, that the Davisian cycle was a special case of the more general situation in which landform development would be subject to varying periods / rates of tectonic uplift (Penck, 1953; Thornes and Brunsden, 1977; Gilchrist, 1995). Penck (1953) was interested in

analysing landscapes to reveal the history of endogenic movements and, as Thorn (1988, p135) points out, envisaged landscapes as following a number of possible sequences which were controlled by the relative interplay of uplift and denudational / denudational intensity rather than time. The inclusion of a fluctuating base level made Penck's proposal "more confused and unsatisfactory than the [Davisian] cycle" (Chorley, 1965a, p24). Chorley (1965a) similarly questioned the single uplift of Davis and suggested that the exclusion of progressive movements by Davis made his cyclic scheme "possible".

Like Davis, L.C. King also proposed a cyclic approach in which landscape development was controlled by denudation cycles initiated by uplift events (King, 1953; 1962). King was highly critical of the Davisian scheme of slope flattening and downwearing which produced the peneplain (Davis, 1899), even going as far as describing the peneplain as "an imaginary landform" (canon 37, 1953, p749). According to King (1953, p742) the secret of landscape evolution lies in the mode of development of hillslopes. In King's "Standard Epigene Cycle of Erosion" the most important denudation activity is the parallel retreat of hillslopes, especially the free face or scarp element of the hillslope, which produce, as they retreat, broad shallow angle pediment slopes (King, 1953; 1962). Over time the parallel retreat destroys the interfluves and the pediments coalesce to form a pediplain, the whole process being known as pediplanation.

Of particular interest, in the context of passive margin landscapes, is King's idea of the "great cyclic scarps" (1953, p743) or "major tectonic and erosional scarps" (1962, p157). Unlike the parallel retreat of hillslopes that are initiated by fluvial incision responding to uniform uplift, these large free faces are produced when a 'sub-continental' scale landmass is subjected to differential tectonic uplift, the effect of which is greatest at the coast (King, 1953; 1962). This initiates a new cycle of erosion involving the parallel retreat of the cyclic scarps that evolve independently of, and mainly perpendicular to, the main drainage basins (Figure 5.8). These scarps are initiated by large coastal monoclines and retreat parallel to the site of their initial formation (1944; 1953; 1962).

An important feature of pediplains, which is a direct consequence of King's preference for parallel retreat to vertical downwearing, is that they persist in the landscape for prolonged periods with little modification, only being destroyed by the parallel retreat of a new, uplift induced, erosion cycle (Figure 5.8). If an area experiences uplift events (or base level lowering) in relatively quick succession, a series of roughly parallel scarps will form separating pediplains, each attributable to different erosion cycles, which will rise step-like from the coast (Figure 5.8). The longevity of these pediplanation surfaces can be verified, according to King, by dating the oldest superficial deposits identified on the relevant surface. Thorn (1988) has pointed out that pediplains are time-transgressive, with the planed surface being progressively older with increasing distance from the scarp which is producing the pediplain.

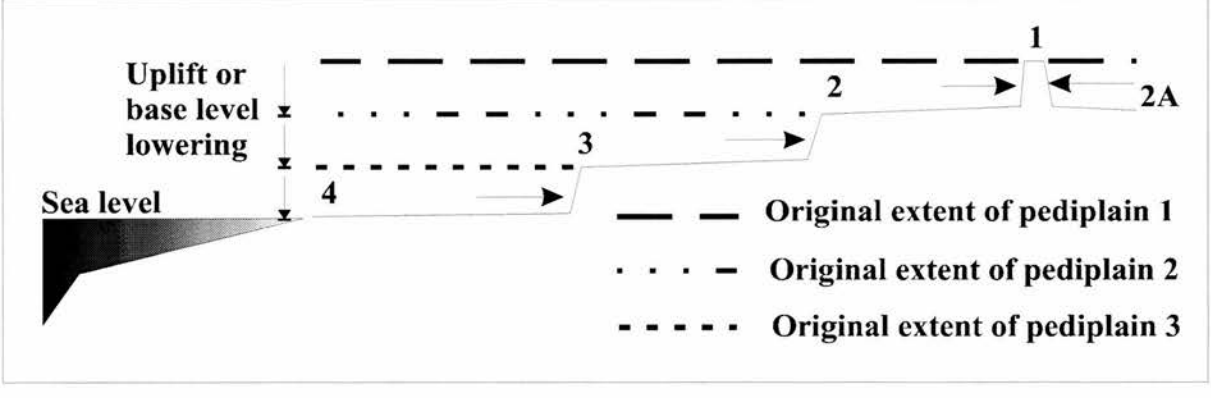

Figure 5.8: King's model of landscape evolution. Uplift or base level lowering induce the parallel retreat of a large cyclic scarp. This reduces the extent of pediplain 1 and creates pediplain 2. Before the complete removal of pediplain 1 another uplift creates a new phase of scarp retreat which reduces the extent of pediplain 2 and initiates a new pediplain 3. A further uplift event leads to the formation of surface 4. Pediplain 1 is the oldest surface while pediplain 4 is the youngest. Each pediplain is progressively older from left to right, except for the small section of pediplain 2 (2A), which is subject to parallel retreat from right to left. (After Summerfield, 1991a).

King's scheme was originally developed to explain the evolution of the southern African passive margin landscape, but was subsequently expanded and modified to account for virtually all global landscapes (King, 1962). The publication of King's ideas coincided with a major shift in emphasis in geomorphology and this meant his approach had much less impact than the Davisian cycle (Ollier, 1995b).

These classic models have been subject to a number of criticisms. The popularity and longevity of the Davisian cycle has been attributed to a simple methodology and its close affinity with studies of denudation chronology (Chorley, 1965a; Thornes and Brunsden,

1977; Thorn, 1988). These studies related the sequential development of denudational forms to base level adjustments. This methodology, which is the same as that proposed by King (1962), involved the identification of surfaces or partial remnants and their correlation, based on summit accordance, over large areas. These surfaces, it was argued, could be dated either by sedimentary deposits or stratigraphic relationships. Such an approach was heavily criticised for its lack of quantitative measurements, preoccupation with time and a lack of concern with processes and structure, although both Davis and King accept that process and structure play a role in landscape evolution (Davis, 1954, p249; King, 1953, canon 1, p747). Chorley went as far as describing the conclusions of studies using this methodology as being a product of "the means of analysis rather than a physical reality" (1965a, p34).

In addition to the foregoing, more recent criticism of these classical models has focussed on their lack of a comprehensive tectonic framework (Summerfield, 1985), although King (1955; 1961; 1983) did try to relate landscape development to endogenic controls. King (1955) sought to explain the periodic uplift of the landsurfaces in his model in terms of the episodic isostatic adjustments of the lithosphere to lateral denudation caused by escarpment retreat. This view interprets isostasy, the mechanism whereby the lithosphere responds to loading / unloading to attain hydrostatic equilibrium, as only occurring once a threshold distance of scarp retreat has been achieved (Gilchrist and Summerfield, 1991). However, Gilchrist and Summerfield (1991) have shown that King's view (1955) (followed by several subsequent workers, including in the context of SE Africa, Partridge and Maud, 1987) is based on a misunderstanding of how the lithosphere reacts, over geological time, to the redistribution of mass by, for example, denudation. Progressive vertical denudation (eg Davis, 1899) and / or progressive lateral denudation (eg King, 1953) over timescales relevant to long-term landscape development induce continuous, rather than episodic, isostatic compensation (Gilchrist and Summerfield, 1991). Hence pulsed uplift events, of the style proposed by King (eg 1953), would require the operation of episodic tectonic, rather than isostatic, mechanisms, which, in the context of passive margin development, are not obvious (Gilchrist and Summerfield, 1991; Kooi and Beaumont, 1994). King (1961) did propose a specific endogenic mechanism, 'cymatogeny', involving upwarping and flexure of continental margins in response to unspecified subcrustal processes, however this lacks a physical basis (Thorn, 1988; Summerfield, 1991a; Kooi and Beaumont, 1994). Gilchrist (1995) discussed the fundamental aspects of these conceptual models with respect to a modern morphotectonic framework and concluded that classical notions of endogenic

activity, based on the existence of cyclic erosional surfaces, are "deficient and require revision" (p21).

5.3.3 Tectonic and Geophysical models

The economic importance of the hydrocarbon reserves in sedimentary basins, which are commonly associated with passive margins, created the impetus for the development of quantitative tectonic and geophysical models (Allen and Allen, 1990). These models need to explain the evolution of such basins and, in particular, the spatial and temporal patterns of post-rift sediment accumulation. The success of such modelling is partly measured by the ability of the model to reproduce not only the sedimentary basin, but also the gross morphology of the passive margin and to constrain the nature and timing of onshore denudation and offshore sedimentation. This field has been dominated by geologists and geophysicists, rather than geomorphologists, and has initiated a series of quantitative models of passive margin development based, originally, solely on the endogenic mechanisms of plate tectonics, but with increasing recognition of the role of exogenic processes.

Detailed reviews of the initial tectonic models of passive margin evolution may be found in Allen and Allen, (1990), Keen and Beaumont (1990) and, from a more geomorphological perspective, Summerfield (1991a) and Gilchrist and Summerfield (1994). The initial tectonic models can be distinguished by their employment of 'active' and 'passive' rifting mechanisms as a means of explaining the lithospheric stretching responsible for continental break-up (Şengör and Burke, 1978). In active rifting models stretching is driven by the tensional forces induced by uplifting or doming of the crust as it responds to a sub-lithospheric thermal anomaly (eg Burke and Dewey, 1973). Passive rifting models require that the extension is induced by horizontal tensional stresses in the lithosphere, resulting from plate driving mechanisms, which allow hot, low-density, asthenospheric material to penetrate the lithosphere (eg McKenzie, 1978). The distinction is one of a temporal nature relating to the sequential order of uplift, thinning, and sub-lithospheric thermal activity which is often difficult to distinguish in reality, with most passive margins exhibiting both 'active' and 'passive' features (Allen and Allen, 1990; Gilchrist and Summerfield, 1994; van der Beek, 1995).

High-elevation passive margins have a distinct marginal upwarp which, if located close to the rift, is known as a rift-flank uplift (Gilchrist and Summerfield, 1990). Marginal upwarps exhibit marked increases in elevation and are usually (cf. southeast Australia) located in the

vicinity of the main escarpment (Figure 5.6). A crucial test of the tectonic models has been their ability to re-produce these marginal upwarps. Four endogenic mechanisms have been put forward to explain such surface uplift - thermal forces, underplating, dynamic forces and flexural isostatic forces (van der Beek *et al*, 1995).

The earliest attempt to model sedimentary basins using passive rifting models involved uniform stretching of both the crust and lithosphere (McKenzie, 1978). The isostatic response to such lithospheric thinning results in a lowering of the surface elevation suitable for sedimentary basin development. The partial replacement of the thinned lithosphere by hot, low-density, asthenospheric material would induce some thermal uplift, but this was regarded as minimal due to the ratio of crust to lithosphere and insufficient to re-produce the onshore topography (Allen and Allen, 1990; Gilchrist and Summerfield, 1994; van der Beek, 1995). Attempts to amend this model to generate rift-flank uplift have included depth-dependent (non-uniform) thinning of the lithosphere (eg Royden and Keen, 1980) and secondary convection (eg Steckler, 1985). Royden and Keen (1980) suggested that de-coupling the lithosphere from the crust, to permit stretching of the lithosphere without extension of the crust, would lead to an increase in the volume and extent of hot, low-density, asthenospheric material capable of creating surface uplift of ≤ 1.5 km. Secondary convection, induced in the sub-lithospheric mantle by extension, is suggested to advect additional heat leading to a proposed rift-flank uplift of ~ 1 km (Steckler, 1985).

The general difficulty with the passive rifting models is their reliance on thermal uplift mechanisms. Whilst this might be suitable for relatively recently formed passive margins (eg the post-Eocene Gulf of Suez, Steckler, 1985; Bohannon *et al*, 1989; Steckler and Omar, 1994) the transient nature of thermal uplift limits its temporal influence to ~ 60 Ma after the plate has moved away from the anomaly (the thermal time constant of the lithosphere). This mechanism therefore fails to account for marginal upwarps identified on mature (> 100 Ma) passive margins.

Active rifting also makes use of thermal isostasy to explain surface elevation at passive margins. The surface uplift is predicted to occur prior to rifting and is induced by the presence of a thermal anomaly, usually in the form of a mantle plume (hot spot, hotline or megaplume – White and McKenzie, 1989; Cox, 1992; Storey and Kyle, 1997). This thermal anomaly is an area of anomalously hot (by ~ +200 °C) mantle thought to be capable of creating a pre-rift domal uplift on the surface with a radius of up to 2000 km and an increase in surface elevation up to 3 – 4 km in the centre (White and McKenzie, 1989; 1995). Whilst

the initial uplift may be due to the thermal impact of the anomaly another mechanism has had to be invoked to explain the persistence of such uplift after the plate has moved away from the plume.

The recognition of the role of mantle anomalies in passive margin formation is, in part, attributable to the presence of large flood basalt provinces at many passive margins (Burke and Dewey, 1973; White and McKenzie, 1989). The extrusion of such large volumes of basalt within ~ 1 Ma is due to decompressive melting of the mantle in response to lithospheric stretching. The geochemical composition of the basalts suggests that a significant additional volume of this melt is accreted to the base of the crust (eg McKenzie, 1984; White and McKenzie, 1989, 1995; Cox, 1993). This underplating thickens the crust and creates 'permanent' surface uplift through isostatic adjustment.

Dynamic models propose that the deformational response of the lithosphere to extensional forces is controlled by the rheological properties of the lithosphere (eg Royden and Keen, 1980; Braun and Beaumont, 1989). The existence of a layered rheology in which layers exhibit a range of resistances to deformation leads to the lithosphere 'necking', around the strongest layer when stretched (Figure 5.9). The depth of the resistant layer within the lithosphere controls the elevation of the rift flanks that are supported by an upward flexure (Braun and Beaumont, 1989) (Figure 5.9). This mechanical approach is sometimes coupled with thermal aspects to explain rift flank uplifts (eg Royden and Keen, 1980; Lister and Etheridge, 1989).

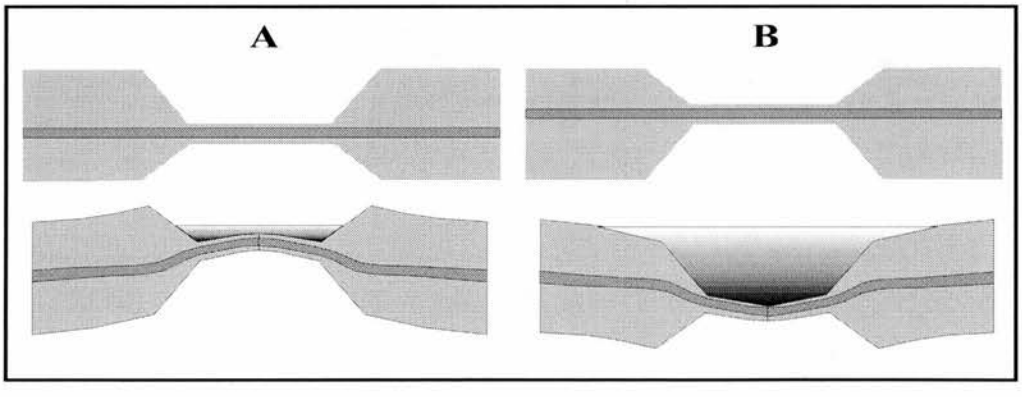

Figure 5.9: Illustration of the concept of lithospheric 'necking'. When stretched, if a layered rheology is assumed, the lithosphere 'necks' around the strongest layer (dark shaded band). If the level of necking is deep (A) upward flexure will occur creating flexurally supported rift flanks. If the level of necking is shallow (B), downward flexure occurs creating a basin. Zones of sediment accumulation are highlighted by the graduated shading. (After Braun and Beaumont, 1989; van der Beek, 1995).

The final commonly encountered uplift mechanism is flexural isostasy. This, in part, is the mechanism employed by Braun and Beaumont (1989). Weissel and Karner (1989) suggest that the permanent uplift of rift flanks is due to flexural isostatic rebound in response to mechanical unloading of a lithosphere during extension. This approach relies on the lithosphere retaining finite mechanical strength (flexural rigidity) even when extended. The isostatic rebound implies either that there is a rheologically strong layer in the lithosphere similar to that proposed by Braun and Beaumont (1989) (Figure 5.9) or a detachment fault which extend through the entire lithosphere, as suggested to account for asymmetric rifts (eg Lister and Etheridge, 1989).

The tectonic / geophysical models, outlined above, have almost exclusively concentrated on rifted, rather than sheared, passive margins due to the more complex structural history of the latter (Scrutton, 1979; Allen and Allen, 1990; Kearey and Vine, 1996). Idealised models of sheared margin development (eg Lorenzo and Vera, 1992; Gadd and Scrutton, 1997) suggest that surface uplift of up to 1400 m will occur only in response to heating from the oceanic lithosphere during the passage of an oceanic spreading ridge. This thermally driven uplift would be transient and would tend to propagate as a wave along the sheared margin. This mechanism cannot explain marginal upwarps on mature passive margins and ignores the impact of any flexural isostatic response induced by exogenic processes. Further tectonic models are needed to explain the evolution of the first-order onshore topography at such sheared margins fully (Gadd and Scrutton, 1997).

For mature passive margins, where the marginal upwarps are located > 100 km inland of the rift site, the tectonic mechanisms that best account for the marginal upwarps are underplating and flexural isostasy (Gilchrist and Summerfield, 1994). Problems, however, exist with both approaches. Underplating would be capable of generating long-wavelength high-elevation areas that persist long after rifting (eg Cox, 1989) but, as pointed out by Gilchrist and Summerfield (1990; 1994), underplating, of itself, does not explain the shorter-wavelength (50 – 300 km) marginal upwarps. The flexural isostatic approach (eg Braun and Beaumont, 1989; Weissel and Karner, 1989) relies on our presently limited knowledge of the rheological properties of the lithosphere and produces uplift at the rift zone without a mechanism for such uplift propagating inland. When offshore sediment loading is included, the long-term persistence of such rift-flank uplifts becomes debatable (Gilchrist and Summerfield, 1994). These criticisms are akin to the suggestion by Summerfield (1991a,1991b) and Beaumont *et al* (2000) that while tectonic models may successfully explain the primary topography of passive margins, the detailed geomorphic evolution post-

break-up requires a consideration of the interplay between denudation and endogenic processes.

5.3.4 SURFACE PROCESS MODELS AND INTEGRATED APPROACHES

Thomas and Summerfield (1987) highlight the major tectonic factors controlling the morphological evolution of passive margins (Figure 5.10). These factors include, in addition to those employed in the foregoing tectonic models, denudational unloading and, possibly, escarpment retreat. Sub-aerial denudation was not regarded as playing a significant role in generating the gross morphology of passive margins prior to the Gilchrist and Summerfield denudational – flexural model (1990; 1994). This model, comprising a conceptual dual terrain denudation component and a quantitative flexural isostatic constituent, envisages a coupling between endogenic isostatic forces and the exogenic processes responsible for onshore denudation and offshore sedimentation. The conceptual component relies on the presence of differential denudation rates inland and seaboard of the main passive margin escarpment. This is supported by apatite fission track data (eg Bohannon *et al*, 1989; Brown *et al*, 1990), and the presence of a dual drainage system comprising high-energy sub-escarpment coastal catchments and lower-energy fluvial systems inland of the main escarpment (eg De Swardt and Bennet, 1974: Summerfield, 1985). Where isostatic compensation occurs regionally, rather than locally, the spatially differentiated denudation rates would be sufficient to induce marginal upwarps through the operation of flexural isostasy.

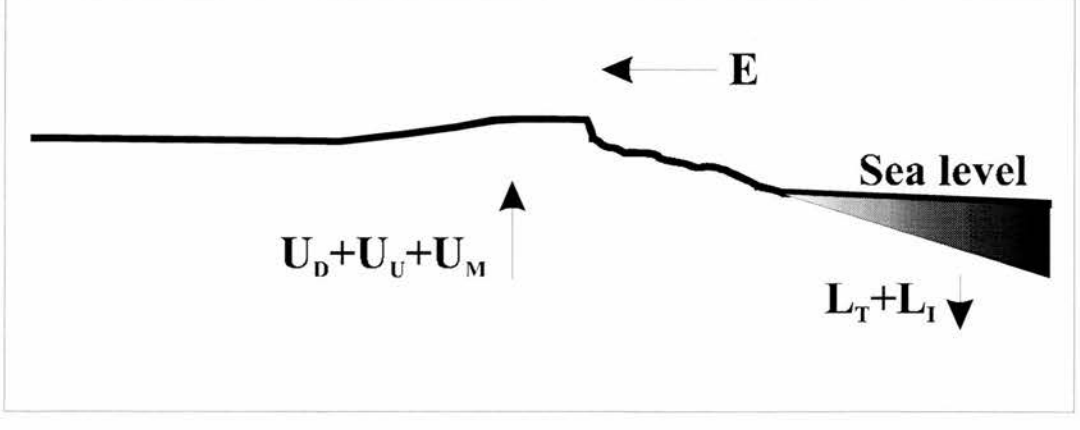

Figure 5.10: Summary of major tectonic factors controlling the long-term morphological development of passive margins. U = isostatic induced uplift due to U_D = denudational unloading; U_U = underplating; U_M = mechanical unloading due to lithospheric stretching. L = isostatic induced subsidence due to L_T = thermal cooling; L_I = sediment and water loading. E = major escarpment retreat (assumes escarpment developed at rifting site and has retreated inland). (After Thomas and Summerfield, 1987).

This study (Gilchrist and Summerfield, 1990; 1994) usefully highlights the need for any model of passive margin evolution to be more integrated and take account of both the impact of denudation / consequent rearrangement of mass and geodynamic forces. It also forms the early part of a growing trend to incorporate the onshore record into models of passive margin evolution and to examine the interactions between tectonics, topography and denudational processes (Bishop and Brown, 1992; Merritts and Ellis, 1994; Gallagher and Brown, 1997, 1999; Beaumont *et al*, 2000; Summerfield, 2000). This change in emphasis, towards a more integrated approach, is largely attributable to three factors – the availability of onshore denudation data; the development of surface process models; and a re-awakening of interest in large-scale geomorphology.

5.3.4.1 ONSHORE DENUDATION DATA

Offshore sediment data has been of some use in helping to constrain the denudational history of the adjacent onshore area (eg Rust and Summerfield, 1990; Pazzaglia and Brandon, 1996). Reconstructing the onshore topographic history using this data is, however, impractical due to problems of constraining the temporal and spatial extent of the onshore source area (Brown *et al*, 1994; Gallagher and Brown, 1997, 1999). In contrast, apatite fission track thermochronology (AFTT) can be used to constrain the regional-scale onshore denudational history of passive margins (eg Gleadow *et al*, 1986; Brown *et al*, 1994; Gallagher and Brown, 1997; Gallagher *et al*, 1998; Summerfield and Brown, 1998; Gleadow and Brown, 2000).

AFTT involves the interpretation of fission tracks, found in the crystal lattice of U-bearing minerals (such as apatite and zircon), which are produced, at a constant rate, by the spontaneous fission of ^{238}U. The number of tracks present is a function of the ^{238}U content and time, while the length of these tracks is a sensitive function of temperature. The tracks form at a constant length and are shortened, or annealed, with increasing temperature, being completely annealed at temperatures > 110 ± 10 °C. The distribution of track lengths therefore reflects the thermal history of the sample as it moves from the ~ 110 °C isotherm to outcrop and may be used to model that history (Gallagher, 1995). If the geothermal gradient is well known, this modelled thermal history can be interpreted to provide a denudational history for the region, temporally constrained by the number of fission tracks (Gallagher and Brown, 1997; Summerfield and Brown, 1998). AFTT data has been used to produce denudational histories for a number of passive margins including southeast Australia (eg Moore *et al*, 1986; Dumitru *et al*, 1991; Brown *et al*, 1994), the Red Sea (eg Omar and

Streckler, 1995); southeast Brazil (eg Harman *et al*, 1998), southern Africa (eg Brown *et al*, 1990; Brown, 1992; Brown *et al*, 2000), east African rift system (van der Beek *et al*, 1998); northeast Atlantic (Clift *et al*, 1998), and western India (Gunnell and Fleitout, 1998).

A finer resolution of denudational histories may be provided by the recent development of a thermochronological technique involving the accumulation of radiogenic helium from uranium and thorium decay in apatite (U-Th/He) (eg Wolf *et al*, 1997). The retention of He is a function of temperature and therefore a thermal history of the sample can be derived and be interpreted as a denudational history in much the same manner as AFTT.

5.3.4.2 Surface process models

Following advances in computing, various quantitative computer models directly applicable to long-term, large-scale (sub-continental), post-break-up landscape evolution have developed (eg Kooi and Beaumont, 1994; Tucker and Slingerland, 1994; Gilchrist *et al*, 1994; van der Beek *et al*, 1995; Braun and Sambridge, 1997; van der Beek and Braun, 1999). In general these numerical surface process models, 'SPM(s)', view post-break-up landscape evolution as governed by the interaction of short-range hillslope and long-range fluvial processes. Based on this assumption, SPMs attempt to provide quantitative predictions of denudation rates and to describe the topographic development of, *inter alia*, passive margins. SPMs provide useful insights into the important factors that control landscape evolution in such settings, particularly when they include dynamic coupling between denudation and flexural isostatic uplift. Kooi and Beaumont (1994) and Tucker and Slingerland (1994) used different SPMs to investigate the role of major exogenic processes in passive margin landscapes and, in particular, the role of escarpments. Gilchrist *et al* (1994) used an SPM to test the prevailing conceptual model of landscape evolution of southwest Africa, while an SPM has also been applied in landscape evolution in southeast Australia (van der Beek and Braun, 1998; 1999; van der Beek *et al*, 1999).

Beaumont *et al* (2000) suggest the need to couple SPMs and tectonic / geophysical models to consider the interactions and feedbacks responsible for shaping the topography of passive margins fully. Simple examples of such an approach, which include interactions but not feedback, are evident in some of the SPMs outlined in the foregoing paragraph which include flexural uplift (eg Kooi and Beaumont, 1994). Kooi and Beaumont (1996) modelled the response of an SPM to tectonic forcing of the scale envisaged by Davis, Penck and King, (they also included the dynamic equilibrium approach of Hack, 1960). The basic form of the

landscape, as envisaged by these different conceptual models, could be reproduced by the coupled SPM-tectonic model and was controlled by the antecedent topography, the timescale of the tectonic process and the response time of the landscape. Although interesting, this study, as those authors admit (p3381), does not prove either that the SPM or the conceptual models accord with natural landscapes.

The further development of these coupled models will, without doubt, increase our knowledge of passive margin evolution, however they rely on integration of data provided by geomorphological, geological and geophysical studies (Summerfield, 1996b; Beaumont *et al*, 2000). An important consideration, which relates to all quantitative models, is that their main value is heuristic (Oreskes *et al*, 1994). The models may be used to illustrate, quantitatively, the consequences of some proposed scenarios for passive margin evolution, but only within the limits of the model simplifications and assumptions (Gunnell and Fleitout, 1998; van der Beek and Braun, 1999). They enable us to explore the "what if" questions (Merritts and Ellis, 1994, p 12139) and, as pointed out by Bishop (1998), the model results constitute synthetic landscapes which should be treated with caution.

5.3.4.3 LARGE-SCALE GEOMORPHOLOGY

The third factor leading to a more integrated approach is the general re-awakening of interest in long-term, large-scale geomorphology (Summerfield, 1981, 1996b, 2000; Bishop, 1988, 1998, 1999; Ahnert, 1996; Sugden *et al*, 1997). In the context of passive margins, exclusively morphological studies have focussed, for example, on reconstructing the drainage history (eg Merritts *et al*, 1994; Pazzaglia and Gardner, 1994). Rivers, particularly bedrock rivers, provide the link between the endogenic processes and the response of the landscape to these (Howard *et al*, 1994). Unravelling the drainage history may therefore provide valuable constraints on the nature and impact of the endogenic processes. Base-level adjustments, induced by tectonics or sea-level changes, are reflected in the long profile of bedrock channels (eg Merritts *et al*, 1994; Goldrick and Bishop, 1995). The analysis of these profiles and their deposits has been used, for example, to demonstrate that flexural isostatic adjustments have occurred along part of the North American passive margin (Pazzaglia and Gardner, 1994), and to assess the impact of passive tectonism in southeast Australia (Bishop and Goldrick, 2000). River long profiles have also been used to constrain the fluvial denudation parameter in an SPM applied to southeast Australia (van der Beek and Braun, 1999).

In the passive margin setting of southeast Australia extensive literature on drainage evolution exists (eg Bishop, 1998; Bishop and Goldrick, 2000). Of particular significance are the identification of the long-term stability of the continental drainage divide and the persistence of the drainage directions from the latest Miocene or early Cenozoic (Bishop, 1986, 1988; Young, 1989; Young and MacDougall, 1993; Bishop and Goldrick, 2000; but cf. Ollier and Pain, 1997). These conclusions are based on the preservation of valley-filling basalts. Although such evidence is not available in other passive margin landscapes, the possibility that endurance of geomorphic form occurs in such landscapes clearly merits consideration.

5.3.5 LANDFORM – SCALE DENUDATION RATES AND ESCARPMENT RETREAT

Research into the long-term development of passive margins has become, over the past few years, a major research theme for the Earth sciences (Summerfield, 1991a; 1996b). As outlined above, advances have been greatest in understanding the geological and geophysical aspects of these landscapes. Although there exists a considerable body of literature on the long-term morphological development of landscapes (Section 5.3.2), this has tended to be qualitative and lacking in empirical data. Summerfield (1991a, 1991b) has pointed out the critical role played by denudation in the development of passive margins and the need to account for the interaction between exogenic and endogenic processes. Accordingly, the continued growth of this integrated approach to understanding passive margin landscape development requires further field-based empirical data about the spatial and temporal patterns of denudation to constrain model parameters. Whilst AFTT (and U-Th/He) provide regional scale denudation data these techniques cannot provide denudation data at the landform-scale. In the context of passive margin evolution, such data is critical to understanding the most dominant onshore topographic expression of high-elevation passive margin landscapes, the escarpment ('Great Escarpment').

King (1953) was among the first to recognise the key role that Great Escarpments must play in the evolution of passive margin landscapes and that their formation / persistence is, in some way, attributable to the interplay of endogenic and exogenic processes. However, despite the widespread acceptance of the relationship between Great Escarpments and continental break-up (eg King, 1962; Ollier, 1985a, 1985b; Summerfield, 1985; Gilchrist and Summerfield, 1990; Steckler and Omar, 1994; Seidl *et al*, 1996; Widdowson, 1997b; Gunnell and Fleitout, 1998) little analysis of these first order topographic features has been undertaken. Several studies of a generally descriptive nature exist (eg Ollier, 1985a; Ollier and Marker, 1985; Ollier and Powar, 1985), and some quantitative studies have examined

the role of lithological resistance in determining slope gradients and gorge head incision into escarpments (eg Moon and Selby, 1983; Young, 1983; Nott *et al*, 1996; Weissel and Seidl, 1997).

The erosional nature of these features has been recognised for almost a century (Suess, 1904, quoted in Partridge and Maud, 1987). Both conceptual (eg King, 1953) and quantitative (eg Gilchrist and Summerfield, 1990, 1994) models of high-elevation passive margins have interpreted these escarpments as retreating over the coastal plain and backwearing into the interior, yet there exist no direct estimates of the rate at which the escarpment retreats. All estimates of the retreat rate to date are indirect and rely on inferences (cf. Fleming *et al*, 1999). King (1953, p729) was the first to estimate an escarpment retreat rate as between "1 foot in 150 years and 1 foot in 300 years", which translates into the commonly quoted rate for all Great Escarpments of 1 – 2 km Ma^{-1} (eg Selby, 1993, p365; Seidl *et al*, 1996, p 301-2). King's "quantitative contribution" (Ollier, 1995b) to geomorphology was based on the assumption that Great Escarpments form at the coast due to break-up and then retreat inland at "a sensibly uniform rate" (1953, p729).

A similar approach has been applied, using the continental edge as the break-up site, by Ollier (1985a), Gilchrist and Summerfield (1990); Steckler and Omar (1994), Seidl *et al* (1996), Widdowson and Cox, (1996); Weissel and Seidl (1997), Ollier and Pain (1997), Widdowson, (1997b), and van der Beek and Braun (1998). An alternative approach has been to estimate the rate by comparing the distance of the present day escarpment from a dated outcrop (eg Young and McDougall, 1982; Young, 1983; Nott *et al*, 1996). A more detailed discussion of the rates derived using these inferential approaches appears in Chapter 8. The direct quantification of Great Escarpment retreat rates over geological timescales, critical to understanding the erosional and evolutionary history of such features, has remained elusive.

SPMs have been applied specifically to the problem of escarpment evolution (Kooi and Beaumont, 1994; Tucker and Slingerland, 1994) and provide a useful insight into the circumstances in which escarpments may be preserved or retreat across a passive margin. Various factors are highlighted by both studies as controlling the evolution of the escarpment within these models. The antecedent topography, and in particular the location of the continental drainage divide, is identified as exerting first order control on escarpment evolution in these models. Escarpment preservation and retreat are favoured when the escarpment top coincides with the continental drainage divide and when continuous backtilting of the escarpment occurs due to flexural isostatic uplift in response to

denudational unloading. The key point to note here is that the ideas generated by these models need to be assessed in the light of empirically derived retreat rates.

5.4 SOUTHEAST AFRICA: EVOLVING IDEAS ABOUT LANDSCAPE DEVELOPMENT

The scenery of southeast Africa and its evolution has been a source of interest for at least a century and the area has been visited by many eminent geomorphologists (eg W.M. Davis, L.C. King, A. Penck, E. Suess). Whilst historical reviews of landscape studies for the whole of southern Africa are provided by Partridge and Maud (1987, 1988) and Birkenhauer (1991) the emphasis here is on southeast Africa and, in particular, the evolution of the Drakensberg and Lesotho Highlands.

5.4.1 THE EARLIEST VIEWS

The initial focus was on the Drakensberg, with Suess (1904) and A. Penck (1908) both concluding that the escarpment was erosional and not faulted (King, 1944). Rogers (1920) introduced the term "Great Escarpment" and argued that the emplacement of the Drakensberg Group basalts would have re-organised the continental drainage system leading to it being "centred round the areas where the volcanic rocks were thickest ..... Basutoland [Lesotho] and Natal [KwaZulu – Natal]" (p xxxi) – a view shared by Dixey (1938). Following late Cretaceous uplift, when the sub-continent "rose as a flat dome with steep slopes to the coast" (Roger, 1920, p xxxi), the Drakensberg was formed by lithological resistance to fluvial erosion of the coastal rivers.

5.4.2 CYCLICAL MODELS

The emphasis after Rogers (1920) switched to the horizontal surface of southern Africa ("...the horizontal surfaces are fundamental rather than the scarps between them", King, 1944, p 259) and the identification and correlation of erosional cycle remnants. The evolution of the Drakensberg was not considered to be a separate development and was placed within this denudational chronology framework. Dixey (1938; 1942) applying the Davisian methodology, correlated erosional surfaces throughout central and southern Africa and postulated successive uplift events. Dixey (1938; 1942) took an almost identical view to Rogers (1920) of the development of the Drakensberg by fluvial erosion induced by uplift events. The highest levels (> ~ 2600 – 2800 m) of the Lesotho Highlands contained the

remnants of a late Jurassic peneplain while the escarpment and dissected coast area were developed by the late Jurassic / early Cretaceous and subsequent uplifts simply added further relief to these features (Dixey, 1938, p 166; 1942, p176).

The work of German scholars, the most influential being Obst and Kayser (1949) and Jessen (1943), has been reviewed by Birkenhauer (1991) and Bremer (1985). Obst and Kayser (1949) introduced the term "Große Randstufe" (great marginal scarp – Birkenhauer, 1991), identified various surfaces and regarded the escarpment as being the product of down-warping and then uplift of the continental margins. Jessen (1943) focussed on the high-elevation continental margins – the 'randschwellen' or marginal swells – which act as a hinge, with the oceanward side subsiding and the continental interior being uplifted (Bremer, 1985). According to Birkenhauer (1991), Jessen identified both uplift and monoclinal tilting as inducing the erosion that created the Drakensberg.

By far the most influential exponent of a cyclical approach to the southeast African landscape was King (1941; 1944; 1947; 1949; 1951; 1953; 1955; 1962; 1982) and his co-workers (eg Fair and King, 1954; King and King, 1959). The two fundamental aspects of King's theory were that the southeast African coast was of monoclinal, rather than faulted, origin (1941, following Penck, 1908) and that parallel scarp retreat and pediplanation, rather than downwearing and peneplanation, were the dominant processes (1947), a view ultimately accepted by Dixey (1955a, 1955b). These two concepts enabled King to interpret the landscape of southeast Africa as being the product of several cycles of erosion, each starting at the coast and each being terminated by an uplift event. The number, aerial extent, names and ages of the surfaces, that evidenced each erosion cycle, vary (King, 1949, 1951, 1962, 1982; Fair and King, 1954; King and King, 1959). The final version identifies six surfaces – named Gondwana; Kretacic; Moorland; Rolling; Widespread; and Youngest – and five 'active episodes', which include the fragmentation of Gondwana and four uplift events centred on the coastal monocline (Figure 5.11). In King's scheme, the fragmentation of Gondwana created uplift along the 'Natal Monocline', the site of which, according to King, is evidenced by the cropping out of the basement inland of the coast (Figure 5.4). The proto-Drakensberg formed at the site of the monocline as the result of a combination of denudation by the coastal rivers during the Kretacic erosion cycle and a hypothesised ~ 1250 m uplift of the monocline in the mid-Cretaceous. Following this the Drakensberg retreated inland to its present-day site (Figure 5.11).

King (1944) estimated the retreat rate of the Drakensberg, based on formation at the monocline, as "1 foot in 233 years" (p 280) (~ 1.3 km Ma^{-1}). King argued that, as denudation was accomplished by backwearing only, little or no denudation had occurred on the topmost parts of the Lesotho Highlands since at least the fragmentation of Gondwana (eg 1982). King (1940) did provide an estimate for denudation of the coastal zone based on the assumption that the rest of the Karoo Supergroup must have, prior to fragmentation, extended over the site of the monocline. This yielded a denudation estimate for the monocline of "1 foot in 9,300 years" (1940, p 155), or ~ 30 m Ma^{-1}.

Various criticisms have led to King's scheme being challenged. The deficiencies in King's proposed uplift mechanisms of isostasy (1955) and the 'arching' cymatogeny (1961) have already been commented on. Maud (1961) and subsequent workers (Martin, 1983 and von Veh and Anderson, 1990) have demonstrated that the southeast African coast is faulted and not of a monocline origin (a view first expressed by Suess, 1904). Moon and Selby (1983) have questioned the notion of parallel slope retreat, central to King's schema. Summerfield (1985) criticised King's methodology of tracing onshore erosion surfaces to offshore unconformities by illustrating that there is no simple relationship between these unconformities and continental denudational cycles. Summerfield (1985) advocated an alternative to the cyclical approach which emphasised plate tectonics, isostatic responses to denudation and an altogether more quantitative approach to understanding landscape evolution.

De Swardt and Bennet (1974), using a combination of aerial photographs and offshore drilling data, argued against King's idea of the survival of relict Gondwana surfaces. They proposed that southern Africa would have had a high overall elevation at break-up and that while uplift may subsequently have occurred along the 'Natal arch' (King's monocline) only minor uplift can have occurred along eastern Lesotho. These authors recognised the importance of a dual drainage system and the impact of structural control in shaping the coastal zone. Structural control and varying lithological resistance dominate the landscape for 30 – 100 kms in front of the Drakensberg and in the Lesotho Highlands. They ruled out the possible existence of planation surfaces of continental extent, but did still adopt a cyclical approach by recognising two erosion surfaces in the coastal zone.

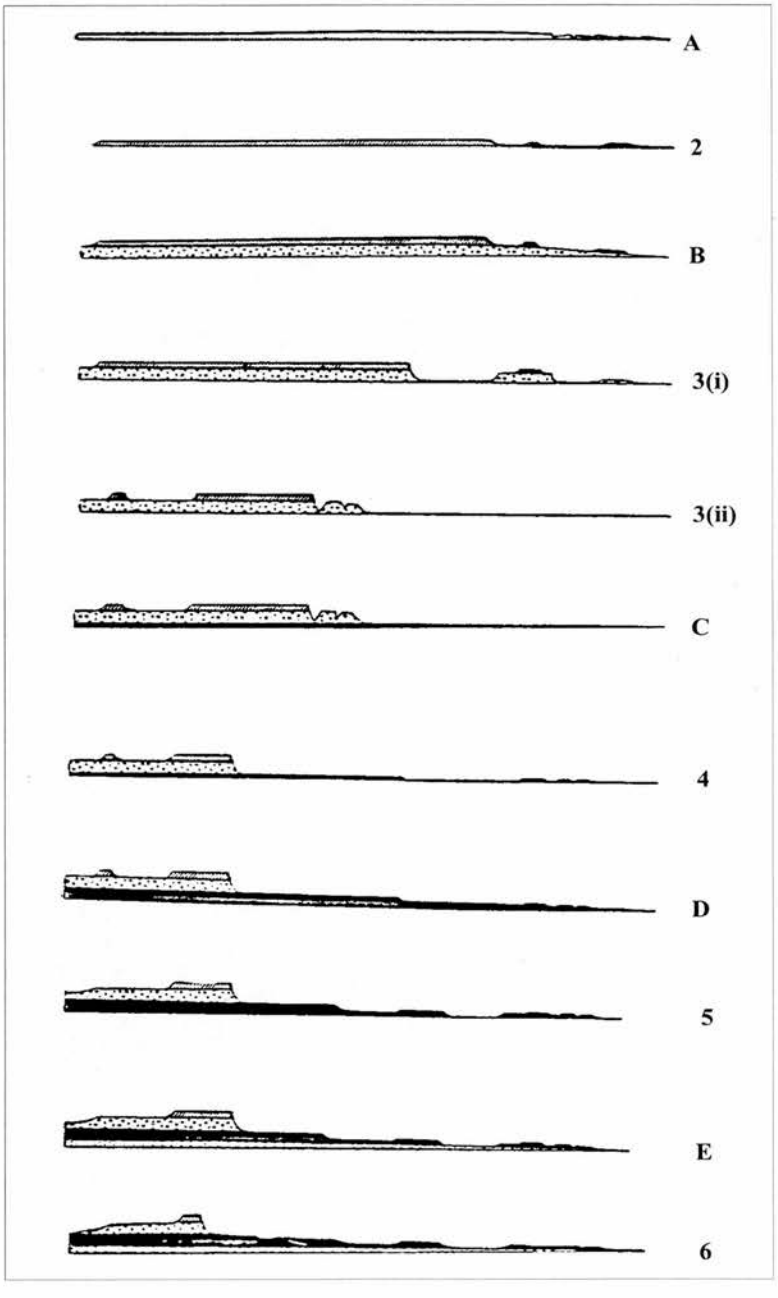

Figure 5.11: King's scheme for the evolution of southeast Africa. Erosion cycle surfaces are represented by numbers, with 2 = Kretacic; 3 = Moorland ((i) being early and (ii) being late); 4 = Rolling; 5 = Widespread; and 6 = Youngest. The earliest erosion cycle, Gondwana, is not shown, but would be as A, only more extensive and without the coastal fragmentation. 'Active episodes' are designated by the letters, A - E. A is the fragmentation of Gondwana which brings to an end the Gondwana erosion cycle and initiates the new Kretacic cycle (2). B, C, D, and E represent uplift events in, respectively, mid-Cretaceous (~ 1250 m); early Miocene (100's m); Pliocene (~ 800 m); and end Pliocene (~ 625 m). In this scheme, the Drakensberg forms as a result of the Kretacic erosion cycle (2) and the mid-Cretaceous uplift (B) and it then retreats inland to its present position. (After King, 1982).

Schmitz and Rooyani (1987) reject King's (1962) scheme for the Lesotho Highlands. They argue (1987, p 85-6) that the original post-basaltic "Gondwana" surface was totally destroyed by fluvial incision and that any flat-lying, low relief, surfaces in Lesotho are structurally controlled or related to climate change. Schmitz and Rooyani (1987) suggest that two phases of "intense vertical erosion" (p 88) occurred in Lesotho post-continental break-up (Figure 5.12). Although they do not provide either dates or mechanisms for such denudational phases, there is a suggestion that the latter phase may relate to Pleistocene climatic variations (1987, p 88). Schmitz and Rooyani (1987) do not relate these incisions to the wider southeast African context.

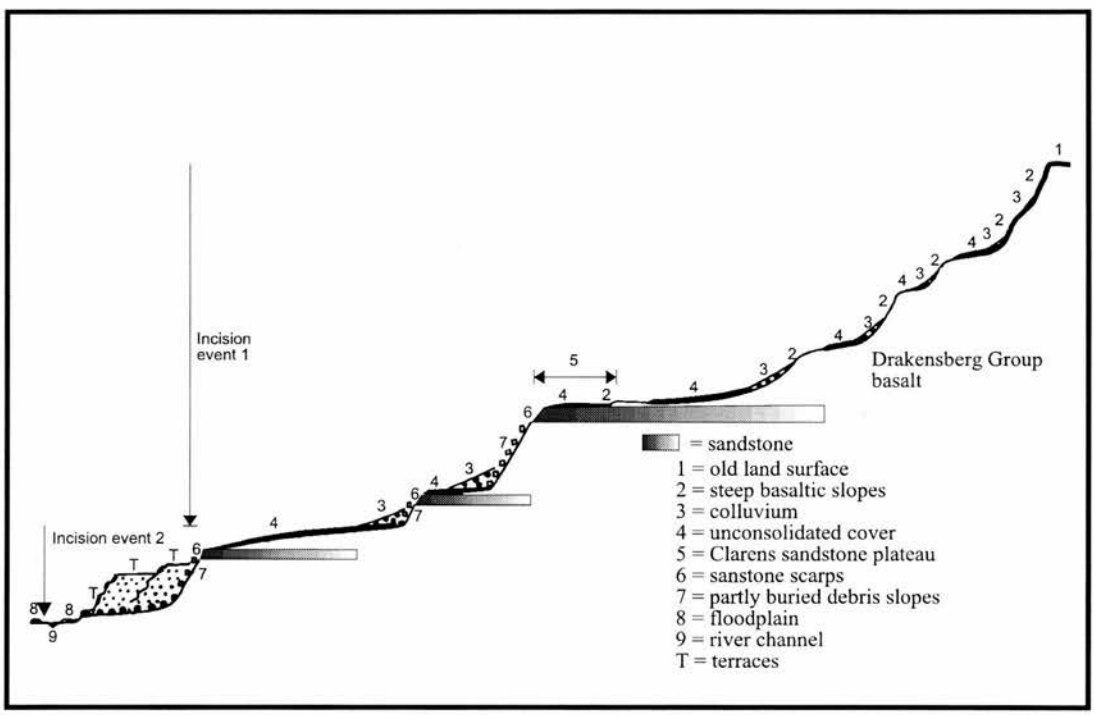

Figure 5.12: Schematic cross-section illustrating the main geomorphologic units in Lesotho and their relationship to the proposed post-Gondwana vertical incision events of Schmitz and Rooyani (1987). Incision event 1 is regarded as being multi-staged. (After Schmitz and Rooyani, 1987).

Partridge and Maud (1987) and subsequent reiterations (Partridge and Maud, 1988; Partridge *et al*, 1995; Maud, 1996; Partridge, 1997b, 1997c, 1998) provide the latest cyclical approach to landscape evolution in southeast Africa. Their methodology has moved away from the "accordance of summits" approach of King (1983, p 179) and seeks to incorporate more "factual data" (1987, p 181) into a framework which is still focussed on horizontal surfaces and their interpretation in terms of denudation cycles and uplift events. This framework, in so far as it relates to most of southern Africa, is shown in Figure 5.13.

Partridge and Maud (1987) envisage three erosion cycles – the African; Post-African I; and Post-African II. The African cycle was initiated by the break-up of Gondwana and lasted from the late Jurassic / early Cretaceous to early Miocene. The polycyclic African cycle was ended by an uplift (~ 300 m) at 18 Ma which initiated the Post-African I cycle. A second uplift (~ 900 m) along the same axis, which is situated roughly 80 – 100 km inland and parallel to the southeast African coast (Figure 5.13), at ~ 2.5 Ma brought the Post-African I cycle to an end and started the Post-African II cycle. In this scheme there is no recognition of any subaerial erosion surface dating to before the break-up of Gondwana as envisaged by King.

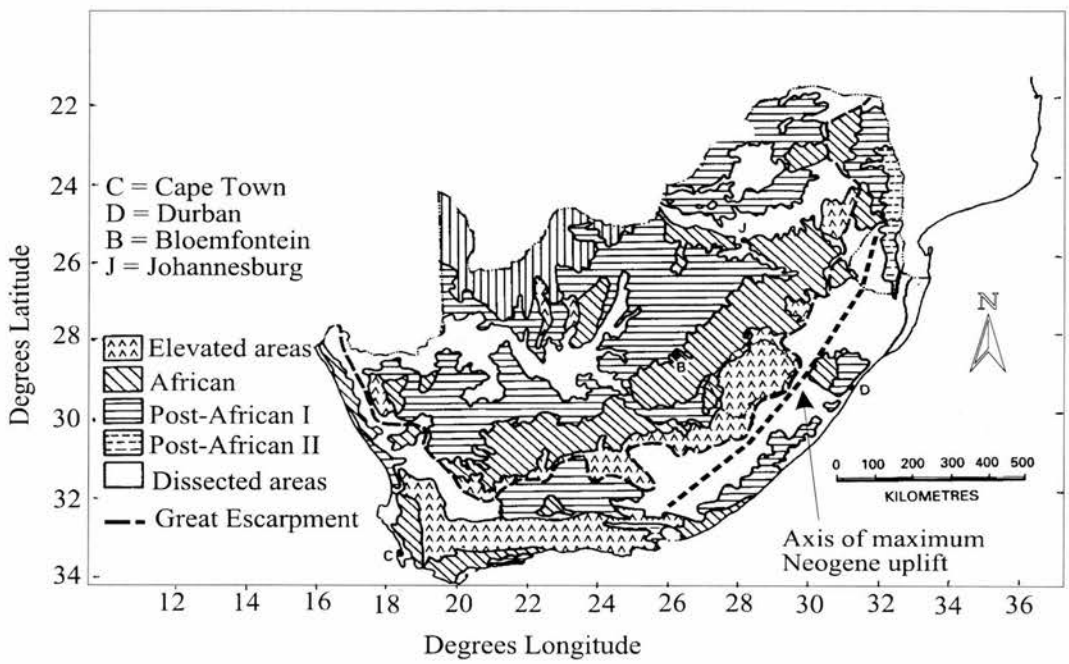

Figure 5.13: Simplified map showing the principal cyclic landsurfaces of southern Africa according to Partridge and Maud, 1987. (After Partridge and Maud, 1987 & Partridge, 1998).

The Lesotho Highlands (part of the elevated areas in Figure 5.13) are viewed as an "erosional residual or high-lying massif" (1987, p192) and part of an "anomalously elevated zone" (1987, p 188), which coincides with the "inner margin of the zone affected by upwarping of the continental hinterland prior to rifting" (1987, p194). Southern Africa is assumed to have had a high elevation prior to rifting sloping from 2350 m at the rift margins

to 1800 m in the interior (1987, p186). The basis for this calculation is, however, erroneous as it confuses relative movements of the crust with surface elevation changes (M. Summerfield, pers. comm.). The Drakensberg is viewed as having formed at the coast (marking the Gondwana break-up site). Following break-up, the Drakensberg receded some 100 km inland from the coast by the mid-Cretaceous, and a further 20 km by the end of the Cretaceous (1987, p 190). Most of the southeast African coastal zone is described as 'dissected' and is recognised to be dominated by structural control and varying lithological resistances to erosion which inhibit the differentiation of Post-African erosion cycles (1987; 1988, p13; Maud, 1996; Partridge, 1997b).

Several criticisms can be made of the Partridge and Maud (1987) model. Firstly, the methodology of using deep weathering profiles and duricrust cappings to correlate erosional surfaces has been questioned (Burke, 1996, p366; Brown *et al*, 2000, p276; M. Summerfield, pers. comm.). These authors dispute the ability of particular weathering profiles to be used as chronological markers given the number of factors, other than time, which can influence their physical, chemical and mineralogical properties. Secondly, the major Pliocene uplift has been challenged (Burke, 1996, p 368) and most of the evidence Partridge and Maud quote in support of this uplift event is, at least, questionable (cf. Partridge, 1998). Such evidence comes, in part, from the distortion of the erosion surfaces which, if the method of correlation is insecure, must also be insecure. River long profiles for five of the main coastal rivers have been used in support of this uplift (Partridge *et al*, 1995), yet no consideration is given to the impact of varying lithological resistance, particularly the abundant dolerite intrusions and other structural control which is well recognised in this area (de Swardt and Bennet, 1974). Lithological variation and structural controls are well known to create steepened reaches, independent of uplift (Hack, 1957). Partridge *et al* (1995) and Partridge (1997b, 1997c, 1998) refer to an increase in east coast offshore sedimentation rates of ~ 50 % in the past 5 Ma, compared to the last 145 Ma, based on data attributed to Martin (1987). This is, in this author's opinion, a mis-reading of the Martin (1987) data. In Martin's paper (1987, table 2 p 719) it is quite clear that there is a difference of only ~ 6 % between the rates for the past 5 Ma and the past 133 Ma, which is easily accounted for by human impact. Lastly, Partridge *et al* (1995) make reference to the spatially restricted onshore early Pliocene marine deposits located at up to ~ 330 m and ~ 35 km inland from the south coast near Port Elizabeth (34°S, 25° 30'E) to support regional southeast African uplift. Several studies of these deposits and local river terraces have explained these in terms of past higher sea levels and local tectonic activity rather than regional-scale uplift (Le Roux, 1990;

McMillan, 1993; Hattingh, 1994; 1996a, 1996b; Hattingh and Geodhart, 1997; Marker and McFarlane, 1997).

All the models discussed in this section, although showing disunity in the matching of erosion surfaces, agree on the cyclical nature of these surfaces, invoking tiered levels of distinct age generated by a sequence of uplift events each followed by prolonged planation during tectonic quiescence. An inherent problem with this methodology, which assumes predominance of backwearing from the coast, is that the only way to explain surfaces at altitudes above the current base-level is by previous uplift or downwarping. Any regional, or local, base-level control is ignored. Thus all the approaches outlined above invoke distinct uplift / downwarping of varying degrees.

5.4.3 ACYCLICAL MODELS

Acyclical approaches have sought to understand the development of the southeast African landscape without reference to repeated erosional cycles and uplift events. Wellington (1955) was opposed to King's denudation chronology and argued that the southeast African landscape reflected the "importance of rock character and structure" (p 11) rather than distinct erosional cycles. For Wellington this landscape could be explained by the "result of downwearing in a single, sustained and still incompleted cycle of erosion" (Barnard, 1997, p140). While Wellington doubted the survival of Gondwana surfaces in the Lesotho Highlands (1958, p4), he did agree with King's view (1944) that the Drakensberg had retreated from the coast in response to headward erosion of the coastal rivers, and that the coast was of monoclinal origin (1955, p 98; 1958, p 5).

De Swardt and Bennet (1974) similarly stressed the lithological and structural control on the evolution of the coastal zone landscape. Birkenhauer (1985) identified three levels (170 – 200 m; 300 m; and 430 – 600 m) roughly parallel to the coast of southeast Africa, which he equated with the erosion surfaces identified by de Swardt and Bennet (1974). Birkenhauer argued that these were marine platforms which have not been subject to any "downwarping, tilting or uplifting" (1985, p232) and that therefore there has been no uplifting and no erosion cycles. The Drakensberg has been located in much the same position since at least the late Cretaceous (1985, p232). Birkenhauer (1991) refined his ideas and identified eight marine benches ('thalassoplains') in total around the coast of southern Africa ranging from 100 to 1000 m above present sea level. These he argued ruled out any uplift younger than late Jurassic / early Cretaceous. Birkenhauer views the position of the Drakensberg as being

controlled by lithological resistance and that it has retreated very little since its formation before the early Cretaceous (1991, p 244). The arguments presented by Birkenhauer to support his views are unclear, in particular his ability to distinguish surface uplift from marine regression in the notable absence of well-dated onshore marine deposits (except in rare isolated coastal locations) (Dingle *et al*, 1983; Summerfield, 1985).

Ollier (1985a) favoured a simple model for southeast Africa and other continental margins with drainage divide escarpments (Seidl *et al*, 1996), in which continental break-up is followed by escarpment retreat without any subsequent uplifts. In a more detailed theoretical analysis, Ollier and Marker (1985) again attribute the formation of the escarpment to the break-up of Gondwana, but then follow King's (1982) view that several distinct period of uplift have affected the region. Ollier and Pain (1996) resurrect King's (1962) idea of downwarping of the continental edge, rather than uplift, to explain the landscape of southeast Africa. Little data, other than the erosion surface remnants identified by Partridge and Maud (1987), which have also been interpreted as uplifted marine erosion benches by Birkenhauer (1985, 1991), is put forward to support this theory.

Burke (1996) discussed the development of the entire African plate over the last 30 Ma, being the period he considered the plate to have been at rest with respect to underlying mantle circulation. In his model (1996, p 363), a previously low-lying erosional surface developed between 65 – 30 Ma following the retreat of late Cretaceous seas from the sub-continent. This surface was uplifted as the African plate came to rest over mantle circulation about 30 Ma ago, and this led to the creation of the Great Escarpment which retreated inland from the coast (Figure 5.14). The Great Escarpment did not exist prior to the uplift at 30 Ma and, in Burke's view, is unrelated to continental break-up (1996, p 367). There are certain problems with Burke's arguments. Firstly, there are no marine Cretaceous sediments in the interior of southern Africa that would support the idea of the region being flooded. Burke attributes this absence to subsequent erosion (1996, p 365). Secondly, the reason behind a 30 Ma uplift is related more to the evidence of volcanism on other parts of the African plate at this time, than any specifically southern African evidence (p 367). Thirdly, Burke argues that escarpment retreat of ~ 1 km Ma^{-1} (based on formation at break-up) is a "slow rate" (p368) and therefore the escarpment must only have formed at 30 Ma. There is very little data on the actual retreat rate of similar escarpments and none for the Drakensberg, and Burke's view conflicts with modelling studies of escarpment retreat (Kooi and Beaumont, 1994; Tucker and Slingerland, 1994).

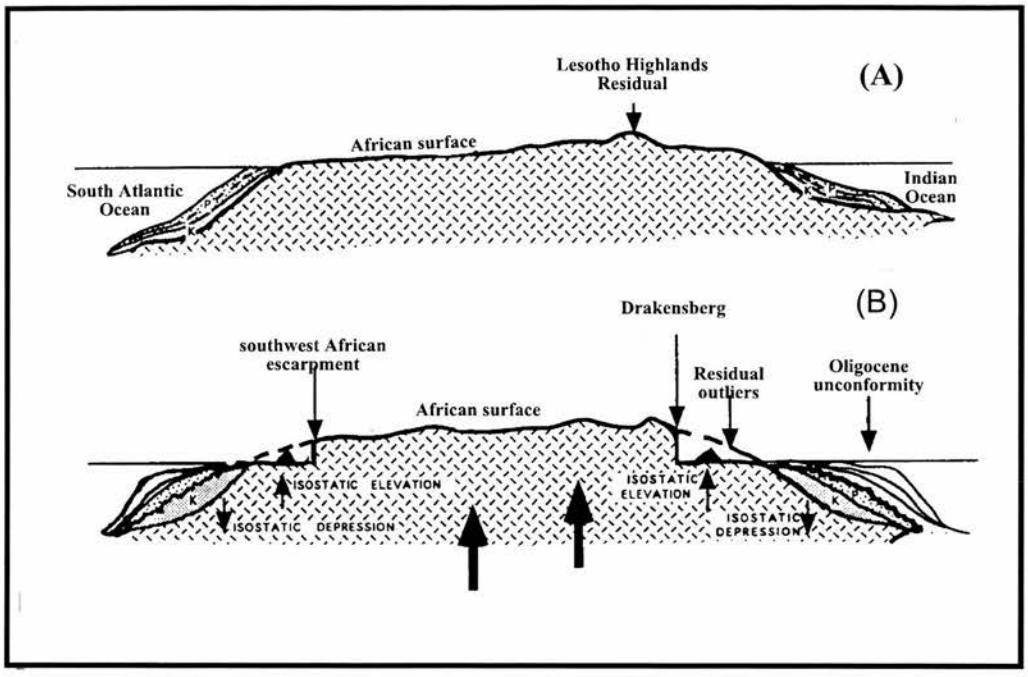

Figure 5.14: Schematic cross-section of southern Africa illustrating Burke's (1996) model of southern African landscape evolution. Prior to the African plate coming to rest (A) the erosional 'African' surface is shown to be close to sea-level and the Lesotho Highlands are a residual. (B) After 30 Ma, when the plate has come to rest, the whole of southern Africa is uplifted on the 'Great Swell of Southern Africa', indicated by the two large black arrows. The Drakensberg, and the equivalent southwest African escarpment, starts to form and erode back into the interior plateau. Isostatic uplift is induced in the coastal zone due to denudational unloading and offshore loading of sediments. (After Burke, 1996).

5.4.5 NEW TECHNIQUES AND NEW APPROACHES

A common difficulty with both cyclical and acyclical models is their comprehensive nature. They all attempt to provide convincing landscape narratives and, given the variety of mechanisms outlined above, all they effectively illustrate is that the concept of equifinality exists at the macroscale of landscape evolution. Each model provides an explanation of the current landscape that is based partly on some data (of variable quality) and partly on assumption. An example of an assumption common to all models is the elevation of the landscape at a particular moment in time. For example, prior to Gondwana break-up King (1962) assumed it was low (~ 600 m) while Partridge and Maud (1987) assumed it was high, varying from ~ 2400 m in east to ~ 1800 m in west. Around 40 Ma, Burke (1996) assumed it was 'close to sea level'. This is a fundamental difficulty (Gilchrist and Summerfield, 1990; Brown *et al*, 2000). Establishing the palaeoelevation is essential to link landscape development and base-level adjustments whether they be attributable to tectonics, eustatic

changes or other mechanisms (eg downwarping, Ollier and Pain, 1997). Other examples of such assumptions include the rate of escarpment retreat and rate of denudation.

Studies of landscape development in southeast Africa have, to date, been dominated by the identification and subsequent attempted correlation of low-relief surfaces (eg Dixey, 1938; King, 1962; De Swardt and Bennet, 1974; Partridge and Maud, 1987; Birkenhauer, 1991). This concentration of effort has provided many competing conceptual landscape narratives and demonstrates that these surfaces are equivocal. For example, such surfaces in the coastal zone have been interpreted as evidence of uplift (eg King, 1953; Birkenhauer, 1985, 1991; Partridge and Maud, 1987), evidence of structural control (eg de Swardt and Bennet, 1974) and as evidence of downwarping (eg Ollier and Pain, 1996).

An alternative approach is to concentrate on collecting reliable data that measure the rates of landscape development, including long-term rates of denudation at a range of scales. Such data can then be compared and combined with other quantitative morphological, geological or geophysical measurements and / or with quantitative models. This type of integrated approach can be used to test existing, more conceptual hypotheses (eg Burke, 1996 as it relates to southern Africa; Partridge and Maud, 1987), or to indicate potentially important constraints. More quantitative research, aimed at establishing denudation rates and quantitative models, is beginning to be applied to the landscape development of southeast Africa.

Summerfield (1996a) commented that the denudation chronologies typical of the cyclical approach yielded little information on the depths of denudation. Offshore sediment volume data partly addresses this issue. Rust and Summerfield (1990) determined that the main volume of sediment within the Orange and Walvis basins offshore of southwest African was deposited during the late Cretaceous / early Tertiary. Averaged over the present day Orange River catchment, which includes the area inland of the Drakensberg in southeast Africa, this equates to a mean depth of ~ 2 km, and a mean denudation rate of ~ 12 m Ma^{-1} for this period. Whilst data exists on offshore sediment sequences for southeast Africa (eg Birch, 1982; Dingle *et al*, 1983; Dingle and Robson, 1985; Martin, 1987; Dingle *et al*, 1987; Hartnady *et al*, 1992; unpublished Soekor Ltd data referred to by Ben-Avraham *et al*, 1994), no attempts have yet been made to calculate average denudation rates from these. In any event, considerable problems exist with trying to re-construct the temporal and spatial variations in the onshore sediment source area and to distinguish changes in the overall rates of onshore denudation from such changes in the source basin area (Summerfield, 1996a).

Additional problems in southeast Africa relate to the narrow continental shelf (Figure 5.5 – only 5 km in some locations – Birch, 1982); the powerful surface Agulhas Current (it can sustain velocities > 2.5 m s^{-1} – Dingle *et al*, 1987) and the North Atlantic Deep Water / Antarctic Bottom Water which re-work and scour sediments (Martin, 1981; Dingle *et al*, 1987; Ben-Avraham *et al*, 1994).

Southeast Africa is a denudational terrain and lacks onshore sedimentary deposits that might be able to constrain denudation rates. An extensive AFTT dataset exists for the whole of southern Africa (Brown, 1992). Published parts of this dataset have so far concentrated on southwest Africa, in particular, an area up to ~ 300 km inland of the coast that includes the southwest African escarpment (Brown *et al*, 1990, 2000). These data have been interpreted to show that ~ 3 – 5 km of denudation occurred along the continental margin post continental break-up in that area (~ 118 Ma), with more limited, but still substantial, denudation in the interior hinterland (Brown *et al*, 1990; 2000).

A broadly similar pattern of denudation has been identified in southeast Africa, with substantial post-Jurassic crustal stripping recorded both west and east of the Lesotho Highlands (Brown, 1992; Brown and Summerfield, in prep.). Oceanward of the Drakensberg, Brown and Summerfield (in prep.) inferred denudation rates range from > 5 km at the coast to ~ 2 – 3 km at Swartberg (~ 50 km oceanward of the Drakensberg) and Ladybrand (~ 200 km northwest of Swartberg) on the inland side of the Lesotho Highlands. These AFTT data also record distinct episodes of accelerated denudation: at the coast between 130 – 110 Ma; at Swartberg at 100 – 80 Ma; and at Ladybrand at 80 – 60 Ma (Brown, 1992). The denudation data for Swartberg implies that the Drakensberg must have lain to the east of this site for at least 80 Ma (Brown and Summerfield, in prep.). This provides a useful constraint on the maximum escarpment retreat rate, assuming constant retreat, for this period (Chapter 8). No AFTT data is available for the basalt outcrop that makes up the Lesotho Highlands, but extrapolation of the Swartberg / Ladybrand data infers ~ 500 – 1000 m of denudation may have occurred (Fleming *et al*, 1999). This renders the survival of intact Gondwana age erosion surfaces in the Lesotho Highlands highly improbable, although the spatial resolution of AFTT data is too coarse to preclude the preservation of isolated remnants as envisaged by King (1962, 1982).

Quantitative modelling in southern Africa has tended to focus on southwest Africa (Gilchrist and Summerfield, 1990; ten Brink and Stern, 1992; Gilchrist *et al*, 1994). These studies are of some interest here as both King (1962) and Partridge and Maud (1987) applied their

cyclical frameworks to landscape evolution in both southwest and southeast Africa. Gilchrist and Summerfield (1990) used isostatic modelling to demonstrate that, if the southwest African escarpment retreated at a constant rate from formation close to the break-up site, then uplift of ~ 600 m could be generated at a marginal upwarp. This modelling was constrained by the denudation data of Rust and Summerfield (1990) and Brown *et al* (1990). Ten Brink and Stern (1992) also modelled the isostatic response of southwest Africa to denudational unloading and sediment loading, but they assumed that the coastal zone had been downwarped. Although the data of Rust and Summerfield (1990) and Brown *et al* (1990) was mentioned, preference was given to the erosional surfaces identified by Partridge and Maud (1987) to constrain the model. Application of the ten Brink and Stern (1992) model to southeast Africa is not appropriate due to the narrow continental shelf and offshore currents that severely limit the build up of sediments offshore. Gilchrist *et al* (1994) suggested a new conceptual model for the landscape development of southwest Africa based on the existence of a dual drainage system and inland drainage divide immediately post-rifting. They applied the Kooi and Beaumont (1994) SPM to this setting, constrained by available data on denudation rates, and concluded that the gross morphology of southwest Africa could be reproduced by denudation induced by the initial rifting and the isostatic response thereto. There was no need to invoke repeated uplift and erosion cycles.

Stüwe (1991) applied a flexural isostasy model to southeast Africa which was able to reproduce the stair-like topography of the coastal zone (Figure 5.3). This modelling used the King (1953) scheme as the only constraint and concluded that flexural rebound, induced by parallel escarpment retreat as envisaged by King, would operate in a cyclic fashion. This modelling lacks any independently determined constraints and, by assuming that escarpment retreat was the only denudation process, ignored any downwearing. This is clearly not the case, given the high local relief in the Lesotho Highlands (Figures 5.1, 5.2). To date, no SPMs have been applied to the problem of landscape evolution in southeast Africa, but modelling using the SPM of Braun and Sambridge (1997) and constrained by the AFTT denudation data of Brown (1992; Brown and Summerfield, in prep.) is ongoing (P. van der Beek, pers. comm.).

The analysis of *in situ*-produced cosmogenic ^{36}Cl can provide direct empirical data on the retreat rate of the key landform in southeast Africa, the Drakensberg, over a geologically useful time span. In addition, by analysing samples from both free face escarpment sites and from flat-lying supra-escarpment sites, a quantitative assessment may be made of the relative importance of scarp retreat and summit lowering in a passive margin setting. The respective

importance of downwearing and backwearing in the long-term denudation of landscapes is the fundamental distinction between the conceptual models of Davis and King. The critical testing of this has been frustrated by a general lack of quantitative data at a suitable scale and has been limited to isolated situations with unique geomorphological circumstances (eg Young, 1983; Nott *et al*, 1996). By applying *in situ*-produced cosmogenic isotope analysis, which yields site and therefore landform specific denudation rates, this project provides a large-scale test of these ideas, in addition to a quantifying escarpment retreat rates.

5.5 Conclusions

What is apparent from this discussion is that the long-term development of passive margin landscapes in general, and southeast Africa in particular, is thought to involve a complex interplay between endogenic and exogenic processes. Therefore, to account for the evolution of such distinctive landscapes quantitative geomorphological, geological and geophysical data needs to be integrated and reconciled (Merritts and Ellis, 1994; Summerfield, 1996b, 2000; Bishop, 1998; Beaumont *et al*, 2000). Over time the interest in these landscapes has switched from the exclusive preserve of geomorphology to geology and geophysics, yet the onshore morphology of these areas has remained the critical test of conceptual, tectonic and geophysical models. Quantitative models, particularly SPMs, have been of considerable value in furthering our understanding of the likely controls on large-scale, long-term landscape evolution, but their role is limited by a lack of empirical data on rates at landscape evolution at the landform scale. This data is essential to constrain the model parameters (Kooi and Beaumont, 1994; van der Beek and Braun, 1998, 1999). Regional scale denudation data is provided by AFTT, but the resolution is too coarse to provide data at the scale of landforms such as the Drakensberg. The recently developed technique of *in situ*-produced cosmogenic isotope analysis provides the first opportunity to obtain direct empirical denudation data at such a scale.

CHAPTER 6: RESULTS I: *IN SITU*-PRODUCED CHLORINE-36 DERIVED DENUDATION RATES FOR FLAT-LYING SITES

6.1 INTRODUCTION

Denudation rates, derived using *in situ*-produced cosmogenic ^{36}Cl analysis, for flat-lying (0 ° - 5 °) sites on the southern Drakensberg escarpment and the Lesotho Highlands are reported in this chapter. Denudation rates for free face sites are dealt with in Chapter 7. In all, 33 samples from flat-lying sites were prepared and analysed, 19 from the Drakensberg and 14 from the Lesotho Highlands. Four samples, all from the Drakensberg, were collected in late 1995 and the results from these, plus two free face samples, were published in Fleming *et al* (1999) (Appendix 9). The rest of the samples were collected in late 1997. This chapter is split into three sections, the first two providing descriptions of the southern Drakensberg and Lesotho Highlands sample sites. The third section contains the analytical results and the estimated denudation rates for the flat-lying samples.

6.2 SOUTHERN DRAKENSBERG SITES

6.2.1 GENERAL MORPHOLOGY AND GEOLOGY

The southern section of the Drakensberg runs for ~ 250 km in a southwest direction from ~ 29 ° 20 ' S to ~ 31 ° 10 ' S (Figure 6.1). The southern section was chosen for two main reasons. Firstly this section runs parallel to the coast and the Agulhas Falkland Fracture Zone (Figure 5.5), which marks the site of continental break-up. If the escarpment did form near the coast and retreat inland by parallel slope retreat, as suggested by, *inter alia,* King (1982) (Chapter 5), then the southern Drakensberg would appear to reflect the operation of this process at its simplest level. Assuming this formational process and that retreat commenced shortly after break-up ~ 135 Ma BP (eg Storey, 1995), a time averaged retreat rate of 1.2 – 1.5 km Ma^{-1} is obtained, which is the same as the rate of one foot in two hundred years proposed by King (1953, p746) for the entire Drakensberg. In contrast, the northern section of the Drakensberg, which runs northwest from approximately 29 ° 20 ' S to 28 ° 52' S, is almost ninety degrees to the coast and hence is less likely to be solely the product of parallel retreat. Secondly, the elevation of the escarpment summit of the southern Drakensberg

declines generally to the southwest from ~ 3100 m to ~ 2500 m and presents more sites of a contrasting geomorphological nature than the northern Drakensberg where the escarpment summit varies between ~ 3000 m and 3300 m only.

Although there is an overall decline in elevation towards the southwest, the southern Drakensberg is made up of series of alternating highs and lows (Figure 6.2; Plate 1) which inspired the local Sotho name for the Drakensberg, 'Qathlamba' (wall of spears). The altitude of the escarpment summit generally varies between 2400 and 3000 m, except for a section around 30 ° 8 ' S where the elevation drops to ~ 2100 m (Figure 6.2). Generally the Drakensberg summit marks the highest local elevation, but this is not always the case, particularly in the northern part (Figure 6.2). For example, the highest point in southern Africa, Thabana-Ntlenyana (3482 m), 12 km north of Sani Pass (Figure 6.2), is ~ 4 km inland of the escarpment.

The continental drainage divide generally coincides with the edge of the escarpment. In a very few isolated areas, for example near Naudesnek (Figure 6.1), there are small, < 2 – 3 km^2, subdued relief, drainage basins which lie inland of the escarpment but drain over it to the Indian Ocean. For example, the one near Naudesnek, has local relief of < 200 m in a ~ 2 km^2 basin. The area inland of the southern Drakensberg is drained by the Orange River, (the Senqu River in Lesotho), and its tributaries, which drains to the Atlantic Ocean. These rivers have, as can be seen in Figure 6.2, incised the area inland of the Drakensberg deeply. This incision can be quite dramatic even near the escarpment. For example, in the area around 30 ° 5 ' S, the Tsoelike River, only ~ 5 km inland of the Drakensberg, is ~ 700 m lower than the elevation of the escarpment summit (~ 2400 m) (Plate 2). The area oceanward of the Drakensberg is drained by rivers flowing to the Indian Ocean. The headwaters of these rivers rise on the escarpment with the first order tributaries being separated by steep-sided (~ 25 – 35 °) narrow (10 – 50 m) ridges that run out for lengths of up to a few kilometres from the main escarpment face (Plate 3).

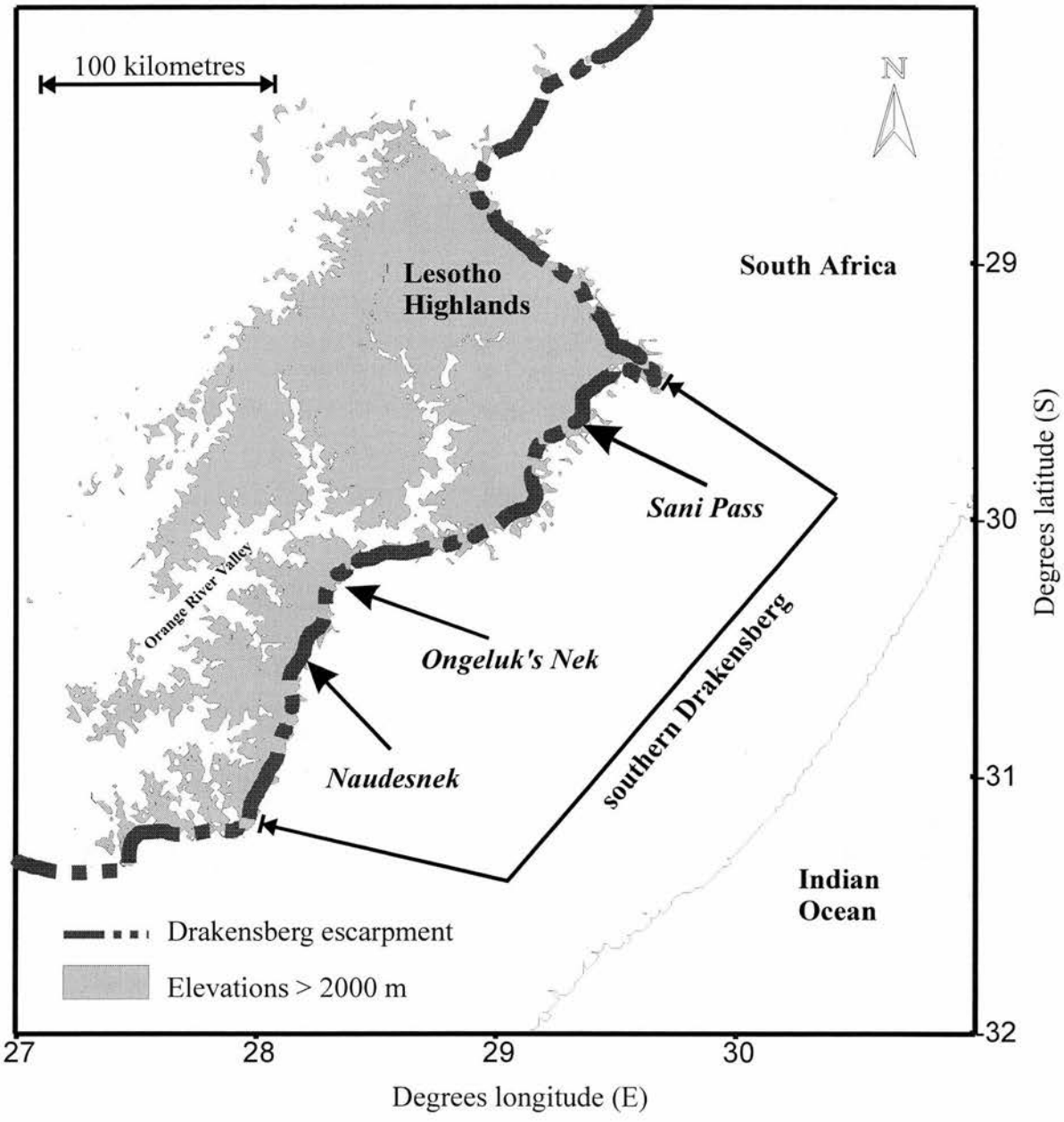

Figure 6.1: Location map showing elevations over 2000 m asl in southeast Africa and the position of the Drakensberg escarpment. Samples were collected from three sites on the southern Drakensberg - Naudesnek; Ongeluk's Nek and Sani Pass - and from various sites within the Lesotho Highlands. Based on US Geological Survey 1 km topographic data.

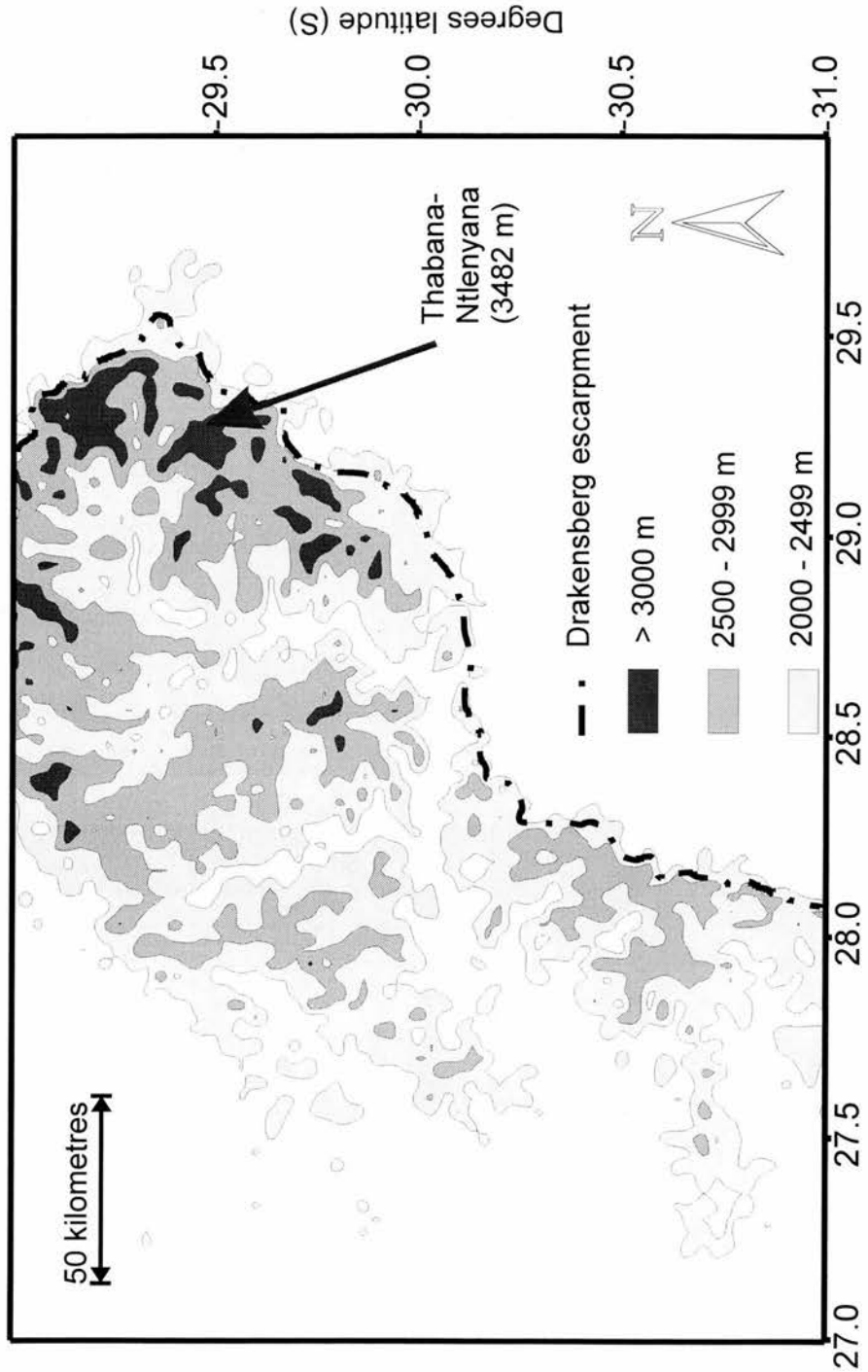

Figure 6.2: Generalised contour map of the area inland of the southern Drakensberg showing the 2000m, 2500m and 3000 m contours. Based on US Geological Survey 1 km topographic data.

The undulating summit of the southern Drakensberg varies between thin (< 1 m) rocky / sandy soil cover and bedrock. The soil cover supports vegetation (the *Merxmuellera drakensbergensis-Festuca caprina* Afroalpine grassland (O'Connor and Bredenkamp, 1997)) which consists mainly of tussock grasses, ericaceous dwarf shrubs and creeping, or mat-forming, plants (van Zinderen Bakker and Werger, 1974; O'Connor and Bredenkamp, 1997). Similar vegetation is also supported by the thin soil that mantles the talus slopes on the oceanward side of the escarpment (Plate 3). Bedrock exposures are generally confined to the highest elevations along the Drakensberg summit. These tend to occur as flat-topped tor-like rock outcrops which stand above the surrounding surface by a few metres on at least three sides (Plate 4). The inland-facing slope was often found to be more gently sloping (~ 5 – 15°) in comparison to the more abrupt step-like slope on the escarpment facing side. Bedrock also crops out as less pronounced local topographic highs along the escarpment summit. Free-face bedrock exposures, with a near vertical drop ranging from a few to several hundred metres, occur extensively along the escarpment edge. Free-face exposures of a generally smaller scale also occur on the inland side of the escarpment.

With the exception of three sections, the whole of the southern Drakensberg is formed in the 183 ± 1 Ma old (Duncan *et al*, 1997) Drakensberg Group basalts. At the three excepted sections, at 29 ° 55 ' S (about 25 km long), 30 ° 4 ' S (about 2 km long) and 30 ° 8' S (about 3 km long), the Drakensberg is formed in predominantly Clarens Formation sandstone. The individual basalt flows of the Drakensberg Group vary considerably in thickness (~ 2 – 50 m) and reach an accumulated thickness in excess of 1.4 km (Cox, 1988; Rehacek, 1995). The compound nature of the flows, the absence of sedimentary or weathering horizons and a general lack of distinguishing petrographic features have prevented the tracing of individual flows in the field and a normal stratigraphic division of the pile (Eales *et al*, 1984; Marsh *et al*, 1997). Marsh *et al* (1997) have recently been able to produce, based on flow geochemistry, a stratigraphic subdivision of the main ~ 1.4 km pile into five major units. Given the problems of describing individual flows, the following general description should be regarded as applying to all the sampling sites used in this study.

The majority of the flows are composed of olivine-poor tholeiitic basalt and are amygdaloidal with the cavities being filled mainly (80 – 95 %) by zeolites (alumino-silicates) and, to a lesser extent, quartz and chalcedony (SiO_2) (Marsh and Eales, 1984, Rehacek, 1995). Zeolites exclusively fill the vesicles above ~ 2500 m (Rehacek, 1995). Amygdales tend to be concentrated in the vesiculated top and bottom of flows, where the

movement of gas bubbles has been halted during cooling, with the central interior part of flows being massive and amygdale-free (Marsh *et al*, 1997). The basalt is mid- to dark grey and, in hand specimen, fine-grained in texture (Plate 5).

With the exception of flows at the base of the pile, which were clearly influenced by the pre-eruption topography (Marsh *et al*, 1997), the flows are very nearly horizontal with a slight (< 2 °) inward dip to the flows all around the main Lesotho remnant (G. Marsh, pers. comm.). This area formed the main depocentre of the Karoo basin during deposition of the Clarens Formation sandstone (Catuneanu *et al*, 1998) and, therefore, such dipping may be attributable to slight basin subsidence during the volcanic extrusions. However, given the general uniformity of the thickness' of the units reported by Marsh *et al* (1997), any subsidence must have been superficial (G. Marsh, pers. comm.).

Dolerite dykes, which acted as feeders to the volcanic pile, intrude and cross cut the basalt flows at numerous sites, decreasing in numbers upwards (Marsh and Eales, 1984; Rehacek, 1995). Dykes vary in length extending up to several tens of kilometres with a mix of widths from a couple of metres to over 50 m (Schmitz and Rooyani, 1987). The basalts and dolerites vary little in texture and composition, but Marsh *et al* (1997) were able to demonstrate that dykes could be classified on the basis of their geochemistry. Marsh *et al* (1997) found that their classification of the dykes was consistent with that of the basalts allowing them to conclude that no intrusion belongs to a unit lower in the sequence than the flows which it intrudes. This study did identify a suite of small intrusions near the top of the pile at 28 ° 45 'S, 28 ° 40' E which could not be correlated with any known lava unit in Lesotho. These dykes appear to have been feeding flows that have been eroded from the top of the pile subsequently (Marsh *et al*, 1997; G. Marsh, pers. comm.).

6.2.2 Sampling strategy

The sampling strategy for this project had to overcome the inherent problem of constraining the denudation rate for a feature that, in the southern Drakensberg alone, is ~ 250 km in length. To achieve this, it was decided that sampling should be concentrated in three separate sites spread along the southern Drakensberg. The sites ultimately chosen were Naudesnek, Ongeluk's Nek and Sani Pass (Figure 6.1) which provided a range of sample settings and relative ease of access. Naudesnek is ~ 50 km south of Ongeluk's Nek and ~ 175 km southwest of Sani Pass. At each site samples were collected from exposed, intact, bedrock on the most representative geomorphic features. Samples were chosen from sites which

appeared to have a simple exposure history, which have been undergoing continuous denudation and which were unlikely to have been subject to prolonged burial by soil, snow or falling detritus.

6.2.3 NAUDESNEK

6.2.3.1 GENERAL DESCRIPTION

Naudesnek (Figure 6.1), 30 ° 45' S, 28 ° 9' E, is the most southerly of the Drakensberg sampling sites. The Drakensberg runs generally north to south in this area and, although this part of the escarpment is less dramatic than the sites further north (Plate 6), Naudesnek, at ~ 2500 m, is the highest pass in South Africa. On either side of the pass the escarpment summit rises to > 2600 m, reaching 2731 m at Scobell's Kop, about 7 km south of Naudesnek (Figure 6.3). On the eastern (oceanward) side of the escarpment, the ground level falls ~ 400 m over a distance of ~ 1 km from the Drakensberg summit. Inland, (west) of the escarpment summit, the altitude also declines, but less markedly, falling about 150 m over 1 km from the highest ground on the summit. The eastern flanks of the escarpment are drained by first order tributaries of the Luzi River, a tributary of the Mzimvubu River which drains to the Indian Ocean (exiting at 31 ° 40 ' S, 29 ° 30 ' E). One unnamed tributary of the Luzi rises just to the north of Scobell's Kop and flows over the escarpment (Figure 6.3). The catchment above the escarpment is only ~ 2 km^2 and local relief within the basin is < 200 m. Inland of the escarpment, drainage is provided by the tributaries of the Bell River, part of the Orange River basin.

The escarpment at Naudesnek is entirely formed in Drakensberg Group basalt. The contact between the basalt and the underlying Clarens Formation sandstone is at ~ 1750 m, making the depth of the basalt pile in the area around Naudesnek, assuming a roughly continuous elevation for the basal contact, of between 750 and 950 m. Given the slight inward dip of the basalt flows, mentioned above, this is likely to be a conservative estimate. The basalt extends for some 10 – 15 km to the east (oceanward) of the escarpment summit in this area, compared to 5 – 10 km at Ongeluk's Nek and 4 – 8 km at Sani Pass.

Figure 6.3: (overleaf). Map of the Drakensberg escarpment at Naudesnek showing the approximate position of the main free face of the escarpment. The flat-lying sampling sites, eight in total, are marked A - H. Based on published 1: 50 000 scale map sheets, 1: 50 000 scale aerial photographs and field observation.

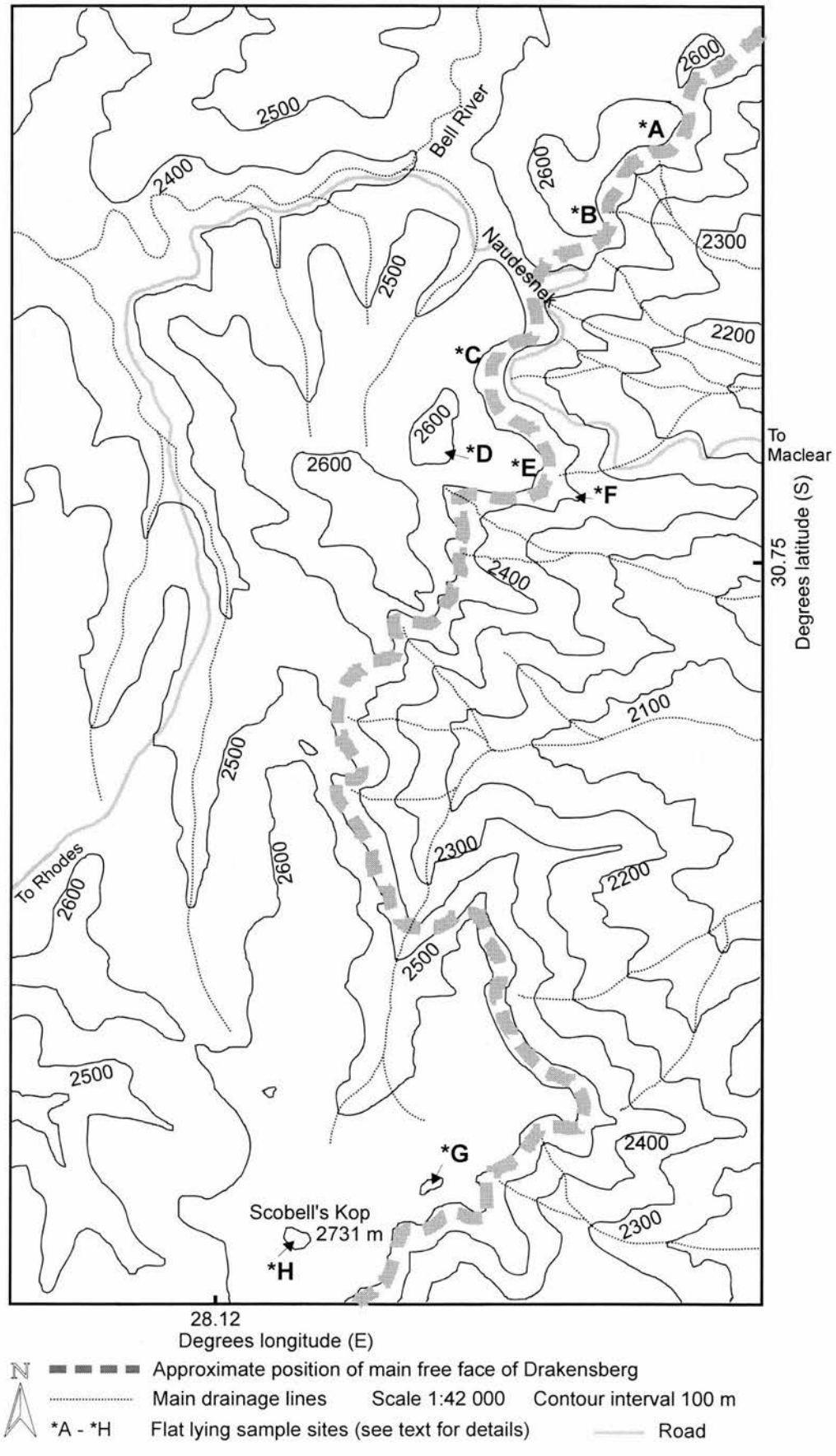
2600
2500
Bell River
2400
*A
2600
*B
2300
Naudesnek
2500
2200
*C
2600
*D
*E
*F
To Maclear
2600
30.75
Degrees latitude (S)
2400
2100
2500
2600
2300
2200
To Rhodes
2600
2500
2500
*G
2400
Scobell's Kop
2731 m
2300
*H
28.12
Degrees longitude (E)
N
Approximate position of main free face of Drakensberg
Main drainage lines
Scale 1:42 000
Contour interval 100 m
*A - *H
Flat lying sample sites (see text for details)
Road

6.2.3.2 SAMPLING SITES

Ten samples were collected and analysed from eight flat-lying sites (A - H in Figure 6.3) at Naudesnek. Three samples (N1/95, N2/95 and N3/95) were collected during the first field season in 1995 and the remaining seven (N1/97, N2/97, N3/97, N4/97, N6/97, N7/97 and N14/97) were collected in late 1997. Sample sites were chosen bearing in the mind the 'Field Procedures' outlined in Chapter 4. Six sites (A, B, C, D, G and H in Figure 6.3) were chosen as representing the highest summits along the escarpment which would constrain the rate of summit lowering. Sites E and F were chosen to quantify the rate of downwearing along a ridge extending from the main escarpment. Samples of varying thickness' of 0.05 – 0.1 m were collected from intact exposed bedrock which was standing ~ 0.5 – 1.0 m above the surrounding surface. Field data, as described in Chapter 4, was recorded at each site and is summarised in Table 6.1.

Table 6.1: Location and field data for flat-lying samples collected at Naudesnek.

Sample	Latitude (d m s) S	Longitude (d m s) E	Altitude (m asl)	Site in Figure 6.3	Surface slope (°)	Thickness (g cm^{-2})	Topographic shielding
1995							
N1/95	30 47 29	28 07 16	2731	H	0	11.6	None
N2/95	30 44 35	28 07 55	2644	D	0	10.2	None
N3/95	30 44 35	28 08 20	2569	E	0	8.7	Partial
1997							
N1/97	30 44 35	28 07 55	2644	D	0	10.15	None
N2/97	30 44 35	28 07 55	2644	D	0	14.5	None
N3/97	30 44 44	28 08 40	2409	F	0	14.5	Partial
N4/97	30 44 20	28 08 00	2595	C	0	13.05	Partial
N6/97	30 43 44	28 08 40	2614	B	0	13.05	Partial
N7/97	30 43 23	28 08 50	2642	A	0	13.05	None
N14/97	30 47 15	28 07 50	2716	G	0	14.5	None

Sample N1/95 was from the bedrock outcrop knoll that forms the summit of Scobell's Kop, which is ~ 500 m inland from the main free face of the escarpment (H on Figure 6.3; Plate 7). This outcrop stands ~ 10 – 15 m above the surrounding surface with the topmost 2 – 3 m

being a marked ~ 80 ° bedrock free face. Below this there is a more gentle (~ 35 °) vegetated slope. The summit is fairly flat but slopes at ~ 5 ° from the middle to the side nearest the escarpment. The sample was taken from the flat middle section. The knoll is ~ 40 m by ~ 20 m, the short axis being parallel to the main escarpment face. Typical of weathered bedrock exposures in this area, the summit has an irregular surface comprising intact bedrock, loose < 0.3 m thick boulders, small-scale pits both within intact bedrock and in joints which contained sand / silt sized sediment some of which supports tussocks of grass (Plate 8). Sample N14/97 was collected from site G in Figure 6.3. This is another flat-topped knoll which is located on the edge of the escarpment ~ 1 km east northeast of sample N1/95. This knoll is smaller, being only ~ 20 m by 10 m and a marked ~ 2 – 3 m free face on the inland sides raises the knoll above the surrounding surface. The surface is flat and the sample was collected ~ 3 m in from the escarpment edge. The summit is similar to that on Scobell's Kop.

N2/95, N1/97 and N2/97 were all collected from the same site (D in Figure 6.3; Plate 7). This is another flat-topped knoll which rises above the surrounding surface by ~ 5 – 10 m. There is a marked free face all round the top of this knoll which is again 2 – 3 m high. The knoll is ~ 0.6 km inland of the main escarpment face and forms the highest point of one of the narrow buttress ridges which extend eastward from the main escarpment. The summit is ~ 50 m by 50 m, and generally flat. The surface is similar to that at Scobell's Kop (Plate 8). Sample N2/95 was taken from ~ 5 m in from the eastern (escarpment) side of the knoll. N1/97 was collected from the central part and N2/97 is from ~ 5 m in from the western (inland) side. These samples were collected to test for variability in the denudation rate across a local surface.

N3/95 and N3/97 (E and F in Figure 6.3 respectively; Plate 7) were collected from bedrock exposures on the buttress ridge which runs eastward from site D in Figure 6.3. The ridge extends for ~ 4 km with the summit elevation dropping from 2664 m to 2131 m. N3/95 is from a high bedrock exposure which occurs just above the main escarpment face and is ~ 0.65 km east of site D. This generally flat outcrop stands ~ 1 m above the surrounding surface and extends for ~ 20 m by 20 m. Again the outcrop shows signs of weathering with an irregular surface made up of bedrock, small < 0.2 m thick boulders and pits filled with sand / silt size material, some of which support grass tussocks. N3/97 was collected from a flat section of the buttress ridge about 600 m east of site E. The ridge at this point is ~ 10 m wide and an exposed section of bedrock is about 4 m by 2 m and stands ~ 0.5 m above the surrounding surface. The sample was taken from the centre. This bedrock surface is similar

in appearance to that from which sample N3/95 was collected. No other suitably exposed bedrock sites were identified along the remainder of the ridge.

N4/97, N6/97 and N7/97 (C, B and A, respectively, in Figure 6.3; Plate 7) are samples taken from bedrock exposed on summits immediately above the main free face of the escarpment. Sample N4/97 was collected from ~ 0.75 km north of site D from a ~ 50 m by ~ 30 m flat-lying bedrock exposure. The sample came from a slightly raised (~ 0.5 m) of this surface which was ~ 15 m from the escarpment edge. The surface was again irregular with some small (~ 0.2 – 0.3 m thick) loose boulders, pits and vegetation. Sample N6/97 (B in Figure 6.3) is from a small, ~ 5 m by 4 m, knoll which is ~ 0.75 m above the surrounding surface. The knoll is set back ~ 10 m from the main escarpment face about 0.65 km northeast of Naudesnek pass. The sample was taken ~ 3 m in from the main escarpment face. The surface is similar to that at N4/97, although there are fewer loose boulders. Sample N7/97 (A in Figure 6.3) is from ~ 0.75 km northeast of site B. This sample site is a small knoll, ~ 5 m by 3 m set back ~ 15 m from the main free face. The surface at this site is, again, a mix of intact bedrock, small (~ 0.2 – 0.3 m thick) boulders, sand / silt sized sediment and vegetation.

6.2.4 Ongeluk's Nek

6.2.4.1 General Description

Ongeluk's Nek, 30 ° 20 ' S, 28 ° 15 ' E, (Figure 6.1) is approximately 50 km north of Naudesnek. In this area the Drakensberg runs north to south (Plate 9) and the summit of the pass is 2547 m. About 1 km south of the pass is Mak'holo (2899 m) the highest point on the escarpment for > 20 km to the south and > 95 km to the north. North of the pass the escarpment summit rises to > 2675 m. Oceanward (east) of the escarpment, the ground level falls ~ 500 m within 1 km of the escarpment summit. West of the Drakensberg summit, the ground falls, generally, ~ 150 m over a distance of 1km, with the exception of the area immediately inland of Mak'holo where the fall is ~ 300 km over the same distance. First order tributaries of the Mabele River (another tributary of the Mzimvubu River) rise on the eastern flanks of the Drakensberg. Inland, the area is drained by tributaries of the Quthing River, part of the Senqu (Orange) River basin.

At Ongeluk's Nek the escarpment is, again, formed entirely in Drakensberg Group basalts. Contact between the basalts and the underlying Clarens Formation occurs at ~ 1680 m (Rehacek, 1995), making the present-day basalt pile thickness in this area, assuming a

roughly continuous elevation for the contact, between 850 – 1200 m. Basalt crops out between 5 and 10 km east (oceanward) of the Drakensberg summit in this area, which is less than the extent encountered at Naudesnek.

6.2.4.2 *Sampling sites*

Four samples from flat-lying sites at Ongeluk's Nek (A - C in Figure 6.4) were obtained during the 1997 field season (O1/97; O5/97; O8/97 and O11/97). Two samples, O1/97 and O5/97 are from the summit of Mak'holo, collected at sites A and B respectively, while sample O11/97 is from site D which marks the highest escarpment summit on the northern side of the pass. Sample O8/97 is from site C, the summit of Maphooaneng Pass, ~ 7.5 km west northwest of Ongeluk's Nek. This sample was collected to provide a comparison between the downwearing rate of escarpment summits and summits at a similar elevation inland. The field data for these samples is summarised in Table 6.2.

Table 6.2: Location and field data for flat-lying samples from Ongeluk's Nek.

Sample	Latitude (d m s) S	Longitude (d m s) S	Altitude (m asl)	Site in Figure 6.4	Surface slope (°)	Thickness (g cm^{-2})	Topographic shielding
O1/97	30 20 56	28 15 25	2880	A	0	13.05	None
O5/97	30 20 44	28 15 23	2898	B	0	14.5	None
O8/97	30 18 53	28 8 20	2560	C	0	9.57	Partial
O11/97	30 19 52	28 14 55	2660	D	0	14.5	Partial

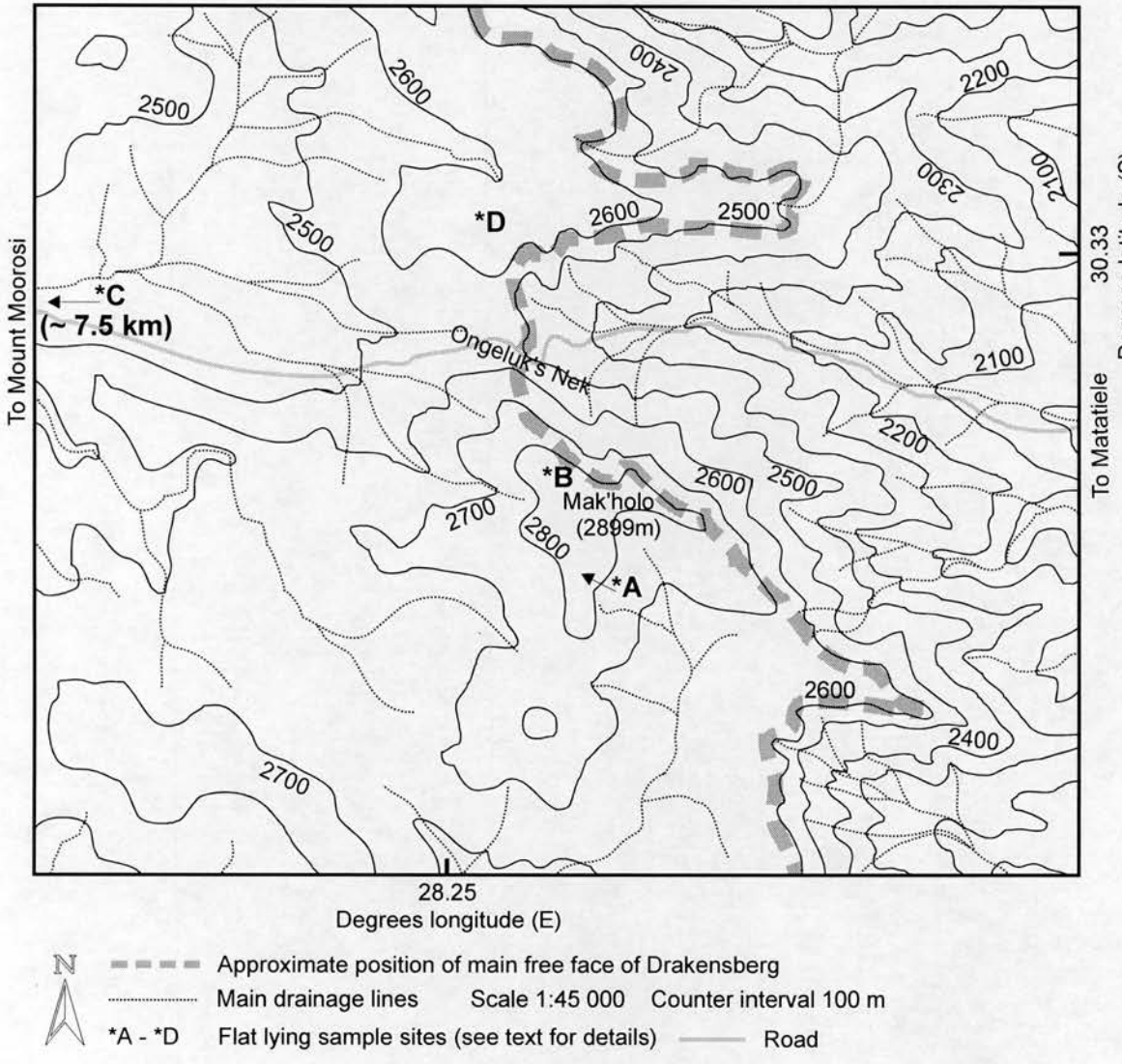

Figure 6.4: Map of the Drakensberg at Ongeluk's Nek showing the approximate position of the main free face of the escarpment. The flat lying sample sites, four in total from this area (of which three are shown on the map) are marked (*A- *D). Site C is ~ 7.5 km inland (west) of Ongeluk's Nek at Maphooaneng Pass and is not shown. Based on published 1: 50 000 scale maps, 1: 50 000 scale aerial photographs and field observations.

Samples O1/97 and O5/97 are both from the bedrock knoll that forms the summit of Mak'holo. This knoll is 'L' shaped with the short axis of the 'L' forming the summit of the Drakensberg and the long axis running inland at ninety degrees to the main escarpment free face. Sample O1/97 (A in Figure 6.4; Plate 11) is from near the end of this long axis, ~ 400 m from the main free face of the escarpment. Sample O5/97 (B in Figure 6.4; Plate 10) was collected from the short axis, ~ 10 m in from the main free face, and about 75 m west of the trig point marking the summit. The knoll has a marked free face on the east and west which is ~ 4 – 15 m high. The northern edge of the knoll marks the main free face of the escarpment while the southern edge has no marked free face and slopes ~ 35 °. The surface of the knoll is irregular and comprises exposed, intact, bedrock, some loose < 0.3 m thick boulders and some vegetation (Plate 9). Both samples were collected from bedrock that stands proud of the surrounding surface by ~ 0.3 – 0.5 m.

O8/97 is from exposed bedrock on the westmost (lower) of the two unnamed summits that form the south side of Maphooaneng Pass (Plate 10). This summit is convex with the only free face being ~ 20 m below the summit on the north (Maphooaneng Pass) side. Between the free face and the summit the slope is ~ 20 °. The surface is, again, a mix of exposed rock, loose < 0.5 m thick boulders, sandy / silly soil and vegetation (Plate 12). The sample is from an exposed outcrop which stands ~ 0.3 m above the surface.

Sample O11/97 (D in Figure 6.4) is from a bedrock knoll that marks the highest point on the northern side of Ongeluk's Nek. This knoll is ~ 100 m x 150 m with marked free faces ~ 2 – 3 m high on all sides. The surface is generally flat with the usual mix of exposed bedrock, loose ~ 0.1 – 0.2 m thick boulders and grass tussocks.

6.2.5 Sani Pass

6.2.5.1 General description

Sani Pass (29 ° 35 ' S, 29 ° 17 ' E, Figure 6.1) is 2874 m above sea level and is the northernmost of the sampling sites on the southern Drakensberg escarpment, located about 30 km south of the point where the escarpment turns to run southeast – northwest. This area has the greatest relief of the three escarpment sites with the ground level falling between ~ 500 m and ~ 750 m over a distance of 1 km on the oceanward (east) side (Plate 13). Inland of the Drakensberg summit the ground falls ~ 200 m over 1 km on the southern side of the pass and ~ 20 m on the northern side in the area known as the Sani Flats which extends for ~ 6

km^2 (Figure 6.5). Hodgson's Peaks (3251 m and 3256 m, Plate 13) form the highest escarpment summits about 4 km south of Sani. North of the pass the escarpment summit rises gently from 2880 m to 2900 m for ~ 5km before reaching 3126 m at Bitso-Lebe (Figure 6.5). The highest summit in southern Africa, Thabana-Ntlenyana (3482 m), is ~ 12.5 km north of Sani. East of the escarpment the area is drained by tributaries of the Mkhomazana River, part of the Mkomazi Drainage Basin which drains to the Indian Ocean. Inland the main river is the Sani, a tributary of the Senqu (Orange) River.

The lithology of the escarpment in this area is Drakensberg Group basalt. Contact between the basalt and the underlying Clarens Formation sandstone is at ~ 2090 m, making the basalt pile ~ 790 – 1160 m thick, again, assuming a roughly continuous elevation for the basal contact. The basalt extends for ~ 4 – 8 km oceanward of the escarpment summit.

Figure 6.5: (overleaf) Map of the Drakensberg at Sani Pass. The approximate position of the main free face of the escarpment is shown as are the main drainage lines. The flat-lying sample sites are marked A - D. Based on 1:50 000 scale topographic maps, 1: 30 000 scale aerial photograph and field observations.

Figure 6.6: (overleaf 2) Aerial photograph of the southern Drakensberg at Sani Pass. North is at the top of the page. The Sani Flats, ~ 6 km^2, form the escarpment summit north of the pass. To the south, the highest summits are the twin peak of Hodgson's Peaks (3251 m and 3256 m). The difference in the relief oceanward and inland of the escarpment is clearly shown. The scale is approximately 1: 30 000.

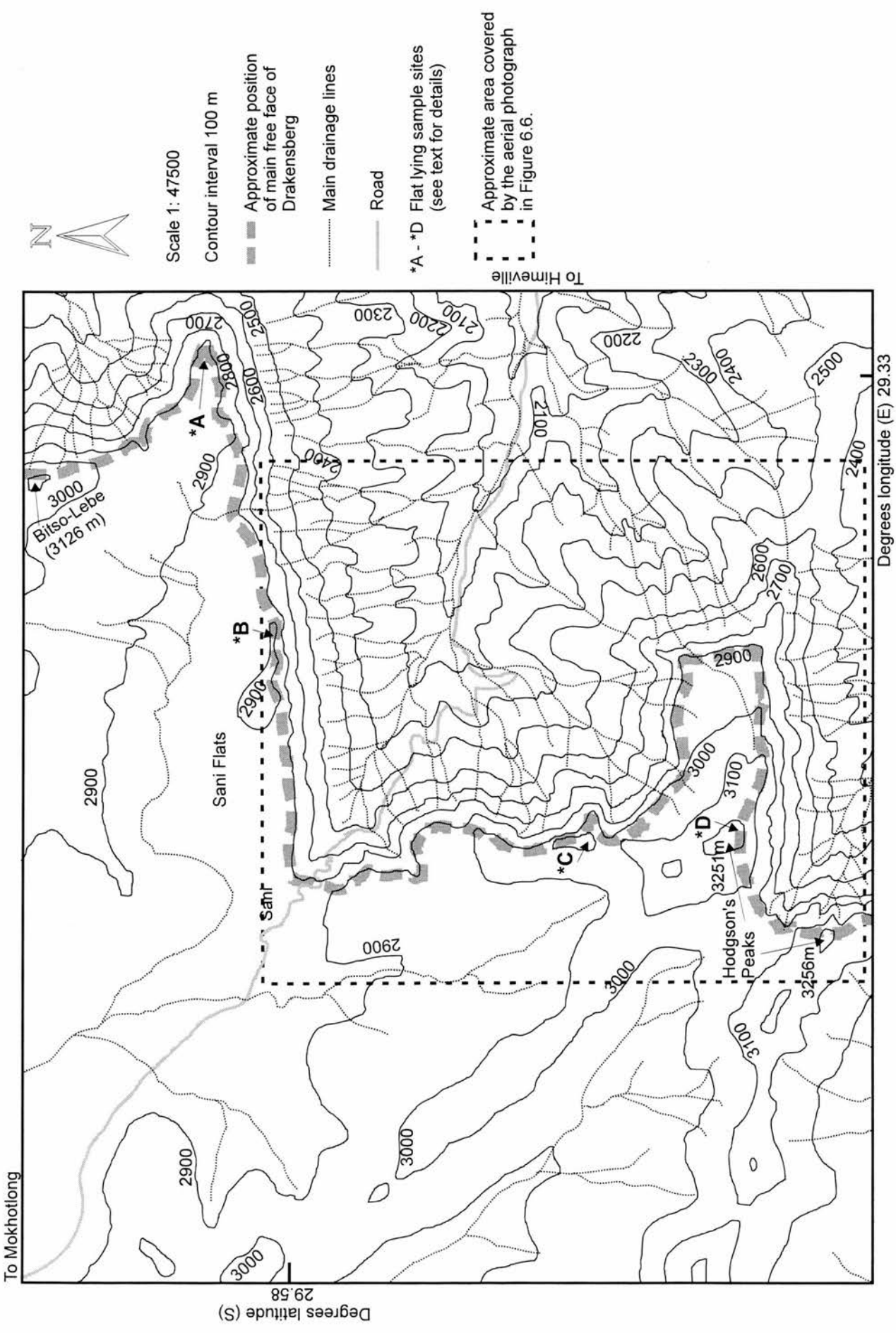
N
Scale 1: 47500
Contour interval 100 m
Approximate position of main free face of Drakensberg
Main drainage lines
Road
*A - *D Flat lying sample sites (see text for details)
Approximate area covered by the aerial photograph in Figure 6.6.
To Himeville
To Mokhotlong
Degrees latitude (S)
29.58
Degrees longitude (E) 29.33
3000 Bitso-Lebe (3126 m)
Sani Flats
Sani
Hodgson's Peaks
3251m
3256m
*A
*B
*C
*D
2900
3000
3100
2700
2600
2500
2400
2300
2200
2100

750
6.7.84
9
1-30000
87
B
C
D
SANI
HODGSON'S
PEAKS

6.2.5.2 SAMPLING SITES

Five samples from four flat-lying sites at Sani (A - D in Figure 6.5) were collected and analysed. Sample S1/95 was collected from site A in 1995, and the remaining four samples (S3/97, S5/97, S8/97 and S10/97) were collected during the second field season. Sites A and B were chosen to establish the rate of lowering of the Sani Flats, the extensive area of low relief which forms the escarpment summit on the northern side of the pass. The other two sites, C and D, were selected as representing the highest summits along the southern part of the escarpment. The location and field data is summarised in Table 6.3.

Table 6.3: Location and field data for flat-lying samples collected at Sani Pass.

Sample	Latitude (d m s) S	Longitude (d m s) E	Altitude (m asl)	Site in Figure 6.5	Surface slope (°)	Thickness (g cm^{-2})	Topographic shielding
1995							
S1/95	29 34 40	29 20 00	2884	A	0	15.9	Partial
1997							
S3/97	29 37 00	29 17 35	3251	D	0	14.5	None
S5/97	29 34 40	29 20 00	2890	A	0	14.5	None
S8/97	29 35 00	29 18 35	2900	B	0	13.05	Partial
S10/97	29 36 30	29 17 25	3129	C	0	14.5	Partial

Samples S1/95 and S5/97 were both collected from exposed bedrock at site A in Figure 6.5. Sample S5/97 was collected to establish the ability of the technique to replicate results from separate samples collected at the same site and prepared in different laboratories (J. Stone prepared S1/95 in the Research School for Earth Sciences, ANU, while the author prepared S5/97 in Edinburgh). This site is the easternmost point of the Sani Flats, ~ 5 km from Sani, and marks the summit of the escarpment (Plate 14). The surface is a mix of exposed bedrock, loose < 0.3 m thick boulders, sandy/ silty sediment and some low growing vegetation. Both samples were collected from similar exposed bedrock which stood proud of the surface about 0.3 m – 0.5 m and which was located ~ 10 m in from the escarpment edge. The samples were located ~ 10 m apart, sample S1/95 being slightly further east than S2/97.

S8/97 is from site B in Figure 6.5. This site is ~ 2.5 km west of site A and is also part of the Sani Flats summit (Plate 14). The surface at site B is similar to that at site A (Plate 15) and

the sample was taken from an exposed section of bedrock which is ~ 0.5 m above the surrounding surface and ~ 5 m from the escarpment edge.

Two samples were collected from summits south of the pass. S3/97 is from site D, the northernmost of the summits at Hodgson's Peaks. This site is a bedrock knoll located ~ 150 m inland of the main free face of the escarpment. The knoll is ~ 5 – 10 m wide, ~ 30 – 40 m long and is flanked by a free face of ~ 3 – 4 m high all sides (Plate 16). The summit is undulating with a series of four bedrock hummocks each with an amplitude of ~ 1 – 2 m. The surface is a mix of intact bedrock and loose < 0.3 m thick boulders. The sample is from the top of one of the bedrock hummocks and is ~ 5 m in from the free face on the southern side of the knoll (side nearest the escarpment). Sample S10/97 is from site C, another bedrock knoll which marks the summit of the Drakensberg located ~ 3 km south of Sani (Plate 17). The knoll is ~ 40 m by ~ 15m and stands ~ 20 – 30 m above the surrounding surface. The only pronounced free face is on the escarpment side, the other sides sloping ~ 25 – 40 ° from the surface below. The surface is convex and the sample was collected from the almost flat summit, ~ 10 m in from the edge of the escarpment. The summit surface is similar to other surfaces sampled in this area.

6.3 Lesotho Highlands' sites

6.3.1 General morphology and geology

The Lesotho Highlands form the ground over 2000 m which lies inland of the Drakensberg (Figure 6.1). This area extends for ~ 15.5 x 10^3 km^2 with elevations ranging from ~ 1500 m near the Senqu (Orange) River and its major tributaries south of 29 ° 30 ' S to 3482 m at Thabana-Ntlenyana (Figure 6.2). The highest elevations are generally found within ~ 35 km of the Drakensberg and this also tends to be where the most extensive areas > 3000 m, are found (Figure 6.7). These areas, generally, have a low relief summit (Plate 18), except where they have been incised by major tributaries of the Senqu River (Plate 19). Apart from this, the highest elevations are concentrated in three mountain ranges – the Central Range, Thaba-Putsoa (Blue Mountain) Range and the Maloti Mountains (Figure 6.7). There is a general decline in elevation from the northeast to the southwest with summits rarely exceeding 3000 m in the Thaba-Putsoa Range. The Highlands are drained entirely by the Senqu River which runs generally south until ~ 30 ° S (within ~ 10 km of the Drakensberg) where it turns to the southwest.

The summits of the Highlands are similar to the Drakensberg, being a mix of exposed bedrock and thin sandy soils that support Afroalpine grassland (O'Connor and Bredenkamp, 1997). In some places flat-topped knolls, similar to those encountered on the Drakensberg summit occur (Plate 20), whilst in other locations bedrock crops out in a less pronounced manner. The slopes support a good ground cover of grasses and ericaceous dwarf shrubs and free face exposures sometimes occur as bedrock steps on the valley sides.

Figure 6.7: (overleaf). Map of the Lesotho Highlands showing the 2000 m, 2500 m and 3000 m contours and the approximate position of the Drakensberg. The flat-lying sample sites from various summits of the Highlands (11 in total) are marked A - K. The most extensive areas of ground > 3000 m occur within ~ 35 km of the Drakensberg and elevations generally decline from the northeast to the southwest. The area is drained by the Senqu (Orange) River and its position, as well as that of some of the main tributaries, is marked.

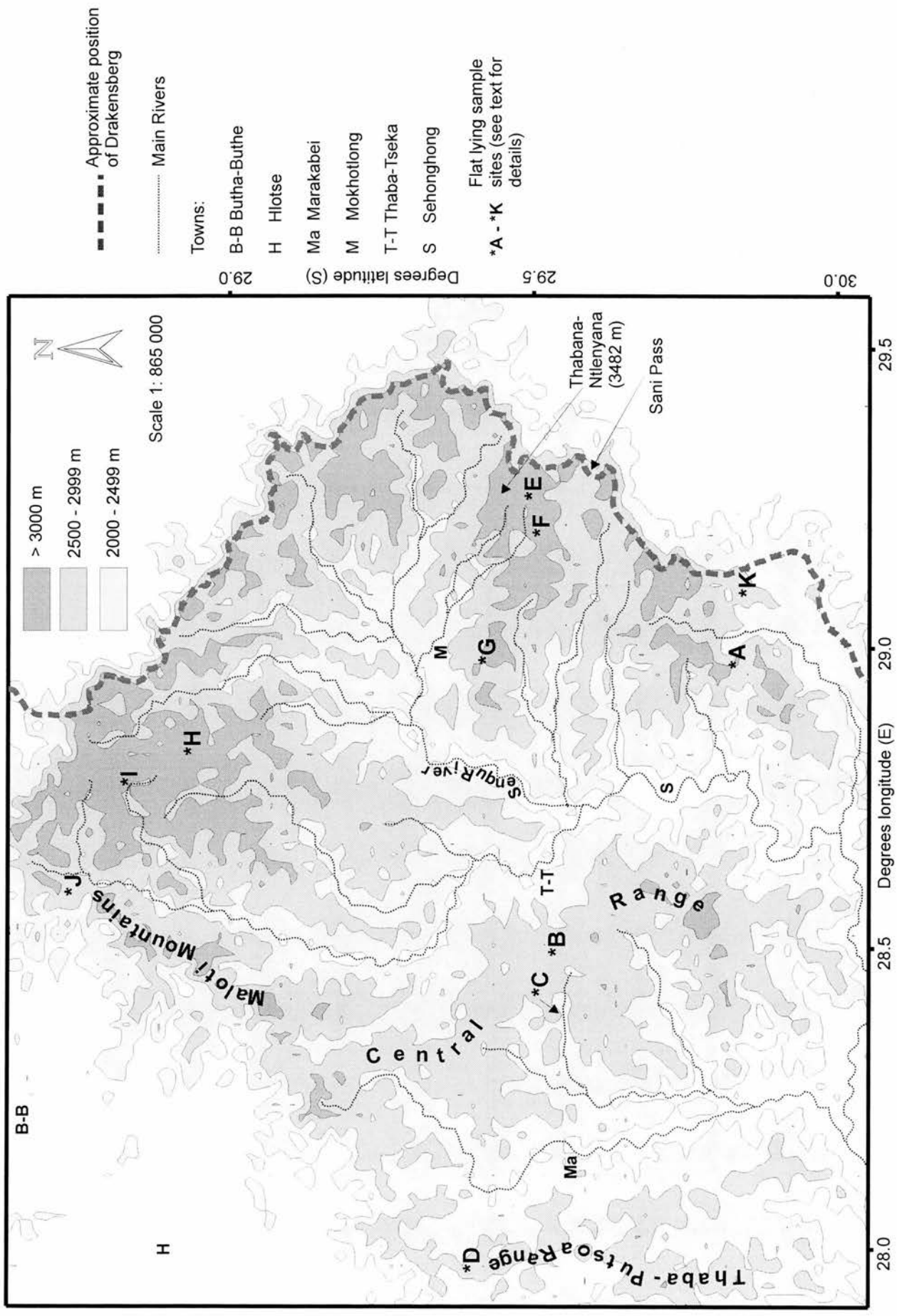
Approximate position of Drakensberg
Main Rivers
Towns:
B-B Butha-Buthe
H Hlotse
Ma Marakabei
M Mokhotlong
T-T Thaba-Tseka
S Sehonghong
Flat lying sample sites (see text for details)
*A - *K
Degrees latitude (S)
29.0
29.5
30.0
> 3000 m
2500 - 2999 m
2000 - 2499 m
Scale 1: 865 000
N
Thabana-Ntlenyana (3482 m)
Sani Pass
Maloti Mountains
Central
Range
Thaba-Putsoa Range
Senqu River
B-B
H
Ma
M
S
T-T
*A
*B
*C
*D
*E
*F
*G
*H
*I
*J
*K
28.0
28.5
29.0
29.5
Degrees longitude (E)

The predominant lithology of the Highlands is the 183 ± 1 Ma old Drakensberg Group basalts. The Senqu River bed is cut into the underlying Clarens Formation sandstone south of Sehonghong (Figure 6.7) and south of 30 ° S the channel has incised into the Elliot Formation sandstone. The basal contact of the basalt with the Clarens sandstone is ~ 1800 m in the Sehonghong area. An example of the influence of the pre-eruption topography on the altitude of this basal contact is found further downstream at ~ 30 ° S, 28 ° 15 ' E where the bed of the Senqu is cut in basalt at ~ 1600 m. In addition to the basalt there are a large number of dolerite dykes and several kimberlite pipes, the latter being mostly concentrated in the area north of 29 ° S.

6.3.2 SAMPLING STRATEGY

In nearly all the landscape development scenarios for southeast Africa, the Lesotho Highlands are regarded as some form of residual and are excluded from the particular evolutionary scheme (eg Partridge and Maud, 1987; Burke, 1996). King (eg 1962) suggested that the highest summit (ie > 3000 m) were intact remnants of the Gondwana surface and that they had experienced little, if any, modification. Although King's view has been challenged theoretically (eg Partridge and Maud, 1987), it has not, previously, been possible to measure the denudation rate on these highest summits. Establishment of denudation rate estimates for this area, derived directly from the basalt bedrock, enables King's theory to be tested critically and, in addition, provide a comparison for denudation rate estimates for the escarpment summit samples. To achieve this, fourteen flat-lying samples were collected from eleven summits ranging in altitude from 2619 m to 3360 m (sites A - K in Figure 6.7). These summits can be grouped into three types – summits from extensive, lower relief, areas (sites B, E, F, H); summits at the head of a river valley (A, G, J and K) and summits above river valley sides (C, D, and I).

6.3.3 SAMPLING SITES

All fourteen samples from the eleven sites shown in Figure 6.7 were collected during the 1997 field season. The field data is summarised in Table 6.4. As before, at each site samples were collected from exposed, intact, bedrock which appeared to have a simple exposure history, to be subject to prolonged ongoing denudation and which was least likely to have experienced burial by snow, soil or falling debris from higher sites.

Table 6.4: Location and field data for flat-lying samples collected from the Lesotho Highlands.

Sample	Lat. (d m s) S	Long. (d m s) E	Alt. (m asl)	Site in Figure 6.7	Summit Type [α]	Surface Slope (°)	Thick. (g cm^{-2})	Topo. Shield.
L1/97	29 53 35	28 58 15	3050	A	VH	0	14.5	Partial
L4/97	29 32 44	28 30 46	2915	B	LR	0	9.28	None
L7/97	29 31 49	28 22 47	2750	C	VS	0	14.5	None
L9/97	29 25 00	27 57 15	2619	D	VS	0	13.05	Partial
L10/97	29 30 45	29 16 12	3266	E	LR	0	11.6	Partial
L11/97	29 30 40	29 16 02	3260	E	LR	0	11.6	Partial
L12/97	29 30 50	29 13 02	3360	F	LR	0	14.5	None
L13/97	29 30 50	29 13 28	3360	F	LR	0	11.6	None
L15/97	29 25 58	28 57 40	3140	G	VH	0	14.5	Partial
L16/97	28 56 25	28 50 12	3295	H	LR	0	13.05	None
L17/97	28 56 26	28 50 05	3292	H	LR	0	14.5	None
L22/97	28 50 00	28 44 25	3055	I	VS	0	10.15	Partial
L23/97	29 51 55	29 05 07	2891	K	VH	0	14.5	None
L28/97	28 45 50	28 36 01	2850	J	VH	0	14.5	Partial

[α] Samples from extensive lower relief summits (LR); valley heads (VH) or valley side summits (VS).

6.3.3.1 Summits at the head of river valleys

Sample L1/97 is from a bedrock outcrop knoll which forms the summit of Matabeng Pass, ~ 15 km west of the Drakensberg (A in Figure 6.7). This summit forms the drainage divide between a tributary of the Tsoelike River (east of the pass) and the Matabeng River on the west. The ground level east and west of the pass falls ~ 380 m within 1 km of the summit. The knoll is ~ 40 m by ~ 25 m and has a marked free face of ~ 10 – 15 m on the east and west sides and ~ 3 – 5 m on the north and south (Plate 20). The summit surface rises towards the centre and the sample was collected from a flat topped outcrop at the centre that is ~ 1 m above the surface. The surface is similar to those at the Drakensberg, being a mix of bedrock, boulders (< 0.3 m thick), and grass tussocks.

L15/97 is from a similar setting at the summit of Menoaneng Pass, ~ 35 km northwest of the escarpment at Sani Pass (G in Figure 6.7). This pass forms the drainage divide between two tributaries of the Senqu River. The ground level falls ~ 350 m within 1 km on the northwest and southeast sides of the pass. The bedrock knoll has a distinct free face ~ 10 – 15 m on the southeast side only. On the other sides there are exposed bedrock free faces but these are ~ 2 – 3 m and slope at ~ 60 °. The knoll is ~ 50 m by 5 – 10 m and has two summits. This sample is from the northern summit and was from an outcrop which stands ~ 1 m above the surface.

Sample L23/97 is from site K in Figure 6.7, the summit of Thaba-Ntso (2891 m) which borders the Sehlabathebe National Park in Lesotho. This summit forms the drainage divide between two tributaries of the Tsoelike River. Although Thaba-Ntso is composed of basalt, the Drakensberg, which is ~ 3 km west, is formed in Stormberg Group sandstones for ~ 25 km. The bedrock knoll which forms the summit is ~ 10 m by 100 m, with a marked free face on the north and south sides of ~ 10 – 12 m. The ground level falls ~ 370 m within 1 km of the summit. The summit surface is a mix of intact bedrock, loose boulders (< 0.3 m thick) and small grass tussocks. Sample L23/97 is from a section of bedrock which stands ~ 0.5 m above surface, ~ 3 m from the north side of the knoll.

L28/97 is from the summit at the head of the drainage divide at Moteng Pass in the Maloti Mountains, which mark the western boundary of the Lesotho Highlands (J in Figure 6.7). This summit separates a tributary which drains to the east to the Malibamatso River and eventually to the Senqu River. On the west the Hololo River rises and drains from the Highlands to the Caledon River in the Lesotho Lowlands (1500 – 2000 m), falling ~ 375 km within 1 km (Plate 21). The summit is, again, marked by a distinct bedrock knoll which is ~ 75 m by 20 m, with a pronounced free face on both the east and west sides. The sample is from a raised section of bedrock ~ 0.5 m higher than the rest of the surface and ~ 10 m from the western edge.

6.3.3.2 Summits from more extensive, lower relief, areas

Sample L4/97 was collected from the summit of Thabana-ea-Manase (2915 m) in the Central Range (B in Figure 6.7). The ground falls between ~ 20 – 200 m within 1 km of the summit. The summit is marked by a ~ 3 – 4 m wide bedrock ridge which stands 2 – 3 m above a 10 – 15° slope which extends for ~ 50 m where it forms the summit of a 10 –12 m free face. The summit of the ridge is made up of a series of blocks, the joints being subject to various

degrees of weathering. Some ~ 0.5 m thick boulders were noted on the well vegetated 10 – 15 ° slope below the ridge (Plate 22). The sample is from ~ 1 m in from the edge of the ridge.

Samples L10/97 and L11/97 are both from site E in Figure 6.7, ~ 4.5 km south of Thabana-Ntlenyana. The samples are from bedrock which crops out on the summit of a broad ridge (~ 100m x ~ 750 m) that is ~ 3 km west of the Drakensberg. Elevations within 1 km of the ridge fall ~ 100 m to the north and ~ 200 m to the south. The summit of the ridge is split into three levels, each marked by a 1 – 2 m step. All levels are mainly exposed bedrock with some limited vegetation growing in weathered joints (Plate 23). L10/97 is from the highest level and L11/97 is from the lowest level. Both samples are from ~ 10 – 15 m from the southern edge of the ridge.

L12/97 and L13/97 were taken from the summit of Kotisephola (3360 m) which is ~ 10 km northwest of Sani Pass (F in Figure 6.7). The summit is roughly 'L' shaped being ~ 50 m wide by ~ 300 m and ~ 150 m. The ground falls, within 1 km of the summit, by ~ 250 m. On the summit surface are three small hummocks (~ 10 m^2) which rise ~ 1 m above the surrounding surface (Plate 24). L12/97 is from the hummock furthest west, while L13/97 is from the one furthest east. The surface of the hummocks comprise intact bedrock and some loose < 0.1 m thick boulders.

Samples L16/97 and L17/97 are from the summit of Mafisoaneng (3295 m) which is ~ 15 km west of the northern Drakensberg (H in Figure 6.7). The surface is this area is generally of low local relief (Plate 18), with elevation falling ~ 150 m within a ~ 1 km radius of the summit. The summit is formed by a bedrock knoll which is ~ 50 – 100 m wide and ~ 400 m in length. It is flanked by a free face ~ 15 m high at the west which tapers to ~ 5 m at the east, with a short ~ 10 m section towards the east where the free face is interrupted by a ~ 40 ° grassed slope. This separates the summit into two knolls, the easternmost of which is ~ 3 m higher. L16/97 was from this eastern section, while L17/97 is from the more extensive western section (Plate 25). The surface at both sites is similar to that at other sites.

6.3.3.3 Summits above river valley sides

Three samples were collected from flat-lying sites above river valleys. L7/97 is from a flat-lying site on the summit of the drainage divide between the Tenane (~ 2260 m, ~ 2 km south) and Likomiking Rivers (~ 2300 m, ~ 3.5 km north) (C in Figure 6.7). The summit is ~ 20 m x 20 m in extent, and formed of exposed intact bedrock with some loose < 0.2 m thick

boulders and grass tussocks (Plate 26). The sample is from a slightly raised area in the central part of the summit.

Sample L9/97 is from a flat-lying site (D in Figure 6.7) above the Makheleng River which drains to the Lesotho Lowlands. The river is ~ 3.5 km west of the site and ~ 500 m lower. The site is a low relief summit (~ 1 km^2) which slopes ~ 2 ° to the west and is ~ 1 km west of Thaba-Putsoa (2900 m) (Plate 27). The summit is mainly grassed with the exception of a ~ 10 m by ~ 30 m outcrop which stands ~ 1 m above the grassed surface and from which the sample was collected. The surface of this outcrop also has some grass tussocks which are growing in some weathered joints.

Flat-lying site I (Figure 6.7) provided L22/97. This site is ~ 130 m above and ~ 500 m east of the Motete River. The outcrop is ~ 20 m by ~ 50 m and forms part of a generally flat surface of ~ 1 – 2 km^2 which extends for ~ 1 km along the river valley (Plate 28). On the river valley side this surface has a distinct ~ 10 – 20 m free face. The sample was collected from ~ 2 m from the free face edge from an outcrop which stands ~ 0.5 m above the surface.

6.4 ANALYTICAL DATA AND ESTIMATED DENUDATION RATES

6.4.1 ANALYTICAL DATA

Chlorine-36 was extracted and recovered from all the samples using the procedures outlined in Chapter 4. Sample S1/95 was prepared by Dr John Stone in the Research School of Earth Sciences (RSES), ANU and samples N1/95, N2/95 and N3/95 were prepared by the author, under Dr Stone's supervision, in the RSES laboratory. The remaining 29 samples were prepared by the author in the ^{36}Cl clean room laboratory in the Department of Geography. Isotopic ratios were measured by Dr Keith Fifield and Dr Richard Cresswell using the 14-UD pelletron accelerator at ANU. Whole rock chloride concentration and the ancillary chemical analyses were determined as summarised in Chapter 4. The major and selected trace element (Li, B, Cl, Cr, Sm, Gd, Th and U) concentrations are detailed in Appendices 3 and 4 respectively.

The location and field data for the sample sites is given in Tables 6.1 to 6.4. Chlorine-36 is produced by reactions involving Ca, K and ^{35}Cl. The concentration of these elements in each sample together with the weight of sample digested and the amount of ^{36}Cl free chloride carrier added is given in Table 6.5. The weight of sample digested varied between ~ 4.5 g and ~14 g, with most being ~ 10 – 12 g. About 1.4 – 1.5 x 10^{-3} g of ^{36}Cl free chloride carrier was added to each sample. The Ca content varied between 5.16 and 7.91 wt. %, while the K content varied between 0.19 and 1.23 wt. %. For the purpose of subsequent calculations, an error of 1 % was included in these values. The whole rock Cl content of all samples was low (~ 1 – 36 ppm, typically ~ 3 – 4 ppm) which reduced the significance of the ^{35}Cl thermal neutron capture reaction in the total ^{36}Cl production rate. Four replicates (N7/97(R), O1/97(R), L15/97(R) and L17/97(R)) were prepared to test the reproducibility of the results. Aliquots for these were taken from the post-leached material and hence have the same Ca, K and Cl content as their principal counterparts.

Table 6.5: Elemental composition of flat-lying samples

Sample	Sample weight (g)	^{36}Cl free chloride carrier (x 10^{-3} g)	Ca (wt%)	K (wt%)	Cl (μg g^{-1})
Naudesnek					
1995					
N1/95	7.8014	1.3985	6.58	0.79	10.3 ± 0.4
N2/95	7.1689	1.3952	6.70	0.32	14.7 ± 0.4
N3/95	7.7952	1.3961	7.91	0.64	9.9 ± 0.3
1997					
N1/97	9.9901	1.4400	6.51	0.40	1.7 ± 0.4
N2/97	10.2543	1.4551	6.26	0.31	3.9 ± 0.3
N3/97	10.5329	1.4377	6.16	0.24	4.0 ± 1.0
N4/97	10.0706	1.4315	6.33	0.64	3.2 ± 0.2
N6/97	14.1788	1.4386	7.21	0.72	3.6 ± 0.9
N7/97	12.3260	1.4367	7.23	0.54	10.9 ± 0.3
N7/97(R)	10.5653	1.4895	7.23	0.54	10.9 ± 0.3
N14/97	10.3351	1.4447	6.49	0.32	1.2 ± 0.3
Ongeluk's Nek					
O1/97	10.4163	1.4353	7.26	0.56	3.4 ± 0.9
O1/97(R)	9.7325	1.4428	7.26	0.56	3.4 ± 0.9
O5/97	10.4061	1.4386	6.69	0.19	2.3 ± 0.6
O8/97	10.5422	1.4447	5.16	1.23	2.7 ±0.7
O11/97	11.3419	1.4395	6.86	0.78	1.0 ± 0.3
Sani Pass					
1995					
S1/95	4.5001	1.3985	6.55	0.95	10.1 ± 0.2
1997					
S3/97	10.5610	1.4405	5.23	1.00	4.9 ± 1.2
S5/97	12.4273	1.4400	7.27	0.48	3.7 ± 0.3
S8/97	10.8225	1.4235	6.51	0.51	7.7 ± 0.3
S10/97	10.6457	1.4490	6.27	0.56	5.1 ± 1.3
Lesotho Highlands					
L1/97	9.9754	1.4367	6.63	0.61	2.6 ± 0.7
L4/97	10.6406	1.4334	6.26	1.22	3.1 ± 0.3
L7/97	10.6882	1.4377	6.13	0.39	1.4 ± 0.3
L9/97	10.6457	1.4475	6.01	0.54	3.1 ± 0.3
L10/97	10.6678	1.4381	6.34	0.85	3.5 ± 0.9
L11/97	10.4603	1.4527	7.12	0.35	2.2 ± 0.6
L12/97	9.0655	1.4461	5.65	0.85	9.1 ± 0.3
L13/97	12.0036	1.4282	5.83	0.47	1.2 ± 0.3
L15/97	10.7104	1.4221	7.02	0.71	3.5 ± 0.3
L15/97(R)	9.2171	1.5719	7.02	0.71	3.5 ± 0.3
L16/97	11.4229	1.4334	7.20	0.35	35.6 ± 0.5
L17/97	13.0043	1.4405	7.46	0.42	12.2 ± 0.5
L17/97(R)	9.1446	1.4621	7.46	0.42	12.2 ± 0.5
L22/97	11.6925	1.4339	5.70	1.33	2.2 ± 0.6
L23/97	10.1297	1.4782	6.49	0.79	6.2 ± 0.3
L28/97	11.5322	1.440	5.74	0.51	3.9 ± 0.7

The isotopic ratios measured by the AMS, together with the total ^{36}Cl, the background ^{36}Cl and cosmogenic ^{36}Cl contents are reported in Table 6.6. The uncertainty in the AMS determined ratio (quoted at the 1 σ level, K. Fifield, pers. comm.) varies between 1.1 % and 7.9 %, with the error tending to increase as the ratio decreases because the counting statistics become more important. The ^{36}Cl blank figure is the total number of ^{36}Cl atoms (and error) which was measured in the relevant procedural blank (one per five samples). This is deducted before the ^{36}Cl total is determined. The measured abundance of ^{36}Cl (atoms g^{-1}) in each sample (^{36}Cl total in Table 6.6) is calculated by multiplying the $^{36}Cl/Cl$ ratio by the relevant atomic concentration of Cl. This absolute concentration includes both a non-cosmogenic nucleogenic component attributable to U-fission (P_{sf}, Equation 3.5, Chapter 3) and (α,n) reactions ($P_{(\alpha,n)}$, Equation 3.6, Chapter 3) as well as the cosmogenic constituent. This background component (^{36}Cl background in Table 6.6) was derived using Equation 3.32 and the relevant U and Th concentrations listed in Appendix 4. The concentration of cosmogenic ^{36}Cl (^{36}Cl cosmogenic in Table 6.6) is derived by deducting the background component from the measured abundance but, given the very low background levels (> 0.1 % of cosmogenic ^{36}Cl), the ^{36}Cl total and ^{36}Cl cosmogenic figures in Table 6.6 are the same.

Table 6.6: Chlorine-36 isotopic ratio and absolute concentrations for flat-lying samples.

Sample	^{36}Cl / Cl AMS ratio (10^{-15})	AMS Uncert. (%)	^{36}Cl blank (10^4 atom)	^{36}Cl total (10^6 atom g^{-1})	^{36}Cl background (10^2 atom g^{-1})	^{36}Cl cosmogenic (10^6 atom g^{-1})
Naudesnek						
1995						
N1/95	500 ± 20	4.0	1.2 ± 1.2	1.61 ± 0.06	3.0 ± 0.8	1.61 ± 0.06
N2/95	1520 ± 55	3.6	1.2 ± 1.2	5.42 ± 0.10	5.7 ± 0.9	5.42 ± 0.10
N3/95	205 ± 9	4.4	1.2 ± 1.2	0.66 ± 0.03	3.4 ± 1.1	0.66 ± 0.03
1997						
N1/97	1850 ± 60	3.2	2.7 ± 1.5	4.60 ± 0.15	0.7 ± 0.2	4.60 ± 0.15
N2/97	2010 ± 70	3.5	2.7 ± 1.5	4.99 ± 0.17	1.4 ± 0.2	4.99 ± 0.17
N3/97	260 ± 15	5.8	2.7 ± 1.5	0.62 ± 0.04	1.7 ± 0.5	0.62 ± 0.04
N4/97	880 ± 40	4.5	2.7 ± 1.5	2.18 ± 0.10	1.0 ± 1.0	2.18 ± 0.10
N6/97	1160 ± 20	1.7	2.4 ± 1.5	2.08 ± 0.04	2.0 ± 0.5	2.08 ± 0.04
N7/97	325 ± 15	4.6	2.4 ± 1.5	0.70 ± 0.03	4.9 ± 0.4	0.70 ± 0.03
N7/97(R)	274 ± 13	4.7	1.2 ± 1.0	0.71 ± 0.03	4.9 ± 0.4	0.71 ± 0.03
N14/97	305 ± 20	6.6	2.2 ± 1.7	0.73 ± 0.05	0.6 ± 0.2	0.73 ± 0.05
Ongeluk's Nek						
O1/97	715 ± 30	4.2	3.4 ± 1.7	1.72 ± 0.07	2.0 ± 0.5	1.72 ± 0.07
O1/97(R)	624 ± 25	4.0	1.2 ± 1.0	1.61 ± 0.07	2.0 ± 0.5	1.61 ± 0.07
O5/97	585 ± 27	4.6	3.4 ± 1.7	1.40 ± 0.07	2.0 ± 0.3	1.40 ± 0.07
O8/97	152 ± 12	7.9	1.0 ± 1.2	0.36 ± 0.03	1.1 ± 0.3	0.36 ± 0.03
O11/97	1940 ± 70	3.6	3.4 ± 1.7	4.23 ± 0.15	0.4 ± 0.1	4.23 ± 0.15
Sani Pass						
1995						
S1/95	450 ± 30	6.7	1.2 ± 1.2	2.46 ± 0.13	3.7 ± 0.6	2.46 ± 0.13
1997						
S3/97	390 ± 20	5.1	3.4 ± 1.7	0.94 ± 0.05	2.3 ± 0.6	0.94 ± 0.05
S5/97	1160 ± 35	3.0	3.4 ± 1.7	2.36 ± 0.07	2.1 ± 0.2	2.36 ± 0.07
S8/97	1330 ± 30	2.3	2.2 ± 1.7	3.15 ± 0.07	3.6 ± 0.2	3.15 ± 0.07
S10/97	527 ± 19	3.6	2.2 ± 1.7	1.27 ± 0.05	2.2 ± 0.6	1.27 ± 0.05
Lesotho Highlands						
L1/97	626 ± 24	3.8	2.2 ± 1.7	1.56 ± 0.06	1.9 ± 0.5	1.56 ± 0.06
L4/97	1350 ± 50	3.7	2.2 ± 1.7	3.17 ± 0.12	1.7 ± 0.2	3.17 ± 0.12
L7/97	410 ± 19	4.6	2.2 ± 1.7	0.95 ± 0.04	0.5 ± 0.1	0.95 ± 0.04
L9/97	396 ± 16	4.0	1.7 ± 1.5	0.94 ± 0.04	1.2 ± 0.1	0.94 ± 0.04
L10/97	1936 ± 63	3.3	1.7 ± 1.5	4.56 ± 0.15	1.9 ± 0.5	4.56 ± 0.15
L11/97	1052 ± 37	3.5	1.7 ± 1.5	2.53 ± 0.09	1.0 ± 0.3	2.53 ± 0.09
L12/97	740 ± 30	4.1	2.2 ± 1.5	2.12 ± 0.09	7.2 ± 0.6	2.12 ± 0.09
L13/97	975 ± 35	3.6	2.2 ± 1.5	2.00 ± 0.07	0.7 ± 0.2	2.00 ± 0.07
L15/97	750 ± 20	2.7	2.2 ± 1.5	1.74 ± 0.05	1.9 ± 0.3	1.74 ± 0.05
L15/97(R)	558 ± 23	4.1	1.2 ± 1.0	1.65 ± 0.07	1.9 ± 0.3	1.65 ± 0.07
L16/97	3245 ± 100	3.1	2.2 ± 1.5	8.90 ± 0.28	19.7 ± 1.1	8.90 ± 0.28
L17/97	2770 ± 30	1.1	2.2 ± 1.5	5.80 ± 0.07	7.2 ± 0.6	5.80 ± 0.07
L17/97(R)	1963 ± 71	3.6	1.2 ± 1.0	5.76 ± 0.21	7.2 ± 0.6	5.76 ± 0.21
L22/97	2290 ± 74	3.2	3.2 ± 1.7	4.87 ± 0.16	1.1 ± 0.3	4.87 ± 0.16
L23/97	889 ± 31	3.5	1.2 ± 1.0	2.30 ± 0.08	2.5 ± 0.2	2.30 ± 0.08
L28/97	275 ± 12	4.4	3.2 ± 1.7	0.60 ± 0.03	1.7 ± 0.3	0.60 ± 0.03

The site-specific spallogenic and muogenic production rates (Table 6.8) were calculated from the measured concentrations of the relevant target nuclei (Table 6.5) and the calibrated production measurements of Stone *et al* (1996a, 1998a) and Evans *et al* (1997), scaled, as appropriate, for altitude, latitude, topographic shielding and the sample thickness. The scaling factors are listed in Table 6.7.

The altitude / latitude scaling factor for spallation induced reactions was derived using the widely accepted form provided by Lal (1991), while that for muogenic reactions was calculated using Equation 2.1. Just prior to submission of this thesis a new scheme was proposed for scaling production rates for altitude and latitude (Dunai, 2000). If this new scheme were to be applied to the results in this study, the overall impact would be to reduce the scaling factors for spallogenic reactions by ~ 5 – 9 %. This would lead to a corresponding reduction in the site-specific ^{36}Cl production rate from spallation of Ca and K (Table 6.8). The overall impact on the calculated denudation rates would be to reduce these systematically by ~ 4 – 7 %. However, as mentioned below, the estimated denudation rates have been calculated assuming a 20 % uncertainty in the production rate, which was specifically included, in part, to account for recognised errors in the Lal (1991) scaling factors (eg Gosse *et al*, 1996). If the scheme proposed by Dunai (2000) becomes widely accepted as the norm, the production rates and, consequently, the denudation rates, can be easily adjusted, however, a systematic reduction of ~ 4 – 7 % would have no significant impact on the overall geomorphic conclusions of this project.

The topographic shielding factor was produced using Equation 2.3. The production rates used in the denudation rate calculation are averaged over the thickness of the sample by multiplying the surface production rate for spallation, spallogenic thermal neutron and epithermal neutron reactions by the sample thickness correction factor (calculated per Appendix 6). Because the samples were ≤ 5 cm thick, the correction factor is < 5 %. No correction was made for muon induced reactions as the production rate is invariant over the depth represented by the sample thickness. Production rates for thermal and epithermal neutron activation were determined from the measured elemental composition of the sample (Table 6.5) with altitude / latitude scaling assuming 90 % of the neutrons are spallogenic in origin and the remainder muogenic.

Table 6.7: Scaling factors applicable to flat-lying samples.

Sample	Altitude / latitude scaling factor		Topographic Shielding Scaling Factor	Sample thickness scaling factor		
	Spallation	Muon induced reactions		Spallation	Thermal Neutrons	Epithermal Neutrons
Naudesnek						
1995						
N1/95	5.8762	2.7555	1.0	0.9559	1.3442	1.0612
N2/95	5.5627	2.6645	1.0	0.9602	1.3164	1.0595
N3/95	5.3185	2.5920	0.9989	0.9645	1.2742	1.0487
1997						
N1/97	5.5611	2.6642	1.0	0.9649	1.3158	1.0593
N2/97	5.5611	2.6642	1.0	0.9521	1.4414	1.0838
N3/97	4.7973	2.4332	0.9874	0.9513	1.4668	1.0846
N4/97	5.3940	2.6147	0.9999	0.9581	1.4083	1.0731
N6/97	5.4568	2.6335	0.9995	0.9572	1.3231	1.0580
N7/97	5.5511	2.6615	1.0	0.9564	1.3147	1.0608
N14/97	5.8223	2.7398	1.0	0.9521	1.4454	1.0747
Ongeluk's Nek						
O1/97	6.3540	2.8989	1.0	0.9581	1.2969	1.0560
O5/97	6.4232	2.9184	1.0	0.9521	1.4511	1.0792
O8/97	5.2141	2.5666	0.9999	0.9675	1.3192	1.0538
O11/97	5.5523	2.6675	0.9997	0.9504	1.4692	1.0935
Sani Pass						
1995						
S1/95	6.2544	2.8685	0.9995	0.9474	1.3835	1.0717
1997						
S3/97	7.7642	3.2836	1.0	0.9539	1.4170	1.0777
S5/97	6.2770	2.8749	0.9999	0.9539	1.3410	1.0597
S8/97	6.3148	2.8856	0.9998	0.9581	1.3347	1.0645
S10/97	7.2334	3.1409	0.9999	0.9539	1.3933	1.0698
Lesotho Highlands						
L1/97	6.9438	3.0671	0.9968	0.9530	1.3570	1.0635
L4/97	6.3680	2.9001	1.0	0.9692	1.2604	1.0492
L7/97	5.7613	2.7253	1.0	0.9504	1.4921	1.0804
L9/97	5.3036	2.5875	0.9992	0.9564	1.4226	1.0757
L10/97	7.8120	3.2939	0.9999	0.9597	1.4088	1.0750
L11/97	7.7853	3.2868	0.9999	0.9623	1.3897	1.0642
L12/97	8.2384	3.4056	1.0	0.9521	1.3513	1.0739
L13/97	8.2384	3.4056	1.0	0.9606	1.3979	1.0716
L15/97	7.2536	3.1429	0.9999	0.9521	1.3327	1.0686
L16/97	7.8497	3.2927	1.0	0.9564	1.3086	1.0665
L17/97	7.8364	3.2892	1.0	0.9521	1.3238	1.0671
L22/97	6.8199	3.0126	0.9988	0.9649	1.3521	1.0643
L23/97	6.3164	2.8916	1.0	0.9521	1.3597	1.0657
L28/97	6.0300	2.7888	0.9972	0.9521	1.4615	1.0838

The site-specific ^{36}Cl production rates for the flat-lying samples are detailed in Table 6.8 and include production from spallation, muon induced reactions and thermal neutron capture reactions involving Ca, K and ^{35}Cl. The production rates for the spallogenic and muogenic reactions involving Ca and K (P_{Ca} and P_K in Table 6.7) were derived from the following calibrated rates: Ca spallation, 48.8 ± 1.7 atoms $g(Ca)^{-1}$ a^{-1} (Stone *et al*, 1996a); muon capture by Ca, 5.3 ± 0.53 atoms $g(Ca)^{-1}$ a^{-1} (Stone *et al*, 1998a); K spallation, 171 ± 15 atoms $g(K)^{-1}$ a^{-1} (Evans *et al*, 1997); and muon capture by K, 9 ± 2 atoms $g(K)^{-1}$ a^{-1} (as assumed by Evans *et al* (1997) – this reaction has still to be independently calibrated). The neutron capture reactions involving ^{35}Cl ($P_{Cl\text{-}35}$) and ^{39}K ($P_{K\text{-}39}$) were calculated using Equations 3.13 (f_{35} and f_{39}), 3.12 ($P_{n,35}$ and $P_{n,39}$), 3.14 ($P_{n,epi}$) with $P_f(0)$ = 586 ± 40 n $(g\ air)^{-1}$ a^{-1} (Phillips *et al*, 1996a). As has already been mentioned (Chapter 2), the production of cosmogenic isotopes is subject to various spatial and temporal influences. To account for these uncertainties in general and specifically for geomagnetic field variations, altitude and latitude scaling uncertainties, calibration uncertainties, etc. (eg Gosse *et al*, 1996) a 20 % uncertainty (1 σ level) was allocated to all production rates. Assuming such uncertainty to be random and independent, this production uncertainty together with uncertainties in target element measurements, were propagated through the production rate calculations by combining errors in quadrature using the standard rules (Taylor, 1997).

The total production rate (P_{TOTAL}) ranges from ~ 17 atoms g^{-1} a^{-1} for N3/97, the lowest elevation site, to > 35 atoms g^{-1} a^{-1} for the highest elevation samples. In all these Cl-poor samples, spallation of Ca and K contribute > 90 % to the total in all but two samples (N2/95 – 84 % and L16/97 – 76 %). Muon induced reactions account for 3 – 5 % of P_{TOTAL}. Reactions involving Ca provide most ^{36}Cl, with the contribution, which is dependent on the chemical composition of the sample, ranging between 55 and 89 %. The production rate from thermal neutron capture by ^{35}Cl is < 2.0 atoms g^{-1} a^{-1} except for N2/95 (2.32 atoms g^{-1} a^{-1}, 14.7 ppm Cl), L16/97 (6.57 atoms g^{-1} a^{-1}, 35.6 ppm Cl) and L17/97 (2.93 atoms g^{-1} a^{-1}, 12.2 ppm Cl). Between 80 – 85 % of the thermal neutrons were captured by the major elements in the sample, with Fe being the major absorber in all samples. The fraction captured by ^{35}Cl (f_{35}) is < 0.1 %, except for the samples with the highest Cl content (N2/95 and L16/97), and < 0.01 % for capture by ^{39}K (f_{39}).

Table 6.8: Site-specific chlorine-36 production rates for flat-lying samples.

Sample	P_{Ca} [α]		P_K [β]		f_{35} [φ]	P_{CL-35} [χ]		f_{39} [ι]	P_{K-39} [δ]	P_{TOTAL} [ε]
	Spallation (atom g^{-1} a^{-1})	Muon (atom g^{-1} a^{-1})	Spallation (atom g^{-1} a^{-1})	Muon (atom g^{-1} a^{-1})		$P_{n,35}$ [γ] (atom g^{-1} a^{-1})	$P_{n,epi}$ [η] (atom g^{-1} a^{-1})		$P_{n,39}$ [φ] (atom g^{-1} a^{-1})	(atom g^{-1} a^{-1})
Naudesnek										
1995										
N1/95	18.04 ± 3.61	1.00 ± 0.20	7.59 ± 1.52	0.10 ± 0.02	0.00093	1.79 ± 0.38	0.20 ± 0.03	0.000079	0.15 ± 0.03	28.87 ± 3.94
N2/95	17.44 ± 3.49	1.01 ± 0.20	2.88 ± 0.58	0.04 ± 0.01	0.00127	2.32 ± 0.48	0.40 ± 0.08	0.000030	0.05 ± 0.01	24.14 ± 3.57
N3/95	19.80 ± 3.96	1.22 ± 0.24	5.60 ± 1.12	0.08 ± 0.02	0.00092	1.51 ± 0.31	0.31 ± 0.06	0.000065	0.11 ± 0.02	28.63 ± 4.14
1997										
N1/97	17.04 ± 3.41	0.98 ± 0.20	3.66 ± 0.74	0.05 ± 0.01	0.00014	0.27 ± 0.08	0.03 ± 0.01	0.000036	0.07 ± 0.01	22.10 ± 3.50
N2/97	16.16 ± 3.23	0.95 ± 0.19	2.78 ± 0.56	0.04 ± 0.01	0.00031	0.66 ± 0.13	0.05 ± 0.01	0.000027	0.06 ± 0.01	20.70 ± 3.29
N3/97	13.71 ± 2.74	0.93 ± 0.19	1.88 ± 0.38	0.03 ± 0.01	0.00033	0.62 ± 0.18	0.04 ± 0.01	0.000022	0.041 ±0.007	17.25 ± 2.78
N4/97	15.94 ± 3.19	0.96 ± 0.20	5.65 ± 1.13	0.08 ± 0.02	0.00027	0.54 ± 0.12	0.034±0.007	0.000059	0.12 ± 0.02	23.32 ± 3.39
N6/97	18.37 ± 3.67	1.10 ± 0.22	6.45 ± 1.29	0.10 ± 0.02	0.00032	0.56 ± 0.17	0.11 ± 0.04	0.000070	0.12 ± 0.03	26.81 ± 3.90
N7/97	18.70 ± 3.74	1.10 ± 0.22	4.90 ± 0.98	0.07 ± 0.01	0.00094	1.61 ± 0.32	0.43 ± 0.09	0.000051	0.09 ± 0.02	26.89 ± 3.89
N14/97	17.52 ± 3.50	0.99 ± 0.20	3.07 ± 0.62	0.04 ± 0.01	0.00010	0.23 ± 0.07	0.015±0.005	0.000031	0.07 ± 0.01	21.93 ± 3.57
Ongeluk's										
Nek										
O1/97	21.53 ± 4.31	1.11 ± 0.22	5.88 ± 1.18	0.07 ± 0.01	0.00030	0.55 ± 0.16	0.16 ± 0.05	0.000054	0.10 ± 0.02	29.41 ± 4.47
O5/97	19.93 ± 3.99	1.01 ± 0.20	2.00 ± 0.41	0.025± 0.005	0.00019	0.47 ± 0.15	0.03 ± 0.01	0.000018	0.04 ± 0.01	23.50 ± 4.01
O8/97	12.69 ± 2.54	0.79 ± 0.16	10.60 ± 2.12	0.16 ± 0.03	0.00024	0.43 ± 0.13	0.03 ± 0.01	0.000121	0.22 ± 0.04	24.92 ± 3.31
O11/97	17.65 ± 3.53	1.03 ± 0.21	7.04 ± 1.41	0.10 ± 0.02	0.00007	0.17 ± 0.05	0.011±0.004	0.000063	0.14 ± 0.03	26.15 ± 3.81
Sani Pass										
1995										
S1/95	18.93 ± 3.79	1.01 ± 0.20	9.68 ± 1.94	0.12 ± 0.02	0.00088	1.85 ± 0.38	0.31 ± 0.06	0.000091	0.19 ± 0.04	32.09 ± 4.27
1997										
S3/97	18.89 ± 3.78	0.80 ± 0.16	12.62 ± 2.53	0.12 ± 0.02	0.00039	1.12 ± 0.33	0.09 ± 0.03	0.000088	0.25 ± 0.05	33.89 ± 4.56
S5/97	21.22 ± 4.24	1.11 ± 0.22	4.93 ± 0.99	0.06 ± 0.01	0.00034	0.67 ± 0.13	0.13 ± 0.03	0.000048	0.10 ± 0.02	28.22 ± 4.37
S8/97	19.21 ± 3.84	0.99 ± 0.20	5.24 ± 1.05	0.06 ± 0.01	0.00063	1.36 ± 0.26	0.19 ± 0.04	0.000046	0.10 ± 0.02	27.16 ± 4.00
S10/97	21.09 ± 4.22	0.95 ± 0.19	6.66 ± 1.34	0.07 ± 0.01	0.00045	1.13 ± 0.36	0.11 ± 0.04	0.000054	0.14 ± 0.03	30.15 ± 4.44

Table 6.8: (cont.).

Sample	P_{Ca} [α]		P_K [β]		f_{35} [ϕ]	P_{CL-35} [χ]		P_{K-39} [δ]		P_{TOTAL} [ε]
	Spallation (atom g^{-1} a^{-1})	Muon (atom g^{-1} a^{-1})	Spallation (atom g^{-1} a^{-1})	Muon (atom g^{-1} a^{-1})		$P_{n,35}$ [γ] (atom g^{-1} a^{-1})	$P_{n,epi}$ [η] (atom g^{-1} a^{-1})	f_{39} [ι]	$P_{n,39}$ [φ] (atom g^{-1} a^{-1})	(atom g^{-1} a^{-1})
Lesotho Highlands										
L1/97	21.38 ± 4.28	1.01 ± 0.20	6.95 ± 1.39	0.08 ± 0.02	0.00023	0.53 ± 0.17	0.09 ± 0.03	0.000060	0.14 ± 0.03	30.17 ± 4.51
L4/97	18.82 ± 3.76	0.96 ± 0.19	12.88 ± 2.58	0.15 ± 0.03	0.00026	0.53 ± 0.12	0.08 ± 0.02	0.000110	0.23 ± 0.05	33.65 ± 4.57
L7/97	16.37 ± 3.27	0.94 ± 0.19	3.65 ± 0.74	0.05 ± 0.01	0.00013	0.27 ± 0.08	0.014±0.004	0.000039	0.08 ± 0.02	21.38 ± 3.36
L9/97	14.87 ± 2.97	0.91 ± 0.18	4.68 ± 0.93	0.07 ± 0.01	0.00026	0.52 ± 0.12	0.033±0.008	0.000049	0.10 ± 0.02	21.18 ± 3.13
L10/97	23.18 ± 4.64	0.95 ± 0.19	10.86 ± 2.17	0.11 ± 0.02	0.00028	0.80 ± 0.26	0.05 ± 0.02	0.000074	0.21 ± 0.05	36.16 ± 5.13
L11/97	26.01 ± 5.20	1.08 ± 0.22	4.47 ± 0.90	0.04 ± 0.01	0.00019	0.52 ± 0.17	0.03 ± 0.01	0.000034	0.09 ± 0.02	32.24 ± 5.29
L12/97	21.60 ± 4.31	0.86 ± 0.17	11.36 ± 2.27	0.11 ± 0.02	0.00065	1.87 ± 0.39	0.34 ± 0.07	0.000067	0.19 ± 0.04	36.32 ± 4.90
L13/97	22.48 ± 4.50	0.88 ± 0.18	6.41 ± 1.29	0.06 ± 0.01	0.00010	0.28 ± 0.09	0.018±0.006	0.000042	0.12 ± 0.03	30.25 ± 4.68
L15/97	23.64 ± 4.73	1.07 ± 0.21	8.34 ± 1.67	0.09 ± 0.02	0.00028	0.63 ± 0.14	0.17 ± 0.04	0.000062	0.14 ± 0.03	34.07 ± 5.02
L16/97	26.35 ± 5.27	1.09 ± 0.22	4.48 ± 0.90	0.04 ± 0.01	0.00273	6.57 ± 1.32	1.89 ± 0.39	0.000029	0.07 ± 0.01	40.49 ± 5.52
L17/97	27.12 ± 5.42	1.13 ± 0.23	5.30 ± 1.06	0.05 ± 0.01	0.00097	2.93 ± 0.59	0.73 ± 0.15	0.000036	0.08 ± 0.02	37.35 ± 5.57
L22/97	18.28 ± 3.66	0.87 ± 0.17	14.95 ± 2.99	0.17 ± 0.03	0.00018	0.43 ± 0.14	0.03 ± 0.01	0.000119	0.29 ± 0.06	35.01 ± 4.73
L23/97	19.01 ± 3.80	0.99 ± 0.20	8.11 ± 1.62	0.10 ± 0.02	0.00055	1.14 ± 0.25	0.20 ± 0.04	0.000077	0.16 ± 0.03	29.71 ± 4.15
L28/97	16.07 ± 3.21	0.87 ± 0.17	4.97 ± 1.00	0.06 ± 0.01	0.00031	0.73 ± 0.19	0.04 ± 0.01	0.000045	0.10 ± 0.02	22.85 ± 3.37

[α] Spallation and muon production from Ca.
[β] Spallation and muon production from K.
[χ] Production from ^{35}Cl.
[δ] Production from ^{39}K.
[ε] Total ^{36}Cl production from Ca, K and ^{35}Cl.
[ϕ] Fraction of stopped neutrons captured by ^{35}Cl.
[γ] Production rate from capture by ^{35}Cl of thermalized neutrons.
η Production rate from capture by ^{35}Cl of epithermal neutrons.
[ι] Fraction of stopped neutrons captured by ^{39}K.
φ Production rate from capture by ^{39}K of thermalized neutrons.

6.4.2 ESTIMATED DENUDATION RATES

Denudation rates for the flat-lying samples were calculated using Equation 3.36. This assumes that the surfaces from which the samples were collected have been exposed for a sufficient period of time for secular equilibrium to have been achieved (Figure 2.5) and that the denudation rate, ε, is in 'steady-state', defined by Nishiizumi *et al* (1991) as meaning the continuous removal of rock of thickness' $< \Lambda_{sp} / \rho$ (assuming $\Lambda_{sp} = 160$ g cm^{-2} and $\rho \approx 2.9$ g cm^{-3} for basalt, this is ~ 0.5 m). The implications for the estimated denudation rates in the event of these assumptions not being fully satisfied by individual samples are considered in Chapter 8.

Table 6.9 lists the estimated denudation rates, assuming 'steady-state' denudation, and an estimate of the minimum period of time over which these rates apply (T_{eff}). The apparent surface exposure age ($T_{eff} = 1 / (\lambda + \rho \varepsilon / \Lambda)$, Lal, 1991), which is the number of years it would take for the measured concentration to be built up in the absence of denudation, provides the minimum timescale over which the modelled rates average denudation. No maximum time period for the rate is imposed by the model. The estimated denudation rates are shown, in relation to the sample's field location, in Figures 6.8 (Naudesnek), 6.9 (Ongeluk's Nek), 6.10 (Sani Pass) and 6.11 (Lesotho Highlands).

All uncertainties are quoted at the 1 σ (68 % confidence) level. Two uncertainties are shown for the estimated denudation rate (Table 6.9). The first uncertainty figure was derived by propagating all analytical errors (including uncertainties in AMS measurements, chemical analyses / measurements, blank, background effects etc.) and assumed random and independent uncertainties in the site-specific production rates (20 %, Table 6.8), decay constant (5 %) and attenuation length (5 %) (eg Bierman *et al*, 1999, Cockburn *et al*, 1999) through the calculations using the standard rules of addition in quadrature (Taylor, 1997). Uncertainties calculated in this way are $\pm$ 15 – 33 % (1 σ level). This estimate of the denudation rate uncertainty was used in the calculation of T_{eff} and will be used in subsequent discussions. For comparison, the second uncertainty figure was derived as above, but ignoring the assumed uncertainties in production, attenuation and decay. Uncertainties calculated in this way reflect the analytical uncertainties only and are $\pm$ 4 – 9 % (1 σ).

Table 6.9: Estimated denudation rates for flat-lying samples.

Sample	Modelled denudation rate, ε ($m\ Ma^{-1}$)	Minimum time period over which denudation rates apply (T_{eff}) (10^3 a)
Naudesnek		
1995		
N1/95	10.4 ± 1.6 (± 0.5)	47.3 ± 6.6
N2/95	1.5 ± 0.4 (± 0.1)	199.1 ± 29.4
N3/95	27.9 ± 4.1 (± 1.7)	18.9 ± 2.7
1997		
N1/97	1.5 ± 0.5 (± 0.1)	199.1 ± 37.1
N2/97	1.2 ± 0.4 (± 0.1)	233.3 ± 37.1
N3/97	17.3 ± 2.9 (± 1.2)	29.7 ± 4.8
N4/97	5.4 ± 1.0 (± 0.3)	82.7 ± 12.7
N6/97	6.7 ± 1.2 (± 0.3)	69.2 ± 10.7
N7/97	24.2 ± 3.6 (± 1.4)	21.7 ± 3.1
N7/97(R)	24.1 ± 3.6 (± 1.4)	21.7 ± 3.1
N14/97	17.8 ± 3.2 (± 1.3)	28.9 ± 4.8
Ongeluk's Nek		
O1/97	9.3 ± 1.6 (± 0.5)	52.2 ± 8.1
O1/97(R)	9.9 ± 1.7 (± 0.6)	49.4 ± 7.7
O5/97	9.2 ± 1.8 (± 0.6)	52.7 ± 9.3
O8/97	43.0 ± 6.6 (± 3.7)	12.5 ± 1.9
O11/97	2.4 ± 0.5 (± 0.2)	150.3 ± 20.9
Sani Pass		
1995		
S1/95	6.9 ± 1.2 (± 0.5)	67.5 ± 4.1
1997		
S3/97	21.5 ± 3.2 (± 1.4)	24.2 ± 3.5
S5/97	6.1 ± 1.1 (± 0.3)	74.9 ± 11.4
S8/97	4.1 ± 0.8 (± 0.2)	102.7 ± 15.6
S10/97	13.9 ± 2.2 (± 0.8)	36.4 ± 5.4
Lesotho Highlands		
L1/97	10.7 ± 1.8 (± 0.6)	46.1 ± 7.1
L4/97	5.1 ± 0.9 (± 0.3)	86.6 ± 12.5
L7/97	12.9 ± 2.2 (± 0.7)	38.9 ± 6.2
L9/97	13.2 ± 2.1 (± 0.7)	38.1 ± 5.7
L10/97	3.5 ± 0.7 (± 0.2)	115.7 ± 17.3
L11/97	6.5 ± 1.3 (± 0.4)	71.0 ± 12.2
L12/97	9.4 ± 1.5 (± 0.5)	51.7 ± 7.4
L13/97	7.8 ± 1.4 (± 0.4)	60.8 ± 9.6
L15/97	10.7 ± 1.8 (± 0.5)	46.1 ± 7.1
L15/97(R)	11.3 ± 1.9 (± 0.6)	43.9 ± 6.8
L16/97	1.7 ± 0.4 (± 0.1)	185.7 ± 25.5
L17/97	2.6 ± 0.6 (± 0.1)	142.5 ± 22.6
L17/97(R)	2.6 ± 0.6 (± 0.2)	142.5 ± 22.6
L22/97	3.0 ± 0.6 (± 0.2)	129.2 ± 18.5
L23/97	6.8 ± 1.1 (± 0.4)	68.4 ± 9.5
L28/97	23.4 ± 3.6 (± 1.3)	22.4 ± 3.3

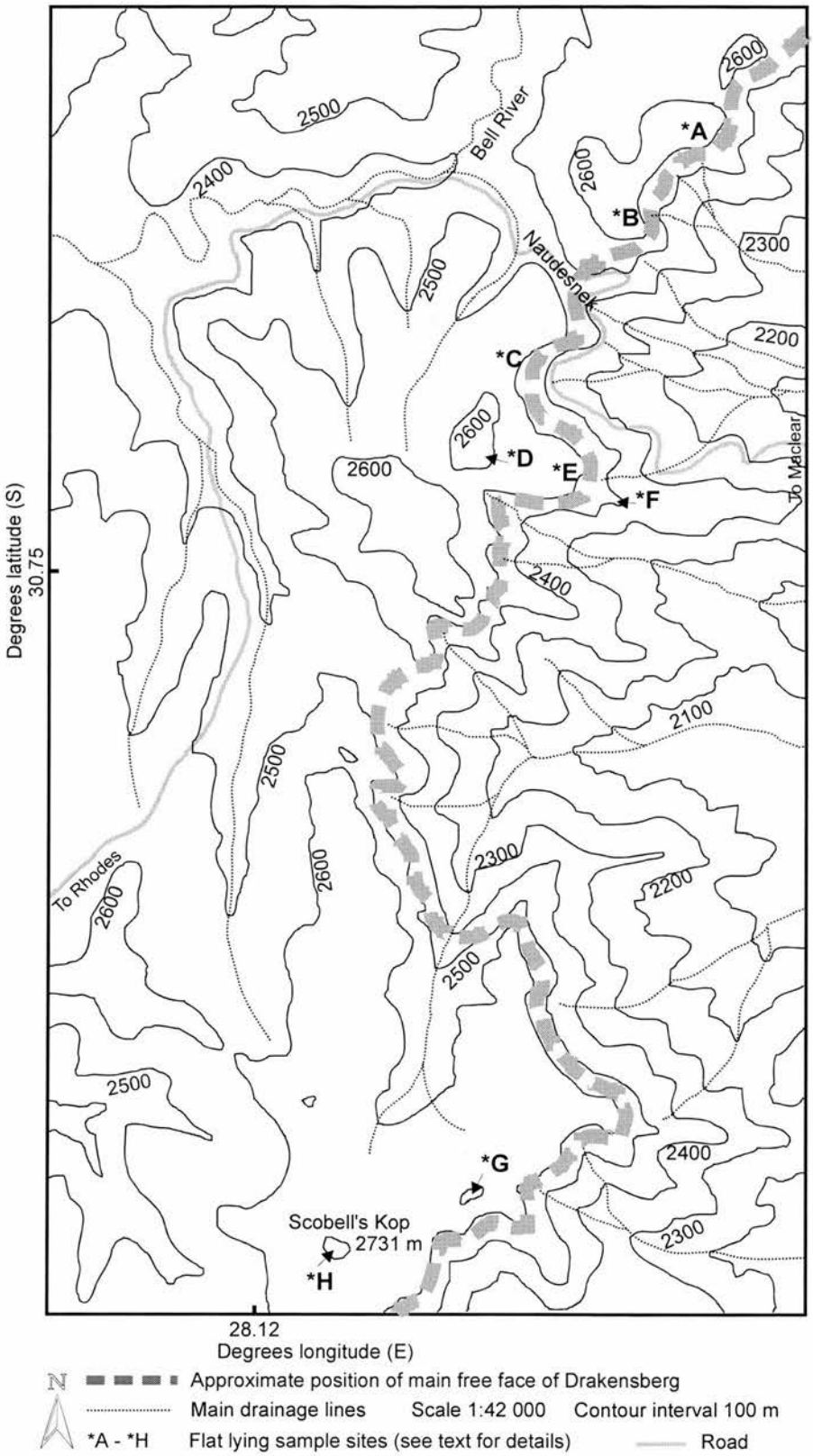

Site / Sample	Denudation rate (m Ma^{-1})
A	
N7/97	24.2 +/- 3.6
N7/97(R)	24.1 +/- 3.6
B	
N6/97	6.7 +/- 1.2
C	
N4/97	5.4 +/- 1.0
D	
N2/95	1.5 +/- 0.4
N1/97	1.5 +/- 0.5
N2/97	1.2 +/- 0.4
E	
N3/95	27.9 +/- 4.1
F	
N3/97	17.3 +/- 2.9
G	
N14/97	17.8 +/- 3.2
H	
N1/95	10.4 +/- 1.6

Figure 6.8: Map of the escarpment at Naudesnek showing the flat lying sample locations and the relevant 'steady-state' model derived denudation rate (in m Ma^{-1}). Based on Figure 6.3.

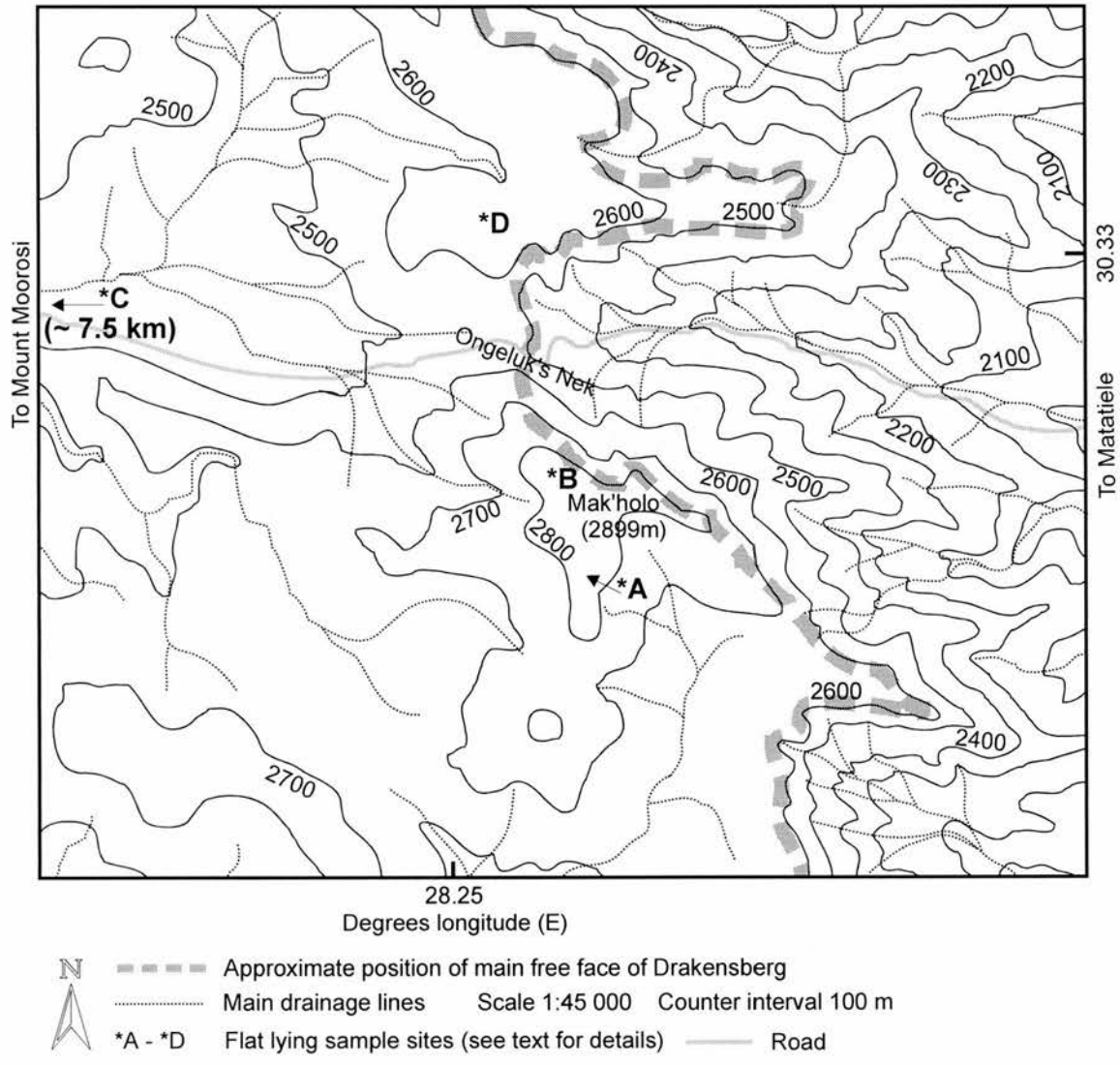

Site	Sample	Denudation rate (m Ma^{-1})
A	O1/97	9.3 +/- 1.6
	O1/97(R)	9.9 +/- 1.7
B	O5/97	9.2 +/- 1.8
C	O8/97	43.0 +/- 6.6
D	O11/97	2.4 +/- 0.5

Figure 6.9: Map of the escarpment at Ongeluk's Nek showing the location of the flat lying sample sites and the relevant 'steady-state' model derived denudation rate (in m Ma^{-1}). Based on Figure 6.4.

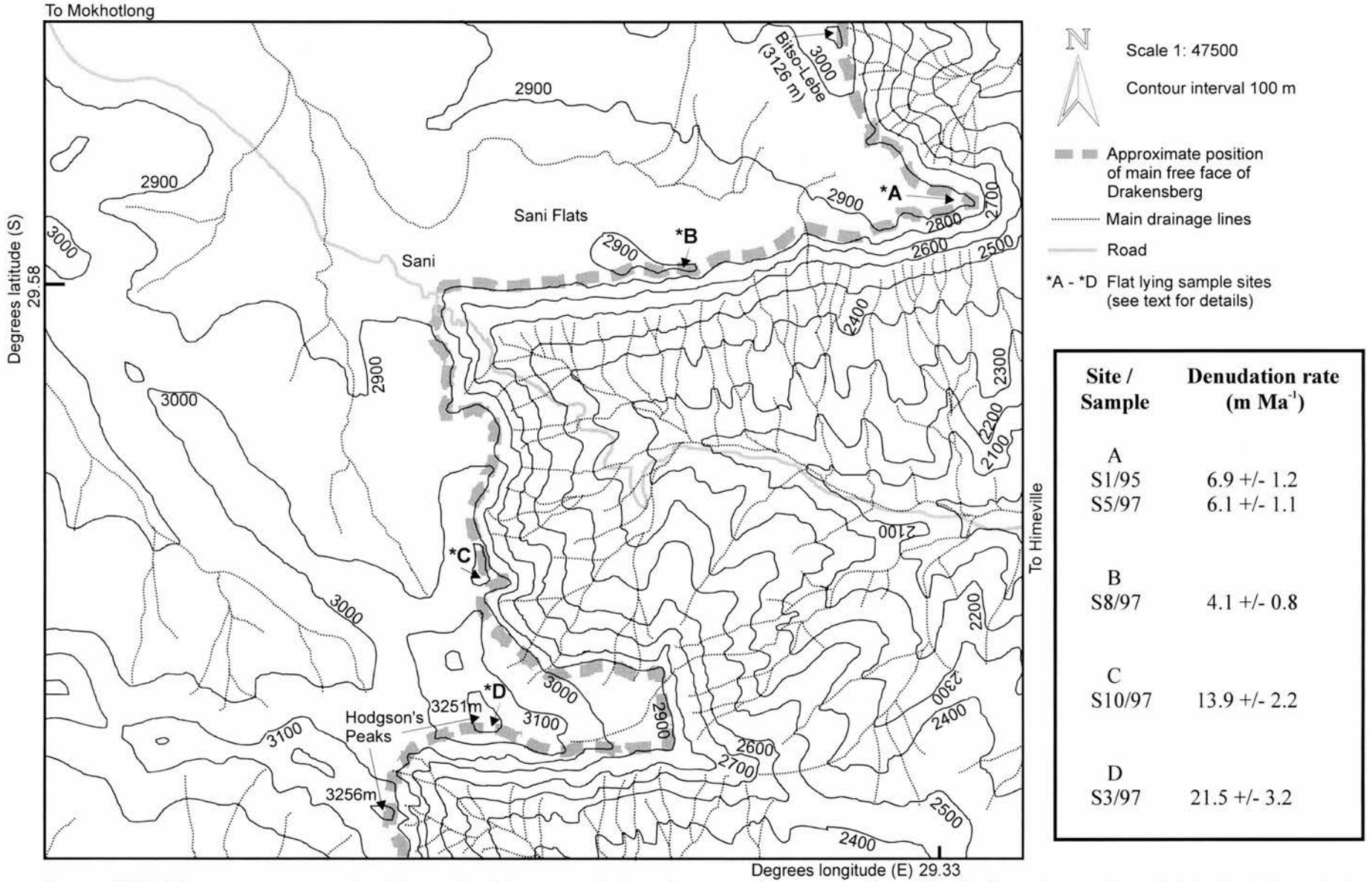

Site / Sample	Denudation rate (m Ma^{-1})
A	
S1/95	6.9 +/- 1.2
S5/97	6.1 +/- 1.1
B	
S8/97	4.1 +/- 0.8
C	
S10/97	13.9 +/- 2.2
D	
S3/97	21.5 +/- 3.2

Figure 6.10: The escarpment at Sani Pass. Flat lying sample locations are shown together with the 'steady-state' model derived denudation rates (in m Ma^{-1}). Based on Figure 6.6.

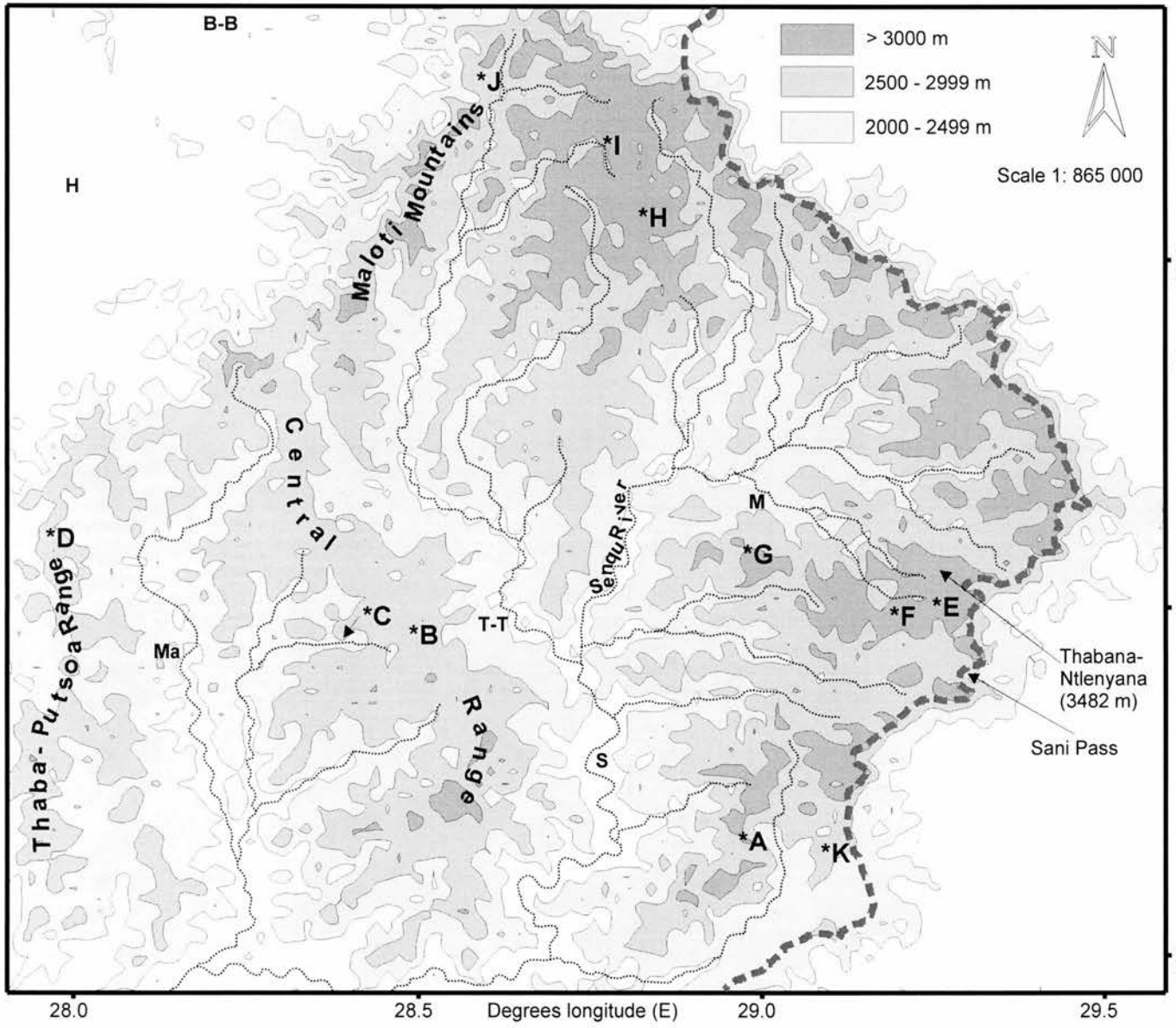

Approximate position of Drakensberg
Main Rivers
*A - *K Flat lying sample sites (see text for details)

Towns:
B-B Butha-Buthe
H Hlotse
Ma Marakabei
M Mokhotlong
T-T Thaba-Tseka
S Sehonghong

Site	Sample	Denudation rate (m Ma^{-1})
A	L1/97	10.7 +/- 1.8
B	L4/97	5.1 +/- 0.9
C	L7/97	12.9 +/- 2.2
D	L9/97	13.2 +/- 2.1
E	L10/97	3.5 +/- 0.7
	L11/97	6.5 +/- 1.3
F	L12/97	9.4 +/- 1.5
	L13/97	7.8 +/- 1.4
G	L15/97	10.7 +/- 1.8
	L15/97(R)	11.3 +/- 1.9
H	L16/97	1.7 +/- 0.4
	L17/97	2.6 +/- 0.6
	L17/97(R)	2.6 +/- 0.6
I	L22/97	3.0 +/- 0.6
J	L28/97	23.4 +/- 3.6
K	L23/97	6.8 +/- 1.1

Figure 6.11: Map of the Lesotho Highlands showing the flat lying sample locations and 'steady-state' model derived denudation rates (in m Ma^{-1}). Based on Figure 6.7.

Modelled denudation rates from flat-lying sites vary between 1.2 ± 0.4 m Ma^{-1} and 43.0 ± 6.6 m Ma^{-1} over timescales, respectively, of ~ 230 ka and ~ 13 ka (Table 6.9). The reproducibility of the modelled denudation rates was tested using four samples chosen at random, which had both principals and replicates prepared – N7/97, O1/97, L15/97 and L17/97. In all cases modelled denudation rates accord very well being within the measurement uncertainty (even if calculated ignoring the assumed uncertainties in production rates, λ and Λ) and with the difference between principal and replicate varying between 1 – 8 %. This is similar to other data sets (eg Ivy-Ochs (1996) 4 – 8 %; Cockburn (1998) 3 – 20 %). Further confirmation of the reliability of the laboratory procedures is provided by the similarity in modelled denudation rates of samples from the same surface, one of which was processed at ANU and the other at Edinburgh. This is the case with samples N2/95 and N1/97 both collected within a 20 m radius on the same summit surface. N2/95 was prepared at ANU, while N1/97 was prepared in Edinburgh. Both samples yield identical denudation rate estimates. Sample N2/97 was also collected from this surface and the modelled denudation rate is ~ 20 % less than that for N2/95 and N1/97 which may, in part, be due to local site variability.

Samples collected from the same surface produce similar denudation rate estimates. The three samples from Naudesnek (N2/95, N1/97 and N2/97, location D, Figure 6.8) were collected along a ~ 40 m transect on the summit of a flat topped knoll. All record a consistently low rate of ~ 1.2 – 1.5 ± 0.5 m Ma^{-1}. Samples O1/97 and O5/97 were collected several hundred metres apart on the flat summit of Mak'holo at Ongeluk's Nek (Figure 6.9) and yield similar estimates of denudation of ~ 9.2 ± 1.8 m Ma^{-1}. At Sani Pass, three samples were collected from the Twelve Apostles, S1/95 and S5/97 being taken from the eastern end and S8/97 being from ~ 2.5 km west of this, but still very much on the Sani Flats (Figure 6.10). Again the three results are relatively consistent (~ 4.1 ± 0.8 – 6.9 ± 1.2 m Ma^{-1}), particularly when the distance between the sites and the differences in elevation (~ 16 m) is taken into account.

In the Lesotho Highlands, multiple samples were collected from three surfaces. Samples L10/97 and L11/97 (E, Figure 6.11) were collected ~ 150 m apart and from distinctly different levels (L11/97 ~ 4 m lower) on the same surface. The estimated rates, 3.5 ± 0.7 m Ma^{-1} and 6.5 ± 1.3 m Ma^{-1} respectively, although outwith the calculated uncertainty, are within the same order of magnitude. On the summit of Kotisephola (F, Figure 6.11), two samples, L12/97 and L13/97, were collected from two small hummocks, both ~ 1 m higher

than the same surface. Calculated denudation rates here are 7.8 ± 1.4 m Ma^{-1} and 9.4 ± 1.5 m Ma^{-1}, respectively, which are within the 68 % confidence level uncertainty. Two samples collected from the summit of Maphisoaneng (H, Figure 6.11), L16/97 and L17/97, are, again from two distinct levels. L16/97 is from the eastern level which is ~ 3m higher than the surface from which L17/97 was collected. The estimated denudation rates are, respectively, 1.7 ± 0.4 m Ma^{-1} and 2.6 ± 0.6 m Ma^{-1}, which are only just within the 1 σ level uncertainty.

Apart from the relative, internal, consistency of rates from samples taken from the same surface, the estimated denudation rates vary quite considerably, even between sample sites which are, morphologically, quite similar. At Naudesnek (Figure 6.8), escarpment summit denudation rates range from 1.2 ± 0.4 m Ma^{-1} to 24.2 ± 3.6 m Ma^{-1}. Samples N4/97, N6/97, N7/97, and N14/97 were all collected from similar summits located on the edge of the escarpment yet estimated rates vary from 5.4 ± 1.0 m Ma^{-1} to 24.2 ± 3.6 m Ma^{-1}. Site D (Figure 6.8), which provided the three samples N2/95, N1/97 and N2/97, and the site from which N1/95 was collected are similar flat topped knolls located ~ 0.5 km inland of the scarp. Although these sites are ~ 5.5 km apart, their similar settings and elevations (2644 m and 2731 m, respectively) suggest that similar denudation rates would be expected yet the rates are ~ 1.2 – 1.5 ± 0.5 m Ma^{-1} and 10.4 ± 1.6 m Ma^{-1} respectively.

Similar variations occur in the escarpment summit denudation rates for Ongeluk's Nek and Sani Pass. The Mak'holo summit at the former is downwearing at an estimated rate of ~ 9.3 ± 1.8 m Ma^{-1}, while the summit on the northern side of the pass, which is ~ 200 m lower in elevation, is denuding a lower rate of 2.4 ± 0.5 m Ma^{-1} (Figure 6.9). At Sani Pass, while the Sani Flats are downwearing at ~ 4.1 ± 0.8 – 6.9 ± 1.2 m Ma^{-1}, the northern summit of Hodgson's Peaks, ~ 350 m higher, is denuding at an estimated rate of 21.5 ± 3.2 m Ma^{-1}. Another summit on the escarpment edge at Sani, ~ 120 m lower than Hodgson's Peaks, yielded a rate of 13.9 ± 2.2 m Ma^{-1} (S8/97) (Figure 6.10).

The estimated denudation rates for the two samples from the buttress ridge at Naudesnek (Figure 6.8), N3/95 and N3/97, vary between 27.9 ± 4.1 m Ma^{-1} and 17.3 ± 2.9 m Ma^{-1}, respectively. Although it was expected that higher rates would be found on the buttress ridge, these rates are similar to the highest estimated denudation rates for the escarpment summits.

The calculated 'steady-state' denudation rates for samples collected in the Lesotho Highlands yield similar variations (Figure 6.11). Although the results from the lower relief

summits vary between 1.7 ± 0.4 m Ma^{-1} (L16/97) and 9.4 ± 1.5 m Ma^{-1} (L12/97), this variation is less than might be expected, particularly given the large distances between these sample sites (up to 70 km – Figure 6.11). Samples from flat topped knolls which form the summits at the head of valleys within the Lesotho Highlands (L1/97, L15/97, L23/97 and L28/97 – Figure 6.11) produce estimated denudation rates ranging from 6.8 ± 1.1 m Ma^{-1} to 23.4 ± 3.6 m Ma^{-1}. Samples from flat-lying areas above river valleys in the Lesotho Highlands (L7/97, L9/97, L22/97 and O8/97, the sample from ~ 7.5 km inland of Ongeluk's Nek – Figures 6.9 and 6.11) yield downwearing rates of 3.0 ± 0.6 m Ma^{-1} to 43.0 ± 6.6 m Ma^{-1} (the highest downwearing rate produced in this study). Given that these valley head and valley side sample sites can be regarded as morphologically similar to the escarpment summit sites (small flat summits adjacent to areas of high local relief), it is interesting that their estimated denudation rates fall into a generally similar range (particularly if O8/97 is ignored) to the downwearing rates estimated for the escarpment summits.

The possible causes of these variations and the implications of the variability in the estimated denudation rates are discussed in Section 8.3. The implications of the denudation rates for our understanding of the development of the southern Drakensberg and Lesotho Highlands' landscapes are discussed in Chapter 8.

CHAPTER 7: RESULTS II: *IN SITU*-PRODUCED CHLORINE-36 DERIVED DENUDATION RATES FOR FREE FACE SITES

7.1 INTRODUCTION

The field and analytical data, together with the modelled ^{36}Cl derived denudation rates, for samples collected from free face sites are reported in this chapter. A total of 44 samples were prepared and analysed, 29 from the three sites on the southern Drakensberg (Naudesnek, Ongeluk's Nek and Sani Pass) and fifteen from the Lesotho Highlands. One sample each from Naudesnek (N4/95) and Sani Pass (S2/95) were collected during the 1995 field season and the results from these, plus four flat-lying results, were reported in Fleming *et al* (1999) (Appendix 9). The remaining samples were collected in late 1997. The first two sections of this chapter provide details of the sampling sites in the southern Drakensberg and Lesotho Highlands while the third reports the analytical data and resulting estimated denudation / backwearing rates.

7.2 SOUTHERN DRAKENSBERG SITES

A detailed description of the morphology and geology of the southern Drakensberg is provided in the preceding chapter. Sampling from free face sites was concentrated in the same areas as used for the flat-lying samples, namely Naudesnek, Ongeluk's Nek and Sani Pass. The rationale for sampling from free faces was that this would yield an estimate of the retreat rate for the escarpment at each site, which, when considered collectively would provide an empirical estimate of the backwearing rate for the southern Drakensberg. In addition estimated rates from these samples can be compared with the results from the flat-lying sites to assess quantitatively the relative importance of downwearing and backwearing in this part of southeast Africa. At each site samples were collected from exposed intact bedrock on the most representative free faces. As before, surfaces were chosen which appeared to have a simple exposure history and to have been subject to prolonged denudation, uninterrupted by temporary burial by soil, snow or falling debris. To reduce the possibility of past cover by talus or snow, samples were taken from ~ 2 m up from the base of the free face exposure. To limit the possibility of *in situ*-produced ^{36}Cl in the free samples being attributable to the deep penetration of cosmic radiation, particularly muons, via the top of the free face, samples were only collected from cliffs that were > ~ 10 m high.

7.2.1 NAUDESNEK

Chapter 6 provides a general description of the morphology of Naudesnek. Twelve samples were collected from nine free face sites in this area (A - I in Figure 7.1). Sample N4/95 was taken from site E in late 1995 while the rest were collected during the 1997 field season. Sites A - E were chosen as representing the main free face of the escarpment and results from the eight samples from these sites will constrain the retreat rate at Naudesnek. Sites G and H are from free faces within the small eastward draining basin which lies inland of the scarp. Sites F and I are from free faces on the westward side of the Drakensberg. These four sites were chosen to provide a comparison between retreat rates for the main free face of the escarpment and those from non-escarpment settings. Samples of ~ 0.05 – 0.1 m were taken from intact exposed bedrock free faces at each site. Field data, as described in Chapter 4, was recorded at the site and is summarised in Table 7.1.

Sample N4/95 is from the free face of the escarpment which, at this site (E in Figure 7.1), is flanked by a narrow buttress ridge. The free face is split by a narrow (2 –3 m wide) gully which provides access from the summit to the buttress ridge. This sample is from the northern section of the free face, ~ 5 m from the gully. The free face has a dip of ~ 82 ° and is ~ 12 m high. The face is irregular due to the preferential weathering of joints, some of which now support vegetation. Denudation appears to be accomplished by a combination of granular disintegration, spalling of thin (< 0.2 m) sheets and the loss of small blocks < 0.5 m thick (Plate 29). The talus slope was well vegetated and lacked loose boulders suggesting either that block fall is relatively uncommon or any blocks coming from the free face are transported downslope rapidly or, alternatively, that such blocks breakdown by granular disintegration / exfoliation of thin sheets, relatively quickly on the talus slope.

Figure 7.1 (overleaf). Map of the southern Drakensberg at Naudesnek showing the position of the nine sites (A-I) from which samples were collected from free face exposure. For details of the sample sites see text.

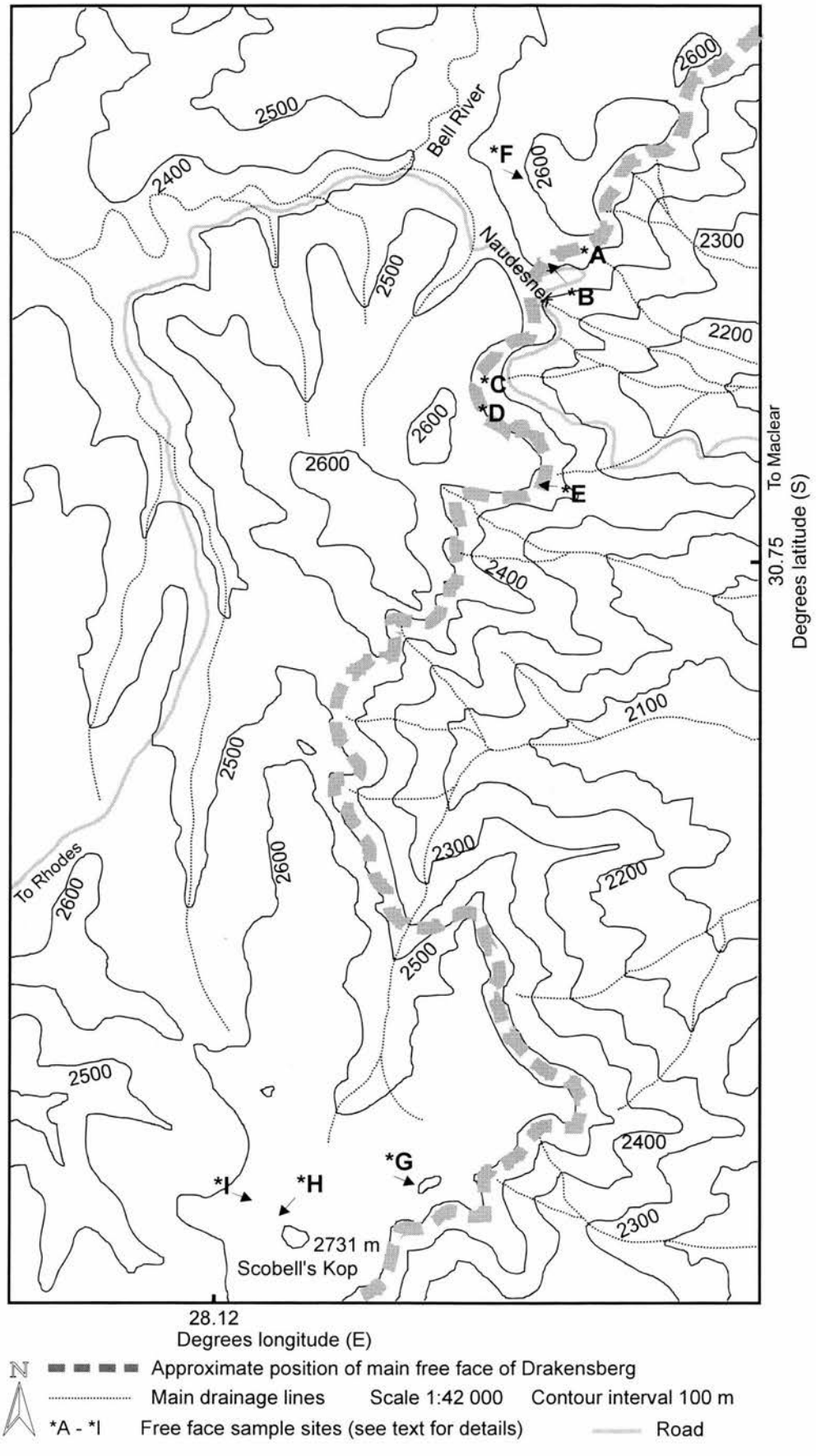
2600
2500
Bell River
*F
2400
2600
2300
Naudesnek
*A
2500
*B
2200
*C
*D
2600
2600
*E
To Maclear
30.75
Degrees latitude (S)
2400
2100
2500
2600
2300
2200
To Rhodes
2600
2500
2500
2400
*G
*I
*H
2731 m
Scobell's Kop
2300
28.12
Degrees longitude (E)
N
Approximate position of main free face of Drakensberg
Main drainage lines
Scale 1:42 000
Contour interval 100 m
*A - *I
Free face sample sites (see text for details)
Road

Table 7.1: Field and location data for free face samples collected at Naudesnek.

Sample	Latitude (d m s) S	Longitude (d m s) E	Altitude (m asl)	Site in Figure 7.1	Surface slope (°)	Thickness (g cm^{-2})	Aspect
1995							
N4/95	30 44 40	28 08 09	2550	E	82	11.6	E
1997							
N5/97	30 43 55	28 08 10	2506	B	88	13.05	SE
N8/97	30 44 21	28 08 01	2582	D	85	14.5	NE
N9/97	30 44 21	28 07 59	2582	D	84	11.6	NE
N10/97	30 44 20	28 07 59	2579	C	85	13.05	S
N11/97	30 44 20	28 08 01	2573	C	85	11.6	SE
N12/97	30 43 53	28 08 42	2529	A	85	14.5	E
N13/97	30 43 53	28 08 41	2520	A	85	14.5	SE
N15/97	30 47 19	28 07 40	2642	G	65	14.5	W
N16/97	30 47 18	28 07 16	2651	H	70	13.05	NE
N17/97	30 47 18	28 07 05	2643	I	80	13.05	NW
N18/97	30 43 35	28 08 02	2480	F	82	10.15	SW

N5/97, N12/97 and N13/97 were all collected from the main free face of the escarpment on the northern side of the pass (A and B in Figure 7.1). This free face becomes lower in height towards the summit of the pass, eventually disappearing ~ 150 m north of the summit. N5/97 is from site B, which is at the western end, ~ 50 m from the point where the free face disappears. The face is ~ 20 m high with a dip of 88 °. N12/97 is from the easternmost part of this free face at the point where the free face starts to run north (A in Figure 7.1; Plate 30). At this site the free face has three distinct steps, N12/97 being from the topmost free face. N13/97 is also from site A, but is ~ 20 m west of sample N12/97 (Plate 30). The talus slope below this free face is ~ 20 – 30 ° and, again, is well vegetated. Some boulders < 0.5 m thick were noted lying on the talus slope (Plate 31) and the denudational processes appear similar to those at noted previously.

N8/97, N9/97, N10/97 N11/97 and N4/95 are from part of the main free face on the southern side of the pass. The free face here is discontinuous, being split by a series of grassed gullies which vary in width from a few to several tens of metres. Sites C (N8/97 and N9/97) and D (N10/97 and N11/97) in Figure 7.1 are split by one such grassed gully which is ~ 10 – 50 m wide (Plate 32). Samples N8/97 and N9/97 were collected from the free face on the southern side of the gully (D in Figure 7.1), N8/97 being ~ 50 m from the gully, while N9/97 is about 10 m closer to the gully. This face is oriented southeast – northwest and is ~ 15 – 20 m high with a dip of ~ 85 °. The talus slope is ~ 25 – 30 °, well vegetated and has a few loose boulders which are < 0.5 m thick (Plate 32). Between the points where the samples were collected was an area where a block ~ 2 – 3 m long and ~ 0.5 m thick has fallen from the face (Plate 32). The face is irregular with joint spacing of ~ 0.3 – 0.5 m noted. Denudational process appear to vary between granular disintegration, exfoliation of thin (< 0.05 m) sheets and the loss of blocks ~ 0.3 – 0.5 m thick.

N10/97 and N11/97 are from the northern side of the gully in Plate 32 (C in Figure 7.1). Sample N10/97 is from the side of the free face which forms the north side of the gully. This part of the face is oriented west – east and slopes at ~ 85 °. The sample was collected from ~ 3 m up from the grassed slope and there was a further 12 m of cliff face above. N11/97 was collected from the east face of this outcrop, ~ 10 m from N10/97. The talus slope at site C is ~ 25 – 30 ° and lacks loose boulders. The face is similar to that at site D with similar denudational processes operating.

N4/95 is from site E (Figure 7.1), a continuation of the main free face on the southern side of Naudesnek. This section of free face forms the side of a step on the buttress ridge from which flat-lying samples N3/95 and N3/97 were collected. Again the free face is split by a series of less steep and grassed gullies. The sampled face slopes at 82 ° and is oriented north – south. Beneath the face the talus slope was well vegetated and lacked loose boulders. The face is irregular and joint spacing is ~ 0.3 – 0.5 m. The face appears to be denuding by a combination of the loss of individual boulders, granular disintegration and exfoliation of thin < 0.1 m sheets.

N15/97 and N16/97 were collected from two free faces which form part of the valley sides of the small drainage basin inland of the escarpment at Scobell's Kop (G and H respectively in Figure 7.1). N15/97 is from a free face which extends for ~ 75 m on the eastern side of this basin (Plate 33). N16/97 is from a ~ 100 m long free face on the western side of the basin (H in Figure 7.1). Both faces vary in height between ~ 5 – 12 m and dip at ~ 65 – 70 °. The slope below these free face is ~ 5 – 10 ° and is well-grassed. Several boulders < 0.5 m thick were found on this surface. Both faces were more irregular than that encountered on the main escarpment, although the joint spacing is similarly ~ 0.3 – 0.5 m (Plate 34).

Samples N17/97 and N18/97 are from two of several free faces which exist on the inland side of the escarpment. N17/97 (I in Figure 7.1) was taken from a free face on the inland (Orange River tributary) side of Scobell's Kop (Plate 35). The face is ~ 1 km inland of the main escarpment face, extends for several hundred metres and is ~ 20 m high with a dip of ~ 80 °. The well-grassed ground below the free face slopes at ~ 5 – 10 ° and several boulders ~ 0.5 m thick were present on this. The face is again being denuded by a combination of the loss of individual boulders, exfoliation of thin sheets and granular disintegration.

Sample N18/97 is from a free face located ~ 600 m inland of the escarpment (F in Figure 7.1). This face is on the north side of a tributary of the Bell River, ~ 60 m above the channel. The face is ~ 150 m long, oriented west – east, and is ~ 15 – 20 m high with a dip of ~ 82 °. The talus slope is again well vegetated and slopes at ~ 20 – 25 °. Some < 0.5 m thick boulders were noted on this slope. The face is similar in appearance to those on the main escarpment with joint spacing of ~ 0.5 m (Plate 36). Again denudation appears to involves a combination of granular disintegration, exfoliation of thin (< 0.1 m) sheets and blocks of ~ 0.5 m thick (Plate 36).

7.2.2 ONGELUK'S NEK

A general description of the morphology and geology of the southern Drakensberg at Ongeluk's Nek is provided in Chapter 6. During the 1997 field season eight samples were collected from eight free face sites at Ongeluk's Nek (A - H in Figure 7.2). Sites B, C, F and G were chosen to represent the main free face of the escarpment at Ongeluk's Nek. The remaining sites are from free face sites inland of the escarpment. The field data for these samples are summarised in Table 7.2.

Table 7.2: Field and location data for free face samples collected at Ongeluk's Nek.

Sample	Latitude (d m s) S	Longitude (d m s) E	Altitude (m asl)	Site in Figure 7.2	Surface slope (°)	Thickness (g cm^{-2})	Aspect
O2/97	30 20 46	28 15 22	2840	A	70	14.5	SE
O3/97	30 20 43	28 15 21	2840	B	85	13.05	N
O4/97	30 20 50	28 15 56	2764	C	88	11.6	E
O6/97	30 20 44	28 15 16	2852	D	85	14.5	W
O7/97	30 18 48	28 08 15	2533	E	84	14.5	N
O9/97	30 20 03	28 15 12	2635	F	85	14.5	SE
O10/97	30 19 55	28 15 24	2620	G	88	14.5	S
O12/97	30 19 50	28 15 18	2631	H	86	13.05	W

Sample O2/97 is from the eastern face of the knoll which forms the summit of Mak'holo (A in Figure 7.2). This free face is ~ 150 m inland of the escarpment and is separated from the main escarpment face by a small (~ 2 km^2) inland draining basin. The face is ~ 12 m high and dips at ~ 70 °. The face is irregular due to the preferential weathering of joints which have a spacing of ~ 0.3 – 0.5 m. Denudation appears to be accomplished by a combination of granular disintegration, spalling of thin (< 0.1 m) sheets and the loss of blocks < 0.5 m thick. The talus slope (~ 15 °) is well vegetated with a few loose boulders < 0.5 m thick.

Samples O3/97 and O4/97 were collected from two sites on the main escarpment free face on the southern side of Ongeluk's Nek (B and C respectively in Figure 7.2; Plate 37). O3/97 is from the northern side of the knoll that forms the summit of Mak'holo, and here the free face is ~ 15 m high and dips at ~ 85°. In front of the face is a narrow grassed ledge which slopes at ~ 25 ° for ~ 3 m before continuing at ~ 85 ° for several ten's of metres. O4/97 was taken

from another free face ~ 1 km east of site B. This face (~ 11 m high) forms the topmost section of the main escarpment free face, from which it is separated by a ~ 3 m wide, 20° dip, rock ledge (Plate 38). Denudational processes appear similar to those noted previously.

Samples O9/97 and O10/97 are from two sites on the northern side of Ongeluk's Nek (F and G respectively in Figure 7.2). The main free face on the northern side of Ongeluk's Nek is discontinuous, being broken up by a series of wide (50 – 150 m) grassed gullies. O9/97 is from the main escarpment free face which forms the westernmost part of the embayment at Ongeluk's Nek (Plate 39). This face is ~ 15 – 20 m high, ~ 250 m long, and highly irregular due to preferential weathering of joints, some of which have been opened to form gullies ~ 1 – 1.5 m deep. The talus slope (~ 15 °) is, again, well vegetated with some loose ~ 0.5 m thick boulders. Sample O10/97 was collected from another free face ~ 200 m east of site F. The free face at site G is much smaller than that at site F, being only ~ 40 m in length and ~ 11 m high. It forms the topmost of a series of stepped faces which occur on the northern side of the embayment (Plate 39). Denudation at both these sites appears to be due, again, to a combination of spalling of sheets, granular disintegration and loss of blocks ~ 0.5 m thick (Plate 40).

Inland of the escarpment, samples O6/97 and O12/97 were collected from western facing free faces (D and H, respectively, in Figure 7.2). O6/97 is from the western face of the knoll that forms the summit of Mak'holo. This face is between 0.1 and 1 km inland of the escarpment, extends for a few hundred metres and is ~ 10 – 15 m high with a dip of ~ 85 ° (Plate 41). In front of the face the ground slopes ~ 5 – 10 ° and is well-grassed with a few < 0.5 m thick boulders. Again the joints have been preferentially weathered and denudation appears to be accomplished by a combination of the processes mentioned previously. O12/97 was taken from the inland face of the knoll which forms the summit on the northern side of Ongeluk's Nek (H in Figure 7.2). This face is ~ 1 km inland and is orientated roughly north / south. The face is ~ 20 m high with a dip of ~ 86 ° (Plate 42). On the gently sloping (~ 5 °), well-grassed, talus slope several boulders ~ 0.5 – 1 m thick were noted.

Sample O7/97 is from a free face at Maphooaneng Pass, ~ 7.5 km west of Ongeluk's Nek (E, Figure 7.2). This free face extends for a few hundred metres on the southern side of the pass and is ~ 10 – 15 m high with a dip of ~ 84 ° (Plate 43). This sample is from the western end of the face which appears to be denuding by the loss of ~ 0.5 m blocks, granular disintegration and sheeting. The talus slope (~ 15 – 20 °) is a mix of vegetation, bare soil and loose boulders ~ 0.5 m thick.

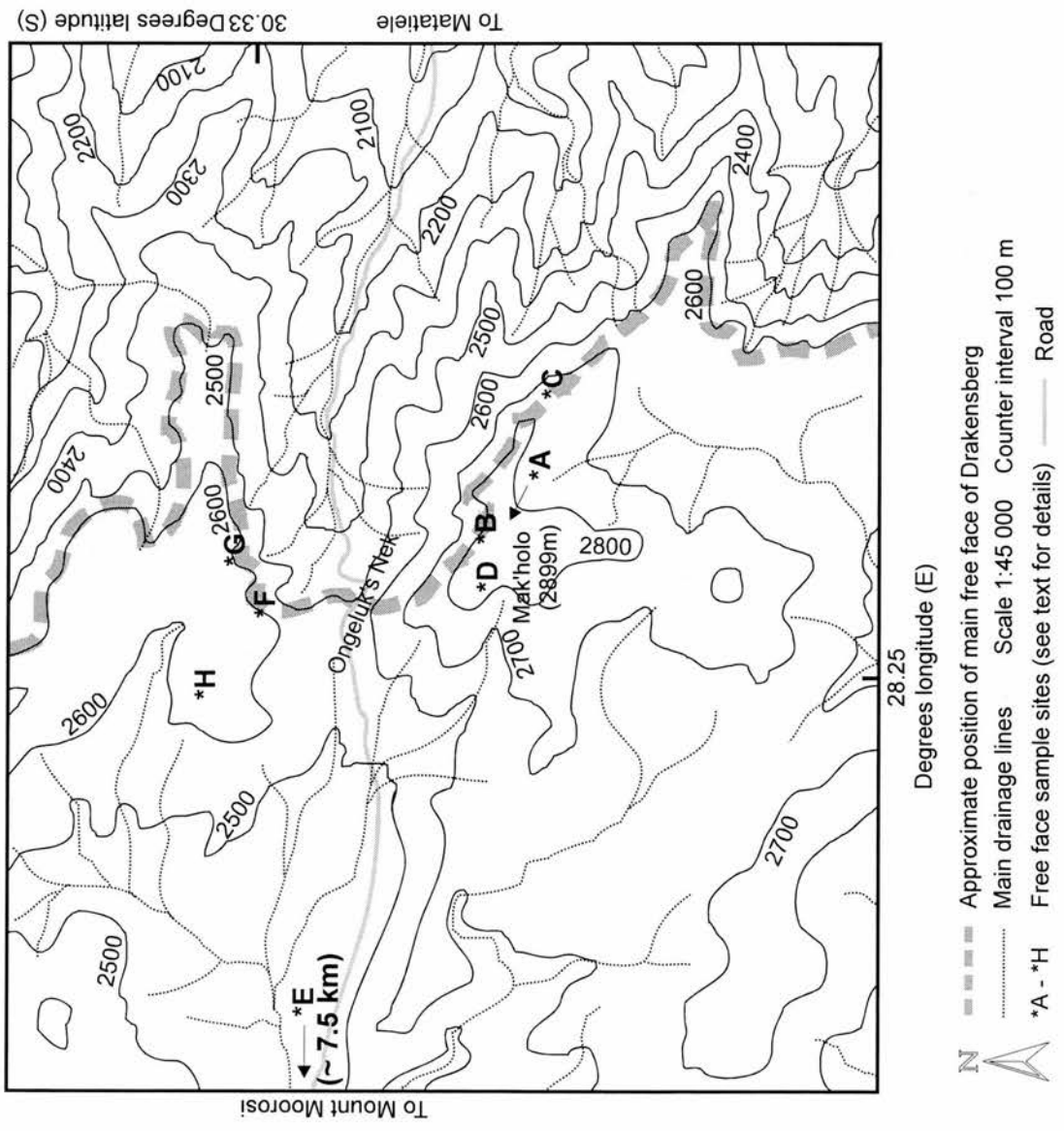

Figure 7.2: Map of the southern Drakensberg at Ongeluk's Nek. The 8 free face sites (A - H) from which the samples were collected are shown. Site E is ~ 7.5 km inland of the escarpment at Maphooaneng Pass and is not shown. For details of the sample sites see text.

7.2.3 SANI PASS

A general description of the morphology and geology of the Drakensberg at Sani Pass can be found in Chapter 6. Nine samples were collected from six free face sites at Sani Pass (A - F, Figure 7.3). Sample S2/95 was collected during the 1995 field season and the remainder were collected in late 1997. Sites A- D are on the main escarpment free face, while sites E and F are from free faces inland of the escarpment. The field and location data for the samples collected at Sani Pass are summarised in Table 7.3.

Table 7.3: Location and field data for free face samples collected at Sani Pass.

Sample	Latitude (d m s) S	Longitude (d m s) E	Altitude (m asl)	Site in Figure 7.3	Surface slope (°)	Thickness (g cm^{-2})	Aspect
1995							
S2/95	29 34 30	29 19 55	2824	A	76	10.2	NE
1997							
S1/97	29 35 18	29 17 20	2900	D	85	13.05	NE
S2/97	29 35 20	29 17 23	2900	D	88	14.5	E
S4/97	29 36 56	29 17 42	3225	F	75	14.5	E
S6/97	29 34 31	29 19 56	2826	A	89	11.6	NE
S7/97	29 34 29	29 19 54	2830	A	75	13.05	NE
S9/97	29 35 00	29 18 35	2880	B	85	13.05	S
S11/97	29 36 25	29 17 23	3000	E	80	14.5	W
S12/97	29 35 02	29 17 40	2890	C	84	13.05	S

Figure 7.3 (overleaf): Map of the Drakensberg at Sani Pass. Nine samples were collected from the six free face sites (A - F) marked. For details of the sample sites see text.

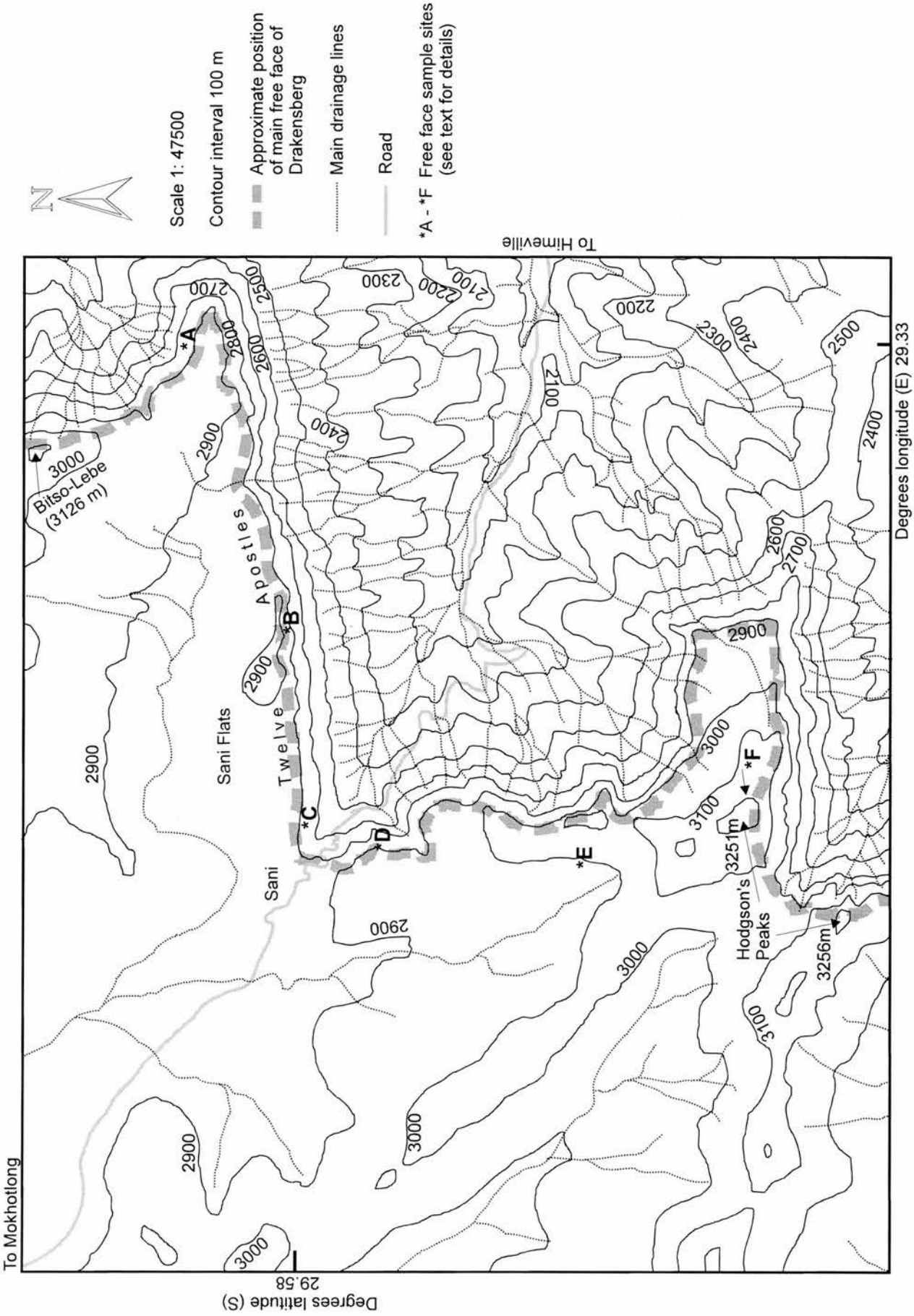
N
Scale 1: 47500
Contour interval 100 m
Approximate position of main free face of Drakensberg
Main drainage lines
Road
*A - *F Free face sample sites (see text for details)
To Himeville
To Mokhotlong
Degrees latitude (S) 29.58
Degrees longitude (E) 29.33
Bitso-Lebe (3126 m)
3000
Apostles
Twelve
Sani Flats
Sani
Hodgson's Peaks
3251m
3256m
*A
*B
*C
*D
*E
*F
2900
3000
3100
2700
2800
2600
2500
2400
2300
2200
2100

Samples S2/95, S6/97 and S7/97 are from the main free face of the Drakensberg at site A (Figure 7.3, Plate 44). The free face at this site is ~ 50 m high and is the northern extension of the face which is 50 – 80 m high that runs unbroken for ~ 7 km from Sani almost to Bitso-Lebe and forms the Twelve Apostles (Plate 45). The samples were collected from ~ 50 m apart, S6/97 being the furthest east and S7/97 the furthest west. S6/97 was collected from the steepest part of the face (~ 89 °), while the other two samples are from sections that slope ~ 75 °. The face at the point where S7/97 was collected extends ~ 5 – 10 m in front of the general line of the rest of the face (Plate 46). At all three sample locations the face appears to be denuding by a combination of granular disintegration, exfoliation of thin (~ 0.1 m) sheets and the loss of individual blocks < 0.5 m thick (Plate 47). The slope in front of the free face (~ 30 – 40 °) is a mix of vegetation, exposed bedrock steps and some loose boulders ~ 0.5 m thick (Plates 44, 47).

Samples S9/97 and S12/97 were collected from the Twelve Apostles section of the main free face of the Drakensberg at sites B and C respectively (Figure 7.3, Plate 45). The face from which S9/97 was collected is about midway along the Twelve Apostles and ~ 25 m high with a dip of ~ 85 °. A narrow (3 – 5 m) grassed step separates this face from another ~ 25 m high free face below (Plate 48). S12/97 is from the western end of the Twelve Apostles where the free face is ~ 15 m high and is, again, separated from another section of free face by a narrow grassed step (Plate 49). At both sites B and C the talus slope below the lower section of free face is ~ 50 ° with a mixture of vegetation and exposed bedrock, part of which forms a pronounced step midway down the slope (Plate 49). Denudation again seems to be accomplished by a combination of granular disintegration, removal of thin (~ 0.1 m) fragments and the periodic loss of blocks ~ 0.5 m thick.

Samples S1/97 and S2/97 are from site D (Figure 7.3) on the main free face on the southern side of Sani Pass (Plate 50). S1/97 is furthest west (inland) of the two taken from where the face has a northeastern aspect, while S2/97 is from ~ 100 m along the same face where the aspect is east. The face at both places is ~ 25 m high with a dip of 85 – 88 °. Again there is a narrow (2 – 5 m) grassed step in front of the face which separates it from another, generally less well defined, face immediately below (Plate 51). At both sampling locations denudation appears to be accomplished by the combination of factors mentioned previously, although at locations between loss of blocks of generally ~ 0.5 m thick appears to be dominant (Plate 51).

Two samples were collected from free faces at sites inland of the main escarpment free face. At site E (Figure 7.3) sample S11/97 was taken from an inland (western) facing free face which runs for several hundred metres about 300 m west of the escarpment (Plate 52). This face is ~ 12 – 15 m high with a dip of ~ 80 °. The talus slope is ~ 10 ° and is well-grassed. At and near the section where this sample was collected there were a few loose ~ 0.5 m thick boulders lying on the talus slope, however at three other sites along this face several boulders up to ~ 1 m thick were noted. At the sample site denudation appears to be due to the usual combination of granular disintegration, exfoliation of this sheets and the loss of individual ~ 0.5 m thick boulders.

Sample S4/97 was also collected from a free face inland of the escarpment (site F, Figure 7.3). This free face is on the eastern side of the northern summit of Hodgson's Peaks (3251 m), ~ 50 m east of the summit, and ~ 20 m below the summit. The face is oriented roughly north – south and runs for ~ 60 m in from the escarpment edge. The sample was taken from midway along the face. Northeast of the site the area is drained by a small < 2 km^2 basin which drains over the escarpment (Plate 53). The face is ~ 10 – 12 m high, with a dip of ~ 80 °. The talus slope is ~ 15 – 20 ° and is well-grassed with a few loose boulders < 0.5 m thick.

7.3 LESOTHO HIGHLANDS' SITES

Chapter 6 provides a detailed description of the morphology and geology of the Lesotho Highlands. The rationale for sampling from free faces within this area was to establish if there was a clear difference between the rate of denudation of free faces at the escarpment and those well inland. In addition estimated rates from these free face sites can be compared with estimates from the flat-lying sites described in the preceding chapter to assess quantitatively the relative importance of downwearing and backwearing in this area. Sampling procedures identical to those used at the southern Drakensberg free face sites were employed.

In total fifteen samples were collected during the 1997 field season from the 10 sites shown in Figure 7.4 (A - J). The location and field data is summarised in Table 7.4. With the exception of sample L29/97 (site I, Figure 7.4), all the free face samples were collected from sites close to those which supplied the flat-lying samples. General descriptions of these sites are provided in Chapter 6 and are not repeated here. No suitable flat-lying site near sample L29/97 was found due to obvious recent human interference (road, transmission cable and radio mast construction). The free face locations are grouped into types similar to those used for the flat-lying sample sites – free faces at the head of a river valley (A, E, H, I and J), free faces forming the sides of summits in lower relief areas (B and F) and free faces at river valleys (C, D and G).

Figure 7.4 (overleaf): Map of the Lesotho Highlands showing the 2000 m, 2500 m and 3000 m contours. Fifteen samples were collected at ten free face sites (A- J). For details of the sample sites see text.

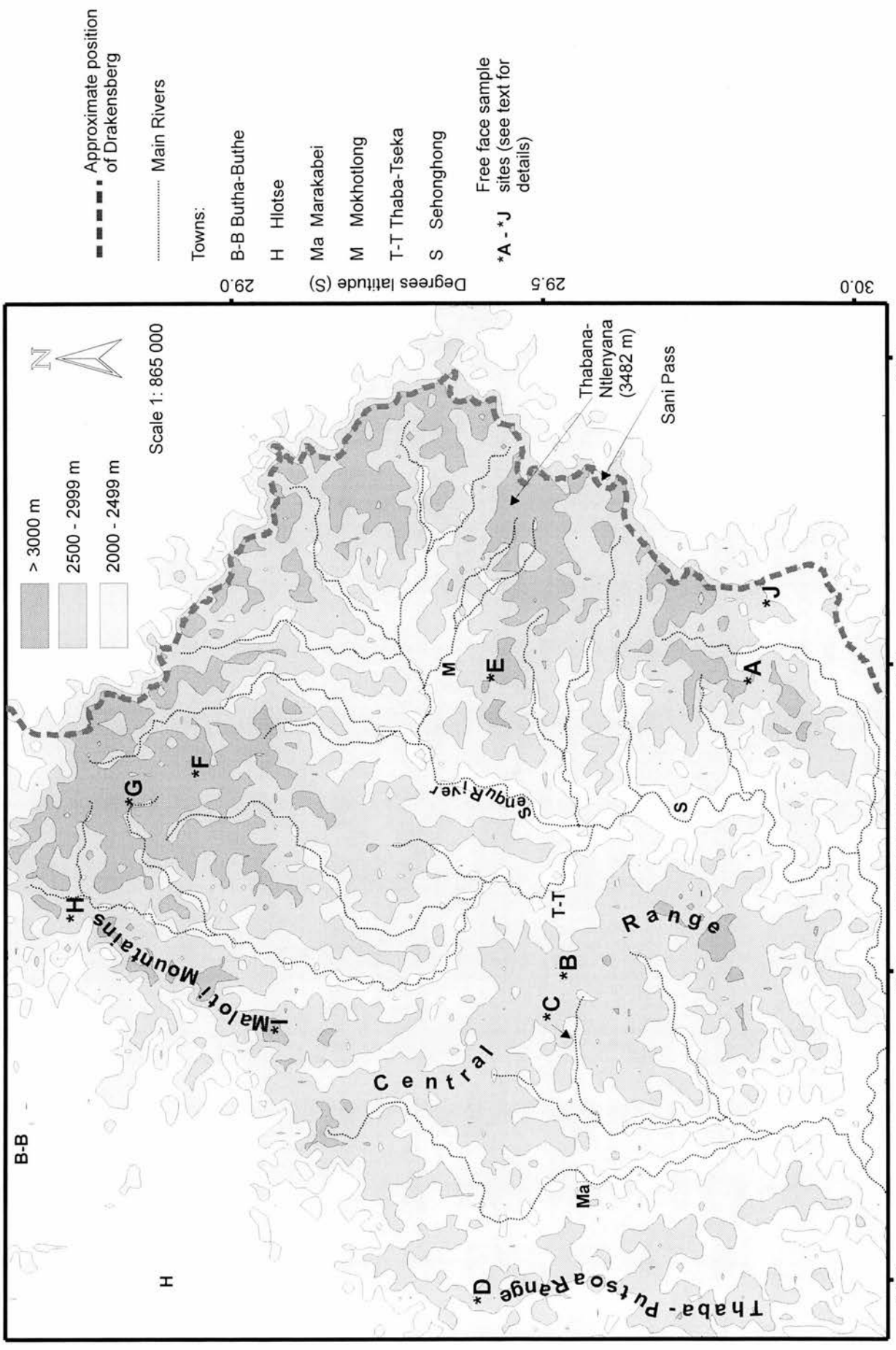
Approximate position of Drakensberg
Main Rivers
Towns:
B-B Butha-Buthe
H Hlotse
Ma Marakabei
M Mokhotlong
T-T Thaba-Tseka
S Sehonghong
Free face sample sites (see text for details)
*A - *J
Degrees latitude (S)
29.0
29.5
30.0
N
Scale 1: 865 000
> 3000 m
2500 - 2999 m
2000 - 2499 m
Thabana-Ntlenyana (3482 m)
Sani Pass
*A
*B
*C
*D
*E
*F
*G
*H
*I
*J
Maloti Mountains
Thaba-Putsoa Range
Central
Range
T-T
M
S
Senqu River
B-B
H
Ma
28.0
28.5
29.0
29.5
Degrees longitude (E)

Table 7.4: Location and field data for free face samples collected in the Lesotho Highlands.

Sample	Lat. (d m s) S	Long. (d m s) E	Alt. (m asl)	Site in Figure 7.4	Free face type [α]	Surface slope (°)	Thick. (g cm^{-2})	Aspect
L2/97	29 53 35	28 58 15	3034	A	VH	88	13.05	SE
L3/97	29 53 34	28 58 15	3018	A	VH	80	13.05	NW
L5/97	29 32 44	28 30 46	2898	B	S	88	11.6	N
L6/97	29 31 49	28 22 47	2730	C	VS	88	14.5	S
L8/97	29 24 57	27 56 56	2400	D	VS	76	10.15	W
L14/97	29 25 58	28 57 40	3125	E	VH	82	14.5	SW
L18/97	28 56 33	28 50 00	3275	F	S	85	14.5	S
L19/97	28 50 52	28 45 50	3050	G	VS	78	13.05	W
L20/97	28 50 53	28 45 25	3050	G	VS	82	14.5	NE
L21/97	28 50 02	28 44 09	3040	G	VS	85	14.5	S
L24/97	29 51 55	29 05 07	2880	J	VH	87	14.5	NW
L25/97	29 51 55	29 05 07	2880	J	VH	86	11.6	SE
L26/97	29 52 41	29 05 09	2745	J	VH	82	13.05	S
L27/97	28 45 50	28 36 01	2825	H	VH	83	10.15	NW
L29/97	29 03 56	28 24 03	3110	I	VH	85	13.05	NE

[α] Samples are from free faces located at valley heads (VH), valley sides (VS) or forming the sides of summits in lower relief areas (S).

7.3.1 FREE FACES AT THE HEAD OF RIVER VALLEYS

Samples L2/97 and L3/97 are from the free faces on the eastern and western sides of the knoll which forms the summit of Matabeng Pass, ~ 15 km west of the Drakensberg (A, Figure 7.4). This location has already been described in Chapter 6 in relation to flat-lying sample L1/97. The two faces are ~ 10 – 15 m high with of ~ 80 – 88 ° dip (Plate 20). Both faces are highly irregular due to weathering of the joints which have a spacing of ~ 0.3 – 0.5 m (Plate 54). The denudational processes operating on both faces appear to be a combination of granular disintegration, exfoliation of thin (< 0.1 m) sheets and the loss of individual 0.3 – 0.5 m thick blocks (Plate 54). The ~ 25 ° talus slopes are well vegetated with occasional

bedrock outcrops which form steps (Plate 20) and there are some loose < 0.5 m thick boulders.

Sample L14/97 is also from a similar setting at Menoaneng Pass which is ~ 35 km northwest of Sani Pass (E, Figure 7.4). The face sampled was that on the southwest side which is ~ 10 – 15 m high (Plate 55). Again weathering has exposed the jointing and denudation appears to be accomplished by a combination of the loss of individual blocks, exfoliation of thin sheets and granular disintegration. There are some loose < 0.5 m thick boulders on the ~ 25 ° talus slope.

Samples L24/97, L25/97 and L26/97 were all collected from site J (Figure 7.4) which is ~ 2.5 km west of the Drakensberg. L24/97 and L25/97 are, respectively, from the northwest and southeast free faces below the summit of Thaba-Ntso (2891 m) which provided the flat-lying sample L23/97 (Plate 56). The free face on both sides is ~ 10 m and the denudational processes appear to be similar to those noted at other sites. The rectilinear talus slope (~ 35 °) is punctuated by bedrock outcrops which form several metre high steps. Some loose ~ 0.5 m thick boulders were noted on the slope. L26/97 was collected from a large (> 50 m high) free face which is sited ~ 1.2 km due south of Thaba-Ntso (Plate 57). The Drakensberg, ~ 6 km west at this point, is formed not in basalt, but in the underlying Stormberg Group Basalt and this face marks the southern boundary of the basalt in this area (Plate 58). This free face again shows signs of the operation of granular disintegration, exfoliation of thin (< 0.2 m) sheets and the loss of individual blocks (~ 0.5 m thick). The talus slope (~ 35 – 40 °) is well vegetated and a few loose ~ 0.5 m thick boulders were noted near the foot of this.

L27/97 is from the free face on the northwest side of Moteng Pass in the Maloti Mountains (H, Figure 7.4; Plate 21). These mountains mark the western boundary of the Lesotho Highlands and form the drainage divide between eastward flowing tributaries of the Orange (Senqu) River and westward flowing tributaries of the Caledon River (the international border between Lesotho and South Africa) which itself is part of the Orange River Basin. This free face is ~ 20 – 25 m high with a dip of ~ 83 °. Denudation appears to be due to a combination of granular disintegration, exfoliation of thin (~ 0.2 m) sheets and the loss of individual boulders ~ 0.5 m thick (Plate 59). The talus slope (~ 30 °) is mainly grassed, but there are some ~ 30 ° sloping bedrock exposures which may be attributable to recent soil erosion. Some loose ~ 0.3 – 0.5 m thick boulders were also noted.

L29/97 is from a free face just below the summit of Mafika-Lisiu (3175 m) in the Maloti Mountains (I, Figure 7.4). This summit separates an eastward flowing tributary of the Bokong River (part of the Senqu Basin) from the westward flowing Mphosong River (Caledon Basin). The elevation falls ~ 525 m within 1 km on the western side (Plate 60) and ~ 125 m within 1 km to the east. The sample was collected from a pronounced free face which again appears to be denuding by a combination of granular disintegration, exfoliation of thin sheets and the loss of individual blocks ~ 0.5 m thick. The talus slope (~ 40 °) is a mix of grassed sections and exposed bedrock steps.

7.3.2 Free faces of summits in lower relief areas

Two samples were collected from free faces of summits in lower relief areas. L5/97 is from a free face just below the summit of Thabana-ea-Manase (2915 m) in the Central Range (B, Figure 7.4). Flat-lying sample L4/97 was collected from this summit and a description of the location can be found in Chapter 6. This face is ~ 6 – 11 m high and is on the northern side of the summit. At the western end of the face the upper 1 – 2 m overhangs the lower section and the periodic collapse of this overhang has produced ~ 1 – 1.5 m thick boulders which are lying on the grassed talus slope (5 – 10 °) (Plate 61). The lowermost section of the face, from which the sample was taken, is being denuded by granular disintegration and the exfoliation of thin (0.1 – 0.2 m) sheets.

Sample L18/97 was collected from the southern free face of the knoll which forms the summit of Mafisoaneng (F, Figure 7.4). Two flat-lying samples (L16/97 and L17/97) are from the summit and Chapter 6 contains a general description of the location. The sample is from western half of the face where it is ~ 12 m high with a dip of ~ 85 ° (Plate 62). The joint spacing, highlighted by preferential weathering, is ~ 0.3 – 0.5 m. Denudation appears to be due to a combination of granular disintegration, exfoliation of thin (< 0.2 m) sheets and the loss of individual boulders and slabs of ~ 0.5 m thickness. The talus slope (~ 15 – 20 °) is well-grassed with some, generally, ~ 0.5 m thick loose boulders. At a couple of sites, near the western end of the face, there are a large number of loose boulders and slabs of ~ 0.5 – 1 m thickness which have been produced by a recent rock fall of this part of the face.

7.3.3 Free faces at river valleys

Five samples were collected from free faces in river valleys at three sites. L6/97 is from a ~ 3 – 11 m high free face directly below the summit of the drainage divide between the Tenane

and Likomiking Rivers (C, Figure 7.4) from which flat-lying sample L7/97 was collected. This face is ~ 100 m in length and is situated ~ 450 m above the Tenane River which is ~ 2 km due south. The talus slope (~ 30 °) is a mix of exposed bedrock, sandy soil, vegetation and a few loose ~ 0.5 m thick boulders (Plate 63). Denudation appears to be due to a combination of the loss of individual ~ 0.5 m thick boulders, exfoliation of thin sheets and granular disintegration.

Sample L8/97 is from a free face which is ~ 400 m above the Makheleng River (D, Figure 7.4; Plate 27). Flat-lying sample L9/97 was collected from ~ 100 m above this site. This free face forms a pronounced step on the eastern side of this river valley, roughly midway, in altitude, to the summit of Thaba-Putsoa (2900 m). The face is discontinuous, being dissected by a series of 2 – 5 m wide 35 – 40 ° gullies, which separate 20 – 50 m wide sections of free face. L8/97 is from a ~ 30 m wide section of free face, ~ 5m from one of the gullies (Plate 64). The talus slope (~ 35 – 40 °) is well-grassed with some loose ~ 0.5 m thick boulders. The denudational processes appear to be similar to those noted at other sites (Plate 64).

Three samples were taken from free face sites at the Motete River (G, Figure 7.4). L19/97 and L20/97 are from pronounced rock steps that occur midway up, respectively, the east and west slopes of the river valley (Plate 65). These faces are discontinuous, extending for ~ 200 – 300 m and other free faces, of varying heights and lengths, also occur as rock steps on these otherwise well-grassed slopes (Plate 65). The face from which L19/97 was taken, on the east bank, is ~ 50 m above the riverbed, while L20/97 is from a face ~ 75 m above the river on the west bank. The slope on the east bank is ~ 10 – 15 °, while that on the west is slightly steeper at ~ 20 °. Although at the places where the samples were collected the face appears to be denuding by the loss of thin (~ 0.1 – 0.2 m) sheets, individual < 0.5 m thick boulders and granular disintegration, at both sites the faces are highly irregular and there is evidence, from the face and talus slope, for the loss of boulders / slabs up to ~ 2 m thick (Plate 66). The collapse of such slabs appears to be due to undercutting of the face by sapping (Plate 66).

Sample L21/97 is from a free face on the midslope of the eastern bank of the Motete River, ~ 3 km downstream from the site described above. This face is ~ 125 m above the channel and forms the face below the surface from which flat-lying sample L22/97 was collected. The face is, again, discontinuous and highly irregular (Plate 67). The talus slope (~ 15 – 20 °) has a large number of loose boulders lying on it which are, generally, ~ 0.5 m thick, with a few of 1 – 2m thickness (Plate 67). These large boulders appear to be produced by a combination

of the collapse of overhangs and the failure of large (several cubic metres) sections of the face which are up to 2 m thick (Plate 67). Other sections of the face, from which the sample was collected, appear to be denuding by the loss of individual boulders of ~ 0.5 m thickness, exfoliation of thin sheets and granular disintegration.

7.4 ANALYTICAL DATA AND ESTIMATED DENUDATION / BACKWEARING RATES

7.4.1 ANALYTICAL DATA

Chlorine-36 was extracted from all samples using the procedures outlined in Chapter 4. With the exception of S2/95 and N4/95, all samples were prepared in the ^{36}Cl clean room laboratory in the Department of Geography. S2/95 was prepared by Dr John Stone in the RSES laboratory, ANU, while N4/95 was prepared by the author, under Dr Stone's supervision, in the RSES laboratory. Isotopic ratios were measured using the 14-UD pelletron accelerator at ANU. Whole rock chloride concentrations and other ancillary chemical analyses were determined as detailed in Chapter 4. Major element and selected trace element (Li, B, Cl, Cr, Sm, Gd, Th and U) concentrations are listed, respectively, in Appendices 3 and 4.

Field and location data for all free face samples are provided in Tables 7.1 – 7. 4. The concentrations of Ca, K and ^{35}Cl, the elements responsible for ^{36}Cl production, together with the mass of sample digested and the quantity of ^{36}Cl free carrier used, are detailed in Table 7.5. Generally a larger mass (~ 15 – 19 g) of sample digested for the free face samples, as a lower ^{36}Cl content was expected than for the samples from flat-lying sites. Approximately 1.4×10^{-3} g of ^{36}Cl free carrier was added to each sample prior to digestion. The Ca content varied between 3.87 and 7.67 wt % while the K content was 0.27 – 1.54 wt %. In subsequent calculations an error of 1 % was assumed in these values. The whole rock Cl content was, again, very low (1.5 – 13.8 ppm) reducing the significance of the ^{35}Cl thermal neutron capture reaction in the total ^{36}Cl production rate.

Table 7.5: Elemental composition of free face samples.

Sample	Mass digested (g)	^{36}Cl free chloride carrier (x 10^{-3} g)	Ca (wt %)	K (wt %)	Cl (μg g^{-1})
Naudesnek					
N4/95	15.3179	1.4031	6.97	0.73	13.8 ± 0.4
N5/97	19.2178	1.4395	7.15	0.76	1.7 ± 0.2
N8/97	19.3329	1.4410	7.29	0.57	3.3 ± 0.8
N9/97	19.2770	1.4381	7.27	0.55	3.7 ± 0.9
N10/97	18.2057	1.4410	7.08	0.56	2.8 ± 0.7
N11/97	17.7500	1.4584	5.95	0.80	3.3 ± 0.8
N12/97	18.4248	1.4485	3.87	1.21	2.1 ± 0.5
N13/97	18.8947	1.4424	6.32	0.51	5.8 ± 1.4
N15/97	19.5441	1.4428	5.77	0.27	1.6 ± 0.3
N16/97	15.2681	1.4287	6.31	0.50	1.7 ± 0.2
N17/97	18.2400	1.4485	7.37	0.61	2.0 ± 0.5
N18/97	18.2068	1.4348	6.12	1.07	4.5 ± 1.1
Ongeluk's Nek					
O2/97	18.1807	1.4400	6.64	0.56	4.7 ± 0.3
O3/97	18.0898	1.4386	7.10	0.58	6.1 ± 1.5
O4/97	18.0269	1.4249	7.40	0.51	7.1 ± 1.8
O6/97	18.0608	1.4320	7.36	0.59	8.3 ± 0.2
O7/97	18.0291	1.4362	6.65	0.56	5.2 ± 0.4
O9/97	15.7099	1.4428	7.39	0.51	1.6 ± 0.4
O10/97	17.6294	1.4395	7.48	0.82	4.9 ± 1.2
O12/97	17.3883	1.4584	6.92	1.07	3.6 ± 0.2
Sani Pass					
S2/95	4.4501	1.3985	6.10	0.51	8.0 ± 0.2
S1/97	17.5720	1.4523	6.70	0.50	1.9 ± 0.5
S2/97	16.2382	1.4443	7.13	0.75	3.3 ± 0.8
S4/97	15.8793	1.4443	6.30	0.50	3.2 ± 0.3
S6/97	15.8534	1.4452	6.75	0.76	4.5 ± 0.3
S7/97	19.9072	1.4419	6.45	0.81	5.1 ± 1.3
S9/97	15.4053	1.4499	7.55	0.54	2.2 ± 0.6
S11/97	17.3459	1.4443	4.72	1.00	11.5 ± 0.2
S12/97	18.4871	1.4400	7.05	0.79	4.2 ± 1.1
Lesotho Highlands					
L2/97	16.9304	1.4377	6.72	0.63	3.5 ± 0.2
L3/97	16.6981	1.4419	7.11	0.63	3.8 ± 0.3
L5/97	17.0244	1.4513	6.69	1.01	2.6 ± 0.3
L6/97	16.5242	1.4113	7.45	0.73	3.9 ± 1.0
L8/97	16.6087	1.4428	7.33	0.59	4.2 ± 0.3
L14/97	16.9683	1.5055	6.94	0.82	2.9 ± 0.3
L18/97	16.3506	1.4607	7.06	0.63	2.4 ± 0.3
L19/97	16.7841	1.4551	6.13	1.54	5.1 ± 0.5
L20/97	16.8198	1.4560	6.07	1.29	5.1 ± 0.4
L21/97	16.3860	1.4428	7.67	0.52	2.4 ± 0.3
L24/97	15.0812	1.4377	7.60	0.37	2.2 ± 0.6
L25/97	15.1345	1.4400	4.57	0.38	1.5 ± 0.4
L26/97	15.2512	1.4395	6.11	0.84	11.2 ± 0.5
L27/97	15.0610	1.4414	7.23	0.66	3.5 ± 0.9
L29/97	15.1072	1.4362	7.43	0.75	3.7 ± 0.2

The isotopic ratios together with total ^{36}Cl, background ^{36}Cl and cosmogenic ^{36}Cl contents are detailed in Table 7.6. Uncertainty in the AMS ratio (quoted at the 1 σ level, K. Fifield, pers. comm.) is larger than for the flat-lying samples because of the generally lower ratios which make the counting statistics more important. Errors generally vary between 3.7 % and 11.5 %, but N12/97 and O4/97 have uncertainties of 22 % - 29 %. These large uncertainties were caused by problems in the pressing of the AgCl pellets into targets for the AMS (R. Cresswell, pers. comm.). This reduced the beam currents and the number of counts on which the ratio was based and, consequently, increased the statistical error. The only way to reduce this error would have been to prepare fresh AgCl pellets for these samples. The ^{36}Cl blank figure is the number of ^{36}Cl atoms present in the procedural blank (one per batch of five samples) and this was deducted before arriving at the ^{36}Cl total figure. The ^{36}Cl total, ^{36}Cl background and ^{36}Cl cosmogenic figures were derived in the same manner as for the flat-lying samples in Chapter 6 (Section 6.4.1).

Table 7.6: ^{36}Cl isotopic ratio and absolute concentrations for free face samples.

Sample	$^{36}Cl/Cl$ ratio (10^{-15})	AMS uncert. (%)	^{36}Cl blank (10^4 atom)	^{36}Cl total (10^5 atom g^{-1})	^{36}Cl background (10^2 atom g^{-1})	^{36}Cl cosmogenic (10^5 atom g^{-1})
Naudesnek						
N4/95	60 ± 5	8.3	1.2 ± 1.2	1.06 ± 0.09	5.7 ± 0.9	1.06 ± 0.09
N5/97	155 ± 13	8.4	2.4 ± 1.5	2.01 ± 0.17	0.79 ± 0.01	2.01 ± 0.17
N8/97	92 ± 6	6.5	2.4 ± 1.5	1.21 ± 0.08	1.5 ± 0.4	1.21 ± 0.08
N9/97	87 ± 5	5.7	2.4 ± 1.5	1.15 ± 0.07	2.3 ± 0.6	1.15 ± 0.07
N10/97	198 ± 15	7.6	2.7 ± 1.5	2.75 ± 0.21	1.4 ± 0.4	2.75 ± 0.21
N11/97	70 ± 7	10.0	2.2 ± 1.7	1.01 ± 0.10	1.3 ± 0.3	1.01 ± 0.10
N12/97	28 ± 8	28.6	2.2 ± 1.7	0.37 ± 0.11	1.1 ± 0.3	0.37 ± 0.11
N13/97	170 ± 8	4.7	2.2 ± 1.7	2.37 ± 0.12	2.3 ± 0.6	2.37 ± 0.12
N15/97	195 ± 10	5.1	2.2 ± 1.7	2.50 ± 0.13	0.6 ± 0.1	2.50 ± 0.13
N16/97	153 ± 8	5.2	1.2 ± 1.5	2.48 ± 0.13	0.7 ± 0.2	2.48 ± 0.13
N17/97	197 ± 13	6.6	2.2 ± 1.5	2.72 ± 0.18	1.6 ± 0.4	2.72 ± 0.18
N18/97	117 ± 6	5.1	2.2 ± 1.5	1.65 ± 0.09	1.9 ± 0.5	1.65 ± 0.09
Ongeluk's Nek						
O2/97	455 ± 19	4.2	2.2 ± 1.5	6.49 ± 0.27	2.5 ± 0.2	6.49 ± 0.27
O3/97	126 ± 8	6.3	2.2 ± 1.5	1.83 ± 0.12	5.1 ± 1.7	1.82 ± 0.12
O4/97	41 ± 9	22.0	1.9 ± 1.2	0.59 ± 0.13	3.1 ± 0.8	0.59 ± 0.13
O6/97	155 ± 8	5.2	1.9 ± 1.2	2.30 ± 0.12	5.1 ± 0.3	2.30 ± 0.12
O7/97	118 ± 6	5.1	1.9 ± 1.2	1.70 ± 0.09	2.1 ± 0.2	1.69 ± 0.09
O9/97	26 ± 3	11.5	1.0 ± 1.2	0.41 ± 0.05	1.0 ± 0.3	0.41 ± 0.05
O10/97	152 ± 8	5.3	1.0 ± 1.2	2.24 ± 0.12	3.2 ± 0.8	2.23 ± 0.12
O12/97	95 ± 6	6.3	1.0 ± 1.2	1.41 ± 0.09	2.0 ± 0.2	1.41 ± 0.09
Sani Pass						
S2/95	27 ± 3	11.1	1.2 ± 1.2	1.48 ± 0.17	4.3 ± 0.4	1.48 ± 0.17
S1/97	124 ± 9	7.3	1.0 ± 1.2	1.78 ± 0.13	1.3 ± 0.4	1.78 ± 0.13
S2/97	81 ± 5	6.2	5.7 ± 1.7	1.24 ± 0.08	1.9 ± 0.5	1.24 ± 0.08
S4/97	162 ± 8	4.9	5.7 ± 1.7	2.57 ± 0.13	1.3 ± 0.2	2.57 ± 0.13
S6/97	61 ± 4	6.6	5.7 ± 1.7	0.96 ± 0.07	3.4 ± 0.5	0.96 ± 0.07
S7/97	222 ± 10	4.5	5.7 ± 1.7	2.91 ± 0.14	3.2 ± 0.8	2.90 ± 0.14
S9/97	62 ± 5	8.1	5.7 ± 1.7	0.98 ± 0.08	1.6 ± 0.4	0.98 ± 0.08
S11/97	143 ± 8	5.6	3.5 ± 2.2	2.29 ± 0.13	8.7 ± 0.3	2.28 ± 0.13
S12/97	195 ± 9	4.6	3.5 ± 2.2	2.71 ± 0.13	3.0 ± 0.8	2.71 ± 0.13
Lesotho Highlands						
L2/97	111 ± 5	4.5	3.5 ± 2.2	1.65 ± 0.08	1.9 ± 0.2	1.65 ± 0.08
L3/97	283 ± 11	3.9	3.5 ± 2.2	4.33 ± 0.17	1.9 ± 0.2	4.33 ± 0.17
L5/97	121 ± 7	5.8	3.5 ± 2.2	1.79 ± 0.11	1.4 ± 0.4	1.79 ± 0.11
L6/97	158 ± 8	5.1	1.7 ± 1.5	2.40 ± 0.13	2.3 ± 0.6	2.39 ± 0.13
L8/97	56 ± 4	7.1	1.7 ± 1.5	0.86 ± 0.06	2.1 ± 0.2	0.86 ± 0.06
L14/97	246 ± 13	5.3	0.7 ± 0.7	3.84 ± 0.20	2.0 ± 0.2	3.84 ± 0.20
L18/97	113 ± 6	5.3	0.7 ± 0.7	1.76 ± 0.09	1.3 ± 0.2	1.76 ± 0.09
L19/97	734 ± 27	3.7	0.7 ± 0.7	11.5 ± 0.4	2.1 ± 0.2	11.5 ± 0.4
L20/97	566 ± 21	3.7	0.7 ± 0.7	8.84 ± 0.33	2.4 ± 0.3	8.84 ± 0.33
L21/97	142 ± 8	5.6	0.7 ± 0.7	2.19 ± 0.12	1.3 ± 0.2	2.18 ± 0.12
L24/97	91 ± 6	6.6	1.2 ± 1.5	1.50 ± 0.10	0.8 ± 0.2	1.50 ± 0.10
L25/97	45 ± 4	8.9	1.2 ± 1.5	0.73 ± 0.07	0.9 ± 0.3	0.73 ± 0.07
L26/97	71 ± 5	7.0	1.2 ± 1.5	1.27 ± 0.09	2.4 ± 0.4	1.27 ± 0.09
L27/97	110 ± 6	5.5	3.2 ± 1.7	1.84 ± 0.10	2.0 ± 0.5	1.84 ± 0.10
L29/97	71 ± 5	7.0	1.2 ± 1.5	1.19 ± 0.08	2.6 ± 0.2	1.18 ± 0.08

The site-specific production rates were derived from the measured concentrations of the relevant target (Table 7.5) and the calibrated production rates for spallogenic and muogenic reactions (Stone *et al*, 1996a, 1998a; Evans *et al*, 1997), scaled, as appropriate for altitude / latitude, slope / topographic shielding and sample thickness. These scaling factors are listed in Table 7.8. The altitude / latitude scaling factor for spallogenic reactions was derived from Lal (1991). For these sloping free face samples muon production was scaled, for altitude and latitude, as described in Section 3.3.3. The comments in Section 6.4.1 relating to the impact of using the scaling factors recently proposed by Dunai (2000) apply equally to the samples collected from free faces. The shielding factor to account for the slope was derived from Equations 3.25 and 3.30, respectively, for spallation and muons, while the correction for the impact of topography (excluding the free face) was derived from Equation 2.3. The production rates used in the denudation rate calculation were averaged over the thickness of the sample by multiplying the site-specific surface production rate by the sample thickness correction factor (calculated per Appendix 6). Although these samples were of a similar thickness to the flat-lying samples, the correction factor is slightly greater (< 8 %) because of the shorter effective attenuation lengths for spallogenic production on these sloping surfaces. Again no correction was made for muon induced reactions. Thermal and epithermal neutron activation production rates were scaled for altitude / latitude by assuming that 90 % of the neutrons were spallogenic in origin with the remainder being due to muon interactions.

Table 7.8: Scaling factors applicable to free face samples.

Sample	Alt. / Lat.	Slope shielding		Topo.	Sample thick. scaling factor		
	Spall.	Spall.	Muon	Shield.	Spall.	Thermal neutrons	Epith. neutrons
Naudesnek							
N4/95	5.2456	0.6039	0.5965	1.0	0.9325	1.3198	1.0211
N5/97	5.0994	0.5308	0.5254	1.0	0.9278	1.3254	1.0132
N8/97	5.3504	0.5681	0.5616	0.9997	0.9250	1.3301	1.0165
N9/97	5.3504	0.5802	0.5734	0.9996	0.9376	1.2873	1.0145
N10/97	5.3403	0.5681	0.5616	0.9929	0.9303	1.3070	1.0141
N11/97	5.3203	0.5681	0.5616	0.9967	0.9383	1.3601	1.0251
N12/97	5.1739	0.5681	0.5616	0.9977	0.9237	1.3863	1.0285
N13/97	5.1446	0.5681	0.5616	0.9991	0.9237	1.4218	1.0268
N15/97	5.5620	0.7786	0.7660	0.9990	0.9354	1.4373	1.0484
N16/97	5.5932	0.7322	0.7210	1.0	0.9421	1.3820	1.0427
N17/97	5.5655	0.6270	0.6189	1.0	0.9365	1.3211	1.0235
N18/97	5.0162	0.6039	0.5965	0.9992	0.9455	1.2824	1.0216
Ongeluk's Nek							
O2/97	6.2025	0.7322	0.7210	0.9993	0.9340	1.3451	1.0335
O3/97	6.2025	0.5681	0.5616	1.0	0.9303	1.2998	1.0147
O4/97	5.9224	0.5308	0.5254	0.9990	0.9362	1.2712	1.0122
O6/97	6.2476	0.5681	0.5616	0.9988	0.9223	1.3231	1.0132
O7/97	5.1265	0.5802	0.5734	0.9996	0.9245	1.3790	1.0266
O9/97	5.4670	0.5681	0.5616	0.9997	0.9264	1.3195	1.0127
O10/97	5.4162	0.5308	0.5254	0.9994	0.9167	1.3593	1.0106
O12/97	5.4533	0.5558	0.5497	1.0	0.9200	1.3577	1.0179
Sani Pass							
S2/95	6.0323	0.6711	0.6617	1.0	0.9389	1.3132	1.0309
S1/97	6.3160	0.5681	0.5616	1.0	0.9289	1.3573	1.0222
S2/97	6.3160	0.5308	0.5254	1.0	0.9210	1.3167	1.0093
S4/97	7.6493	0.6817	0.6720	1.0	0.9310	1.4516	1.0443
S6/97	6.0323	0.5180	0.5129	0.9983	0.9325	1.2738	1.0112
S7/97	6.0542	0.6817	0.6720	0.9953	0.9383	1.3043	1.0298
S9/97	6.2394	0.5681	0.5616	0.9944	0.9317	1.3182	1.0140
S11/97	6.7061	0.6270	0.6189	1.0	0.9276	1.3319	1.0355
S12/97	6.2770	0.5802	0.5734	1.0	0.9338	1.2929	1.0155
Lesotho Highlands							
L2/97	6.8787	0.5308	0.5254	0.9983	0.9292	1.2904	1.0132
L3/97	6.8141	0.6270	0.6189	0.9983	0.9352	1.2884	1.0207
L5/97	6.3035	0.5308	0.5254	0.9982	0.9376	1.2758	1.0115
L6/97	5.6913	0.5308	0.5254	1.0	0.9224	1.3326	1.0127
L8/97	4.6210	0.6711	0.6617	0.9983	0.9487	1.2893	1.0251
L14/97	7.1906	0.6039	0.5965	1.0	0.9261	1.3211	1.0235
L18/97	7.7610	0.5681	0.5616	1.0	0.9168	1.3215	1.0235
L19/97	6.8013	0.6494	0.6406	0.9997	0.9352	1.3549	1.0390
L20/97	6.8013	0.6039	0.5965	1.0	0.9261	1.3641	1.0282
L21/97	6.6419	0.5681	0.5616	1.0	0.9250	1.3353	1.0148
L24/97	6.2748	0.5434	0.5376	1.0	0.9219	1.3420	1.0073
L25/97	6.2748	0.5558	0.5497	1.0	0.9376	1.3291	1.0179
L26/97	5.7825	0.6039	0.5965	1.0	0.9352	1.3485	1.0260
L27/97	5.9398	0.5922	0.5850	1.0	0.9449	1.2709	1.0176
L29/97	7.0766	0.5681	0.5616	0.9977	0.9303	1.3396	1.0183

The site-specific ^{36}Cl surface production rates for the free face samples are listed in Table 7.9. The production rates for spallogenic and muogenic reactions involving Ca and K (P_{Ca} and P_K) are derived from the calibrated rates in Stone *et al* (1996a, 1998a) and Evans *et al* (1997). The neutron capture reactions involving ^{35}Cl ($P_{Cl\text{-}35}$) and ^{39}K ($P_{K\text{-}39}$) were calculated using $P_f(0) = 586 \pm 40$ n (g air)$^{-1}$ a^{-1} (Phillips *et al*, 1996) and Equations 3.13 (f_{35} and f_{39}), 3.12 ($P_{n,35}$ and $P_{n,39}$) and 3.14 ($P_{n,epi}$). Again, to account for general uncertainties in production rates (eg Gosse *et al*, 1996), a 20 % uncertainty (1 σ level) was allocated to all production rates. Assuming all uncertainties, including this allocated error and target element measurements, to be independent and random, these uncertainties were propagated through the production rate calculations by combining errors in quadrature (Taylor, 1997).

The total, site-specific, ^{36}Cl production rate (P_{TOTAL}) varies between ~ 10 atoms g^{-1} a^{-1} for L25/97 and ~ 25 atoms g^{-1} a^{-1} for L19/97. Production at all sites is dominated by spallation of Ca and K, which contributes ~ 90 – 94 %. Negative muon induced reactions account for ~ 3 –5 %. In these Cl-poor basalts, neutron activation reactions account for < 5 %, with rates for thermal neutron capture by ^{35}Cl being ~ 0.5 – 1.2 atoms g^{-1} a^{-1}. Iron is the major absorber of all thermalized neutrons, with 80 – 85 % being absorbed by the major elements. Chlorine –35 captured < 0.1 % while ^{39}K captured an order of magnitude less.

Table 7.9: Site-specific chlorine-36 production rates for free face samples.

Sample	P_{Ca} [α]		P_K [β]		f_{35} [φ]	P_{CL-35} [χ]		f_{39} [ι]	P_{K-39} [δ]	P_{TOTAL} [ε]
	Spallation (atom g^{-1} a^{-1})	Muon (atom g^{-1} a^{-1})	Spallation (atom g^{-1} a^{-1})	Muon (atom g^{-1} a^{-1})		$P_{n,35}$ [γ] (atom g^{-1} a^{-1})	$P_{n,epi}$ [η] (atom g^{-1} a^{-1})		$P_{n,39}$ [φ] (atom g^{-1} a^{-1})	(atom g^{-1} a^{-1})
Naudesnek										
N4/95	10.04 ± 2.01	0.63 ± 0.25	3.67 ± 0.74	0.05 ± 0.02	0.00121	1.20 ± 0.26	0.21 ± 0.04	0.000073	0.07 ± 0.02	15.88 ± 2.17
N5/97	8.76 ± 1.75	0.56 ± 0.23	3.28 ± 0.66	0.05 ± 0.02	0.00015	0.13 ± 0.03	0.020±0.005	0.000076	0.06 ± 0.01	12.86 ± 1.89
N8/97	9.99 ± 2.00	0.62 ± 0.25	2.75 ± 0.55	0.04 ± 0.02	0.00030	0.27 ± 0.08	0.05 ± 0.02	0.000057	0.05 ± 0.01	13.78 ± 2.09
N9/97	10.31 ± 2.06	0.63 ± 0.25	2.73 ± 0.55	0.04 ± 0.02	0.00034	0.30 ± 0.09	0.06 ± 0.02	0.000056	0.05 ± 0.01	14.12 ± 2.15
N10/97	9.67 ± 1.93	0.60 ± 0.24	2.71 ± 0.54	0.04 ± 0.02	0.00025	0.22 ± 0.07	0.05 ± 0.02	0.000056	0.05 ± 0.01	13.33 ± 2.02
N11/97	8.20 ± 1.64	0.50 ± 0.20	3.85 ± 0.77	0.06 ± 0.02	0.00030	0.29 ± 0.09	0.02 ± 0.01	0.000079	0.08 ± 0.02	12.99 ± 1.83
N12/97	5.11 ± 1.02	0.33 ± 0.13	5.62 ± 1.12	0.09 ± 0.03	0.00018	0.17 ± 0.05	0.02 ± 0.01	0.000112	0.11 ± 0.02	11.44 ± 1.53
N13/97	8.31 ± 1.66	0.54 ± 0.21	2.34 ± 0.47	0.04 ± 0.01	0.00053	0.52 ± 0.16	0.04 ± 0.01	0.000051	0.05 ± 0.01	11.82 ± 1.75
N15/97	11.39 ± 2.28	0.69 ± 0.28	1.84 ± 0.37	0.03 ± 0.01	0.00015	0.22 ± 0.06	0.015±0.004	0.000027	0.04 ± 0.01	14.23 ± 2.33
N16/97	11.87 ± 2.37	0.70 ± 0.28	3.29 ± 0.66	0.05 ± 0.02	0.00015	0.21 ± 0.05	0.015±0.004	0.000047	0.07 ± 0.01	16.20 ± 2.48
N17/97	11.74 ± 2.35	0.69 ± 0.28	3.39 ± 0.68	0.05 ± 0.02	0.00018	0.20 ± 0.06	0.03 ± 0.01	0.000061	0.07 ± 0.01	16.16 ± 2.46
N18/97	8.55 ± 1.71	0.55 ± 0.22	5.24 ± 1.05	0.08 ± 0.03	0.00040	0.37 ± 0.11	0.05 ± 0.02	0.000104	0.10 ± 0.02	14.94 ± 2.02
Ongeluk's Nek										
O2/97	13.72 ± 2.74	0.75 ± 0.30	4.09 ± 0.82	0.05 ± 0.02	0.00042	0.59 ± 0.13	0.11 ± 0.02	0.000055	0.08 ± 0.02	19.39 ± 2.88
O3/97	11.36 ± 2.27	0.60 ± 0.24	3.26 ± 0.65	0.04 ± 0.02	0.00055	0.54 ± 0.16	0.13 ± 0.04	0.000058	0.06 ± 0.01	15.98 ± 2.38
O4/97	10.61 ± 2.12	0.58 ± 0.23	2.55 ± 0.51	0.03 ± 0.01	0.00063	0.54 ± 0.17	0.13 ± 0.04	0.000049	0.04 ± 0.01	14.50 ± 2.20
O6/97	11.74 ± 2.35	0.63 ± 0.25	3.30 ± 0.66	0.04 ± 0.02	0.00075	0.75 ± 0.16	0.19 ± 0.04	0.000059	0.06 ± 0.01	16.69 ± 2.46
O7/97	8.91 ± 1.78	0.57 ± 0.23	2.65 ± 0.53	0.04 ± 0.02	0.00045	0.45 ± 0.10	0.05 ± 0.01	0.000053	0.05 ± 0.01	12.72 ± 1.88
O9/97	10.36 ± 2.07	0.63 ± 0.25	2.49 ± 0.50	0.04 ± 0.01	0.00015	0.14 ± 0.04	0.03 ± 0.01	0.000052	0.05 ± 0.01	13.73 ± 2.15
O10/97	9.61 ± 1.92	0.60 ± 0.24	3.70 ± 0.74	0.05 ± 0.02	0.00045	0.40 ± 0.12	0.06 ± 0.02	0.000083	0.07 ± 0.02	14.49 ± 2.08
O12/97	9.41 ± 1.88	0.57 ± 0.23	5.11 ± 1.02	0.07 ± 0.03	0.00031	0.30 ± 0.07	0.05 ± 0.01	0.000102	0.10 ± 0.02	15.61 ± 2.16
Sani Pass										
S2/95	11.30 ± 2.26	0.62 ± 0.25	3.35 ± 0.67	0.04 ± 0.02	0.00064	0.84 ± 0.18	0.15 ± 0.03	0.000048	0.06 ± 0.01	16.36 ± 2.38
S1/97	10.89 ± 2.18	0.57 ± 0.23	2.84 ± 0.57	0.03 ± 0.01	0.00017	0.19 ± 0.06	0.021±0.007	0.000049	0.06 ± 0.01	14.61 ± 2.26
S2/97	10.73 ± 2.15	0.57 ± 0.23	3.95 ± 0.79	0.05 ± 0.02	0.00030	0.28 ± 0.08	0.07 ± 0.02	0.000074	0.07 ± 0.02	15.70 ± 2.30

Table 7.9: (cont.).

Sample	P_{Ca} [α]		P_K [β]		f_{35} [ϕ]	P_{CL-35} [χ]		f_{39} [ι]	P_{K-39} [δ]	P_{TOTAL} [ε]
	Spallation (atom g^{-1} a^{-1})	Muon (atom g^{-1} a^{-1})	Spallation (atom g^{-1} a^{-1})	Muon (atom g^{-1} a^{-1})		$P_{n,35}$ [γ] (atom g^{-1} a^{-1})	$P_{n,epi}$ [η] (atom g^{-1} a^{-1})		$P_{n,39}$ [φ] (atom g^{-1} a^{-1})	(atom g^{-1} a^{-1})
Sani Pass										
S4/97	14.92 ± 2.98	0.65 ± 0.26	4.14 ± 0.83	0.04 ± 0.02	0.00029	0.51 ± 0.12	0.030±0.007	0.000047	0.09 ± 0.02	20.38 ± 3.11
S6/97	9.58 ± 1.92	0.54 ± 0.22	3.76 ± 0.75	0.05 ± 0.02	0.00039	0.33 ± 0.07	0.09 ± 0.02	0.000072	0.06 ± 0.01	14.41 ± 2.07
S7/97	12.12 ± 2.42	0.66 ± 0.26	5.36 ± 1.07	0.07 ± 0.03	0.00043	0.53 ± 0.16	0.12 ± 0.04	0.000075	0.09 ± 0.02	18.95 ± 2.67
S9/97	12.09 ± 2.42	0.64 ± 0.26	3.03 ± 0.61	0.04 ± 0.02	0.00021	0.21 ± 0.07	0.03 ± 0.01	0.000055	0.06 ± 0.01	16.10 ± 2.51
S11/97	8.98 ± 1.80	0.44 ± 0.18	6.70 ± 1.34	0.08 ± 0.03	0.00082	1.13 ± 0.23	0.22 ± 0.04	0.000079	0.11 ± 0.02	17.66 ± 2.26
S12/97	11.70 ± 2.34	0.61 ± 0.25	4.59 ± 0.92	0.06 ± 0.02	0.00037	0.39 ± 0.12	0.09 ± 0.03	0.000077	0.08 ± 0.02	17.51 ± 2.53
Lesotho Highlands										
L2/97	11.10 ± 2.22	0.53 ± 0.21	3.66 ± 0.73	0.04 ± 0.02	0.00030	0.30 ± 0.07	0.08 ± 0.02	0.000059	0.06 ± 0.01	15.76 ± 2.35
L3/97	13.83 ± 2.77	0.67 ± 0.27	4.30 ± 0.86	0.05 ± 0.02	0.00033	0.38 ± 0.09	0.11 ± 0.02	0.000061	0.07 ± 0.02	19.42 ± 2.91
L5/97	10.21 ± 2.04	0.53 ± 0.21	5.42 ± 1.09	0.07 ± 0.03	0.00023	0.22 ± 0.05	0.04 ± 0.01	0.000100	0.09 ± 0.02	16.59 ± 2.32
L6/97	10.13 ± 2.03	0.59 ± 0.24	3.48 ± 0.70	0.05 ± 0.02	0.00035	0.32 ± 0.10	0.05 ± 0.02	0.000071	0.07 ± 0.01	14.68 ± 2.16
L8/97	10.50 ± 2.10	0.74 ± 0.30	2.96 ± 0.59	0.05 ± 0.02	0.00038	0.37 ± 0.08	0.05 ± 0.01	0.000059	0.06 ± 0.01	14.73 ± 2.20
L14/97	13.61 ± 2.72	0.63 ± 0.25	5.65 ± 1.13	0.06 ± 0.02	0.00024	0.30 ± 0.07	0.07 ± 0.02	0.000074	0.09 ± 0.02	20.42 ± 2.96
L18/97	13.92 ± 2.78	0.60 ± 0.24	4.36 ± 0.87	0.04 ± 0.02	0.00019	0.22 ± 0.05	0.08 ± 0.02	0.000054	0.06 ± 0.01	19.29 ± 2.93
L19/97	12.35 ± 2.47	0.60 ± 0.24	10.91 ± 2.18	0.12 ± 0.05	0.00040	0.60 ± 0.14	0.06 ± 0.01	0.000135	0.20 ± 0.04	24.84 ± 3.31
L20/97	11.25 ± 2.25	0.55 ± 0.22	8.43 ± 1.69	0.10 ± 0.04	0.00043	0.57 ± 0.12	0.07 ± 0.02	0.000120	0.16 ± 0.03	21.13 ± 2.82
L21/97	13.05 ± 2.61	0.65 ± 0.26	3.12 ± 0.63	0.04 ± 0.01	0.00022	0.25 ± 0.06	0.04 ± 0.01	0.000054	0.06 ± 0.01	17.21 ± 2.70
L24/97	11.66 ± 2.33	0.62 ± 0.25	2.01 ± 0.40	0.03 ± 0.01	0.00022	0.21 ± 0.07	0.04 ± 0.01	0.000042	0.04 ± 0.01	14.60 ± 2.38
L25/97	7.29 ± 1.46	0.38 ± 0.15	2.14 ± 0.43	0.03 ± 0.01	0.00014	0.15 ± 0.05	0.014±0.005	0.000040	0.04 ± 0.01	10.04 ± 1.53
L26/97	9.73 ± 1.95	0.55 ± 0.22	4.68 ± 0.94	0.06 ± 0.03	0.00100	1.12 ± 0.21	0.11 ± 0.02	0.000082	0.09 ± 0.02	16.35 ± 2.18
L27/97	11.71 ± 2.34	0.64 ± 0.26	3.78 ± 0.76	0.05 ± 0.02	0.00031	0.32 ± 0.10	0.06 ± 0.02	0.000066	0.07 ± 0.01	16.61 ± 2.48
L29/97	13.51 ± 2.70	0.63 ± 0.25	4.77 ± 0.96	0.05 ± 0.02	0.00033	0.40 ± 0.09	0.05 ± 0.01	0.000073	0.09 ± 0.02	19.51 ± 2.88

[α] Spallation and muon production from Ca; [β] Spallation and muon production from K; [χ] Production from ^{35}Cl; [δ] Production from ^{39}K; [ε] Total ^{36}Cl production from Ca, K and ^{35}Cl; [ϕ] Fraction of stopped neutrons captured by ^{35}Cl; [γ] Production rate from capture by 35Cl of thermalized neutrons; η Production rate from capture by ^{35}Cl of epithermal neutrons; [ι] Fraction of stopped neutrons captured by ^{39}K; φ Production rate from capture by ^{39}K of thermalized neutrons.

7.4.2 ESTIMATED DENUDATION / BACKWEARING RATES

Denudation rates for the free face sampling sites were calculated using two models. The first approach uses Equation 3.36 which assumes that the surface has been exposed for a sufficient period for secular equilibrium (Figure 2.5) to be achieved and that the denudation rate, ε, is in 'steady-state' (Nishiizumi *et al*, 1991). Steady-state denudation here means the continuous removal of rock that is no thicker than Λ/ρ. Unlike the samples from the flat-lying sites, the attenuation length for spallogenic reactions is not 160 g cm^{-2}, but is some shorter length related to the angle of the dipping surface (Equation 3.26, Table 7.10). This means that the thickness, perpendicular to the cliff face, varies from ~ 0.3 m for the steepest faces, to ~ 0.4 m for the less steep ones. In the field this assumption is impossible to verify over the timescale applicable to the technique. At some sample sites there was clear evidence from the free face that thin sheets were spalling and that granular disintegration was currently ongoing. However, the depth of rock removed and the rate of such removal is likely to vary temporally because of the impact of climatic change and the nature of the rock structure (eg massive or jointed, joint spacing etc.). For this reason, and because of the presence of ~ 0.5 m thick boulders on the talus slope at most sites, a second model, described below, was employed.

The attenuation lengths for spallogenic reactions on these free faces (derived using Equation 3.26), the modelled denudation rates (assuming 'steady-state' denudation), and the minimum timescales over which the rates are applicable (T_{eff}, Lal, 1991) are detailed in Table 7.10. In addition the modelled denudation rates have been converted to backwearing rates by trigonometric correction (ε / sin α, where α is the relevant slope angle).

All uncertainties are quoted at the 1 σ (68 %confidence) level. Two uncertainties are shown for the estimated denudation rate, both calculated in the same manner as for the flat-lying samples. The first uncertainty, which includes assumed random and independent errors in the site-specific production rates (20 %), decay constant (5 %) and the attenuation length (increased to 10 % for inclined surfaces), ranges between $\pm$ 17 – 32 % (1 σ level). This uncertainty is used in the calculation of T_{eff} and in subsequent discussions. For comparison, the second uncertainty, which reflects analytical errors only, generally ranges between $\pm$ 5 – 13 % (1 σ level), with the largest errors (16 % and 27 %) being recorded for the samples with large AMS uncertainties, O4/97 and N12/97.

Table 7.10: Modelled 'steady-state' denudation and backwearing rates.

Sample	Spall. Attn. length (Λ) (cm^{-2})	'Steady-state' denudation rate (ε) (m Ma^{-1})	'Steady-state' backwearing rate (m Ma^{-1})	Minimum period for denudation rates (T_{eff}) (10^3 a)
Naudesnek				
N4/95	103	63.8 ± 11.3 (± 6.8)	64.4 ± 11.4	5.5 ± 1.0
N5/97	96	23.0 ± 4.5 (± 2.0)	23.0 ± 4.5	14.0 ± 2.8
N8/97	100	44.0 ± 8.3 (± 3.2)	44.2 ± 8.3	7.7 ± 1.5
N9/97	101	48.3 ± 9.0 (± 3.3)	48.6 ± 9.0	7.1 ± 1.3
N10/97	100	17.9 ± 3.5 (± 1.5)	18.0 ± 3.5	18.5 ± 3.6
N11/97	100	49.8 ± 9.6 (± 5.1)	50.0 ± 9.6	6.8 ± 1.3
N12/97	100	117.9 ± 37.0 (± 31.2)	118.4 ± 37.1	2.9 ± 1.0
N13/97	100	19.3 ± 3.5 (± 1.2)	19.4 ± 3.5	17.2 ± 3.1
N15/97	121	26.1 ± 5.1 (± 1.6)	28.8 ± 5.6	15.4 ± 3.0
N16/97	116	28.6 ± 5.4 (± 1.8)	30.4 ± 5.7	13.6 ± 2.6
N17/97	105	23.2 ± 4.5 (± 1.7)	23.6 ± 4.6	15.1 ± 2.9
N18/97	103	36.0 ± 6.3 (± 2.4)	36.4 ± 6.4	9.6 ± 1.7
Ongeluk's Nek				
O2/97	116	12.4 ± 2.3 (± 0.7)	13.2 ± 2.4	30.0 ± 5.3
O3/97	100	33.6 ± 6.2 (± 2.5)	33.7 ± 6.2	10.0 ± 1.9
O4/97	96	94.9 ± 24.9 (± 15.0)	95.0 ± 24.9	3.5 ± 1.0
O6/97	100	27.8 ± 5.0 (± 1.6)	27.9 ± 5.0	12.1 ± 2.2
O7/97	101	29.4 ± 5.3 (± 3.0)	29.6 ± 5.3	11.5 ± 2.1
O9/97	100	131.0 ± 27.2 (± 15.0)	131.5 ± 27.3	2.6 ± 0.6
O10/97	96	23.7 ± 4.3 (± 1.6)	23.7 ± 4.3	13.5 ± 2.5
O12/97	98	41.7 ± 7.4 (± 3.0)	41.8 ± 7.4	8.0 ± 1.4
Sani Pass				
S2/95	110	49.2 ± 9.7 (± 6.3)	50.7 ± 10.0	7.6 ± 1.5
S1/97	100	30.6 ± 6.0 (± 2.4)	30.7 ± 6.0	11.0 ± 2.2
S2/97	96	46.2 ± 8.5 (± 3.3)	46.2 ± 8.5	7.0 ± 1.3
S4/97	111	33.2 ± 6.1 (± 2.0)	34.4 ± 6.3	11.2 ± 2.1
S6/97	95	54.8 ± 10.1 (± 4.1)	54.8 ± 10.1	5.9 ± 1.1
S7/97	111	27.1 ± 4.8 (± 1.7)	28.1 ± 5.0	13.7 ± 2.4
S9/97	100	62.6 ± 12.3 (± 5.5)	62.8 ± 12.3	5.4 ± 1.1
S11/97	105	31.5 ± 5.2 (± 2.1)	32.0 ± 5.3	11.2 ± 1.8
S12/97	101	24.3 ± 4.4 (± 1.5)	24.4 ± 4.4	13.9 ± 2.5
Lesotho Highlands				
L2/97	96	34.2 ± 6.3 (± 2.0)	34.2 ± 6.3	9.5 ± 1.8
L3/97	105	17.0 ± 3.2 (± 0.9)	17.3 ± 3.2	20.3 ± 3.8
L5/97	96	33.0 ± 5.9 (± 2.3)	33.0 ± 6.0	9.8 ± 1.8
L6/97	96	22.0 ± 4.1 (± 1.4)	22.0 ± 4.1	14.5 ± 2.7
L8/97	110	75.8 ± 14.1 (± 5.8)	78.1 ± 14.5	5.0 ± 1.0
L14/97	103	19.7 ± 3.7 (± 1.3)	19.9 ± 3.7	17.3 ± 3.2
L18/97	100	40.1 ± 7.5 (± 2.5)	40.3 ± 7.5	8.4 ± 1.6
L19/97	107	7.9 ± 1.4 (± 0.5)	8.1 ± 1.4	42.2 ± 6.9
L20/97	103	8.5 ± 1.5 (± 0.5)	8.6 ± 1.5	38.1 ± 6.3
L21/97	100	29.3 ± 5.6 (± 1.9)	29.4 ± 5.6	11.5 ± 2.2
L24/97	97	35.7 ± 7.1 (± 2.6)	35.7 ± 7.1	9.2 ± 1.9
L25/97	98	51.8 ± 10.1 (± 4.8)	51.9 ± 10.1	6.5 ± 1.3
L26/97	103	52.6 ± 9.3 (± 4.1)	53.1 ± 9.4	6.7 ± 1.2
L27/97	102	35.0 ± 6.5 (± 2.3)	35.3 ± 6.5	9.8 ± 1.8
L29/97	100	62.5 ± 11.6 (± 4.8)	62.7 ± 11.6	5.4 ± 1.0

The large number of sites at which ~ 0.5 m thick boulders were noticed on the well-vegetated talus slopes and the joint spacing of the basalt exposed at the free faces, suggests that faces may retreat predominantly by the intermittent shedding of blocks ~ 0.5 m thick. This process may be the sole denudation mechanism at some sites, or may operate in addition to the regular spalling of thin sheets or individual grains. If denudation does occur by the falling of blocks similar to or thicker than the attenuation length for spallogenic ^{36}Cl production (by far the most dominant production mechanism at these sites, Table 7.9), the measured ^{36}Cl content should be interpreted in terms of a surface exposure age. Given the attenuation length for these samples (Table 7.10), this would apply to blocks thicker than ~ 0.3 – 0.4 m.

Equation 2.7 was used to derive the surface exposure ages for this denudation model, P_{sp} being substituted by P_{total} for ^{36}Cl production, and assuming that periodic shedding of blocks was the sole denudation mechanism. The total production rate for the surface of the free face sites is given in Table 7.9, however, this needs to be modified before calculating the exposure age for the intermittent shedding of ~ 0.5 m thick blocks. Because ^{36}Cl is produced beneath the surface, part of the measured ^{36}Cl concentration, $^{36}Cl_{cosmogenic}$ (Table 7.6), will have been produced while the sampled surface was, respectively, 0.5 m, 1.0 m, 1.5 m, 2.0 m etc., perpendicularly beneath the surface. The removal of each previous 0.5 m thick block brings the sampled surface closer to the surface and therefore into a higher ^{36}Cl production zone. Therefore in interpreting the measured ^{36}Cl concentration as an exposure age, account needs to be taken of this 'prior' exposure. Ignoring subsurface production leads to an overestimate of the surface exposure age and corresponding underestimate in the denudation rate derived from this. This 'prior' exposure was dealt with by calculating the total ^{36}Cl production rate (again assuming a 20 % uncertainty at the 1 σ level) at depths of 2 m, 1.5 m, 1.0 m and 0.5 m perpendicularly beneath the sloping surface (Appendix 7) and integrating these with the surface production rate (P_{total}, Table 7.9). Production at depths below 2 m at these sites is insignificant even from negative muon reactions and therefore was ignored.

Assuming that denudation by this process proceeds by the regular shedding of blocks of comparable thickness, surface exposure ages calculated as described above represent the minimum time interval between shedding events. These ages therefore provide maximum limits on the denudation rate for the regular shedding of ~ 0.5 m thick blocks. Using the same trigonometric correction as for the 'steady-state' model denudation rates, maxima backwearing rates have been derived. These rates, together with the relevant surface exposure ages, are detailed in Table 7.11. Uncertainties in the production rates (20 %) and

the decay constant (5 %) (both assumed random and independent), together with measurement uncertainties in the AMS ratio and target elements, were propagated as before. Uncertainties are quoted at the 1 σ (68 % confidence) level.

Table 7.11: Modelled 'regular 0.5 m thick block fall' denudation and backwearing rates.

Sample	Surface Exposure Age (10^3 a)	Maximum Perpendicular Denudation Rate (m Ma^{-1})	Maximum Backwearing Rate (m Ma^{-1})
Naudesnek			
N4/95	5.3 ± 1.2	94.3 ± 22.5	95.3 ± 22.7
N5/97	12.0 ± 2.6	41.7 ± 9.5	41.7 ± 9.5
N8/97	6.6 ± 1.4	75.8 ± 16.8	76.0 ± 16.9
N9/97	6.0 ± 1.3	83.3 ± 18.9	83.8 ± 19.0
N10/97	15.5 ± 3.4	32.3 ± 7.4	32.4 ± 7.5
N11/97	5.8 ± 1.3	86.2 ± 20.3	86.5 ± 20.4
N12/97	2.4 ± 0.9	208.3 ± 90.9	209.1 ± 91.3
N13/97	15.1 ± 3.2	33.1 ± 7.3	33.2 ± 7.4
N15/97	11.8 ± 2.5	42.4 ± 9.4	46.8 ± 10.4
N16/97	10.7 ± 2.2	46.7 ± 10.0	49.7 ± 10.7
N17/97	12.4 ± 2.7	40.3 ± 9.2	40.9 ± 9.4
N18/97	8.2 ± 1.7	61.0 ± 13.2	61.6 ± 13.3
Ongeluk's Nek			
O2/97	23.9 ± 5.0	20.9 ± 4.6	22.3 ± 4.9
O3/97	8.6 ± 1.9	58.1 ± 13.5	58.4 ± 13.6
O4/97	3.1 ± 1.0	161.3 ± 58.1	161.4 ± 58.1
O6/97	10.4 ± 2.2	48.1 ± 10.6	48.3 ± 10.7
O7/97	9.9 ± 2.1	50.5 ± 11.2	50.8 ± 11.3
O9/97	2.2 ± 0.5	227.3 ± 54.5	228.1 ± 54.7
O10/97	11.8 ± 2.5	42.4 ± 9.4	42.4 ± 9.4
O12/97	6.8 ± 1.5	73.5 ± 17.0	73.7 ± 17.1
Sani Pass			
S2/95	6.2 ± 1.5	80.6 ± 20.7	83.1 ± 21.4
S1/97	9.2 ± 2.0	54.3 ± 12.4	54.6 ± 12.4
S2/97	6.0 ± 1.3	83.3 ± 18.9	83.4 ± 19.0
S4/97	9.1 ± 1.9	54.9 ± 12.0	56.9 ± 12.4
S6/97	5.1 ± 1.1	98.0 ± 22.2	98.1 ± 22.2
S7/97	11.0 ± 2.3	45.5 ± 9.9	47.1 ± 10.3
S9/97	4.5 ± 1.0	111.1 ± 26.0	111.5 ± 26.1
S11/97	9.6 ± 2.3	52.1 ± 13.2	52.9 ± 13.4
S12/97	11.6 ± 2.5	43.1 ± 9.7	43.3 ± 9.8
Lesotho Highlands			
L2/97	8.0 ± 1.7	62.5 ± 13.9	62.5 ± 13.9
L3/97	16.6 ± 3.5	30.1 ± 6.6	30.6 ± 6.7
L5/97	8.3 ± 1.8	60.2 ± 13.7	60.3 ± 13.7
L6/97	12.5 ± 2.6	40.0 ± 8.7	40.0 ± 8.7
L8/97	4.1 ± 0.9	122.0 ± 28.1	125.7 ± 29.0
L14/97	14.1 ± 3.0	35.5 ± 7.9	35.8 ± 8.0
L18/97	6.9 ± 1.4	72.5 ± 15.3	72.7 ± 15.4
L19/97	35.1 ± 7.3	14.2 ± 3.1	14.6 ± 3.2
L20/97	32.2 ± 6.8	15.5 ± 3.4	15.7 ± 3.5
L21/97	9.5 ± 2.0	52.6 ± 11.6	52.8 ± 11.6
L24/97	7.8 ± 1.7	64.1 ± 14.7	64.2 ± 14.7
L25/97	5.5 ± 1.2	90.9 ± 20.8	91.1 ± 20.9
L26/97	5.8 ± 1.3	86.2 ± 20.3	87.1 ± 20.5
L27/97	8.2 ± 1.7	61.0 ± 13.2	61.4 ± 13.3
L29/97	4.5 ± 1.0	111.1 ± 26.0	111.5 ± 26.1

The backwearing results derived using the 'steady-state' model ('SSM', Table 7.10) and the 0.5 m block fall model ('BFM', Table 7.11) are shown in relation to their field settings in Figures 7.5 (Naudesnek), 7.6 (Ongeluk's Nek), 7.7 (Sani Pass) and 7.8 (Lesotho Highlands). Again, like the denudation estimates for the flat-lying samples, the backwearing results are variable, both within sampling locations and between morphological settings.

At Naudesnek (Figure 7.5), estimated backwearing rates for the main escarpment free face vary between 18.0 ± 3.5 m Ma^{-1} and 118.4 ± 37.1 m Ma^{-1} (SSM) or 32.4 ± 7.5 m Ma^{-1} and 209.1 ± 91.3 m Ma^{-1} (BFM). Interestingly this highest rate (N12/97) and one of the lowest rates (N13/97) of 19.4 ± 3.5 m Ma^{-1} (SSM) or 33.2 ± 7.4 m Ma^{-1} (BFM), are produced by two samples from the same location. N12/97 is from the eastmost face of the uppermost exposed flow on the northern side of Naudesnek (A, Figure 7.5), while N13/97 is from the southeast side of the same face, but from a lower flow. A similar backwearing rate, 23.0 ± 4.5 m Ma^{-1} (SSM) or 41.7 ± 9.5 m Ma^{-1} (BFM), was estimated for N5/97 (also southeast aspect) which was collected at the western end of the same free face (B, Figure 7.5).

On the southern side of Naudesnek (Figure 7.5), similar backwearing estimates of 44.2 ± 8.3 m Ma^{-1} (SSM) or 76.0 ± 16.9 m Ma^{-1} (BFM) and 48.6 ± 9.0 m Ma^{-1} (SSM) or 83.8 ± 19.0 m Ma^{-1} (BFM), respectively, were determined for samples N8/97 and N9/97. These were collected from the same section of free face, ~ 40 m apart. Sample N11/97, collected from another section of free face ~ 100 m further north, also yielded a similar rate of 50.0 ± 9.6 m Ma^{-1} (SSM) or 86.5 ± 20.4 m Ma^{-1} (BFM). N10/97 yielded the lowest backwearing estimate at Naudesnek (18.0 ± 3.5 m Ma^{-1} (SSM) or 32.4 ± 7.5 m Ma^{-1} (BFM)). This sample is from the free face on the north side of the grassed gully which separates the face from which N8/97 and N9/97 were collected from the face which provided N11/97 (Figure 7.5). N4/95, which is from a another section of free face, ~ 600 m south of the location of N8/97 (Figure 7.5), produces a backwearing rate of 64.4 ± 11.4 m Ma^{-1} (SSM) or 95.3 ± 22.7 m Ma^{-1} (BFM). This is similar, within the 1 σ level uncertainty, to the results from N8/97, N9/97 and N11/97 (Figure 7.5).

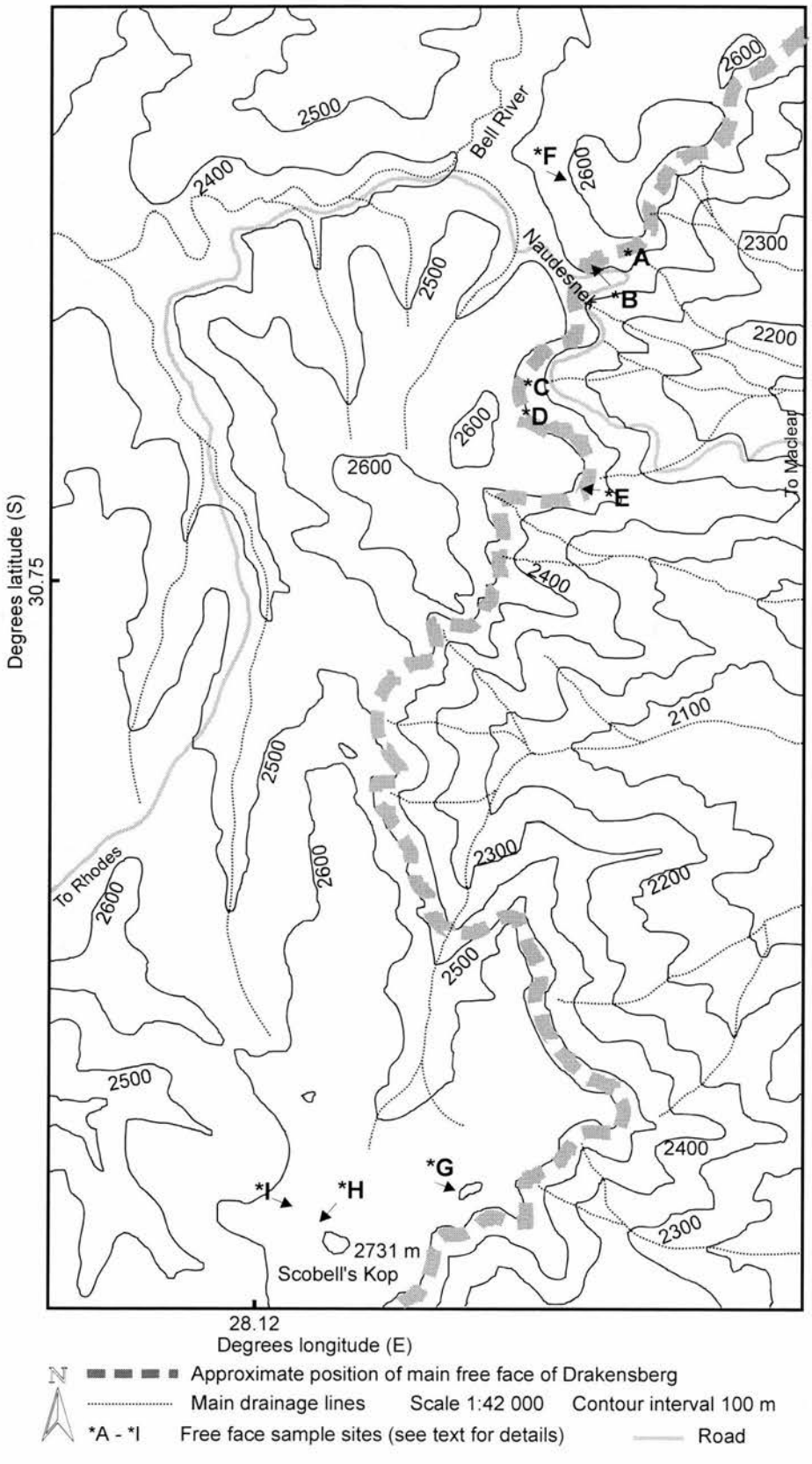

Site / Sample	Model	Backwearing rate (m Ma^{-1})
A		
N12/97	SSM	118.4 +/- 37.1
	BFM	209.1 +/- 91.3
N13/97	SSM	19.4 +/- 3.5
	BFM	33.2 +/- 7.4
B		
N5/97	SSM	23.0 +/- 4.5
	BFM	41.7 +/- 9.5
C		
N10/97	SSM	18.0 +/- 3.5
	BFM	32.4 +/- 7.5
N11/97	SSM	50.0 +/- 9.6
	BFM	86.5 +/- 20.4
D		
N8/97	SSM	44.2 +/- 8.3
	BFM	76.0 +/- 16.9
N9/97	SSM	48.6 +/- 9.0
	BFM	83.8 +/- 19.0
E		
N4/95	SSM	64.4 +/- 11.4
	BFM	95.3 +/- 22.7
F		
N18/97	SSM	36.4 +/- 6.4
	BFM	61.6 +/- 13.3
G		
N15/97	SSM	28.8 +/- 5.6
	BFM	46.8 +/- 10.4
H		
N16/97	SSM	30.4 +/- 5.7
	BFM	49.7 +/- 10.7
I		
N17/97	SSM	23.6 +/- 4.6
	BFM	40.9 +/- 9.4

Figure 7.5: The escarpment at Naudesnek showing the location of the free face sample sites and the backwearing rates calculated using both the 'steady-state' model (SSM) and the regular shedding of 0.5 m thick blocks model (BFM). All backwearing rates in m Ma^{-1}. Based on Figure 7.1.

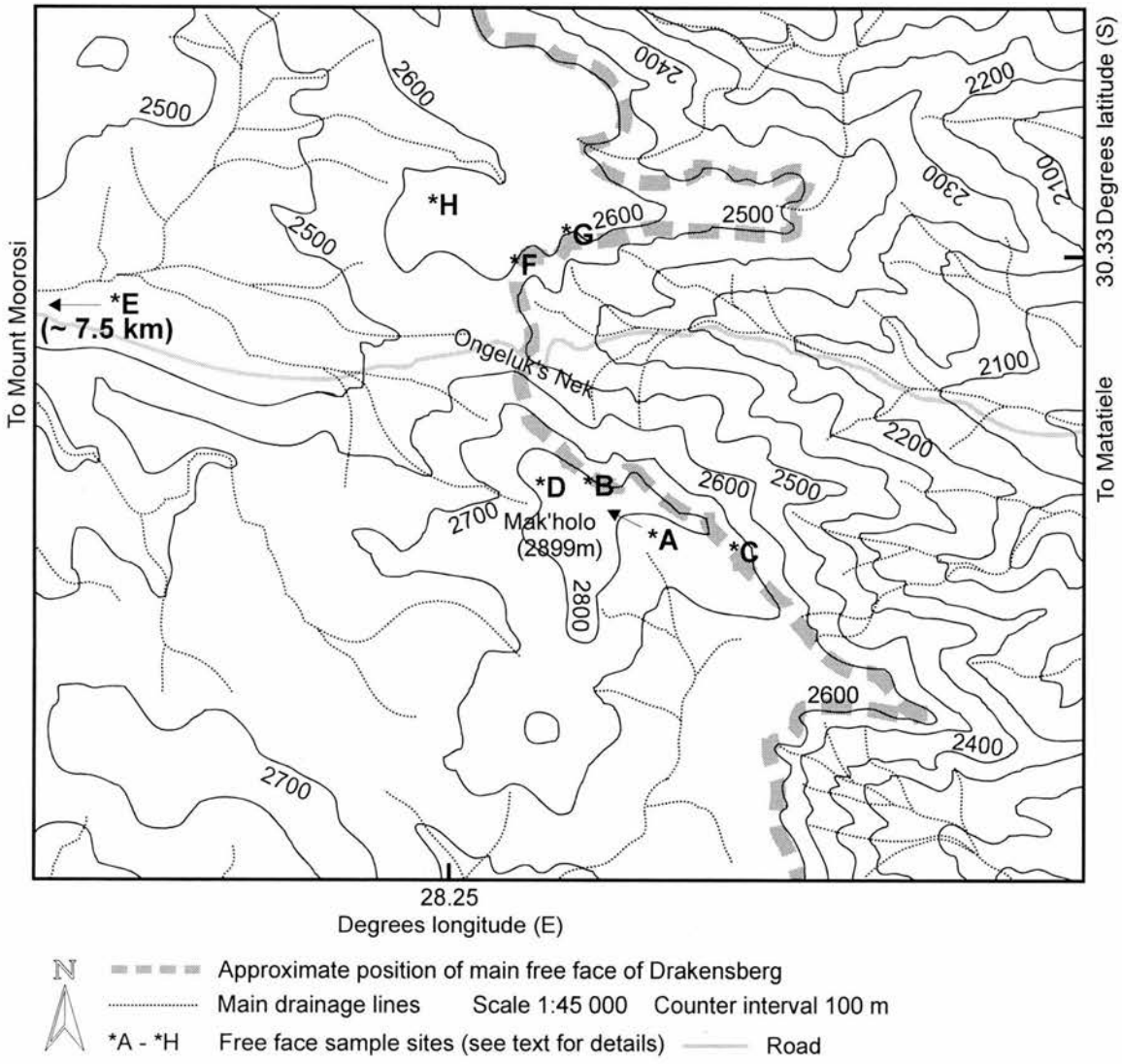

Site	Sample	Model	Backwearing rate (m Ma^{-1})
A	O2/97	SSM	13.2 +/- 2.4
		BFM	22.3 +/- 4.9
B	O3/97	SSM	33.7 +/- 6.2
		BFM	58.4 +/- 13.6
C	O4/97	SSM	95.0 +/- 24.9
		BFM	161.4 +/- 58.1
D	O6/97	SSM	27.9 +/- 5.0
		BFM	48.3 +/- 10.7
E	O7/97	SSM	29.6 +/- 5.3
		BFM	50.8 +/- 11.3
F	O9/97	SSM	131.5 +/- 27.3
		BFM	228.1 +/- 54.7
G	O10/97	SSM	23.7 +/- 4.3
		BFM	42.4 +/- 9.4
H	O12/97	SSM	41.8 +/- 7.4
		BFM	73.7 +/- 17.1

Figure 7.6: The location of free face samples at Ongeluk's Nek. Backwearing rates shown were calculated using both the SSM and BFM models. All rates in m Ma^{-1}. Based on Figure 7.2.

The samples from the main escarpment free face at Ongeluk's Nek (Figure 7.6) also show variability. O3/97 and O4/97 (B and C, Figure 7.6) collected from ~ 1 km apart on the main free face below the summit of Mak'holo on the southern side of the pass, produce estimated backwearing rates of, respectively, 33.7 ± 6.2 m Ma^{-1} (SSM) or 58.4 ± 13.6 m Ma^{-1} (BFM) and 95.0 ± 24.9 m Ma^{-1} (SSM) or 161.4 m Ma^{-1} (BFM). On the lower altitude, northern side of Ongeluk's Nek, similar variability is encountered. O9/97 (F, Figure 7.6) yields the highest estimated backwearing rate of all samples in this study of 131.5 ± 27.3 m Ma^{-1} (SSM) or 228.1 ± 54.7 m Ma^{-1} (BFM). Sample O10/97, which was collected from another section of free face ~ 200 m east of O9/97, produced a much smaller estimated backwearing rate of 23.7 ± 4.3 m Ma^{-1} (SSM) or 42.4 ± 9.4 m Ma^{-1} (BFM).

The estimates for the rate of backwearing of the main escarpment free face at Sani Pass (Figure 7.7) are similarly variable. Three samples (S2/95, S6/97 and S7/97) were collected within a ~ 100m long section at the eastern end of the main free face that forms the Twelve Apostles (A, Figure 7.7). Similar estimates were produced by S2/95, 50.7 ± 10.0 m Ma^{-1} (SSM) or 83.1 ± 21.4 m Ma^{-1} (BFM), and S6/97, 54.8 ± 10.1 m Ma^{-1} (SSM) or 98.1 ± 22.2 m Ma^{-1} (BFM), which are from sites ~ 50 m apart. S7/97 is the furthest west of these samples and is from a site which juts out ~ 5 – 10 m from the general line of the rest of the face. This sample yielded a lower backwearing estimate of 28.1 ± 5.0 m Ma^{-1} (SSM) or 47.1 ± 10.3 m Ma^{-1} (BFM). Samples from two other sites on the Twelve Apostles (B and C, Figure 7.7), produced similarly variable estimates. S9/97 (B, Figure 7.7) produced an estimated rate of 62.8 ± 12.3 m Ma^{-1} (SSM) or 111.5 ± 26.1 m Ma^{-1} (BFM), while a lower rate of 24.4 ± 4.4 m Ma^{-1} (SSM) or 43.3 ± 9.8 m Ma^{-1} (BFM) was determined for S12/97 (C, Figure 7.7). On the southern side of Sani Pass, S1/97 (D, Figure 7.7) yielded an estimated backwearing rate of 30.7 ± 6.0 m Ma^{-1} (SSM) or 54.6 ± 12.4 m Ma^{-1} (BFM). S2/97, which was collected ~ 100 m further east along the same face, produced an estimated backwearing rate 50 % higher at 46.2 ± 8.5 m Ma^{-1} (SSM) or 83.4 ± 19.0 m Ma^{-1} (BFM).

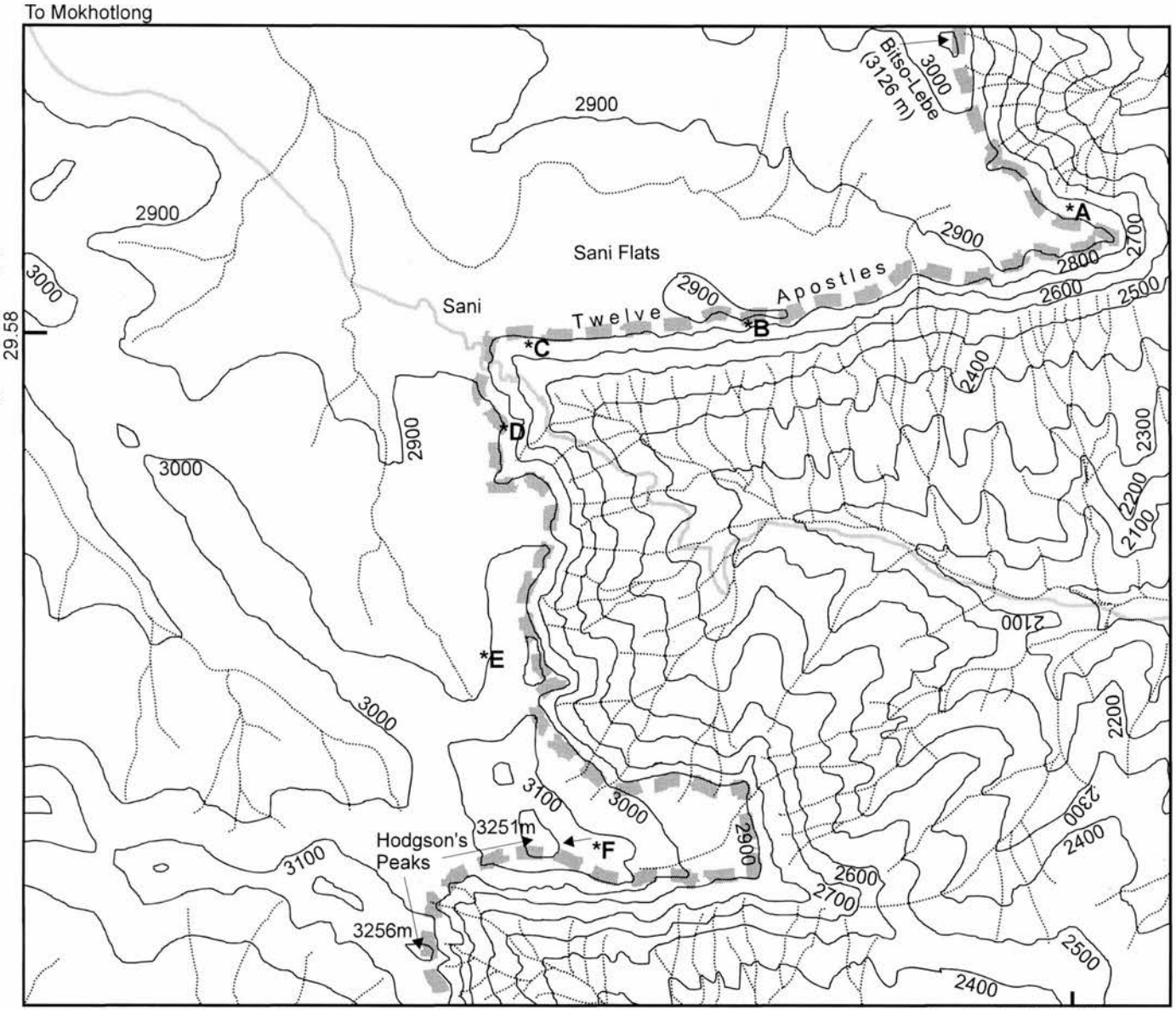

Site	Sample	Model	Backwearing rate (m Ma^{-1})
A	S2/95	SSM	50.7 +/- 10.0
		BFM	83.1 +/- 21.4
	S6/97	SSM	54.8 +/- 10.1
		BFM	98.1 +/- 22.2
	S7/97	SSM	28.1 +/- 5.0
		BFM	47.1 +/- 10.3
B	S9/97	SSM	62.8 +/- 12.3
		BFM	111.5 +/- 26.1
C	S12/97	SSM	24.4 +/- 4.4
		BFM	43.3 +/- 9.8
D	S1/97	SSM	30.7 +/- 6.0
		BFM	54.6 +/- 12.4
	S2/97	SSM	46.2 +/- 8.5
		BFM	83.4 +/- 19.0
E	S11/97	SSM	32.0 +/- 5.3
		BFM	52.9 +/- 13.4
F	S4/97	SSM	34.4 +/- 6.3
		BFM	56.9 +/- 12.4

Figure 7.7: Free face sample sites at Sani Pass. Backwearing rates shown are derived using both SSM and BFM models. All rates in m Ma^{-1}. Based on Figure 7.3.

Estimated backwearing rates for samples collected from non-main escarpment free faces settings at Naudesnek, Ongeluk's Nek and Sani Pass are not substantially different from the rates discussed above. At Naudesnek, N15/97 and N16/97 from the west facing and northeast facing, respectively, valley sides of the small inland drainage basin at Scobell's Kop (G and H, Figure 7.5), yielded similar estimated backwearing rates of 28.8 ± 5.6 m Ma^{-1} (SSM) or 46.8 ± 10.4 m Ma^{-1} (BFM) and 30.4 ± 5.7 m Ma^{-1} (SSM) or 49.7 ± 10.7 m Ma^{-1} (BFM), respectively. These are comparable to the estimated backwearing rates from other inland facing free faces at Naudesnek (F and I, Figure 7.5). N17/97 (I, Figure 7.5) yielded a rate of 23.6 ± 4.6 m Ma^{-1} (SSM) or 40.9 ± 9.4 m Ma^{-1} (BFM), while N18/97 (F, Figure 7.5) produced an estimated backwearing rate of 36.4 ± 6.4 m Ma^{-1} (SSM) or 61.6 ± 13.3 m Ma^{-1} (BFM).

The three inland facing free faces sampled at Ongeluk's Nek (Figure 7.6) yielded rates ranging from 13.2 ± 2.4 m Ma^{-1} to 41.8 ± 7.4 m Ma^{-1} (SSM) or 22.3 ± 4.9 m Ma^{-1} to 73.7 ± 17.1 m Ma^{-1} (BFM). O2/97, from the eastern side of the summit of Mak'holo, ~ 150 m inland of the main escarpment free face (Figure 7.6), yielded a backwearing rate of 13.2 ± 2.4 m Ma^{-1} (SSM) or 22.3 ± 4.9 m Ma^{-1} (BFM). Meanwhile, O6/97, from the eastern side of this summit, which is ~ 300m inland of the escarpment edge, produced a estimated rate of 27.9 ± 5.0 m Ma^{-1} (SSM) or 48.3 ± 10.7 m Ma^{-1} (BFM). Site H (Figure 7.6), which is the inland face of the knoll which forms the summit on the northern side of the pass, provided sample O12/97. This yielded an estimated backwearing rate of 41.8 ± 7.4 m Ma^{-1} (SSM) or 73.7 ± 17.1 m Ma^{-1} (BFM).

At Sani Pass, two samples were collected from free faces which were not part of the main escarpment free face. S4/97 (F, Figure 7.7) is from a free face which forms part of the western edge of a small drainage basin which drains over the escarpment to the northeast of Hodgson's Peaks. This sample yielded an estimated backwearing rate of 34.4 ± 6.3 m Ma^{-1} (SSM) or 56.9 ± 12.4 m Ma^{-1} (BFM), which is similar to the results from Naudesnek for the same type of setting. An estimated backwearing rate of 32.0 ± 5.3 m Ma^{-1} (SSM) or 52.9 ± 13.4 m Ma^{-1} (BFM) was produced by S11/97 (E, Figure 7.7), an inland facing free face which is ~ 300 m inland of the escarpment edge at Sani Pass.

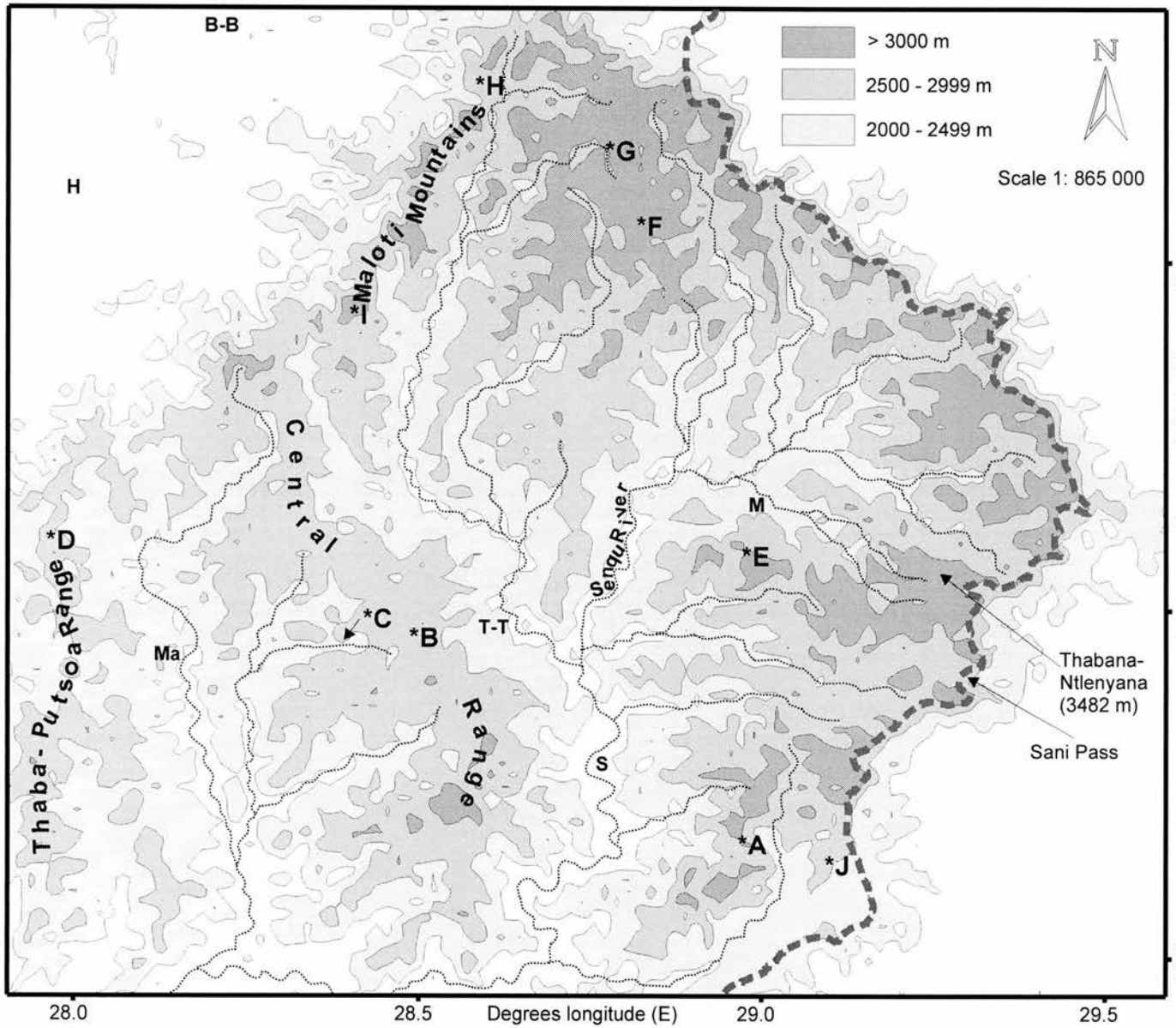

Approximate position of Drakensberg
Main Rivers
*A - *J Free face sample sites (see text for details)

Towns:
B-B Butha-Buthe
H Hlotse
Ma Marakabei
M Mokhotlong
T-T Thaba-Tseka
S Sehonghong

Site	Sample	Model	Backwearing rate (m Ma^{-1})
A	L2/97	SSM	34.2 +/- 6.3
		BFM	62.5 +/- 13.9
	L3/97	SSM	17.3 +/- 3.2
		BFM	30.6 +/- 6.7
B	L5/97	SSM	33.0 +/- 6.0
		BFM	60.3 +/- 13.7
C	L6/97	SSM	22.0 +/- 4.1
		BFM	40.0 +/- 8.7
D	L8/97	SSM	78.1 +/- 14.5
		BFM	125.7 +/- 29.0
E	L14/97	SSM	19.9 +/- 3.7
		BFM	35.8 +/- 8.0
F	L18/97	SSM	40.3 +/- 7.5
		BFM	72.7 +/- 15.4
G	L19/97	SSM	8.1 +/- 1.4
		BFM	14.6 +/- 3.2
	L20/97	SSM	8.6 +/- 1.5
		BFM	15.7 +/- 3.5
	L21/97	SSM	29.4 +/- 5.6
		BFM	52.8 +/- 11.6
H	L27/97	SSM	35.3 +/- 6.5
		BFM	61.4 +/- 13.3
I	L29/97	SSM	62.7 +/- 11.6
		BFM	111.5 +/- 26.1
J	L24/97	SSM	35.7 +/- 7.1
		BFM	64.2 +/- 14.7
	L25/97	SSM	51.9 +/- 10.1
		BFM	91.1 +/- 20.9
	L26/97	SSM	53.1 +/- 9.4
		BFM	87.1 +/- 20.5

Figure 7.8: Free face sample sites in the Lesotho Highlands. Backwearing rates calculated using both the SSM and BFM models. All rates in m Ma^{-1}. Based on Figure 7.4.

Figure 7.8 shows the estimated backwearing rates derived from samples collected in the Lesotho Highlands. The estimated backwearing rates for free faces at the head of river valleys (Table 7.4) range from 17.3 ± 3.2 m Ma^{-1} (L3/97) to 62.7 ± 11.6 m Ma^{-1} (L29/97) (SSM) or 30.6 ± 6.7 m Ma^{-1} (L3/97) to 111.5 ± 26.1 m Ma^{-1} (L29/97) (BFM). Samples collected from free faces at valley sides (Table 7.4) have produced a greater range. The lowest rates were returned by samples L19/97 and L20/97 which are from free faces that crop out midway up the east and west valley sides of the Motete River valley (G, Figure 7.8). These yielded very low rates of 8.1 ± 1.4 m Ma^{-1} (SSM) or 14.6 ± 3.2 m Ma^{-1} (BFM) and 8.6 ± 1.5 m Ma^{-1} (SSM) or 15.7 ± 3.5 m Ma^{-1} (BFM), respectively. About 3 km downstream in the Motete Valley, L21/97, also from a midslope free face, yielded an estimated backwearing rate of 29.4 ± 5.6 m Ma^{-1} (SSM) or 52.8 ± 11.6 m Ma^{-1} (BFM). This is similar to the results from free faces just below the drainage divides at sites near Ongeluk's Nek (O7/97, E, Figure 7.6) and above the Tenane River (L6/97, C, Figure 7.8). The highest estimated backwearing rate from a free face occurring in a valley side is from sample L8/97. This sample is from the midslope on the western side of Thaba-Putsoa (D, Figure 7.8) and yielded a rate of 78.1 ± 14.5 m Ma^{-1} (SSM) or 125.7 ± 29.0 m Ma^{-1} (BFM).

Two samples were collected from free faces which form the sides of summits in lower relief areas of the Lesotho Highlands. Despite these being collected ~ 75 km apart (Figure 7.8), the estimated backwearing rates are similar with L5/97 yielding a rate of 33.0 ± 6.0 m Ma^{-1} (SSM) or 60.3 ± 13.7 m Ma^{-1} (BFM) and L18/97 producing a rate of 40.3 ± 7.5 m Ma^{-1} (SSM) or 72.7 ± 15.4 m Ma^{-1} (BFM). These rates are similar to the estimated backwearing rates yielded by the inland facing free faces at the escarpment sites (Figures 7.5, 7.6, 7.7) which are similarly fronted by lower relief regions.

Possible causes and the implications of the variations in the individual results are assessed in Section 8.3. The broader implications of the backwearing rates for the development of the southern Drakensberg escarpment and the Lesotho Highlands are discussed in Chapter 8.

CHAPTER 8: IMPLICATIONS OF THE RESULTS FOR THE DEVELOPMENT OF THE SOUTHERN DRAKENSBERG AND LESOTHO HIGHLANDS LANDSCAPES

8.1 INTRODUCTION

Estimated denudation rates for flat-lying samples and backwearing rates for free face sites, derived from the analysis of *in situ*-produced cosmogenic ^{36}Cl, were presented in Chapters 6 and 7. For ease of reference these results are summarised below. The main focus of this chapter is the discussion of the implications of these results for our understanding of the development of the southern Drakensberg and Lesotho Highlands landscapes. This discussion is split into three sections which consider the implications of the denudation and backwearing results separately and then collectively. Where possible the results are also considered in the light of independent, longer term, constraints on rates of long-term landscape change in the study area, and with general predictions from passive margin modelling. However, before discussing the significance of the denudation / backwearing data, the possible causes and implications of variations in the site-to-site results are considered.

8.2 SUMMARY OF DENUDATION AND BACKWEARING RESULTS

8.2.1 DENUDATION RATES FOR FLAT-LYING SAMPLES

The estimated denudation rates for the flat-lying sample sites, derived using the 'steady-state' model (Lal, 1991), are summarised in Figure 8.1 in which the samples have been grouped on the basis of their general morphological setting. Figure 8.1A shows the denudation rates for the samples (and analytical replicates) collected at the three locations on the escarpment summit and on the buttress ridge at Naudesnek. Figure 8.1B summarises the denudation estimates for the samples (and analytical replicates) collected from the Lesotho Highlands (including O8/97), grouped according to whether they were collected from lower relief summits, valley head summits or valley side summits. Where samples were taken from the same surface this is also indicated. The starred letters (eg A, B etc.) refer to the sample's

location on the relevant location map (Figure 6.8: Naudesnek; Figure 6.9: Ongeluk's Nek; Figure 6.10: Sani Pass; and Figure 6.11: Lesotho Highlands).

8.2.2 FREE FACE BACKWEARING RATES

A summary of the estimated backwearing rates for the free face samples, determined using both the 'steady-state' model (Lal, 1991) (SSM) and the regular shedding of 0.5 m thick blocks model (Chapter 7) (BFM), are given in Figure 8.2. Again, this figure shows the results grouped according to their morphological settings. Figure 8.2A compares the backwearing rates, calculated using both models, for the samples collected from the main free face of the escarpment at Naudesnek, Ongeluk's Nek and Sani Pass. The backwearing results for samples collected at these three locations from non-main escarpment free faces (eg from free faces which were inland facing) are summarised in Figure 8.2B. This figure also shows the backwearing rates for the sites in the Lesotho Highlands (including O7/97, collected from ~ 7.5 km west of Ongeluk's Nek). These are grouped according to whether the free face was situated at the head of a river valley, at a valley side or formed the side of a summit in a lower relief area. The starred letter after the sample name refers to the sample's location on the appropriate location map (Naudesnek – Figure 7.5; Ongeluk's Nek – Figure 7.6; Sani Pass – Figure 7.7; and Lesotho Highlands – Figure 7.8).

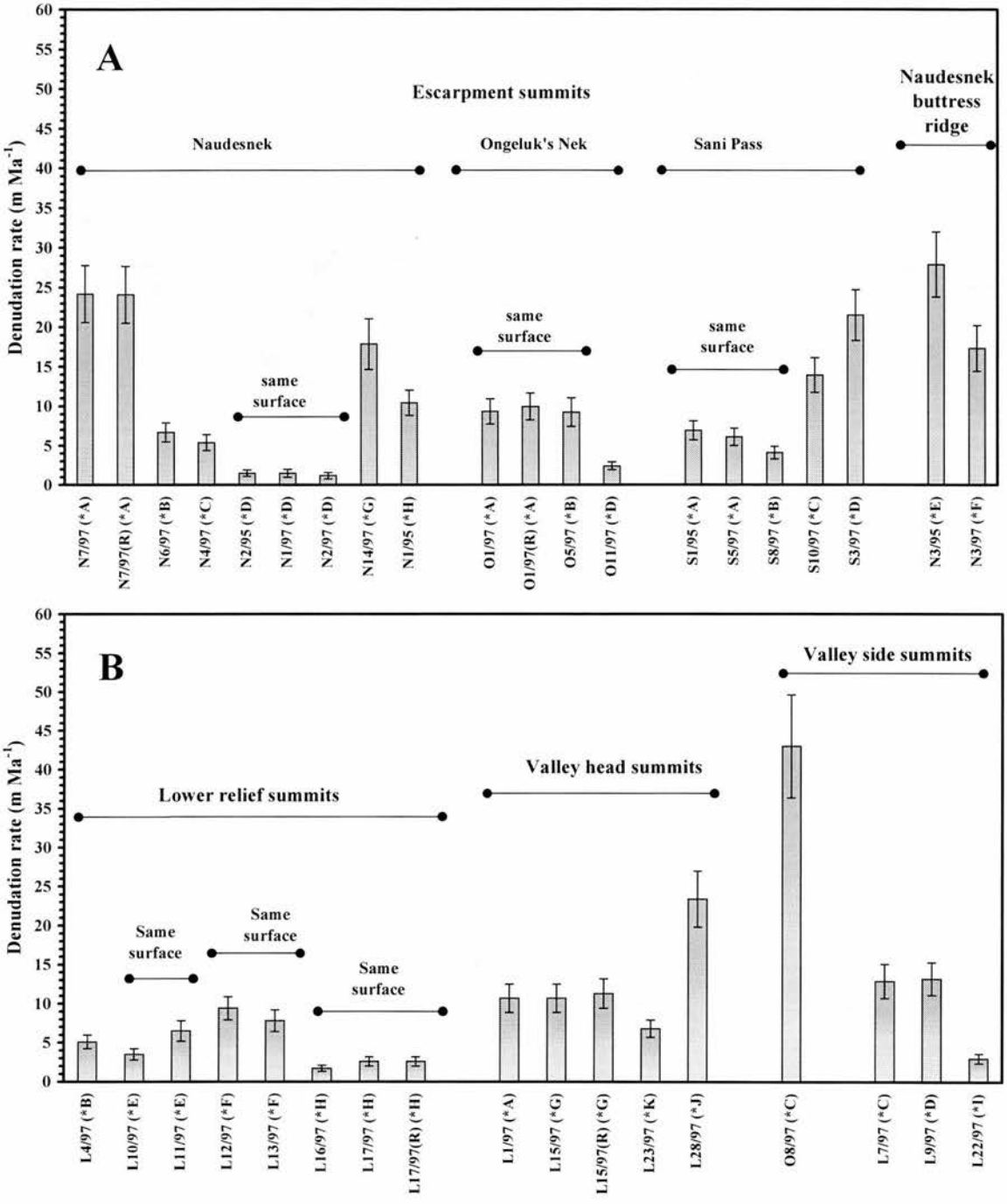

Figure 8.1: Estimated denudation rates for flat-lying samples, grouped according to morphological setting. Figure A summarises the results for the samples from the summit of the southern Drakensberg at Naudesnek, Ongeluk's Nek and Sani Pass, as well as the samples from the buttress ridge at Naudesnek. Figure B summarises the results for the samples collected from the Lesotho Highlands' sites (including O8/97). In both, samples collected from the same surface are indicated. The starred letter after each sample refers to the sample's location on the relevant map (Figures 6.8 (Naudesnek); 6.9 (Ongeluk's Nek); 6.10 (Sani Pass) and 6.11 (Lesotho Highlands)). Error bars for the 1 σ (68 % confidence) level are shown with the uncertainty being derived as explained in Chapter 6.

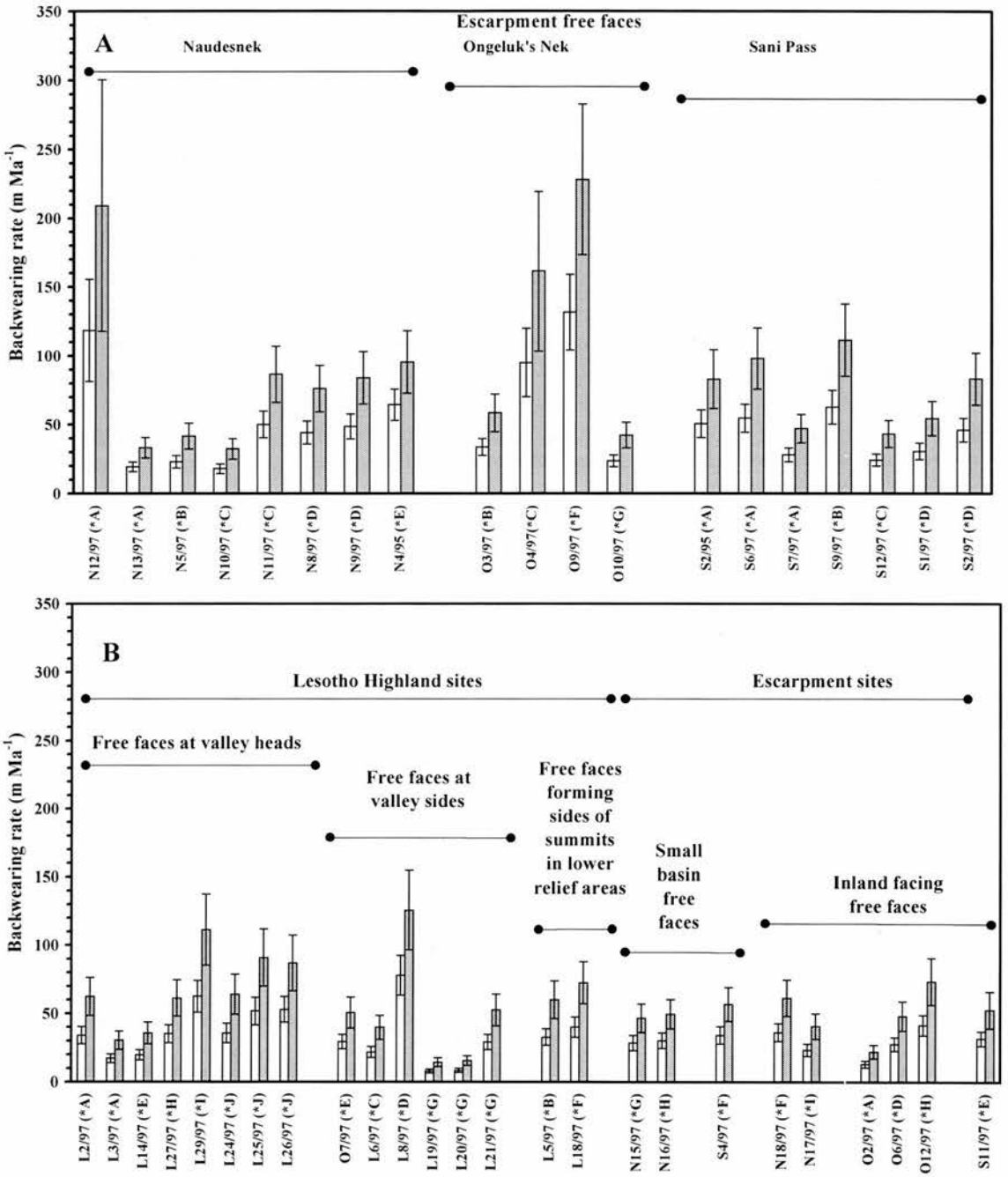

Figure 8.2: Backwearing rates estimated using both the 'steady-state' model (Lal, 1991) - white column - and the regular loss of 0.5 m thick blocks (Chapter 7) - grey column. Figure A summarises the results for samples collected from the main escarpment free face sites at Naudesnek, Ongeluk's Nek and Sani Pass. Figure B shows the results for samples collected from free face sites in the Lesotho Highlands and from non-main escarpment free face sites at Naudesnek, Ongeluk's Nek and Sani Pass. The starred letter refers to the sample's location on the relevant map (Naudesnek - Figure 7.5; Ongeluk's Nek - Figure 7.6; Sani Pass - Figure 7.7; and Lesotho Highlands - Figure 7.8). Error bars for the 1 σ (68 % confidence) level uncertainties are shown (derived as explained in Chapter 7).

8.3 ASSESSING THE POSSIBLE CAUSES AND IMPLICATIONS OF VARIABILITY IN THE DENUDATION / BACKWEARING ESTIMATES

Although samples which were collected from the same surface have yielded similar denudation rates (Figure 8.1), variability is generally encountered within both the denudation and backwearing estimate datasets (Figures 8.1 and 8.2). Whilst this might be expected for samples collected from different morphological settings, the variability also exists in results from samples taken from similar morphological settings. For example, at Ongeluk's Nek, main escarpment free face retreat rate estimates, calculated using the block fall model, vary between ~ 42 m Ma^{-1} (O10/97) and ~ 228 m Ma^{-1} (O9/97). Samples from non-escarpment free faces at Ongeluk's Nek, again derived using the BFM, yield rates, which although generally lower, vary between ~ 22 m Ma^{-1} (O2/97) and ~ 74 m Ma^{-1}. Therefore, before considering the significance of the *in situ*-produced cosmogenic ^{36}Cl derived denudation and backwearing rates for the landscape development in the study area, it is worth assessing the possible causes of these variations and what the implications of such variability might be. The possible causes of variations can be broadly grouped into those related to incomplete fulfilment of the interpretive model assumptions and those related to the field characteristics of the particular sample site.

8.3.1 INTERPRETIVE MODEL ASSUMPTIONS

One potential cause of variability is the nature of the models used to interpret the measured ^{36}Cl abundances and, in particular, the possibility that the underlying assumptions of the models have not been fully satisfied by a particular sample. Two assumptions of particular importance are those relating to the exposure of the sampled surface and 'steady-state' denudation (Lal, 1991).

Denudation and backwearing rates derived using the 'steady-state' model (Equation 3.36) incorporate the implicit assumptions that the sampled surface has been exposed for a sufficient time to enable secular equilibrium to be achieved and that the surface, once subaerially exposed, remains so without interruption by intermittent and / or prolonged burial. Backwearing rates quantified from the block fall model (Chapter 7) are also affected by the latter assumption. The assumptions, achieving of secular equilibrium and simple exposure, may be checked by comparing results from two or more cosmogenic isotopes (Chapter 2). However, this option is only available for substrates which have suitable mineralogies to enable a multi-isotope approach to be used (eg ^{26}Al and ^{10}Be in quartz,

Bierman *et al*, 1999). Such a check was precluded in this study because of the lack of olivine / pyroxene phenocrysts in the Drakensberg Group basalts. If olivine / pyroxene had been present it may have been possible to analyse cosmogenic ^{21}Ne or ^{3}He in addition to ^{36}Cl which would have enabled these assumptions to be verified.

Samples were chosen from surfaces which, on the basis of field evidence (eg weathered nature of surface, field location, etc.), were thought to fulfil these assumptions; however, the possibility of insufficient length of exposure for the achievement of secular equilibrium or intermittent burial cannot be entirely ruled out. The implication of either of these assumptions not being entirely satisfied is that the measured ^{36}Cl abundance is lower than it would be if the assumptions were fulfilled. This means that the denudation / backwearing rates derived, using the 'steady-state' model, for surfaces which do not fulfil the assumptions of secular equilibrium and simple exposure, will be higher than the 'true' rate and should be regarded as maximum rates (Lal, 1991). The same conclusion would apply to backwearing rates derived using the block fall model where the assumption of simple exposure is not fulfilled.

One denudation estimate to which this may apply is the result for O8/97. An estimated denudation rate of 43.0 ± 6.6 m Ma^{-1} was derived from this sample using Equation 3.36. The measured ^{36}Cl abundance was $0.36 \pm 0.03 \times 10^{6}$ atom g^{-1} which was ~ 50 % of the total of the next smallest yield (N3/95, Table 6.6). Immediately to the west of this site (Plate 12) is an area which has recently become exposed and it is possible that the surface from which the sample was collected has not been exposed for a sufficient period for secular equilibrium to be achieved. If this is indeed the case then the measured ^{36}Cl abundance does not reflect secular equilibrium and the estimated denudation rate based on this is consequently higher than the 'true' rate. Therefore the result from sample O8/97 may overestimate the 'true' denudation rate at that site.

The other, fundamental, assumption of Lal's interpretative model (1991) is that the denudation rate is in 'steady-state'. As discussed in Chapter 2, Lal defined 'steady-state' in the context of his model as meaning a constant denudation rate, involving the continuous removal of rock much thinner than Λ_{sp} / ρ (~ 0.55 m for the Drakensberg basalts) (Lal, 1991; Nishiizumi *et al*, 1991). This assumption is unlikely to be applicable to most field situations, including the present study, because of the impact of, for example, climatic change, range fires, lithological characteristics, etc. which are likely to vary both the thickness of rock being shed and rate at which it is shed.

Lal's model (1991) does allow for the possibility of episodic, one-off, loss of material that is thicker than normal. In this case the ^{36}Cl concentration will take time to return to the saturated level (ie return to secular equilibrium). If the sample is collected during this re-adjustment period, the measured concentration will be lower than for the 'true' steady-state situation. Consequently the model rate will overestimate the 'true' denudation rate. Therefore denudation rates derived using the 'steady-state' model of Lal (1991) will be overestimates of the 'true' denudation rate if the sampled surface has experienced the episodic loss of material that is thicker than normal.

Small *et al* (1997) envisaged another scenario in which a flat-lying surface was denuded by the episodic removal of blocks of constant thickness, $< \Lambda_{sp} / \rho$, with no other denudation occurring between the removal of blocks. In this situation the relationship of the 'steady-state' modelled denudation rate to the 'true' rate is dependent on the time of sampling in relation to the time of removal of the last block. A sample collected shortly after the removal of a block will overestimate the 'true' denudation rate, while one taken just before a removal event would lead to an underestimation of the 'true' rate. Small *et al* (1997) showed that the magnitude of the under- and overestimation varies with the thickness of the block, being at least 20 % for blocks ~ 0.25 m thick. If the situation envisaged by Small *et al* (1997) is applicable then they suggest, assuming episodic removal of blocks is non-synchronous between sampled surfaces, that taking the mean value of many 'steady-state' model derived denudation estimates should provide a more accurate estimate of the 'true' mean denudation rate for an area.

Given the acknowledged (eg Lal, 1991, Gillespie and Bierman, 1995, Small *et al*, 1997) inability of the assumption of a 'steady-state' denudation rate to be tested, even using paired cosmogenic isotopes, and its likely inapplicability in most field settings, it is reasonable to suggest that this may account for some, if not all, of the variability in the estimated denudation and backwearing rates in this study. The similarity of results from samples collected from the same surface (Figure 8.1A) suggests that each surface behaves as a whole and that variability in the denudational processes and rates is extremely limited within a particular surface unit. This observation neither confirms nor refutes that 'steady-state' denudation is actually occurring on these surfaces, but rather suggests that if changes in the rate or type of process affecting the surface have occurred then they have affected the whole surface unit in the same manner. Variations between different surfaces, particularly between sites which have similar morphological settings, could be attributable to violation of the 'steady-state' assumption. If surfaces are subject to the periodic loss of thicker than 'normal'

material, then this process is likely to be asynchronous across sample sites. Applying the scenario envisaged by Lal (1991), some surfaces would be recording the 'true' rate while samples from surfaces which have recently lost thicker blocks would tend to overestimate the denudation rate. Equally if the Small *et al* (1997) denudation process applies at some, or even all, of the sites, some samples may be overestimating the 'true' rate, while others are underestimating it.

Field evidence (Chapter 6) suggests that the flat-lying surfaces are being denuded by a combination of granular disintegration, exfoliation of thin < 0.1 m sheets and the loss of individual blocks or larger sheets < 0.3 m thick. This supports a more complex denudational regime, at least involving periodic loss of thicker material, than that envisaged by the 'steady-state' model (Lal, 1991).

Denudation at the free face sample sites, again based on the field evidence (Chapter 7) is even more unlikely to fulfil the simple 'steady-state' model criteria. Based on the evidence from the talus slopes and the irregular nature of most of the free faces, the periodic loss of individual blocks seems to be the dominant process. While the proposed block fall model takes account of this, variability in results is likely because the calculated rate is dependent on the relationship between the timing of the sample collection and the timing of block fall events. If the sample was taken, relatively, soon after a block fall event the ^{36}Cl concentration would be lower than if the sample was collected just before the next block fall event. This lower concentration would yield a higher denudation rate than if the sample was collected just before the block fall event, thereby overestimating the 'true' rate. Although samples were taken from what appeared to be the 'oldest' and most stable part of each face and 'fresh' faces were avoided, it is impossible to differentiate accurately between surfaces which are, for example, 5000 or 10000 years old, but which would yield backwearing rates, using the BFM, which differed by ~50 %.

8.3.2 NATURAL SPATIAL VARIABILITY

In view of the large number of surfaces sampled, an alternate, or additional, cause of variability in the results may be the natural diversity in field site characteristics. Differences may occur in lithological resistance or in factors such as altitude and aspect which affect the intensity of the denudational processes. Such differences may act individually or collectively to create variations between the denudation rate recorded at one site and that at another.

One of the reasons for the choice of the Drakensberg and Lesotho Highlands for this study was the ability to collect samples from a single homogeneous lithology and thereby substantially reduce the impact of lithological variability on the denudation / backwearing estimates. Although the Drakensberg Group basalt forms a single lithology, basalt, by its nature is composed of individual flows, the chemical, mineralogical and geotechnical / physical characteristics of which are subject to some variation (eg Whalley *et al*, 1982; Douglas *et al*, 1991, 1994; Ramluckan, 1992; Rehacek, 1995; Marsh *et al*, 1997).

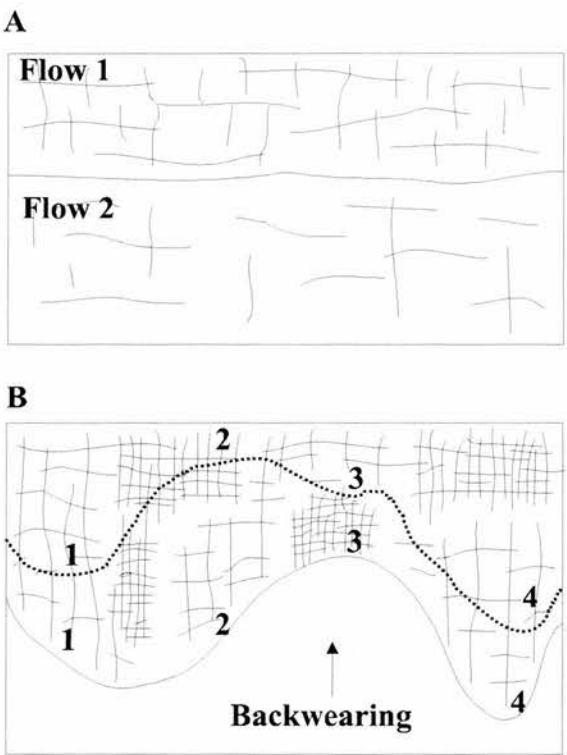

Figure 8.3: A is a cross-section through two flows. Flow 1 has a more dense and integrated joint pattern than flow 2 and hence will be more readily broken down. A sample from flow 1 would be expected to yield a higher denudation rate than one from flow 2. B is a planform view of an embayment on the escarpment. Higher denudation rates would be expected from sites where the joint spacing was closer and more integrated, for example at site 3. The form of the escarpment is expected to change over time as represented by the dotted line, and that form is influenced by the jointing pattern which in turn affects the expected backwearing rates. In this scenario, whilst the rate would be expected, *ceteris paribus*, to remain relatively constant at sites 1 and 4, it would show an increase at site 2 and a decrease at site 3. Figure B after Nicholas and Dixon, 1986.

Of particular importance in establishing the rate of downwearing or backwearing are the physical characteristics of the individual flows which might influence the ability of rock to resist the denudational processes. In basalts these physical factors include the presence of any breaks in the continuity of the rock, especially jointing and other partings, sub-millimetre microfractures, flow boundaries and vesicles (eg Whalley *et al*, 1982; Douglas *et al*, 1991, 1994). The orientation, continuity, width and infilling of such partings affect the opportunity of water and weathering processes to weaken the bedrock further and enable its removal by erosional processes (eg Selby, 1980, 1993; Douglas *et al*, 1991; Allison, 1996; Weissel and Seidl, 1997; Allison and Kimber 1998; Kimber *et al*, 1998). Although Moon and Selby (1983) have shown that outcrops of Drakensberg Group basalts can have remarkably uniform strength characteristics, that study was restricted to one location and it is possible that more variation would be encountered over the spatial range of the present study. Vertical and horizontal alterations in the pattern of such partings both within flows (which can be of considerable thickness (up to 30 m) and length (Rehacek, 1995)) and between flows would influence the rate of break-up and hence the denudation rate from site to site. Such spatial variation in rock fabric was identified by Nicholas and Dixon (1986) to be the cause of the typical embayment and headland planform of escarpments. They viewed the planform in a sandstone escarpment as being the product of variations in the backwearing rate which were governed by differences in the parting density of the lithology. These points are illustrated in Figure 8.3.

One possible example of the influence of flow characteristics is the difference in the backwearing rates estimated for samples N12/97 and N13/97. These two samples were collected from different flows at the same site at Naudesnek. N12/97 recorded a backwearing rate of 209.1 ± 91.3 m Ma^{-1} (BFM) while N13/97 from the lower flow yielded a rate of 33.2 ± 7.4 m Ma^{-1} (BFM). In the field (Plate 31) the lower flow forms a distinct step beneath the one from which N12/97 was collected, which suggests that it is being denuded at a lower rate.

Another natural cause of variability between results from widely dispersed sites would be the impact of variations in factors which control the intensity of the denudational processes. Two of the key controls on the effectiveness of chemical / physical weathering and the operation of erosional processes are temperature and the availability of water (eg Summerfield, 1991a; Selby, 1993). Water is important as a weathering agent being involved in the dissolution of minerals and chemical reactions as well as affecting the strength of jointed bedrock. In

addition precipitation as rain / snow remove weathering products by, for example, rainsplash and overland flow, and provide lubricants to aid rockfall. Temperature affects the rate of chemical reactions and determines if water is present as a liquid or solid form. Ice crystallisation / volumetric expansion during its formation, combined with the number and duration of freeze-thaw cycles, affect the rate of frost weathering. Ice formation within joints will aid mass movements and the removal of infill, thereby reducing the rock mass strength.

In very general terms altitude affects both precipitation and temperature. Although increases in precipitation with increasing altitude are generally recognised as occurring in the mid-latitudes and sub-tropics, other factors, such as orographic effects complicate this picture (Barry, 1992). In the free atmosphere the average temperature decreases at a rate of 6 °C km^{-1}, but again this relationship is complicated by factors such as nocturnal inversions which cause diurnal changes in the rate (Barry, 1992). Further complications are introduced for free face sites by the importance of aspect and slope angle which control the solar radiation receipt and hence temperature conditions (Barry, 1992). Therefore, although it might be expected that the efficiency of weathering and erosional processes will vary from site to site, the exact magnitude and impact on denudation and backwearing rates is difficult to quantify and assess. This is further complicated by the lack of site-specific climatic data for the summits of the Drakensberg and Lesotho Highlands.

A plot of increasing altitude against the denudation rate estimates for the flat-lying samples (Figure 8.4) does not reveal any apparent relationship between these two variables. Three of the highest denudation rate estimates are derived from the lowest altitudes, but this is probably because two of these are from the buttress ridge at Naudesnek and the third is sample O8/97 which, as suggested above, may have been subject to relatively recent exposure. Otherwise there is no obvious correlation in this plot, with both very low and relatively high denudation rates being estimated throughout the altitudinal range. This is perhaps not surprising, given that, for example, all the sites are likely to be affected by both chemical and physical weathering and that any potential reduction in chemical weathering rates caused by decreasing temperatures might well be offset by potential increases in physical weathering rates attributable to increased freeze-thaw activity.

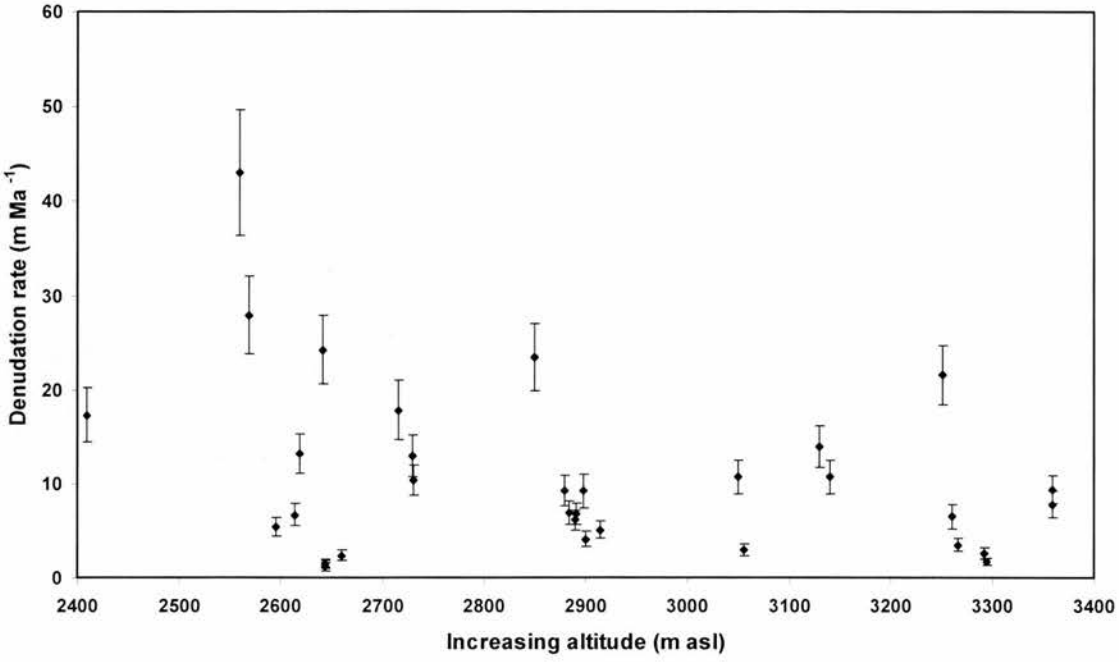

Figure 8.4: Plot of the estimated denudation rate for the flat-lying samples against increasing altitude. Both low and relatively high denudation rates were estimated at lower and higher elevation sites. This suggests either that altitude has no impact on the denudation rate, or, more likely, that this relationship is more complex and non-linear and / or other factors, either acting in concert or individually, are influencing the denudation rate estimates.

Similarly when the backwearing results (BFM version) are grouped by the aspect of the free face (Figure 8.5) no relationship is apparent. Indeed all aspects show variability. The mean backwearing rate and standard deviation for each aspect are given in Table 8.1. This shows that, with the exception of east and southeast aspects, the rates for each aspect fall within a similar range (Table 8.1). Both the mean and standard deviation are higher for the E and SE aspect faces because of the influence of two large estimates for the east facing free faces and one for the southeast aspect (Figure 8.5).

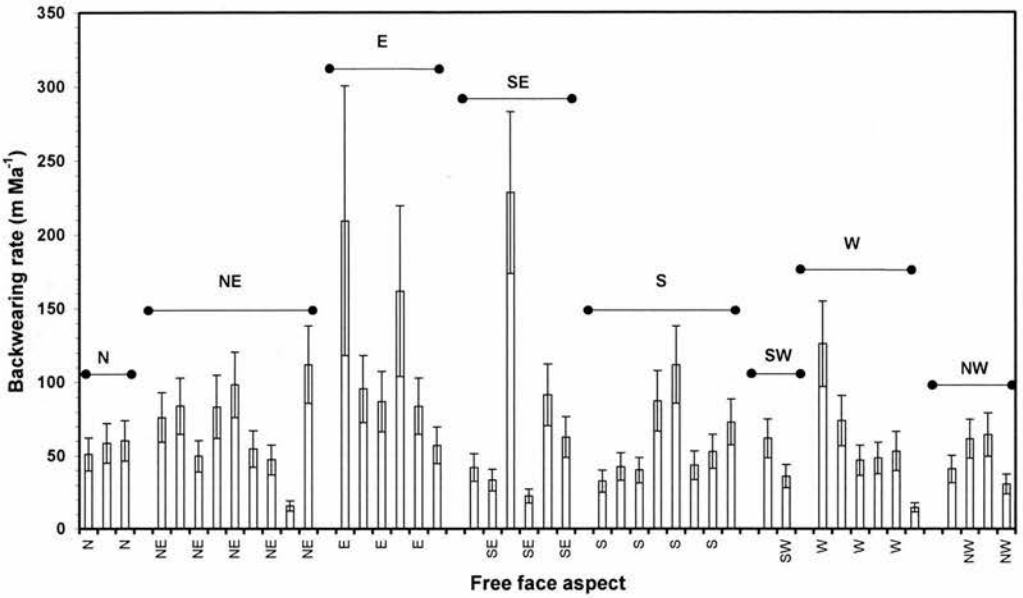

Figure 8.5: Backwearing rates, derived using the 0.5 m block fall model (Chapter 7), for the free face samples grouped according to the aspect of the sampled face. Although aspect is likely to influence the moisture and temperature regime, and hence backwearing rate, no such relationship is evident from this data.

Table 8.1: Mean backwearing rates (derived using the 0.5 m thick block fall model) based on free face aspect.

Aspect	Mean backwearing rate (m Ma^{-1})	Standard deviation (m Ma^{-1})
N	56.6 (n = 3)	5
NE	68.8 (n = 9)	29.6
E	115.0 (n = 6)	57.5
SE	79.8 (n = 6)	76.6
S	60.3 (n = 8)	27.6
SW	48.7 (n = 2)	18.2
W	60.3 (n = 6)	37.2
NW	49.3 (n = 4)	16.2

8.3.3 IMPLICATIONS OF VARIABILITY

Although general causes of variability in the denudation and backwearing datasets have been highlighted, it has not been possible in this study to identify the impact of these different causes on individual results. Whilst it may be possible to investigate, for example, the impact of the physical characteristics of the individual basalt flows on results from different, but morphologically similar, sites (particularly free face sites where the flows are well exposed)

this would require a more detailed analysis of the exposed flows, particularly the prevailing small and large scale rock mechanics of each flow, than was undertaken for this study. In any event such an assessment would be of limited value unless the other factors which influence variability, in particular those related to the interpretive model assumptions, could be independently assessed.

If the variability in the individual results is caused by natural site-to-site variability then these results accurately reflect the rate of denudation and backwearing in the southern Drakensberg and Lesotho Highlands. If, however, the variability is caused by incomplete fulfilment of the interpretive model assumptions by one or all of the individual results then, as explained in Section 8.3.1, the affected samples could be yielding either overestimates or a combination of over- and underestimates of the 'true' denudation / backwearing rates. Therefore, whilst this inability to separate the potential influence of the interpretive model assumptions from field based characteristics probably precludes a detailed site by site comparison of the individual results, it does not necessarily prevent the individual denudation or backwearing results from being considered collectively.

In situations like these Small *et al* (1997) showed that the mean of many denudation rate estimates should provide a reasonably accurate estimate of the actual mean denudation rate. This is based on two assumptions. Firstly that some values will overestimate the 'true' rate while others underestimate it. Hence deriving a mean will enable some cancellation to take place. Secondly, it assumes that episodic events are asynchronous between sample sites. As discussed in Section 8.3.1, such assumptions can reasonably be applied to the rates derived using either the SSM or BFM approaches. Therefore, following the Small *et al* (1997) approach, the best estimate of the 'true' rate of denudation / backwearing is likely to be derived by taking the mean of a number of site-specific rates produced by spatially distinct samples from similar morphological settings.

The mean values of the site-specific denudation and backwearing rates are given in Tables 8.2 and 8.3 respectively. In addition to mean denudation and backwearing rates derived from the total sample population, mean values have also been determined on the basis of the morphological settings in Figures 8.1 and 8.2. Where replicate samples were analysed the rate for that site, for the purpose of determining the mean rate, was taken as the weighted average of the result from the two samples (Taylor, 1997). Mean rates are quoted with an uncertainty which is the standard deviation of the mean at the 1 σ level. The dispersion of

the individual results is quantified by the standard deviation, quoted at the 68 % confidence level, and the range.

The mean denudation rate (Table 8.2) derived from all 33 flat-lying samples is 10.6 ± 1.6 m Ma^{-1}. The high standard deviation, σ, 9.2 m Ma^{-1}, reflects the wide range of denudation estimates. If the result from sample O8/97 (43.0 ± 6.6 m Ma^{-1}) is treated as being anomalous and caused by relatively recent exposure, the mean for all sites reduces to 9.2 ± 1.2 m Ma^{-1}, with σ reducing to 7.1 m Ma^{-1}. The mean backwearing rate (Table 8.3), based on the backwearing rates derived using the 'steady-state' model for all 44 free face samples, is 40.8 ± 3.9 m Ma^{-1}, with σ = 25.7 m Ma^{-1}. This standard deviation value again reflects the wide range of backwearing rates. Using the 0.5 m thick block fall model, this mean increases to 70.4 ± 6.7 m Ma^{-1}, with a standard deviation of 44.2 m Ma^{-1}.

Table 8.2: Mean denudation rates for flat-lying sample locations. The uncertainty in the mean is the standard deviation of the mean quoted at the 1 σ level.

Morphological setting	Location	Number of samples	Mean denudation rate (m Ma^{-1})	Standard deviation (m Ma^{-1})	Range (m Ma^{-1})
Escarpment summits	Naudesnek	n = 8	8.6 ± 3.0	8.5	23.0
	Ongeluk's Nek	n = 3	7.1 ± 2.3	4.0	7.2
	Sani Pass	n = 5	10.5 ± 3.2	7.2	17.4
	All	n = 16	8.9 ± 1.8	7.1	23.0
Buttress ridge summit	Naudesnek	n = 2	22.6 ± 5.3	7.6	10.6
Lower relief summits	Lesotho Highlands	n = 7	5.2 ± 1.1	2.8	7.7
Valley head summits	Lesotho Highlands	n = 4	13.0 ± 3.6	7.2	16.6
Valley side summits	Lesotho Highlands	n = 4	18.0 ± 8.7	17.3	40
All Lesotho Highlands' summits	Lesotho Highlands	n = 15	10.7 ± 2.7	10.5	41.3
All flat lying sites	Drakensberg & Lesotho Highlands	n = 33	10.6 ± 1.6	9.2	41.8

Table 8.3: Mean backwearing rates from all free face sample sites. The uncertainty in the mean is the standard deviation of the mean quoted at the 1 σ level.

Morphological setting	Location	Number of samples	Steady state model			0.5 m block fall model		
			Mean backwearing rate (m Ma^{-1})	Standard deviation (m Ma^{-1})	Range (m Ma^{-1})	Mean backwearing rate (m Ma^{-1})	Standard deviation (m Ma^{-1})	Range (m Ma^{-1})
Escarpment free faces	Naudesnek	n = 8	48.3 ± 11.6	32.9	100.4	82.3 ± 20.2	57.1	176.7
	Ongeluk's Nek	n = 4	71.0 ± 25.7	51.2	107.8	122.6 ± 44.0	87.9	185.6
	Sani Pass	n = 7	42.5 ± 5.6	14.8	38.4	74.4 ± 10.0	26.5	68.2
	All	n = 19	50.9 ± 7.4	32.4	113.5	87.9 ± 12.9	56.1	195.7
Small basin free faces	Escarpment sites	n = 3	31.2 ± 1.7	2.9	5.6	51.1 ± 3.0	5.2	10.1
Inland facing free faces	Escarpment sites	n = 6	29.2 ± 4.1	10.1	28.6	50.0 ± 7.2	17.7	32.8
All non-scarp free faces	Escarpment sites	n = 9	29.8 ± 2.7	8.2	28.6	50.3 ± 4.7	14.2	32.8
Valley head free faces	Lesotho Highlands	n = 8	38.8 ± 5.7	16.1	45.4	68.0 ± 9.7	27.6	80.9
Valley side free faces	Lesotho Highlands	n = 6	29.3 ± 10.5	25.7	70.0	49.9 ± 16.6	40.7	111.1
Free faces at summit sides	Lesotho Highlands	n = 2	36.7 ± 3.6	5.1	7.1	66.5 ± 6.2	8.8	12.4
All Lesotho Highlands free faces	Lesotho Highlands	n = 16	35.0 ± 4.8	19.1	70.0	61.1 ± 7.9	31.5	111.1
All free faces	Drakensberg & Lesotho Highlands	n = 44	40.8 ± 3.9	25.7	123.4	70.4 ± 6.7	44.2	213.5

8.4 IMPLICATIONS OF THE NEW DENUDATION RATE ESTIMATES FOR THE LANDSCAPE DEVELOPMENT OF THE SOUTHERN DRAKENSBERG AND LESOTHO HIGHLANDS

The mean denudation rates produced in Table 8.2 demonstrate that denudation is occurring, at roughly the same rate, on all flat-lying summits on the southern Drakensberg and Lesotho Highlands. The mean rate derived from all samples (n = 33) is 10.6 ± 1.6 m Ma^{-1} (σ = 9.2 m Ma^{-1}), which is necessarily integrated over the past ~ 50 ka. Both the lowest mean rate, 5.2 ± 1.1 m Ma^{-1}, and lowest standard deviation, 2.8 m Ma^{-1}, are produced by the results from the lower relief summits in the Lesotho Highlands (n = 7), while the highest mean rate, 22.6 ± 5.3 m Ma^{-1}, comes from the buttress ridge at Naudesnek (n = 2) (Figure 8.1). Whilst this might suggest that more extensive low relief summits are being denuded at a lower rate than the rather narrow summits found on ridges, the comments in Section 8.3 about variability, imply that other causes (ie model, lithological, process) may also be playing a part. Without the ability to distinguish between the contributory factors, it is safest to consider the implications of the mean denudation rate based on all samples.

8.4.1 LONGER TERM ESTIMATES OF DENUDATION FOR THE STUDY AREA

Although there are no other direct measurements of denudation rates applicable to the past *circa* $10^3 - 10^5$ a for the flat-lying summits of the southern Drakensberg and Lesotho Highlands, one of the advantages of choosing this study area is the availability of existing independent, longer term, quantitative assessments of denudation. The ^{36}Cl derived rates from this study can be compared usefully with these existing $10^7 - 10^8$ a timescale estimates which have been provided by studies involving zeolite zonation, kimberlite pipe morphology and apatite fission track thermochronology (AFTT).

8.4.1.1 DENUDATION ESTIMATES FROM ZEOLITE ZONATION STUDIES

Zeolites are hydrothermal alteration products found within amygdales or other cavities in basaltic rocks (Wilson, 1993). A distinct vertical zonation of these products has been identified in many thick basalt sequences, including those in Iceland, India (Deccan), Brazil (Parana) and southern Africa (Karoo) (Mehegan *et al*, 1982; Sukheswala *et al*, 1974; Murata *et al*, 1987; Potgieter *et al*, 1982; Ramluckan, 1992; Dunlevey *et al*, 1993). Different zeolites have been shown to have distinct crystallisation temperature boundaries and the zonation with depth below the surface of the original pile is thought to be caused by the geothermal gradient prevailing during zeolitization (eg Murata *et al*, 1987). The presence of one

particular zeolite, laumontite, and its location within the present day pile has then been used to suggest both an original depth for the relevant basalt pile and the depth of basalt removed since emplacement (eg Murata *et al*, 1987; Potgieter *et al*, 1982; Ramluckan, 1992; Dunlevey *et al*, 1993).

In the case of the Drakensberg Group basalts, Potgieter *et al* (1982) identified laumontite in the basal flows at the extreme west of the existing pile at 30° 45' S, 27° 15, E, ~ 90 km east of Naudesnek (Figure 6.1). These workers inferred from this that the Drakensberg Group had an original thickness of ~ 2 km, of which a maximum thickness of ~ 1.4 km still remains in the highest parts of Lesotho. Another zeolite zonation study has been carried out at Sani Pass (Ramluckan, 1992; Dunlevey *et al*, 1993). Based on the depth of the laumontite zeolites, which occurs between 170 and 420 m above the base of the pile (this distribution is unrelated to the geochemistry of the basalts in this area - Ramluckan, 1992), and comparison with the zonation in the Parana (Brazil) and Antrim (Ireland) basalts, these studies suggested that the original pile was 1600 – 1800 m thick. Based on this Dunlevey *et al* (1993) argue that ~ 200 – 400 m has been removed from the summit of Thabana-Ntlenyana (3482 m, Figure 6.11) since emplacement of the basalts.

Further evidence for denudation of the basalt pile since emplacement is provided by Marsh *et al* (1997). They identified dykes near the top of the basalt sequence in the Oxbow area (28° 45' S, 28° 40' E, Figure 6.11) which had a distinctive chemistry but which did not correspond to any basalt flows in Lesotho. On the basis that no flows were identified Marsh *et al* (1997) argued that that these flows, assuming they were erupted from the Oxbow fissures (dykes), must have been eroded. The thickness of the missing flows is unknown, however the Oxbow dykes have a similar geochemistry to the upper part of another remnant of the Karoo igneous province which crops out at the Springbok Flats, ~ 400 km north of Lesotho (Marsh *et al*, 1997). This Springbok Flats unit is ~ 370 m thick and forms the top of that sequence (G. Marsh, pers. comm.). Assuming that this unit has experienced some, presently unknown, subaerial denudation, this 370 m would represent a minimum thickness which has been eroded from the summit of the basalts in the vicinity of Oxbow. The basalt pile at Oxbow is presently ~ 1500 m thick and the addition of this 'missing' unit would bring the minimum thickness of the original pile to ~ 1900 m, close to the estimates from the zeolite studies.

Given that the age of the Drakensberg Group has now been resolved at 183 ± 1 Ma (Duncan *et al*, 1997), it is possible to derive a rough estimate of denudation rates from these original

pile thickness estimates. This requires two assumptions; firstly, that there was no post-basaltic-emplacement sediment or other lithological accumulation or burial, and, secondly, that the post-eruptive topography was generally flat-lying with minimal relief. With regard to post-eruptive burial, the basalts and rhyolites that form the ~ 8 km thick Lebombo volcanic sequence, ~ 200 km northwest of Lesotho, continued to be extruded after the cessation of volcanism in the Lesotho area (Marsh *et al*, 1997; Duncan *et al*, 1997). Flows from the Lebombo sequence, which are geochemically distinct from the basalts in Lesotho (Marsh *et al*, 1997; Duncan *et al*, 1997), are completely absent from the Lesotho pile and are thought to have only flowed to the east of the Lebombo mountains because of the presence of the Lebombo monocline and related rifting (G. Marsh pers. comm.). The absence of an obvious source of post-eruptive sedimentation, other than localised redistribution of basalt-derived sediments, argues against post-eruptive burial. The post-eruptive topography is thought to have been generally flat-lying (Marsh *et al*, 1997). This is based partly on the horizontal nature of the upper units identified in that study (eg the upper Mafika Lisiu unit is known, from boreholes, to be horizontal for at least 40 km – G. Marsh pers. comm.), and partly on the ability of flood basalts to flow over distances of many tens of kilometres on shallow angle surfaces, < 1 ° (eg Beeson and Tolan, 1990; Cashman *et al*, 1998).

Table 8.4: Time averaged denudation rates based on estimates of original basalt pile thickness for selected sites.

Location	**Estimated present thickness of basalt pile (m)**	**Estimated time averaged denudation rate, assuming original 2 km thick pile and age of 183 Ma for basalts (m Ma^{-1})**	**Mean denudation rate derived in this study (from Table 8.2) (m Ma^{-1})**
Naudesnek	750 – 950	6 – 7	8.6 ± 3.0
Ongeluk's Nek	850 – 1200	4 – 6	7.1 ± 2.3
Sani Pass	790 – 1160	5 – 7	10.5 ± 3.2
All Lesotho Highlands' sites	750 – 1500 [α]	4 – 8	10.7 ± 2.7
Highest elevation Lesotho Highlands (L10/97, L11/97; L12/97, L13/97; L16/97, L17/97; Figure 6.11)	1100 – 1300 [α]	4 – 5	5.3 ± 1.3 [β]

[α] See text for how this was derived.

β Based on mean of results from listed samples. Uncertainty is the standard deviation of the mean.

Based on these assumptions and estimates of the current depth of the pile (Chapter 6) we can determine a very rough time averaged denudation rate for parts of the southern Drakensberg and Lesotho Highlands (Table 8.4). The depth of pile is used in preference to the elevation of sample sites to avoid complications introduced by isostatic adjustments related to denudational unloading. The present depth of the pile at specific sites in the Lesotho Highlands is difficult to estimate as the basal contact remains buried beneath the basalt. The thickness at Thabana-Ntlenyana (3482 m) is estimated at 1400 m (eg Dunlevey *et al*, 1993) and at Mont-aux-Source (3282 m) (28° 45' S, 28° 55' E, Figure 6.11), at the western end of the northern Drakensberg, is ~ 1200 m thick. Based on these figures this basal contact would appear to be located at ~ 2100 m asl. Over long distances and large areas it is unlikely that the basal contact will be at a roughly continuous elevation – earliest flows are known to have filled in existing local relief (eg Eales *et al*, 1984). However, if the contact is assumed to be ~ 2100 m asl for the purpose of this rough calculation, a range of estimates can be derived for all the Lesotho Highlands' sites as well. A separate estimate is included for the Lesotho Highlands' sample sites which lie along a line through the highest elevations from Thabana-Ntlenyana to Mont-aux-Source and from which more than one sample was collected (near Thabana-Ntlenyana - L10/97 & L11/97; Kotisephola – L12/97 & L13/97; and Mafisoaneng – L16/97 & L17/97, Figure 6.11). When compared to the mean denudation rates derived in this study the rates are very similar for the different locations (Table 8.4).

8.4.1.2 Denudation estimates based on kimberlite pipe morphology

A site-specific estimate of denudation in the Lesotho Highlands has been provided by Hawthorne's (1975) model of the morphology of kimberlite pipes. Hawthorne suggested that the differences in shape and composition of the kimberlite pipes in southern Africa reflected the depth of denudation experienced by the pipe since its emplacement. One pipe in the Lesotho Highlands, at Letseng-la-Terae (29° 00′ S, 28° 50′ E, Figure 6.11) was examined by Hawthorne (1975) from which he estimated that ~ 300 m had been denuded from the pipe since emplacement. This pipe was emplaced ~ 90 Ma BP (Davis, 1977, quoted in Partridge and Maud, 1987, p186), which suggests a time averaged denudation rate, since emplacement, for the area around Letseng-la-Terae of ~ 3 m Ma^{-1}. The closest samples (L 16/97 and L17/97) to Letseng-la-Terae are from the summit of Mafisoaneng (3295 m), which is ~ 7 km north and ~ 150 m higher (Figure 6.11). These two samples yielded ^{36}Cl derived denudation estimates of 1.7 ± 0.4 m Ma^{-1} and 2.6 ± 0.6 m Ma^{-1} respectively, which are very similar to the kimberlite pipe based estimate. Unfortunately, although there are numerous kimberlite

pipes in Lesotho (eg Dawson, 1962), this is the only published estimate of denudation using this method.

8.4.1.3 Denudation estimated by AFTT data

Although an extensive apatite fission track thermochronology (AFTT) dataset exists for southern Africa which provides information of long-term (10^7 a) regional scale denudation (Brown, 1992), a lack of apatites means that there are no data available for the area covered by the basalt outcrop. However, extrapolation of denudation depths from AFTT analysis of samples from two boreholes, one located ~ 30 km oceanward of the Drakensberg at Swartberg (30° 09′ S, 29° 16′ E) and the other located ~ 50 km northwest of the Lesotho Highlands at Ladybrand (29° 05′ S, 27° 28′ E) (Figure 6.11), has yielded an estimate of the total amount of crustal stripping of the Lesotho Highlands (Brown and Summerfield, in prep.). The Brown and Summerfield (in prep.) data suggest that 3.1 ± 1.2 km and 1.7 ± 0.5 km, respectively, has been stripped since ~ 90 Ma from the regions immediately oceanward and inland of the Lesotho Highlands. A straight line extrapolation, assuming an originally low relief summit for the basalt pile (see above), yields a maximum estimate of ~ 1 – 2km of crustal stripping since the early Cretaceous (Brown and Summerfield, in prep.). This equates to a mean denudation rate of 8 – 15 m Ma^{-1}. However, although this is very similar to the ^{36}Cl derived rates, it has to be borne in mind that this estimate is derived from an interpolated surface which itself is derived from regionally averaged depth of denudation (ie encompassing river valleys and interfluves) calculated at sites outside the basalt pile.

The ^{36}Cl derived mean denudation rate estimates determined by the present study are entirely compatible with the range of denudation rates, ~ 3 – 15 m Ma^{-1} for the Lesotho Highlands and the summit of the southern Drakensberg, yielded by the zeolite zonation, kimberlite pipe and AFTT approaches. This gross similarity of denudation rates is particularly remarkable given the orders of magnitude differences in the time scales over which these independent techniques yield denudation data.

8.4.2 IMPLICATIONS OF THE MEAN DENUDATION RATE ESTIMATES

The major implication of the *in situ*-produced cosmogenic ^{36}Cl derived denudation estimates from the flat-lying samples, is that it demonstrates that denudation is ongoing across a wide variety of sites in the southern Drakensberg and Lesotho Highlands. Lester King asserted on several occasions (eg 1944, 1949, 1953, 1962, 1982) that the highest surfaces within the Lesotho Highlands were the remnants of a more extensive, but now dissected, Jurassic age erosion surface which had been planed to an "extensive, flat landscape" (1982, p 50) with some minor hills prior to the break-up of Gondwana (Figure 8.6). What is unclear from King's writings is whether these surfaces were thought to have survived without alteration (eg 1962, p 164 – "With landsurfaces not wasting away *in situ*, the ages of existing landsurfaces may be extended backwards in time almost indefinitely...."), or whether he envisaged that, although subject to some denudation, they retained their original minimal relief (eg 1982, p 54 "Denudation ...has etched minor details of later date into the pristine surface....").

Albeit that King's view has been subject to theoretical challenge (eg De Swardt and Bennet, 1974; Partridge and Maud, 1987), the cosmogenic ^{36}Cl isotope data from the flat-lying samples confirm, for the first time, that denudation at a mean rate of 10.6 ± 1.6 m Ma^{-1} has been occurring actively over at least the past $10^4 - 10^5$ years (T_{eff}, Table 6.9) on both the summits of the southern Drakensberg and the Lesotho Highlands. On the basis of Figure 8.6, samples collected from the escarpment summit at Ongeluk's Nek (O1/97; O5/97; O11/97) and from all sites within the Lesotho Highlands (except K, Figure 6.11), are all from King's 'Gondwana' surface. Individual results from these sites range from $1.7 - 23.4$ m Ma^{-1}, reflecting modification, rather than preservation, at all sites.

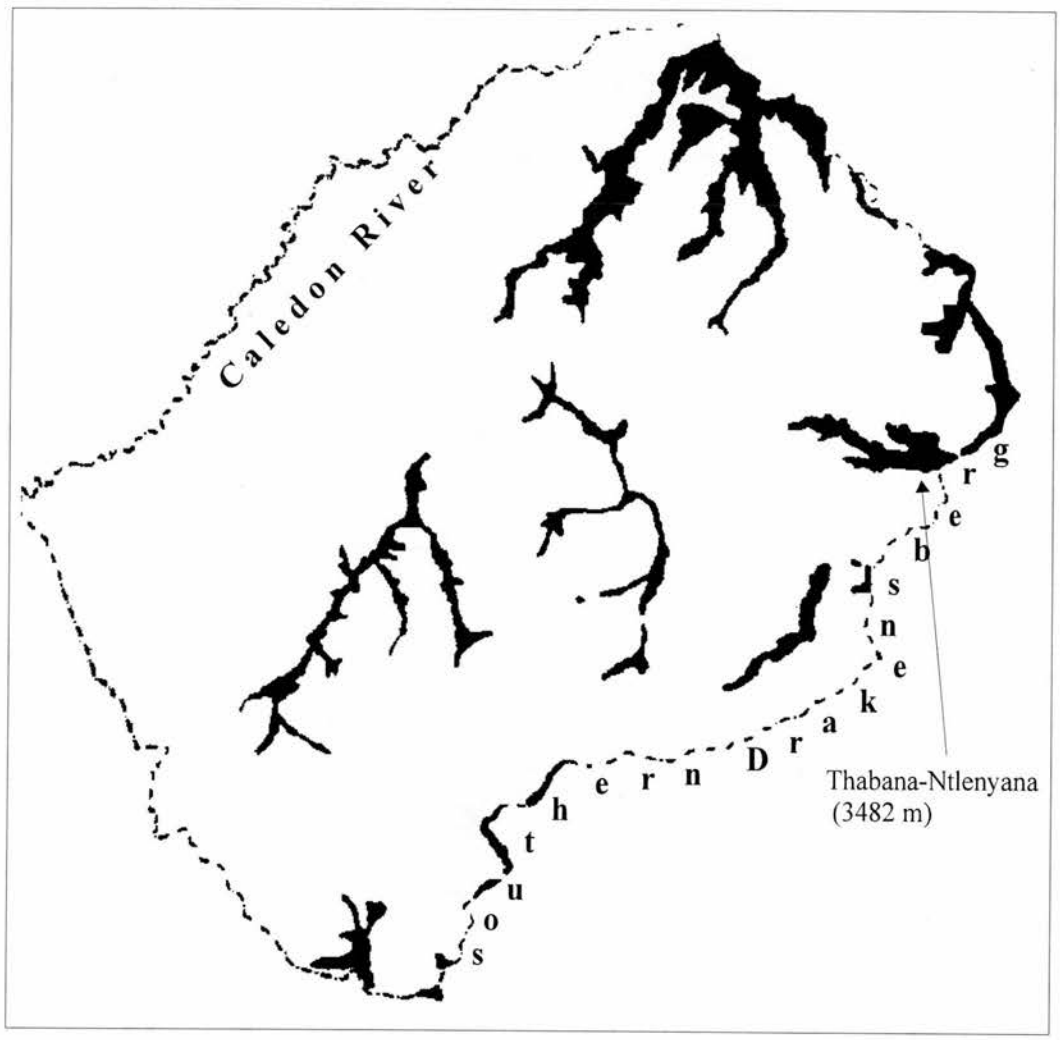

Figure 8.6: The position of the remnants of the Jurassic age, 'Gondwana', erosion surface in Lesotho as proposed by Lester King. King described the Lesotho Highlands as being remnants of Mesozoic planation which have been exposed continuously since then to the "weather" and proposed that this area has "remained with only minor alteration until they are destroyed utterly by encroachment of [a] fresh cyclic scarp" (King, 1962, p159). (After King, 1944, 1962).

Although the ^{36}Cl derived denudation rates are necessarily integrated over a range of timescales of the order of $10^4 - 10^5$ years (T_{eff} for the mean rate of 10.6 ± 1.6 m Ma^{-1} is ~ 47 ka), they may characterise the mean denudation rate for longer periods, perhaps since the start of the Quaternary. Southern Africa, like the rest of the world, has experienced climatic fluctuations throughout at least the last 200 ka (the longest terrestrial record in this area – Partridge *et al*, 1997) and most probably the entire Quaternary. Available evidence (Table 5.2) suggests that the southern Drakensberg and Lesotho Highlands have, in the past, experienced periglacial conditions. Although the features listed in Table 5.2 lack dating control, their preservation suggests that they were formed during the same period as the last glacial maximum, ~ 24 – 16 ka BP. If so, the effects of periglaciation on denudation rates during that period are 'integrated' in the ^{36}Cl derived denudation rates. In any event, past periglaciation may have had little impact on denudation rates, as evidence from several studies (Section 5.4.4.2) suggest that colder conditions also meant drier, with available precipitation tending to fall during the summer months as at present. Increased bedrock breaking down and removal by erosional processes may therefore have been negligible.

Further support for this view is provided by studies of bedrock breakdown under freeze-thaw weathering. Several studies of basalt presently subject to freeze-thaw weathering (eg Whalley *et al*, 1982; Douglas *et al*, 1991, 1995) have shown that bedrock disintegration is as much a function of rock properties as climate. This view is supported by André (1997) who suggests that the importance of frost weathering in periglacial environments has been exaggerated and has a very limited impact on hard igneous rocks, such as basalt.

Taking all these factors into account it seems reasonable to suggest that the calculated mean rate probably characterises the average denudation rate for the whole of the Quaternary. Indeed the striking overall similarity between these direct ^{36}Cl derived rates of denudation with the longer term estimates of the gross denudation of the basalt pile (Section 8.4.1), suggests that denudation may have been ongoing for at least the past 10^7 a at this order of magnitude rate. In any event, the ^{36}Cl derived denudation rates demonstrate that unmodified Gondwana bevelled surface remnants cannot have survived as suggested by King (eg 1982).

King (eg 1962, 1982) identified this 'Gondwana' surface using the much criticised (eg Chorley, 1965a & b; De Swardt and Bennet, 1974) technique of accordance of summit levels. If the variability in the individual ^{36}Cl derived denudation rates is due to field (ie lithological and process), rather than interpretive model characteristics (an unresolved issue), then such order of magnitude differences (Figure 8.1, Table 6.4) between individual, but

presently accordant summits, suggests such summits may never have been part of an extensive flat landscape produced by denudational, rather than depositional, processes. In other words, present accordance of erosional summits cannot be taken as present accordance of denudation rates.

It has been suggested, without any supporting evidence, that the erosional surfaces in the Lesotho Highlands may have been formed by etch processes under a thick weathering regolith (possibly implied to be Jurassic age) which has subsequently been stripped (Twidale, 1990; 1992). No thick weathering deposits have been identified in the Lesotho Highlands where the soils and any regolith in the summits areas are generally thin (< 1m thick, Schmitz and Rooyani, 1987). The oldest radiocarbon age from a sedimentary sequence in the Lesotho Highlands is ~ 13.5 ka BP (Marker, 1998). The tor-like summits from which some samples were collected are most probably either residuals of more resistant flows (De Swardt and Bennet, 1974) or the product of cryoplanation processes during past periglacial conditions (French, 1996; Grab, 1999), than the sub-surface product of a now stripped weathering horizon. Although the climatic fluctuations ushered in with the start of the Quaternary may have created conditions in which a pre-existing weathering mantle could have been stripped, the high local relief found in the Lesotho Highlands suggests that if a thick weathering mantle did exist it must have been substantially stripped prior to the start of the Pleistocene. In any event the ^{36}Cl derived denudation data presented in this study cannot resolve this issue, although it does demonstrate that denudation has been an active process on the summits of the Drakensberg and Lesotho Highlands for at least the past $10^4 - 10^5$ year period.

Overall the mean (n = 33) ^{36}Cl derived denudation rate for the Lesotho Highlands and Drakensberg, 10.6 ± 1.6 m Ma^{-1}, is of the same order of magnitude as the rate of plateau lowering, ~ 1 – 10 m Ma^{-1} (during the Cenozoic) of the southeast Australian Highlands inland of the continental drainage divide (Bishop and Goldrick, 2000). Although these data are also from another passive margin setting and areas that are distant from base levels (the ultimate base level for the Lesotho Highlands is the Atlantic Ocean), it is not directly comparable as the SE Australian data is mainly derived from rates of fluvial incision (eg Bishop *et al*, 1985; Young and MacDougall, 1993). The denudation data for the Lesotho Highlands and Drakensberg presented here are site-specific rates for summits and other interfluve settings. The rate of fluvial incision in the Lesotho Highlands is currently unknown. The presence of deeply incised river channels (eg Plate 2) might suggest high rates of incision. However the ability of the Drakensberg Group basalt to maintain steep free faces

(not just on the Drakensberg escarpment), which have yielded relatively low ^{36}Cl derived rates of backwearing, may have favoured the creation, over time, of deeper and narrower river valleys, even for relatively modest rates of fluvial incision.

8.5 IMPLICATIONS OF THE NEW BACKWEARING RATE ESTIMATES FOR THE LANDSCAPE DEVELOPMENT OF THE SOUTHERN DRAKENSBERG AND LESOTHO HIGHLANDS

8.5.1 CHOICE OF BACKWEARING RATES

Free face backwearing rates have been estimated from the measured ^{36}Cl abundances using both the 'steady-state' model of Lal (1991) (SSM) and an alternative model based on regular shedding of 0.5 m thick blocks (BFM). Mean backwearing rates (Table 8.3) calculated using the BFM, although generally ~ 70 – 80 % higher than those derived using the SSM approach, are of the same order of magnitude. For the purpose of this discussion, the backwearing rates will be regarded as being more accurately estimated by the BFM results. This is because the predominant thickness of loose boulders below the free face sample sites, in both the southern Drakensberg and Lesotho Highlands, was ~ 0.5 m and the physical appearance of those free faces suggested that loss of individual blocks of this thickness has been the dominant denudational process.

A potential drawback of using the block fall model to constrain mean backwearing rates is that the retreat rate is, fundamentally, a function of the thickness of the blocks that are being shed. Thus while the age of exposure of the sampled free face surface determined from the measured ^{36}Cl concentration would remain nearly the same (the use of different block sizes affects the total production rate calculation and hence the derived exposure age), the rate of backwearing, being a direct function of the thickness of material falling from the face, increases with increasing block thickness. The impact of this is illustrated in Table 8.5 for the regular shedding of 1 m, 2 m, 3 m and 5 m thick blocks, with backwearing rates being calculated as described in Chapter 7. For comparison, the mean rate calculated using 0.5 m thick blocks for the escarpment free faces is 87.9 ± 12.9 m Ma^{-1} (averaged over the past ~ 6 ka), and for the Lesotho Highlands' free faces is 61.1 ± 7.9 m Ma^{-1} (averaged over the past ~ 8 ka).

During this study the thickest slab of basalt noted as being lost from a free face was ~ 2 m thick from another part of the face from which sample L19/97 was collected (Plate 66). This sample, L19/97, yielded the highest ^{36}Cl concentration of all the free face samples, and thus

the oldest exposure age (~ 35 ka). Hence even if the free face from which L19/97 was taken is retreating by the regular loss of ~ 2 m thick blocks, the backwearing rate for this site would still only be 41.6 ± 9.2 m Ma^{-1}. At the other free face sites, both in the Lesotho Highlands and the southern Drakensberg, evidence from the joint spacing on the sampled free faces, the irregular nature of the free faces, the thickness of loose boulders on the talus slopes and their generally angular nature, all suggest that the regular shedding of ~ 0.5 m thick boulders is the dominant mode of denudation.

Table 8.5: Mean backwearing rate for the Drakensberg derived for different thickness' of block shed from the free face sample sites. The uncertainty in the backwearing rate is the standard deviation of the mean.

Setting / location	**Location**	**Mean backwearing rate (m Ma^{-1}) based on regular shedding of blocks**			
		1.0 m thick block	**2.0 m thick block**	**3.0 m thick block**	**5.0 m thick block**
Escarpment	All (n = 19)	140.1 ± 23.9	261.3 ± 56.0	391.9 ± 91.8	653.2 ± 164.1
Lesotho Highlands	All (n = 16)	97.0 ± 15.5	179.7 ± 38.1	269.9 ± 63.7	449.3 ± 115.2

Based on the BFM approach, the mean backwearing estimate (Table 8.3) for the main southern Drakensberg escarpment free face (n = 19), 87.9 ± 12.9 m Ma^{-1}, is ~ 44 % higher than the mean rate yielded by the 16 samples collected from the Lesotho Highlands' free faces, 61.1 ± 7.9 m Ma^{-1}. The mean rate from the non-escarpment free face samples collected at the southern Drakensberg sites, 50.3 ± 4.7 m Ma^{-1} (n = 9), is very similar to the rates from the Lesotho Highlands' sites (Figure 8.2). Whilst this might imply that free faces on the escarpment are backwearing at a faster rate than those located in non-scarp settings, both at the southern Drakensberg and within the Lesotho Highlands, the range of results at each setting, reflected in the standard deviations and large range values (Table 8.3), precludes this from being a firm conclusion. What is perhaps surprising is that the difference in backwearing rates between the escarpment and other free faces is not greater than the ~ 44 % implied by the means, particularly given the generally higher free faces and higher local relief of the southern Drakensberg. This may, in part, reflect relatively uniform strength

characteristics of the Drakensberg Group basalts that crop out as free faces (Moon and Selby, 1983).

8.5.2 Comparison of the backwearing estimates for free faces in the southern Drakensberg and Lesotho Highlands with other general estimates of free face retreat

Although this research is one of the first to use the analysis of *in situ*-produced cosmogenic isotopes to yield backwearing rates for bedrock free faces, several other studies have attempted to constrain rockwall retreat rates in various field locations using a variety of direct and indirect approaches. An interesting question therefore arises as to how the rates derived in this project compare with these other estimates of free face retreat. However, before undertaking such a comparison a number of general caveats need to be stressed.

Firstly, the diverse techniques employed yield retreat rate estimates that apply over considerably different temporal scales. Shorter term studies suffer from their inherent inability to include the impact of high magnitude / low frequency events, which are more likely to be included in longer term averaged rates, such as those provided by cosmogenic isotope analysis. Secondly, other techniques which do yield long-term retreat rates use an indirect approach which relies on assumptions about past morphological relationships. The technique employed here provides a direct measure of the retreat rate. Thirdly, lithology plays a key role in the rate at which free faces retreat. In particular, compound free faces, formed of different lithologies, are likely to experience high retreat rates if the caprock is undermined as a result of weaker underlying lithologies or the presence of hydro-geological conditions which favour basal sapping. The Drakensberg Group basalts have been shown to have a uniformly high rock mass strength (Moon and Selby, 1983) and the absence of undercuts at the foot of free faces demonstrate that basal sapping is not an important process in this area. Lastly, climate will also play an important role in determining the type of denudational processes that affect the free face. Free faces in areas which have only recently become ice free may yield atypically high rates as a result of deglaciation stress release. These general caveats should be borne in mind in the following discussion.

A range of free face retreat estimates derived over a wide range of settings and timescales using a variety of techniques, all converted to a common measurement (m Ma^{-1}), are given in Table 8.6. The studies can be grouped into four broad climatic settings – arctic / subarctic, alpine, temperate, and arid / semi-arid. There is a general absence of studies of free face

retreat rates in sub tropical / tropical environments (Thomas, 1994), with the rate for such environments sometimes being quoted as 1000 – 1500 m Ma^{-1} (eg Young, 1972). This rate is usually derived from King's (1953) estimate of the retreat rate of the Drakensberg which is discussed in Section 8.5.3.

Both within the broad climatic settings in Table 8.6 and between these settings there is considerable variation. Whilst difference between climatic settings might be expected to reflect the relative efficacy of disparate denudational processes (ranging from frost-induced spalling to major collapses caused by hydro-geological conditions which favour spring sapping), differences within settings more likely reflect the contrasting levels of lithological resistance and the diverse techniques used to quantify these rates. These techniques range from the collection of fragments from rock faces (eg Rapp, 1960; Becht, 1995), to estimates of the age and volume of slope debris (eg André, 1986; Ballantyne and Kirkbride, 1987), reconstructions based on talus flatiron ages and morphological relationships to scarp faces (eg Schmidt, 1996; Gutiérrez *et al*, 1998), reconstructions based on beheaded consequent valleys (eg Schmidt, 1989), and the relationship of escarpments to dated geological features (eg Yair and Gerson, 1974; Cole and Mayer, 1982; Schmidt, 1989; Young and MacDougall, 1982; Nott *et al*, 1991, 1996).

Short term studies ('present' in Table 8.6) quantify rates for small rockwall sections over a few years and present considerable difficulties in scaling up to the larger temporal and spatial scales represented by the backwearing rates derived in this study. The section of face selected may be more (or less) active than others and present day estimates may be misleading by ignoring both the influence of rockfalls of varying magnitude / frequency and the impact of climate change on the efficiency of denudational processes (eg Douglas *et al*, 1991; McCarroll *et al*, 1998). Thus while mean backwearing rates derived from all sites in this study (70.4 ± 6.7 m Ma^{-1} - BFM) fall within the lower end of the range of present day estimates in Table 8.6 (9 – 500 m Ma^{-1} in different lithologies and settings), this similarity has to be treated with some caution.

Table 8.6: General estimates of free face (rockwall / scarp) retreat rates for different climatic settings, lithologies and applicable to a range of timescales.

Climatic setting / Location	Lithology	Retreat rate (m Ma^{-1})	Age range	Study
Arctic / subarctic				
Lappland	mica schist / limestone	40 – 150	present	Rapp, 1960
Spitsbergen	limestone / chert /sandstone	20 – 500	present	Rapp (quoted in Rapp, 1960)
Spitsbergen	limestone / chert / sandstone	340 – 500	~ 10 ka	Rapp (quoted in Rapp, 1960)
West Greenland	basalt	500 – 1500	5.8 – 7.9 ka	Frich & Brandt, 1985
Spitsbergen	various	100 – 700	800 – 1800 a	André, 1986
Spitsbergen	mica schist /quartzite	110	present	André, 1986
Spitsbergen	various	7 – 1500	?	André, in French, 1996
Spitsbergen	amphibolite	0 – 4.2	1300 a	André, 1997 :- biogenic flaking;
	amphibolite / quartzite	30 – 220	1300 – 1600 a	frost weathering;
	quartzite	100 – 1580	1800 a	pressure release
Alpine				
Poland	various	20 – 1000	?	Kotarba *et al*, in Saunders & Young, 1983
Swiss Alps	various	2500	?	Barsch, in Saunders & Young, 1983.
Yukon, Canada	igneous metasedimentary	7 – 30	?	Gray, in Saunders & Young, 1983.
Swiss Alps	gneiss / mica schist	10 – 100	present	Becht, 1995
Canadian Rockies	siliceous	2.5 – 17.7	~ 300 a	Luckman & Fiske, 1995
Temperate				
UK	various	1430 – 4020	400 – 800 a (Stadial)	Ballantyne & Kirkbride, 1987
UK	sandstone / quartz-dolerite	9 – 63	present	Ballantyne & Eckford, in Ballantyne & Kirkbride, 1987
UK	volcanics	10 – 21	present	Stuart, in Ballantyne & Kirkbride, 1987
SE Australia	various	< 170	Neogene	Young & MacDougall, 1982
SE Australia	various	50	Neogene	Nott *et al*, 1991
SE Australia	sandstone / siltstone	< 0.3	Neogene	Nott *et al*, 1996
Arid / semi-arid				
Sinai, Israel	various	100 – 400	250 ka	Yair & Gerson 1974
Colorado Plateau	limestone	180 – 750	13 ka	Cole & Mayer, 1982
Colorado Plateau	sandstone / limestone / conglomerates	500 – 6700	Cenozoic	Schmidt, 1989
Gulf of Suez	limestone / sandstone	~ 6000	20 Ma	Steckler & Omar, 1994
Colorado Plateau	marine shale	2000 – 3500	100 ka	Schmidt, 1996
NE Spain	limestone	900 – 1000	25 – 7000 a	Gutiérrez *et al*, 1998

The longer term ($10^2 - 10^6$ a) estimates provide more realistic comparators for the ^{36}Cl derived data, which average retreat rates over the 10^3 - 10^4 a timescale. These longer term estimates range from very slow rates of retreat, < 0.3 – 18 m Ma^{-1}, measured in both the Canadian Rockies (averaged over 300 a) and SE Australia (averaged over ~ 23 Ma), to the kilometre scale rates, averaged over ~ 65 Ma, reported for the Colorado Plateau (Schmidt, 1989, 1996). The highest long-term rates are estimated for locations which are clearly dissimilar to the settings encountered in this study.

Ballantyne and Kirkbride (1987) estimated rates of ~ 1500 – 4000 m Ma^{-1} (the lowest rate is for a basalt free face), but these are for stadial conditions and a situation where rockfall may be related to pressure release of over-steepened free faces following recent ice sheet deglaciation. Frich and Brandt (1985) determined retreat rates of 500 – 1500 m Ma^{-1} for basalt free faces, however, this is an averaged rate over the period since deglaciation of their study area and the high rate is, again, likely to reflect pressure release following this event rather than the sole impact of periglacial weathering. André (1997) has been able to show that higher rates are yielded in situations of deglaciation stress relaxation.

Although some of the assumptions underlying the techniques employed by Cole and Mayer (1982) and Schmidt (1989) have been questioned (eg Hama, 1983; Oberlander, 1997), the highest retreat rates have been estimated for the compound scarps of the Colorado Plateau. These scarps are composed of alternating layers of different lithologies which yield different retreat rates. Schmidt (1989) showed that his retreat rates were seemingly related to the thickness and resistance of the caprock, the highest retreat rates being recorded where these combined values were lowest. The results from Schmidt's 1996 study are for a marine shale which is 'of very low resistance' (p139). The compound scarps in the Colorado Plateau are also subject to specific hydro-geological conditions which favour basal sapping by groundwater as the process of scarp backwasting (eg Ahnert, 1960; Laity and Malin, 1985). In comparison, the Drakensberg escarpment and Lesotho Highlands are formed entirely in one lithology, basalt, which is generally regarded as a very resistant rock. In addition Moon and Selby (1983) have demonstrated that free face outcrops of this Drakensberg Group basalt have uniformly high rock mass strength characteristics. With the possible exception of the mid-slope free face from which L19/97 was collected (Plate 66), which shows some signs of undercutting, there is no evidence for basal sapping being an active process at the free faces sampled either at the southern Drakensberg or in the Lesotho Highlands. Other results from arid / semi-arid environments are also from compound slope settings and generally for

weaker lithologies (eg Gutiérrez *et al*, 1998 – limestone caprock over quartzitic gravels; Yair and Gerson, 1974 – limestone over clastic sedimentary units yielded the highest rates, while intact granite yielded low rates of 100 – 200 m Ma^{-1}; Steckler and Omar, 1994 – limestone over friable and easily eroded sandstone).

The Drakensberg and Lesotho Highlands probably experienced periglacial conditions in the past (Table 5.2), and mechanical weathering is clearly ongoing in the Drakensberg / Lesotho Highlands. The region also experiences frosts, therefore we might expect some similarity with rates in the colder environments. Long-term retreat rates for arctic /subarctic environments are slightly higher than those produced by the present study, being generally of the order of 100's m Ma^{-1}, while for alpine environments, the study of Luckman and Fiske (1995) yields a very low rate, which may be attributable to the limited length of that study. However several studies (Douglas, 1981; Whalley *et al*, 1982; Douglas *et al*, 1991, 1995) have shown that, at least in the case of basalt, the disintegration of free faces is as much controlled by the large and small scale rock properties as by the climate. Hence disparities in retreat rate between the present study and those from colder environments are just as likely to be explicable in terms of lithological (structural and mineralogical) differences as variations in the climatic parameters that control the denudational processes. In addition, because the localised effectiveness of frost weathering in breaking down particularly susceptible lithologies is more conspicuous in the Arctic, André suggests that the overall importance of frost weathering as a process may have been exaggerated (1997, p 436). In any event, the present study area is within the summer rainfall region of southern Africa and therefore little moisture is available in the form of precipitation (and given the field setting of most sample sites at interfluves in the form of surface seepage) during the coldest months which will limit the efficiency of any freeze-thaw activity. Past decreases in temperature, due to global climate change, is thought to have been accompanied by an increase in aridity which would have limited any increase in efficiency of frost weathering and hence retreat rate.

The long-term rates which most closely bracket this study's mean rates are those averaged over the past ~ 23 Ma for SE Australia (Table 8.6). Although these rates are for different lithologies in a different climatic setting, these estimates, based on well dated geological evidence, are for scarp / free faces in another passive margin setting. Both Young and MacDougall (1982) and Nott *et al* (1991) were able to infer low retreat rates (< 170 m Ma^{-1} and ~ 50 m Ma^{-1}, respectively) for the major erosional escarpment in this area (a similar feature to the Drakensberg) based on the distance of the escarpment from dated rocks (basalt

flow and sediments) on the coastal plain. Unpublished data, again based on dated basalt flows, suggest similarly very slow scarp retreat rates for the escarpment in northern Queensland (P. Stephenson, pers. comm.). At a smaller spatial scale, Nott *et al*, (1996) have shown that free faces in the uppermost parts of gorge walls have been retreating at < 0.3 m Ma^{-1} since the Oligocene, which is three orders of magnitude less than the gorge head (~ 2500 m Ma^{-1}) of the same Shoalhaven River. The rate from this gorge head setting is not comparable with the retreat rates in this study as no rivers flow over any of the free faces sampled.

Overall the mean backwearing rates derived in this study fall within the lower end of the range of other longer term rockwall / scarp retreat estimates. However, when the particular circumstances of these other studies (ie varying lithologies, compound nature of scarps, climate setting, denudational processes etc.) are compared to the free face settings in this study (ie single lithology with high degree of resistance and limited freeze-thaw activity), it is perhaps to be expected that free face backwearing rates from this study would be generally lower. Of most significance is that very long-term rates from another passive margin setting neatly bracket those derived here, a point which is discussed further in Section 8.5.3.

To date, other than the initial results from this study (Fleming *et al*, 1999), there have been no published estimates of backwearing rates derived using this technique. Cockburn (1998) estimated backwearing rates of 5.9 – 17.9 m Ma^{-1} (n = 4) for the quartzite caprock summit of part of the Namibian escarpment. These were modelled using the 'steady-state' model without adjustment for the impact of the sloping surface on production. Lower estimates of 4.5 – 12.5 m Ma^{-1} have been derived using the amendments to the model suggested in Fleming *et al* (1999) and this thesis (Cockburn *et al*, in press). Using the alternative block fall model proposed here would lead to a substantial increase in the Namibian rates, in the same way as it has for this study (Figure 8.2A, shaded columns). The Cockburn *et al* (in press) results are from a very similar morphological setting, passive margin escarpment free face, to the results shown in Figure 8.2A (unshaded column) which vary between 18.0 – 131.5 m Ma^{-1} (SSM) (n = 19). Whilst the lower rates for the Namibian study may reflect the impact of the different lithology and arid climatic setting, what is interesting is that these separate studies yield rates of free face escarpment retreat that are of a similar order of magnitude, despite the lithological and climatic differences.

These order of magnitude similarities in the backwearing data presented in this study and this other cosmogenic isotope analysis study, although interesting, do not, of themselves,

indicate the likely level of accuracy of this new backwearing data. Because backwearing rates on the timescale provided by this technique ($10^3 - 10^4$ a) have not been obtainable previously for the study area, the very nature of the data makes assessing the level of accuracy problematic. However, the choice of study area enables the mean backwearing rate for the main free face of the southern Drakensberg to be assessed against maximum limits of retreat for the Drakensberg provided by independent field evidence.

8.5.3 SOUTHERN DRAKENSBERG ESCARPMENT RETREAT

BFM results from the three separate escarpment sites are relatively consistent, being 82.3 ± 20.2 m Ma^{-1} (σ = 57.1 m Ma^{-1}), 122.6 ± 44.0 m Ma^{-1} (σ = 87.9 m Ma^{-1}) and 74.4 ± 10.0 m Ma^{-1} (σ = 26.5 m Ma^{-1}), for Naudesnek, Ongeluk's Nek and Sani Pass, respectively (Table 8.3). The results become even more consistent if the very high individual backwearing rates yielded by sample N12/97 from Naudesnek (209.1 ± 91.3 m Ma^{-1}) and O9/97 from Ongeluk's Nek (228.1 ± 54.7 m Ma^{-1}) are regarded as anomalous. When these two samples are excluded, the mean rates for Naudesnek (n = 7) and Ongeluk's Nek (n = 3) reduce to 64.1 ± 10.3 m Ma^{-1} (σ = 27.3 m Ma^{-1}) and 87.4 ± 37.3 m Ma^{-1} (σ = 64.6 m Ma^{-1}) respectively.

This relative consistency between three escarpment sites which are ~ 175 km apart, suggests that a mean backwearing rate based on all the individual free face site results from these separate locations will reasonably represent the mean retreat rate for the main free face of the southern Drakensberg. This approach yields a mean (n = 19) backwearing rate for the southern Drakensberg of 87.9 ± 12.9 m Ma^{-1} (σ = 56.1 m Ma^{-1}), averaged over the past ~ 6 ka years.

8.5.3.1 OTHER GROSS ESTIMATES OF THE RETREAT RATE OF THE DRAKENSBERG

There is a lack of data on the retreat rate of the Drakensberg escarpment (the rationale for this part of the study); however, some very broad constraints can be placed on the maximum rate by other geological evidence – the location of a dated tuff deposit; stream pebble analysis and AFTT data. A ~ 50 m thick carbonate tuff deposit and associated vent have been reported at Melkfontein Farm (30° 30′ S, 29° 00′ E), ~ 50 km oceanward of the Drakensberg summit (Nixon, 1975; Nixon *et al*, 1983; Boctor *et al*, 1984). Zircon from this deposit has been dated at 63.4 Ma (Davis, 1978, quoted in Nixon *et al*, 1983). If this tuff was

truly erupted subaerially (rather than being intrusive) then it would limit the maximum rate of mean escarpment backwearing over the past ~ 63 Ma to < 800 m Ma^{-1}.

An unpublished study has compared the dispersal pattern of basalt clasts in the Mkomazi River, which rises on the Drakensberg escarpment, ~ 12 km northeast of Sani Pass and drains to the Indian Ocean, ~ 160 km to the southeast, to the size of basalt clasts in Cretaceous age coastal conglomerates (Matthews and Maud, 1988). Preliminary results from this suggested that by the end of the early Cretaceous (97 Ma), the escarpment was only ~ 35 km from its present position (Mathews and Maud, 1988). This yields a time averaged retreat rate since the start of the late Cretaceous of ~ 360 m Ma^{-1}. Suggestions, based on the Matthews and Maud (1988) study, that the Drakensberg was only ~ 20 km from its present position by the end of the Cretaceous (eg Partridge and Maud, 1987; Partridge, 1998), which yields a mean retreat rate since then of ~ 300 m Ma^{-1}, have to be treated with great caution as this result appears to be based on only one basalt clast from a core taken from a late Cretaceous deposit (Mathews and Maud, 1988). Indeed all results from this study should be treated with caution as there is no discussion of reworking or post-depositional weathering of basalt clasts. Basalt is known to weather *in situ* by spheroidal weathering (eg Sarracino and Prasad, 1988) and hence any analysis reliant on the shape and size of basalt clasts preserved in deposits, such as the Mathews and Maud (1988) study, has to address this issue critically.

The AFTT data from the borehole at Swartberg mentioned earlier (Brown and Summerfield, in prep.) show that this site experienced accelerated denudation in the late Cretaceous (~ 91 – 69 Ma BP) involving the removal of ~ 3 km of crustal section. If this accelerated denudation is assumed to reflect either the passage of the retreating escarpment or, as favoured by Brown and Summerfield, fluvial incision seaward of a new escarpment that developed inland of Swartberg, this AFTT data suggest that the escarpment must have been east of this site since at least ~ 65 Ma BP. Given that Swartberg is ~ 30 km east of the southern Drakensberg, a maximum time-averaged retreat rate of ~ 460 m Ma^{-1} can be derived.

These three studies all provide at least extreme limits on the mean rate of backwearing of the southern Drakensberg for the Cenozoic. This is clearly less than the kilometre scale rates suggested by Schmidt (1989, 1996) for the Colorado Plateau for the same period, but more than the low rates derived for the SE Australian escarpment for the Neogene (Young and MacDougall, 1982; Nott *et al*, 1991). The mean rates for the past 65 Ma for the Drakensberg are higher than those determined by the present study but this might be expected given the shorter timeframe (10^4 a) over which these rates apply.

8.5.3.2 *Implications of the mean retreat rate derived for the southern Drakensberg*

The mean (n = 19) backwearing rate for the main free face of the southern Drakensberg averaged over sites that are ~ 175 km apart, is 87.9 ± 12.9 m Ma^{-1} (σ = 56.1 m Ma^{-1}). Although this directly measured rate is averaged over the past ~ 6 ka only, its order of magnitude is entirely compatible with indirect constraints imposed by the independent geological evidence discussed in Section 8.5.3.1. However this direct rate is more than an order of magnitude less than the various rates proposed by Lester King for major erosional scarps (scarp meaning the free face, King, 1962, p143) of "1 foot in 150 years to 1 foot in 300 years" (~ 1000 – 2000 m Ma^{-1}) (1953, canon 43). Specifically for the Drakensberg the rate ranged from an average "1 foot in 200 years" (~ 1500 m Ma^{-1}) (King, 1953, p746) to an approximate rate of "1 foot in 100 years" (~ 3000 m Ma^{-1}) (King, 1962, p 158). Based on the method employed by King to determine these rates (distance between present day site and inferred site of initiation divided by a period of time) (eg 1953, p746), these rates should probably be regarded as average rather than constant rates, although this is not made explicit by King. An even higher rate is implied by Burke's (1996) suggestion that the Drakensberg formed at the coast ~ 30 Ma BP and has retreated inland since then (equivalent average retreat rate of at least 5300 m Ma^{-1}).

Is it possible that the ^{36}Cl derived backwearing rate for the southern Drakensberg is atypically low? As indicated in Section 8.5.1, a potential drawback of the BFM approach is that the retreat rate is essentially controlled by the thickness of the blocks being modelled. To achieve mean backwearing rates for the Drakensberg of the order suggested by King (eg 1953, 1962, 1982), the measured ^{36}Cl concentrations would require the regular shedding of blocks well in excess of 5 m thick (Table 8.5). No field evidence exists at the sites visited on the southern Drakensberg or, indeed, in the Lesotho Highlands, which supports the shedding of such thickness' of basalt.

The mean escarpment retreat rate is necessarily integrated over the past 6 ka, thus while it might reflect the typical interglacial climatic conditions of the Quaternary, it does not include the impact of glacial maxima conditions. Mention has already been made of the fact that during past glacial maxima, the Drakensberg and Lesotho Highlands experienced colder and drier climatic conditions. In this situation denudational processes, in particular freeze-thaw break down of the free faces, may not have been any more effective than they are at present. In addition, if results from the studies of basalt in present freeze-thaw environments (eg Whalley *et al*, 1982; Douglas *et al*, 1991, 1995) are correct, then the physical properties

of the basalts are just as critical in controlling rock break down as climatic parameters. Taken together these factors imply that retreat rates of the Drakensberg free faces during past glacial maxima climatic conditions may have been essentially similar to those estimated here for the past 6 ka. However, even if retreat rates did increase during glacial maxima conditions to, say, double the present estimate, the low ratio of the length of past glacial maxima periods (~ 10 ka) to interglacial periods (~ 100 ka) during the Pleistocene, would mean such increased rates during glacial maxima had little impact on the average retreat rate for the whole ~ 1.6 Ma. Therefore it may be reasonable to suggest that the mean rate of backwearing determined here is likely to be fairly typical of the average rate for the whole of the Pleistocene.

Longer term extrapolations become increasingly more tenuous. However, the rates determined here are consistent with, if slightly lower than, the maximum escarpment retreat estimates for the past ~ 65 Ma provided by the Melkfontein tuff deposit and the AFTT data (Section 8.5.3.1). The low rates are also comparable with field, rather than theoretical, estimates of the retreat rate of other passive margin escarpments. In southeast Australia, field relationships of the escarpment (a gorge-like escarpment, Seidl *et al*, 1996) to dated basalt flows and sediments yield a retreat rate of 50 – 170 m Ma^{-1} (Young and MacDougall, 1982; Nott *et al*, 1991, 1996), while theoretical calculations, based on similar considerations to those employed by King, produce retreat rates of 1000 – 2000 m Ma^{-1} (eg Seidl *et al*, 1996; Weissel and Seidl, 1997). Analysis of *in situ*-produced cosmogenic ^{10}Be and ^{26}Al at one site on the Namibian margin has produced, using the 'steady-state' model (Lal, 1991) a mean rate of escarpment retreat of ~ 10 m Ma^{-1} (Cockburn *et al*, in press), well below the average rate of ~ 1000 m Ma^{-1} often assumed (eg Gilchrist and Summerfield, 1990).

Taken together, these comparisons suggest that the low rates of escarpment retreat determined here may be typical of a considerable longer timeframe (10^6 – 10^7a). Although it is not possible to be certain that this is the case, it is possible to speculate about the consequences of accepting that the ^{36}Cl derived retreat rate of ~ 90 m Ma^{-1} applies to much longer intervals than the ~ 6 ka period imposed by the technique. If extrapolated back in time, retreat of the southern Drakensberg at the mean rate of ~ 90 m Ma^{-1} would limit the total distance of escarpment retreat to < 15 km over the period since break-up along the SE African margin, ~ 135 Ma BP (Storey, 1995). Whilst this is still compatible with the Melkfontein tuff deposit's location, the AFTT data imply that considerable denudation (~ 3 km) occurred ~ 30 km east of the southern Drakensberg between ~ 91 – 69 Ma BP (Brown and Summerfield, in prep.). If this ~ 3 km of crustal stripping recorded by the AFTT data

reflects escarpment retreat then clearly the rate of retreat must have decreased considerably (order of magnitude) since the late Cretaceous. Such a dramatic reduction would have to be caused either by a increase in the lithological resistance of the basalts (unlikely given the broad similarity of backwearing and denudation rates derived here) or a major reduction in the efficiency of the denudational processes perhaps attributable to changes in the climatic regime. In general terms the climate of southern Africa is thought to have become both cooler and drier throughout the Cenozoic (Partridge, 1997a). However, conclusive onshore proxy data for the Tertiary climate are lacking which creates problems in deriving definitive interpretations (Dingle *et al*, 1983). Hence the exact climatic change experienced by the Drakensberg and Lesotho Highlands since the Cretaceous is unknown and consequently the impact on the efficiency of the denudational processes is similarly unknown.

Another possibility is that the present escarpment was not formed at the break-up site, but was formed some distance inland instead. Surface process models (SPMs), described in Chapter 5, have specifically considered the issue of passive margin escarpment evolution in general (eg Gilchrist *et al*, 1994; Kooi and Beaumont, 1994; Tucker and Slingerland, 1994; van der Beek and Braun, 1999; Beaumont *et al*, 2000). These SPMs identify the pre-break-up topography, and specifically the location of the antecedent continental drainage divide, as exerting first order control on the subsequent development of passive margin escarpments. The synthetic landscapes, produced by the SPMs, suggest that escarpment preservation and slow retreat are favoured where the summit of the escarpment broadly coincides with a drainage divide (as is extensively the case with the southern Drakensberg) and when continuous backtilting of the escarpment occurs because of flexural isostatic uplift induced by denudational unloading. Generally, where the drainage divide is significantly inland of any break-up related (tectonic) escarpment, fluvial incision caused by the discharge of large inland catchments draining over such an escarpment to the new base level will degrade this initial 'tectonic' escarpment (eg Kooi and Beaumont, 1994; Tucker and Slingerland, 1994; van der Beek and Braun, 1999; Beaumont *et al*, 2000). The SPMs predict that, in time, another escarpment would develop at the locus of this antecedent drainage divide (or, in exceptional circumstances, at the site of maximum isostatic rebound, van der Beek and Braun, 1999) and that escarpment preservation coupled with slow retreat would then be favoured by this coincidence of drainage divide and escarpment crest (eg Gilchrist *et al*, 1994; Beaumont *et al*, 2000).

Is it possible that the scenario predicted by the SPMs has applied to the development of the southern Drakensberg? Current conceptual models (eg King, 1951, 1982; Partridge and

Maud, 1987) envisage the immediate post-break-up landscape of southeast Africa as having a major escarpment, whose formation is related to the break-up event, and drainage divide located at or near the continental edge. The subsequent landscape development is then characterised by progressive inland retreat of the escarpment. However, there is no direct evidence of the drainage pattern immediately before or after break-up. Therefore the possibility exists that a major drainage divide existed some distance inland. Indeed the presence of such a topographic barrier may help to explain the geographical provinciality of the chemically distinct basalts of the Karoo igneous province (eg the lack of coeval and later Lebombo basalts in the Lesotho pile) (G. Marsh, pers. comm.). Such a drainage divide would have separated, presumably, low gradient interior rivers from higher gradient drainage flowing to the newly formed base level of the Indian Ocean. If this was the case then, based on the results from the simulated landscapes produced by the SPMs, any escarpment created along the coast as a consequence of break-up would rapidly have been destroyed by fluvial incision. The present day escarpment, in this scenario, would have grown vertically through differential denudation as a feature pinned at the seaward flank of the drainage divide, with subsequent inland retreat of only a few kilometres (Fleming *et al*, 1999). Such a scenario is favoured by Brown and Summerfield (in prep.) as a means of explaining their AFTT data. Their data record both an early Cretaceous phase of accelerated denudation at the coast and the somewhat later (~ 91 – 69 Ma BP) ~ 3 km of crustal stripping which occurred at a site only ~ 30 km east of the southern Drakensberg. Formation of the present escarpment at a site to the west of Swartberg some 65 Ma ago is consistent with the ^{36}Cl derived backwearing rate which, if it is typical of long-term retreat rates, would imply that the southern Drakensberg has retreated only ~ 6 km during the Cenozoic.

Considered on its own the ^{36}Cl derived backwearing rate for the southern Drakensberg is incapable of discriminating between the long-term (10^7 - 10^8 a) scenarios of the landscape development of southeast Africa. However, when considered in conjunction with regional scale denudation data (eg AFTT data) and the heuristic value of quantitative modelling, it provides a powerful means of constraining, at the landform scale, the implications of different landscape development schemes. Although such an approach may never conclusively determine the exact sequence of events, the only conclusive evidence for which is long since destroyed by denudation, it does present the opportunity to question and test critically some long held, but essentially, qualitative statements on long-term landscape development.

8.6 BACKWEARING VERSUS DOWNWEARING

The issue of whether landscapes are developed under the long-term influence of slope flattening, as proposed by Davis (1899, 1954), or the parallel retreat of slopes, as propounded by, *inter alia*, King (eg 1953), was the fundamental issue for geomorphology in the first half of the last century. Despite the critical importance attached to downwearing in the Davisian geographical cycle (Davis, 1899) and to backwearing in King's 'Standard Epigene Cycle of Erosion' (1962), neither approach was substantiated by empirical data. A general lack of adequate data at the scale of landforms and over timescales applicable to landscape formation means this debate remains essentially unresolved (Nott *et al*, 1996). Data from southeast Australia, based on the widespread preservation of basalts, demonstrate that both downwearing and backwearing are ongoing, but, at least in the context of that study area, they are both relatively insignificant when compared to the rate of gorge head extension (Nott *et al*, 1996). The ^{36}Cl derived data for the southern Drakensberg and Lesotho Highlands also show that both denudation (downwearing) and backwearing have occurred at least over the $10^4 - 10^5$ a timescale of the ^{36}Cl data, and, as suggested above, probably over a longer term (10^6 a).

Based on the mean denudation rates in Tables 8.2 and 8.3, the overall ratio of downwearing (denudation), based on all 33 flat-lying samples, ~ 10 m Ma^{-1}, to backwearing, based on the 0.5 m block fall model for all 44 free face samples, ~ 70 m Ma^{-1}, is 1:7. If the mean backwearing rates for the escarpment, ~ 90 m Ma^{-1}, and the Lesotho Highland free faces, ~ 60 m Ma^{-1}, are considered separately, the ratio becomes 1:9 and 1:6, respectively. In other words, in southeast Africa, the southern Drakensberg is backwearing at a rate which is 9 times faster than summit lowering, while in the Lesotho Highlands' free faces are backwearing six times faster than summit lowering. The main free face of the escarpment is also backwearing at ~ 1.4 times the mean rate of free face retreat in the Lesotho Highlands. Interestingly the ratio of downwearing to backwearing for the southern Drakensberg is of the same order as the ratio of 1: 5 – 17 for plateau lowering (~1 – 10 m Ma^{-1}, Bishop, 1988; Young and MacDougall, 1993; Bishop and Goldrick, 2000) to escarpment retreat (50 – 170 m Ma^{-1}, Young and MacDougall, 1982; Nott *et al*, 1991) in SE Australia. However, plateau lowering is not directly comparable to summit lowering as it includes, *inter alia*, fluvial incision.

These ratios suggest that backwearing of free faces is more influential in denuding the remainder of the basalt pile than downwearing of flat summits. However, without data on the

rate of fluvial incision or non-free face slope denudation within the Lesotho Highlands, presently unconstrained, a general conclusion that backwearing is more important than downwearing in denuding the Lesotho Highlands cannot be drawn. Some indication of these rates may be provided by calculating the potential denudation rate predicted by Ahnert's (1970) empirical relationship between local relief and denudation.

Local relief in the Lesotho Highlands, calculated from the maximum and minimum elevation values contained in the 10-minute resolution NGDC database (Summerfield and Hulton, 1994), ranges from ~ 600 m to 2000 m for 10-minute grid units (~ 16.2 km by 18.5 km at latitude 30°). Although less than the 20 km x 20 km cells used by Ahnert (1970) to derived his relationship of denudation rate, d, (m Ma^{-1}) to local relief, h, (m) (d = 0.1535 h), the grid dimensions are sufficiently comparable to enable Ahnert's relationship to be applied (Summerfield, 1991b; Summerfield and Hulton, 1994). This range of local relief suggests that present denudation rates for the Lesotho Highlands should be of the order of ~ 90 – 300 m Ma^{-1}, with a mean of ~ 165 m Ma^{-1}. Comparable denudation rates for the southern Drakensberg (local relief ranging from 900 – 2000 m) are ~ 140 – 330 m Ma^{-1}, with a mean of ~ 215 m Ma^{-1}, about 1.3 times the rate for the Lesotho Highlands. Interestingly this is similar to the difference in ^{36}Cl derived backwearing rates for these two areas (~ 1.4 times). The rates for both the Lesotho Highlands and southern Drakensberg are similar to the estimates derived by Summerfield (1991b) using 15′ x 15′ size grids.

The denudation rates predicted by Ahnert's (1970) relationship are higher than the site-specific summit denudation and free face backwearing rates, although it should be borne in mind that the latter are not strictly comparable to denudation rates. An exact split of the contribution of each landscape component to the predicted mean denudation rate is not feasible, but a possible implication is that fluvial incision is responsible for the higher rate predicted by Ahnert's (1970) model. If the mean rate of fluvial incision is speculated to be of the order of 100 m Ma^{-1}, then the long-term (10^6 – 10^7 a) operation of this rate would imply that the headwaters of the Orange River could have incised the original ~ 2 km thick basalt pile in ~ 20 Ma. Indeed, if the predicted mean denudation rate for the Lesotho Highlands of ~ 165 m Ma^{-1} applies to the longer term, the majority of the pile would be removed in ~ 15 Ma. This might suggest that fluvial incision of this magnitude is a recent phenomenon perhaps related to uplift or base level adjustment (the base level for the Lesotho Highlands is the Atlantic Ocean). If so, why isn't the same amount of local relief encountered in the area inland (west and southwest) of the Lesotho Highlands (Summerfield, 1991b)? Any suggestion that the basalt may not be as resistant to denudation as the underlying Karoo

sedimentary sequence runs counter to the fact that the Lesotho Highlands still retains up to 70 % of the original thickness of the basalt pile some 183 Ma after emplacement and ~ 135 Ma after the opening of the South Atlantic. An accurate estimate of rates and timings of fluvial incision in the Lesotho Highlands, beyond the scope of this study, is essential in answering this question.

In any event, if the mean denudation rate predicted by Ahnert's (1970) relationship is taken as averaging denudation from both downwearing (eg summit lowering, fluvial incision) and backwearing (eg free face retreat), then the overall ratio of downwearing to backwearing in the Lesotho Highlands will be less than implied by the site-specific ^{36}Cl derived data. The ^{36}Cl data derived ratio of downwearing to backwearing of 1:9, for the southern Drakensberg, holds good for the relationship of the summit crest and main free face. However, if the whole escarpment zone is considered (ie the buttress ridges and slopes below the free faces) then, based on the higher denudation rates recorded by the samples from the buttress ridge at Naudesnek (mean ~ 23 m Ma^{-1} (n = 2), Table 8.2), and the existence of those ridges, which implies higher mean rates of fluvial incision, the ratio is also likely to be less than 1:9. Regardless of the exact magnitude of the ratio, the ^{36}Cl data have shown that both backwearing and downwearing are operating in at least part of the landscape proposed by King as being the consequence of the sole operation of backwearing and pediplanation.

CHAPTER 9: CONCLUSIONS AND FUTURE DIRECTIONS

9.1 CONCLUSIONS

A number of conclusions may be drawn from this research. These are grouped broadly in terms of the specific application of the denudation and backwearing results derived from *in situ*-produced ^{36}Cl data to the evolution of the SE African landscape and the more general application of the analysis of *in situ*-produced cosmogenic isotopes to research into long-term landscape development.

The main conclusions of this research relating to the development of the SE African landscape are:

- The mean (n = 33) denudation rate for bedrock summits in the southern Drakensberg and Lesotho Highlands, derived from the analysis of *in situ*-produced cosmogenic ^{36}Cl, is 10.6 ± 1.6 m Ma^{-1}. This mean rate is integrated over the past ~ 50 ka, but may be applicable to at least the Quaternary. Denudation rates determined for individual samples fluctuate between 1.2 ± 0.4 m Ma^{-1} and 43.0 ± 6.6 m Ma^{-1}. The cause of this observed, site-to-site variability, which exists in both summit and free face sample datasets, is unclear. However, it may simply reflect the natural site-to-site variations in the lithological resistance of individual basalt flows or the intensity of the denudational processes. Alternatively it may be caused by the underlying assumptions of the interpretive models not having been fully satisfied by a particular sample. The mean summit lowering rate is consistent with longer term ($10^7 - 10^8$ a), regional scale, estimates of crustal stripping provided by, for example, zeolite zonation studies and AFTT. Denudation of these summit flats at the measured rates demonstrates that Jurassic age erosion surface remnants have not survived unaltered since the break-up of Gondwana as suggested by King (eg 1982).

- The mean backwearing rate (n = 19) for the main free face of the southern Drakensberg, based on samples from 3 separate locations spread ~ 175 km along the escarpment, is 87.9 ± 12.9 m Ma^{-1} (range = 195.7 m Ma^{-1}). This rate is derived from measured ^{36}Cl abundances using an interpretive model, based on field evidence, which assumes that the predominant mode of retreat is the regular shedding of ~ 0.5 m thick blocks. The mean retreat rate is averaged over the past ~ 6 ka, but may be applicable to at least the past 1.6

Ma. Although this mean rate is of the same order as field-data-derived retreat rates for the SE Australian and Namibian passive margin escarpments, it is more than an order of magnitude less than the theoretically determined average retreat rate specifically suggested for the Drakensberg and, generally, applied to other passive margin escarpments. However, the slow retreat rate for the southern Drakensberg, derived from the ^{36}Cl data, is consistent with: (i) indirect inferences from geological and AFTT data which imply similarly slow rates of Drakensberg escarpment retreat during the Cenozoic and (ii) predictions from numerical models of synthetic passive margin escarpments which propose that slow escarpment retreat rates will occur, in situations like that encountered at the southern Drakensberg, where the escarpment summit coincides generally with the continental drainage divide. Taken together these independent data, including the ^{36}Cl derived retreat rates, suggest that the present southern Drakensberg escarpment has been retreating slowly throughout the Cenozoic. This implies that the southern Drakensberg may not have retreated from a site of formation near the coast. Such a conclusion does not preclude the formation of the southern Drakensberg escarpment being a direct consequence of Gondwana break-up: rather integration of these independent data suggests that existing qualitative models of post-Gondwana landscape development along the SE African continental margin require some re-appraisal.

- In the Lesotho Highlands, the mean (n = 16) free face backwearing rate, derived using the 0.5 m thick block fall model, is 61.1 ± 7.9 m Ma^{-1} (range = 111.1 m Ma^{-1}). This is ~ 40 % less than the retreat rate of the main free face of the escarpment. Nevertheless, backwearing is clearly an important mechanism of denudation in the Lesotho Highlands. The ratio of the ^{36}Cl derived mean summit lowering to free face backwearing rate is 1:7, however, the overall downwearing to backwearing rate in the Lesotho Highlands is likely to reduce if the impact of fluvial incision, currently unknown, is taken into account. Therefore although backwearing, as suggested by King (eg 1953), is a very important modifier of this landscape it does not operate exclusively.

Conclusions relating to the general application of the analysis of *in situ*-produced cosmogenic isotopes to research into long-term landscape development are:

- Previous research has demonstrated the general potential of *in situ*-produced cosmogenic isotope analysis to yield denudation data applicable to the $10^3 - 10^6$ a timescale (eg Nishiizumi *et al*, 1993). This project has confirmed the ability of *in situ*-produced

cosmogenic ^{36}Cl analysis to yield site-specific denudation data for flat-lying sites and backwearing rate estimates for free face sites over timescales of $10^3 - 10^5$ years. This technique therefore presents an important opportunity to assess landscape change directly at the scale of individual landforms and over timescales appropriate to landscape development. Although the technique is affected by acknowledged uncertainties in production rates (eg Gosse *et al*, 1996; Dunai, 2000) and limitations in the interpretive models (eg Small *et al*, 1997; Bierman *et al*, 1999), the denudation estimates it provides are important as first order information which has not previously been obtainable. Refinement of the technique is ongoing (eg Dunne *et al*, 1999; Dunai, 2000) and, given time, uncertainties in production rates will decrease and interpretive models will become more advanced.

- Results from this project demonstrate that cosmogenic isotope analysis, by providing denudation information at the landform scale, has considerable potential as a tool for addressing long-standing questions of landscape development, such as the retreat rate of passive margin escarpments. Whilst this technique may be usefully employed as a 'standalone' tool for addressing long-term landscape development, this project illustrates that a better understanding of long-term morphological evolution is achieved when the shorter term, site-specific, cosmogenic data are considered together with results both from other techniques which quantify longer term, regional scale, landscape change (eg AFTT) and the heuristic predictions of numerical models of landscape development. This study therefore confirms the value of taking an integrated approach to understanding long-term landscape development.

- This study illustrates the practical application of cosmogenic isotope analysis to quantifying denudation of steeply dipping surfaces (ie free faces). This has previously only been discussed theoretically (eg Dunne *et al*, 1999). Although the 'steady-state' model of Lal (1991) may be applicable to free faces formed in massive lithologies, where denudation is more likely to proceed by granular disintegration, its application is considered questionable for free faces evolved in jointed lithologies, such as the Drakensberg Group basalts. In this situation it is proposed that a more realistic model, to interpret the measured isotopic concentration, is one based on the regular shedding of individual blocks, the thickness of which is constrained by the field evidence. This highlights an important general point which is that the application of this technique requires the employment of models which are appropriate to the field circumstances. Although data can be derived from the measured concentration using any interpretive

model, the use of 'off-the-shelf' models (eg Lal, 1991) should always be subject to a critical assessment of the underlying model assumptions and their likely applicability to the field setting. Future work (section 9.2) is needed to derive and test other interpretive models.

9.2 FUTURE DIRECTIONS

Opportunities for future research suggested by this project cover both the further advancement of the cosmogenic isotope analysis technique as a tool for quantifying denudation and future applications of the technique to research into the development of landscapes in southern Africa and beyond.

The use of cosmogenic isotope analysis to determine reliable data for geomorphological application relies on the ability of the models (used to interpret the measured cosmogenic isotope abundance as a surface exposure age or denudation rate) to mirror geomorphic processes realistically. The applicability of the underlying assumptions of these models to 'real' geomorphic settings, in particular the ability of the 'steady-state' model (Lal, 1991) to reflect denudational processes accurately, has been the subject of some debate (eg Gillespie and Bierman, 1995; Small *et al*, 1997; Bierman *et al*, 1999). Although considerable effort has been expended in establishing the accuracy of cosmogenic isotope derived surface exposure ages by reference to independently established ages, no attempt has yet been made (or at least published) which investigates, by reference to other field evidence, the precision of denudation rates quantified by modelling cosmogenic isotope yields. This may, in part, reflect the lack of other techniques which can provide such site-specific denudation data over the same timescale. However, the ability to derive retreat rates for free faces using the technique, as demonstrated in this thesis, does present the opportunity to assess the accuracy of backwearing rates derived from different models (eg SSM, BFM) in field settings where independent estimates of retreat, over similar timescales, have been made (Table 8.6). Such research should enable refinement of these existing models and perhaps suggest other novel approaches and solutions.

Although this project has quantified the retreat rate of the southern Drakensberg, other issues relating to the development of the Great Escarpment of southern Africa remain, some of which can be addressed by the analysis of *in situ*-produced cosmogenic isotopes, again within an integrated framework. For example: is the northern Drakensberg, which runs at right angles to the coast for over 90 km, backwearing at the same ~ 90 m Ma^{-1} rate?; what

are the retreat rates of other escarpments in SE Africa which are formed in the upper Karoo sedimentary sequence (Clarens / Elliot / Molteno Formations)? More generally the technique is capable of being used to assess the relative importance of the extensive outcrops of Karoo igneous province dolerite sheets and dykes in the landscape evolution of southern Africa. Where exposed, these tend to form positive relief, for example, as flat-topped inselbergs, and the use of the technique would enable the denudation and backwearing rate of these features to be assessed. Such results could be integrated with the regional scale denudation data already quantified by AFTT (eg Brown, 1992) and currently ongoing numerical modelling of the morphological evolution of this region (P. van der Beek, pers. comm.).

Major escarpments are fundamental morphological features which exist in all high-elevation passive margins (Gilchrist and Summerfield, 1990), and both qualitative and conceptual models regard these escarpments as playing a critical role in the development of such landscapes. This study has shown the ability of *in situ*-produced cosmogenic isotope analysis to quantify both the summit denudation and free face retreat rate of such key features. A similar approach has been applied to the Namibian margin escarpment (Cockburn 1998, Cockburn *et al*, in press) and research using *in situ*-produced ^{10}Be and ^{26}Al is currently ongoing on the southeast Australian margin (H. Cockburn, pers. comm.). The analysis of *in situ*-produced ^{36}Cl could usefully be applied to the sections of the Western Ghats escarpment in India which are formed in Deccan flood basalts. Some AFTT and offshore sediment volume data already exist (Gunnell and Fleitout, 1998, 2000) and escarpment retreat rates provided by the analysis of *in situ*-produced cosmogenic isotopes could be integrated with this and used to test existing theoretical estimates of the Western Ghats retreat rate (eg Widdowson, 1997b).

Establishing retreat rates from these 'mature' escarpments in high-elevation passive margins are critically important to furthering our understanding of the long-term landscape history of these areas. However, equally important, given the numerical modelling predictions as to the morphological conditions which favour the survival and retreat of these escarpments (eg Kooi and Beaumont, 1994), is the establishment of retreat rates for escarpments that are located at sites of more recent continental break-up. The Gulf of Suez / Red Sea, formed by the break-up of the African and Arabian plates, is one such example. AFTT denudation data already exists for this margin (Omar and Steckler, 1995) and estimates, based on inferences from indirect field evidence, of an average escarpment retreat rate as high as 6 km Ma^{-1} have been made (Steckler and Omar, 1994). Whilst a higher retreat rate would be expected for this

escarpment formed, as it is, in a limestone caprock which overlies and is being actively undercut by the removal of a friable and easily eroded sandstone (Steckler and Omar, 1994), no direct estimate of escarpment retreat exists. The analysis of *in situ*-produced ^{36}Cl in the carbonate caprock would enable a direct estimate of such retreat to be made.

This study has demonstrated the ability of *in situ*-produced cosmogenic isotope analysis to address long-standing questions of landscape evolution and has gone some way to taking up Nishiizumi *et al's* (1993, p424) challenge "to rethink and create innovative test of some long-held assumptions about how landscapes evolve". Overall a growing acceptance of a more integrated approach to understanding long-term morphological evolution will lead to a wider range of applications of this technique thereby further enabling problems of landscape development to be addressed quantitatively.

REFERENCES

Ahnert, F., 1960. The influence of Pleistocene climates upon the morphology of cuesta scarps on the Colorado Plateau. *Annals of the Association of American Geographers*, **50**, 139-156.

Ahnert, F., 1970. Functional relationships between denudation, relief and uplift in large mid-latitude drainage basins. *American Journal of Science*, **268**, 243-263.

Ahnert, F., 1994. Equilibrium, scale and inheritance in geomorphology. *Geomorphology*, **11**, 125-140.

Ahnert, F., 1996. The point of modelling geomorphological systems. In S. B. McCann and D. C. Ford (eds.) *Geomorphology sans frontières*, Wiley, 91-113.

Albrecht, A., Herzog, G.F., Klein, J., Dezloufly-Arjomandy, B., and Goff, F., 1993. Quaternary erosion and cosmic-ray-exposure history derived from ^{10}Be and ^{26}Al produced in situ - An example from Pajarito plateau, Valles caldera region. *Geology*, **21,** 551-554.

Allen, P.A. and Allen, J.R., 1990. *Basin analysis: principles and applications.* Blackwell, Oxford.

Allison, R.J., 1996. Slope and slope processes. *Progress in Physical Geography*, **20**, 453-465.

Allison, R.J. and Kimber, O.G., 1998. Modelling failure mechanisms to explain rock slope change along the Isle of Purbeck coast, UK. *Earth Surface Processes and Landforms,* **23**, 731-750.

Allkofer, O.C. and Jokisch, H., 1973. A survey on the recent measurements of the absolute vertical cosmic-ray muon flux at sea level. *Nuovo Cimento*, 15, 371-389.

Anderson, R.S., Repka, J.L., and Dick, G.S., 1996. Explicit treatment of inheritance in dating depositional surfaces using in situ ^{10}Be and ^{26}Al. *Geology*, **24**, 47-51.

André, M-F., 1986. Dating slope deposits and estimating rates of rock wall retreat in northwest Spitsbergen by lichenometry. *Geografiska Annaler*, **60A**, 65-75.

André, M-F., 1997. Holocene rockwall retreat in Svalbard: A triple rate evolution. *Earth Surface Processes and Landforms,* **22**, 423-440.

Andrews, J.N., Fontes, J-Ch., Michelot, J-L., and Elmore, D., 1986. In-situ neutron flux, ^{36}Cl production and groundwater evolution in crystalline rocks at Stripa, Sweden. *Earth and Planetary Science Letters*, **77**, 49-58.

Anthony, E.Y., and Poths, J., 1992. ^{3}He surface exposure dating and its implications for magma evolution in the Potrillo volcanic field, Rio Grande Rift, New Mexico, USA.. *Geochimica et Cosmochimica Acta*, **56**, 4105-4108.

Antoine, L.A.G. and Moyes, A.B., 1992. Geophysical evidence for a causative process for fragmentation in western Gondwana. *Geology*, **20**, 605-608.

Ballantyne, C.K., and Kirkbride, M.P., 1987. Rockfall activity in upland Britain during the Loch Lomond stadial. *The Geographical Journal*, **153**, 86-92.

Ballantyne, C.K., Stone, J.O., and Fifield, L.K., 1998. Cosmogenic Cl-36 dating of postglacial landsliding at The Storr, Isle of Skye, Scotland. *The Holocene*, **8**, 347-351.

Barnard, W.S., 1997. Classics in physical geography revisited: Wellington, J.H., 1955, Southern Africa: a geographical study. Part 1. Physical Geography. *Progress in Physical Geography*, 21, 137-144.

Barry, R.G., 1992. *Mountain weather and climate*. Routledge, London.

Baumgartner, S., Beer, J., Masarik, J., Wagner, G., Meynadier, L., and Synal, H.-A., 1998. Geomagnetic modulation of the ^{36}Cl Flux in the GRIP Ice Core, Greenland. *Science,* **279**, 1330-1332.

Beaumont, C., Kooi, H., and Willett, S., 2000. Coupled tectonic – surface process models with applications to rifted margins and collisional orogens. In M.A. Summerfield (ed.) *Geomorphology and Global Tectonics.* Wiley, Chichester.

Becht, M., 1995. Slope erosion processes in the Alps. In O. Slaymaker, (ed.), *Steepland Geomorphology*. Wiley, Chichester.

Beeson, M.H. and Tolan, J.L., 1990. The Columbia River Basalt Group in the Cascade Range: a middle Miocene reference datum for structural analysis. *Journal of Geophysical Research*, **95**, 19,547-19,559.

Bell, J.W., Brune, J.N., Liu, T., Zreda, M., and Young, J.C., 1998. Dating precariously balanced rocks in seismically active parts of California and Nevada. *Geology*, **26**, 495-498.

Ben-Avraham, Z., 1995. Neotectonic activity offshore southeast Africa and its implications. *South African Journal of Geology,* **98**, 202-207.

Ben-Avraham, Z., Hartnady, C.J.H., and Le Roux, A.P., 1995. Neotectonic activity on continental fragments in the southwest Indian Ocean, Agulhas Plateau and Mozambique Ridge. *Journal of Geophysical Research*, **100**, 6199-6211.

Ben-Avraham, Z., Hartnady, C.J.H., and Malam, J.A., 1993. Early tectonic extension between the Agulhas Bank and the Falkland Plateau due to the rotation of the Lafonia microplate. *Earth and Planetary Science Letters*, **117**, 43-58.

Ben-Avraham, Z., Nieme, T.M., and Hartnady, C.J.H., 1994. Mid-Tertiary changes in deep ocean circulation patterns in the Natal Valley and Transkei Basin, southwest Indian Ocean. *Earth and Planetary Science Letters*, **121**, 639-646.

Bentley, H.W., Phillips, F.M., Davis, S.N., Gifford, S., Elmore, D., Tubbs, L.E., and Gove, H.E., 1982. Thermonuclear ^{36}Cl pulse in natural water. *Nature*, **300**, 737-740.

Bentley, H.W., Phillips, F.M., and Davis, S.N., 1986. Chlorine-36 in the Terrestrial Environment. In: P., Fritz and J-Ch., Fontes, (eds.), *Handbook of Environmental Isotope Geochemistry*. Elsevier, Amsterdam, 427-480.

Bierman, P.R., 1993. *In situ produced cosmogenic isotopes and the evolution of granitic landforms.* Unpublished Ph.D. thesis, University of Washington.

Bierman, P.R., 1994. Using in situ produced cosmogenic isotopes to estimate rates of landscape evolution: A review from the geomorphic perspective. *Journal of Geophysical Research*, **99, B7**, 13 885-13 896.

Bierman, P.R., Albrecht, A., Bothner, M.H., Brown, E.T., Bullen, T.D., Gray, L.B., and Turpin, L., 1998. Erosion, weathering and sedimentation. In C. Kendall and J.J. McDonnell (eds.) *Isotope tracers in catchment hydrology*, Elsevier.

Bierman, P.R., and Gillespie, A.R., 1991. Range fires: A significant factor in exposure-age determination and geomorphic surface evolution. *Geology*, **33**, 148-156.

Bierman, P.R., Gillespie, A.R., and Caffee, M.W., 1995. Cosmogenic ages for earthquake recurrence intervals and debris flow fan deposition, Owens Valley, California. *Science*, **270**, 447-450.

Bierman, P.R., Marsella, K.A., Patterson, C., Davis, P.T., and Caffee, M., 1999. Mid-Pleistocene cosmogenic minimum-age limits for the pre-Wisconsinan glacial surfaces in southwestern Minnesota and southern Baffin Island: a multiple nuclide approach. *Geomorphology*, **27**, 25-39.

Bierman, P., and Steig, E.J., 1996. Estimating rates of denudation using cosmogenic isotope abundances in sediment. *Earth Surface Processes and Landforms,* **21**, 125-139.

Bierman, P., and Turner, J., 1995. ^{10}Be and ^{26}Al evidence for exceptionally low rates of Australian bedrock erosion and the likely existence of Pre-Pleistocene landscapes. *Quaternary Research,* **44**, 378-382.

Bilokon, H., Cini Castagnoli, G., Castellina, A., D'Ettorre Piazzoli, B., Mannocchi, G., Meroni, E., Picchi, P., and Vernetto, S., 1989. Flux of the vertical negative muons stopping at depths of 0.35 – 1000 hg/cm^2. *Journal of Geophysical Research*, **94**, 12145-12152.

Birch, G.F., 1982. Sedimentological and geophysical investigations of a major sediment exit point on the south-east African continental margin (vicinity of Port St. Johns). *Transactions of the Geological Society of South Africa*, **85**, 91-103.

Birkenhauer, J., 1985. Some thoughts on coastal levels and their significance in the geomorphological development of Natal. *South African Geographical Journal,* **67**, 228-233.

Birkenhauer, J., 1991. *The Great Escarpment of Southern Africa and its coastal forelands - A Re-Appraisal.* Münchener Geographische Abhandlungen Reihe B, Institut für Geographie der Universität München.

Bishop, P., 1985. Southeast Australian Late Mesozoic and Cenozoic denudation rates: a test for Late Tertiary increases in continental denudation. *Geology*, **13**, 479-482.

Bishop, P., 1986. Horizontal stability of the Australian continental drainage divide in south central New South Wales during the Cainozoic. *Australian Journal of Earth Sciences*, **33**, 295-307.

Bishop, P., 1988. The Eastern Highlands of Australia: the evolution of an intraplate highland belt. *Progress in Physical Geography*, **12**, 159-181.

Bishop, P., 1998. Griffith Taylor and the SE Australian Highlands: issues of data sources and testability in interpretations of long-term drainage history and landscape evolution. *Australian Geographer*, **29**, 7-29.

Bishop, P., 1999. Mega-geomorphology: 'Old' physical geography back in fashion. *The Journal of the Scottish Association of Geography Teachers*, 28, 5-14.

Bishop, P. and Brown, R.W., 1992. Denudational isostatic rebound of intraplate highlands: The Lachlan River Valley, Australia. *Earth Surface Processes and Landforms,* **17**, 345-360.

Bishop, P. and Goldrick G., 2000. Eastern Australia. In: M.A. Summerfield, (ed.), *Geomorphology and Global Tectonics*, Wiley, Chichester.

Bishop, P., Young, R.W., and McDougall, I., 1985. Stream profile change and long-term landscape evolution - Early Miocene and modern rivers of the east Australian highland crest, central New South Wales. *Journal of Geology*, **93**, 455-474.

Boctor, N.Z., Nixon, P.H., Buckley, F., and Boyd., F.R., 1984. Petrology of carbonate tuff from Melkfontein, East Griqualand, southern Africa. In: J. Kornprobst (ed.) *Kimberlites I: kimberlites and related rocks*. Elsevier, Amsterdam.

Boelhowers, J., 1994. Periglacial landforms at Giant's Castle, Natal Drakensberg, South Africa. *Permafrost and Periglacial Process,* **5**, 129-136.

Bohannon, R.G., Naeser, C.W., Schmidt, D.L., and Zimmermann, R.A., 1989. The timing of uplift, volcanism, and rifting peripheral to the red Sea: A case for passive rifting? *Journal of Geophysical Research*, **94**, 1683-1701.

Braucher, R., Bourlès, D.L., Colin, F., Brown, E.T., and Boulangé, B., 1998b. Brazilian laterite dynamics using in situ-produced ^{10}Be. *Earth and Planetary Science Letters*, **163**, 197-205.

Braucher, R., Bourlès, D.L., Colin, F., Brown, E.T., and Boulangé, B., 1999. Brazilian laterite dynamics using in situ-produced ^{10}Be (Vol 163, P197). *Earth and Planetary Science Letters*, **165**, 295.

Braucher, R., Colin, F., Brown, E.T., Bourlès, D.L., Bamba, D., Raisbeck, G.M., Yiou, F., and Koud, J.M., 1998a. African laterite dynamics using in situ-produced ^{10}Be. *Geochimica et Cosmochimica Acta*, **62**, 1501-1507.

Braun, J., and Beaumont, C., 1989. A physical explanation of the relation between flank uplifts and the breakup unconformity at rifted continental margins. *Geology*, **17**, 760-764.

Braun, J. and Sambridge, M., 1997. Modelling landscape evolution on geological time scales: a new method based on irregular spatial discretization. *Basin Research*, **9**, 27-52.

Bremer, H., 1985. Randschwellen: a link between plate tectonics and climatic geomorphology. *Zeitschrift für Geomorphologie NF, Supplement Band*, **54**, 11-21.

Briner, J.P., and Swanson, T.W., 1998. Using inherited cosmogenic ^{36}Cl to constrain glacial erosion rates of the Cordilleran ice sheet. *Geology*, **26**, 3-6.

Brook, E.J., Brown, E.T., Kurz, M.D., Ackert, R.P., Raisbeck, G.M., and Yiou, F., 1995a. Constraints on age, erosion, and uplift of Neogene glacial deposits in the Transantarctic Mountains determined from on situ cosmogenic ^{10}Be and ^{26}Al. *Geology*, **23**, 1063-1066.

Brook, E.J., and Kurz, M.D., 1993. Surface-exposure chronology using *in situ* cosmogenic ^{3}He in Antarctic quartz sandstone boulders. *Quaternary Research,* **39**, 1-10.

Brook, E.J., Kurz, M.D., Ackert, R.P., Denton, G.H., Brown, E.T., Raisbeck, G.M., and Yiou, F., 1993. Chronology of Taylor Glacier advances in Arena Valley, Antarctica, using *in situ* cosmogenic ^{3}He and ^{10}Be. *Quaternary Research*, **39**, 11-23.

Brook, E.J., Kurz, M.D., Ackert, R.P., Raisbeck, G.M., and Yiou, F., 1995b. Cosmogenic nuclide exposure ages and glacial history of late Quaternary Ross Sea drift in McMurdo Sound, Antarctica. *Earth and Planetary Science Letters*, **131**, 41-56.

Brook, E.J., Nesje, A., Lehman, S.J., Raisbeck, G.M., and Yiou, F., 1996. Cosmogenic nuclide exposure ages along a vertical transect in western Norway: implications for the Height of the Fennoscandian ice sheet. *Geology*, **24**, 207-210.

Brown, E.T., Bourlès, D.L., Burchfiel, B.C., Qidong, D., Jun, L., Molnar, P., Raisbeck, G.M., Yiou, F., 1998a. Estimation of slip rates in the southern Tien Shan using cosmic ray exposure dates of abandoned alluvial fans. *Geological Society of America Bulletin*, **110**, 377-386.

Brown, E.T., Bourlès, D.L., Colin, F., Raisbeck, G.M., Yiou, F., and Desgarceaux, S., 1995a. Evidence for muon-induced production of ^{10}Be in near surface rock from the Congo. *Geophysical Research Letters*, **22**, 703-706.

Brown, E.T., Brook, E.J., Raisbeck, G.M., Yiou, F., and Kurz, M.D., 1992. Effective attenuation lengths of cosmic rays producing ^{10}Be and ^{26}Al in quartz: implications for exposure age dating. *Geophysical Research Letters*, **19**, 369-372.

Brown, E.T., Edmond, J.M., Raisbeck, G.M., Yiou, F., Kurz, M.D., and Brook, E.J., 1991. Examination of surface exposure ages of Antarctic moraines using *in situ* produced ^{10}Be and ^{26}Al. *Geochimica et Cosmochimica Acta*, **55**, 2269-2283.

Brown, E.T., Stallard, R.F., Larsen, M.C., Raisbeck, G.M., and Yiou, F., 1995b. Denudation rates determined from the accumulation of in situ- produced ^{10}Be in the Luquillo Experimental Forest, Puerto Rico. *Earth and Planetary Science Letters*, **129**, 193-202.

Brown, E.T., Stallard, R.F., Larsen, M.C., Bourlès, D.L., Raisbeck, G.M., and Yiou, F., 1998b. Determination of predevelopment denudation rates of an agricultural watershed (Cayaguás River, Puerto Rico) using in-situ-produced ^{10}Be in river-borne quartz. *Earth and Planetary Science Letters*, **160**, 723-728.

Brown, R.W., 1992. *A fission track thermochronology study of the tectonic and geomorphic development of the sub-aerial continental margins of southern Africa.* Unpublished Ph.D. Thesis, La Trobe University, Bundoora, Victoria.

Brown, R.W., Gallagher, K., Gleadow, A.J.W., and Summerfield, M.A., 2000. Morphotectonic evolution of the South Atlantic margins of south Africa and South America. In M.A. Summerfield (ed.) *Geomorphology and Global Tectonics,* Wiley.

Brown, R.W., Rust, D.J., Summerfield, M.A., Gleadow, A.J.W., and de Wit, M.C.J., 1990. An early Cretaceous phase of accelerated erosion on the south-western margin of Africa: evidence from apatite fission track analysis and the offshore sedimentary record. *Nuclear Tracks and Radiation Measurements,* **17**, 339-350.

Brown, R.W., and Summerfield, M.A., in prep. Denudational history along a transect across the eastern margin (Drakensberg Escarpment) of southern Africa derived from apatite fission-track thermochronology.

Brown, R.W., Summerfield, M.A., and Gleadow, A.J.W., 1994. Apatite fission track analysis: Its potential for the estimation of denudation rates and implications for models of long-term landscape development. In: M.J. Kirkby (ed.) *Process models and theoretical geomorphology*, Wiley, London.

Bruno, L.A., Baur, H., Graf, T., Schlüchter, C., Signer, P., and Wieler, R., 1997. Dating of Sirius Group tillites in the Antarctic Dry Valleys with cosmogenic ^{3}He and ^{21}Ne. *Earth and Planetary Science Letters*, **147**, 37-54.

Burbank, D.W., Leland, J., Fielding, E., Anderson, R.S., Brozovic, N., Reid, M.R., and Duncan, C., 1996. Bedrock incision , rock uplift and threshold hillslopes in the northwestern Himalayas. *Nature*, **379**, 505-510.

Burke, K., 1996. The African Plate. *South African Journal of Geology,* **99**, 341-409.

Burke, K., and Dewey, J.F., 1973. Plume-generated triple junctions: key indicators in applying plate tectonics to older rocks. *Journal of Geology*, **81**, 406-433.

Butzer, K.W., 1984. Late Quaternary environments in South Africa. In: J.C. Vogel (ed.) *Late Cainozoic Palaeoclimates of the Southern Hemisphere*. A.A. Balkema, Rotterdam.

Campbell, I.H. and Griffiths, R.W., 1990. Implications of mantle plume structure for the evolution of flood basalts. *Earth and Planetary Science Letters*, **99**, 79-93.

Cashman, K., Pinkerton, H., and Stephenson, J., 1998. Introduction to special section; Long lava flows. *Journal of Geophysical Research*, **103**, 27,281-27,289.

Catuneanu, O., Hancox, P.J., and Rubidge, B.S., 1998. Reciprocal flexural behaviour and contrasting stratigraphies: a new basin development model for the Karoo retroarc foreland system, South Africa. *Basin Research*, **10**, 417-439.

Cerling, T.E., 1990. Dating geomorphologic surfaces using cosmogenic ^{3}He. *Quaternary Research*, **33**, 148-156.

Cerling, T.E. and Craig, H., 1994a. Geomorphology and in-situ cosmogenic isotopes. *Annual Review of Earth and Planetary Science,* **22**, 273-317.

Cerling, T.E. and Craig, H., 1994b. Cosmogenic ^{3}He production rates from 39° N and 46° N latitude western USA and France. *Geochimica et Cosmochimica Acta*, **58**, 249-255.

Cerling, T.E., Poreda, R.J., and Rathburn, S.L., 1994. Cosmogenic ^{3}He and ^{21}Ne age of the Big Lost River Flood, Snake River Plain, Idaho. *Geology*, 22, 227-230.

Cerling, T.E., Webb, R.H., Poreda, R.J., Rigby, A.D., and Melis, T.S., 1999. Cosmogenic ^{3}He ages and frequency of late Holocene debris flows from Prospect Canyon, Grand Canyon, USA. *Geomorphology*, **27**, 93-111.

Charalambus, S., 1971. Nuclear transmutation by negative stopped muons and the activity induced by the cosmic-ray muons. *Nuclear Physics*, **A166**, 145-161.

Chorley, R.J., 1965a. A re-evaluation of the geomorphic system of W.M. Davis. In: R.J. Chorley and P. Haggett (eds.) *Frontiers in Geographical Teaching*, Metheun, London.

Chorley, R.J., 1965b. The application of quantitative methods to geomorphology. In: R.J. Chorley and P. Haggett (eds.) *Frontiers in Geographical Teaching*, Metheun, London.

Clark, D.H., Bierman, P.R., and Larsen, P., 1995. Improving *in situ* cosmogenic chronometers. *Quaternary Research,* **44**, 367-377.

Clift, P.D., Carter, A., and Hurford, A.J., 1998. The erosional and uplift history of NE Atlantic passive margins: constraints on a passing plume. *Journal of the Geological Society, London*, **155**, 787-800.

Cockburn, H.A.P., 1998. *Landscape evolution in Namibia and Antarctica: Quantifying denudation rates using in-situ cosmogenic isotope analysis.* Unpublished Ph.D. Thesis, University of Edinburgh.

Cockburn, H.A.P., Brown, R.W., Summerfield, M.A., and Seidl, M.A., In press. Quantifying passive margin denudation and landscape development using a combined fission-track thermochronology and cosmogenic isotope analysis approach. *Earth and Planetary Science Letters*.

Cockburn, H.A.P., Seidl, M.A. and Summerfield, M.A., 1999. Quantifying denudation rates on inselbergs in the central Namib desert using in situ-produced cosmogenic ^{10}Be and ^{26}Al. *Geology*, **27**, 399-402.

Cole, K.L., and Mayer, L., 1982. Use of packrat middens to determine rates of cliff retreat in the eastern Grand Canyon, Arizona. *Geology*, **10**, 597-599.

Cole, D.I., 1992. Evolution and development of the Karoo Basin. In M.J. de Wit and I.G.D. Ransome (eds.) *Inversion tectonics of the Cape Fold Belt, Karoo and Cretaceous Basins of southern Africa.* Balkema, Rotterdam.

Conrad, N.J., Elmore, D., Kubik, P., Gove, H.E., Tubbs, L.E., Chrunyk, B.A., and Wahlen, M., 1986. The chemical preparation of AgCl for measuring ^{36}Cl in polar ice with accelerator mass spectrometry. *Radiocarbon,* **28**, 556-560.

Cornett, R.J., Chant, L., Andrews, H.R., Davies, W.G., Greiner, B.F., Imahori, Y., Koslowsky, V.T., Kotzer, T., Milton, J.C.D. and Milton, G.M., 1997. ^{36}Cl and ^{129}I in teeth and bones. *Nuclear Instruments and Methods in Physics Research*, **B123**, 249- 253.

Courtillot, V., Jaupart, C., Manighetti, I., Tapponier, P., and Besse, J., 1999. On causal links between flood basalts and continental breakup. *Earth and Planetary Science Letters*, **166**, 177-195.

Cox, K.G., 1988. The Karoo Province. In J.D. MacDougall (ed.) *Continental Flood Basalts*. Kluwer, Dordrecht.

Cox, K.G., 1989. The role of mantle plumes in the development of continental drainage patters. *Nature*, **342**, 873-876.

Cox, K.G., 1992. Karoo igneous activity, and the early stages of the break-up of Gondwanaland. In B.C. Storey, T. Alabaster and R.J. Parkhurst (eds.) *Magmatism and the Causes of Continental Break-up*. Geological Society Special Publication Number 68.

Cox, K.G., 1993. Continental magmatic underplating. *Philosophical Transactions of the Royal Society of London*, **A342**, 155-166.

Davis, R. and Schaeffer O.A., 1955. Chlorine-36 in nature. *Annals of the New York Academy of Sciences*, **62**, 105-122.

Davis, W.M., 1899. The Geographical Cycle. *Geographical Journal,* **xiv**, 481-504.

Davis, W.M., 1954. *Geographical Essays* (edited by D.W. Johnson). Dover, New York.

Dawson, J.B., 1962. Basutoland kimberlites. *GSA Bulletin*, **73**, 545-560.

Deacon, J. and Lancaster, N., 1988. *Late Quaternary Palaeoenvironments of Southern Africa.* Clarendon Press, Oxford.

Dep, L., Elmore, D., Lipschutz, M., Vogt, S., Phillips, F.M., and Zreda, M., 1994a. Depth dependence of cosmogenic neutron-capture-produced ^{36}Cl in a terrestrial rock. *Nuclear Instruments and Methods in Physics Research*, **B92**, 301-307.

Dep, L., Elmore, D., Fabryka-Martin, J., Masarik, J., and Reedy, R.C., 1994b. Production rate systematics of in-situ-produced cosmogenic nuclides in terrestrial rocks; Monte Carlo approach of investigating $^{35}Cl(n, \gamma)^{36}Cl$. *Nuclear Instruments and Methods in Physics Research*, **B92**, 321-325.

De Swardt, A.M.J. and Bennet, G., 1974. Structural and physiographic development of Natal since the Late Jurassic. *Transactions of the Geological Society of South Africa*, **77**, 309-322.

Dickin, A.P., 1995. *Radiogenic Isotope Geology*. Cambridge University Press, Cambridge.

Dingle, R.V., Birch, G.F., Bremner, J.M., De Decker, R.H., Du Plessis, A., Engelbrecht, J.C., Fincham, M.J., Fitton, T., Flemming, B.W., Gentle, R.I., Goodlad, S.W., Martin, A.K., Mills, E.G., Moir, G.J., Parker, R.J., Robson, S.H., Rogers, J., Salmon, D.A., Siesser, W.G., Simpson, E.S.W., Summerhayes, C.P., Westall, F., Winter, A., and Woodborne, M.W., 1987. Deep-sea sedimentary environments around southern Africa (south-east Atlantic and south-west Indian Oceans). *Annals of the South African Museum*, **98**, 1-27.

Dingle, R.V. and Hendey, Q.B., 1984. Late Mesozoic and Tertiary sediment supply to the eastern Cape Basin (SE Atlantic) and paleo-drainage systems in south western Africa. *Marine Geology*, **56**, 13-26.

Dingle, R.V. and Robson, S., 1985. Slumps, canyons and related features on the continental margin off East London, SE Africa (SW Indian Ocean). *Marine Geology*, **67**, 37-54.

Dingle, R.V., Siesser, W.G., and Newton, A.R., 1983. *Mesozoic and Tertiary Geology of Southern Africa*, A.A. Balkema, Rotterdam.

Dixey, F., 1938. Some observations on the physiographical development of central and southern Africa. *Transactions of the Geological Society of South Africa*, **41**, 113-172.

Dixey, F., 1942. Erosion cycles in central and southern Africa. *Transactions of the Geological Society of South Africa*, **45**, 151-181.

Dixey, F., 1955a. Some aspects of the geomorphology of central and southern Africa. *Transactions of the Geological Society of South Africa*, **58**, 1-58.

Dixey, F., 1955b. Erosion surfaces in Africa: some consideration of age and origin. *Transactions of the Geological Society of South Africa*, **58**, 265-280.

Dockhorn, B., Neumaier, S., Hartmann, F.J., Petitjean, C., Faestermann, H., Korschinek, G., Morinaga, H., and Nolte, E., 1991. Determination of erosion rates with cosmic ray produced ^{36}Cl. *Zeitschrift für Physik A - Hadrons and Nuclei*, **341**, 117-119.

Donahue, D.J., Jull, A.J.T., and Toolin, L.J., 1990. Radiocarbon measurements at the University of Arizona AMS facility. *Nuclear Instruments and Methods in Physics Research*, **B52**, 224-228.

Douglas, G.R., 1981. The development of bonded discontinuities in basalt, and their significance to freeface weathering. *Jökull*, **31**, 1-9.

Douglas, G.R., McGreevy, J.P., and Whalley, W.B., 1994. Mineralogical aspects of crack development and free face activity in some basalt cliffs, County Antrim, Northern Ireland. In D.A. Robinson and R.B.G. Williams (eds.) *Rock weathering and landform evolution* Wiley, Chichester.

Douglas, G.R., Whalley, W.B., and McGreevy, J.P., 1991. Rock properties as controls on free-face debris fall activity. *Permafrost and periglacial processes*, **2**, 311-319.

Duk-Rodkin, A., Barendregt, R.W., Tarnocai, C., and Phillips, F.M., 1996. Late Tertiary to Late Quaternary record in the McKenzie Mountains, Northwest Territories, Canada: stratigraphy, paleosols, paleomagnetism and chlorine-36. *Canadian Journal of Earth Sciences*, **33**, 875-895.

Dumitru, T.A., Hill, K.C., Coyle, D.A., Duddy, I.R., Foster, D.A., Gleadow, A.J.W., Green, P.F., Kohn, B.P., Laslett, G.M., and O'Sullivan, A.J., 1991. Fission track thermochronology: application to continental rifting of south-eastern Australia. *The APEA Journal*, **31**, 131-141.

Dunai, T.J., 2000. Scaling factors for production of in situ produced cosmogenic nuclides: a critical reevaluation. *Earth and Planetary Science Letters*, **176**, 157-169.

Duncan, R.A., Hooper, P.R., Rehacek, J., Marsh, J.S., and Duncan, A.R., 1997. The timing and duration of the Karoo igneous event, southern Gondwana. *Journal of Geophysical Research*, **102**, 18,127-18,138.

Dunlevey, J.N., Ramluckan, V.R., and Mitchell, A.A., 1993. Secondary mineral zonation in the Drakensberg basalt formation, South Africa. *South African Journal of Geology*, **96**, 216-220.

Dunne, J., Elmore, D., and Muzikar, P., 1999 Scaling factors for the rates of production of cosmogenic nuclides for geometric shielding and attenuation at depth on sloped surfaces. *Geomorphology*, **27**, 3-11.

Du Toit, A.L., 1954. *The Geology of South Africa*, (Third edition edited and prepared by S.H. Haughton), Oliver and Boyd, Edinburgh.

Dyer, T.G.J. and Marker, M.E., 1979. On some aspects of Lesotho hollows. *Zeitschrift für Geomorphologie NF*, **23**, 256-270.

Eales, H.V., Marsh, J.S., and Cox, K.G., 1984. The Karoo Igneous Province: an introduction. In: A.J. Erlank (ed.) *Petrogenesis of the Volcanic Rocks of the Karoo Province*. Geological Society of South Africa Special Publication Number 13.

Elmore, D. and Phillips, F.M., 1987. Accelerator mass spectrometry for measurement of long-lived radioisotopes. *Science*, **236**, 542-550.

Elmore, D., Conrad, N.J., Kubik, P.W., Gove, H., Wahlen, M., Beer, J., and Suter, M., 1987. ^{36}Cl and ^{10}Be profiles in Greenland ice: dating and production rate variations. *Nuclear Instruments and Methods in Physics Research*, **B29**, 207-210.

Encarnacion, J., Fleming, T.H., Elliot, D.H., and Eales, H.V., 1996. Synchronous emplacement of Ferrar and Karoo dolerites and the early breakup of Gondwana. *Geology*, **24**, 535-538.

Evans, J.M., Stone, J.O.H., Fifield, L.K., and Cresswell, R.G., 1997. Cosmogenic chlorine-36 production in K-feldspar. *Nuclear Instruments and Methods in Physics Research*, **B123**, 334-340.

Fabryka-Martin, J.T., 1988. *Production of radionuclides in the Earth and their hydrogeologic significance, with emphasis on chlorine-36 and iodine-129.* Unpublished Ph.D. Thesis, University of Arizona.

Fabryka-Martin, J.T., Davis, S.N., and Elmore, D., 1987. Applications of ^{129}I and ^{36}Cl in hydrology. *Nuclear Instruments and Methods in Physics Research*, **B29**, 361-371.

Fabryka-Martin, J.T., Davis, S.N., Elmore, D., and Kubik, P.W., 1989. *In situ* production and migration of ^{129}I in the Stripa granite, Sweden. *Geochimica et Cosmochimica Acta*, **53**, 1817-1823.

Fair, T.J.D. and King, L.C., 1954. Erosional land-surfaces in the eastern marginal areas of South Africa. *Transactions of the Geological Society of South Africa*, **62**, 19-26.

Faure, G., 1986. *Principles of Isotope Geology*. (2nd Edition). Wiley, New York.

Feige, Y., Oltman, B.G., and Kastner, J., 1968. Production rates of neutrons in soils due to natural radioactivity. *Journal of Geophysical Research*, **73**, 3135-3142.

Fifield, L.K., 1999. Accelerator mass spectrometry and its applications. *Reports on Progress in Physics*, **62**, 1223-1274.

Fifield, L.K., Ophel, T.R., Allan. G.L., Bird, J.R., and Davie, R.F., 1990. Accelerator mass spectrometry at the Australian National University's 14UD accelerator: experience and developments. *Nuclear Instruments and Methods in Physics Research*, **B52**, 233-237.

Fifield, L.K., Allan, G.L., Stone, J.O.H., and Ophel, T.R., 1994. The ANU AMS system and research program. *Nuclear Instruments and Methods in Physics Research*, **B92**, 85-88.

Finkel, R.C. and Suter, M., 1993. AMS in the Earth sciences: Technique and applications. *Advances in Analytical Geochemistry*, **1**, 1-114.

Fitton, J.G., Saunders, A.D., Larsen, L.M., Hardarson, B.S., and Norry, M.J., 1998. Volcanic rocks from the southeast Greenland margin at 63 °N: composition, petrogenesis, and mantle sources. In A.D. Saunders, H.C. Larsen and S.W. Wise, Jr., (eds.) *Proceedings of the Ocean Drilling Program, Scientific Results*, **152**, 331-350.

Fitzpatrick, R.W., 1978. Periglacial soils with fossil permafrost horizons. *Annals of the Natal Museum*, **23**, 475-484.

Fleming, A., Summerfield, M.A., Stone, J.O., Fifield, L.K., and Cresswell, R.G., 1999. Denudation rates for the southern Drakensberg escarpment, SE Africa, derived from *in-situ*-produced cosmogenic ^{36}Cl: initial results. *Journal of the Geological Society, London*, **156**, 209-212.

Frich, P., and Brandt, E., 1985. Holocene talus accumulation rates, - and their influence on rock glacier growth. A case study from Igpik, Disko – west Greenland. *Geografisk Tidsskrift*, **85**, 32-44.

French, H.M., 1996. *The Periglacial Environment*. (2nd Edition). Longman, Harlow.

Gadd, S.A. and Scrutton, R.A., 1997. An integrated thermomechanical model for transform continental margin evolution. *Geo-Marine Letters*, **17**, 21-30.

Gallagher, K., 1995. Evolving temperature histories from apatite fission – track data. *Earth and Planetary Science Letters*, **136**, 421-435.

Gallagher, K. and Brown, R., 1997. The onshore record of passive margin evolution. *Journal of the Geological Society, London*, **154**, 451-457.

Gallagher, K., and Brown, R.W., 1999. Denudation and uplift at passive margins: the record of the Atlantic Margin of southern Africa. *Philosophical Transactions of the Royal Society of London, Series A*, **357**, 835-859.

Gallagher, K., Brown, R., and Johnson, C., 1998. Fission track analysis and its applications to geological problems. *Annual Review of Earth and Planetary Science*, **26**, 519-572.

Gilchrist, A.R., 1995. On appraising classical models of landscape evolution for passive continental margins. In: O. Slaymaker (ed.) *Steepland Geomorphology*, Wiley, London.

Gilchrist, A.R., Kooi, H., and Beaumont, C., 1994. Post-Gondwana geomorphic evolution of southwestern Africa: implications for the controls on landscape development from observations and numerical experiments. *Journal of Geophysical Research*, **99**, 12,211-12,228.

Gilchrist, A.R. and Summerfield, M.A., 1990. Differential denudation and flexural isostasy in formation of rifted-margin upwarps. *Nature*, **346**, 739-742.

Gilchrist, A.R. and Summerfield, M.A., 1991. Denudation, isostasy and landscape evolution. *Earth Surface Processes and Landforms,* **16**, 555-562.

Gilchrist, A.R. and Summerfield, M.A., 1994. Tectonic models of passive margin evolution and their implications for theories of long-term landscape development. In: M.J. Kirkby (ed.) *Process Models and Theoretical Geomorphology*, Wiley, London.

Gillespie, A.R. and Bierman, P.R., 1995. Precision of terrestrial exposure ages and erosion rates estimated from analysis of cosmogenic isotopes produced in situ. *Journal of Geophysical Research*, **100**, 24637-24649.

Gleadow, A.J.W. and Brown, R.W., 2000. Fission – track thermochronology and long –term denudation response to tectonics. In M.A. Summerfield (ed.) *Geomorphology and Global Tectonics* Wiley, Chichester.

Gleadow, A.J.W., Duddy, I.R., Green, P.F., and Lovering, J.F., 1986. Confined fission track lengths in apatite: a diagnostic tool for thermal history analysis. *Contributions to Mineralogy and Petrology*, **94**, 405-415.

Goldrick, G. and Bishop, P., 1995. Distinguishing the roles of lithology and relative uplift in the steepening of the long profiles of bedrock rivers. *Journal of Geology*, **103**, 227-231.

Goodlad, S.W., Martin, A.K., and Hartnady, C.J.H., 1982. Mesozoic magnetic anomalies in the southern Natal Valley. *Nature*, **295**, 686-688.

Gosse, J.C., Evenson, E.B., Klein, J., Lawn, B., and Middleton, R., 1995a. Precise cosmogenic ^{10}Be measurements in western North America; support for a global Younger Dryas cooling event. *Geology*, **23**, 877-880.

Gosse, J.C., Klein, J., Evenson, E.B., Lawn, B., and Middleton, R., 1995b. Beryllium-10 dating of the duration and retreat of the last Pinedale Glacial Sequence. *Science*, **268**, 1329-1333.

Gosse, J.C., Reedy, R.C., Harrington, C.D., and Poths, J., 1996. Overview of the workshop on secular variations in production rates of cosmogenic nuclides on Earth. *Radiocarbon,* **38**, 135-147.

Goudie, A., 1995. *The Changing Earth: Rates of Geomorphological Processes*, Blackwell, Oxford.

Goudie, A.S., 1996. Climate: Past and Present. In: W.M. Adams, A.S. Goudie and A.R. Orme (eds.) *The Physical Geography of Africa*, Oxford University Press, Oxford.

Grab, S.W., 1994. Thufur in the Mohlesi Valley, Lesotho, southern Africa. *Permafrost and Periglacial Process,* **5**, 111-118.

Grab, S.W., 1996. Debris deposits in the high Drakensberg, South Africa: possible indicators of plateau, niche and cirque glaciation. *Zeitschrift für Geomorphologie NF, Supplementband*, **103**, 389-403.

Grab, S.W., 1997a. Annually re-forming miniature sorted patterned ground in the high Drakensberg, southern Africa. *Earth Surface Processes and Landforms,* **22**, 733-745.

Grab, S., 1997b. Thermal regime for a thufa apex and its adjoining depression, Mashai Valley, Lesotho. *Permafrost and Periglacial Process,* **8**, 437-445.

Grab, S., 1998a. Periglacial research in Africa: past, present and future. *Progress in Physical Geography*, **22**, 375-384.

Grab, S., 1998b. Non-sorted patterned ground in the high Drakensberg, southern Africa: some new data. *The Geographical Journal*, **164**, 19-31.

Grab, S., 1999. Block and debris deposits in the high Drakensberg, Lesotho, southern Africa: implications for high altitude slope processes. *Geografiska Annaler*, **81A**, 1-16.

Grab, S. and Hall, K., 1996. North-facing hollows in the Lesotho / Drakensberg mountains: hypothetical palaeoenvironmental reconstructions. *South African Journal of Science*, **92**, 183-184.

Graf, T.H., Kohl, C.P., Marti, K., and Nishiizumi, K., 1991. Cosmic-ray produced neon in Antarctic rocks. *Geophysical Research Letters*, **18**, 203-206.

Granger, D.E., Kirchner, J.W., and Finkel, R., 1996. Spatially averaged long-term erosion rates measured from in situ-produced cosmogenic nuclides in alluvial sediment. *Journal of Geology*, **104**, 249-257.

Granger, D.E., Kirchner, J.W., and Finkel, R.C., 1997. Quaternary downcutting rate of the New River, Virginia measured from differential decay of cosmogenic ^{26}Al and ^{10}Be in cave-deposited alluvium. *Geology*, **25**, 107-110.

Gunnell, Y. and Fleitout, L., 1998. Shoulder uplift of the Western Ghats passive margin, India: a denudational model. *Earth Surface Processes and Landforms*, **23**, 391-404.

Gunnell, Y. and Fleitout, L., 2000. Morphotectonic evolution of the Western Ghats, India. In M.A. Summerfield (ed.) *Geomorphology and Global Tectonics,* Wiley.

Gutiérrez, M., Sancho, C., and Arauzo, T., 1998. Scarp retreat rates in semiarid environments from talus flatirons (Ebro Basin, NE Spain). *Geomorphology*, **25**, 111-121.

Guyodo, Y., and Valet, J-P., 1999. Global change sin intensity of the Earth's magnetic field during the past 800 kyr. *Nature*, **399**, 249-252.

Hack, J.T., 1957. Physiographic divisions and differential uplift in the Piedmont and Blue Ridge. *U. S. Geological Survey Professional Paper*, **1265**.

Hack, J.T., 1960. Interpretation of erosional topography in humid temperate regions. *American Journal of Science*, **258A**, 80-97.

Hall, K., 1992. A discussion of the need for greater rigour in southern African cryogenic studies. *South African Geographical Journal*, **74**, 69-71.

Hallet, B. and Putkonen, J., 1994. Surface dating of dynamic landforms: Young boulders on ageing moraines. *Science*, **265**, 937-940.

Haman, J.F., 1983. Comments and replies on Cole, K.L. and Mayer, L. 'Use of packrat middens to determine rates of cliff retreat in the eastern Grand Canyon, Arizona'. *Geology*, **11**, 315.

Hancock, G.S., Anderson, R.S., Chadwick, O.A., and Finkel, R.C., 1999. Dating fluvial terraces with ^{10}Be and ^{26}Al profiles: application to the Wind River, Wyoming. *Geomorphology*, **27**, 41-60.

Handwerger, D.A., Cerling, T.E., and Bruhn, R.L., 1999. Cosmogenic ^{14}C in carbonate rocks. *Geomorphology*, **27**, 13-24.

Hanvey, P.M. and Lewis, C.A., 1991. Sedimentology and genesis of slope deposits at Sonskyn, eastern Cape Drakensberg. *Permafrost and Periglacial Process,* **2**, 31-38.

Hanvey, P.M. and Marker, M.E., 1992. Present-day periglacial microforms in the Lesotho Highlands: implications for present and past climatic conditions. *Permafrost and Periglacial Process,* **3**, 353-361.

Hanvey, P.M. and Marker, M.E., 1994. Sedimentary sequences in the Tlaeeng Pass area, Lesotho. *South African Geographical Journal*, **76**, 63-67.

Harman, R., Gallagher, K., Brown, R., Raza, A., and Bizzi, L., 1998. Accelerated denudation and tectonic/geomorphic reactivation of the cratons of northeastern Brazil during the Late Cretaceous. *Journal of Geophysical Research*, **103**, 27,091-27,105.

Hartnady, C.J.H., 1985. Uplift, faulting, seismicity, thermal spring and possible incipient volcanic activity in the Lesotho-Natal region, SE Africa: The Quathlamba hotspot hypothesis. *Tectonics*, **4**, 371-377.

Hartnady, C.J.H., Ben-Avraham, Z., and Rogers, J., 1992. Deep-ocean basins and submarine rises off the continental margin of SE Africa: new geological research. *South African Journal of Science*, **88**, 534-539.

Hastenrath, S. and Wilkinson, J., 1973. A contribution to the periglacial morphology of Lesotho, southern Africa. *Biuletyn Peryglacjalny*, **22**, 157-167.

Hattingh, J., 1994. Depositional environment of some gravel terraces in the Sundays River Valley, Eastern Cape. *South African Journal of Geology*, **97**, 156-166.

Hattingh, J., 1996a. Fluvial response to allocyclic influences during the development of the Lower Sundays river, Eastern Cape, South Africa. *Quaternary International*, **33**, 3-10.

Hattingh, J., 1996b. Fluvial systems and landscape evolution. In C.A. Lewis (ed.) *The geomorphology of the Eastern Cape South Africa*, Grocott and Sherry, Grahamstown.

Hattingh, J. and Geodhart, M.L., 1997. Neotectonic control on drainage evolution in the Algoa Basin, southeastern Cape Province. *South African Journal of Geology*, **100**, 43-52.

Hawthorne, J.B., 1975. Model of a kimberlite pipe. In: L.H. Ahrens, J.B. Dawson, A.R. Duncan and A.J. Erlank (eds.) *Physics and Chemistry of the Earth*. Pergamon, Oxford.

Heimsath, A.M., Dietrich, W.E., Nishiizumi, K., and Finkel, R.C., 1997. The soil production function and landscape equilibrium. *Nature*, **388**, 358-361.

Heimsath, A.M., Dietrich, W.E., Nishiizumi, K., and Finkel, R.C., 1999. Cosmogenic nuclides, topography, and the spatial variation of soil depth. *Geomorphology*, **27**, 151-172.

Henning, H.J., Bell, W.A., Billquist, P.J., Glagola, B.G., Kutschera, W., Liu, Z., Lucas, H.F., Paul, M., Rehim, K.E., and Yntema, J.L., 1987. Calcium-41 concentration in terrestrial materials: prospects for dating of Pleistocene samples. *Science*, **236**, 725.

Honda, M. and Arnold, J.R., 1967. Effects of cosmic rays on meteorites. In: K. Sitte, (ed.), *Handbuch der Physik*, Springer-Verlag, New York.

Howard, A.D., Dietrich, W.E., and Seidl, M.A., 1994. Modeling fluvial erosion on regional to continental scales. *Journal of Geophysical Research*, **99**, 13,971-13,986.

Ishikawa, T and Nakamura, E., 1990. Suppression of boron volatilization from a hydrofluoric acid solution using a boron-mannitol complex. *Analytical Chemistry*, **62**, 2612-2616.

Ivy-Ochs, S.D., 1996. *The dating of rock surfaces using in situ produced ^{10}Be, ^{26}Al and ^{36}Cl, with examples from Antarctica and the Swiss Alps.* Ph.D. Thesis, Swiss Federal Institute of Technology, Zürich. Diss. ETH No. 11763.

Ivy-Ochs, S., Schlüchter, C., Kubik, P.W., Dittrich-Hannen, B., and Beer, J., 1995. Minimum ^{10}Be exposure ages of early Pliocene for the Table Mountain plateau and the Sirius Group at Mount Fleming, Dry Valleys, Antarctica. *Geology*, **23**, 1007-1010.

Jackson, J. (1997) (ed.) *The Glossary of Geology*. 4th Edition. American Geological Institution.

Jackson, L.E., Phillips, F.M., Shimamura, K., and Little, E.C., 1997. Cosmogenic ^{36}Cl dating of the foothills erratics train, Alberta, Canada. *Geology*, **25**, 195-198.

Jannick, N.O., Phillips, F.M., Smith, G.I., and Elmore, D., 1991. A ^{36}Cl chronology for lacustrine sedimentation in the Pleistocene Owens River system. *GSA Bulletin*, **103**, 1146-1159.

Jarvis, K.E., Gray, A.L., and Houk, R.S., 1992. *Handbook of inductively coupled plasma mass spectrometry*. Blackie, Glasgow.

Jeffrey, A., 1996. *Mathematics for Engineers and Scientists* (5th edition). Chapman and Hall.

Jessen, O., 1943. *Die Randschwellen der Kontinente*. Petermans. Geog. Mitt., Ergänzungsh.

Jull, A.J.T., Wilson, A.E., Burr, G.S., Toolin, L.J., and Donahue, D.J., 1992. Measurements of cosmogenic ^{14}C produced by spallation in high-latitude rocks. *Radiocarbon*, **34**, 737-744.

Kearey, P. and Vine, F.J., 1996. *Global Tectonics* (2nd edition). Blackwell, Oxford.

Keen, C.E. and Beaumont, C., 1990. Geodynamics of rifted continental margins. In M.J. Keen and G.L. Williams (eds.) *Geology of the Continental Margin of Eastern Canada*. Geology of Canada, No. 2, Geological Survey of Canada, p 391-472.

Kerr, A., Sugden, D.E. and Summerfield, M.A., 2000. Linking tectonics and landscape development in a passive margin setting: the Transantarctic Mountains. In M.A. Summerfield (ed.), *Geomorphology and Global Tectonics*. Wiley, Chichester.

Kimber, O.G., Allison, R.J., and Cox, N.J., 1998. Mechanisms of failure and slope development in rock masses. *Transactions of the Institute of British Geographers NS*, **23**, 353-370.

King, L.C., 1940. Attempt at a measure of erosion in Natal. *Transactions of the Geological Society of South Africa*, **XLIII**, 153-157.

King, L.C., 1941. The monoclinal coast of Natal, South Africa. *Journal of Geomorphology*, **3**, 144-153.

King, L.C., 1944. Geomorphology of the Natal Drakensberg. *Transactions of the Geological Society of South Africa*, **47**, 255-282.

King, L.C., 1947. Landscape study in southern Africa. *Proceedings of the Geological Society of South Africa*, **47**, 255-282.

King, L.C., 1949. On the ages of African landsurfaces. *Quarterly Journal of the Geological Society of London*, **104**, 439-453.

King, L.C., 1951. *South African Scenery (2nd Edition)*. Oliver and Boyd, Edinburgh.

King, L.C., 1953. Canons of landscape evolution. *Bulletin of the Geological Society of America*, **64**, 721-752.

King, L.C., 1955. Pediplanation and isostacy: an example from South Africa. *Quarterly Journal of the Geological Society of London*, **111**, 353-359.

King, L.C., 1961. Cymatogeny. *Transactions of the Geological Society of South Africa*, **64**, 1-22.

King, L.C., 1962. *The Morphology of the Earth.* Oliver and Boyd, Edinburgh.

King, L.C., 1982. *The Natal Monocline: explaining the origin and scenery of Natal, South Africa (2nd Edition)*. University of Natal Press, Pietermaritzburg.

King, L.C., 1983. *Wandering Continents and Spreading Sea Floors on an Expanding Earth.* Wiley, Chichester.

King, L.C. and King, L.A., 1959. A reappraisal of the Natal Monocline. *South African Geographical Journal*, **41**, 15-30.

Klein, J., Giegengack, R., Middleton, R., Sharma, P., Underwood, J.R., and Weeks, R.A., 1986. Revealing histories of exposure using *in situ* produced ^{26}Al and ^{10}Be in Libyan desert glass. *Radiocarbon,* **28**, 547-555.

Kohl, C.P. and Nishiizumi, K., 1992. Chemical isolation of quartz for measurement of *in-situ*-produced cosmogenic nuclides. *Geochimica et Cosmochimica Acta*, **56**, 3583-3587.

Kooi, H. and Beaumont, C., 1994. Escarpment evolution on high-elevation rifted margins: insights derived from a surface processes model that combines diffusion, advection and reaction. *Journal of Geophysical Research*, **99**, 12,191-12,209.

Kooi, H. and Beaumont, C., 1996. Large-scale geomorphology: classical concepts reconciled and integrated with contemporary ideas via a surface process model. *Journal of Geophysical Research*, **101**, 3361-3386.

Koons, P.O., 1995. Modeling the topographic evolution of collisional belts. *Annual Review of Earth and Planetary Science,* **23**, 375-408.

Kubik, P.W., Ivy Ochs, S., Masarik, J., Frank, M., and Schlüchter, C, 1998. ^{10}Be and ^{26}Al production rates deduced from an instantaneous event within the dendo-calibration curve, the landslide of Köfels, Ötz Valley, Austria. *Earth and Planetary Science Letters*, **161**, 231-241.

Kurz, M.D., 1986a. Cosmogenic helium in a terrestrial igneous rock. *Nature*, **320**, 435-439.

Kurz, M.D., 1986b. In situ production of terrestrial cosmogenic helium and some applications to geochronology. *Geochimica et Cosmochimica Acta*, **50**, 2855-2862.

Kurz, M.D., 1987. Erratum to Kurz 1986 In situ production of terrestrial cosmogenic helium and some applications to geochronology. *Geochimica et Cosmochimica Acta*, **51**, 1019.

Kurz, M.D., Colodner, D., Trull, T.W., Moore, R.B., and O'Brien, K., 1990. Cosmic ray exposure dating with in situ produced cosmogenic ^{3}He: results from young Hawaiian lava flows. *Earth and Planetary Science Letters*, **97**, 177-189.

Kutschera, W., 1997. Conference summary: trends in AMS. *Nuclear Instruments and Methods in Physics Research*, **B123**, 594-598.

Laity, J.E., and Malin, M.C., 1985. Sapping processes and the development of theatre-headed valley networks on the Colorado Plateau. *Bulletin of the Geological Society of America*, **96**, 203-217.

Lal, D., 1986. On the study of continental erosion rates and cycles using cosmogenic ^{10}Be and ^{26}Al and other isotopes. In: A.J. Hurford, E. Jäger, and J.A.M. Ten Cate (eds.) *Dating Young Sediments*. CCOP Technical Secretariat, Bangkok.

Lal, D., 1987a. Cosmogenic nuclides produced *in situ* in terrestrial solids. *Nuclear Instruments and Methods in Physics Research*, **B29**, 238-245.

Lal, D., 1987b. Production of ^{3}He in terrestrial rocks. *Chemical Geology*, **66**, 89-98.

Lal, D., 1988. In situ-produced cosmogenic isotopes in terrestrial rocks. *Annual Review of Earth and Planetary Science*, **16**, 355-388.

Lal, D., 1991. Cosmic ray labeling of erosion surfaces: *in situ* nuclide production rates and erosion models. *Earth and Planetary Science Letters*, **104**, 424-439.

Lal, D., 1995. On cosmic-ray exposure ages of terrestrial rocks: A suggestion. *Radiocarbon*, **37**, 889-898.

Lal, D. and Arnold, J.R., 1985. Tracing quartz through the environment. *Proceedings of the Indian Academy of Science*, **94**, 1-5.

Lal, D., Arnold, J.R., and Honda, M., 1960. Cosmic-ray production rates of ^{7}Be in oxygen and P^{32}, P^{33}, S^{35} in argon in mountain altitudes. *Physical Review*, **118**, 1626-1632.

Lal, D, Jull, A.J.T., Donahue, D.J., Burtner, D., and Nishiizumi, K, 1990. Polar ice ablation rates measured using *in situ* cosmogenic ^{14}C. *Nature*, **346**, 350-352.

Lal, D. and Peters, B., 1967. Cosmic ray produced radioactivity in the Earth. In: K. Sitte (ed.) *Handbuch der Physik*. Springer-Verlag, New York.

Lawver, L.A., Royer, J-Y, Sandwell, D.T., and Scotese, C.R., 1991. Evolution of the Antarctic continental margins. In M.R.A. Thomson, J.A. Crame and J.W. Thomson (eds.) *geological evolution of Antarctica*. Cambridge University Press, Cambridge.

Leavy, B.D., 1987. Surface-exposure dating of young volcanic rocks using the in situ buildup of cosmogenic isotopes. Unpublished Ph.D. Thesis, New Mexico Institute of Mining and Technology.

Leland, J., Reid, M.R., Burbank, D.W., Finkel, R. and Caffee, M., 1998. Incision and differential bedrock uplift along the Indus River near Nanga Parbat, Pakistan Himalaya, from ^{10}Be and ^{26}Al exposure age dating of bedrock straths. *Earth and Planetary Science Letters*, **154**, 93-107.

Le Roux, F.G., 1990. Palaeontological correlation of Cenozoic marine deposits of the southeastern, southern and western coasts Cape Province. *South African Journal of Geology*, **93**, 514-518.

Lewis, C.A., 1988a. Periglacial landforms. In: B.P. Moon and G.F. Darbis (eds.) *The Geomorphology of Southern Africa*. Southern, Johannesburg.

Lewis. C.A., 1988b. Periglacial features in southern Africa: A review. *Palaeoecology of Africa*, **19**, 357-370.

Lewis, C.A., 1994. Protalus ramparts and the altitude of the local equilibrium line during the last glacial stage in Bokspruit, East cape, Drakensberg, South Africa. *Geografiska Annaler*, **76A**, 37-48.

Lewis, C.A. and Darbis, G.F., 1985. Periglacial ice-wedge cast and head deposits at Dynevor Park, Barkly East area, north-eastern Cape Province, South Africa. *South African Journal of Science*, **81**, 673-677.

Lewis, C.A. and Hanvey, P.M., 1988. Sedimentology of debris slope accumulations at Rhodes, Eastern Cape Drakensberg, South Africa. In: G.F. Darbis and B.P. Moon, *Geomorphological Studies in Southern Africa*. Balkema, Rotterdam.

Lewis, C.A. and Hanvey, P.M., 1991. Quaternary fan and river terrace deposits, Glen Orchy, east Cape Drakensberg, South Africa. *Permafrost and Periglacial Process,* **2**, 39-48.

Lewis, C.A. and Hanvey, P.M., 1993. The remains of rock glaciers in Bottelnek, East Cape Drakensberg, South Africa. *Transactions of the Royal Society of South Africa*, **48**, 265-289.

Licciardi, J.M., Kurz, M.D., Clark, P., and Brook, E.J., 1999. Calibration of cosmogenic ^{3}He production rates from Holocene lava flows in Oregon, USA and effects of the Earth's magnetic field. *Earth and Planetary Science Letters*, **172**, 261-271.

Lide, D.R., 1995. *CRC Handbook of Chemistry and Physics*. CRC Press.

Lister, G.S. and Etheridge, M.A., 1989. Detachment models for uplift and volcanism in the Eastern Highlands, and their application to the origin of passive margin mountains. In: R.W. Johnson (ed.) *Intraplate Volcanism in Eastern Australia and New Zealand*. (Cambridge university Press, Cambridge).

Liu. B., Phillips, F.M., Fabryka-Martin, J.T., Fowler, M.M., and Stone, W.D., 1994a. Cosmogenic ^{36}Cl accumulation in unstable landforms 1. Effects of the thermal neutron distribution. *Water Resources Research*, **30**, 3115-3125.

Liu. B.L., Phillips, F.M., Elmore, D., and Sharma, P., 1994b. Depth dependence of soil carbonate accumulation based on cosmogenic Cl-36 dating. *Geology*, **22**, 1071-1074.

Liu. B., Phillips, F.M., Fabryka-Martin, J.T., Fowler, M.M., and Stones, W.D., 1995. Correction to "Cosmogenic ^{36}Cl accumulation in unstable landforms1. Effects of thermal neutron distribution". *Water Resources Research*, **31**, 1159.

Liu, B., Phillips, F.M., Pohl, M.M., and Sharma, P., 1996. An alluvial surface chronology based on cosmogenic ^{36}Cl dating, Ajo Mountains (Organ Pipe Cactus National Monument), southern Arizona. *Quaternary Research,* **45**, 30-37.

Lock, B.E., Paverd, A.L., and Broderick, T.J., 1974. Stratigraphy of the Karroo volcanic rocks of the Barkly East district. *Transactions of the Geological Society of South Africa*, **77**, 117-129.

Lorenzo, J.M., and Vera, E.E., 1992. Thermal uplift and erosion across the continent – ocean boundary of the southern Exmouth Plateau. *Earth and Planetary Science Letters*, **108**, 79-92.

Luckman, B.F., and Fiske, C.J., 1995. Estimating long-term rockfall accretion rates by lichenometry. In O. Slaymaker, (ed.), *Steepland Geomorphology*. Wiley, Chichester.

Marker, M.E., 1991. The evidence for cirque glaciation in Lesotho. *Permafrost and Periglacial Process*, **2**, 21-30.

Marker, M.E., 1994. Sedimentary sequences at Sani Top, Lesotho Highlands, southern Africa. *The Holocene*, **4**, 406-412.

Marker, M.E., 1995a. Late Quaternary environmental implications from sedimentary sequences at two high altitude Lesotho sites. *South African Journal of Science*, **91**, 294-298.

Marker, M.E., 1995b. Further data for a Pleistocene periglacial gradient in southern Africa. *Transactions of the Royal Society of South Africa*, **50**, 49-58.

Marker, M.E., 1998. New radiocarbon dates from Lesotho. *South African Journal of Science*, **94**, 239-240.

Marker, M.E. and McFarlane, M.J., 1997. Cartographic analysis of the African Surface Complex between Albertina and Mossel Bay, Southern Cape, South Africa. *South African Journal of Geology*, **100**, 185-194.

Marsh, J.S. and Eales, H.V., 1984. The chemistry and petrogenesis of igneous rocks of the Karoo Central area, southern Africa. In: A.J. Erlank (ed.) *Petrogenesis of the Volcanic Rocks of the Karoo Province*. Geological Society of South Africa Special Publication Number 13.

Marsh, J.S., Hooper, P.R., Rehacek, J., Duncan, R.A., and Duncan, A.R., 1997. Stratigraphy and age of Karoo basalts of Lesotho and implications for correlations within the Karoo igneous province. In: J.J. Mahoney and M.F. Coffin (eds.) *Large Igneous Provinces: Continental, Oceanic and planetary Flood Volcanism*. AGU Geophysical Monograph Number 100.

Marshall, J.E.A., 1994. The Falkland Islands: a key element in Gondwana paleogeography. *Tectonics*, **13**, 499-514.

Marti, K. and Craig, H., 1987 Cosmic-ray-produced neon and helium in the summit lavas of Maui. *Nature*, **325**, 335-336.

Martin, A.K., 1981. Evolution of the Agulhas current and its palaeo-ecological implications. *South African Journal of Science*, **77**, 547-554.

Martin, A.K., 1983. Fault pattern of coastal Natal - a results of strike-slip motion during Gondwanaland break-up. *Joint Geological Survey University of Cape Town Marine Geoscience Unit Technical Report 14.*

Martin, A.K., 1987. Comparison of sedimentation rates in the natal Valley, south-western Indian Ocean with modern sediment yields in east coast rivers in southern Africa. *South African Journal of Science*, **83**, 716-724.

Martin, A.K. and Hartnady, C.J.H., 1986. Plate tectonic development of the south west Indian Ocean: a revised reconstruction of East Antarctica and Africa. *Journal of Geophysical Research*, **91**, 4767-4786.

Masarik, J. and Reedy, R.C., 1995. Terrestrial cosmogenic-nuclide production systematics calculated from numerical simulations. *Earth and Planetary Science Letters*, **136**, 381-395.

Matthews, P.E. and Maud, R.R., 1988. Paleographic implications of a river-pebble dispersal pattern across southern Natal. *Extended Abstracts, 22nd Earth Science Congress, Geological Society of South Africa.*

Maud, R.R., 1961. A preliminary review of the structure of coastal Natal. *Transactions of the Geological Society of South Africa*, **64**, 247-256.

Maud, R.R., 1996. The macro-geomorphology of the Eastern Cape. In C.A. Lewis (ed.) *The geomorphology of the Eastern Cape South Africa*, Grocott and Sherry, Grahamstown.

Mehegan, J.M., Robinson, P.T., and Delaney, J.R., 1982. Secondary mineralization and hydrothermal alteration in the Reydarfjord drill core, eastern Iceland. *Journal of Geophysical Research*, **87**, 6511-6524.

Merritts, D. and Ellis, M., 1994. Introduction to special section on tectonics and topography. *Journal of Geophysical Research*, **99**, 12,135-12,141.

Merritts, D., Vincent, K.R., and Wohl, E.E., 1994. Long river profiles, tectonism, and eustacy: A guide to interpreting fluvial terraces. *Journal of Geophysical Research*, **99**, 14,031-14,050.

Mitchell, P.J., 1996. The Late Quaternary of the Lesotho Highlands, southern Africa: preliminary results and future potential of ongoing research at Sehonghong Shelter. *Quaternary International*, **33**, 35-43.

Molnar, P., and England, P., 1990. Late Cenozoic uplift of mountain ranges and global climate change: chicken or egg? *Nature*, **346**, 29-34.

Montaser, A., (ed.) 1998. *Inductively coupled plasma mass spectrometry*. Wiley-VCH, New York.

Moon, B.P. and Selby, M.J., 1983. Rock mass strength and scarp-forms in southern Africa. *Geografiska Annaler*, **65A**, 135-145.

Moore, M.E., Gleadow, A.J.W. and Lovering, J.F., 1986. Thermal evolution of rifted continental margins: new evidence from fission tracks in basement apatites from southeastern Australia. *Earth and Planetary Science Letters*, **78**, 255-270.

Muller, R.A., 1977. Radioisotope dating with a cyclotron. *Science*, **196**, 489-494.

Murata, K.J., Milton, L., Formoso, L., and Roisenberg, A., 1987. Distribution of zeolites in lavas of southeastern Parana Basin, State of Rio Grande do Sul, Brazil. *Journal of Geology*, **95**, 455-467.

McCarroll, D., Shakesby, R.A., and Matthews, J.A., 1998. Spatial and temporal patterns of Late Holocene rockfall activity on a Norwegian Talus slope: a lichenometric and simulation – modeling approach. *Arctic and Alpine Research*, *30*, 51-60.

McKean, J.A., Dietrich, W.E., Finkel, R.C., Southon, J.R. and Caffee, M., 1993. Quantification of soil production and downslope creep rates from cosmogenic ^{10}Be accumulations on a hillslope profile. *Geology*, **21**, 343-346.

McKenzie, D.P., 1978. Some remarks on the development of sedimentary basins. *Earth and Planetary Science Letters*, **40**, 25-31.

McKenzie, D.P., 1984. A possible mechanism of epeirogenic uplift. *Nature*, **307**, 616-619.

McMillan, I.K., 1993. Foraminiferal biostratigraphy, sequence stratigraphy and interpreted chronostratigraphy of marine Quaternary sedimentation on the South African continental shelf. *South African Journal of Science*, **89**, 83-89.

Nakamura, E., Ishikawa, T, Birck, J-L and Allègre, C.J., 1992. Precise boron isotopic analysis of natural rock samples using a boron-mannitol complex. *Chemical Geology (Isotope Geoscience Section)*, **94**, 193-204.

Nicholas, R.M., and Dixon, J.C., 1986. Sandstone scarp form and retreat in the Land of Standing Rocks, Canyonlands National Park, Utah. *Zeitschrift für Geomorphologie*, **30**, 167-187.

Niedermann, S., Graf, Th., Kim, J.S., Kohl, C.P., Marti, K., and Nishiizumi, K., 1994. Cosmic-ray-produced ^{21}Ne in terrestrial quartz: the neon inventory of Sierra Nevada quartz separates. *Earth and Planetary Science Letters*, **125**, 341-355.

Niedermann, S., Graf, Th. and Marti, K., 1993. Mass spectrometric identification of cosmic-ray-produced neon in terrestrial rocks with multiple neon components. *Earth and Planetary Science Letters*, **118**, 65-73.

Nishiizumi, K., Arnold, J.R., Elmore, D., Ma, X., Newman, D, and Gove, H.E., 1983. ^{36}Cl and ^{53}Mn in Antarctic meteorites and ^{10}Be – ^{36}Cl dating of Antarctic ice. *Earth and Planetary Science Letters*, **62**, 407-417.

Nishiizumi, K., Elmore, D., Ma, X.Z., and Arnold, J.R., 1984. ^{10}Be and ^{36}Cl depth profiles in an Apollo 15 drill core. *Earth and Planetary Science Letters*, **70**, 157-163.

Nishiizumi, K., Finkel, R.C., Klein, J., and Kohl, C.P., 1996. Cosmogenic production of ^{7}Be and ^{10}Be in water targets. *Journal of Geophysical Research*, **B10**, 22225-22232.

Nishiizumi, K., Klein, J., Middleton, R., and Craig, H., 1990. Cosmogenic ^{10}Be, ^{26}Al and ^{3}He in olivine in Maui lavas. *Earth and Planetary Science Letters*, **98**, 263-266.

Nishiizumi, K., Kohl, C.P., Arnold, J.R., Dorn, R., Klein, J., Fink, D., Middleton, R., and Lal. D., 1993. Role of *in situ* cosmogenic nuclides ^{10}Be and ^{26}Al in the study of diverse geomorphic processes. *Earth Surface Processes and Landforms,* **18**, 407-425.

Nishiizumi, K., Kohl, C.P., Arnold, J.R., Klein, J., Fink, D., and Middleton, R., 1991. Cosmic ray produced ^{10}Be and ^{26}Al in Antarctic rocks: exposure and erosion history. *Earth and Planetary Science Letters*, **104**, 440-454.

Nishiizumi, K., Lal, D., Klein, J., Middleton, R., and Arnold, J.R., 1986. Production of ^{10}Be and ^{26}Al by cosmic rays in terrestrial quartz *in situ* and implications for erosion rates. *Nature*, **319**, 134-136.

Nishiizumi, K., Winterer, E.L., Kohl, C.P., Klein, J., Middleton, R., Lal, D., and Arnold, J.R., 1989. Cosmic ray production rates of ^{10}Be and ^{26}Al in quartz from glacially polished rocks. *Journal of Geophysical Research*, **B12**, 17907-17915.

Nixon, P.H., 1975. Melkfontein carbonate tuff, East Griqualand, South Africa. *19th Annual Report, Research Institute of African Geology, University of Leeds*, 36-37.

Nixon, P.H., Boyd, F.R., and Boctor, N.Z., 1983. East Griqualand kimberlites. *Transactions of the Geological Society of South Africa*, **86**, 221-236.

Norrish, K. and Hutton, J.T., 1969. An accurate X-ray spectographic method for the analysis of a wide range of geological samples. *Geochimica et Cosmochimica Acta*, **33**, 431-453.

Nott, J.F., Idnurm, M and Young, R.W., 1991. Sedimentology, weathering, age and geomorphological significance of Tertiary sediments in the far south coast of New South Wales. *Australian Journal of Earth Sciences*. **38**, 357-373.

Nott, J., Young, R., and McDougall, I., 1996. Wearing down, wearing back and gorge extension in the long-term evolution of a highland mass: quantitative evidence from the Shoalhaven Catchment, southeast Australia. *Journal of Geology*, **104**, 224-232.

O'Brien, K., 1979. Secular variations in the production of cosmogenic isotopes in the Earth's atmosphere. *Journal of Geophysical Research*, **84**, 423-431.

O'Brien, K., Sandmeier, H.A., Hansen, G.E., and Campbell, J.E., 1978. Cosmic ray induced neutron background sources and fluxes for geometries of air over water, ground, iron and aluminium. *Journal of Geophysical Research*, **83**, 114-120.

O'Connor, T.G. and G.J. Bredenkamp, 1997. Grassland. In R.M. Cowling, D.M. Richardson and S.M. Pierce (eds.) *Vegetation of southern Africa*, Cambridge University Press.

Oberlander. T.M., 1997. Slope and pediment systems. In D.S.G. Thomas, (ed.), *Arid zone geomorphology; process, form and change.* Wiley, Chichester.

Obst, E. and Kayser, K., 1949. *Die Große Randstufe auf der Ostseite Südafrikas und ihr vorland.* Geographische Gesellschaft zu Hannover.

Ollier, C.D., 1985a. Morphotectonics of continental margins with great escarpments. In: M. Morisawa and J.T. Hack (eds.) *Tectonic Geomorphology*, Allen and Unwin, Boston.

Ollier, C.D., 1985b. Morphotectonics of passive continental margins: Introduction. *Zeitschrift für Geomorphologie, N.F. Supplement Band*, **54**, 1-9.

Ollier, C.D., 1995a. Tectonics and landscape evolution in southeast Australia. *Geomorphology*, **12**, 37-44.

Ollier, C.D., 1995b. Classics in physical geography: King, L.C., 1953. Canons of landscape evolution. *Progress in Physical Geography*, **19**, 371-377.

Ollier, C.D. and Marker, M.E., 1985. The great escarpment of southern Africa. *Zeitschrift für Geomorphologie, N.F. Supplement Band*, **54**, 37-56.

Ollier, C.D. and Pain, C.F., 1997. Equating the basal unconformity with the palaeoplain: a model for passive margins. *Geomorphology*, **19**, 1-15.

Ollier, C.D. and Powar, K.B., 1985. The Western Ghats and the morphotectonics of peninsular India. *Zeitschrift für Geomorphologie, N.F. Supplement Band*, 54, 57-69.

Omar, G.I. and Steckler, M.S., 1995. Fission – track evidence on the initial rifting of the Red Sea: two phases, no propagation. *Science*, **270**, 1341-1344.

Oreskes, N., Shrader-Frechette, K., and Belitz, K., 1994. Verification, validation and confirmation of numerical models in the earth sciences. *Science*, **263**, 641-646.

Partridge, T.C., 1990. Cainozoic environmental changes in southern Africa. *South African Journal of Science*, **86**, 315-317.

Partridge, T.C., 1997a. Cainozoic environmental change in southern Africa, with special emphasis on the last 200,000 years. *Progress in Physical Geography*, **21**, 3-22.

Partridge, T.C., 1997b. Late Neogene uplift in Eastern and Southern Africa and its paleoclimatic implications. In W.F. Ruddiman (ed.) *Tectonic uplift and climate change*, Plenum Press, New York.

Partridge, T.C., 1997c. Evolution of landscapes. In R.M. Cowling, D.M. Richardson and S.M. Pierce (eds.) *Vegetation of southern Africa*, Cambridge University Press, 5 - 20.

Partridge, T.C., 1998. Of diamonds, dinosaurs and diastrophism: 150 million years of landscape evolution in southern Africa. *South African Journal of Geology,* **101**, 167-184.

Partridge, T.C., Avery, D.M., Botha, G.A., Brink, J.S., Deacon, J., Herbert, R.S., Maud, R.R., Schaltz, A., Scott, L., Talma, A.S., and Vogel, J.C., 1990. Late Pleistocene and Holocene climatic change in southern Africa. *South African Journal of Science*, **86**, 302-307.

Partridge, T.C., Demenocal, P.B., Lorentz, S.A., Paiker, M.J., and Vogel, J.C., 1997. Orbital forcing of climate over South Africa: a 200,000 year rainfall record from the Pretoria saltpan. *Quaternary Science Reviews*, **16**, 1125-1133.

Partridge, T.C., Kerr, S.J., Metcalfe, S.E., Scott, L., Talma, A.S. and Vogel, J.C., 1993. The Pretoria Saltpan: a 200,000 year southern African lacustrine sequence. *Palaeogeography, Palaeoclimatology, Palaeoecology*, **101**, 317-337.

Partridge, T.C. and Maud, R.R., 1987. Geomorphic evolution of southern Africa since the Mesozoic. *South African Journal of Geology,* **90**, 179-208.

Partridge, T.C. and Maud, R.R., 1988. The geomorphic evolution of southern Africa: a comparative review. In: G.F. Darbis and B.P. Moon (eds.) *Geomorphological Studies in Southern Africa*, A.A. Balkema, Rotterdam.

Partridge, T.C., Scott, L., and Hamilton, J.E., 1999. Synthetic reconstructions of southern African environments during the Last Glacial Maximum (21-18 kyr) and the Holocene Altithermal (8-6 kyr). *Quaternary International*, **57/58**, 207-214.

Partridge, T.C., Wood, B.A., and De Menocal, P.B., 1995. The influence of global climatic change and regional uplift on large-mammalian evolution in east and southern Africa. In E.S. Vrba, G.H. Denton, T.C. Partridge, and L.H. Burckle (eds.) *Paleoclimate and Evolution, with Emphasis on Human Origins*, Yale university Press, New Haven.

Pazzaglia, F.J. and Brandon, M.T., 1996. Macrogeomorphic evolution of the post-Triassic Appalachian mountains determined by deconvolution of the offshore basin sedimentary record. *Basin Research*, **8**, 255-278.

Pazzaglia, F.J. and Gardner, T.W., 1994. Late Cenozoic flexural deformation of the middle US Atlantic passive margin. *Journal of Geophysical Research*, **99**, 12143-12157.

Penck, A. 1908. Der Drakensberg und der Quathlambabruch. Sitz. Ber. D. Kgl. Preuß. Akademie d. Wiss., **9**, 230-258.

Penck, W., 1953. *Morphological Analysis of Land Forms* (Translated by H. Czech and K.C. Boswell). MacMillan, London.

Phillips, F.M., 1995. The use of isotopes and environmental tracers in subsurface hydrology. *Reviews of Geophysics*, **33**, 1029-1033.

Phillips, F.M., Leavy, B.D., Jannik, N.O., Elmore, D., and Kubik, P.W., 1986. The accumulation of cosmogenic chlorine-36 in rocks: A method for surface exposure dating. *Science*, **231**, 41-43.

Phillips, F.M. and Plummer, M.A., 1996. CHLOE: A program for interpreting *in-situ* cosmogenic nuclide data for surface exposure dating and erosion studies. *Radiocarbon,* **38**, 1.

Phillips, F.M., Rogers, D.B., Dreiss, S.J., Jannik, N.O., and Elmore, D., 1995. Chlorine-36 in Great Basin waters – revisited. *Water Resources Research*, **31**, 3195-3204.

Phillips, F.M., Zreda, M.G., Flinsch, M.R., Elmore, D., and Sharma, P., 1996a. A reevaluation of cosmogenic ^{36}Cl production rates in terrestrial rocks. *Geophysical Research Letters*, **23**, 949-952.

Phillips, F.M., Zreda, M.G., Benson, L.V., Plummer, M.A., Elmore, D., and Sharma, P., 1996b. Chronology for fluctuations in Late Pleistocene Sierra Nevada glaciers and lakes. *Science*, **274**, 749-751.

Phillips, F.M., Zreda, M., Gosse, J.C., Klein, J., Evenson, E.E., Hall, R.D., Chadwick, O.A., and Sharma, P., 1997. Cosmogenic ^{36}Cl and ^{10}Be ages of Quaternary glacial and fluvial deposits of the Wind River Range, Wyoming. *Geological Society of America Bulletin*, **109**, 1453-1463.

Phillips, F.M., Zreda, M.G., Ku, T-H., Luo, S., Huang, Q., Elmore, D., Kubik, P.W., and Sharma, P., 1993. ^{230}Th / ^{234}U and ^{36}Cl dating of evaporite deposits from the western Qaidam Basin, China: Implications for glacial-period dust export from Central Asia. *Geological Society of America Bulletin*, **105**, 1606-1616

Phillips, F.M., Zreda, M.G., Smith, S.S., Elmore, D., Kubik, P.W., Dorn, R.I., and Roddy, D.J., 1991. Age and geomorphic history of Meteor Crater, Arizona, from cosmogenic ^{36}Cl and ^{14}C in rock varnish. *Geochimica et Cosmochimica Acta*, **55**, 2695-2698.

Phillips, F.M., Zreda, M.G., Smith, S.S., Elmore, D., Kubik, P.W., and Sharma, P., 1990. Cosmogenic chlorine-36 chronology for glacial deposits at Bloody Canyon, Eastern Sierra Nevada. *Science*, **284**, 1529-1532.

Phillips, W.M., McDonald, E.V., Reneau, S.L., and Poths, J., 1998. Dating soils and alluvium with cosmogenic ^{21}Ne depth profiles: case studies from the Pajarito Plateau, New Mexico, USA. *Earth and Planetary Science Letters*, **160**, 209-223.

Plummer, M.A., Phillips, F.M., Fabryka-Martin, J., Turin, H.J., Wigard, P.E., and Sharma, P., 1997. Chlorine-36 in fossil rat urine: An archive of cosmogenic nuclide deposition during the past 40,000 years. *Science*, **227**, 538-541.

Poreda, R.J. and Cerling, T.E., 1992. Cosmogenic neon in recent lavas from the western United States. *Geophysical Research Letters*, **19**, 1863-1866.

Porteous, N.C., Walsh, J.N., and Jarvis, K.E., 1995. Measurement of boron isotope ratios in groundwater studies. *Analyst*, **120**, 1397-1400.

Potgieter, C.D., Snyman, C.P., and Fortsch, E.B., 1982. Epigenetic laumontite in the Jurassic Clarens and Drakensberg Groups of the Karoo sequence. *Transactions of the Geological Society of South Africa*, **85**, 203-210.

Potts, P.J., 1987. *A Handbook of Silicate Rock Analysis*. Blackie, Glasgow.

Quenby, J.J. and Webber, W.R., 1959. Cosmic ray cut-off rigidities and the Earth's magnetic field. *Philosophical Magazine*, **4**, 90-113.

Raisbeck, G.M. and Yiou, F., 1989. Dating by cosmogenic isotopes ^{10}Be, ^{26}Al and ^{41}Ca. In: E. Roth and B. Poty, (eds.) *Nuclear methods of dating*, CEA, Paris.

Raisbeck, G., Yiou, F., and Zhou, S.Z., 1994. Paleointensity puzzle. *Nature*, **371**, 207-208.

Rama and Honda, M., 1961. Cosmic-ray-induced radioactivity in terrestrial materials. *Journal of Geophysical Research*, **66**, 3533-3539.

Ramluckan, V.R., 1992. *The petrology and geochemistry of the Karoo sequence basaltic rocks in the Natal Drakensberg at Sani Pass*. Unpublished M.Sc. Thesis, University of Durban-Westville.

Rapp, A., 1960. Recent development of mountain slopes in Kärkevagge and surroundings, northern Scandinavia. *Geografiska Annaler*, **A42**, 71 –200.

Reedy, R.C., Arnold, J.R., and Lal, D., 1983a. Cosmic ray record in solar system matter. *Science*, **219**, 127-135.

Reedy, R.C., Arnold, J.R., and Lal, D., 1983b. Cosmic ray record in solar system matter. *Annual Review of Nuclear and Particle Science*, **33**, 505-537.

Reedy, R.C., Tuniz, C. and Fink, D., 1994. Report on the workshop on production rates of terrestrial in-situ-produced cosmogenic nuclides. *Nuclear Instruments and Methods in Physics Research*, **B92**, 335-339.

Rehacek, J., 1995. *Chemical and Paleomagnetic Stratigraphy of Basalts in Northern Lesotho, Karoo Province*. Unpublished Ph.D. Thesis, Washington State University.

Repka, J.L., Anderson, R.S., and Finkel, R.C., 1997. Cosmogenic dating of fluvial terraces, Fremont River, Utah. *Earth and Planetary Science Letters*, **152**, 59-73.

Ritz, J.F., Brown, E.T., Bourlès, D.L., Philip, H., Schlupp, A., Raisbeck, G.M., Yiou, F., and Enkhtuvshin, B., 1995. Slip rates along active faults estimated with cosmic-ray-exposure dates: Application to the Bogd fault, Gobi-Altaï, Mongolia. *Geology*, **23**, 1019-1022.

Rogers, A.W., 1920. Geological survey and its aims: and a discussion on the origin of the Great Escarpment. *Proceedings of the Geological Society of South Africa*, **23**, xix-xxxiii.

Roth, E., 1989. Principles and general aspects. In: E., Roth and B. Poty, (eds.), *Nuclear Methods of Dating*, Kluwer, Dordrecht.

Royden, L and Keen, C.E., 1980. Rifting process and thermal evolution of the continental margins of eastern Canada determined by subsidence curves. *Earth and Planetary Science Letters*, **15**, 343-361.

Rust, D.J. and Summerfield, M.A., 1990. Isopach and borehole data as indicators of rifted margin evolution in southwestern Africa. *Marine and Petroleum Geology*, **7**, 277-287.

SACS (South African Committee for Stratigraphy), 1980. *Stratigraphy of South Africa, Part 1,* (compiled by L.E. Kent). Handbook 8, Geological Survey of South Africa.

Santa Fe Workshop Abstracts, 1996. *Radiocarbon*, **38**, 149-173.

Sarda, P., Staudacher, T., Allègre, C.J., and Lecomte, A., 1993. Cosmogenic neon and helium at Réunion: measurement of erosion rate. *Earth and Planetary Science Letters*, **119**, 405-411.

Sarracino, R. and Prasad, G., 1988. Spheroidal weathering in the Lesotho Formation Basalts. In: G.F. Darbis and B.P. Moon (eds.) *Geomorphological Studies in Southern Africa*, A.A. Balkema, Rotterdam.

Saunders, I. and Young, A., 1983. Rates of surface processes on slopes, slope retreat and denudation. *Earth Surface Processes and Landforms,* **8**, 473-502.

Schmidt, K-H., 1989. The significance of scarp retreat for Cenozoic landform evolution on the Colorado Plateau, USA. *Earth Surface Processes and Landforms,* **14**, 93-105.

Schmidt, K-H., 1996. Talus and pediment flatirons – indicators of climate change on scarp slopes on the Colorado Plateau, USA. *Zeitschrift für Geomorphologie*, **103**, 135-158.

Schmitz, G. and Rooyani, F., 1987. *Lesotho Geology, Geomorphology, Soils*. National University of Lesotho.

Schulze, B.R., 1972. South Africa. In: J.F. Griffiths (ed.) *Climates of Africa. World Survey of Climatology, Volume 10*. Elsevier, Amsterdam.

Schulze, R.E., 1997. Climate. In R.M. Cowling, D.M. Richardson, and S.M. Pierce (eds.) *Vegetation of southern Africa.* Cambridge University Press, Cambridge.

Scott, L., 1984. Palynological evidence for Quaternary paleoenvironments in southern Africa. In: R.G. Klein (ed.) *Southern African Prehistory and Paleoenvironments*. Balkema, Rotterdam.

Scrutton, R.A., 1979. On sheared passive continental margins. *Tectonophysics*, **59**, 293-305.

Seidl, M.A., Finkel, R.C., Caffee, M.W., Hudson, B., and Dietrich, W.E.,1997. Cosmogenic isotope analyses applied to river longitudinal profile evolution: problems and interpretations. *Earth Surface Processes and Landforms,* **22**, 195-209.

Seidl, M.A., Weissel, J.K., and Pratson, L.F., 1996. The kinematics and pattern of escarpment retreat across the rifted continental margin of SE Australia. *Basin Research*, **12**, 301-316.

Selby, M.J., 1980. A rock mass strength classification for geomorphic purposes: with tests from Antarctica and New Zealand. *Zeitschrift für Geomorphologie*, **24**, 31-51.

Selby, M.J., 1985. *Earth's changing surface*. Clarendon Press, Oxford.

Selby, M.J., 1993. *Hillslope Materials and Processes*. (2nd edition) Open University Press.

Sene, K.J., Jones, D.A., Meigh, J.R., and Farquharson, F.A.K., 1998. Rainfall and flow variations in the Lesotho Highlands. *International Journal of Climatology*, **18**, 329-345.

Şengör, A.H.C. and Burke, K, 1978. Relative timing of rifting and volcanism on earth and its tectonic implications. *Geophysical Research Letters*, **5**, 419-421.

Shee, S.R., Bristow, J.W., Bell, D.R., Smith, C.B., Allsopp, H.l., and Shee, P.B., 1989. The petrology of kimberlites, related rocks and associated mantle xenoliths from the Kuruman Province, South Africa. In: J. Ross, A.L. Jaques, J. Ferguson, D.H. Green, S.Y. O'Reilly, R.V. Danchin, and A.J.A. Janse (eds.) *Kimberlites and Related Rocks Volume 1: their composition, occurrence, origin and emplacement*. Proceedings of the 4th International Kimberlite conference, Geological Society of Australia.

Shepard, M.K., Arvidson, R.E., Caffee, M., Finkel, R., and Harris, L., 1995. Cosmogenic exposure ages of basalt flows: Lunar Crater volcanic field, Nevada. *Geology*, **23**, 21-24.

Siame, L.L., Bourlès, D.L., Sébrier, M., Bellier, O., Casatano, J.C., Araujo, M., Perez, M., Raisbeck, G.M., and Yiou, F., 1997. Cosmogenic dating ranging from 20 to 700 ka of a series of alluvial fan surfaces affected by the El Tigre fault, Argentina. *Geology*, **25**, 975-978.

Siame, L.L. Sébrier, M., Bellier, O., and Bourlès, D.L., 1999. Active tectonics and in situ-produced ^{10}Be datings along the Las Tapias fault (Eastern Argentine Precordillera, Central Andes). *Journal of Conference Abstract*, **4**, 447-448.

Skinner, E.M.W., Clement, C.R., Gurney, C.R., Apter, D.B., and Hatton, C.J., 1992. The distribution and tectonic setting of South African kimberlites. *Geol. I. Geof.*, **33**, 33-40.

Small, E.E., Anderson, R.S., and Hancock, G.S., 1999. Estimates of the rate of regolith production using ^{10}Be and ^{26}Al from an alpine hillslope. *Geomorphology*, **27**, 131-150.

Small, E.E., Anderson, R.S., Repka, J.L., and Finkel, R., 1997. Erosion rates of alpine bedrock summit surfaces deduced from *in situ* ^{10}Be and ^{26}Al. *Earth and Planetary Science Letters*, **150**, 413-425.

Smith, B.J., Whalley, W.B., Warke, P.A., and Ruffell. A., 1999. Introduction and background: interpretations of landscape change. In B.J. Smith, W.B. Whalley and P.A. Warke (eds.) *Uplift, erosion and stability: Perspectives on long-term landscape development.* Geological Society, London, Special Publications, **162**, vii-xi.

Smith, C.B., Allsopp, H.L., Kramers, J.D., Hutchinson, G., and Roddick, J.C., 1985. Emplacement ages of Jurassic-Cretaceous South African kimberlites by the Rb-Sr method on phlogopite and whole rock samples. *Transactions of the Geological Society of South Africa*, **88**, 249-266.

Smith, J.A., and Duller, N.M., 1959. Effects of Pi meson decay-absorption phenomena on the high-energy mu meson zenithal variation at sea level. *Journal of Geophysical Research*, **64**, 2297-2305.

Smith, R.M.H., Eriksson, P.G., and Botha, W.J., 1993. A review of the stratigraphy and sedimentary environments of the Karoo-aged basins of southern Africa. *Journal of African Earth Sciences*, **16**, 143-169.

Steckler, M.S., 1985. Uplift and extension at the Gulf of Suez: Indications of induced mantle convection. *Nature*, **317**, 135-139.

Steckler, M.S. and Omar, G.I., 1994. Controls on erosional retreat of the uplifted rift flanks at the Gulf of Suez and northern Red Sea. *Journal of Geophysical Research*, **99**, 12,159-12,173.

Steig, E.J., Brook, E.J., White, J.W.C., Sucher, C.M., Bender, M.L., Lehman, S.J., Morse, D.L., Waddington, E.D., and Clow, G.D., 1998. Synchronous climate changes in Antarctica and the North Atlantic. *Science*, **282**, 92-95.

Stone, J.O., Allan, G.L., Fifield, L.K., and Cresswell, R.G., 1996a. Cosmogenic chlorine-36 from calcium spallation. *Geochimica et Cosmochimica Acta*, **60**, 679-692.

Stone, J., Allan., G.L., Fifield, L.K., Evans, J.M., and Chivas, A.R., 1994. Limestone erosion measurements with cosmogenic chlorine-36 in calcite - preliminary results from Australia. *Nuclear Instruments and Methods in Physics Research*, **B92**, 311-316.

Stone, J.O., Ballantyne, C.K., and Fifield, L.K., 1998b. Exposure dating and validation of periglacial weathering limits, northwest Scotland. *Geology*, **26**, 577-572.

Stone, J.O.H., Evans, J.M., Fifield, L.K., Allan, G.L., Cresswell, R.G., 1998a. Cosmogenic chlorine-36 production in calcite by muons. *Geochimica et Cosmochimica Acta*, **62**, 433-454.

Stone, J., Lambeck, K., Fifield, L.K., Evans, J.M., and Cresswell, R.G., 1996b. A Lateglacial age for the Main Rock Platform, western Scotland. *Geology*, **24**, 707-710.

Storey, B.C., 1995. The role of mantle plumes in continental break-up: case histories from Gondwanaland. *Nature*, **377**, 301-308.

Storey, B.C., Curtis, M.L., Ferris, J.K., Hunter, M. A., and Livermore, R.A., 1999. Reconstruction and break-out model for the Falkland Islands within Gondwana. *Journal of African Earth Sciences*, 29, 153-163.

Storey, B.C. and Kyle, P.R., 1997. An active mantle mechanism for Gondwana breakup. *South African Journal of Geology,* **100**, 283-290.

Strack, E., Heisinger, B., Dockhorn, B., Hartmann, F.J., Korschinek, G., Nolte, E., Morteani, G., Petitjean, C., and Neumaier, S., 1994. Determination of erosion rates with cosmogenic ^{26}Al. *Nuclear Instruments and Methods in Physics Research*, **B92**, 317-320.

Stüwe, K., 1991. Flexural constraints on the denudation of asymmetric mountain belts. *Journal of Geophysical Research*, **96**, 10,401-10,408.

Sueker, J.K., Turk, J.T., and Michel, R.L., 1999. Use of cosmogenic ^{35}S for comparing ages of water from three alpine-subalpine basins in the Colorado Front Range. *Geomorphology*, **27**, 61-74.

Suess, E., 1904. *The Face of the Earth.* Clarendon Press, Oxford.

Sugden, D., Denton, G.H., and Marchant, D.R., 1995. Landscape evolution of the Dry Valleys, Transantarctic Mountains: tectonic implications. *Journal of Geophysical Research*, **100**, 9949-9967.

Sugden, D.E., Summerfield, M.A., and Burt, T.P., 1997. Editorial: linking short-term geomorphic processes to landscape evolution. *Earth Surface Processes and Landforms,* **22**, 193-194.

Summerfield, M.A., 1981. Macroscale geomorphology. *Area*, **13**, 3-8.

Summerfield, M.A., 1985. Plate tectonics and landscape development on the African continent. In: M. Morisawa and J.T. Hack (eds.) *Tectonic Geomorphology*, Allen and Unwin, Boston.

Summerfield, M.A., 1991a. *Global Geomorphology: an introduction to the study of landforms.* Longman, Harlow.

Summerfield, M.A., 1991b. Sub-aerial denudation of passive margins: regional elevation versus local relief models. *Earth and Planetary Science Letters*, **102**, 460-469.

Summerfield, M.A., 1996a. Tectonics, geology, and long-term landscape development. In: W.M. Adams, A.S. Goudie, and A.R. Orme (eds.) *The Physical Geography of Africa.* Oxford University Press, Oxford.

Summerfield, M.A., 1996b. Understanding landscape development: the evolving interface between geomorphology and other earth sciences. *Area*, **28**, 211-220.

Summerfield, M.A., 2000. Geomorphology and global tectonics: introduction. In M.A. Summerfield (ed.) *Geomorphology and Global Tectonics.* Wiley, Chichester.

Summerfield, M.A. and Brown, R.W., 1998. Geomorphic factors in the interpretation of fission-track data. In: P. Van Den Haute and F. De Corte (eds.) *Advances in Fission-Track Geochronology.* Kluwer, Netherlands, 269-284.

Summerfield, M.A. and Hulton, N.J., 1994. Natural controls of fluvial denudation rates in major drainage basins. *Journal of Geophysical Research*, **99**, 13,871-13,883.

Summerfield, M.A., Stuart, F.M., Cockburn, H.A.P., Sugden, D.E., Denton, G.H., Dunai, T., and Marchant, D.R., 1999a. Long-term rates of denudation in the Dry Valleys, Transantarctic Mountains, southern Victoria Land, Antarctica based on *in-situ*-produced cosmogenic ^{21}Ne. *Geomorphology*, **27**, 113-129.

Summerfield, M.A., Sugden, D.E., Denton, G.H., Merchant, D.R., Cockburn, H.A.P., and Stuart, F.M., 1999b. Cosmogenic isotope data support previous evidence of extremely low rates of denudation in the Dry Valleys region, southern Victoria Land, Antarctica. In B.J. Smith, W.B. Whalley, and P.A. Warke (eds.) *Uplift, erosion and stability: Perspectives on long-term landscape development.* Special Publication of the Geological Society number 162.

Sumner, P., 1995. Cutbacks in the Natal Drakensberg escarpment: comments on an hypothesis on their origin. *South African Journal of Science*, **91**, 285-286.

Sukheswala, R.N., Avasia, R.K., and Gangopadhyay, M., 1974. Zeolites and associated secondary minerals in the Deccan Traps of western India. *Mineralogy Magazine*, 39, 658-671.

Swanson, T.W., and Caffee, M.L., in prep. Determination of ^{36}Cl production rates from the deglaciation history of Whidbey and Fidalgo Islands, Washington.

Tankard, A.J., Jackson, M.P.A., Ericksson, K.A., Hobday, D.K., Hunter, D.R., and Mintel, W.E.L., 1982. *Crustal evolution of South Africa.* Springer-Verlag, New York.

Taylor, J.R., 1997. *An introduction to error analysis: the study of uncertainties in physical measurements.* University Science Books, California.

Ten Brink, U. and Stern, T., 1992. Rift flank uplifts and hinterland basins: comparison of the Transantarctic Mountains with the Great Escarpment of southern Africa. *Journal of Geophysical Research*, **97**, 569-585.

Thorn, C.E., 1988. *An introduction to theoretical geomorphology*, Unwin Hyman, London.

Thornes, J.B. and Brunsden, D., 1977. *Geomorphology and time.* Metheun, London.

Thomas, M.F., 1994. *Geomorphology in the Tropics: a study of weathering and denudation in low latitudes.* Wiley, Chichester.

Thomas, M.F., 1995. Models for landform development on passive margins. Some implications for relief development in glaciated areas. *Geomorphology*, **12**, 3-15.

Thomas, M.F. and Summerfield, M.A., 1987. Long-term landform development: key themes and research problems. In V. Gardiner (ed.) *International Geomorphology 1986 Part II*, Wiley, ps 935-956.

Thomas, R.J., von Veh, M.W., and McCourt, S., 1993. The tectonic evolution of southern Africa: an overview. *Journal of African Earth Sciences*, **16**, 5-24.

Trimble, S.W., 1977. The fallacy of stream equilibrium in contemporary denudation studies. *American Journal of Science*, **277**, 876-887.

Tucker, G.E. and Slingerland, R.L., 1994. Erosional dynamics, flexural isostasy, and long-lived escarpments: a numerical modelling study. *Journal of Geophysical Research*, **99**, 12,229-12,243.

Trull, T.W., Brown, E.T., Marty, B., Raisbeck, G.M., and Yiou, F., 1995. Cosmogenic ^{10}Be and ^{3}He accumulation in Pleistocene beach terraces in Death Valley, California, USA: implications for cosmic-ray exposure dating of young surfaces in hot climates. *Chemical Geology*, **119**, 191-207.

Trull, T.W., Kurz, M.D., and Jenkins, W.J., 1991. Diffusion of cosmogenic ^{3}He in olivine and quartz: implications for surface exposure dating. *Earth and Planetary Science Letters*, **103**, 241-256.

Twidale, C.R., 1990. The origin and implications of some erosional landforms. *Journal of Geology*, **98**, 343-364.

Twidale, C.R., 1992. King of the plains: Lester King's contributions to geomorphology. *Geomorphology*, **5**, 491-509.

Tyson, P.D., 1986. *Climatic Change and Variability in Southern Africa.* OUP, Cape Town.

van der Beek, P.A., 1995. *Tectonic evolution of continental rifts: inferences from numerical modelling and fission track thermochronology.* Ph.D., Thesis, Proefschrift Vrije Universiteit, Amsterdam.

van der Beek, P., Andriessen, P., and Cloetingh, S., 1995. Morphotectonic evolution of rifted continental margins; inferences from a coupled tectonic-surface processes model and fission track thermochronology. *Tectonics*, **14**, 406-421.

van der Beek, P. and Braun, J., 1998. Numerical modelling of landscape evolution on geological time-scales; a parameter analysis and comparison with the south-eastern highlands of Australia. *Basin Research*, **10**, 49-68.

van der Beek, P. and Braun, J., 1999 Controls on post-Mid-Cretaceous landscape evolution in the southeastern highlands of Australia: insights from numerical surface process models. *Journal of Geophysical Research*, **104**, 4945-4966.

van der Beek, P., Braun, J., and Lambeck, K., 1999. Post-palaeozoic uplift of southeastern Australia revisited: results from a process-based model of landscape evolution. *Australian Journal of Earth Sciences*, **46**, 157-172.

van der Beek, P., Mbede, E., Andriessen, P., and Delvaux, D., 1998. Denudation history of the Malawi and Rukwa rift flanks (East African Rift System) from apatite fission track thermochronology. *Journal of African Earth Sciences*, **26**, 363-385.

van Zinderen Bakker, E.M. and Werger, M.J.A., 1974. Environment, vegetation and phytogeography of the high-altitude bogs of Lesotho. *Vegetatio*, **29**, 37-49.

Von Egidy, T and Hartmann, F.J., 1982. Average muonic coulomb capture probabilities for sixty-five elements. *Physics Reviews*, A26, 2355-2360.

Von Veh, M.W. and Anderson, N.J.B., 1990. Normal-slip faulting in the coastal areas of northern Natal and Zululand, South Africa. *South African Journal of Geology,* **93**, 574-582.

Weissel, J.K., and Karner, G.D., 1989. Flexural uplift of rift flanks due to mechanical unloading of the lithosphere during extension. *Journal of Geophysical Research*, **94**, 13,919-13,950.

Weissel, J.K. and Seidl, M.A., 1997. Influence of rock strength properties on escarpment retreat across passive continental margins. *Geology*, **25**, 631-634.

Wellington, J.H., 1955. *Southern Africa: A Geographical Study. Volume 1: Physical Geography*. Cambridge University Press.

Wellington, J.H., 1958. The evolution of the Orange River Basin: some outstanding problems. *South African Geographical Journal*, **40**, 3-30.

Wells, S.G., McFadden, L.D., Poths, J., and Olinger, C.T., 1995. Cosmogenic ^{3}He surface-exposure dating of stone pavements: implications for landscape evolution in deserts. *Geology*, **23**, 613-616.

Whalley, W.B., Douglas, G.R., and McGreevy, J.P., 1982. Crack propagation and associated weathering. *Zeitschrift für Geomorphologie*, **26**, 33-54.

Whipple, K.X., Kirby, E., and Brocklehurst, S.H., 1999. Geomorphic limits to climate-induced increases in topographic relief. *Nature*, **401**, 39-43.

White, R.S., 1997. Mantle plume origin for the Karoo and Ventersdorp flood basalts, South Africa. *South African Journal of Geology,* **100**, 271-282.

White, R.S. and McKenzie, D.P., 1989. Volcanism at rifts. *Scientific American*, 261, 44-55.

White. R.S. and McKenzie, D., 1995. Mantle plumes and flood basalts. *Journal of Geophysical Research*, **100**, 17,543-17,585.

Widdowson, M., 1997a. The geomorphological and geological importance of palaeosurfaces. In: M. Widdowson (ed.) *Palaeosurfaces: recognition, Reconstruction and Palaeoenvironmental Interpretation.* Geological Society Special Publication Number 120.

Widdowson, M., 1997b. Tertiary palaeosurfaces of the SW Deccan, Western India: implications for passive margin uplift. In: M. Widdowson (ed.) *Palaeosurfaces: recognition, Reconstruction and Palaeoenvironmental Interpretation.* Geological Society Special Publication Number 120.

Widdowson, M. and Cox, K.G., 1996. Uplift and erosional history of the Deccan traps, India: evidence from laterites and drainage patterns of the Western Ghats and Konkan Coast. *Earth and Planetary Science Letters*, **137**, 57-69.

Wilson, M., 1993. *Igneous petrogenesis*. Chapman and Hall, London.

Wolf, R.A., Farley, K.A., and Silver, L.T., 1997. Assessment of (U-Th)/He thermochronometry: the low-temperature history of the San Jacinto mountains, California. *Geology*, **25**, 65-68.

Yair, A., and Gerson, R., 1974. Mode and rate of escarpment retreat in an extremely arid environment (Sharm el Sheikh, southern Sinai Peninsula. *Zeitschrift für Geomorphologie, Supplementband*, **21**, 202-215.

Yamashita, M., Stephens, L.D., and Patterson, H.W., 1966. Cosmic-ray-produced neutrons at ground level: neutron production rate and flux distribution. *Journal of Geophysical Research*, **71**, 3817-3834.

Yokoyama, Y., Reyss, J-L., and Guichard, F., 1977. Production of radionuclides by cosmic rays at mountain altitudes. *Earth and Planetary Science Letters*, **36**, 44-50.

Young, A., 1972. *Slopes*. Oliver and Boyd, Edinburgh.

Young, R.W., 1983. The tempo of geomorphological change: evidence from southeastern Australia. *Journal of Geology*, **91**, 221-230.

Young, R.W., 1989. Crustal constraints on the evolution of the continental divide of eastern Australia. *Geology*, **17**, 528-530.

Young, R.W. and McDougall, I., 1982. Basalts and silcretes on the coast near Ulladulla, southern New South Wales. *Journal of the Geological Society of Australia*, **29**, 425-430.

Young, R. and McDougall, I., 1993. Long-term landscape evolution: Early Miocene and modern rivers in southern New South Wales, Australia. *Journal of Geology*, **101**, 35-49.

Zreda, M., England, J., Phillips, F., Elmore, D., and Sharma, P., 1999. Unblocking of the Nares Strait by Greenland and Ellesmere ice-sheet retreat 10,000 years ago. *Nature*, 398, 139-142.

Zreda, M., and Noller, J.S., 1998. Ages of prehistoric earthquakes revealed by cosmogenic chlorine-36 in a bedrock fault scarp at Hebgen lake. Science, 282, 1097-1099.

Zreda, M.G. and Phillips, F.M., 1995. Insights into alpine moraine development from cosmogenic ^{36}Cl buildup dating. *Geomorphology*, **14**, 149-156.

Zreda, M.G., Phillips, F.M., and Elmore, D., 1994. Cosmogenic ^{36}Cl accumulation in unstable landforms 2: simulations and measurements on eroding moraines. *Water Resources Research*, **30**, 3127-3136.

Zreda, M.G., Phillips, F.M., Elmore, D., Kubik, P.W., Sharma, P., and Dorn, R.I., 1991. Cosmogenic chlorine-36 production rates in terrestrial rocks. *Earth and Planetary Science Letters*, **105**, 94-109.

Zreda, M.G., Phillips, F.M., Kubik, P., Sharma, P., and Elmore, D., 1993. Cosmogenic ^{36}Cl dating of a young basaltic eruption complex, Lathrop Wells, Nevada. *Geology*, **21**, 57-60.

Zreda, M.G., Phillips, F.M., and Smith, S.S., 1990. *Cosmogenic ^{36}Cl dating of geomorphic surfaces.* Hydrology Report H90-1, Hydrology Program, New Mexico Institute of Mining and Technology, Socorro, New Mexico.

Personal Communicants

H. Cockburn, University of Melbourne, Melbourne, Australia.

R. Cresswell, Australian National University, Canberra, Australia.

K. Fifield, Australian National University, Canberra, Australia

D. James, University of Edinburgh.

K. Jarvis, NERC ICP-MS Facility, Kingston University.

G. Marsh, Rhodes University, Grahamstown, South Africa.

P. Stephenson, James Cook University, Townsville, Australia.

J. Stone, University of Washington, Seattle, USA.

M. Summerfield, University of Edinburgh.

P. van der Beek, Université Joseph Fourier, Grenoble, France.

Appendices

Appendix Number	Contents
1	Plates.
2	Comparison of denudation rates derived using different calibrated Ca and K spallation rates.
3	Major element analysis results.
4	Trace element analysis results.
5	Isotope dilution curve fitting results.
6	Determination of the sample thickness correction factor.
7	Site-specific sub-surface ^{36}Cl production rates for the 0.5 m thick block fall model for the free face samples.
8	Copy of the *Mathematica* ® program used to calculate the denudation rates for samples from free face surfaces.
9	Fleming, A., *et al*, 1999. Denudation rates for the southern Drakensberg escarpment, SE Africa, derived from *in-situ*-produced cosmogenic ^{36}Cl: initial results. *Journal of the Geological Society, London.* **156**, 209-212.

Appendix 1: Plates

Plate 1: View of the southern Drakensberg at ~ 29 ° 45 ' S (Garden Castle). The highest peak, left of centre, is Wilson's Peak (3310 m).

Plate 2: The Tsoelike River at 30 ° 5 ' S, looking north. This riverbed is ~ 700 m below the elevation of the escarpment summit which is only ~ 5 km to the south. Note buildings for scale. The mountains in the far distance are part of the Central Range of the Lesotho Highlands.

Plate 3: View oceanward from the Drakensberg at Naudesnek showing the steep-sided narrow ridges which separate the first order tributaries which rise on the escarpment.

Plate 4: View of one of the bedrock knolls at Naudesnek.

Plate 5: Sample O2/97 after sawing but prior to crushing. This sample is typical of the fine-grained Drakensberg Group basalt samples used in this study.

Plate 6: View of the southern Drakensberg near Naudesnek taken from about 20 km away on the oceanward side of the escarpment and looking west.

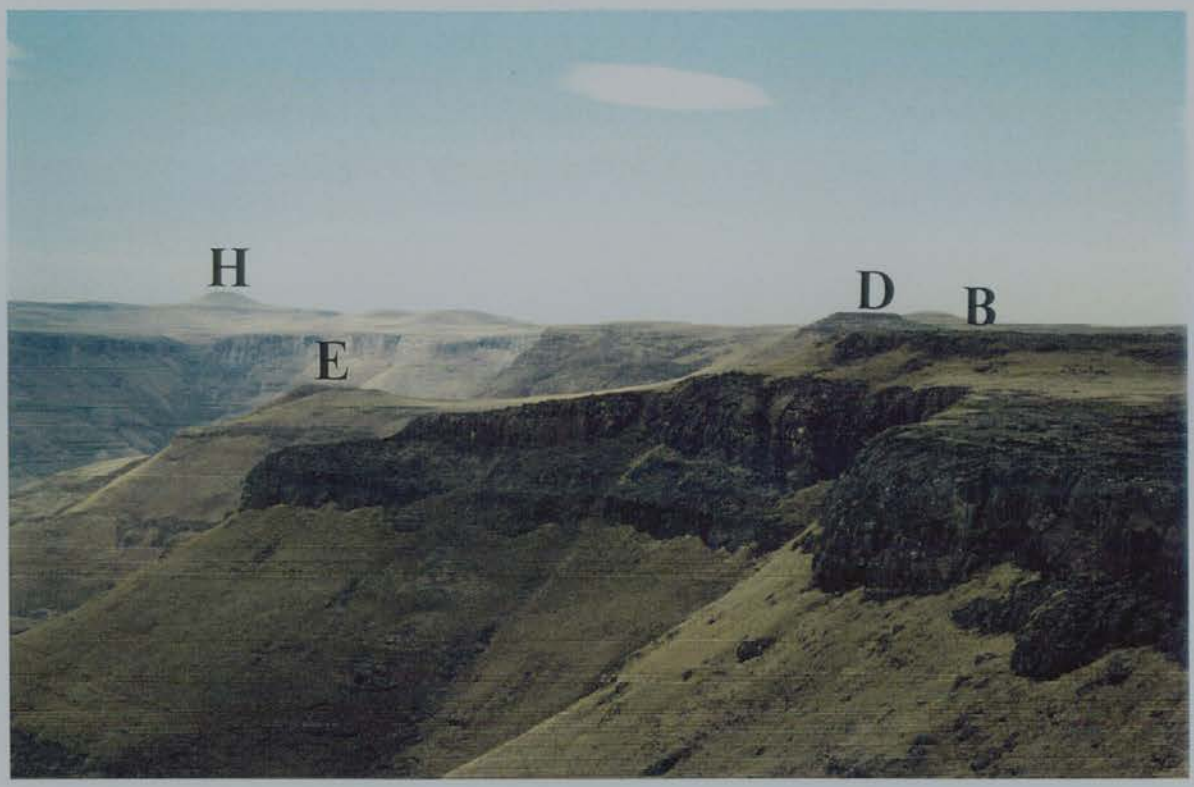

Plate 7: General view of the southern Drakensberg at Naudesnek, taken from site A in Figure 6.3, looking north. Sites B, D, E and H are shown. Sites F and G are out of shot on the left-hand side. Site C is also out of sight.

Plate 8: Example of a typical weathered bedrock exposure on a summit on the southern Drakensberg. This is the site from which sample N1/97 was collected.

Plate 9: View looking north along the Drakensberg escarpment from the summit of Mak'holo (2899 m).

Plate 10: View looking west (inland) from the summit of Mak'holo (2899 m). The location of sample O5/97 is shown as is the summit at Maphooaneng Pass ~ 7.5 km to the west from which sample O8/97 was collected. The mountains on the horizon are the Thaba-Putsoa Range (~ 2900 m high and ~ 70 km west) which mark the western limit of the basalt outcrop in the part of Lesotho.

Plate 11: The surface of the knoll which marks the summit of Mak'holo (2899 m). This is the exposed bedrock from which sample O1/97 was taken.

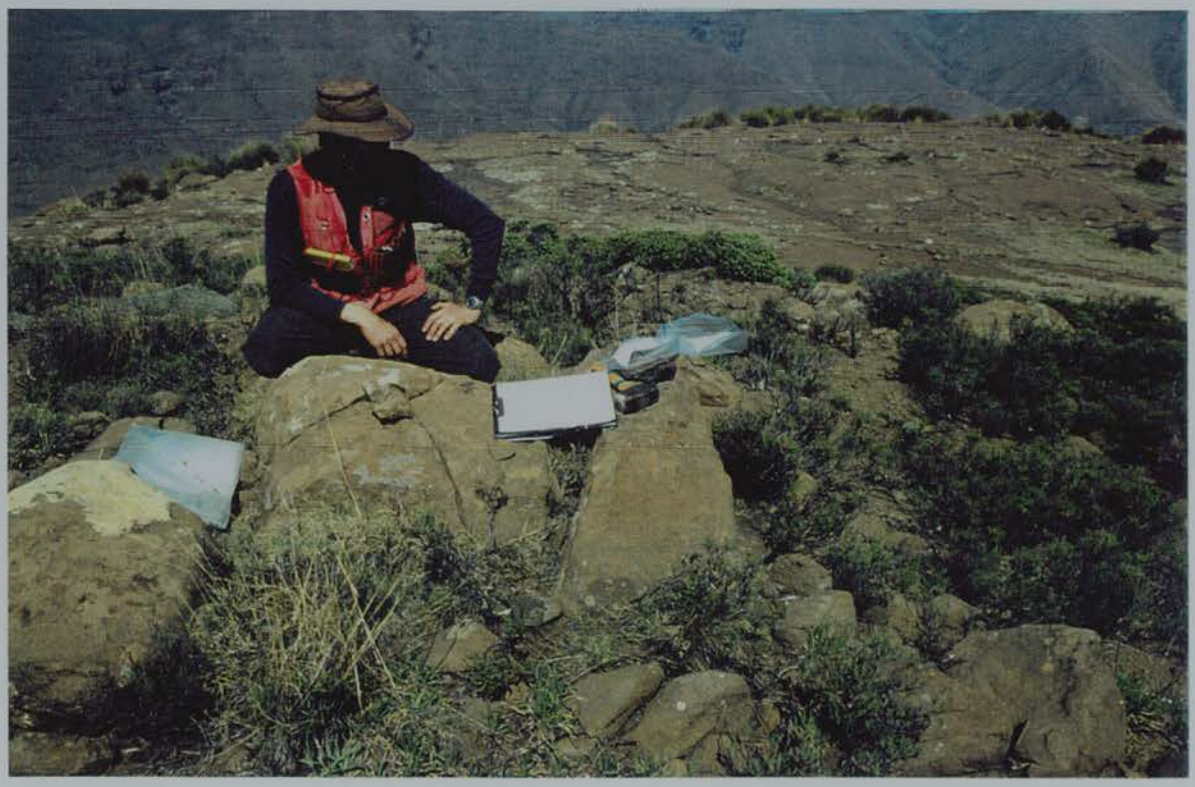

Plate 12: Sample O8/97 collected from the westernmost summit (2560 m) at Maphooaneng Pass, ~ 7.5 km west of Ongeluk's Nek.

Plate 13: View of Hodgson's Peaks (3256 m on left and 3251 m on right) the highest summits on the Drakensberg in the Sani Pass area.

Plate 14: View of the easternmost part of the Sani Flats taken from near the summit of the northernmost of the twin summits of Hodgson's Peaks. Sample sites A (S1/95 and S5/97) and B (S8/97) are marked.

Plate 15: Site B in Figure 6.6, looking east to site A. The main free face of the escarpment is on the left-hand side.

Plate 16: View of the bedrock knoll which forms the summit of the northernmost of the twin summits of Hodgson's Peaks. Looking from the inland side of the escarpment southeast. The location of sample S3/97 is shown.

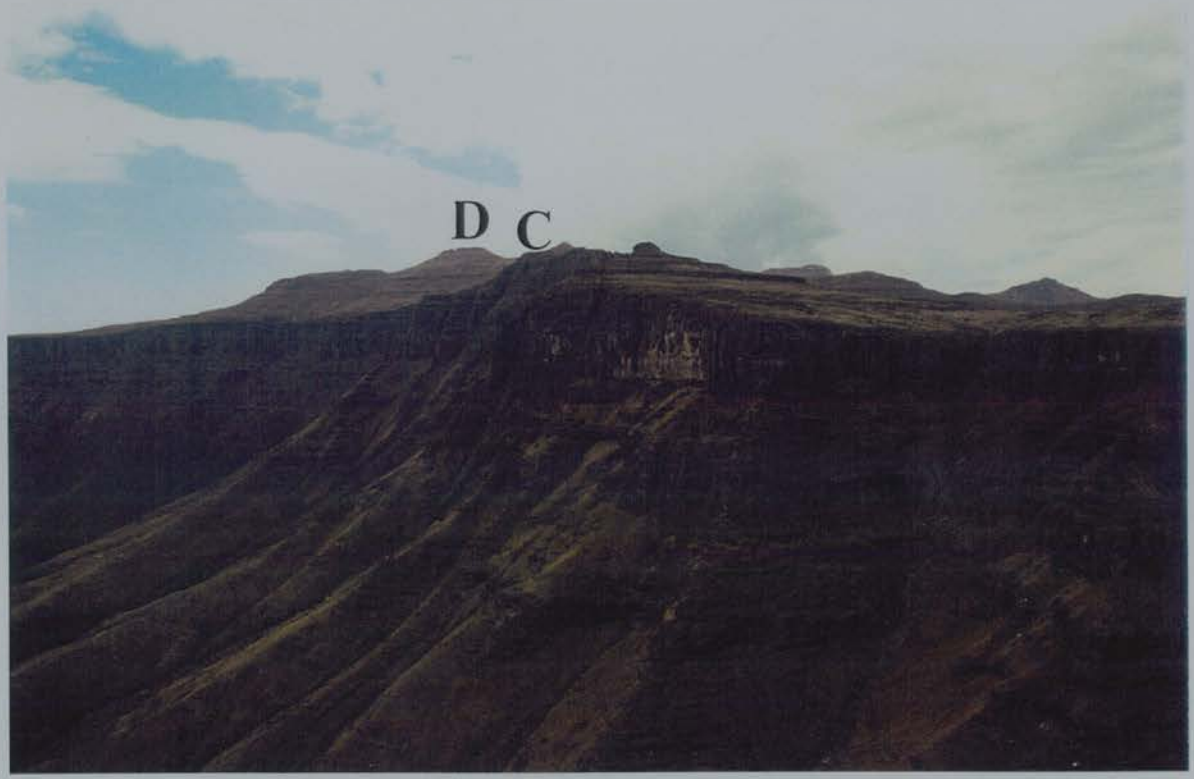

Plate 17: View from the Sani Flats looking south along the escarpment. Sites D (S3/97), one of the summits of Hodgson's Peaks, and C (S10/97), a summit on the escarpment are shown.

Plate 18: View of part of the low relief summit > 3000 m in the northwest of the Lesotho Highlands (north of 29 ° S). Photo taken from near sample site H in Figure 6.7, looking southeast.

Plate 19: View from near sample site I in Figure 6.7, looking southeast to the valley incised by the Motete River, a major tributary of the Senqu, into the extensive area of ground > 3000 m. The valley floor (not visible) is ~ 400 m below the summit surface.

Plate 20: The bedrock knoll at Matabeng Pass which forms the drainage divide between two rivers. Distinct bedrock knolls were also encountered at the other valley head summit sites (G, J and K in Figure 6.7).

Plate 21: View from the summit of Moteng Pass (2850 m) in the Maloti Mountains (J in Figure 6.7) looking down the Hololo River valley to the Lesotho Lowlands (1500 - 2000 m). Other summits of the Maloti can be seen in the distance.

Plate 22: The summit of Thabana-ea-Manase (2915 m) in the Central Range. Sample L4/97 was taken from the summit ridge, the left hand side of which can be seen. Note the boulders on the 10 - 15 ° slope below the ridge which are assumed to have fallen from the ridge. The view is to the east and the valley in the distance is that of the Malibamatso River, just north of its confluence with the Senqu.

Plate 23: Sample site E in Figure 6.7. This is the ridge from which samples L10/97 and L11/97 were collected. Thabana-Ntlenyana (3482 m), the highest summit in southern Africa is in the distance.

Plate 24: The summit of Kotisephola (3360 m). Sample L12/97 is from the furthest away hummock. Site of L13/97 sample is out of shot on the left-hand side. View looking northwest.

Plate 25: The summit at Mafisoaneng (3295 m), looking east. Sample L16/97 is from the hummock, while L17/97 is from near the site of the bag in the centre of the frame.

Plate 26: The summit of the drainage divide between the Tenane (left hand side) and Likomiking (fight hands side) Rivers, looking west. Sample L7/97 is from this site.

Plate 27: View of Lekhalong-la-Thaba-Putsoa (Blue Mountain Pass) from the west. Site D in Figure 6.7, from which sample L9/97 was collected, is indicated. The main valley is that of the Makheleng River, a tributary of the Senqu River.

Plate 28: Site I in Figure 6.7, looking northwest down the Motete River valley. Sample L22/97 was collected from an outcrop on this flat surface, which extends for ~ 1 - 2 km^2, and which is separated from the river valley by a ~ 10 - 20 m free face.

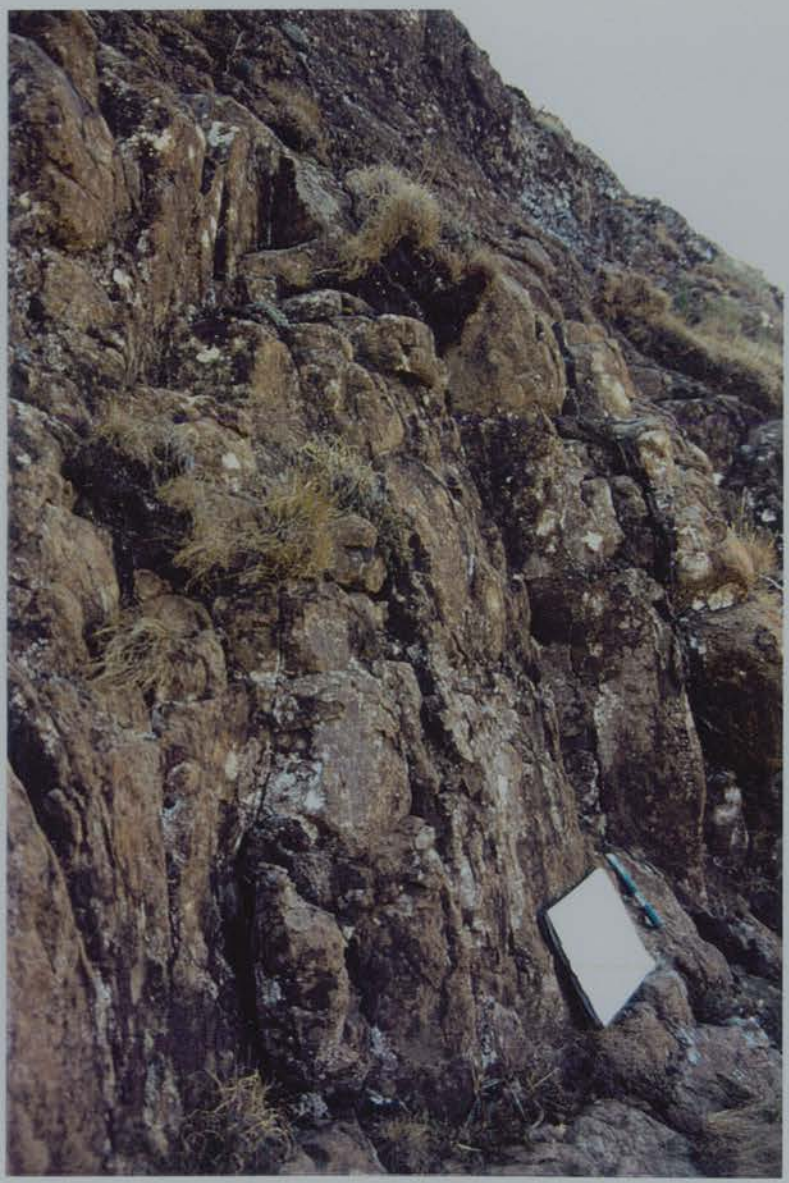

Plate 29: Free face from which sample N4/95 was collected. This face is being eroded by a combination of granular disintegration, spalling of thin < 0.2 m sheets and the loss of blocks < 0.5 m thick.

Plate 30: The free face from which samples N12/97 and N13/97 were collected. Note the stepped nature of the free face at this site. N5/97 was taken from the south-western (left-hand side) continuation of this face, ~ 250 m west.

Plate 31: The free face on the northern side of Naudesnek. Sample N5/97 was collected from this end (western) of the face, while N12/97 and N13/97 are from the same face ~ 250 m east.

Plate 32: View looking from the oceanward side of the escarpment, at the main free face of the escarpment on the southern side of Naudesnek. Samples N8/97 and N9/97 are from the left hand free face, while N11/97 is from the face on the right-hand side of the grassed gully. N10/97 was collected from the same face as N11/97, but in the gully.

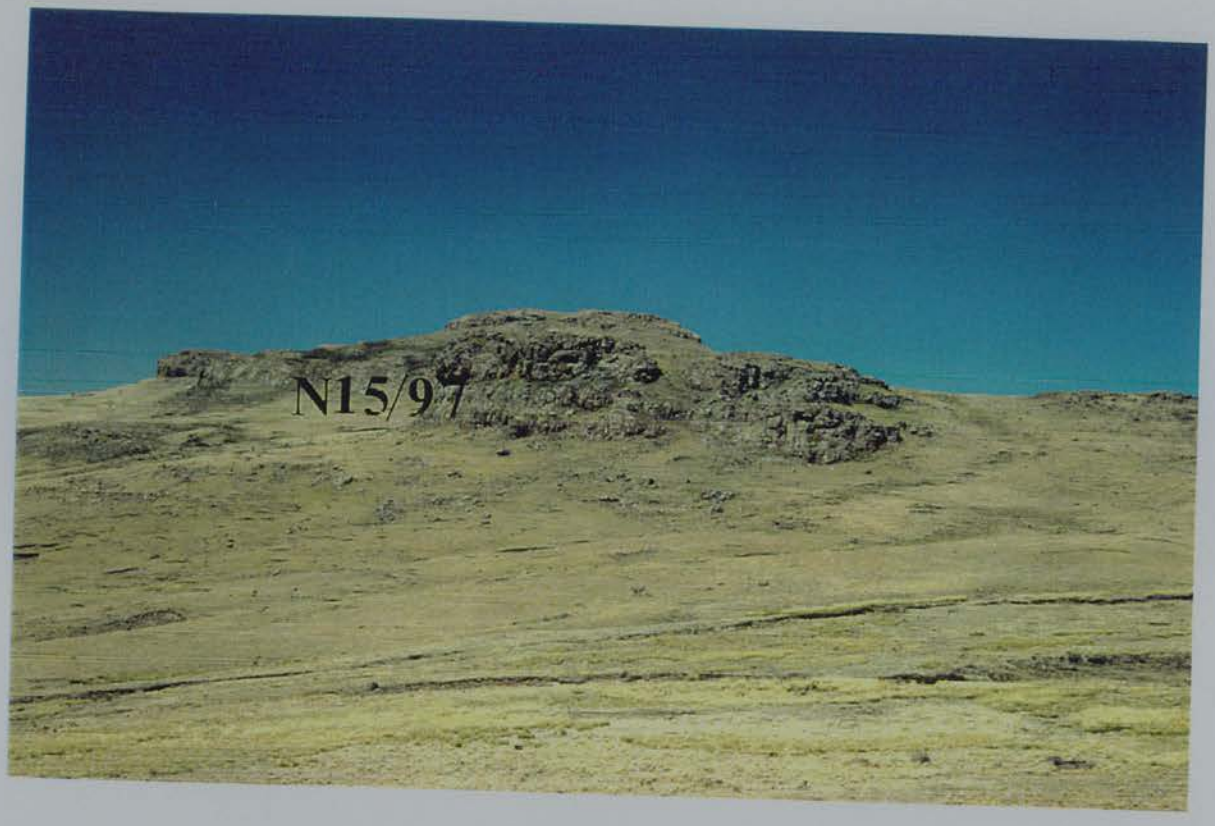

Plate 33: The free face on the eastern side of the small drainage basin inland of the escarpment at Scobell's Kop (G in Figure 7.1). Sample N15/97 was collected from this face.

Plate 34: The free face on the western side of the small drainage basin at Scobell's Kop from which sample N16/97 is from. This face, and that from which provided N15/97, are more irregular than those on the main free face.

Plate 35: View of the inland side of the escarpment at Scobell's Kop, the summit in the centre of the photograph. Sample N17/97 is from the southern (left-hand side) of the free face which is ~ 80 m below Scobell's Kop summit. This area is drained by a tributary of the Bell River, part of the Orange River Basin.

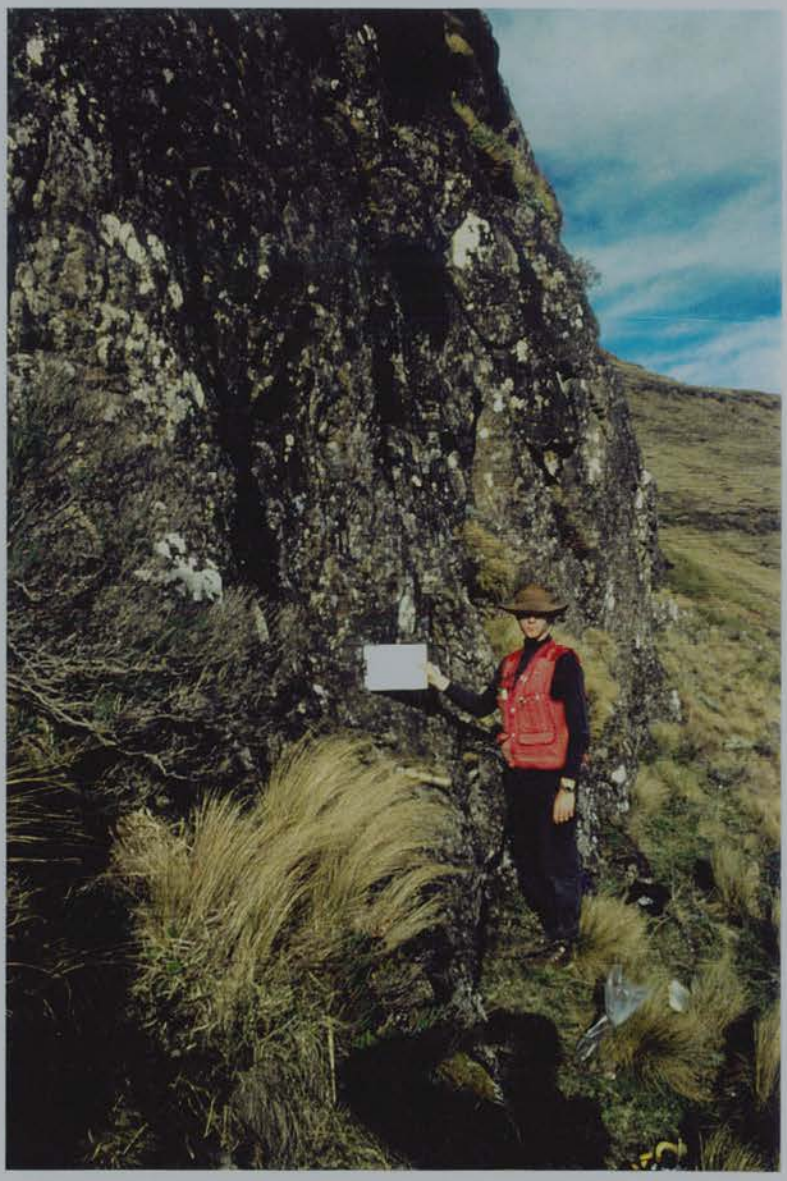

Plate 36: The free face that provided sample N18/97. This is located on the inland side of the escarpment, the summit of which, at Naudesnek, can be seen on the horizon. This face is similar in appearance to those on the escarpment. This face is being denuded by a combination of granular disintegration, exfoliation of thin sheets and the loss of blocks ~ 0.5 m thick.

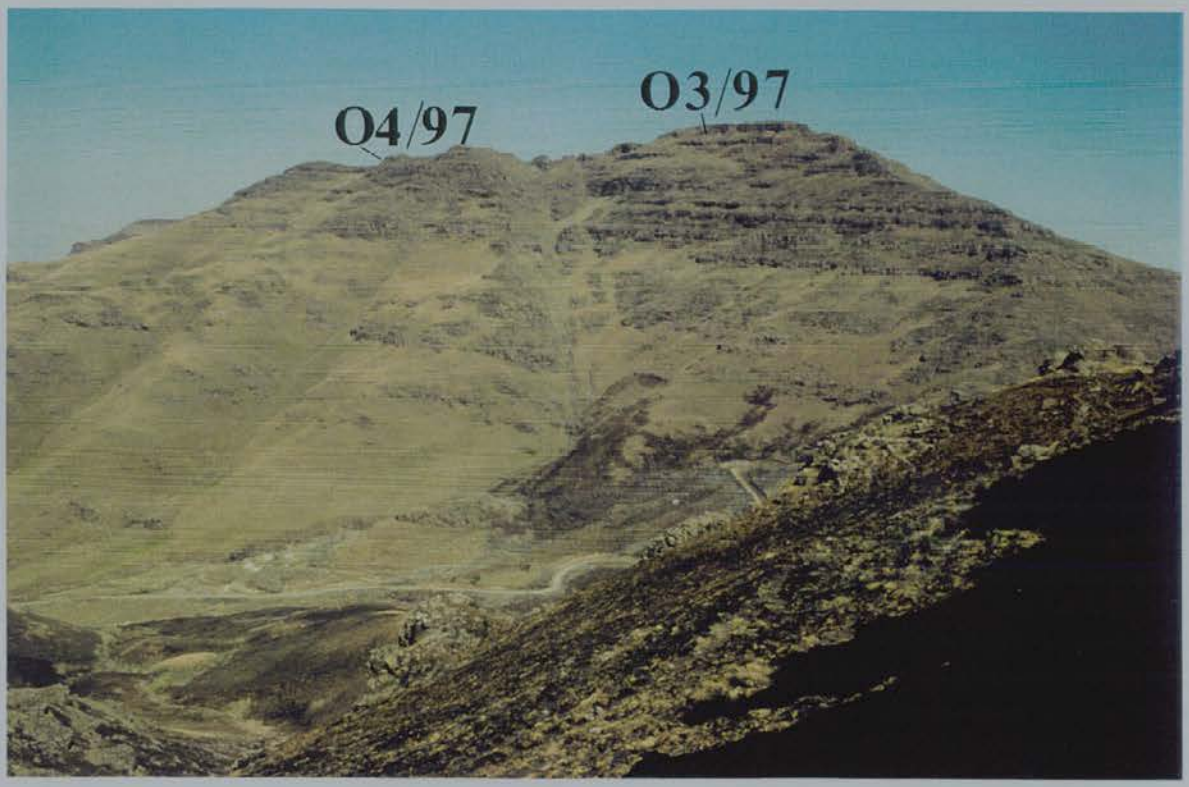

Plate 37: View of the southern side of the escarpment at Ongeluk's Nek. Samples O3/97 and O4/97 were collected from this free face at the sites shown.

Plate 38: The free face from which sample O4/97 was collected. This is the topmost part of the main escarpment free face and is separated from it by a ~ 3 m wide rock ledge.

Plate 39: View of the free face that forms the western extremity of the embayment at Ongeluk's Nek. Sample O9/97 was collected from this face. The free face from which sample O10/97 was taken is visible on the left hand side of the photograph.

Plate 40: Close up of the face from which sample O10/97 was collected. Note that the face is being denuded by a combination of processes involving granular disintegration, exfoliation of thin sheets and the loss of blocks.

Plate 41: The free face on the inland (western) side of the knoll which forms the summit of Mak'holo. Sample O6/97 comes from this face.

Plate 42: Sample O12/97 was taken from this free face which is on the inland side of the knoll which forms the summit on the northern side of Ongeluk's Nek.

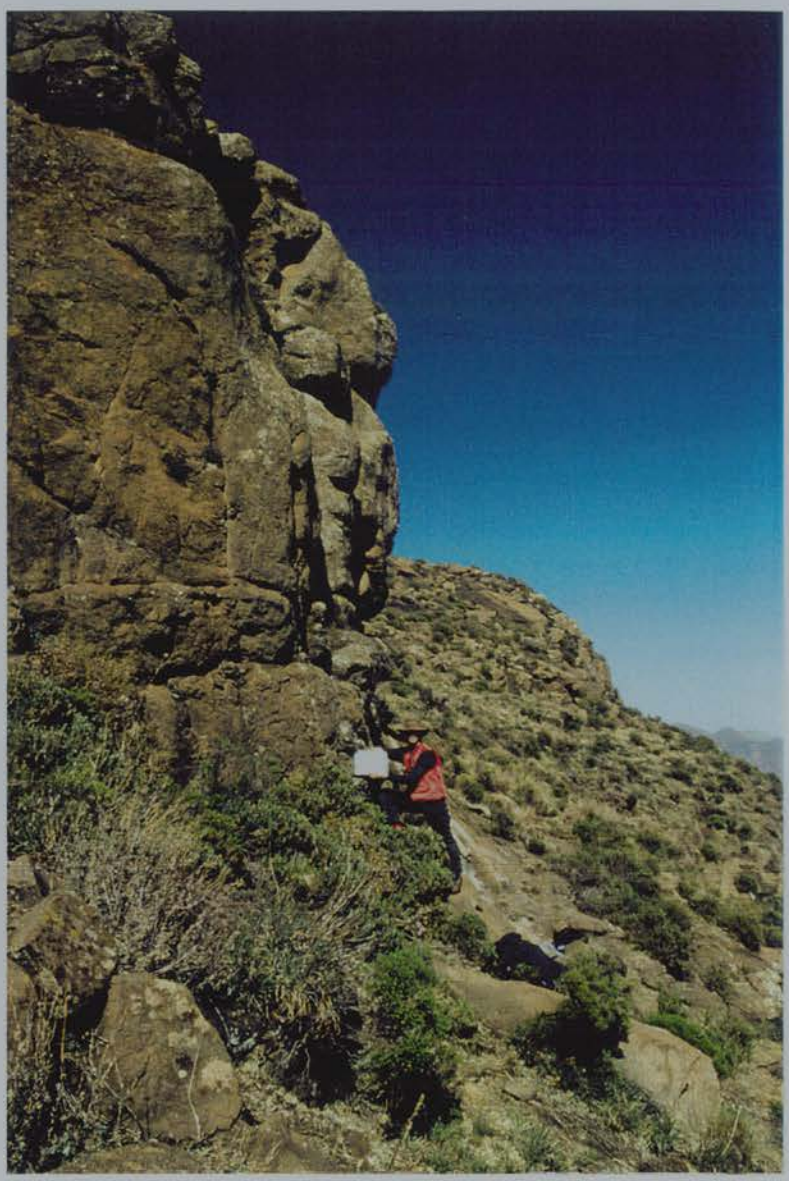

Plate 43: The free face on the southern side of Maphooaneng Pass, ~ 7.5 km west of Ongeluk's Nek. Sample O7/97 is from this site.

Plate 44: View of the main escarpment free face at site A in Figure 7.3. Samples S2/95, S6/97 and S7/97 were all collected from this face.

Plate 45: The Twelve Apostles viewed from the eastern (oceanward) side of the escarpment. The position of samples S9/97 and S12/97 are shown. Samples S2/95, S6/97 and S7/97 are from the northern continuation of this face. The lowermost free face is formed in Clarens Formation sandstone.

Plate 46: Looking west along the escarpment to the protruding part of the face from which sample S7/97 was collected (near where person is standing). The highest point on the left of the photo is Bitso-Lebe (3126 m).

Plate 47: The face from which sample S6/97 was collected. Note that the face here appears to be losing material through the removal of thin ~ 0.1 - 0.3 m wide sheets, but that further along this face individual blocks ~ 0.5 m have been lost.

Plate 48: Site B in Figure 7.3, about midway along the Twelve Apostles. Sample S9/97 was taken from this face. Note the grassed ledge which separates this part of the free face from a similar face below. The height of the face from the ledge to the surface is ~ 25 m.

Plate 49: View of the Twelve Apostles from the southern side of Sani Pass. S12/97 is from the western end while S9/97 is from midway.

Plate 50: The main free face of the Drakensberg on the southern side of Sani Pass. The sites from which samples S1/97 and S2/97 were collected are shown.

Plate 51: Looking south along the main free face on the southern side of Sani Pass. Sample S2/97 was collected from the rockface next to the person in the centre of the photograph. Note that at the point where this photo was taken the face appears to be denuding by the loss of individual boulders of varying sizes, generally < 0.5 m thick.

Plate 52: The free face on the inland side of the escarpment at Sani Pass from which sample S11/97 was collected. The second peak from the right is the northern summit of Hodgson's Peaks.

Plate 53: Looking east from the northern summit of Hodgson's Peaks. Sample S4/97 was taken from the eastern side of the knoll (out of sight). This area is drained by a series of channels that flow to the escarpment edge, which is visible on the right and left hand sides of the photo.

Plate 54: The eastern free face of the summit at Matabeng Pass from which sample L2/97 was collected. This face appears to be denuding by granular disintegration, exfoliation of thin (few centimetres) sheets and the occasional loss of individual < 0.5 m thick boulders.

Plate 55: The free face at site E, Figure 7.4, from which sample L14/97 was collected.

Plate 56: The free face on the northwest side of Thaba-Ntso from which sample L24/97 was collected.

Plate 57: The large free face from which L26/97 was taken is on the extreme right. This marks the southern boundary of the basalt in this area. The summit of Thaba-Ntso, from which L24/97 and L25/97 were collected, is marked. The bedrock exposed on the lower slopes is Clarens Formation sandstone.

Plate 58: The view looking southeast from the location of L26/97. The edge of the escarpment is marked by the more distant edge of the dark green hills in the middle distance (~ 5 - 10 km away). The escarpment here is formed in Stormberg Group sandstones.

Plate 59: The free face at Moteng Pass from which sample L27/97 was taken. The face shows signs of the past loss of thin (< 0.2 m) sheets and individual blocks < 0.5 m thick.

Plate 60: The free face at the summit of Mafika-Lisiu in the Maloti Mountains and the view west down the Mphosong River valley.

Plate 61: The free face at site B, Figure 7.4 from which sample L5/97 was collected. The collapse of part of the upper overhang has produced the ~ 1- 2m thick boulders which can be seen lying on the talus slope.

Plate 62: The free face on the southern side of the summit at Mafisoaneng (3295 m) from which L18/97 was collected.

Plate 63: The free face above the Tenane River from which sample L6/97 was collected.

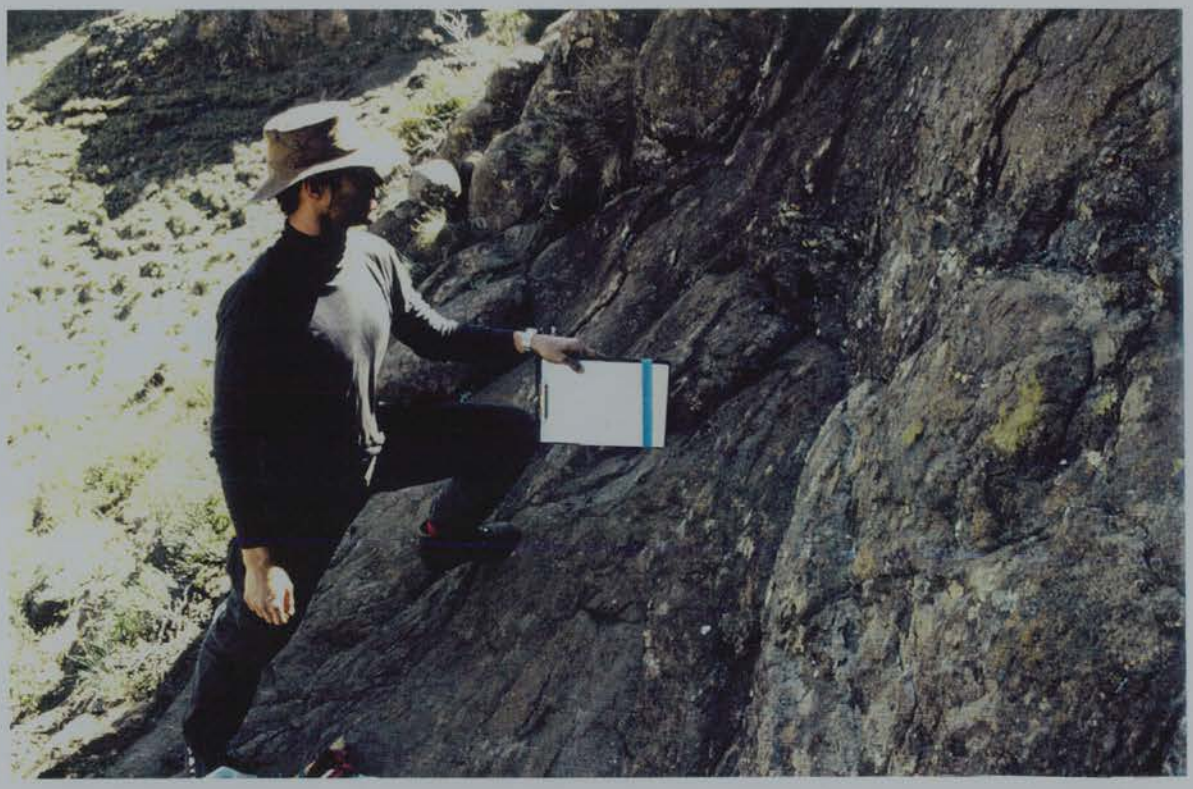

Plate 64: The free face from which sample L8/97 was collected. One of the gullies which dissect this bedrock step can be seen in the background.

Plate 65: View of the east slope of part of the Motete River valley. L19/97 was collected from the lower of the two main free faces. Sample L20/97 is from a similar position on the western bank.

Plate 66: Looking north along the face from which L19/97 was collected. Part of the face, ~ 6m to the south of the sample site, has lost a slab of ~ 2 m thick. This collapse appears to be due to undercutting caused by sapping.

Plate 67: View, looking west, of the free face on the eastern bank of the Motete River valley from which sample L21/97 was collected. Most boulders on the talus slope are ~ 0.5 m thick, but there are some boulders of ~ 1 - 2 m thickness which are produced by the collapse of overhangs (such as that at the southern end of the face) and the failure of ~ 1 - 2m thick slabs.

Appendix 2

A. Comparison of denudation rates derived using the calibrated Ca spallation rates of Stone *et al* (1996a), Phillips *et al*, (1996a) and Swanson and Caffee (in prep.).

Sample	Ca (wt %)	K (wt %)	Denudation Rate (m Ma^{-1}) derived using steady-state model (Lal, 1991) and one of following Ca spallation production rates:			% increase in denudation rate derived using Stone *et al* (1996a) Ca spallation production rate	
			P_{Ca} = 48.8 atoms $(g\ Ca)^{-1}\ a^{-1}$ (Stone *et al*, 1996a)	P_{Ca} = 73.3 atoms $(g\ Ca)^{-1}\ a^{-1}$ (Phillips *et al*, 1996a)	P_{Ca} = 81.9 atoms $(g\ Ca)^{-1}\ a^{-1}$ (Swanson and Caffee, in prep.)	if Phillips *et al* (1996a) rate used	if Swanson and Caffee (in prep.) rate used
L25/97	4.57	0.38	51.8	68.4	75.0	32	45
S11/97	4.72	1.00	31.5	38.7	41.2	23	31
O8/97	5.16	1.23	43.0	53.4	56.8	24	32
L19/97	6.13	1.54	7.9	9.9	10.6	25	34
S9/97	7.55	0.54	62.6	84.4	91.8	35	47
O9/97	7.39	0.51	131.0	176.1	191.4	35	46
L21/97	7.67	0.52	29.3	39.8	43.3	36	48

B. Comparison of denudation rates derived using the calibrated K spallation rates of Evans *et al* (1997), Phillips *et al*, (1996a) and Swanson and Caffee (in prep.).

Sample	K (wt %)	Ca (wt %)	Denudation Rate (m Ma^{-1}) derived using steady-state model (Lal, 1991) and one of following K spallation production rates:			% increase (decrease) in denudation rate derived using Evans *et al* (1997) K spallation production rate	
			P_K = 171 atoms $(g\ K)^{-1}\ a^{-1}$ (Evans *et al*, 1997)	P_K = 154 atoms $(g\ K)^{-1}\ a^{-1}$ (Phillips *et al*, 1996a)	P_K = 209 atoms $(g\ K)^{-1}\ a^{-1}$ (Swanson and Caffee, in prep.)	if Phillips *et al* (1996a) rate used	if Swanson and Caffee (in prep.) rate used
O5/97	0.19	6.69	9.2	9.1	9.4	(1)	2
N3/97	0.24	6.16	17.3	17.1	17.7	(1)	2
O9/97	0.51	7.39	131.0	130.0	135.3	(1)	3
L10/97	0.85	6.34	3.5	3.3	3.8	(5)	8
O8/97	1.23	5.16	43.0	41.6	46.8	(3)	9
L20/97	1.29	6.07	8.5	8.1	9.2	(5)	8
L19/97	1.54	6.13	7.9	7.5	8.7	(5)	10

APPENDIX 3

MAJOR ELEMENT ANALYSIS RESULTS

Samples were prepared for major element analysis using the procedures outlined in Section 4.4.1. The prepared fused glass discs were analysed by D. James using the Phillips PW 1480 wavelength-dispersive automatic XRF spectrometer in the Department of Geology and Geophysics, University of Edinburgh.

Table 1: Major element composition of samples collected during 1995 field season.

Major Element (%)	Samples					
	S1/95β	**S2/95β**	**N1/95**	**N2/95**	**N3/95**	**N4/95**
SiO_2	50.61	52.77	51.84	51.35	53.13	52.43
TiO_2	1.14	1.26	1.09	1.21	1.26	1.20
Al_2O_3	13.17	11.26	13.30	12.63	10.59	14.13
Fe_2O_3 (total)	12.35	12.65	11.40	12.72	11.56	10.70
MnO	0.19	0.20	0.16	0.20	0.19	0.17
MgO	6.05	7.32	6.19	6.61	8.21	6.34
CaO	9.16	8.53	9.21	9.38	11.07	9.75
Na_2O	2.34	3.25	2.10	2.47	2.10	2.84
K_2O	1.15	0.62	0.95	0.38	0.77	0.88
P_2O_5	0.08	0.06	0.11	0.17	0.07	0.13
LoIα	3.76	2.08	3.08	2.69	0.49	0.93
Total	100.00	100.00	99.43	99.81	99.44	99.50

α loss on ignition.
β analysed at Australian National University.

Table 2: Major element composition of samples collected during 1997 field season.

Major Element (%)	Samples								
	N1 /97	**N2 /97**	**N3 /97**	**N4 /97**	**N5 /97**	**N6 /97**	**N7 /97**	**N8 /97**	**N9 /97**
SiO_2	54.17	55.84	57.13	55.19	55.06	55.96	54.38	54.28	56.00
TiO_2	1.35	1.20	1.22	1.14	1.04	1.14	1.51	1.36	1.11
Al_2O_3	10.49	10.05	9.04	11.55	11.86	10.57	11.94	13.70	13.23
Fe_2O_3 (total)	13.60	12.33	12.32	12.00	11.23	10.85	12.05	10.31	9.52
MnO	0.21	0.19	0.18	0.19	0.15	0.18	0.19	0.18	0.19
MgO	6.63	6.19	6.27	5.08	6.71	7.30	6.65	6.01	6.33
CaO	9.11	8.76	8.62	8.85	10.01	10.09	10.11	10.20	10.17
Na_2O	2.02	1.62	1.14	1.50	2.32	2.13	2.20	2.61	2.58
K_2O	0.48	0.37	0.29	0.77	0.92	0.87	0.65	0.69	0.66
P_2O_5	0.01	0.02	0.07	0.02	0.01	0.01	0.01	0.01	0.01
LoIα	1.70	3.07	3.41	3.31	0.83	0.46	0.15	0.57	0.41
Total	99.77	99.64	99.69	99.60	100.14	99.56	99.84	99.92	100.21

Major Element (%)	Samples								
	N10 /97	**N11 /97**	**N12 /97**	**N13 /97**	**N14 /97**	**N15 /97**	**N16 /97**	**N17 /97**	**N18 /97**
SiO_2	55.14	56.03	57.43	55.44	58.74	57.95	54.51	54.26	55.60
TiO_2	1.24	0.95	1.21	1.06	1.04	0.94	1.04	1.16	1.07
Al_2O_3	13.50	11.73	12.26	12.87	9.62	10.42	11.19	12.04	12.04
Fe_2O_3 (total)	10.03	10.20	10.95	10.15	11.07	10.59	11.86	11.05	11.39
MnO	0.17	0.16	0.16	0.14	0.16	0.16	0.17	0.17	0.16
MgO	5.95	5.80	3.78	5.01	5.26	5.73	6.77	6.98	5.77
CaO	9.90	8.32	5.41	8.84	9.07	8.08	8.83	10.31	8.57
Na_2O	2.57	2.35	4.66	2.41	1.13	2.73	1.96	2.13	2.50
K_2O	0.68	0.96	1.46	0.61	0.39	0.32	0.60	0.73	1.29
P_2O_5	0.01	0.04	0.03	0.04	0.05	0.03	0.07	0.01	0.02
LoIα	0.41	2.99	2.07	2.92	2.93	2.73	2.75	0.93	1.06
Total	99.60	99.53	99.42	99.49	99.46	99.68	99.75	99.77	99.47

Major Element (%)	Samples								
	O1 /97	**O2 /97**	**O3 /97**	**O4 /97**	**O5 /97**	**O6 /97**	**O7 /97**	**O8 /97**	**O9 /97**
SiO_2	53.52	55.77	54.13	53.44	55.47	53.41	54.97	58.60	54.64
TiO_2	1.42	1.25	1.31	1.35	1.17	1.16	1.26	1.06	1.17
Al_2O_3	14.12	14.16	14.54	13.30	11.71	15.92	12.28	11.60	14.13
Fe_2O_3 (total)	11.10	10.66	10.59	11.53	11.94	9.81	11.27	9.81	9.43
MnO	0.19	0.15	0.18	0.19	0.17	0.19	0.19	0.12	0.17
MgO	5.84	4.44	5.44	6.26	5.10	5.04	5.65	4.31	5.91
CaO	10.15	9.29	9.94	10.36	9.35	10.30	9.30	7.22	10.34
Na_2O	2.58	2.48	2.44	2.28	1.79	2.71	2.54	2.87	2.80
K_2O	0.68	0.68	0.70	0.61	0.23	0.71	0.68	1.48	0.61
P_2O_5	0.01	0.02	0.01	0.01	0.06	0.01	0.04	0.02	0.01
LoIα	0.05	0.62	0.27	0.29	3.10	0.23	1.73	2.59	0.44
Total	99.66	99.52	99.55	99.62	100.09	99.49	99.91	99.68	99.65

Major Element (%)	Samples								
	O10 /97	**O11 /97**	**O12 /97**	**S1 /97**	**S2 /97**	**S3 /97**	**S4 /97**	**S5 /97**	**S6 /97**
SiO_2	55.38	51.66	54.60	54.64	54.72	56.04	55.52	53.47	55.52
TiO_2	1.06	1.30	1.06	1.14	1.15	1.26	1.05	1.16	1.50
Al_2O_3	11.53	10.59	11.62	12.22	13.78	10.74	11.87	14.30	12.63
Fe_2O_3 (total)	9.48	13.83	11.04	11.01	10.33	12.31	10.92	10.67	11.12
MnO	0.17	0.20	0.16	0.18	0.18	0.19	0.17	0.19	0.20
MgO	7.36	5.96	7.17	6.25	5.90	5.43	5.33	6.02	5.92
CaO	10.47	9.60	9.68	9.38	9.97	7.32	8.82	10.17	9.45
Na_2O	2.25	1.69	2.17	2.42	2.41	2.66	1.37	2.82	2.47
K_2O	0.99	0.94	1.29	0.60	0.90	1.20	0.60	0.58	0.91
P_2O_5	0.01	0.02	0.01	0.01	0.01	0.05	0.03	0.01	0.01
LoIα	0.77	3.67	0.89	1.58	0.23	2.71	3.73	0.41	0.13
Total	99.47	99.46	99.69	99.43	99.58	99.91	99.41	99.80	99.86

Major Element (%)	Samples								
	S7 /97	**S8 /97**	**S9 /97**	**S10 /97**	**S11 /97**	**S12 /97**	**L1 /97**	**L2 /97**	**L3 /97**
SiO_2	54.63	53.91	55.01	55.29	55.06	54.06	55.14	54.74	54.19
TiO_2	1.40	1.32	1.04	1.16	1.83	1.10	1.27	1.56	1.34
Al_2O_3	11.25	13.12	13.20	11.59	10.69	13.78	13.54	13.62	13.55
Fe_2O_3 (total)	12.03	11.31	9.24	11.26	13.79	10.37	10.32	11.19	11.12
MnO	0.18	0.17	0.17	0.17	0.20	0.18	0.17	0.20	0.19
MgO	6.97	5.82	6.07	5.99	5.21	5.90	5.47	5.73	5.89
CaO	9.02	9.11	10.56	8.77	6.61	9.87	9.27	9.40	9.95
Na_2O	2.73	2.94	2.66	2.85	4.18	2.78	2.95	2.44	2.36
K_2O	0.98	0.61	0.65	0.68	1.21	0.95	0.74	0.76	0.76
P_2O_5	0.01	0.02	0.01	0.08	0.01	0.02	0.01	0.01	0.01
LoIα	0.43	1.11	0.83	1.83	0.79	0.39	0.71	0.27	0.12
Total	99.63	99.44	99.44	99.67	99.58	99.40	99.59	99.92	99.48

Major Element (%)	Samples								
	L4 /97	**L5 /97**	**L6 /97**	**L7 /97**	**L8 /97**	**L9 /97**	**L10 /97**	**L11 /97**	**L12 /97**
SiO_2	54.78	55.06	54.21	57.37	54.27	55.48	54.27	56.60	57.04
TiO_2	1.28	1.26	1.13	0.98	1.06	1.31	1.19	1.03	1.94
Al_2O_3	13.41	13.94	11.98	11.26	13.45	11.60	11.39	11.33	11.52
Fe_2O_3 (total)	11.53	9.91	10.57	10.11	10.14	11.61	12.28	10.34	12.4
MnO	0.15	0.18	0.19	0.17	0.16	0.18	0.19	0.16	0.24
MgO	4.58	5.44	7.25	4.89	5.70	5.03	5.65	4.74	3.95
CaO	8.75	9.36	10.43	8.58	10.26	8.41	8.87	9.96	7.90
Na_2O	2.45	2.46	2.48	1.81	2.66	2.01	1.50	1.16	2.51
K_2O	1.47	1.22	0.88	0.47	0.71	0.65	1.02	0.42	1.02
P_2O_5	0.01	0.01	0.01	0.02	0.03	0.04	0.05	0.04	0.06
LoIα	1.09	0.61	0.69	3.78	1.20	3.26	3.67	3.72	0.84
Total	99.50	99.46	99.82	99.44	99.64	99.58	100.08	99.50	99.42

Major Element (%)	Samples								
	L13 /97	**L14 /97**	**L15 /97**	**L16 /97**	**L17 /97**	**L18 /97**	**L19 /97**	**L20 /97**	**L21 /97**
SiO_2	55.55	53.50	54.01	51.80	53.04	53.34	53.44	54.60	54.45
TiO_2	1.25	1.59	1.78	1.90	1.68	2.03	1.52	1.30	1.12
Al_2O_3	11.42	14.17	11.84	12.68	12.62	11.84	11.61	11.96	11.91
Fe_2O_3 (total)	11.85	11.30	12.38	14.20	12.54	13.45	12.59	12.15	9.96
MnO	0.17	0.19	0.24	0.20	0.24	0.21	0.24	0.18	0.20
MgO	4.74	4.88	5.93	5.51	5.86	5.83	5.89	5.79	7.69
CaO	8.15	9.71	9.82	10.07	10.43	9.88	8.58	8.49	10.73
Na_2O	2.11	2.80	2.34	2.62	2.59	2.35	1.83	2.12	2.31
K_2O	0.57	0.99	0.85	0.42	0.50	0.76	1.86	1.56	0.63
P_2O_5	0.03	0.02	0.01	0.01	0.01	0.01	0.04	0.01	0.01
LoIα	3.62	0.41	0.22	0.20	0.05	(+0.19)	1.87	1.34	0.62
Total	99.46	99.56	99.42	99.61	99.56	99.88	99.47	99.50	99.63

Major Element (%)	Samples							
	L22 /97	**L23 /97**	**L24 /97**	**L25 /97**	**L26 /97**	**L27 /97**	**L28 /97**	**L29 /97**
SiO_2	55.43	54.51	55.99	58.85	55.20	54.24	57.13	54.81
TiO_2	1.19	1.23	1.05	1.04	0.98	1.17	1.28	1.10
Al_2O_3	11.62	12.28	13.31	11.91	13.04	13.33	9.43	10.88
Fe_2O_3 (total)	11.63	11.31	8.83	9.04	9.94	9.94	12.17	10.05
MnO	0.17	0.18	0.17	0.13	0.12	0.20	0.22	0.17
MgO	5.05	6.69	6.54	4.32	5.82	6.38	5.48	7.97
CaO	7.97	9.07	10.64	6.40	8.55	10.11	8.03	10.39
Na_2O	1.54	2.64	2.22	5.44	3.12	2.88	1.41	2.01
K_2O	1.60	0.95	0.45	0.46	1.01	0.80	0.61	0.90
P_2O_5	0.02	0.01	0.01	0.02	0.06	0.02	0.03	0.01
LoIα	3.19	0.60	0.54	1.85	1.89	0.72	3.63	1.29
Total	99.41	99.47	99.75	99.46	99.73	99.79	99.42	99.58

α loss on ignition.

APPENDIX 4

TRACE ELEMENT RESULTS

Samples were prepared for trace element analysis using the procedures outlined in Sections 4.3.4 (Cl) 4.4.2 (Li, Cr, Sm, Gd, Th ,U) and 4.4.3 (B). For the Cl measurement, the AgCl pellet was analysed by K. Fifield and R. Cresswell using the 14-UD pelletron accelerator at ANU. The rest of the trace elements (excluding B), were analysed at the NERC ICP-MS facility at Imperial College with the assistance of K. Jarvis and L. Clarke. Boron measurements were made by XRAL Laboratories, Ontario.

Table 1: Trace element composition of samples collected during 1995 field season.

Trace Element (ppm)	Samples					
	S1/95	**S2/95**	**N1/95**	**N2/95**	**N3/95**	**N4/95**
Li	6.3 ± 0.2	4.1 ± 0.6	6.5 ± 0.8	5.5 ± 0.3	4.9 ± 0.4	4.5 ± 1.9
B[α]	5 ± 5	5 ± 5	5 ± 5	5 ± 5	5 ± 5	5 ± 5
Cl	10.1 ± 0.2	8.0 ± 0.2	10.3 ± 0.4	14.7 ± 0.4	9.9 ± 0.3	13.8 ± 0.4
Cr	177 ± 3	182 ± 2	201 ± 7	158 ± 3	237 ± 6	315 ± 5
Sm	3.1 ± 0.1	3.95 ± 0.06	3.16 ± 0.04	3.52 ± 0.06	3.02 ± 0.08	3.12 ± 0.05
Gd	3.6 ± 0.1	4.51 ± 0.04	3.8 ± 0.1	4.09 ± 0.03	3.48 ± 0.07	3.5 ± 0.1
Th	1.19 ± 0.05	1.57 ± 0.02	0.99 ± 0.03	1.31 ± 0.08	1.24 ± 0.03	1.29 ± 0.04
U	0.22 ± 0.01	0.342±0.001	0.16 ± 0.01	0.22 ± 0.03	0.15 ± 0.02	0.199±0.006

[α] Boron was not measured in these samples due to problems with the ICP-MS. For denudation rate calculation purposes, the boron content was assumed to be 5 ± 5 ppm.

Table 2: Trace element composition of samples collected during 1997 field season.

Trace Element (ppm)	Samples					
	N1/97	**N2/97**	**N3/97**	**N4/97**	**N5/97**	**N6/97**
Li	7.76 ± 0.06	7.05 ± 0.02	8.5 ± 0.3	5.9 ± 0.1	6.17 ± 0.08	8.8 ± 0.2
B	< 0.1 [β]	15	11	< 10	3 [β]	< 10
Cl	1.7 ± 0.4 [χ]	3.9 ± 0.3	4.0 ± 1.0 [χ]	3.2 ± 0.2	1.7 ± 0.2	3.6 ± 0.9 [χ]
Cr	172 ± 5	159 ± 10	142 ± 2	193 ± 4	182 ± 6	116 ± 2
Sm	3.6 ± 0.4	3.6 ± 0.2	2.85 ± 0.07	3.3 ± 0.2	3.17 ± 0.08	4.9 ± 0.5
Gd	5.1 ± 0.3	4.3 ± 0.2	3.7 ± 0.3	4.0 ± 0.4	4.1 ± 0.3	5.0 ± 0.3
Th	1.5 ± 0.2	1.4 ± 0.2	1.5 ± 0.3	1.2 ± 0.1	1.5 ± 0.2	1.8 ± 0.1
U	0.31 ± 0.04	0.27 ± 0.02	0.4 ± 0.2	0.22 ± 0.03	0.25 ± 0.01	0.38 ± 0.02

Trace Element (ppm)	Samples					
	N7/97	**N8/97**	**N9/97**	**N10/97**	**N11/97**	**N12/97**
Li	7.0 ± 0.2	5.3 ± 0.5	7.3 ± 0.1	6.37 ± 0.07	7.5 ± 0.1	6.1 ± 0.1
B	< 10	< 10	< 10	< 10	< 10	< 10
Cl	10.9 ± 0.3	3.3 ± 0.8 [χ]	3.7 ± 0.9 [χ]	2.8 ± 0.7 [χ]	3.3 ± 0.8 [χ]	2.1 ± 0.5 [χ]
Cr	107 ± 2	172 ± 1	186 ± 3	163 ± 4	188 ± 6	231± 5
Sm	3.5 ± 0.2	3.3 ± 0.4	3.4 ± 0.1	3.43 ± 0.03	2.9 ± 0.2	2.9 ± 0.3
Gd	4.2 ± 0.4	4.1 ± 0.4	4.8 ± 0.5	4.8 ± 0.4	3.5 ± 0.3	3.87 ± 0.09
Th	1.39 ± 0.09	1.4 ± 0.1	1.6 ± 0.1	1.63 ± 0.09	1.23 ± 0.03	1.5 ± 0.1
U	0.31 ± 0.07	0.24 ± 0.02	0.43 ± 0.03	0.26 ± 0.01	0.23 ± 0.01	0.31 ± 0.01

Trace Element (ppm)	Samples					
	N13/97	**N14/97**	**N15/97**	**N16/97**	**N17/97**	**N18/97**
Li	6.0 ± 0.1	7.6 ± 0.1	8.95 ± 0.08	9.37 ± 0.3	6.9 ± 6.9 [δ]	8.1 ± 0.2
B	< 10	< 10	< 10	< 10	< 10	< 10
Cl	5.8 ± 1.4 [χ]	1.2 ± 0.3 [χ]	1.6 ± 0.3	1.7 ± 0.2	2.0 ± 0.5 [χ]	4.5 ± 1.1 [χ]
Cr	173 ± 7	153 ± 6	120 ± 4	155 ± 5	143 ± 9	131 ± 2
Sm	2.9 ± 0.2	4.1 ± 0.3	3.4 ± 0.1	3.5 ± 0.2	2.9 ± 0.6	3.1 ± 0.3
Gd	3.4 ± 0.3	5.0 ± 0.5	3.7 ± 0.3	3.7 ± 0.3	3.1 ± 0.3	3.7 ± 0.1
Th	1.20 ± 0.05	1.9 ± 0.2	1.18 ± 0.08	1.36 ± 0.04	2.3 ± 0.3	1.30 ± 0.04
U	0.24 ± 0.05	0.42 ± 0.03	0.18 ± 0.01	0.27 ± 0.03	0.49 ± 0.04	0.29 ± 0.01

Trace Element (ppm)	Samples					
	O1/97	**O2/97**	**O3/97**	**O4/97**	**O5/97**	**O6/97**
Li	6.81 ± 0.06	8.37 ± 0.2	5.88 ± 0.07	7.5 ± 0.2	9.7 ± 0.4	7.8 ± 0.3
B	4 [β]	< 10	< 10	< 10	< 10	< 10
Cl	3.4 ± 0.9 [χ]	4.7 ± 0.3	6.1 ± 1.5 [χ]	7.1 ± 1.8 [χ]	2.3 ± 0.6 [χ]	8.3 ± 0.2
Cr	129 ± 3	140 ± 6	87 ± 1	195 ± 7	87 ± 3	123 ± 4
Sm	3.63 ± 0.08	3.8 ± 0.4	3.5 ± 0.3	3.1 ± 0.4	3.1 ± 0.2	3.6 ± 0.2
Gd	4.7 ± 0.1	4.5 ± 0.4	4.2 ± 0.3	4.0 ± 0.2	4.2 ± 0.5	4.6 ± 0.3
Th	1.78 ± 0.08	1.7 ± 0.1	2.8 ± 0.9	1.28 ± 0.06	1.54 ± 0.06	1.7 ± 0.1
U	0.34 ± 0.03	0.32 ± 0.02	0.38 ± 0.05	0.29 ± 0.04	0.29 ± 0.04	0.36 ± 0.03

Trace Element (ppm)	Samples					
	O7/97	**O8/97**	**O9/97**	**O10/97**	**O11/97**	**O12/97**
Li	8.4 ± 0.2	5.37 ± 0.07	10.2 ± 0.1	9.8 ± 0.2	7.9 ± 0.2	13.8 ± 0.3
B	< 10	3 [β]	< 10	< 10	11	< 10
Cl	5.2 ± 0.4	2.7 ± 0.7 [χ]	1.6 ± 0.4 [χ]	4.9 ± 1.2 [χ]	1.0 ± 0.3 [χ]	3.6 ± 0.2
Cr	64 ± 2	100 ± 2	194 ± 7	266 ± 6	133 ± 2	175 ± 6
Sm	3.3 ± 0.1	3.2 ± 0.4	4.0 ± 0.5	4.0 ± 0.2	3.8 ± 0.3	3.6 ± 0.3
Gd	4.2 ± 0.3	4.1 ± 0.3	4.2 ± 0.4	4.6 ± 0.3	4.7 ± 0.3	4.7 ± 0.6
Th	1.18 ± 0.09	1.25 ± 0.08	1.67 ± 0.01	2.1 ± 0.1	1.7 ± 0.2	1.75 ± 0.09
U	0.30 ± 0.03	0.25 ± 0.02	0.36 ± 0.06	0.34 ± 0.05	0.33 ± 0.07	0.35 ± 0.03

Trace Element (ppm)	Samples					
	S1/97	**S2/97**	**S3/97**	**S4/97**	**S5/97**	**S6/97**
Li	8.51 ± 0.07	9.24 ± 0.02	9.4 ± 0.3	10.07 ± 0.06	6.0 ± 0.1	8.44 ± 0.07
B	< 10	< 10	3 [β]	< 10	< 1.0 [β]	< 10
Cl	1.9 ± 0.5 [χ]	3.3 ± 0.8 [χ]	4.9 ± 1.2 [χ]	3.2 ± 0.3	3.7 ± 0.3	4.5 ± 0.3
Cr	139 ± 1	125 ± 5	135 ± 3	177 ± 5	143 ± 3	116 ± 3
Sm	3.5 ± 0.2	3.9 ± 0.4	3.8 ± 0.1	3.2 ± 0.3	3.8 ± 0.3	3.9 ± 0.1
Gd	3.7 ± 0.2	4.5 ± 0.5	5.0 ± 0.3	4.0 ± 0.4	4.8 ± 0.2	4.3 ± 0.1
Th	2.0 ± 0.3	1.66 ± 0.03	1.64 ± 0.04	1.5 ± 0.1	1.52 ± 0.06	2.3 ± 0.4
U	0.46 ± 0.05	0.37 ± 0.02	0.32 ± 0.01	0.24 ± 0.04	0.35 ± 0.06	0.51 ± 0.09

Trace Element (ppm)	Samples					
	S7/97	**S8/97**	**S9/97**	**S10/97**	**S11/97**	**S12/97**
Li	7.1 ± 0.2	7.05 ± 0.07	9.63 ± 0.06	9.9 ± 0.3	7.3 ± 0.1	6.8 ± 0.3
B	< 10	13	< 10	< 10	< 10	< 10
Cl	5.1 ± 1.3 [χ]	7.7 ± 0.3	2.2 ± 0.6 [χ]	5.1 ± 1.3 [χ]	11.5 ± 0.2	4.2 ± 1.1 [χ]
Cr	115 ± 2	102 ± 3	120 ± 4	142 ± 5	43 ± 1	187 ± 5
Sm	4.3 ± 0.4	3.9 ± 0.1	3.7 ± 0.2	3.5 ± 0.2	6.1 ± 0.2	3.6 ± 0.5
Gd	4.8 ± 0.3	4.2 ± 0.4	4.4 ± 0.4	3.6 ± 0.4	7.0 ± 0.1	4.8 ± 0.4
Th	1.94 ± 0.06	1.54 ± 0.06	1.93 ± 0.09	1.27 ± 0.06	2.57 ± 0.07	2.0 ± 0.1
U	0.42 ± 0.02	0.28 ± 0.02	0.44 ± 0.02	0.27 ± 0.03	0.55 ± 0.01	0.44 ± 0.06

Trace Element (ppm)	Samples					
	L1/97	**L2/97**	**L3/97**	**L4/97**	**L5/97**	**L6/97**
Li	8.0 ± 0.3	8.2 ± 0.2	5.49 ± 0.2	9.69 ± 0.06	7.0 ± 0.1	7.9 ± 0.2
B	< 10	< 10	< 1.0 [β]	< 10	< 10	< 10
Cl	2.6 ± 0.7 [χ]	3.5 ± 0.2	3.8 ± 0.3	3.1 ± 0.3	2.6 ± 0.3	3.9 ± 1.0 [χ]
Cr	196 ± 12	180 ± 7	113 ± 4	156 ± 2	106 ± 3	115 ± 3
Sm	3.5 ± 0.1	4.1 ± 0.4	3.6 ± 0.3	4.1 ± 0.3	3.4 ± 0.3	3.7 ± 0.1
Gd	4.4 ± 0.4	4.5 ± 0.2	4.9 ± 0.7	5.0 ± 0.4	4.2 ± 0.4	4.5 ± 0.3
Th	2.1 ± 0.3	1.75 ± 0.04	1.5 ± 0.1	1.8 ± 0.1	1.8 ± 0.1	1.89 ± 0.05
U	0.43 ± 0.07	0.35 ± 0.05	0.33 ± 0.05	0.38 ± 0.05	0.26 ± 0.3	0.31 ± 0.05

Trace Element (ppm)	Samples					
	L7/97	**L8/97**	**L9/97**	**L10/97**	**L11/97**	**L12/97**
Li	6.0 ± 0.2	9.50 ± 0.09	9.8 ± 0.2	10.87 ± 0.06	10.5 ± 0.1	10.8 ± 0.3
B	< 10	< 10	< 10	< 10	< 10	< 10
Cl	1.4 ± 0.3	4.2 ± 0.3	3.1 ± 0.3	3.5 ± 0.9 [χ]	2.2 ± 0.6 [χ]	9.1 ± 0.3
Cr	132 ± 2	85 ± 0.4	115 ± 4	191 ± 2	145 ± 4	43 ± 2
Sm	2.9 ± 0.4	3.5 ± 0.2	3.6 ± 0.2	4.1 ± 0.1	3.6 ± 0.2	6.7 ± 0.4
Gd	3.7 ± 0.3	4.1 ± 0.3	4.0 ± 0.3	4.6 ± 0.4	4.1 ± 0.2	8.5 ± 0.7
Th	1.36 ± 0.08	1.4 ± 0.1	1.41 ± 0.09	2.2 ± 0.3	1.72 ± 0.05	3.2 ± 0.3
U	0.23 ± 0.01	0.31 ± 0.01	0.24 ± 0.03	0.38 ± 0.03	0.32 ± 0.01	0.66 ± 0.05

Trace Element (ppm)	Samples					
	L13/97	**L14/97**	**L15/97**	**L16/97**	**L17/97**	**L18/97**
Li	11.1 ± 0.1	8.0 ± 0.3	5.36 ± 0.04	6.2 ± 0.1	7.3 ± 0.2	7.1 ± 0.1
B	< 10	< 10	< 10	< 10	< 10	< 10
Cl	1.2 ± 0.3 [χ]	2.9 ± 0.3	3.5 ± 0.3	35.6 ± 0.5	12.2 ± 0.5	2.4 ± 0.3
Cr	139 ± 6	183 ± 3	148 ± 4	98 ± 2	132 ± 4	151 ± 5
Sm	4.5 ± 0.3	4.3 ± 0.5	4.7 ±0.5	4.50 ± 0.08	4.7 ± 0.5	4.4 ± 0.2
Gd	5.4 ± 0.3	5.7 ± 0.2	5.6 ± 0.4	5.3 ± 0.3	6.0 ± 0.2	5.0 ± 0.5
Th	2.19 ± 0.02	2.09 ± 0.07	2.0 ± 0.2	1.9 ± 0.1	1.9 ± 0.2	1.83 ± 0.08
U	0.4 ± 0.1	0.48 ± 0.01	0.38 ± 0.09	0.42 ± 0.04	0.45 ± 0.04	0.41 ± 0.09

Trace Element (ppm)	Samples					
	L19/97	**L20/97**	**L21/97**	**L22/97**	**L23/97**	**L24/97**
Li	6.7 ± 0.1	6.74 ± 0.05	5.6 ± 0.2	9.6 ± 0.1	9.5 ± 0.1	5.0 ± 0.2
B	< 10	< 1.0 [β]	< 10	< 10	< 10	3 [β]
Cl	5.1 ± 0.5	5.1 ± 0.4	2.4 ± 0.3	2.2 ± 0.6 [χ]	6.2 ± 0.3	2.2 ± 0.6 [χ]
Cr	271± 6	166 ± 6	173 ± 10	225 ± 11	185 ± 1	163 ± 7
Sm	3.3 ± 0.2	3.5 ± 0.2	3.3 ± 0.2	3.7 ± 0.1	2.98 ± 0.06	2.3 ± 0.2
Gd	3.8 ± 0.2	4.4 ± 0.4	3.9 ± 0.3	4.3 ± 0.4	3.8 ± 0.6	3.5 ± 0.1
Th	1.52 ± 0.05	1.7 ± 0.2	1.52 ± 0.07	1.92 ± 0.01	1.04 ± 0.07	0.90 ± 0.06
U	0.30 ± 0.02	0.274 ± 0.001	0.31 ± 0.02	0.36 ± 0.03	0.29 ± 0.03	0.21 ± 0.03

Trace Element (ppm)	Samples				
	L25/97	**L26/97**	**L27/97**	**L28/97**	**L29/97**
Li	6.3 ± 0.1	11.6 ± 0.2	6.5 ± 0.4	7.19 ± 0.07	7.7 ± 0.1
B	< 10	11	< 10	5 [β]	< 10
Cl	1.5 ± 0.4 [χ]	11.2 ± 0.5	3.5 ± 0.9 [χ]	3.9 ± 0.7	3.7 ± 0.2
Cr	149 ± 1	394 ± 7	129 ± 1	110 ± 1	76 ± 3
Sm	2.9 ± 0.4	2.3 ± 0.2	3.8 ± 0.2	4.0 ± 0.3	4.0 ± 0.2
Gd	3.10 ± 0.09	2.9 ± 0.3	4.5 ± 0.3	5.2 ± 0.2	5.3 ± 0.3
Th	1.3 ± 0.4	1.2 ± 0.1	1.65 ± 0.06	1.79 ± 0.06	1.96 ± 0.03
U	0.30 ± 0.03	0.27 ± 0.05	0.31 ± 0.05	0.37 ± 0.02	0.53 ± 0.06

[β] Determined by prompt gamma neutron activation (detection limit 1 ppm).
[χ] Estimated from the asymptotic value of $^{35}Cl : ^{37}Cl$ ratio – see Chapter 4 for details.
[δ] The mean value of the lithium content of all Naudesnek samples.

Table 3: USGS Reference materials.

Reference Material		Trace Element (ppm)					
		Li	Cr	Sm	Gd	Th	U
1995 Samples							
BH-VO1	Measured	3.6 ± 0.4	280 ± 6	6.16 ± 0.05	6.09 ± 0.09	1.22 ± 0.03	0.46 ± 0.02
	Expected	4.6	289	6.2	6.4	1.08	0.42
	Recovery	78 %	97 %	99 %	95 %	113 %	109 %
BCR-1	Measured	38 ± 2	13.35 ± 0.07	6.94 ± 0.05	6.93 ± 0.03	6.02 ± 0.06	1.75 ± 0.02
	Expected	12.9	16	6.59	6.68	5.98	1.75
	Recovery	295 %	83 %	105 %	104 %	101 %	100 %
1997 Samples							
W-2	Measured	11.1 ± 0.3	85 ± 2	3.2 ± 0.1	3.6 ± 0.3	2.2 ± 0.1	0.49 ± 0.07
	Expected	9.6 ± 0.6	92 ± 4	3.3 ± 0.1	-	2.4 ± 0.1	0.53 ± -
	Recovery	116 %	92 %	97 %	-	92 %	88 %
BCR-2	Measured	10.6 ± 0.2	15.4 ± 0.5	6.3 ± 0.3	6.9 ± 0.8	6.2 ± 0.3	1.63 ± 0.04
	Expected	9 ± 2	18 ± 2	6.7 ± 0.3	6.8 ± 0.3	6.2 ± 0.7	1.69 ± 0.19
	Recovery	121 %	86 %	94 %	101 %	100 %	96 %
GSP-2	Measured	34 ± 2	12.9 ± 0.5	23.3 ± 0.3	15.7 ± 0.4	103 ± 4	2.0 ± 0.1
	Expected	36 ± 1	20 ± 6	27 ±1	12 ± 2	105 ± 8	2.4 ± 0.19
	Recovery	95 %	65 %	86 %	131 %	98 %	83 %
AGV-2	Measured	11.5 ± 0.2	13.5 ± 0.7	5.0 ± 0.6	5.0 ± 0.3	6.3 ± 0.3	1.9 ± 0.1
	Expected	11± -	17 ± 2	5.7 ± 0.3	4.7 ± 0.26	6.1 ± 0.6	1.9 ± 0.16
	Recovery	105 %	79 %	88 %	106 %	103 %	100 %

Reference Material		Boron content (ppm)
W-2	Measured	16
	Expected	12
	Recovery	133%
AC-E	Measured	18
	Expected	21
	Recovery	86%
GSD-1	Measured	<10
	Expected	4.6
	Recovery	-
NIST-688	Measured	<10
	Expected	1.4
	Recovery	-

Table 4: Trace element results from replicate samples.

Sample		Trace Element (ppm)					
		Li	**Cr**	**Sm**	**Gd**	**Th**	**U**
N2/97	# 1	7.05± 0.02	159 ± 10	3.5 ± 0.2	4.3 ± 0.2	1.4 ± 0.2	0.27±0.02
	# 2	5.13± 0.06	75 ± 3	3.5 ± 0.7	4.2 ± 0.2	1.32±0.09	0.26±0.03
	Recovery	137 %	212 %	100 %	102 %	106 %	104 %
O7/97	# 1	8.4 ± 0.2	64 ± 2	3.3 ± 0.1	4.2 ± 0.3	1.18±0.09	0.30±0.03
	# 2	8.4 ± 0.2	78 ± 4	3.1 ± 0.1	4.20±0.07	1.23±0.08	0.28±0.03
	Recovery	100 %	82 %	106 %	100 %	96 %	107 %
O10/97	# 1	9.8 ± 0.2	266 ± 6	4.0 ± 0.2	4.6 ± 0.3	2.1 ± 0.1	0.34±0.05
	# 2	9.0 ± 0.3	133 ± 3	4.1 ± 0.3	4.3 ± 0.3	2.19±0.03	0.34±0.01
	Recovery	109 %	200 %	98 %	107 %	96 %	100 %
S11/97	# 1	7.3 ± 0.1	43 ± 1	6.1 ± 0.2	7.0 ± 0.1	2.57±0.07	0.55±0.01
	# 2	6.27±0.02	28 ± 1	5.9 ± 0.5	6.6 ± 0.2	2.4 ±0.1	0.49±0.07
	Recovery	116 %	153 %	103 %	106 %	107 %	112 %
L14/97	#1	8.0 ± 0.3	183 ± 3	4.3 ± 0.5	5.7 ± 0.2	2.09±0.07	0.48±0.01
	#2	7.9 ± 0.2	105 ± 2	5.1 ± 0.2	5.7 ± 0.3	2.3 ± 0.2	0.48±0.03
	Recovery	101 %	174 %	84 %	100 %	91 %	100 %

APPENDIX 5
ISOTOPE DILUTION CURVE FITTING

The following plots show the results of the least-squares fitting procedure that was employed to obtain the asymptotic value for the ^{35}Cl / ^{37}Cl ratio (^{35}Cl / ^{37}Cl *meas* in Equation 4.3). The correlation coefficient (r) is given for each curve.

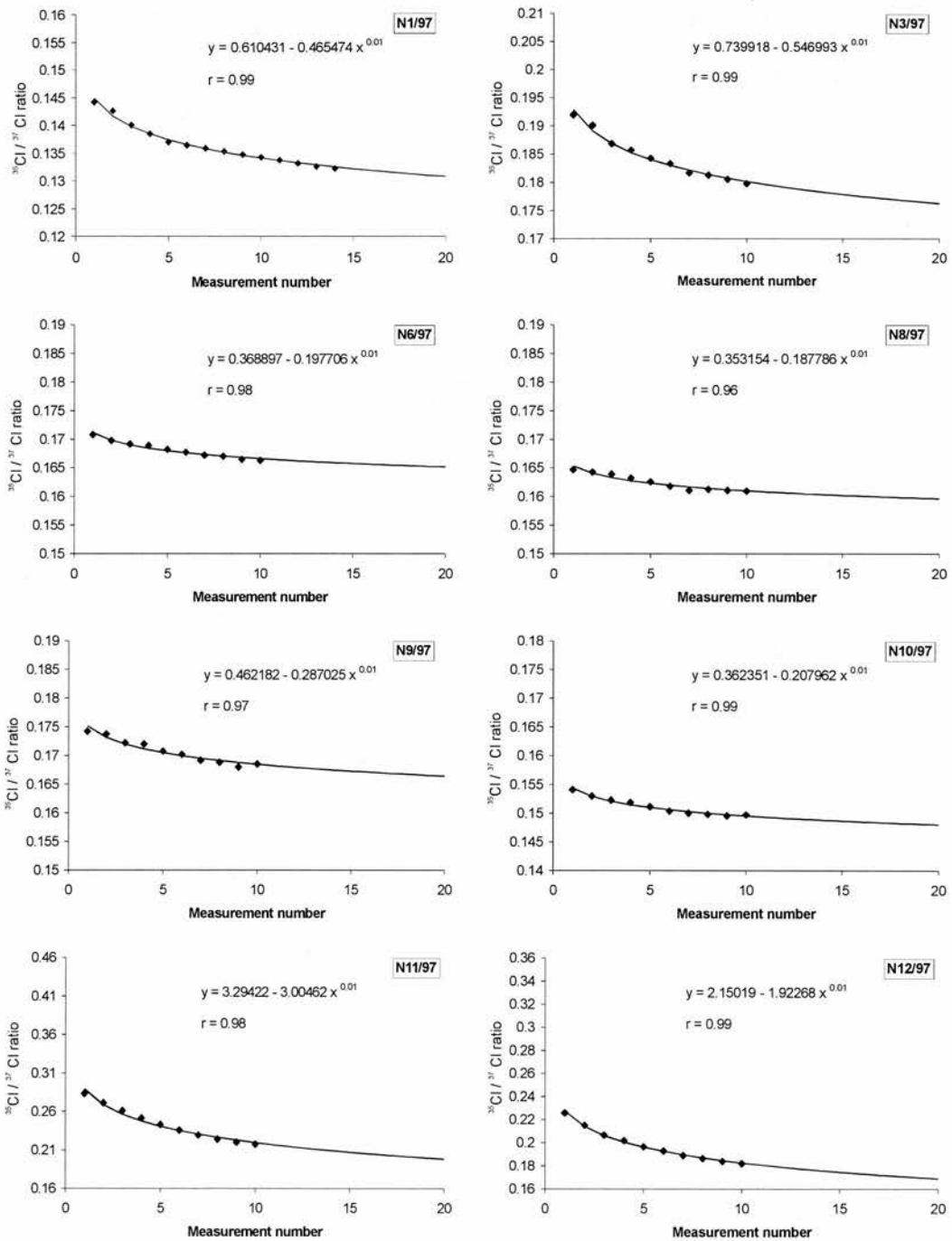

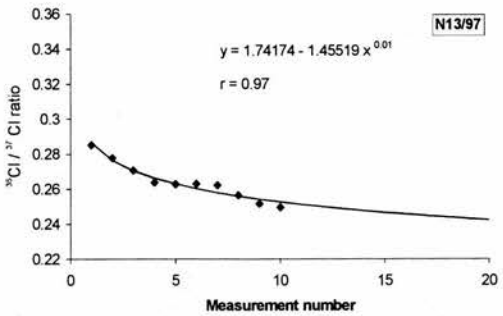
N13/97
y = 1.74174 - 1.45519 x 0.01
r = 0.97
35Cl / 37 Cl ratio
Measurement number

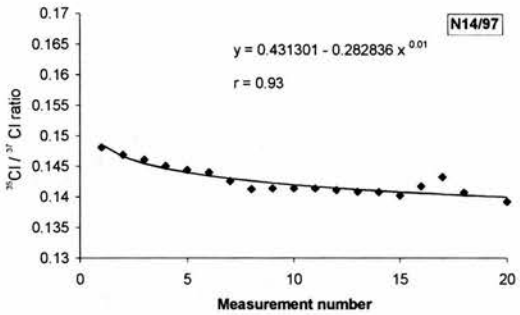
N14/97
y = 0.431301 - 0.282836 x 0.01
r = 0.93
35Cl / 37 Cl ratio
Measurement number

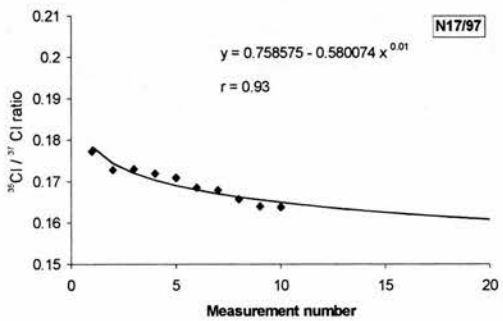
N17/97
y = 0.758575 - 0.580074 x 0.01
r = 0.93
35Cl / 37 Cl ratio
Measurement number

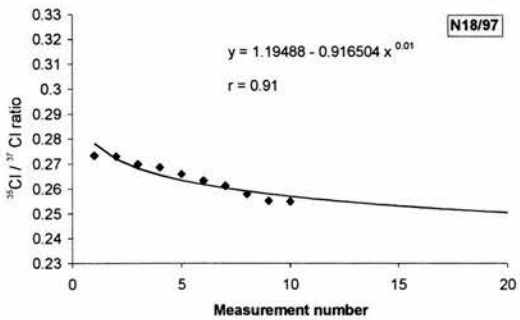
N18/97
y = 1.19488 - 0.916504 x 0.01
r = 0.91
35Cl / 37 Cl ratio
Measurement number

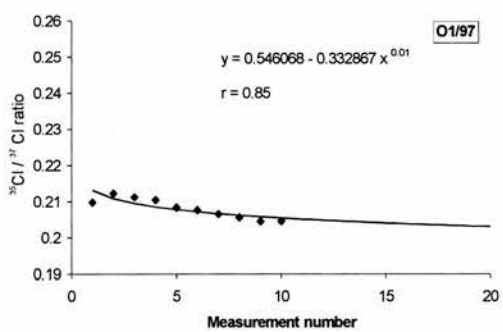
O1/97
y = 0.546068 - 0.332867 x 0.01
r = 0.85
35Cl / 37 Cl ratio
Measurement number

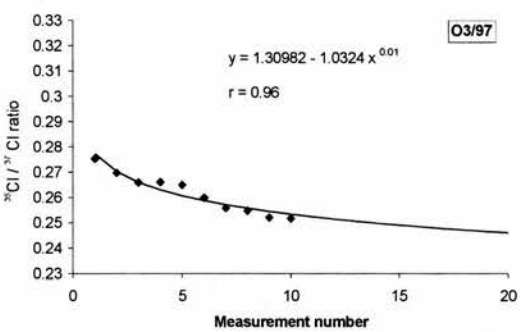
O3/97
y = 1.30982 - 1.0324 x 0.01
r = 0.96
35Cl / 37 Cl ratio
Measurement number

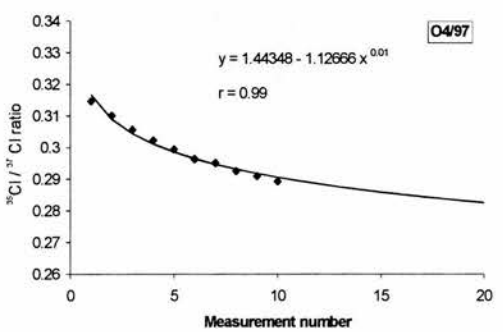
O4/97
y = 1.44348 - 1.12666 x 0.01
r = 0.99
35Cl / 37 Cl ratio
Measurement number

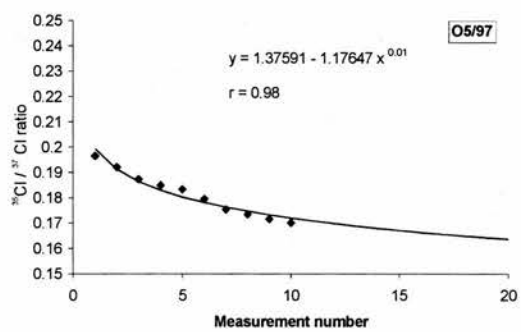
O5/97
y = 1.37591 - 1.17647 x 0.01
r = 0.98
35Cl / 37 Cl ratio
Measurement number

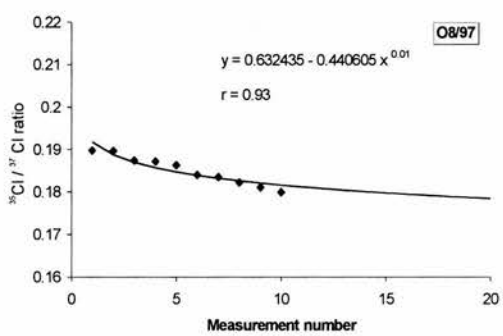
O8/97
y = 0.632435 - 0.440605 x 0.01
r = 0.93
35Cl / 37 Cl ratio
Measurement number

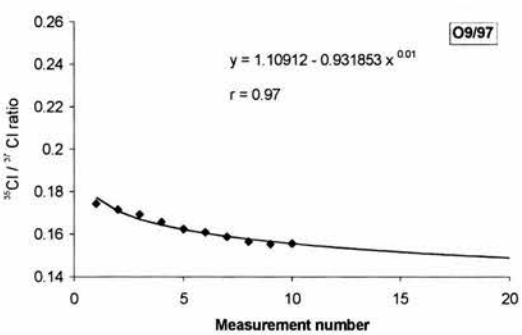
O9/97
y = 1.10912 - 0.931853 x 0.01
r = 0.97
35Cl / 37 Cl ratio
Measurement number

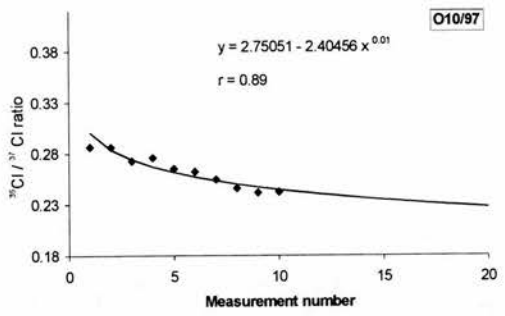
O10/97
y = 2.75051 - 2.40456 x 0.01
r = 0.89
35Cl / 37 Cl ratio
Measurement number

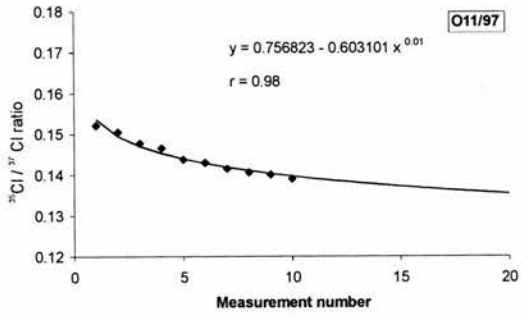
O11/97
y = 0.756823 - 0.603101 x 0.01
r = 0.98
35Cl / 37 Cl ratio
Measurement number

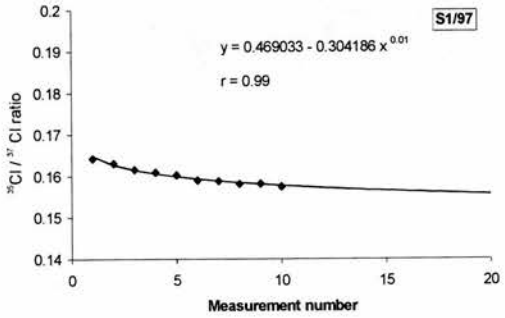
S1/97
y = 0.469033 - 0.304186 x 0.01
r = 0.99
35Cl / 37 Cl ratio
Measurement number

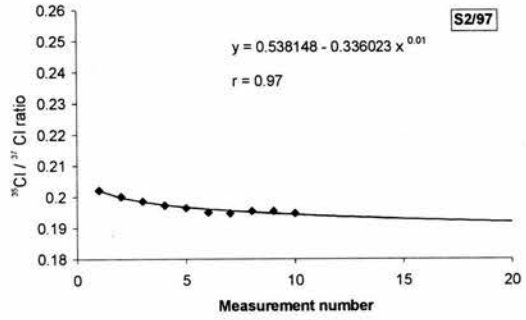
S2/97
y = 0.538148 - 0.336023 x 0.01
r = 0.97
35Cl / 37 Cl ratio
Measurement number

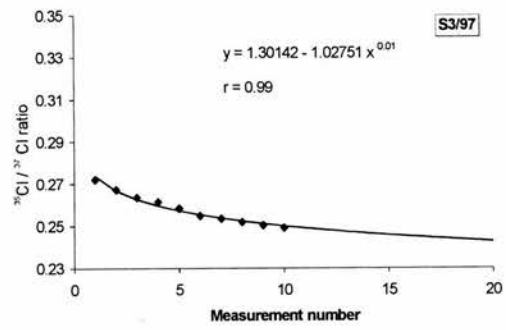
S3/97
y = 1.30142 - 1.02751 x 0.01
r = 0.99
35Cl / 37 Cl ratio
Measurement number

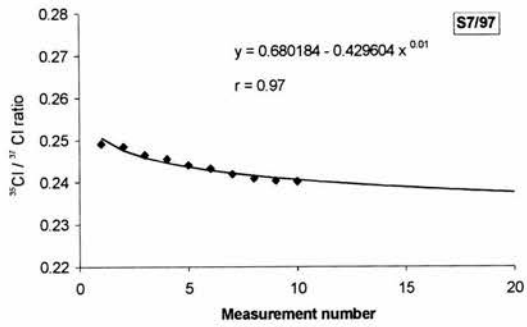
S7/97
y = 0.680184 - 0.429604 x 0.01
r = 0.97
35Cl / 37 Cl ratio
Measurement number

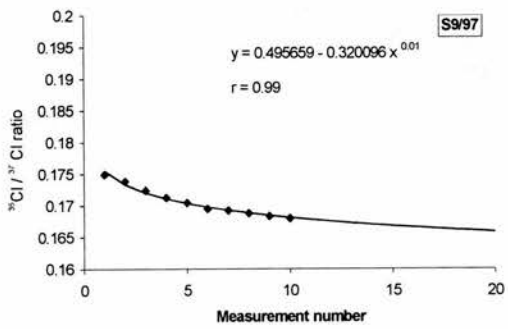
S9/97
y = 0.495659 - 0.320096 x 0.01
r = 0.99
35Cl / 37 Cl ratio
Measurement number

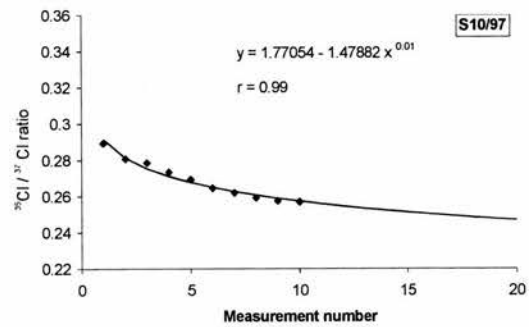
S10/97
y = 1.77054 - 1.47882 x 0.01
r = 0.99
35Cl / 37 Cl ratio
Measurement number

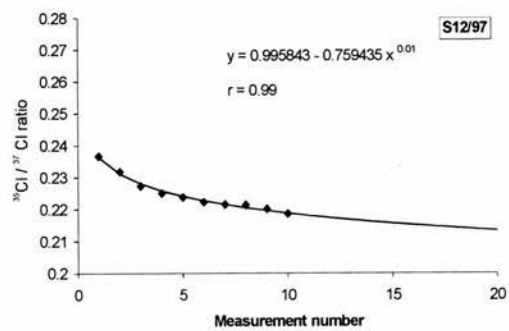
S12/97
y = 0.995843 - 0.759435 x 0.01
r = 0.99
35Cl / 37 Cl ratio
Measurement number

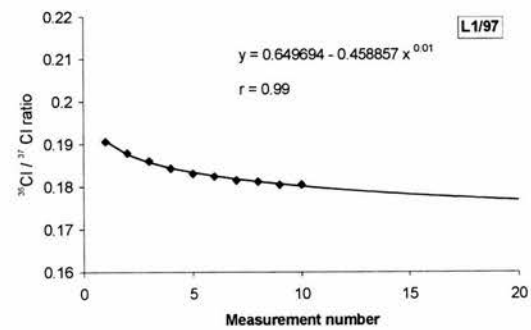
L1/97
y = 0.649694 - 0.458857 x 0.01
r = 0.99
35Cl / 37 Cl ratio
Measurement number

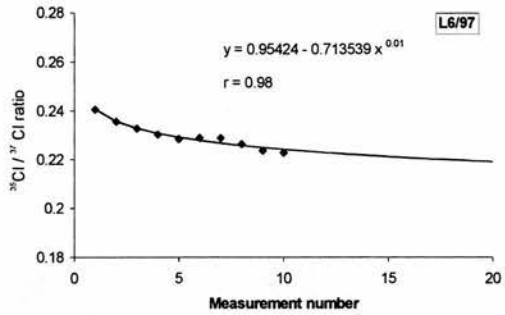
L6/97
y = 0.95424 - 0.713539 x 0.01
r = 0.98
35Cl / 37 Cl ratio
Measurement number

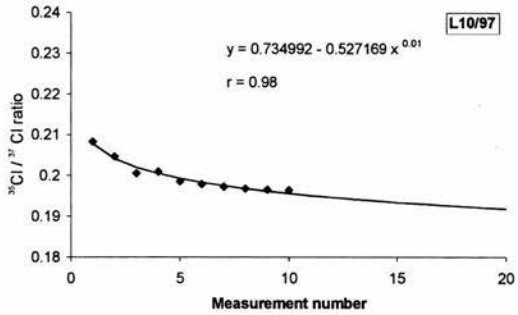
L10/97
y = 0.734992 - 0.527169 x 0.01
r = 0.98
35Cl / 37 Cl ratio
Measurement number

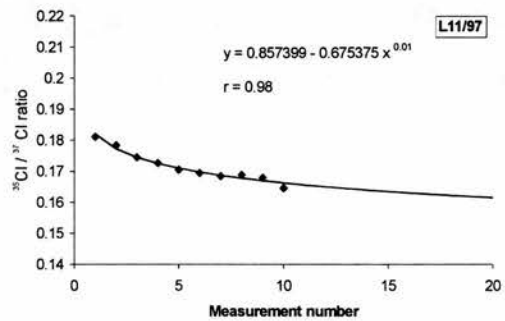
L11/97
y = 0.857399 - 0.675375 x 0.01
r = 0.98
35Cl / 37 Cl ratio
Measurement number

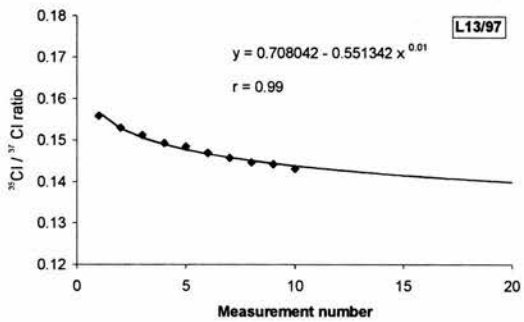
L13/97
y = 0.708042 - 0.551342 x 0.01
r = 0.99
35Cl / 37 Cl ratio
Measurement number

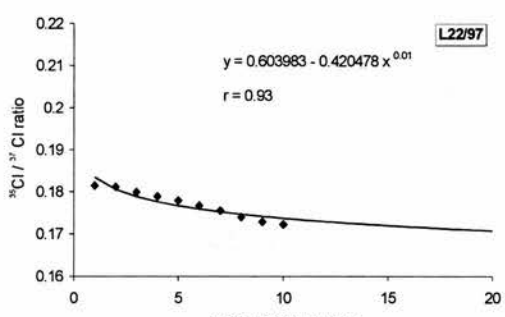
L22/97
y = 0.603983 - 0.420478 x 0.01
r = 0.93
35Cl / 37 Cl ratio
Measurement number

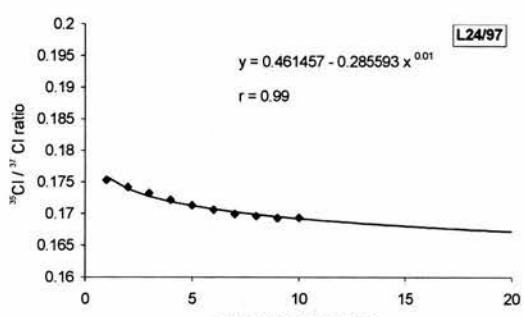
L24/97
y = 0.461457 - 0.285593 x 0.01
r = 0.99
35Cl / 37 Cl ratio
Measurement number

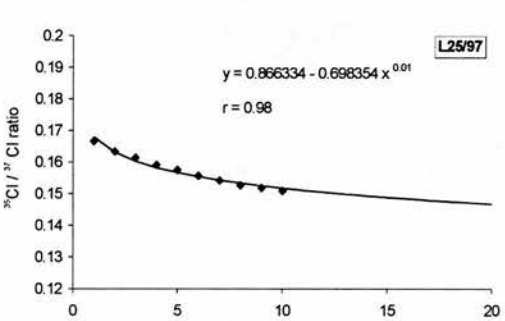
L25/97
y = 0.866334 - 0.698354 x 0.01
r = 0.98
35Cl / 37 Cl ratio
Measurement number

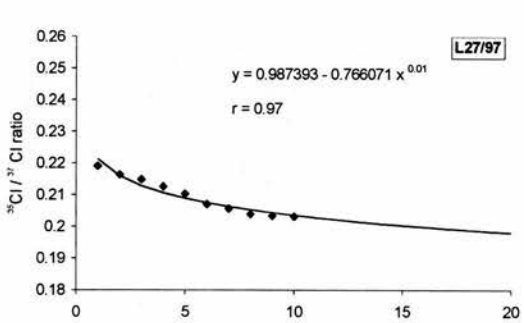
L27/97
y = 0.987393 - 0.766071 x 0.01
r = 0.97
35Cl / 37 Cl ratio
Measurement number

Appendix 6

Determination of the sample thickness correction factor

Spallation

The sample thickness correction factor, DF_{sp}, was determined using the following equation:

$$DF_{sp} = \left(\frac{\Lambda}{\rho z_s}\right)\left(e^{(-(\rho z_t)/\Lambda)} - e^{(-(\rho z_b)/\Lambda)}\right)$$

where, Λ is the effective attenuation length for spallogenic production (g cm^{-2}), ρ is density (g cm^{-3}), z_s is the total thickness of the sample (cm). Z_t and z_b require some explanation. Before the sample is crushed any weathered material on the surface is ground off (Chapter 4) hence, z_t is the depth from the original surface to the top of the sample (ie the depth of the weathered rind that is removed) (cm) and z_b is the depth from the original surface to the base of the sample (cm).

Thermal neutron activation

The sample thickness correction factor for thermal neutron production, DF_n, was calculated using the following:

$$DF_n = \int_{z=\rho z_t}^{\rho z_b} \Phi^*_{ss} e^{(-z/\Lambda)} + F\Delta\Phi^* e^{(-z/L_{ss})} \Big/ \left(\left(\Phi^*_{ss} + F\Delta\Phi^*\right)\left(\rho z_b - \rho z_t\right)\right)$$

where, Λ, ρ, z_b and z_t are as defined before. The remaining terms, Φ^*_{ss}, F, $\Delta\Phi^*$, L_{ss}, are as defined in Section 3.2.3.5.

Epithermal neutron capture

The correction factor for the sample thickness for epithermal neutron activation, DF_{epi} was determined as follows:

$$DF_{epi} = \int_{z=\rho z_t}^{\rho z_b} e^{(-z/\Lambda)} - 0.4e^{\left(-z/\Lambda_{epi}\right)} \Big/ \left(0.6\left(\rho z_b - \rho z_t\right)\right)$$

where, Λ, ρ, z_b and z_t are as previously defined and Λ_{epi} is the epithermal neutron attenuation length. The constants, 0.4 and 0.6 are, respectively, the fractional reduction in the epithermal flux at the air-ground interface and one minus this fractional reduction (J. Stone, pers. comm.).

Appendix 7

Table 1: Site specific ^{36}Cl production rates for 50 cm perpendicularly below free face surfaces.

Sample	Combined $P_{Ca}{}^{\alpha}$ & $P_K{}^{\beta}$ Spallation (atom g^{-1} a^{-1})	$P_{Ca}{}^{\alpha}$ Muon (atom g^{-1} a^{-1})	$P_K{}^{\beta}$ Muon (atom g^{-1} a^{-1})	$P_{n,35}{}^{\chi}$ (atom g^{-1} a^{-1})	$P_{n,\,epi}{}^{\delta}$ (atom g^{-1} a^{-1})	$P_{n,39}{}^{\varepsilon}$ (atom g^{-1} a^{-1})	$P_{TOTAL}{}^{\phi}$ (atom g^{-1} a^{-1})
Naudesnek							
N4/95	3.47 ± 0.52	0.34 ± 0.14	0.03 ± 0.01	0.28 ± 0.12	0.04 ± 0.01	0.02 ± 0.01	4.18 ± 0.55
N5/97	2.66 ± 0.41	0.29 ± 0.12	0.03 ± 0.01	0.03 ± 0.01	0.003 ± 0.001	0.014 ± 0.003	3.02 ± 0.43
N8/97	2.99 ± 0.49	0.33 ± 0.13	0.022 ± 0.009	0.06 ± 0.03	0.009 ± 0.002	0.012 ± 0.005	3.42 ± 0.51
N9/97	3.10 ± 0.51	0.34 ± 0.14	0.021± 0.009	0.07 ± 0.03	0.011 ± 0.002	0.012 ± 0.005	3.56 ± 0.53
N10/97	2.90 ± 0.47	0.32 ± 0.13	0.021 ± 0.008	0.05 ± 0.02	0.009 ± 0.002	0.011 ± 0.005	3.32 ± 0.49
N11/97	2.83 ± 0.42	0.27 ± 0.11	0.03 ± 0.01	0.06 ± 0.03	0.004 ± 0.001	0.02 ± 0.01	3.21 ± 0.44
N12/97	2.52 ± 0.36	0.18 ± 0.07	0.05 ± 0.02	0.04 ± 0.02	0.003 ± 0.001	0.02 ± 0.01	2.80 ± 0.36
N13/97	2.50 ± 0.40	0.29 ± 0.12	0.019 ± 0.008	0.11 ± 0.05	0.007 ± 0.001	0.010 ± 0.005	2.93 ± 0.42
N15/97	3.99 ± 0.70	0.45 ± 0.18	0.17 ± 0.07	0.06 ± 0.02	0.003 ± 0.001	0.010 ± 0.004	4.69 ± 0.72
N16/97	4.34 ± 0.70	0.44 ± 0.18	0.03 ± 0.01	0.05 ± 0.02	0.003 ± 0.001	0.02 ± 0.01	4.89 ± 0.73
N17/97	3.80 ± 0.61	0.39 ± 0.16	0.03 ± 0.01	0.05 ± 0.02	0.006 ± 0.001	0.02 ± 0.01	4.29 ± 0.64
N18/97	3.37 ± 0.49	0.31 ± 0.12	0.04 ± 0.02	0.09 ± 0.04	0.009 ± 0.002	0.02 ± 0.01	3.85 ± 0.51
Ongeluk's Nek							
O2/97	5.10 ± 0.82	0.47 ± 0.19	0.03 ± 0.01	0.15 ± 0.05	0.024 ± 0.005	0.02 ± 0.01	5.80 ± 0.84
O3/97	3.43 ± 0.55	0.33 ± 0.13	0.022 ± 0.009	0.12 ± 0.06	0.023 ± 0.005	0.013 ± 0.006	3.93 ± 0.57
O4/97	2.91 ± 0.48	0.30 ± 0.12	0.017 ± 0.007	0.12 ± 0.06	0.022 ± 0.004	0.009 ± 0.004	3.38 ± 0.50
O6/97	3.53 ± 0.57	0.34 ± 0.14	0.022 ± 0.009	0.16 ± 0.07	0.034 ± 0.007	0.013 ± 0.006	4.10 ± 0.59
O7/97	2.75 ± 0.44	0.30 ± 0.12	0.021 ± 0.008	0.10 ± 0.04	0.009 ± 0.002	0.011 ± 0.005	3.19 ± 0.46
O9/97	3.01 ± 0.50	0.34 ± 0.14	0.019 ± 0.008	0.03 ± 0.01	0.005 ± 0.001	0.011 ± 0.005	3.42 ± 0.52
O10/97	2.94 ± 0.45	0.31 ± 0.12	0.03 ± 0.01	0.08 ± 0.04	0.010 ± 0.002	0.015 ± 0.007	3.38 ± 0.47
O12/97	3.31 ± 0.49	0.31 ± 0.12	0.04 ± 0.02	0.06 ± 0.03	0.008 ± 0.002	0.021 ± 0.009	3.74 ± 0.50
Sani Pass							
S2/95	4.15 ± 0.63	0.37 ± 0.15	0.03 ± 0.01	0.21 ± 0.08	0.031 ± 0.006	0.015 ± 0.06	4.79 ± 0.65
S1/97	3.22 ± 0.53	0.31 ± 0.12	0.019 ± 0.008	0.04 ± 0.02	0.004 ± 0.001	0.012 ± 0.005	3.60 ± 0.54
S2/97	3.24 ± 0.51	0.29 ± 0.12	0.03 ± 0.01	0.06 ± 0.03	0.012 ± 0.002	0.014 ± 0.007	3.65 ± 0.52

Table 1: cont.

Sample	Combined $P_{Ca}{}^{\alpha}$ & $P_K{}^{\beta}$ Spallation (atom g^{-1} a^{-1})	$P_{Ca}{}^{\alpha}$ Muon (atom g^{-1} a^{-1})	$P_K{}^{\beta}$ Muon (atom g^{-1} a^{-1})	$P_{n,35}{}^{\chi}$ (atom g^{-1} a^{-1})	$P_{n,epi}{}^{\delta}$ (atom g^{-1} a^{-1})	$P_{n,39}{}^{\varepsilon}$ (atom g^{-1} a^{-1})	$P_{TOTAL}{}^{\phi}$ (atom g^{-1} a^{-1})
S4/97	5.16 ± 0.84	0.39 ± 0.16	0.03 ± 0.01	0.11 ± 0.05	0.006 ± 0.001	0.019 ± 0.008	5.71 ± 0.85
S6/97	2.90 ± 0.45	0.29 ± 0.12	0.03 ± 0.01	0.07 ± 0.03	0.015 ± 0.003	0.013 ± 0.006	3.32 ± 0.46
S7/97	4.73 ± 0.72	0.40 ± 0.16	0.04 ± 0.02	0.13 ± 0.06	0.025 ± 0.005	0.024 ± 0.008	5.36 ± 0.74
S9/97	3.55 ± 0.59	0.34 ± 0.14	0.02 ± 0.01	0.05 ± 0.02	0.005 ± 0.001	0.013 ± 0.006	3.98 ± 0.60
S11/97	3.94 ± 0.56	0.25 ± 0.10	0.04 ± 0.02	0.26 ± 0.09	0.043 ± 0.009	0.025 ± 0.008	4.56 ± 0.58
S12/97	3.88 ± 0.60	0.33 ± 0.13	0.03 ± 0.01	0.09 ± 0.04	0.017 ± 0.003	0.018 ± 0.008	4.36 ± 0.61
Lesotho Highlands							
L2/97	3.26 ± 0.52	0.28 ± 0.11	0.021 ± 0.009	0.06 ± 0.03	0.013 ± 0.003	0.013 ± 0.006	3.65 ± 0.53
L3/97	4.56 ± 0.73	0.38 ± 0.15	0.03 ± 0.01	0.09 ± 0.04	0.021 ± 0.004	0.017 ± 0.008	5.10 ± 0.75
L5/97	3.45 ± 0.51	0.28 ± 0.11	0.03 ± 0.01	0.05 ± 0.02	0.007 ± 0.001	0.020 ± 0.009	3.84 ± 0.52
L6/97	3.01 ± 0.47	0.31 ± 0.12	0.025 ± 0.009	0.07 ± 0.03	0.008 ± 0.002	0.014 ± 0.006	3.42 ± 0.49
L8/97	3.60 ± 0.58	0.44 ± 0.18	0.03 ± 0.01	0.10 ± 0.04	0.010 ± 0.002	0.015 ± 0.006	4.20 ± 0.61
L14/97	4.71 ± 0.72	0.35 ± 0.14	0.03 ± 0.01	0.07 ± 0.03	0.014 ± 0.003	0.021 ± 0.008	5.20 ± 0.73
L18/97	4.29 ± 0.68	0.32 ± 0.13	0.02 ± 0.01	0.05 ± 0.02	0.014 ± 0.003	0.014 ± 0.006	4.71 ± 0.70
L19/97	6.00 ± 0.85	0.35 ± 0.14	0.07 ± 0.03	0.14 ± 0.05	0.012 ± 0.002	0.05 ± 0.02	6.61 ± 0.86
L20/97	4.82 ± 0.69	0.31 ± 0.12	0.05 ± 0.02	0.12 ± 0.03	0.013 ± 0.003	0.035 ± 0.008	5.35 ± 0.70
L21/97	3.79 ± 0.63	0.35 ± 0.14	0.020 ± 0.008	0.05 ± 0.03	0.007 ± 0.001	0.013 ± 0.006	4.24 ± 0.65
L24/97	3.07 ± 0.53	0.33 ± 0.13	0.013 ± 0.005	0.04 ± 0.01	0.006 ± 0.001	0.008 ± 0.002	3.46 ± 0.55
L25/97	2.15 ± 0.35	0.20 ± 0.08	0.014 ± 0.006	0.03 ± 0.02	0.002 ± 0.001	0.009 ± 0.004	2.41 ± 0.36
L26/97	3.53 ± 0.53	0.31 ± 0.12	0.03 ± 0.01	0.25 ± 0.06	0.020 ± 0.004	0.020 ± 0.005	4.16 ± 0.55
L27/97	3.74 ± 0.59	0.35 ± 0.14	0.03 ± 0.01	0.07 ± 0.04	0.011 ± 0.002	0.016 ± 0.007	4.22 ± 0.61
L29/97	4.29 ± 0.67	0.34 ± 0.14	0.03 ± 0.01	0.08 ± 0.04	0.009 ± 0.002	0.019 ± 0.009	4.77 ± 0.69

$^{\alpha}$ Spallation and muon production from Ca; $^{\beta}$ Spallation and muon production from K; $^{\chi}$ Production rate from capture by ^{35}Cl of thermalized neutrons; $^{\delta}$ Production rate from capture by ^{35}Cl of epithermal neutrons; $^{\varepsilon}$ Production rate from capture by ^{39}K of thermalized neutrons; $^{\phi}$ Total ^{36}Cl production from Ca, K and ^{35}Cl.

Table 2: Site specific ^{36}Cl production rates for 100 cm perpendicularly below free face surfaces.

Sample	Combined $P_{Ca}{}^{\alpha}$ & $P_K{}^{\beta}$ Spallation (atom g^{-1} a^{-1})	$P_{Ca}{}^{\alpha}$ Muon (atom g^{-1} a^{-1})	$P_K{}^{\beta}$ Muon (atom g^{-1} a^{-1})	$P_{n,35}{}^{\chi}$ (atom g^{-1} a^{-1})	$P_{n,epi}{}^{\delta}$ (atom g^{-1} a^{-1})	$P_{n,39}{}^{\varepsilon}$ (atom g^{-1} a^{-1})	$P_{TOTAL}{}^{\phi}$ (atom g^{-1} a^{-1})
Naudesnek							
N4/95	0.85 ± 0.13	0.21 ± 0.08	0.018 ± 0.007	0.10 ± 0.02	0.010 ± 0.002	0.006 ± 0.001	1.19 ± 0.15
N5/97	0.59 ± 0.09	0.17 ± 0.07	0.015 ± 0.006	0.009 ± 0.002	0.0007 ± 0.0001	0.005 ± 0.001	0.79 ± 0.11
N8/97	0.70 ± 0.11	0.20 ± 0.08	0.013 ± 0.005	0.021 ± 0.004	0.0020 ± 0.0004	0.0040 ± 0.0008	0.94 ± 0.14
N9/97	0.74 ± 0.12	0.20 ± 0.08	0.013 ± 0.005	0.025 ± 0.005	0.0026 ± 0.0005	0.0041 ± 0.0008	0.98 ± 0.15
N10/97	0.68 ± 0.11	0.19 ± 0.08	0.013 ± 0.005	0.018 ± 0.004	0.0020 ± 0.0004	0.0039 ± 0.0008	0.91 ± 0.13
N11/97	0.66 ± 0.10	0.16 ± 0.06	0.018 ± 0.007	0.021 ± 0.004	0.0008 ± 0.0002	0.006 ± 0.001	0.87 ± 0.12
N12/97	0.59 ± 0.08	0.10 ± 0.04	0.027 ± 0.011	0.013 ± 0.003	0.0007 ± 0.0001	0.008 ± 0.002	0.74 ± 0.09
N13/97	0.59 ± 0.09	0.17 ± 0.07	0.011 ± 0.005	0.037 ± 0.007	0.0016 ± 0.0003	0.0035 ± 0.0007	0.81 ± 0.12
N15/97	1.20 ± 0.21	0.29 ± 0.11	0.108 ± 0.043	0.022 ± 0.004	0.0010 ± 0.0002	0.0040 ± 0.0008	1.62 ± 0.24
N16/97	1.24 ± 0.20	0.28 ± 0.11	0.018 ± 0.007	0.020 ± 0.004	0.0009 ± 0.0002	0.006 ± 0.001	1.57 ± 0.23
N17/97	0.96 ± 0.15	0.24 ± 0.09	0.016 ± 0.006	0.016 ± 0.003	0.0015 ± 0.0003	0.006 ± 0.001	1.23 ± 0.18
N18/97	0.83 ± 0.12	0.18 ± 0.07	0.027 ± 0.011	0.032 ± 0.006	0.0023 ± 0.0005	0.008 ± 0.002	1.08 ± 0.14
Ongeluk's Nek							
O2/97	1.46 ± 0.23	0.29 ± 0.12	0.020 ± 0.008	0.06 ± 0.01	0.0069 ± 0.001	0.008 ± 0.002	1.84 ± 0.26
O3/97	0.80 ± 0.13	0.19 ± 0.08	0.013 ± 0.005	0.041 ± 0.008	0.0055 ± 0.001	0.0043 ± 0.0009	1.06 ± 0.15
O4/97	0.64 ± 0.11	0.18 ± 0.07	0.010 ± 0.004	0.040 ± 0.008	0.0049 ± 0.001	0.0031 ± 0.0006	0.88 ± 0.13
O6/97	0.83 ± 0.13	0.20 ± 0.08	0.013 ± 0.005	0.06 ± 0.01	0.008 ± 0.002	0.0044 ± 0.0009	1.11 ± 0.16
O7/97	0.65 ± 0.11	0.18 ± 0.07	0.013 ± 0.005	0.034 ± 0.007	0.0021 ± 0.0004	0.0040 ± 0.0008	0.89 ± 0.13
O9/97	0.71 ± 0.12	0.20 ± 0.08	0.011 ± 0.005	0.010 ± 0.002	0.0012 ± 0.0002	0.0036 ± 0.0008	0.93 ± 0.14
O10/97	0.65 ± 0.10	0.18 ± 0.07	0.016 ± 0.007	0.028 ± 0.006	0.0022 ± 0.0004	0.005 ± 0.001	0.88 ± 0.12
O12/97	0.75 ± 0.11	0.18 ± 0.07	0.023 ± 0.009	0.022 ± 0.004	0.0019 ± 0.0004	0.007 ± 0.001	0.99 ± 0.13
Sani Pass							
S2/95	1.11 ± 0.17	0.22 ± 0.09	0.015 ± 0.006	0.07 ± 0.01	0.008 ± 0.002	0.005 ± 0.001	1.43 ± 0.19
S1/97	0.76 ± 0.12	0.18 ± 0.07	0.011 ± 0.004	0.013 ± 0.003	0.0008 ± 0.0002	0.0038 ± 0.0008	0.96 ± 0.14
S2/97	0.72 ± 0.11	0.17 ± 0.07	0.015 ± 0.006	0.019 ± 0.004	0.0026 ± 0.0005	0.005 ± 0.001	0.93 ± 0.13

Table 2: cont.

Sample	Combined P_{Ca} [α] & P_K [β] Spallation (atom g^{-1} a^{-1})	P_{Ca} [α] Muon (atom g^{-1} a^{-1})	P_K [β] Muon (atom g^{-1} a^{-1})	$P_{n,35}$ [χ] (atom g^{-1} a^{-1})	$P_{n,epi}$ [δ] (atom g^{-1} a^{-1})	$P_{n,39}$ [ε] (atom g^{-1} a^{-1})	P_{TOTAL} [ϕ] (atom g^{-1} a^{-1})
S4/97	1.40 ± 0.23	0.24 ± 0.09	0.015 ± 0.009	0.037 ± 0.008	0.0016 ± 0.0003	0.0063 ± 0.0013	1.70 ± 0.25
S6/97	0.63 ± 0.10	0.17 ± 0.07	0.016 ± 0.006	0.025 ± 0.005	0.0032 ± 0.0006	0.0045 ± 0.0009	0.85 ± 0.12
S7/97	1.28 ± 0.19	0.24 ± 0.10	0.025 ± 0.010	0.05 ± 0.01	0.0068 ± 0.0014	0.0087 ± 0.0017	1.61 ± 0.22
S9/97	0.83 ± 0.14	0.20 ± 0.08	0.012 ± 0.005	0.016 ± 0.003	0.0012 ± 0.0002	0.0042 ± 0.0008	1.07 ± 0.16
S11/97	0.99 ± 0.14	0.15 ± 0.06	0.026 ± 0.011	0.09 ± 0.02	0.0107 ± 0.0021	0.0084 ± 0.0017	1.27 ± 0.16
S12/97	0.92 ± 0.14	0.20 ± 0.08	0.018 ± 0.007	0.030 ± 0.006	0.0039 ± 0.0008	0.0061 ± 0.0012	1.18 ± 0.16
Lesotho Highlands							
L2/97	0.72 ± 0.11	0.16 ± 0.06	0.012 ± 0.005	0.020 ± 0.004	0.0030 ± 0.0006	0.0040 ± 0.0008	0.92 ± 0.13
L3/97	1.15 ± 0.18	0.23 ± 0.09	0.017 ± 0.007	0.032 ± 0.006	0.0054 ± 0.0011	0.0059 ± 0.0011	1.43 ± 0.20
L5/97	0.76 ± 0.11	0.16 ± 0.06	0.020 ± 0.008	0.015 ± 0.003	0.0016 ± 0.0003	0.0065 ± 0.0013	0.97 ± 0.13
L6/97	0.66 ± 0.10	0.18 ± 0.07	0.014 ± 0.006	0.022 ± 0.004	0.0018 ± 0.0004	0.0045 ± 0.0009	0.89 ± 0.13
L8/97	0.96 ± 0.16	0.27 ± 0.11	0.018 ± 0.007	0.037 ± 0.007	0.0027 ± 0.0005	0.0057 ± 0.0011	1.29 ± 0.19
L14/97	1.15 ± 0.18	0.21 ± 0.08	0.020 ± 0.008	0.023 ± 0.005	0.0033 ± 0.0007	0.0071 ± 0.0014	1.41 ± 0.20
L18/97	1.01 ± 0.16	0.19 ± 0.08	0.014 ± 0.006	0.016 ± 0.003	0.0033 ± 0.0007	0.0046 ± 0.0009	1.23 ± 0.18
L19/97	1.55 ± 0.22	0.21 ± 0.08	0.044 ± 0.017	0.046 ± 0.009	0.0031 ± 0.0006	0.0155 ± 0.0031	1.86 ± 0.24
L20/97	1.18 ± 0.17	0.18 ± 0.07	0.032 ± 0.013	0.041 ± 0.008	0.0032 ± 0.0006	0.0115 ± 0.0031	1.45 ± 0.18
L21/97	0.89 ± 0.15	0.21 ± 0.08	0.012 ± 0.005	0.017 ± 0.003	0.0017 ± 0.0003	0.0042 ± 0.0008	1.13 ± 0.17
L24/97	0.69 ± 0.12	0.19 ± 0.08	0.008 ± 0.003	0.015 ± 0.003	0.0014 ± 0.0003	0.0028 ± 0.0006	0.90 ± 0.14
L25/97	0.50 ± 0.08	0.12 ± 0.05	0.008 ± 0.003	0.010 ± 0.002	0.0006 ± 0.0001	0.0028 ± 0.0006	0.63 ± 0.09
L26/97	0.86 ± 0.13	0.18 ± 0.07	0.021 ± 0.008	0.08 ± 0.02	0.0050 ± 0.0010	0.0069 ± 0.0014	1.16 ± 0.15
L27/97	0.90 ± 0.14	0.21 ± 0.08	0.016 ± 0.006	0.025 ± 0.005	0.0028 ± 0.0006	0.0054 ± 0.0011	1.16 ± 0.17
L29/97	1.01 ± 0.16	0.20 ± 0.08	0.017 ± 0.007	0.027 ± 0.005	0.0022 ± 0.0004	0.0061 ± 0.0012	1.26 ± 0.18

[α] Spallation and muon production from Ca; [β] Spallation and muon production from K; [χ] Production rate from capture by ^{35}Cl of thermalized neutrons; [δ] Production rate from capture by ^{35}Cl of epithermal neutrons; [ε] Production rate from capture by ^{39}K of thermalized neutrons; [ϕ] Total ^{36}Cl production from Ca, K and ^{35}Cl.

Table 3: Site specific ^{36}Cl production rates for 150 cm perpendicularly below free face surfaces.

Sample	Combined $P_{Ca}{}^{\alpha}$ & $P_K{}^{\beta}$ Spallation (atom g^{-1} a^{-1})	$P_{Ca}{}^{\alpha}$ Muon (atom g^{-1} a^{-1})	$P_K{}^{\beta}$ Muon (atom g^{-1} a^{-1})	$P_{n,35}{}^{\chi}$ (atom g^{-1} a^{-1})	$P_{n,epi}{}^{\delta}$ (atom g^{-1} a^{-1})	$P_{n,39}{}^{\varepsilon}$ (atom g^{-1} a^{-1})	$P_{TOTAL}{}^{\phi}$ (atom g^{-1} a^{-1})
Naudesnek							
N4/95	0.208 ± 0.031	0.14 ± 0.06	0.012 ± 0.005	0.070 ± 0.014	0.0074 ± 0.0015	0.0042 ± 0.0008	0.44 ± 0.07
N5/97	0.130 ± 0.020	0.12 ± 0.05	0.011 ± 0.004	0.006 ± 0.001	0.0005 ± 0.0001	0.0032 ± 0.0006	0.27 ± 0.05
N8/97	0.164 ± 0.027	0.13 ± 0.05	0.009 ± 0.003	0.015 ± 0.003	0.0015 ± 0.0003	0.0028 ± 0.0006	0.32 ± 0.06
N9/97	0.176 ± 0.029	0.14 ± 0.05	0.008 ± 0.003	0.017 ± 0.003	0.0019 ± 0.0004	0.0029 ± 0.0006	0.34 ± 0.06
N10/97	0.160 ± 0.026	0.13 ± 0.05	0.008 ± 0.003	0.012 ± 0.002	0.0015 ± 0.0003	0.0027 ± 0.0005	0.31 ± 0.06
N11/97	0.155 ± 0.023	0.11 ± 0.04	0.012 ± 0.005	0.015 ± 0.003	0.0006 ± 0.0001	0.0040 ± 0.0008	0.29 ± 0.05
N12/97	0.138 ± 0.020	0.07 ± 0.03	0.018 ± 0.007	0.009 ± 0.002	0.0005 ± 0.0001	0.0055 ± 0.0011	0.24 ± 0.03
N13/97	0.137 ± 0.022	0.11 ± 0.05	0.008 ± 0.003	0.026 ± 0.005	0.0012 ± 0.0002	0.0025 ± 0.0005	0.29 ± 0.05
N15/97	0.363 ± 0.063	0.20 ± 0.08	0.075 ± 0.030	0.019 ± 0.004	0.0009 ± 0.0002	0.0034 ± 0.0007	0.66 ± 0.11
N16/97	0.357 ± 0.058	0.19 ± 0.07	0.012 ± 0.005	0.016 ± 0.003	0.0008 ± 0.0002	0.0050 ± 0.0010	0.58 ± 0.09
N17/97	0.240 ± 0.039	0.16 ± 0.06	0.011 ± 0.004	0.012 ± 0.002	0.0011 ± 0.0002	0.0040 ± 0.0008	0.43 ± 0.07
N18/97	0.202 ± 0.029	0.12 ± 0.06	0.018 ± 0.007	0.023 ± 0.005	0.0017 ± 0.0003	0.0059 ± 0.0011	0.37 ± 0.06
Ongeluk's Nek							
O2/97	0.419 ± 0.067	0.20 ± 0.08	0.014 ± 0.006	0.045 ± 0.009	0.0059 ± 0.0012	0.0059 ± 0.0012	0.69 ± 0.10
O3/97	0.189 ± 0.030	0.13 ± 0.05	0.009 ± 0.003	0.029 ± 0.006	0.0040 ± 0.0008	0.0030 ± 0.0006	0.36 ± 0.06
O4/97	0.142 ± 0.023	0.12 ± 0.05	0.0117 ± 0.003	0.027 ± 0.005	0.0033 ± 0.0007	0.0021 ± 0.0004	0.30 ± 0.05
O6/97	0.194 ± 0.032	0.13 ± 0.05	0.009 ± 0.004	0.039 ± 0.008	0.0057 ± 0.0011	0.0030 ± 0.0006	0.38 ± 0.06
O7/97	0.156 ± 0.025	0.12 ± 0.05	0.009 ± 0.003	0.024 ± 0.005	0.0016 ± 0.0003	0.0028 ± 0.0006	0.32 ± 0.06
O9/97	0.166 ± 0.027	0.13 ± 0.05	0.008 ± 0.003	0.007 ± 0.001	0.0001 ± 0.0002	0.0026 ± 0.0005	0.32 ± 0.06
O10/97	0.143 ± 0.022	0.13 ± 0.05	0.012 ± 0.005	0.019 ± 0.004	0.0015 ± 0.0003	0.0036 ± 0.0007	0.31 ± 0.06
O12/97	0.171 ± 0.025	0.12 ± 0.05	0.015 ± 0.006	0.015 ± 0.003	0.0014 ± 0.0003	0.0048 ± 0.0010	0.33 ± 0.05
Sani Pass							
S2/95	0.397 ± 0.045	0.15 ± 0.06	0.010 ± 0.004	0.055 ± 0.011	0.0065 ± 0.0013	0.0040 ± 0.0008	0.52 ± 0.08
S1/97	0.177 ± 0.029	0.12 ± 0.05	0.007 ± 0.003	0.009 ± 0.002	0.0006 ± 0.0001	0.0027 ± 0.0005	0.32 ± 0.06
S2/97	0.158 ± 0.025	0.12 ± 0.05	0.011 ± 0.004	0.013 ± 0.003	0.0018 ± 0.0004	0.0033 ± 0.0007	0.31 ± 0.05

Table 3: cont.

Sample	Combined $P_{Ca}{}^{\alpha}$ & $P_K{}^{\beta}$ Spallation (atom g^{-1} a^{-1})	$P_{Ca}{}^{\alpha}$ Muon (atom g^{-1} a^{-1})	$P_K{}^{\beta}$ Muon (atom g^{-1} a^{-1})	$P_{n,35}{}^{\chi}$ (atom g^{-1} a^{-1})	$P_{n,epi}{}^{\delta}$ (atom g^{-1} a^{-1})	$P_{n,39}{}^{\varepsilon}$ (atom g^{-1} a^{-1})	$P_{TOTAL}{}^{\phi}$ (atom g^{-1} a^{-1})
S4/97	0.379 ± 0.061	0.16 ± 0.06	0.010 ± 0.004	0.030 ± 0.006	0.0014 ± 0.0003	0.0050 ± 0.0010	0.59 ± 0.09
S6/97	0.137 ± 0.021	0.11 ± 0.04	0.010 ± 0.004	0.016 ± 0.003	0.0021 ± 0.0004	0.0030 ± 0.0006	0.28 ± 0.05
S7/97	0.347 ± 0.053	0.16 ± 0.07	0.017 ± 0.007	0.036 ± 0.007	0.0053 ± 0.0011	0.0064 ± 0.0013	0.58 ± 0.08
S9/97	0.195 ± 0.032	0.14 ± 0.05	0.008 ± 0.003	0.011 ± 0.002	0.0009 ± 0.0002	0.0029 ± 0.0006	0.35 ± 0.06
S11/97	0.249 ± 0.036	0.10 ± 0.04	0.018 ± 0.007	0.059 ± 0.012	0.0074 ± 0.0015	0.0057 ± 0.0011	0.44 ± 0.06
S12/97	0.220 ± 0.034	0.13 ± 0.05	0.012 ± 0.005	0.021 ± 0.004	0.0029 ± 0.0006	0.0043 ± 0.0009	0.39 ± 0.06
Lesotho Highlands							
L2/97	0.159 ± 0.025	0.11 ± 0.05	0.009 ± 0.004	0.014 ± 0.003	0.0020 ± 0.0004	0.0028 ± 0.0006	0.30 ± 0.05
L3/97	0.287 ± 0.046	0.15 ± 0.06	0.011 ± 0.005	0.023 ± 0.005	0.0040 ± 0.0008	0.0042 ± 0.0008	0.48 ± 0.08
L5/97	0.168 ± 0.025	0.11 ± 0.05	0.014 ± 0.006	0.011 ± 0.002	0.0011 ± 0.0002	0.0046 ± 0.0009	0.31 ± 0.05
L6/97	0.147 ± 0.023	0.13 ± 0.05	0.010 ± 0.004	0.015 ± 0.003	0.0012 ± 0.0002	0.0032 ± 0.0006	0.30 ± 0.06
L8/97	0.258 ± 0.042	0.18 ± 0.07	0.012 ± 0.005	0.028 ± 0.006	0.0022 ± 0.0004	0.0043 ± 0.0009	0.49 ± 0.08
L14/97	0.282 ± 0.043	0.14 ± 0.06	0.014 ± 0.005	0.016 ± 0.003	0.0023 ± 0.0004	0.0049 ± 0.0010	0.46 ± 0.07
L18/97	0.236 ± 0.038	0.13 ± 0.05	0.009 ± 0.004	0.011 ± 0.002	0.0022 ± 0.0004	0.0031 ± 0.0006	0.39 ± 0.06
L19/97	0.399 ± 0.057	0.14 ± 0.06	0.029 ± 0.012	0.033 ± 0.007	0.0023 ± 0.0005	0.0112 ± 0.0022	0.62 ± 0.08
L20/97	0.288 ± 0.041	0.12 ± 0.05	0.022 ± 0.009	0.029 ± 0.006	0.0024 ± 0.0005	0.0081 ± 0.0016	0.47 ± 0.06
L21/97	0.209 ± 0.035	0.14 ± 0.06	0.008 ± 0.003	0.012 ± 0.002	0.0023 ± 0.0003	0.0030 ± 0.0006	0.37 ± 0.07
L24/97	0.154 ± 0.027	0.13 ± 0.05	0.005 ± 0.002	0.010 ± 0.002	0.0020 ± 0.0002	0.0019 ± 0.0004	0.30 ± 0.06
L25/97	0.111 ± 0.018	0.08 ± 0.03	0.006 ± 0.002	0.007 ± 0.001	0.0004 ± 0.0001	0.0020 ± 0.0004	0.21 ± 0.04
L26/97	0.211 ± 0.032	0.12 ± 0.05	0.014 ± 0.006	0.061 ± 0.012	0.0038 ± 0.0008	0.0050 ± 0.0010	0.42 ± 0.06
L27/97	0.218 ± 0.035	0.14 ± 0.06	0.011 ± 0.004	0.018 ± 0.004	0.0021 ± 0.0004	0.0038 ± 0.0008	0.39 ± 0.07
L29/97	0.236 ± 0.037	0.13 ± 0.05	0.011 ± 0.004	0.019 ± 0.004	0.0016 ± 0.0003	0.0043 ± 0.0009	0.41 ± 0.07

$^{\alpha}$ Spallation and muon production from Ca; $^{\beta}$ Spallation and muon production from K; $^{\chi}$ Production rate from capture by ^{35}Cl of thermalized neutrons; $^{\delta}$ Production rate from capture by ^{35}Cl of epithermal neutrons; $^{\varepsilon}$ Production rate from capture by ^{39}K of thermalized neutrons; $^{\phi}$ Total ^{36}Cl production from Ca, K and ^{35}Cl.

Table 4: Site specific ^{36}Cl production rates for 200 cm perpendicularly below free face surfaces.

Sample	Combined $P_{Ca}{}^{\alpha}$ & $P_K{}^{\beta}$ Spallation (atom g^{-1} a^{-1})	$P_{Ca}{}^{\alpha}$ Muon (atom g^{-1} a^{-1})	$P_K{}^{\beta}$ Muon (atom g^{-1} a^{-1})	$P_{n,35}{}^{\chi}$ (atom g^{-1} a^{-1})	$P_{n,epi}{}^{\delta}$ (atom g^{-1} a^{-1})	$P_{n,39}{}^{\varepsilon}$ (atom g^{-1} a^{-1})	$P_{TOTAL}{}^{\phi}$ (atom g^{-1} a^{-1})
Naudesnek							
N4/95	0.051 ± 0.008	0.10 ± 0.04	0.0088 ± 0.0035	0.0279 ± 0.0056	0.00059 ± 0.00012	0.0017 ± 0.0003	0.19 ± 0.04
N5/97	0.029 ± 0.004	0.08 ± 0.03	0.0073 ± 0.0029	0.0027 ± 0.0005	0.00004 ± 0.00001	0.0014 ± 0.0003	0.12 ± 0.03
N8/97	0.039 ± 0.006	0.09 ± 0.04	0.0062 ± 0.0025	0.0061 ± 0.0012	0.00011 ± 0.00002	0.0012 ± 0.0002	0.15 ± 0.04
N9/97	0.042 ± 0.007	0.10 ± 0.04	0.0061 ± 0.0024	0.0071 ± 0.0014	0.00014 ± 0.00003	0.0012 ± 0.0002	0.15 ± 0.04
N10/97	0.037 ± 0.006	0.09 ± 0.04	0.0060 ± 0.0024	0.0050 ± 0.0010	0.00011 ± 0.00002	0.0011 ± 0.0002	0.14 ± 0.04
N11/97	0.036 ± 0.005	0.08 ± 0.03	0.0085 ± 0.0034	0.0057 ± 0.0011	0.00005 ± 0.00001	0.0015 ± 0.0003	0.13 ± 0.03
N12/97	0.032 ± 0.005	0.05 ± 0.02	0.0130 ± 0.0052	0.0034 ± 0.0007	0.00004 ± 0.00001	0.0021 ± 0.0004	0.10 ± 0.02
N13/97	0.032 ± 0.005	0.08 ± 0.03	0.0054 ± 0.0022	0.0100 ± 0.0020	0.00009 ± 0.00002	0.0010 ± 0.0002	0.13 ± 0.03
N15/97	0.110 ± 0.019	0.14 ± 0.06	0.0545 ± 0.0218	0.0060 ± 0.0012	0.00009 ± 0.00002	0.0011 ± 0.0002	0.31 ± 0.06
N16/97	0.102 ± 0.017	0.14 ± 0.05	0.0088 ± 0.0035	0.0053 ± 0.0011	0.00008 ± 0.00002	0.0017 ± 0.0003	0.25 ± 0.06
N17/97	0.060 ± 0.010	0.11 ± 0.05	0.0078 ± 0.0031	0.0045 ± 0.0009	0.00009 ± 0.00002	0.0015 ± 0.0003	0.19 ± 0.05
N18/97	0.049 ± 0.007	0.09 ± 0.04	0.0129 ± 0.0052	0.0091 ± 0.0018	0.00014 ± 0.00003	0.0024 ± 0.0005	0.16 ± 0.04
Ongeluk's Nek							
O2/97	0.120 ± 0.019	0.14 ± 0.06	0.0101 ± 0.0040	0.0154 ± 0.0031	0.00057 ± 0.00011	0.0020 ± 0.0004	0.29 ± 0.06
O3/97	0.044 ± 0.007	0.09 ± 0.04	0.0063 ± 0.0025	0.0114 ± 0.0023	0.00030 ± 0.00006	0.0012 ± 0.0002	0.16 ± 0.04
O4/97	0.031 ± 0.005	0.09 ± 0.03	0.0048 ± 0.0019	0.0115 ± 0.0023	0.00024 ± 0.00005	0.0009 ± 0.0002	0.13 ± 0.03
O6/97	0.046 ± 0.007	0.10 ± 0.04	0.0064 ± 0.0026	0.0153 ± 0.0031	0.00044 ± 0.00009	0.0012 ± 0.0002	0.17 ± 0.04
O7/97	0.037 ± 0.006	0.09 ± 0.04	0.0063 ± 0.0025	0.0009 ± 0.0019	0.00012 ± 0.00002	0.0011 ± 0.0002	0.14 ± 0.04
O9/97	0.039 ± 0.006	0.10 ± 0.04	0.0055 ± 0.0022	0.0030 ± 0.0006	0.00007 ± 0.00001	0.0010 ± 0.0002	0.14 ± 0.04
O10/97	0.032 ± 0.005	0.09 ± 0.04	0.0080 ± 0.0032	0.0080 ± 0.0016	0.00011 ± 0.00002	0.0015 ± 0.0003	0.14 ± 0.04
O12/97	0.039 ± 0.006	0.09 ± 0.03	0.0111 ± 0.0044	0.0061 ± 0.0012	0.00010 ± 0.00002	0.0020 ± 0.0004	0.15 ± 0.04
Sani Pass							
S2/95	0.080 ± 0.012	0.11 ± 0.04	0.0076 ± 0.0030	0.0195 ± 0.0039	0.00060 ± 0.00012	0.0015 ± 0.0003	0.22 ± 0.05
S1/97	0.042 ± 0.007	0.09 ± 0.03	0.0054 ± 0.0021	0.0035 ± 0.0007	0.00005 ± 0.00001	0.0010 ± 0.0002	0.14 ± 0.04
S2/97	0.035 ± 0.005	0.08 ± 0.03	0.0072 ± 0.0029	0.0054 ± 0.0011	0.00013 ± 0.00003	0.0013 ± 0.0003	0.13 ± 0.03

Table 4: cont.

Sample	Combined P_{Ca}^{α} & P_K^{β} Spallation (atom g^{-1} a^{-1})	P_{Ca}^{α} Muon (atom g^{-1} a^{-1})	P_K^{β} Muon (atom g^{-1} a^{-1})	$P_{n,35}^{\chi}$ (atom g^{-1} a^{-1})	$P_{n,epi}^{\delta}$ (atom g^{-1} a^{-1})	$P_{n,39}^{\varepsilon}$ (atom g^{-1} a^{-1})	P_{TOTAL}^{ϕ} (atom g^{-1} a^{-1})
S4/97	0.103 ± 0.017	0.02 ± 0.05	0.0076 ± 0.0003	0.0087 ± 0.0017	0.00012 ± 0.00002	0.0014 ± 0.0003	0.24 ± 0.05
S6/97	0.030 ± 0.005	0.08 ± 0.03	0.0072 ± 0.0003	0.0071 ± 0.0014	0.00015 ± 0.00003	0.0013 ± 0.0003	0.12 ± 0.03
S7/97	0.094 ± 0.014	0.12 ± 0.05	0.0124 ± 0.0005	0.0135 ± 0.0027	0.00050 ± 0.00010	0.0024 ± 0.0005	0.24 ± 0.05
S9/97	0.046 ± 0.008	0.10 ± 0.04	0.0058 ± 0.0002	0.0042 ± 0.0008	0.00007 ± 0.00001	0.0011 ± 0.0002	0.16 ± 0.04
S11/97	0.063 ± 0.009	0.07 ± 0.03	0.0129 ± 0.0005	0.0219 ± 0.0044	0.00068 ± 0.00014	0.0021 ± 0.0004	0.17 ± 0.03
S12/97	0.052 ± 0.008	0.10 ± 0.04	0.0089 ± 0.0004	0.0080 ± 0.0016	0.00022 ± 0.00004	0.0017 ± 0.0003	0.17 ± 0.04
Lesotho Highlands							
L2/97	0.035 ± 0.006	0.08 ± 0.03	0.0061 ± 0.0002	0.0055 ± 0.0011	0.00015 ± 0.00003	0.0011 ± 0.0002	0.13 ± 0.03
L3/97	0.072 ± 0.012	0.11 ± 0.04	0.0082 ± 0.0003	0.0085 ± 0.0017	0.00034 ± 0.00007	0.0016 ± 0.0003	0.20 ± 0.05
L5/97	0.037 ± 0.005	0.08 ± 0.03	0.0098 ± 0.0004	0.0041 ± 0.0008	0.00008 ± 0.00002	0.0018 ± 0.0004	0.13 ± 0.03
L6/97	0.032 ± 0.005	0.09 ± 0.03	0.0070 ± 0.0003	0.0063 ± 0.0013	0.00009 ± 0.00002	0.0013 ± 0.0003	0.13 ± 0.04
L8/97	0.069 ± 0.011	0.13 ± 0.05	0.0087 ± 0.0003	0.0107 ± 0.0021	0.00019 ± 0.00004	0.0017 ± 0.0003	0.22 ± 0.05
L14/97	0.069 ± 0.011	0.10 ± 0.04	0.0099 ± 0.0004	0.0058 ± 0.0012	0.00020 ± 0.00004	0.0018 ± 0.0004	0.19 ± 0.04
L18/97	0.055 ± 0.009	0.09 ± 0.04	0.0067 ± 0.0003	0.0042 ± 0.0008	0.00018 ± 0.00004	0.0012 ± 0.0002	0.16 ± 0.04
L19/97	0.103 ± 0.015	0.10 ± 0.04	0.0213 ± 0.0009	0.0114 ± 0.0023	0.00020 ± 0.00005	0.0038 ± 0.0002	0.24 ± 0.04
L20/97	0.071 ± 0.010	0.09 ± 0.04	0.0155 ± 0.0006	0.0103 ± 0.0021	0.00019 ± 0.00004	0.0029 ± 0.0008	0.19 ± 0.04
L21/97	0.049 ± 0.008	0.10 ± 0.04	0.0056 ± 0.0002	0.0045 ± 0.009	0.00009 ± 0.00002	0.0011 ± 0.0006	0.16 ± 0.04
L24/97	0.035 ± 0.006	0.09 ± 0.04	0.0037 ± 0.0015	0.0040 ± 0.0008	0.00007 ± 0.00001	0.0008 ± 0.0002	0.14 ± 0.04
L25/97	0.025 ± 0.004	0.06 ± 0.02	0.0040 ± 0.0016	0.0025 ± 0.0005	0.00003 ± 0.00001	0.0007 ± 0.0001	0.09 ± 0.02
L26/97	0.052 ± 0.008	0.09 ± 0.04	0.0101 ± 0.0040	0.0222 ± 0.0044	0.00030 ± 0.00006	0.0018 ± 0.0004	0.18 ± 0.04
L27/97	0.053 ± 0.008	0.10 ± 0.04	0.0077 ± 0.0031	0.0069 ± 0.0014	0.00016 ± 0.00003	0.0015 ± 0.0003	0.17 ± 0.04
L29/97	0.055 ± 0.009	0.10 ± 0.04	0.0080 ± 0.0032	0.0068 ± 0.0014	0.00012 ± 0.00002	0.0015 ± 0.0003	0.17 ± 0.04

$^{\alpha}$ Spallation and muon production from Ca; $^{\beta}$ Spallation and muon production from K; $^{\chi}$ Production rate from capture by ^{35}Cl of thermalized neutrons; $^{\delta}$ Production rate from capture by ^{35}Cl of epithermal neutrons; $^{\varepsilon}$ Production rate from capture by ^{39}K of thermalized neutrons; $^{\phi}$ Total ^{36}Cl production from Ca, K and ^{35}Cl.

Appendix 8

Copy of the *Mathematica*® (version 3.0) computer program used to calculate the denudation rates for samples from free face surfaces.

Sloping surfaces: Denudation Rate Program

(1) Enter the sample data in to the two cells, Chlorine - 36 Data and Chemical Data - the latter has two sections to complete, one for the major elements and one for the relevant trace elements. The text that appears in (*.....*) is known as commentary text and does not form part of the program. Such text gives the units required and any comment. Once the data is entered you need to press the 'enter' key on the keyboard - this is NOT the same as the return key and Mathematica know s the difference!!

(2) Position the cursor in all the cells, starting at the Input Data and Initialization Cells and working through the cells in the correct sequence. Calculations will be performed in all the cells, but no output is produced except in the last grouping of cells, Cl - 36 Results.

(3) This is a modified version of John Stone's erosion rate program, produced by Alastair Fleming.

■ Input Data and Initialization Cells

```
Off[General::Spell];
Off[General::spell1];
```

```
gamma = 160.0; (*attenuation length in g/cm^2*)
attnlength[dip_] := 161.804 - 0.302406 dip - 0.00506263 dip^2;
(*For sloping surface : attenuation length as a function of dip angle (in degrees)*)
hzncorrn[dip_] := 1 + 0.002034 * dip - 0.000083706 * dip^2;
(*For sloping surface : correction to surface
    spallation production rate as a function of dip angle (in degrees)*)
lamda = 2.303 * 10^-6; (*decay constant of chlorine-36 per year*)

(*Reference neutron stopping rate and production rates at sea level and latitude >
  60 deg. Neutron stopping rate from
   Phillips et al 1996. Breakdown into muon and nucleon components
   from JS Wombeyan data. Ca spallation rate from Tabernacle Hill.*)

pfast =
 586.0; (*neutrons/g/yr in 'infinite' air. Presently lumps spallogenic and muon-
  produced neutrons together. Figure is from
   Phillips et al 1996 and is equivalent to Pf(0) in Liu et al 1994.*)
 pfaststddvn = 117.2; (*20 % uncertainty in above again in neutrons/g/year*)
 neutronmufrn = 0.1; (*fraction of secondary neutrons derived from muon captures -
  1-neutronmufrn is fraction of spallogenic secondary neutrons*)

caspall = 0.3485; (*atoms of chlorine-36 per gram per year % CaO*,
 based on the production rate in Stone et al 1996 of 48.8 atoms/gCa/yr*)
 caspallstddvn = 0.0697; (*20 % of above production in Ca *)
camu = 0.03786; (*atoms Cl-36/g/yr % CaO, based on Stone et al 1998
  figure of 2.1 atoms/gCaCO3/yr which converts to 5.31 atoms/gCa/yr*)
 camustddvn = 0.00757; (*20 % of above, converted as above.*)

kspall = 1.420; (* atoms Cl-36 per gram per year % K2O, based on the production
  rate involving K of 171 atoms/gK/yr from Evans et al 1997, converted for % K2O*)
 kspallstddvn = 0.284; (* 20 % of above in atoms Cl-36/g/yr % K2O*)
kmu = 0.0747; (* atoms Cl-36/g/a/% K2O,
 based on the estimate (NB this reaction has not been independently calibrated)
  in Evans et al 1997 of 9 atoms/gK/yr*)
 kmustddvn = 0.0166; (* atoms Cl-36/g/a % K2O, based on the estimate of the standard
  deviation given by JS in the Drakensberg manuscript (Fleming et al 1999) ~ 22 %*)

(*List of atomic weights in order from periodic table - H, Li, B, C, O, Na, Mg,
  Al, Si, P, Cl, K, Ca, Ti, Cr, Mn, Fe, Sm, Gd. NB all lists in same order!*)

ai = {1.0, 6.94, 10.81, 12.01, 16.00, 22.99, 24.31, 26.98, 28.09, 30.97,
   35.45, 39.10, 40.08, 47.88, 52.00, 54.94, 55.85, 150.36, 157.25};

(*List of the cross sections for thermal neutron absorption
   of the elements in the above list (same order) in barns per atom*)

sigmathermali = 10^-24
   {0.333, 70.5, 765, 0.0035, 0.00028, 0.53, 0.063, 0.233, 0.171, 0.18, 33.5, 2.1,
    0.43, 6.1, 3.1, 13.3, 2.56, 9460 (*NB Westcott factor = 1.7 for Sm*),
    41560 (*NB Westcott factor = 0.85 for Gd*)};
```

```
(*Trace element cross sections for
   thermal neutron absorption from above list, in barns per atom*)

sigmathermaltr =
  10^-24 {70.5, 765, 33.5, 3.1, 9640 (*NB Westcott factor = 1.7 for Sm*),
    41560 (*NB Westcott factor = 0.85 for Gd*)};

(*Scattering cross sections in barns per atom for the main list of elements*)

  sigmascatteri = 10^-24 {20.5, 0.95, 4.27, 4.74, 3.76, 3.025, 3.42,
    1.41, 2.04, 5.0, 15.8, 2.04, 2.93, 4.09, 3.38, 2.20, 11.35, 38, 172};

(*Dilute resonance integrals for the main list of elements*)

  iai = 10^-24 {0, 0, 343, 0.0016, 0.0004, 0.311, 0.038, 0.17, 0.127,
    0.08, 13.7, 1.0, 0.235, 3.1, 1.6, 14, 1.39, 1400, 390};

(*Values for average log decrement
   in E per neutron collision for the main list of elements*)

  elossi = {1.0, 0.264, 0.174, 0.158, 0.12, 0.084, 0.08, 0.072, 0.07,
    0.063, 0.055, 0.05, 0.049, 0.041, 0.038, 0.036, 0.035, 0.013, 0.013};

(*Neutron yield per gram oxide per year per ppm U
    and per ppm Th for (alpha, n) reactions with rock-forming oxides*)

sio2yieldu = 0.45; sio2yieldth = 0.20;
tio2yieldu = 0.09; tio2yieldth = 0.03;
al2o3yieldu = 2.81; al2o3yieldth = 1.41;
fe2o3yieldu = 0.20; fe2o3yieldth = 0.17;
feoyieldu = 0.20; feoyieldth = 0.18;
mnoyieldu = 0.05; mnoyieldth = 0.02;
mgoyieldu = 3.59; mgoyieldth = 1.60;
caoyieldu = 0.07; caoyieldth = 0.02;
na2oyieldu = 10.82; na2oyieldth = 5.07;
k2oyieldu = 0.41; k2oyieldth = 0.27;
p2o5yieldu = 0.13; p2o5yieldth = 0.04;
h2oyieldu = 0.20; h2oyieldth = 0.07;
co2yieldu = 0.29; co2yieldth = 0.11;

(*Combine into matrix, with oxides in same
   order as list for the major elements in the Chemical Data cell*)

nyields = {{sio2yieldu, sio2yieldth}, {tio2yieldu, tio2yieldth},
   {al2o3yieldu, al2o3yieldth}, {fe2o3yieldu, fe2o3yieldth},
   {feoyieldu, feoyieldth}, {mnoyieldu, mnoyieldth}, {mgoyieldu, mgoyieldth},
   {caoyieldu, caoyieldth}, {na2oyieldu, na2oyieldth}, {k2oyieldu, k2oyieldth},
   {p2o5yieldu, p2o5yieldth}, {h2oyieldu, h2oyieldth}, {co2yieldu, co2yieldth}};
```

```
(*Polynomial fits of Lal 1991 for nuclear disintegration rates in the atmosphere,
  per gram per year. JS has converted this from km in the original Lal version
     to metres (hence the division by 1000). The division by 563.4 is
     required to normalise the rate to that at sea level and latitude >
    60 deg where the reference production rates are defined. The 563.4 is
      arrived at by using the polynomial for 60-90 deg and altitude =
   zero. The polynomial for 60-90 deg has to be divided by this
     as well to make the factor 1 for sea level and this latitude.*)

nucleonsfactor0[y_] :=
  (330.7 + 255.9*(y/1000) + 98.43*(y/1000)^2 + 20.50*(y/1000)^3) / 563.4;
 (*rate at 0 deg geomagnetic latitude*)
 nucleonsfactor10[y_] :=
  (337.9 + 252.1*(y/1000) + 111.0*(y/1000)^2 + 20.73*(y/1000)^3) / 563.4;
 (*rate at 10 deg geomagnetic latitude*)
 nucleonsfactor20[y_] :=
  (382.1 + 272.1*(y/1000) + 132.5*(y/1000)^2 + 24.83*(y/1000)^3) / 563.4;
 (*rate at 20 deg geomagnetic latitude*)
 nucleonsfactor30[y_] :=
  (469.3 + 394.6*(y/1000) + 97.76*(y/1000)^2 + 47.20*(y/1000)^3) / 563.4;
 (*rate at 30 deg geomagnetic latitude*)
 nucleonsfactor40[y_] :=
  (525.6 + 505.4*(y/1000) + 142.0*(y/1000)^2 + 58.87*(y/1000)^3) / 563.4;
 (*rate at 40 deg geomagnetic latitude*)
 nucleonsfactor50[y_] :=
  (571.1 + 588.1*(y/1000) + 170.9*(y/1000)^2 + 76.12*(y/1000)^3) / 563.4;
 (*rate at 50 deg geomagnetic latitude*)
 nucleonsfactor60[y_] :=
  (563.4 + 621.8*(y/1000) + 177.3*(y/1000)^2 + 78.91*(y/1000)^3) / 563.4;
 (*rate at 60 - 90 deg geomagnetic latitude*)

(*Factors for scaling muon stopping rate
    relative to its rate at sea level and latitude >60 deg. These
     are used to scale both muon capture reactions and the rate of muon-
    induced secondary neutron production. Method is one used by Lal,
  1988, Nishiizumi et al, 1989 *)

muonsfactor0[y_] := (330.7 / 563.4) Exp[(1033 - (1032.92 -
        121.95*(y/1000) + 5.657*(y/1000)^2 - 0.1095*(y/1000)^3)) / 247];
muonsfactor10[y_] := (337.9 / 563.4) Exp[(1033 - (1032.92 -
        121.95*(y/1000) + 5.657*(y/1000)^2 - 0.1095*(y/1000)^3)) / 247];
muonsfactor20[y_] := (382.1 / 563.4) Exp[(1033 - (1032.92 -
        121.95*(y/1000) + 5.657*(y/1000)^2 - 0.1095*(y/1000)^3)) / 247];
muonsfactor30[y_] := (469.3 / 563.4) Exp[(1033 - (1032.92 -
        121.95*(y/1000) + 5.657*(y/1000)^2 - 0.1095*(y/1000)^3)) / 247];
muonsfactor40[y_] := (525.6 / 563.4) Exp[(1033 - (1032.92 -
        121.95*(y/1000) + 5.657*(y/1000)^2 - 0.1095*(y/1000)^3)) / 247];
muonsfactor50[y_] := (571.1 / 563.4) Exp[(1033 - (1032.92 -
        121.95*(y/1000) + 5.657*(y/1000)^2 - 0.1095*(y/1000)^3)) / 247];
muonsfactor60[y_] := Exp[
   (1033 - (1032.92 - 121.95*(y/1000) + 5.657*(y/1000)^2 - 0.1095*(y/1000)^3)) /
    247];
```

```
(*2 π horizon shielding correction factor.
 Variable 'x' is a list with the first term being an arc subtended by a
   shielded sector and the second term being the elevation angle to the
   shielded  horizon of the sector. Summed over sectors totalling 360 deg,
  the function calculates the fraction of incoming
   cosmic ray flux seen by a sample with a partially shielded horizon.*)

horizoncorrection[x_] := (x[[1]] / 360) (1 - Sin[x[[2]] Degree]^2.3) // N;

(*Assign a value to the flag '
    steady state' used when specifying initial Cl-36 abundance*)
steadystate = 1;

(*List of per-atom negative muon capture ratios,
  most values from von Egidy and Hartmann (1982),
  value for C from Knight et al. (1980). Value for H assumed zero,
  value for Li set below value for Be. Same order as the wt % list above: H,
  Li, B, C, O, Na, Mg,Al, Si, P, Cl, K, Ca, Ti, Cr, Mn, Fe, Sm,Gd.*)

fci = {0.0, 0.10, 0.22, 0.766, 1.0, 1.00, 0.93, 0.76, 0.84, 1.04, 1.32,
   1.54, 1.90, 2.66, 2.98, 2.73, 3.28, 4.4, 5.8};

(*List of nuclear capture probabilities for negative muons captured by elements i,
  from Tennent (1964);values for H & B (~ zero) and Sm &
   Gd (~ 1) inferred. Same order as the wt % list above: H,
  Li, B, C, O, Na, Mg, Al, Si,P, Cl, K, Ca, Ti, Cr, Mn, Fe, Sm, Gd.*)

fdi = {0.0, 0.08, 0.10, 0.11, 0.20, 0.46, 0.55, 0.63, 0.63, 0.69, 0.75,
   0.82, 0.85, 0.87, 0.90, 0.89, 0.91, 0.97, 0.97};

(*List of average neutron emission probabilities following nuclear negative
   muon capture. Values for Al. Si, K, Ca, and Fe from Charalambus
   (1971). Others set to 1.0 (light elements),1.4 (heavy elements) or
   1.23 (recommended av' ge value). Same order as the wt % list above: H,
  Li, B, C, O, Na, Mg, Al,Si, P, Cl, K, Ca, Ti, Cr, Mn, Fe, Sm,Gd.*)

avpn = {1.0, 1.0, 1.0, 1.0, 1.0, 1.23, 1.23, 1.29, 1.09, 1.23, 1.23,
   1.25, 1.10, 1.23, 1.23, 1.23, 1.23, 1.4, 1.4};
```

■ Chlorine-36 data

```
(*Complete sample details and press 'enter' key on keyboard*)

 rundate = 110200; (*enter as a six digit string*)
 cl36runblank = {2.4*10^4, 1.5*10^4}; (*{atoms Cl-36, uncertainty}*)
 clrunblank = 5; (*μg chloride*)

 samplename = "N5/97 - CN0597";
 (*best to put text in " ". Otherwise no spaces, '/' or '-' characters -
   these are recognised symbols in Mathematica.*)
  samplewt = 19.2178; (*wt in g*)
 density = 2.9; (*g cm^-3*)
 top = 0.5; (*depth from original surface to top of sample -
   ie depth of weathered rind removed - in cm*)
  bottom = 4.5; (*depth from original surface to base of sample in cm*)

 latitude = 30.73; (*geographic latitude (decimal degrees) unless
   sample is very young (< 1000 a), in which case geomagnetic latitude*)
  longitude = 28.14; (*reference purposes only*)
 altitude = 2506; (*in metres asl*)
 shielding = {{10, 3.65}, {20, 1.84}, {20, 1.23}, {5, 0.62}, {305, 0}};
 (*elements are {sector width, angle to horizon} in degrees*)

dip = 88; (* for sloping surface, insert average dip of cliff face, in degrees*)
slopestop[p_] = slope88stop[p]; (*insert appropriate polynomial for dip angle,
  chose from slope65stop[p], slope70stop[p],slope75stop[p],slope76stop[p],
  slope78stop[p],slope79stop[p],slope80stop[p],slope81stop[p],slope82stop[p],
  slope83stop[p],slope84stop[p],slope85stop[p],slope86stop[p],
  slope87stop[p],slope88stop[p],slope89stop[p],slope90stop[p]*)

 cl = {1.7, 0.2};
 (*chloride concentration of the sample and the standard deviation in ppm wt.*)
 carriercl = 1.4395413; (*amount of carrier cl in mg*)
 cl36ratio = {155, 13}; (*Cl-36/Cl ratio and uncertainty in units of 10^-15*)
```

■ Chemical data

```
(* These data are used to determine the neutron capture
  characteristics of the sample rock. Enter the oxide weight
  % of each element in the whole rock and the relative standard
  deviation assigned to each. Press the 'enter' key when complete.*)

sio2 = {55.06, 0.01};
tio2 = {1.04, 0.01};
al2o3 = {11.86, 0.01};
fe2o3 = {11.23, 0.01};
feo = {0.0, 0.01};
mno = {0.15, 0.01};
mgo = {6.71, 0.01};
cao = {10.01, 0.01};
na2o = {2.32, 0.01};
k2o = {0.92, 0.01};
p2o5 = {0.01, 0.01};
h2o = {0.62, 0.05};
co2 = {0.21, 0.01};

(*Enter trace element concentrations in ppm wt and absolute
  uncertainties (ie also ppm wt). Press 'enter' when complete.*)

li = {6.17, 0.08};
b = {3.0, 0.3};
wholerockcl = {1.7, 0.2};
cr = {182.0, 6.0};
sm = {3.17, 0.08};
gd = {4.1, 0.3};

u = {0.25, 0.01};
th = {1.5, 0.2};
```

■ Calculation stage (1) : Cl-36 concentration

```
cl36concentration = (cl36ratio[[1]]*10^-15 * 1.698635*10^16 *
     (samplewt*cl[[1]] + 1000*carriercl + clrunblank) - cl36runblank[[1]]) /
  samplewt;

cl36concentrationstddvn = (288.5360863225*cl36ratio[[1]]^2 * cl[[2]]^2 +
    (288.5360863225*cl36ratio[[1]]^2 * (0.5*clrunblank)^2) / samplewt^2 +
    cl36runblank[[2]]^2 / samplewt^2 + (288.5360863225*cl36ratio[[2]]^2 *
       (1000*carriercl + clrunblank + cl[[1]]*samplewt)^2) / samplewt^2)^
  0.5;
```

■ Calculation stage (2) : Fate of neutrons

```
(*First make up the list of element wt%s from oxide wt%s and ppm values. This will
be used wherever a summation involving Ni is required ....*)

wtpercents = {0.1111 h2o[[1]], 10^-4 li[[1]], 10^-4 b[[1]], 0.2729 co2[[1]],
0.88888 h2o[[1]] + 0.7271 co2[[1]] + 0.2581 na2o[[1]] + 0.3970 mgo[[1]] + 0.4708
al2o3[[1]] + 0.5326 sio2[[1]] + 0.5636 p2o5[[1]] + 0.1699 k2o[[1]] + 0.2853
cao[[1]] + 0.4006 tio2[[1]] + 0.2255 mno[[1]] + 0.3006 fe2o3[[1]] + 0.2227
feo[[1]], 0.7419 na2o[[1]], 0.6030 mgo[[1]], 0.5292 al2o3[[1]], 0.4674 sio2[[1]],
0.4364 p2o5[[1]], 10^-4 wholerockcl[[1]], 0.8301 k2o[[1]], 0.7147 cao[[1]], 0.5994
tio2[[1]], 10^-4 cr[[1]], 0.7745 mno[[1]], 0.6994 fe2o3[[1]] + 0.7773 feo[[1]],
10^-4 sm[[1]], 10^-4 gd[[1]]};

(*For error propagation, make up a corresponding list of absolute uncertainties in
wt% element concentrations. For major elements, terms are: wt frn element x wt%
oxide x rsd wt% oxide.  For trace elements, terms are 10^-4 x absolute sd in ppm*)

deltawtpercents = {0.1111 h2o[[1]] h2o[[2]], 10^-4 li[[2]], 10^-4 b[[2]], 0.2729
co2[[1]] co2[[2]], ((*absolute error in [O]*)((0.88888 h2o[[1]] h2o[[2]])^2 +
(0.7271 co2[[1]] co2[[2]])^2 + (0.2581 na2o[[1]] na2o[[2]])^2 + (0.3970 mgo[[1]]
mgo[[2]])^2 + (0.4708 al2o3[[1]] al2o3[[2]])^2 + (0.5326 sio2[[1]] sio2[[2]])^2 +
(0.5636 p2o5[[1]] p2o5[[2]])^2 + (0.1699 k2o[[1]] k2o[[2]])^2 + (0.2853 cao[[1]]
cao[[2]])^2 + (0.4006 tio2[[1]] tio2[[2]])^2 + (0.2255 mno[[1]] mno[[2]])^2 +
(0.3006 fe2o3[[1]] fe2o3[[2]])^2 + (0.2227 feo[[1]] feo[[2]])^2)^0.5), 0.7419
na2o[[1]] na2o[[2]], 0.6030 mgo[[1]] mgo[[2]], 0.5292 al2o3[[1]] al2o3[[2]], 0.4674
sio2[[1]] sio2[[2]], 0.4364 p2o5[[1]] p2o5[[2]], 10^-4 wholerockcl[[2]], 0.8301
k2o[[1]] k2o[[2]], 0.7147 cao[[1]] cao[[2]], 0.5994 tio2[[1]] tio2[[2]], 10^-4
cr[[2]], 0.7745 mno[[1]] mno[[2]], ((0.6994 fe2o3[[1]] fe2o3[[2]])^2 + (0.7773
feo[[1]] feo[[2]])^2)^0.5, 10^-4 sm[[2]], 10^-4 gd[[2]]};


(*Use these lists to calculate mean atomic weight,  macroscopic x-sections for
thermal neutron absorption; (Σth,rock) and thermal neutron scattering (Σsc,rock);
effective resonance integral; and log energy decrement in scattering (and
uncertainties in these parameters).*)

(*Mean atomic weight A*)

arock = Apply[Plus, wtpercents ai] / 100;

arockstddvn = (Apply[Plus, deltawtpercents^2 ai^2])^0.5 / 100;

(*Macroscopic cross section for thermal neutron absorption for whole rock. Formula
for Σth,rock. NB in cm^2/g! Multiply by density to get value in cm^-1*)

abs = 6.0222*10^21(*Avogadro constant / 100*) * wtpercents * sigmathermali / ai;

sigmathermalrock = Apply[Plus, abs];(*fraction stopped by trace elements*)

sigmathermalrockstddvn = 6.0222*10^21 (*Avogadro constant / 100*) (Apply[Plus,
deltawtpercents^2 * sigmathermali^2 / ai^2])^0.5;

(*Fraction of thermalised neutrons captured by Cl-35*)

cl35capturefrn = cl[[1]] 43.6*10^-24 (*σth Cl-35*) * 1.6986*10^16 (*atom Cl per ppm
per g*) * 0.7577 (*Cl-35/Cl*) / sigmathermalrock;

(*error in above*)
```

```
cl35capturefrnstddvn = ((cl35capturefrn cl[[2]] / cl[[1]])^2 + (-cl35capturefrn
sigmathermalrockstddvn / sigmathermalrock)^2)^0.5;

(*Fraction of thermalised neutrons captured by K-39*)

k39capturefrn = k2o[[1]] 0.0043*10^-24 (*σth K-39(n, α)Cl-36*) * 1.2787*10^20
(*atom K per %K20*) * 0.93258 (*K-39/K*) / sigmathermalrock;

(*error in above*)

k39capturefrnstddvn = ((k39capturefrn k2o[[2]] / k2o[[1]])^2 + (-k39capturefrn
sigmathermalrockstddvn / sigmathermalrock)^2)^0.5;

(*Macroscopic cross section for thermal neutron absorptions by trace elements only
(Σth,trace absorbers) in cm^2/g.*)

sigmathermaltr = Apply[Plus,
{abs[[2]], abs[[3]], abs[[11]], abs[[15]], abs[[18]], abs[[19]]}];

(*Fraction of thermal neutron captures by (major, trace) elements.*)

stopping = {1 - (sigmathermaltr / sigmathermalrock), (sigmathermaltr /
sigmathermalrock)};

(*Macroscopic X-section for neutron scattering*)

sigmascatterrock = 6.0222*10^21 (*Avogadro constant / 100*) Apply[Plus, wtpercents
* sigmascatteri / ai];

(*error in above*)

sigmascatterrockstddvn = 6.0222*10^21 (*Avogadro constant / 100*) (Apply[Plus,
deltawtpercents^2 * sigmascatteri^2 / ai^2])^0.5;

(*Effective resonance integral*)

ieffrock = 6.0222*10^21 (*Avogadro constant / 100*) Apply[Plus, wtpercents * iai /
ai];

(*error in above*)

ieffrockstddvn = 6.0222*10^21 (*Avogadro constant / 100*) (Apply[Plus,
deltawtpercents^2 * iai^2 / ai^2])^0.5;

(*Energy loss rate in down-scattering*)

edecrement = 6.0222*10^21 (*Avogadro constant / 100*) Apply[Plus, wtpercents *
elossi *sigmascatteri / ai];

(*error in above*)

edecrementstddvn = 6.0222*10^21 (*Avogadro constant / 100*) (Apply[Plus,
deltawtpercents^2 * elossi^2 *sigmascatteri^2 / ai^2])^0.5;

(*Use the basic composition-dependent parameters above to determine thermal and
epithermal neutron diffusion parameters; Diffusion coefficient D, attenuation
length L, Resonance escape probability and "escape ratio" relative to air*)

(*Thermal neutron diffusion coefficient*)

drock = (3 sigmascatterrock (1 - 2 (3 arock)^-1))^-1;

(*error in above*)

drockstddvn = ((-1/(3*(1 - 2/(3*arock))*sigmascatterrock^2) *
sigmascatterrockstddvn)^2 + (-2/(9*(1 - 2/(3*arock))^2*arock^2*sigmascatterrock) *
arockstddvn)^2)^0.5;

(*Thermal neutron attenuation length*)

lrock = (drock / sigmathermalrock)^0.5;

(*error in above*)

lrockstddvn = ((0.5/(drock^0.5*sigmathermalrock^0.5) * drockstddvn)^2 +
((-0.5*drock^0.5)/sigmathermalrock^1.5 * sigmathermalrockstddvn)^2)^0.5;

(*Epithermal neutron attenuation length - used only in calculating epithermal
production vs z, and thickness correction for production by epithermal neutrons*)

lepi = (3 sigmascatterrock ieffrock)^-0.5;

(*Resonance escape probability*)

pethermalrock = Exp[-ieffrock / edecrement];

(*error in above*)

pethermalrockstddvn = ((-(1/(E^(ieffrock/edecrement)*edecrement)) *
ieffrockstddvn)^2 + (ieffrock/(E^(ieffrock/edecrement)*edecrement^2) *
edecrementstddvn)^2)^0.5;

(*Resonance escape ratio*)

r = (pethermalrock / 0.56 (*p(Eth)air*)) (arock / 14.675 (*Aair*))^0.5;

(*error in above*)

rstddvn =
((0.466147*arock^0.5 * pethermalrockstddvn)^2 + ((0.23307*pethermalrock)/arock^0.5
* arockstddvn)^2)^0.5;

(*Epithermal neutron capture ratio*)

repi = ((1 - pethermalrock) / 0.44(*1 - p(Eth)air*)) (arock / 14.675(*Aair*))^0.5;

(*error in above*)

repistddvn = ((-0.593278 arock^0.5 pethermalrockstddvn)^2 + (((0.29664*(1 -
pethermalrock))/arock^0.5) * arockstddvn)^2)^0.5;

(*Fraction of epithermal captures by Cl-35*)

fepi = cl[[1]] * 1.6986*10^16 (*atom Cl per ppm per g*) * 0.7577 (*Cl-35/Cl*) *
15*10^-24(*σth Cl-35*) / ieffrock;

(*error in above*)

fepistddvn = ((cl[[2]] * 1.6986*10^16 * 0.7577 * 15*10^-24 / ieffrock)^2 +
(-cl[[1]] * 1.6986*10^16 * 0.7577 * 15*10^-24 * ieffrockstddvn /
ieffrock^2)^2)^0.5;

(*Terms in Fred Phillip's final diffusion equation (in Liu et al 1994), determined
by the parameters calculated above.*)

(*Thermal neutron flux that would be observed at the land surface if thermal
```

```
neutrons did not diffuse upwards into the atmosphere. This is Φ* in Liu et al 1994
eqn 14. NB JS has moved the Pf(0) (= pfast in this program, the production rate of
secondary cosmogenic neutrons) to the production rate calculation later on.*)

phistar (* Φ* *)= 0.56(*p(Eth)air*) r / sigmathermalrock;

(*error in above*)

phistarstddvn =
((0.56 rstddvn / sigmathermalrock)^2 +
    ((-0.56*r)sigmathermalrockstddvn / sigmathermalrock^2)^2)^0.5;

(*difference between the thermal neutron fluxes in the air and the ground at the
ground surface. This is ΔΦ* in eqn 15 of Liu et al 1994. Again JS has moved the
Pf(0) part of the production rate calculation.*)

deltaphi (* ΔΦ* *)= 0.56 (16.611 (*g/cm^2 attn length in air*) - (r /
sigmathermalrock));

(*error in above*)

deltaphistddvn = ((((-0.56)/sigmathermalrock) * rstddvn)^2 +
(((0.56*r)/sigmathermalrock^2) * sigmathermalrockstddvn)^2)^0.5;

attn = attnlength[dip];(*for calculating fthermal for sloping surface - adjusts the
attenuation length to reflect the dip of the slope*)

(*weighting factor that determines the balance between the end-members in the
actual interface fluxes, F in eqn 16 in Liu et al 1994. Attenuation length adjusted
for sloping surface.*)

fthermal = ((0.915 / (3.9 drock)) + attn^-1) / ((0.915 / (3.9 drock)) + lrock^-1);

(*error in above*)

fthermalstddvn = (((0.234615*(0.234615/drock + attn^(-1)))/(drock^2*(0.234615/drock
+ lrock^(-1))^2) - 0.234615/(drock^2*(0.234615/drock + lrock^(-1))))^2
drockstddvn^2 + ((0.234615/drock + attn^(-1))/((0.234615/drock +
lrock^(-1))^2*lrock^2))^2 lrockstddvn^2)^0.5;

(*Conditional statements figure out which element is the major neutron absorber*)

Which[
Position[abs, Max[abs]] == {{3}}, maxabsorber = Boron,

Position[abs, Max[abs]] == {{6}}, maxabsorber = Sodium,

Position[abs, Max[abs]] == {{8}}, maxabsorber = Aluminium,

Position[abs, Max[abs]] == {{9}}, maxabsorber = Silicon,

Position[abs, Max[abs]] == {{11}}, maxabsorber = Chlorine,

Position[abs, Max[abs]] == {{12}}, maxabsorber = Potassium,

Position[abs, Max[abs]] == {{13}}, maxabsorber = Calcium,

Position[abs, Max[abs]] == {{16}}, maxabsorber = Manganese,

Position[abs, Max[abs]] == {{17}}, maxabsorber = Iron,

Position[abs, Max[abs]] == {{19}}, maxabsorber = Gadolinium];
```

■ Calculation stage (3) : Production rates

```
(*conditional statements to determine which set of latitude / altitude correction
  polynomials to apply. NB linear interpolation for latitude between polynomials*)

 If[latitude >= 0 && latitude < 10,

spallationfactor = (nucleonsfactor0[altitude] +
     ((latitude / 10) * (nucleonsfactor10[altitude] - nucleonsfactor0[altitude])));

muonfactor = (muonsfactor0[altitude] + ((latitude / 10)
 (muonsfactor10[altitude] -
 muonsfactor0[altitude])))];

If[latitude >= 10 && latitude < 20,

spallationfactor = (nucleonsfactor10[altitude]
 + (((latitude - 10) / 10)
 (nucleonsfactor20[altitude] -
 nucleonsfactor10[altitude])));

 muonfactor = (muonsfactor10[altitude] +
 (((latitude - 10) / 10)
 (muonsfactor20[altitude] -
 muonsfactor10[altitude])))];

If[latitude >= 20 && latitude < 30,

spallationfactor = (nucleonsfactor20[altitude]
 + (((latitude - 20) / 10)
 (nucleonsfactor30[altitude] -
 nucleonsfactor20[altitude])));

 muonfactor = (muonsfactor20[altitude] +
 (((latitude - 20) / 10)
 (muonsfactor30[altitude] -
 muonsfactor20[altitude])))];

If[latitude >= 30 && latitude < 40,

spallationfactor = (nucleonsfactor30[altitude]
 + (((latitude - 30) / 10)
 (nucleonsfactor40[altitude] -
 nucleonsfactor30[altitude])));

 muonfactor = (muonsfactor30[altitude] +
 (((latitude - 30) / 10)
 (muonsfactor40[altitude] -
 muonsfactor30[altitude])))];

If[latitude >= 40 && latitude < 50,

spallationfactor = (nucleonsfactor40[altitude]
```

```
 + (((latitude - 40) / 10)
 (nucleonsfactor50[altitude] -
 nucleonsfactor40[altitude])));

 muonfactor = (muonsfactor40[altitude] + (((latitude - 40) / 10)
 (muonsfactor50[altitude] -
 muonsfactor40[altitude])))];

If[latitude >= 50 && latitude < 60,

spallationfactor = (nucleonsfactor50[altitude]
 + (((latitude - 50) / 10)
 (nucleonsfactor60[altitude] -
 nucleonsfactor50[altitude])));

 muonfactor = (muonsfactor50[altitude] +
 (((latitude - 50) / 10)
 (muonsfactor60[altitude] -
 muonsfactor50[altitude])))];

If[latitude >= 60,

spallationfactor = nucleonsfactor60[altitude];

muonfactor = muonsfactor60[altitude]];

 (*Reduction in production rate for 2π surface caused by topographic obstructions*)

 horizonfactor = Apply[Plus, Map[horizoncorrection, shielding]];

(*Depth and thickness correction factor for spallation rate*)

 depthfactor = (attn / (density * (bottom - top))) *
   (Exp[-((density * top) / attn)] - Exp[-((density * bottom) / attn)]);

 (* Depth and thickness correction factors for
   thermal and epithermal neutron capture reactions (by integration)*)

 nthermalzcorrection = NIntegrate[phistar Exp[-z / attn] +
     fthermal deltaphi Exp[-z / lrock], {z, density top, density bottom}] /
   ((phistar + fthermal deltaphi) (density bottom - density top));

nepizcorrection = NIntegrate[Exp[-z / attn] - 0.4 Exp[-z / lepi],
    {z, density top, density bottom}] / (0.6 (density bottom - density top));

(*depth point below surface for calculation of muon production mechanisms*)
 zcalc = density * top + 0.5 (density * bottom - density * top);

  horizonfactordip = hzncorrn[dip] * horizonfactor; (*redefines the surface production
   rate for a dipping surface taking into account topography and slope angle*)

 (*muon production for sloping surface. Need
   to generate the capture fractions for muon capture on Ca and K,
  and the chlorine-36 production per stopped muon. *)
```

```
atomfrns = (wtpercents / ai) / Apply[Plus, (wtpercents / ai)];

pcaperstoppedmuon = 0.9694(*isotopic abdce Ca-40*) * 0.85(*fdCa*) * 0.043
   (*P alpha*) * 1.90 atomfrns[[13]] / Apply[Plus, atomfrns * fci]; (*fcCa*)

pkperstoppedmuon = 0.82(*fdK*) * 0.043(*P alpha - assume as for Ca*) *
   1.54 atomfrns[[12]] / Apply[Plus, atomfrns * fci]; (*fcK*)

pnperstoppedmuon = Apply[Plus, atomfrns * fci * fdi * avpn];

 (*correction to muon stopping rate as a function of dip angle of
   slope (in degrees). Function derived offline from polynomials below*)

muonhzncorrn[dip_] = 0.977927 + 0.002059 * dip - 0.00008184 * dip^2;

(*muon production for sloping surface. Polynomials
   for stopping muon profile beneath a sloping surface as
   a function of perpendicular depth for Drakensberg and Lesotho
   Highland sites. Derived from Polynomials for muons on slopes.nb*)

slope65stop[p_] = 10^(2.57394 - 0.0278965 Log[p] - 0.00937001 Log[p]^2 +
     0.0142109 Log[p]^3 - 0.00356543 Log[p]^4 + 0.000194251 Log[p]^5);

slope70stop[p_] = 10^(2.54443 - 0.0387563 Log[p] + 0.00191775 Log[p]^2 +
     0.0103093 Log[p]^3 - 0.0030864 Log[p]^4 + 0.000175061 Log[p]^5);

slope75stop[p_] = 10^(2.50997 - 0.0499376 Log[p] + 0.0136535 Log[p]^2 +
     0.00618233 Log[p]^3 - 0.00257007 Log[p]^4 + 0.000153954 Log[p]^5);

slope76stop[p_] = 10^(2.50249 - 0.0521943 Log[p] + 0.0160331 Log[p]^2 +
     0.00533496 Log[p]^3 - 0.00246274 Log[p]^4 + 0.000149512 Log[p]^5);

slope78stop[p_] = 10^(2.48695 - 0.0567122 Log[p] + 0.0208007 Log[p]^2 +
     0.00362448 Log[p]^3 - 0.00224464 Log[p]^4 + 0.000140429 Log[p]^5);

slope79stop[p_] = 10^(2.47891 - 0.0589699 Log[p] + 0.0231808 Log[p]^2 +
     0.00276361 Log[p]^3 - 0.0021341 Log[p]^4 + 0.000135796 Log[p]^5);

slope80stop[p_] = 10^(2.4707 - 0.0612251 Log[p] + 0.0255527 Log[p]^2 +
     0.00190065 Log[p]^3 - 0.00202273 Log[p]^4 + 0.000131107 Log[p]^5);

slope81stop[p_] = 10^(2.46232 - 0.0634775 Log[p] + 0.0279115 Log[p]^2 +
     0.00103712 Log[p]^3 - 0.00191071 Log[p]^4 + 0.000126369 Log[p]^5);

slope82stop[p_] = 10^(2.45381 - 0.0657294 Log[p] + 0.0302525 Log[p]^2 +
     0.000174731 Log[p]^3 - 0.00179823 Log[p]^4 + 0.00012159 Log[p]^5);

slope83stop[p_] = 10^(2.44517 - 0.0679861 Log[p] + 0.0325712 Log[p]^2 -
     0.000684866 Log[p]^3 - 0.00168549 Log[p]^4 + 0.000116778 Log[p]^5);

slope84stop[p_] = 10^(2.43643 - 0.0702581 Log[p] + 0.0348642 Log[p]^2 -
     0.00153996 Log[p]^3 - 0.00157272 Log[p]^4 + 0.000111942 Log[p]^5);

slope85stop[p_] = 10^(2.42764 - 0.0725658 Log[p] + 0.0371317 Log[p]^2 -
     0.00238934 Log[p]^3 - 0.0014601 Log[p]^4 + 0.000107091 Log[p]^5);
```

```
slope86stop[p_] = 10^(2.41885 - 0.0749437 Log[p] + 0.0393776 Log[p]^2 -
      0.00323218 Log[p]^3 - 0.00134783 Log[p]^4 + 0.000102235 Log[p]^5);

slope87stop[p_] = 10^(2.41012 - 0.0774456 Log[p] + 0.0416102 Log[p]^2 -
      0.00406726 Log[p]^3 - 0.0012363 Log[p]^4 + 0.0000973963 Log[p]^5);

slope88stop[p_] = 10^(2.40152 - 0.0799551 Log[p] + 0.0436564 Log[p]^2 -
      0.00482881 Log[p]^3 - 0.00113507 Log[p]^4 + 0.0000930531 Log[p]^5);

slope89stop[p_] = 10^(2.39331 + 0.0142414 Log[p] - 0.0451335 Log[p]^2 +
      0.0251653 Log[p]^3 - 0.00531006 Log[p]^4 + 0.000296545 Log[p]^5);

slope90stop[p_] = 10^(2.3853 + 0.0142414 Log[p] - 0.0451335 Log[p]^2 +
      0.0251653 Log[p]^3 - 0.00531006 Log[p]^4 + 0.000296545 Log[p]^5);

 (*Thermal neutron capture by Cl - 35*)

 pnthermal = ((1 - neutronmufrn) * spallationfactor + neutronmufrn * muonfactor) *
   pfast * horizonfactordip * nthermalzcorrection * cl[[1]] * 43.6 *
   10^-24 (*σth Cl-35*) * 1.6986*10^16 (*atom Cl per microgram*) *
   0.7577 (*Cl - 35 / Cl*) * (phistar + fthermal*deltaphi);

(*Thermal neutron capture by Cl - 35 - from muons*)

pnmuoncl35 = cl35capturefrn*pnperstoppedmuon*slopestop[zcalc]*horizonfactor;

(*Total thermal neutron capture by Cl - 35*)

pneutronscl35total = pnthermal + pnmuoncl35;

(*Thermal neutron capture by K-39*)

 p39 = ((1 - neutronmufrn) * spallationfactor + neutronmufrn * muonfactor) *
   pfast * horizonfactordip * nthermalzcorrection *
   k2o[[1]] * 0.0043*10^-24 (*σth K-39 (n,α) Cl-36*) * 1.2787*10^20
   (*atom k per % k2o*) * 0.93258 (*k-39/k*) * (phistar + fthermal*deltaphi);

(*Thermal neutron capture by K-39 - from muons*)

pnmuonk39 = k39capturefrn*pnperstoppedmuon*slopestop[zcalc]*horizonfactor;

(*Total thermal neutron capture by K-39*)

pneutronsk39total = p39 + pnmuonk39;

(*Epithermal neutron capture by Cl-35*)

 pnepithermal = ((1 - neutronmufrn) * spallationfactor + neutronmufrn * muonfactor) *
   pfast * horizonfactordip * nepizcorrection *
   0.44 (*1-p (Eth) a*) * fepi * repi * 0.6 (*(1 - Feth),
  the fractional reduction in epithermal flux at the air ground interface.*);

(*spallation of Ca*)

 pcaspallx = horizonfactordip*depthfactor*spallationfactor * caspall * cao[[1]];

 (*spallation of Ca for denudation calculation - same as pcaspallx,
  but ignores horizonfactor*)

 pcaspall = depthfactor*spallationfactor * caspall * cao[[1]];

(*spallation of K*)

 pkspallx = horizonfactordip*depthfactor* spallationfactor * kspall * k2o[[1]];

(*spallation of K for denudation calculation - same as pkspallx,
  but ignores horizonfactor*)

 pkspall = depthfactor* spallationfactor * kspall * k2o[[1]];

 (*muon capture by Ca*)

 pcamu = pcaperstoppedmuon*slopestop[zcalc]*horizonfactor;

(*muon capture by K*)

 pkmu = pkperstoppedmuon*slopestop[zcalc]*horizonfactor;

(*Uncertainties in each of the production rates*)

 pnthermalstddvn =
  ((pnthermal * pfaststddvn / pfast)^2 + (pnthermal * cl[[2]] / cl[[1]])^2 +
     (((1 - neutronmufrn) * spallationfactor + neutronmufrn * muonfactor) *
        pfast * horizonfactordip *
        nthermalzcorrection * 5.6114*10^-7 * cl[[1]] * phistarstddvn)^2 +
     (((1 - neutronmufrn) * spallationfactor + neutronmufrn * muonfactor) *
        pfast * horizonfactordip * nthermalzcorrection *
        5.6114*10^-7 * cl[[1]] * deltaphi * fthermalstddvn)^2 +
     (((1 - neutronmufrn) * spallationfactor + neutronmufrn * muonfactor) *
        pfast * horizonfactordip * nthermalzcorrection *
        5.6114*10^-7 * cl[[1]] * fthermal * deltaphistddvn)^2)^
   0.5;

pnmuoncl35stddvn =
  ((cl35capturefrnstddvn / cl35capturefrn)^2 + (0.4)^2)^0.5 * pnmuoncl35;

pneutronscl35totalstddvn = ((pnthermalstddvn)^2 + (pnmuoncl35stddvn)^2)^0.5;

 p39stddvn = ((p39 * pfaststddvn / pfast)^2 + (p39 * k2o[[2]] / k2o[[1]])^2 +
     (((1 - neutronmufrn) * spallationfactor + neutronmufrn * muonfactor) *
        pfast * horizonfactordip *
        nthermalzcorrection * 5.1277*10^-7 * k2o[[1]] * phistarstddvn)^2 +
     (((1 - neutronmufrn) * spallationfactor + neutronmufrn * muonfactor) *
        pfast * horizonfactordip * nthermalzcorrection *
        5.1277*10^-7 * k2o[[1]] * deltaphi * fthermalstddvn)^2 +
     (((1 - neutronmufrn) * spallationfactor + neutronmufrn * muonfactor) *
        pfast * horizonfactordip * nthermalzcorrection *
        5.1277*10^-7 * k2o[[1]] * fthermal * deltaphistddvn)^2)^
   0.5;
```

```
pnmuonk39stddvn = ((k39capturefrnstddvn / k39capturefrn) ^ 2 + (0.4) ^ 2) ^ 0.5 * pnmuonk39;

pneutronsk39totalstddvn = ((p39stddvn) ^ 2 + (pnmuonk39stddvn) ^ 2) ^ 0.5;

 pnepithermalstddvn = pnepithermal *
   ((fepistddvn / fepi) ^ 2 + (pfaststddvn / pfast) ^ 2 + (repistddvn / repi) ^ 2) ^ 0.5;

 pcaspallxstddvn = horizonfactordip * depthfactor * spallationfactor *
   ((caspall * cao[[2]]) ^ 2 + (cao[[1]] * caspallstddvn) ^ 2) ^ 0.5;

 pcaspallstddvn = depthfactor * spallationfactor *
   ((caspall * cao[[2]]) ^ 2 + (cao[[1]] * caspallstddvn) ^ 2) ^ 0.5;

 pkspallxstddvn = horizonfactordip * depthfactor * spallationfactor *
   ((kspall * k2o[[2]]) ^ 2 + (k2o[[1]] * kspallstddvn) ^ 2) ^ 0.5;

 pkspallstddvn = depthfactor * spallationfactor *
   ((kspall * k2o[[2]]) ^ 2 + (k2o[[1]] * kspallstddvn) ^ 2) ^ 0.5;

 pcamustddvn = 0.4 * pcamu;

 pkmustddvn = 0.4 * pkmu;

(*Total site specific production rate for sample, taking account of elevation,
  latitude, horizon shielding, thickness and composition*)

    ptotal = pneutronscl35total +
   pneutronsk39total + pnepithermal + pcaspallx + pkspallx + pcamu + pkmu;

(*error in above*)

 ptotalstddvn =
  (pneutronscl35totalstddvn^2 + pneutronsk39totalstddvn^2 + pnepithermalstddvn^2 +
     pcaspallxstddvn^2 + pkspallxstddvn^2 + pcamustddvn^2 + pkmustddvn^2) ^ 0.5;

(*intrinsic neutron production due to U and Th and uncertainties*)

 (*neutron production by spontaneous fission of U-238*)

 ufissionneutrons =
  0.427 (*constant = Uatom/ppm * λUsf * n yeild per fission*) * u[[1]];

(*error in above - assumes 2.23 % combined error in λUsf and n yield per fission*)

 ufissionneutronsstddvn =
  ufissionneutrons * ((4.973 * 10^-4 + (u[[2]] / u[[1]]) ^ 2) ^ 0.5);

(*major elements*)

 majorelts = {sio2[[1]], tio2[[1]], al2o3[[1]], fe2o3[[1]], feo[[1]], mno[[1]],
   mgo[[1]], cao[[1]], na2o[[1]], k2o[[1]], p2o5[[1]], h2o[[1]], co2[[1]]};

 (*error in above*)

 rsdmajorelts = {sio2[[2]], tio2[[2]], al2o3[[2]], fe2o3[[2]], feo[[2]], mno[[2]],
   mgo[[2]], cao[[2]], na2o[[2]], k2o[[2]], p2o5[[2]], h2o[[2]], co2[[2]]};

(*Total neutron yield per ppm U
  and per ppm Th for (alpha, n) reactions, for rock composition*)

 alphaneutronyields = ((majorelts / 100) . nyields);
 (*Dot product gives output in form {total n per ppm U, total n per ppm Th}*)

 (*error in above*)

 alphaneutronyieldsstddvn = (((rsdmajorelts * majorelts / 100) ^ 2) . (nyields^2)) ^ 0.5;

 (*total neutrons / g / yr produced by U*)

 ualphaneutrons = u[[1]] * alphaneutronyields[[1]];

(*error in above*)

 ualphaneutronsstddvn = ((u[[2]] ^ 2) * (alphaneutronyields[[1]] ^ 2) +
     (u[[1]] ^ 2) * (alphaneutronyieldsstddvn[[1]] ^ 2)) ^ 0.5;

 (*total neutrons / g / yr produced by Th*)

 thalphaneutrons = th[[1]] * alphaneutronyields[[2]];

(*error in above*)

 thalphaneutronsstddvn = ((th[[2]] ^ 2) * (alphaneutronyields[[2]] ^ 2) +
     (th[[1]] ^ 2) * (alphaneutronyieldsstddvn[[2]] ^ 2)) ^ 0.5;

(*background neutron production rate*)

 bckgdneutrons = ufissionneutrons + ualphaneutrons + thalphaneutrons;

(*error in above*)

 bckgdneutronsstddvn = (ufissionneutronsstddvn^2 +
     ualphaneutronsstddvn^2 + thalphaneutronsstddvn^2) ^ 0.5;

(*Cl-36 produced by these background neutrons*)

 pbckgd = bckgdneutrons * cl35capturefrn;

(*error in above*)

 pbckgdstddvn = ((bckgdneutrons * cl35capturefrnstddvn) ^ 2 +
     (bckgdneutronsstddvn * cl35capturefrn) ^ 2) ^
   0.5;
```

■ Calculation stage (4): Denudation rate

```
(*Cl-36 produced by the background neutron flux,
  taking into account the decay in Cl-36. Equals the grow
    in due to background neutrons if surface started with zero Cl-36,
  otherwise steady-state level supported by background neutrons*)

 cl36bckgd = bckgdneutrons * cl35capturefrn / lamda;

(*error in above*)

 cl36bckgdstddvn = ((bckgdneutrons * cl35capturefrnstddvn) ^2 +
      (bckgdneutronsstddvn * cl35capturefrn) ^2) ^0.5 / lamda;

(*cosmogenic produced Cl-36,
  ie the Cl-36 total concentration less the background produced Cl-36*)

 cosmocl36 = cl36concentration - cl36bckgd;

(*error in above*)

 cosmocl36stddvn = (cl36concentrationstddvn^2 + cl36bckgdstddvn^2) ^0.5;

 (*erosional steady-state concentration for spallation*)

  cliffspalln[dip_, erosionrate_] = horizonfactordip
   (pcaspall + pkspall) / (lamda + erosionrate density / attnlength[dip]);

 (*erosional steady-state for thermal neutron capture by Cl*)

 nthermalsteadystate[erosionrate_] =
  ((1 - neutronmufrn) spallationfactor + neutronmufrn muonfactor)
   pfast horizonfactordip nthermalzcorrection cl[[1]] 43.6 *
   10^-24 (*σth Cl-35*) * 1.6986 * 10^16 (*atom Cl per microgram*) *
   0.7577 (*Cl-35/Cl*) ((phistar / (lamda + (density erosionrate / attn))) +
     (fthermal * deltaphi / (lamda + (density erosionrate / lrock))));

 (*erosional steady-state for thermal neutron capture by K*)

 nthermalksteadystate[erosionrate_] =
  ((1 - neutronmufrn) spallationfactor + neutronmufrn muonfactor)
   pfast horizonfactordip nthermalzcorrection k2o[[1]] 0.0043 * 10^-24
   (*σth K-39 (n,alpha) Cl-36*) * 1.2787 * 10^20 (*atom K per % k2o*) *
   0.93258 (*k39/k*) ((phistar / (lamda + (density erosionrate / attn))) +
     (fthermal * deltaphi / (lamda + (density erosionrate / lrock))));

  (*erosional steady-state for muon production*)

 nmuonsdip[erosionrate_] = NIntegrate[
   (pcaperstoppedmuon + pkperstoppedmuon + pnperstoppedmuon cl35capturefrn) *
    horizonfactor * slopestop[zcalc + density erosionrate t] Exp[-lamda t],
   {t, 0, 3000.0 / (erosionrate + 0.0000001)
    (*avoids div'n by zero*)(*integrates over time for 30 m of denudation*)}];

 (*denudation estimate*)
```

```
erosionestimate =
 Select[eros /.
 Solve[cosmocl36 ==
       (horizonfactordip (pcaspall + pkspall) / (lamda + density * eros / attn)) +

   ((1 - neutronmufrn) spallationfactor + neutronmufrn muonfactor)
        pfast horizonfactordip
        nthermalzcorrection cl[[1]] 43.6 * 10^-24 (*σth Cl-35*) * 1.6986 *
        10^16 (*atom Cl per microgram*) * 0.7577 (*Cl-35/Cl*)
        ((phistar / (lamda + (density eros / attn))) +
          (fthermal * deltaphi / (lamda + (density eros / lrock)))) +
       ((1 - neutronmufrn) spallationfactor + neutronmufrn muonfactor)
        pfast horizonfactordip nthermalzcorrection k2o[[1]] 0.0043 * 10^-24
        (*σth K-39 (n,alpha) Cl-36*) * 1.2787 * 10^20 (*atom K per % k2o*) *
        0.93258 (*k39/k*) ((phistar / (lamda + (density eros / attn))) +
          (fthermal * deltaphi / (lamda + (density eros / lrock)))),
     eros],
 (# > 0 &)][[1]];

erosiontrial = {0.8 erosionestimate, 1.5 erosionestimate};

fwdtrial =
Table[{0.0001 i, cliffspalln[dip, 0.0001 i] + nthermalsteadystate[0.0001 i] +
     nthermalksteadystate[0.0001 i] + nmuonsdip[0.0001 i] },
   {i, 10^4 erosiontrial[[1]],
    10^4 erosiontrial[[2]], 10^4 (erosiontrial[[2]] - erosiontrial[[1]]) / 30}];

concabove = Select[fwdtrial, (#[[2]] > cosmocl36 + cosmocl36stddvn &)];
concbelow = Select[fwdtrial, (#[[2]] < cosmocl36 - cosmocl36stddvn &)];

lowerosion = Last[concabove][[1]];
higherosion = First[concbelow][[1]];

fwdtrial2 =
  Table[{0.0001 i, cliffspalln[dip, 0.0001 i] + nthermalsteadystate[0.0001 i] +
     nthermalksteadystate[0.0001 i] + nmuonsdip[0.0001 i]},
   {i, 10^4 lowerosion, 10^4 higherosion, 10^4 (higherosion - lowerosion) / 20}];

deltalist = Map[(Abs[# - {0, cosmocl36}] &), fwdtrial2];

evalue = 10000 * Sort[deltalist, (#2[[2]] > #1[[2]] &)][[1, 1]];

deltaevalueiterative = Max[{10^4 higherosion - evalue, evalue - 10^4 lowerosion}];

(*Propagated uncertainty at the 1 sigma level of denudation rate calculation. Uses
   partial derivatives derived in the calculation of denudation
   error v2.nb. Propagates errors from Ca and K spallation production,
  Cl-36 cosmogenic concentration, Cl-35 and K-39 neutron capture production,
  Ca and K muon production, 5 % error in lamda and 10 % in attenuation length
   (for sloping samples) into denudation error. Based on rule in Taylor, 1997*)
deltaevalue = (10^4 * ((1 / (cosmocl36 density^2)
          (4.53279844764821504`*^-23 E^ (-zcalc / attn - zcalc / lrock)
            (1.10307132729322798`*^22 attn density E^ (zcalc / attn + zcalc / lrock)
               horizonfactordip + (4.86706541238577372`*^44
                  attn cosmocl36 density^2 E^ ((2 zcalc) / attn + (2
```

```
zcalc) / lrock) horizonfactordip lamda lrock -
2.20614265458645597`*^22 attn density^2 E^ (zcalc /
attn + zcalc / lrock) horizonfactordip
(1.10307132729322798`*^22 attn cosmocl36 E^ (zcalc /
attn + zcalc /
lrock) lamda + 1.10307132729322798`*^22 cosmocl36 E^ (zcalc /
attn + zcalc / lrock) lamda lrock -
1.10307132729322798`*^22 attn E^ (zcalc / attn + zcalc /
lrock) horizonfactordip pcaspall - 6.18982673067167876`*^15
cl[[1]] deltaphi E^ (zcalc / attn) fthermal
horizonfactordip lrock muonfactor neutronmufrn pfast -
5.65622678464828432`*^15 deltaphi E^ (zcalc / attn + zcalc /
lrock) fthermal horizonfactordip k2o[[1]]
lrock muonfactor neutronmufrn nthermalzcorrection
pfast - 6.18982673067167876`*^15 attn cl[[1]] E^ (zcalc /
lrock) horizonfactordip muonfactor neutronmufrn pfast
phistar - 5.65622678464828432`*^15 attn E^ (zcalc /
attn + zcalc / lrock) horizonfactordip k2o[[1]]
muonfactor neutronmufrn nthermalzcorrection pfast
phistar - 1.10307132729322798`*^22 attn E^ (zcalc /
attn + zcalc / lrock) horizonfactordip pkspall -
6.18982673067167876`*^15 cl[[1]] deltaphi E^ (zcalc /
attn) fthermal horizonfactordip lrock pfast spallationfactor +
6.18982673067167876`*^15 cl[[1]] deltaphi E^ (zcalc /
attn) fthermal horizonfactordip lrock neutronmufrn pfast
spallationfactor - 5.65622678464828432`*^15 deltaphi E^ (zcalc /
attn + zcalc / lrock) fthermal horizonfactordip k2o[[1]]
lrock nthermalzcorrection pfast spallationfactor +
5.65622678464828432`*^15 deltaphi E^ (zcalc / attn + zcalc /
lrock) fthermal horizonfactordip k2o[[1]] lrock
neutronmufrn nthermalzcorrection pfast spallationfactor -
6.18982673067167876`*^15 attn cl[[1]] E^ (zcalc /
lrock) horizonfactordip pfast phistar spallationfactor +
6.18982673067167876`*^15 attn cl[[1]] E^ (zcalc /
lrock) horizonfactordip neutronmufrn pfast phistar
spallationfactor - 5.65622678464828432`*^15 attn E^ (zcalc /
attn + zcalc / lrock) horizonfactordip k2o[[1]]
nthermalzcorrection pfast phistar spallationfactor +
5.65622678464828432`*^15 attn E^ (zcalc / attn + zcalc /
lrock) horizonfactordip k2o [[1]] neutronmufrn
nthermalzcorrection pfast phistar spallationfactor)) /
(2 √(-4.41228530917291195`*^22 attn cosmocl36 density^2 E^ (zcalc /
attn + zcalc / lrock) lamda
lrock (1.10307132729322798`*^22 cosmocl36 E^ (zcalc /
attn + zcalc /
lrock) lamda - 1.10307132729322798`*^22 E^ (zcalc /
attn + zcalc / lrock) horizonfactordip pcaspall -
6.18982673067167876`*^15 cl[[1]] deltaphi E^ (zcalc /
attn) fthermal horizonfactordip muonfactor neutronmufrn
pfast - 5.65622678464828432`*^15 deltaphi E^ (zcalc /
attn + zcalc / lrock) fthermal horizonfactordip k2o [[1]]
muonfactor neutronmufrn nthermalzcorrection
pfast - 6.18982673067167876`*^15 cl[[1]] E^ (zcalc /
lrock) horizonfactordip muonfactor neutronmufrn
pfast phistar - 5.65622678464828432`*^15 E^ (zcalc /
attn + zcalc / lrock) horizonfactordip k2o[[1]]
muonfactor neutronmufrn nthermalzcorrection
pfast phistar - 1.10307132729322798`*^22 E^ (zcalc /
attn + zcalc / lrock) horizonfactordip pkspall -
6.18982673067167876`*^15 cl[[1]] deltaphi E^ (zcalc /
attn) fthermal horizonfactordip pfast spallationfactor +
6.18982673067167876`*^15 cl[[1]] deltaphi E^ (zcalc /
attn) fthermal horizonfactordip neutronmufrn pfast spallationfactor -
5.65622678464828432`*^15 deltaphi E^ (zcalc /
attn + zcalc / lrock) fthermal horizonfactordip k2o [[1]]
nthermalzcorrection pfast spallationfactor +
5.65622678464828432`*^15 deltaphi E^ (zcalc /
attn + zcalc / lrock) fthermal horizonfactordip k2o[[1]]
neutronmufrn nthermalzcorrection pfast spallationfactor -
6.18982673067167876`*^15 cl[[1]] E^ (zcalc /
lrock) horizonfactordip pfast phistar spallationfactor +
6.18982673067167876`*^15 cl[[1]] E^ (zcalc /
lrock) horizonfactordip neutronmufrn pfast phistar
spallationfactor - 5.65622678464828432`*^15 E^ (zcalc /
attn + zcalc / lrock) horizonfactordip
k2o[[1]] nthermalzcorrection pfast phistar
spallationfactor + 5.65622678464828432`*^15 E^ (zcalc /
attn + zcalc / lrock) horizonfactordip k2o[[1]]
neutronmufrn nthermalzcorrection pfast phistar
spallationfactor) + density^2 (1.10307132729322798`*^22
attn cosmocl36 E^ (zcalc / attn +
zcalc / lrock)
lamda + 1.10307132729322798`*^22 cosmocl36 E^ (zcalc / attn +
zcalc / lrock) lamda
lrock - 1.10307132729322798`*^22 attn E^ (zcalc / attn +
zcalc / lrock) horizonfactordip pcaspall -
6.18982673067167876`*^15 cl[[1]] deltaphi E^ (zcalc /
attn) fthermal
horizonfactordip lrock muonfactor neutronmufrn
pfast - 5.65622678464828432`*^15 deltaphi E^ (zcalc / attn +
zcalc / lrock) fthermal horizonfactordip k2o[[1]]
lrock muonfactor neutronmufrn nthermalzcorrection
pfast - 6.18982673067167876`*^15 attn cl[[1]] E^ (zcalc /
lrock) horizonfactordip muonfactor neutronmufrn pfast
phistar - 5.65622678464828432`*^15 attn E^ (zcalc / attn +
zcalc / lrock) horizonfactordip k2o[[1]]
muonfactor neutronmufrn nthermalzcorrection pfast
phistar - 1.10307132729322798`*^22 attn E^ (zcalc / attn +
zcalc / lrock) horizonfactordip pkspall -
6.18982673067167876`*^15 cl[[1]] deltaphi E^ (zcalc /
attn) fthermal
horizonfactordip lrock pfast spallationfactor +
6.18982673067167876`*^15 cl[[1]] deltaphi E^ (zcalc /
attn) fthermal horizonfactordip
lrock neutronmufrn pfast spallationfactor -
5.65622678464828432`*^15 deltaphi E^ (zcalc / attn +
zcalc / lrock) fthermal horizonfactordip k2o[[1]]
lrock nthermalzcorrection pfast spallationfactor +
5.65622678464828432`*^15 deltaphi E^ (zcalc / attn +
```

```
                zcalc / lrock) fthermal horizonfactordip k2o[[1]] lrock
              neutronmufrn nthermalzcorrection pfast spallationfactor -
             6.18982673067167876`*^15 attn cl[[1]] E^ (zcalc /
                lrock) horizonfactordip pfast phistar spallationfactor +
             6.18982673067167876`*^15 attn cl[[1]] E^ (zcalc /
                lrock) horizonfactordip
              neutronmufrn pfast phistar spallationfactor -
             5.65622678464828432`*^15 attn E^ (zcalc / attn +
                zcalc / lrock) horizonfactordip k2o[[1]]
              nthermalzcorrection pfast phistar spallationfactor +
             5.65622678464828432`*^15 attn E^ (zcalc / attn +
                zcalc / lrock) horizonfactordip k2o[[1]] neutronmufrn
              nthermalzcorrection pfast phistar spallationfactor) ^2)))) *
  pcaspallstddvn) ^2 +
(1 / (cosmocl36 density^2) (4.53279844764821504`*^-23
    E^ (-zcalc / attn - zcalc / lrock) (1.10307132729322798`*^22 attn
      density E^ (zcalc / attn + zcalc / lrock) horizonfactordip +
      (4.86706541238577372`*^44 attn cosmocl36 density^2 E^ ((2
              zcalc) / attn + (2 zcalc) / lrock)
          horizonfactordip lamda lrock - 2.20614265458645597`*^22 attn
          density^2 E^ (zcalc / attn + zcalc / lrock) horizonfactordip
           (1.10307132729322798`*^22 attn cosmocl36 E^ (zcalc / attn + zcalc /
                lrock) lamda + 1.10307132729322798`*^22 cosmocl36 E^ (zcalc /
                attn + zcalc / lrock) lamda lrock -
            1.10307132729322798`*^22 attn E^ (zcalc / attn + zcalc /
                lrock) horizonfactordip pcaspall - 6.18982673067167876`*^15
             cl[[1]] deltaphi E^ (zcalc / attn) fthermal
             horizonfactordip lrock muonfactor neutronmufrn pfast -
            5.65622678464828432`*^15 deltaphi E^ (zcalc / attn + zcalc /
                lrock) fthermal horizonfactordip k2o[[1]] lrock
             muonfactor neutronmufrn nthermalzcorrection pfast -
            6.18982673067167876`*^15 attn cl[[1]] E^ (zcalc / lrock)
             horizonfactordip muonfactor neutronmufrn pfast phistar -
            5.65622678464828432`*^15 attn E^ (zcalc / attn + zcalc /
                lrock) horizonfactordip k2o[[1]] muonfactor
             neutronmufrn nthermalzcorrection pfast phistar -
            1.10307132729322798`*^22 attn E^ (zcalc / attn + zcalc / lrock)
             horizonfactordip pkspall - 6.18982673067167876`*^15 cl[[1]]
             deltaphi E^ (zcalc / attn) fthermal horizonfactordip
             lrock pfast spallationfactor + 6.18982673067167876`*^15
             cl[[1]] deltaphi E^ (zcalc / attn) fthermal
             horizonfactordip lrock neutronmufrn pfast spallationfactor -
            5.65622678464828432`*^15 deltaphi E^ (zcalc / attn + zcalc /
                lrock) fthermal horizonfactordip k2o[[1]]
             lrock nthermalzcorrection pfast spallationfactor +
            5.65622678464828432`*^15 deltaphi E^ (zcalc / attn + zcalc /
                lrock) fthermal horizonfactordip k2o[[1]] lrock
             neutronmufrn nthermalzcorrection pfast spallationfactor -
            6.18982673067167876`*^15 attn cl[[1]] E^ (zcalc /
                lrock) horizonfactordip pfast phistar spallationfactor +
            6.18982673067167876`*^15 attn cl[[1]] E^ (zcalc / lrock)
             horizonfactordip neutronmufrn pfast phistar spallationfactor -
            5.65622678464828432`*^15 attn E^ (zcalc / attn + zcalc / lrock)
             horizonfactordip k2o[[1]] nthermalzcorrection pfast phistar
             spallationfactor + 5.65622678464828432`*^15 attn E^ (zcalc /
                attn + zcalc / lrock) horizonfactordip k2o[[1]] neutronmufrn
              nthermalzcorrection pfast phistar spallationfactor)) /
(2 √(-4.41228530917291195`*^22 attn cosmocl36 density^2 E^ (zcalc /
                attn + zcalc / lrock) lamda
            lrock (1.10307132729322798`*^22 cosmocl36 E^ (zcalc /
                attn + zcalc /
                lrock) lamda - 1.10307132729322798`*^22 E^ (zcalc /
                attn + zcalc / lrock) horizonfactordip pcaspall -
              6.18982673067167876`*^15 cl[[1]] deltaphi E^ (zcalc /
                attn) fthermal horizonfactordip muonfactor neutronmufrn
              pfast - 5.65622678464828432`*^15 deltaphi E^ (zcalc /
                attn + zcalc / lrock) fthermal horizonfactordip k2o[[1]]
              muonfactor neutronmufrn nthermalzcorrection
              pfast - 6.18982673067167876`*^15 cl[[1]] E^ (zcalc /
                lrock) horizonfactordip muonfactor neutronmufrn
              pfast phistar - 5.65622678464828432`*^15 E^ (zcalc /
                attn + zcalc / lrock) horizonfactordip k2o[[1]]
              muonfactor neutronmufrn nthermalzcorrection
              pfast phistar - 1.10307132729322798`*^22 E^ (zcalc /
                attn + zcalc / lrock) horizonfactordip pkspall -
              6.18982673067167876`*^15 cl[[1]] deltaphi E^ (zcalc /
                attn) fthermal horizonfactordip pfast spallationfactor +
              6.18982673067167876`*^15 cl[[1]] deltaphi E^ (zcalc /
                attn) fthermal
              horizonfactordip neutronmufrn pfast spallationfactor -
              5.65622678464828432`*^15 deltaphi E^ (zcalc /
                attn + zcalc / lrock) fthermal horizonfactordip k2o[[1]]
              nthermalzcorrection pfast spallationfactor +
              5.65622678464828432`*^15 deltaphi E^ (zcalc /
                attn + zcalc / lrock) fthermal horizonfactordip k2o[[1]]
              neutronmufrn nthermalzcorrection pfast spallationfactor -
              6.18982673067167876`*^15 cl[[1]] E^ (zcalc /
                lrock) horizonfactordip pfast phistar spallationfactor +
              6.18982673067167876`*^15 cl[[1]] E^ (zcalc /
                lrock) horizonfactordip neutronmufrn pfast phistar
              spallationfactor - 5.65622678464828432`*^15 E^ (zcalc /
                attn + zcalc / lrock) horizonfactordip
              k2o[[1]] nthermalzcorrection pfast phistar
              spallationfactor + 5.65622678464828432`*^15 E^ (zcalc /
                attn + zcalc / lrock) horizonfactordip k2o[[1]]
              neutronmufrn nthermalzcorrection pfast phistar
              spallationfactor) + density^2 (1.10307132729322798`*^22
               attn cosmocl36 E^ (zcalc / attn +
                zcalc / lrock)
               lamda + 1.10307132729322798`*^22 cosmocl36 E^ (zcalc / attn +
                zcalc / lrock) lamda
               lrock - 1.10307132729322798`*^22 attn E^ (zcalc / attn +
                zcalc / lrock) horizonfactordip pcaspall -
              6.18982673067167876`*^15 cl[[1]] deltaphi E^ (zcalc /
                attn) fthermal
               horizonfactordip lrock muonfactor neutronmufrn
               pfast - 5.65622678464828432`*^15 deltaphi E^ (zcalc / attn +
                zcalc / lrock) fthermal horizonfactordip k2o[[1]]
               lrock muonfactor neutronmufrn nthermalzcorrection
               pfast - 6.18982673067167876`*^15 attn cl[[1]] E^ (zcalc /
```

```
lrock) horizonfactordip muonfactor neutronmufrn pfast
phistar - 5.65622678464828432`*^15 attn E^ (zcalc / attn +
zcalc / lrock) horizonfactordip k2o[[1]]
muonfactor neutronmufrn nthermalzcorrection pfast
phistar - 1.10307132729322798`*^22 attn E^ (zcalc / attn +
zcalc / lrock) horizonfactordip pkspall1 -
6.18982673067167876`*^15 cl[[1]] deltaphi E^ (zcalc /
attn) fthermal
horizonfactordip lrock pfast spallationfactor +
6.18982673067167876`*^15 cl[[1]] deltaphi E^ (zcalc /
attn) fthermal horizonfactordip
lrock neutronmufrn pfast spallationfactor -
5.65622678464828432`*^15 deltaphi E^ (zcalc / attn +
zcalc / lrock) fthermal horizonfactordip k2o[[1]]
lrock nthermalzcorrection pfast spallationfactor +
5.65622678464828432`*^15 deltaphi E^ (zcalc / attn +
zcalc / lrock) fthermal horizonfactordip k2o [[1]] lrock
neutronmufrn nthermalzcorrection pfast spallationfactor -
6.18982673067167876`*^15 attn cl[[1]] E^ (zcalc /
lrock) horizonfactordip pfast phistar spallationfactor +
6.18982673067167876`*^15 attn cl[[1]] E^ (zcalc /
lrock) horizonfactordip
neutronmufrn pfast phistar spallationfactor -
5.65622678464828432`*^15 attn E^ (zcalc / attn +
zcalc / lrock) horizonfactordip k2o[[1]]
nthermalzcorrection pfast phistar spallationfactor +
5.65622678464828432`*^15 attn E^ (zcalc / attn +
zcalc / lrock) horizonfactordip k2o[[1]] neutronmufrn
nthermalzcorrection pfast phistar spallationfactor) ^2)))) *
pkspallstddvn) ^2 +
(1 / (cosmocl36 density^2) (4.53279844764821504`*^-23
E^ (-zcalc / attn - zcalc / lrock) (-1.` density (-6.18982673067167876`*^15
cl[[1]] deltaphi E^ (zcalc / attn) fthermal horizonfactordip lrock
muonfactor neutronmufrn - 5.65622678464828432`*^15 deltaphi
E^ (zcalc / attn + zcalc / lrock) fthermal horizonfactordip k2o[[1]]
lrock muonfactor neutronmufrn nthermalzcorrection -
6.18982673067167876`*^15 attn cl[[1]] E^ (zcalc / lrock)
horizonfactordip muonfactor neutronmufrn phistar -
5.65622678464828432`*^15 attn E^ (zcalc / attn + zcalc /
lrock) horizonfactordip k2o[[1]] muonfactor neutronmufrn
nthermalzcorrection phistar - 6.18982673067167876`*^15 cl[[1]]
deltaphi E^ (zcalc / attn) fthermal horizonfactordip lrock
spallationfactor + 6.18982673067167876`*^15 cl[[1]] deltaphi
E^ (zcalc / attn) fthermal horizonfactordip lrock neutronmufrn
spallationfactor - 5.65622678464828432`*^15 deltaphi E^ (zcalc /
attn + zcalc / lrock) fthermal horizonfactordip k2o[[1]] lrock
nthermalzcorrection spallationfactor + 5.65622678464828432`*^15
deltaphi E^ (zcalc / attn + zcalc / lrock) fthermal horizonfactordip
k2o[[1]] lrock neutronmufrn nthermalzcorrection spallationfactor -
6.18982673067167876`*^15 attn cl[[1]] E^ (zcalc /
lrock) horizonfactordip phistar spallationfactor +
6.18982673067167876`*^15 attn cl[[1]] E^ (zcalc / lrock)
horizonfactordip neutronmufrn phistar spallationfactor -
5.65622678464828432`*^15 attn E^ (zcalc / attn + zcalc /
lrock) horizonfactordip k2o[[1]] nthermalzcorrection phistar
spallationfactor + 5.65622678464828432`*^15 attn E^ (zcalc /
attn + zcalc / lrock) horizonfactordip k2o[[1]]
neutronmufrn nthermalzcorrection phistar spallationfactor) +
(-4.41228530917291195`*^22 attn cosmocl36 density^2 E^ (zcalc / attn +
zcalc / lrock) lamda lrock (-6.18982673067167876`*^15 cl[[1]]
deltaphi E^ (zcalc / attn) fthermal horizonfactordip
muonfactor neutronmufrn - 5.65622678464828432`*^15
deltaphi E^ (zcalc / attn + zcalc / lrock)
fthermal horizonfactordip k2o[[1]] muonfactor neutronmufrn
nthermalzcorrection - 6.18982673067167876`*^15 cl[[1]] E^
(zcalc / lrock) horizonfactordip muonfactor
neutronmufrn phistar - 5.65622678464828432`*^15 E^ (zcalc /
attn + zcalc / lrock) horizonfactordip k2o[[1]]
muonfactor neutronmufrn nthermalzcorrection phistar -
6.18982673067167876`*^15 cl[[1]] deltaphi E^ (zcalc /
attn) fthermal horizonfactordip spallationfactor +
6.18982673067167876`*^15 cl[[1]] deltaphi E^ (zcalc /
attn) fthermal horizonfactordip neutronmufrn
spallationfactor - 5.65622678464828432`*^15 deltaphi E^ (zcalc /
attn + zcalc / lrock) fthermal horizonfactordip
k2o[[1]] nthermalzcorrection spallationfactor +
5.65622678464828432`*^15 deltaphi E^ (zcalc / attn + zcalc /
lrock) fthermal horizonfactordip k2o[[1]] neutronmufrn
nthermalzcorrection spallationfactor - 6.18982673067167876`*^15
cl[[1]] E^ (zcalc / lrock) horizonfactordip phistar
spallationfactor + 6.18982673067167876`*^15 cl[[1]] E^ (zcalc /
lrock) horizonfactordip neutronmufrn phistar
spallationfactor - 5.65622678464828432`*^15 E^ (zcalc / attn +
zcalc / lrock) horizonfactordip k2o[[1]] nthermalzcorrection
phistar spallationfactor + 5.65622678464828432`*^15 E^ (zcalc /
attn + zcalc / lrock) horizonfactordip k2o[[1]] neutronmufrn
nthermalzcorrection phistar spallationfactor) + 2 density^2
(-6.18982673067167876`*^15 cl[[1]] deltaphi E^ (zcalc / attn)
fthermal horizonfactordip lrock muonfactor neutronmufrn -
5.65622678464828432`*^15 deltaphi E^ (zcalc / attn + zcalc /
lrock) fthermal horizonfactordip k2o[[1]]
lrock muonfactor neutronmufrn nthermalzcorrection -
6.18982673067167876`*^15 attn cl[[1]] E^ (zcalc /
lrock) horizonfactordip muonfactor neutronmufrn phistar -
5.65622678464828432`*^15 attn E^ (zcalc / attn + zcalc /
lrock) horizonfactordip k2o[[1]] muonfactor neutronmufrn
nthermalzcorrection phistar - 6.18982673067167876`*^15 cl[[1]]
deltaphi E^ (zcalc / attn) fthermal horizonfactordip
lrock spallationfactor + 6.18982673067167876`*^15 cl[[1]]
deltaphi E^ (zcalc / attn) fthermal horizonfactordip
lrock neutronmufrn spallationfactor - 5.65622678464828432`*^15
deltaphi E^ (zcalc / attn + zcalc / lrock)
fthermal horizonfactordip k2o[[1]] lrock nthermalzcorrection
spallationfactor + 5.65622678464828432`*^15 deltaphi E^ (zcalc /
attn + zcalc / lrock) fthermal horizonfactordip k2o[[1]] lrock
neutronmufrn nthermalzcorrection spallationfactor -
6.18982673067167876`*^15 attn cl[[1]] E^ (zcalc /
lrock) horizonfactordip phistar spallationfactor +
6.18982673067167876`*^15 attn cl[[1]] E^ (zcalc / lrock)
horizonfactordip neutronmufrn phistar spallationfactor -
```

```
5.65622678464828432`*^15 attn E^ (zcalc / attn + zcalc / lrock)
 horizonfactordip k2o[[1]] nthermalzcorrection phistar
 spallationfactor + 5.65622678464828432`*^15 attn E^ (zcalc /
     attn + zcalc / lrock) horizonfactordip k2o[[1]] neutronmufrn
 nthermalzcorrection phistar spallationfactor)
(1.10307132729322798`*^22 attn cosmocl36 E^ (zcalc / attn + zcalc /
     lrock) lamda + 1.10307132729322798`*^22 cosmocl36 E^ (zcalc /
     attn + zcalc / lrock) lamda lrock -
 1.10307132729322798`*^22 attn E^ (zcalc / attn + zcalc /
     lrock) horizonfactordip pcaspall - 6.18982673067167876`*^15
 cl[[1]] deltaphi E^ (zcalc / attn) fthermal
 horizonfactordip lrock muonfactor neutronmufrn pfast -
 5.65622678464828432`*^15 deltaphi E^ (zcalc / attn + zcalc /
     lrock) fthermal horizonfactordip k2o[[1]] lrock
 muonfactor neutronmufrn nthermalzcorrection pfast -
 6.18982673067167876`*^15 attn cl[[1]] E^ (zcalc / lrock)
 horizonfactordip muonfactor neutronmufrn pfast phistar -
 5.65622678464828432`*^15 attn E^ (zcalc / attn + zcalc /
     lrock) horizonfactordip k2o[[1]] muonfactor
 neutronmufrn nthermalzcorrection pfast phistar -
 1.10307132729322798`*^22 attn E^ (zcalc / attn + zcalc / lrock)
 horizonfactordip pkspall - 6.18982673067167876`*^15 cl[[1]]
 deltaphi E^ (zcalc / attn) fthermal horizonfactordip
 lrock pfast spallationfactor + 6.18982673067167876`*^15
 cl[[1]] deltaphi E^ (zcalc / attn) fthermal
 horizonfactordip lrock neutronmufrn pfast spallationfactor -
 5.65622678464828432`*^15 deltaphi E^ (zcalc / attn + zcalc /
     lrock) fthermal horizonfactordip k2o[[1]]
 lrock nthermalzcorrection pfast spallationfactor +
 5.65622678464828432`*^15 deltaphi E^ (zcalc / attn + zcalc /
     lrock) fthermal horizonfactordip k2o[[1]] lrock
 neutronmufrn nthermalzcorrection pfast spallationfactor -
 6.18982673067167876`*^15 attn cl[[1]] E^ (zcalc /
    lrock) horizonfactordip pfast phistar spallationfactor +
 6.18982673067167876`*^15 attn cl[[1]] E^ (zcalc / lrock)
 horizonfactordip neutronmufrn pfast phistar spallationfactor -
 5.65622678464828432`*^15 attn E^ (zcalc / attn + zcalc / lrock)
 horizonfactordip k2o[[1]] nthermalzcorrection pfast phistar
 spallationfactor + 5.65622678464828432`*^15 attn E^ (zcalc /
     attn + zcalc / lrock) horizonfactordip k2o[[1]] neutronmufrn
 nthermalzcorrection pfast phistar spallationfactor)) /
(2 √(-4.41228530917291195`*^22 attn cosmocl36 density^2 E^ (zcalc /
     attn + zcalc / lrock) lamda
 lrock (1.10307132729322798`*^22 cosmocl36 E^ (zcalc /
       attn + zcalc /
       lrock) lamda - 1.10307132729322798`*^22 E^ (zcalc /
       attn + zcalc / lrock) horizonfactordip pcaspall -
   6.18982673067167876`*^15 cl[[1]] deltaphi E^ (zcalc /
      attn) fthermal horizonfactordip muonfactor neutronmufrn
  pfast - 5.65622678464828432`*^15 deltaphi E^ (zcalc /
       attn + zcalc / lrock) fthermal horizonfactordip k2o[[1]]
  muonfactor neutronmufrn nthermalzcorrection
  pfast - 6.18982673067167876`*^15 cl[[1]] E^ (zcalc /
     lrock) horizonfactordip muonfactor neutronmufrn
  pfast phistar - 5.65622678464828432`*^15 E^ (zcalc /
     attn + zcalc / lrock) horizonfactordip k2o[[1]]
 muonfactor neutronmufrn nthermalzcorrection
 pfast phistar - 1.10307132729322798`*^22 E^ (zcalc /
     attn + zcalc / lrock) horizonfactordip pkspall -
 6.18982673067167876`*^15 cl[[1]] deltaphi E^ (zcalc /
    attn) fthermal horizonfactordip pfast spallationfactor +
 6.18982673067167876`*^15 cl[[1]] deltaphi E^ (zcalc /
    attn) fthermal
 horizonfactordip neutronmufrn pfast spallationfactor -
 5.65622678464828432`*^15 deltaphi E^ (zcalc /
     attn + zcalc / lrock) fthermal horizonfactordip k2o[[1]]
 nthermalzcorrection pfast spallationfactor +
 5.65622678464828432`*^15 deltaphi E^ (zcalc /
     attn + zcalc / lrock) fthermal horizonfactordip k2o[[1]]
 neutronmufrn nthermalzcorrection pfast spallationfactor -
 6.18982673067167876`*^15 cl[[1]] E^ (zcalc /
    lrock) horizonfactordip pfast phistar spallationfactor +
 6.18982673067167876`*^15 cl[[1]] E^ (zcalc /
    lrock) horizonfactordip neutronmufrn pfast phistar
 spallationfactor - 5.65622678464828432`*^15 E^ (zcalc /
     attn + zcalc / lrock) horizonfactordip
 k2o[[1]] nthermalzcorrection pfast phistar
 spallationfactor + 5.65622678464828432`*^15 E^ (zcalc /
     attn + zcalc / lrock) horizonfactordip k2o[[1]]
 neutronmufrn nthermalzcorrection pfast phistar
 spallationfactor) + density^2 (1.10307132729322798`*^22
  attn cosmocl36 E^ (zcalc / attn +
     zcalc / lrock)
  lamda + 1.10307132729322798`*^22 cosmocl36 E^ (zcalc / attn +
     zcalc / lrock) lamda
  lrock - 1.10307132729322798`*^22 attn E^ (zcalc / attn +
     zcalc / lrock) horizonfactordip pcaspall -
 6.18982673067167876`*^15 cl[[1]] deltaphi E^ (zcalc /
     attn) fthermal
  horizonfactordip lrock muonfactor neutronmufrn
  pfast - 5.65622678464828432`*^15 deltaphi E^ (zcalc / attn +
     zcalc / lrock) fthermal horizonfactordip k2o[[1]]
  lrock muonfactor neutronmufrn nthermalzcorrection
  pfast - 6.18982673067167876`*^15 attn cl[[1]] E^ (zcalc /
     lrock) horizonfactordip muonfactor neutronmufrn pfast
  phistar - 5.65622678464828432`*^15 attn E^ (zcalc / attn +
     zcalc / lrock) horizonfactordip k2o[[1]]
  muonfactor neutronmufrn nthermalzcorrection pfast
  phistar - 1.10307132729322798`*^22 attn E^ (zcalc / attn +
     zcalc / lrock) horizonfactordip pkspall -
 6.18982673067167876`*^15 cl[[1]] deltaphi E^ (zcalc /
     attn) fthermal
  horizonfactordip lrock pfast spallationfactor +
 6.18982673067167876`*^15 cl[[1]] deltaphi E^ (zcalc /
     attn) fthermal horizonfactordip
  lrock neutronmufrn pfast spallationfactor -
 5.65622678464828432`*^15 deltaphi E^ (zcalc / attn +
     zcalc / lrock) fthermal horizonfactordip k2o[[1]]
  lrock nthermalzcorrection pfast spallationfactor +
 5.65622678464828432`*^15 deltaphi E^ (zcalc / attn +
```

```
zcalc / lrock) fthermal horizonfactordip k2o[[1]] lrock
 neutronmufrn nthermalzcorrection pfast spallationfactor -
6.18982673067167876`*^15 attn cl[[1]] E^ (zcalc /
    lrock) horizonfactordip pfast phistar spallationfactor +
6.18982673067167876`*^15 attn cl[[1]] E^ (zcalc /
    lrock) horizonfactordip
 neutronmufrn pfast phistar spallationfactor -
5.65622678464828432`*^15 attn E^ (zcalc / attn +
    zcalc / lrock) horizonfactordip k2o[[1]]
 nthermalzcorrection pfast phistar spallationfactor +
5.65622678464828432`*^15 attn E^ (zcalc / attn +
    zcalc / lrock) horizonfactordip k2o[[1]] neutronmufrn
 nthermalzcorrection pfast phistar spallationfactor) ^2)))) *
pfaststddvn) ^2 +
(1 / (cosmocl36 density^2) (4.53279844764821504`*^-23
  E^ (-zcalc / attn - zcalc / lrock) (-1.` density (-6.18982673067167876`*^15
      deltaphi E^ (zcalc / attn) fthermal horizonfactordip lrock muonfactor
      neutronmufrn pfast - 6.18982673067167876`*^15 attn E^ (zcalc / lrock)
      horizonfactordip muonfactor neutronmufrn pfast phistar -
     6.18982673067167876`*^15 deltaphi E^ (zcalc / attn)
      fthermal horizonfactordip lrock pfast spallationfactor +
     6.18982673067167876`*^15 deltaphi E^ (zcalc / attn) fthermal
      horizonfactordip lrock neutronmufrn pfast spallationfactor -
     6.18982673067167876`*^15 attn E^ (zcalc / lrock) horizonfactordip
      pfast phistar spallationfactor + 6.18982673067167876`*^15 attn
      E^ (zcalc / lrock) horizonfactordip neutronmufrn pfast phistar
      spallationfactor) + (-4.41228530917291195`*^22 attn
      cosmocl36 density^2 E^ (zcalc / attn + zcalc / lrock) lamda lrock
      (-6.18982673067167876`*^15 deltaphi E^ (zcalc / attn) fthermal
         horizonfactordip muonfactor neutronmufrn pfast -
        6.18982673067167876`*^15 E^ (zcalc / lrock) horizonfactordip
         muonfactor neutronmufrn pfast phistar - 6.18982673067167876`*^15
         deltaphi E^ (zcalc / attn) fthermal horizonfactordip
         pfast spallationfactor + 6.18982673067167876`*^15 deltaphi E^
          (zcalc / attn) fthermal horizonfactordip neutronmufrn
         pfast spallationfactor - 6.18982673067167876`*^15 E^ (zcalc /
            lrock) horizonfactordip pfast phistar spallationfactor +
        6.18982673067167876`*^15 E^ (zcalc / lrock) horizonfactordip
         neutronmufrn pfast phistar spallationfactor) +
      2 density^2 (-6.18982673067167876`*^15 deltaphi E^ (zcalc /
            attn) fthermal horizonfactordip lrock muonfactor neutronmufrn
         pfast - 6.18982673067167876`*^15 attn E^ (zcalc /
            lrock) horizonfactordip muonfactor neutronmufrn pfast
         phistar - 6.18982673067167876`*^15 deltaphi E^ (zcalc /
            attn) fthermal horizonfactordip lrock pfast spallationfactor +
        6.18982673067167876`*^15 deltaphi E^ (zcalc / attn) fthermal
         horizonfactordip lrock neutronmufrn pfast spallationfactor -
        6.18982673067167876`*^15 attn E^ (zcalc / lrock) horizonfactordip
         pfast phistar spallationfactor + 6.18982673067167876`*^15
         attn E^ (zcalc / lrock) horizonfactordip
         neutronmufrn pfast phistar spallationfactor)
       (1.10307132729322798`*^22 attn cosmocl36 E^ (zcalc / attn + zcalc /
            lrock) lamda + 1.10307132729322798`*^22 cosmocl36 E^ (zcalc /
            attn + zcalc / lrock) lamda lrock -
        1.10307132729322798`*^22 attn E^ (zcalc / attn + zcalc /
```

```
lrock) horizonfactordip pcaspall - 6.18982673067167876`*^15
 cl[[1]] deltaphi E^ (zcalc / attn) fthermal
 horizonfactordip lrock muonfactor neutronmufrn pfast -
5.65622678464828432`*^15 deltaphi E^ (zcalc / attn + zcalc /
    lrock) fthermal horizonfactordip k2o[[1]] lrock
 muonfactor neutronmufrn nthermalzcorrection pfast -
6.18982673067167876`*^15 attn cl[[1]] E^ (zcalc / lrock)
 horizonfactordip muonfactor neutronmufrn pfast phistar -
5.65622678464828432`*^15 attn E^ (zcalc / attn + zcalc /
    lrock) horizonfactordip k2o[[1]] muonfactor
 neutronmufrn nthermalzcorrection pfast phistar -
1.10307132729322798`*^22 attn E^ (zcalc / attn + zcalc / lrock)
 horizonfactordip pkspall - 6.18982673067167876`*^15 cl[[1]]
 deltaphi E^ (zcalc / attn) fthermal horizonfactordip
 lrock pfast spallationfactor + 6.18982673067167876`*^15
 cl[[1]] deltaphi E^ (zcalc / attn) fthermal
 horizonfactordip lrock neutronmufrn pfast spallationfactor -
5.65622678464828432`*^15 deltaphi E^ (zcalc / attn + zcalc /
    lrock) fthermal horizonfactordip k2o[[1]]
 lrock nthermalzcorrection pfast spallationfactor +
5.65622678464828432`*^15 deltaphi E^ (zcalc / attn + zcalc /
    lrock) fthermal horizonfactordip k2o[[1]] lrock
 neutronmufrn nthermalzcorrection pfast spallationfactor -
6.18982673067167876`*^15 attn cl[[1]] E^ (zcalc /
    lrock) horizonfactordip pfast phistar spallationfactor +
6.18982673067167876`*^15 attn cl[[1]] E^ (zcalc / lrock)
 horizonfactordip neutronmufrn pfast phistar spallationfactor -
5.65622678464828432`*^15 attn E^ (zcalc / attn + zcalc / lrock)
 horizonfactordip k2o[[1]] nthermalzcorrection pfast phistar
 spallationfactor + 5.65622678464828432`*^15 attn E^ (zcalc /
    attn + zcalc / lrock) horizonfactordip k2o[[1]] neutronmufrn
 nthermalzcorrection pfast phistar spallationfactor)) /
(2 √(-4.41228530917291195`*^22 attn cosmocl36 density^2 E^ (zcalc /
    attn + zcalc / lrock) lamda
 lrock (1.10307132729322798`*^22 cosmocl36 E^ (zcalc /
       attn + zcalc /
       lrock) lamda - 1.10307132729322798`*^22 E^ (zcalc /
       attn + zcalc / lrock) horizonfactordip pcaspall -
   6.18982673067167876`*^15 cl[[1]] deltaphi E^ (zcalc /
      attn) fthermal horizonfactordip muonfactor neutronmufrn
    pfast - 5.65622678464828432`*^15 deltaphi E^ (zcalc /
       attn + zcalc / lrock) fthermal horizonfactordip k2o[[1]]
    muonfactor neutronmufrn nthermalzcorrection
    pfast - 6.18982673067167876`*^15 cl[[1]] E^ (zcalc /
      lrock) horizonfactordip muonfactor neutronmufrn
    pfast phistar - 5.65622678464828432`*^15 E^ (zcalc /
       attn + zcalc / lrock) horizonfactordip k2o[[1]]
    muonfactor neutronmufrn nthermalzcorrection
    pfast phistar - 1.10307132729322798`*^22 E^ (zcalc /
       attn + zcalc / lrock) horizonfactordip pkspall -
   6.18982673067167876`*^15 cl[[1]] deltaphi E^ (zcalc /
      attn) fthermal horizonfactordip pfast spallationfactor +
   6.18982673067167876`*^15 cl[[1]] deltaphi E^ (zcalc /
      attn) fthermal
    horizonfactordip neutronmufrn pfast spallationfactor -
```

```
5.65622678464828432`*^15 deltaphi E^(zcalc/
      attn + zcalc/lrock) fthermal horizonfactordip k2o[[1]]
 nthermalzcorrection pfast spallationfactor +
5.65622678464828432`*^15 deltaphi E^(zcalc/
      attn + zcalc/lrock) fthermal horizonfactordip k2o[[1]]
 neutronmufrn nthermalzcorrection pfast spallationfactor -
6.18982673067167876`*^15 cl[[1]] E^(zcalc/
     lrock) horizonfactordip pfast phistar spallationfactor +
6.18982673067167876`*^15 cl[[1]] E^(zcalc/
     lrock) horizonfactordip neutronmufrn pfast phistar
 spallationfactor - 5.65622678464828432`*^15 E^(zcalc/
      attn + zcalc/lrock) horizonfactordip
 k2o[[1]] nthermalzcorrection pfast phistar
 spallationfactor + 5.65622678464828432`*^15 E^(zcalc/
      attn + zcalc/lrock) horizonfactordip k2o[[1]]
 neutronmufrn nthermalzcorrection pfast phistar
 spallationfactor) + density^2 (1.10307132729322798`*^22
  attn cosmocl36 E^(zcalc/attn +
      zcalc/lrock)
  lamda + 1.10307132729322798`*^22 cosmocl36 E^(zcalc/attn +
      zcalc/lrock) lamda
  lrock - 1.10307132729322798`*^22 attn E^(zcalc/attn +
      zcalc/lrock) horizonfactordip pcaspall -
6.18982673067167876`*^15 cl[[1]] deltaphi E^(zcalc/
      attn) fthermal
  horizonfactordip lrock muonfactor neutronmufrn
  pfast - 5.65622678464828432`*^15 deltaphi E^(zcalc/attn +
      zcalc/lrock) fthermal horizonfactordip k2o[[1]]
  lrock muonfactor neutronmufrn nthermalzcorrection
  pfast - 6.18982673067167876`*^15 attn cl[[1]] E^(zcalc/
      lrock) horizonfactordip muonfactor neutronmufrn pfast
  phistar - 5.65622678464828432`*^15 attn E^(zcalc/attn +
      zcalc/lrock) horizonfactordip k2o[[1]]
  muonfactor neutronmufrn nthermalzcorrection pfast
  phistar - 1.10307132729322798`*^22 attn E^(zcalc/attn +
      zcalc/lrock) horizonfactordip pkspall -
6.18982673067167876`*^15 cl[[1]] deltaphi E^(zcalc/
      attn) fthermal
  horizonfactordip lrock pfast spallationfactor +
6.18982673067167876`*^15 cl[[1]] deltaphi E^(zcalc/
      attn) fthermal horizonfactordip
  lrock neutronmufrn pfast spallationfactor -
5.65622678464828432`*^15 deltaphi E^(zcalc/attn +
      zcalc/lrock) fthermal horizonfactordip k2o[[1]]
  lrock nthermalzcorrection pfast spallationfactor +
5.65622678464828432`*^15 deltaphi E^(zcalc/attn +
      zcalc/lrock) fthermal horizonfactordip k2o[[1]] lrock
  neutronmufrn nthermalzcorrection pfast spallationfactor -
6.18982673067167876`*^15 attn cl[[1]] E^(zcalc/
      lrock) horizonfactordip pfast phistar spallationfactor +
6.18982673067167876`*^15 attn cl[[1]] E^(zcalc/
      lrock) horizonfactordip
  neutronmufrn pfast phistar spallationfactor -
5.65622678464828432`*^15 attn E^(zcalc/attn +
      zcalc/lrock) horizonfactordip k2o[[1]]
```

```
      nthermalzcorrection pfast phistar spallationfactor +
     5.65622678464828432`*^15 attn E^(zcalc/attn +
         zcalc/lrock) horizonfactordip
      k2o[[1]] neutronmufrn nthermalzcorrection pfast
      phistar spallationfactor)^2)))) * cl[[2]])^2 +
(1/(cosmocl36 density^2) (4.53279844764821504`*^-23
    E^(-zcalc/attn - zcalc/lrock) (-1.` density (-6.18982673067167876`*^15
      attn cl[[1]] E^(zcalc/lrock) horizonfactordip muonfactor
      neutronmufrn pfast - 5.65622678464828432`*^15 attn E^(zcalc/attn +
         zcalc/lrock) horizonfactordip k2o[[1]] muonfactor neutronmufrn
      nthermalzcorrection pfast - 6.18982673067167876`*^15 attn cl[[1]]
      E^(zcalc/lrock) horizonfactordip pfast spallationfactor +
     6.18982673067167876`*^15 attn cl[[1]] E^(zcalc/lrock)
      horizonfactordip neutronmufrn pfast spallationfactor -
     5.65622678464828432`*^15 attn E^(zcalc/attn + zcalc/
         lrock) horizonfactordip k2o[[1]] nthermalzcorrection pfast
      spallationfactor + 5.65622678464828432`*^15 attn E^(zcalc/
         attn + zcalc/lrock) horizonfactordip k2o[[1]]
      neutronmufrn nthermalzcorrection pfast spallationfactor) +
   (-4.41228530917291195`*^22 attn cosmocl36 density^2 E^(zcalc/attn +
      zcalc/lrock) lamda lrock (-6.18982673067167876`*^15 cl[[1]] E^
       (zcalc/lrock) horizonfactordip muonfactor
      neutronmufrn pfast - 5.65622678464828432`*^15 E^(zcalc/
         attn + zcalc/lrock) horizonfactordip
      k2o[[1]] muonfactor neutronmufrn nthermalzcorrection
      pfast - 6.18982673067167876`*^15 cl[[1]] E^(zcalc/
         lrock) horizonfactordip pfast
      spallationfactor + 6.18982673067167876`*^15 cl[[1]] E^(zcalc/
         lrock) horizonfactordip neutronmufrn pfast spallationfactor -
     5.65622678464828432`*^15 E^(zcalc/attn + zcalc/
         lrock) horizonfactordip k2o[[1]] nthermalzcorrection pfast
      spallationfactor + 5.65622678464828432`*^15 E^(zcalc/
         attn + zcalc/lrock) horizonfactordip k2o[[1]] neutronmufrn
      nthermalzcorrection pfast spallationfactor) +
   2 density^2 (-6.18982673067167876`*^15 attn cl[[1]] E^(zcalc/
         lrock) horizonfactordip muonfactor neutronmufrn
      pfast - 5.65622678464828432`*^15 attn E^(zcalc/
         attn + zcalc/lrock) horizonfactordip
      k2o[[1]] muonfactor neutronmufrn nthermalzcorrection
      pfast - 6.18982673067167876`*^15 attn cl[[1]] E^(zcalc/
         lrock) horizonfactordip pfast spallationfactor +
     6.18982673067167876`*^15 attn cl[[1]] E^(zcalc/
         lrock) horizonfactordip neutronmufrn pfast spallationfactor -
     5.65622678464828432`*^15 attn E^(zcalc/attn + zcalc/
         lrock) horizonfactordip k2o[[1]] nthermalzcorrection pfast
      spallationfactor + 5.65622678464828432`*^15 attn E^(zcalc/
         attn + zcalc/lrock) horizonfactordip k2o[[1]]
      neutronmufrn nthermalzcorrection pfast spallationfactor)
    (1.10307132729322798`*^22 attn cosmocl36 E^(zcalc/attn + zcalc/
         lrock) lamda + 1.10307132729322798`*^22 cosmocl36 E^(zcalc/
         attn + zcalc/lrock) lamda lrock -
     1.10307132729322798`*^22 attn E^(zcalc/attn + zcalc/
         lrock) horizonfactordip pcaspall - 6.18982673067167876`*^15
      cl[[1]] deltaphi E^(zcalc/attn) fthermal
      horizonfactordip lrock muonfactor neutronmufrn pfast -
```

```
5.65622678464828432`*^15 deltaphi E^ (zcalc / attn + zcalc /
      lrock) fthermal horizonfactordip k2o[[1]] lrock
 muonfactor neutronmufrn nthermalzcorrection pfast -
6.18982673067167876`*^15 attn cl[[1]] E^ (zcalc / lrock)
 horizonfactordip muonfactor neutronmufrn pfast phistar -
5.65622678464828432`*^15 attn E^ (zcalc / attn + zcalc /
      lrock) horizonfactordip k2o[[1]] muonfactor
 neutronmufrn nthermalzcorrection pfast phistar -
1.10307132729322798`*^22 attn E^ (zcalc / attn + zcalc / lrock)
 horizonfactordip pkspall - 6.18982673067167876`*^15 cl[[1]]
 deltaphi E^ (zcalc / attn) fthermal horizonfactordip
 lrock pfast spallationfactor + 6.18982673067167876`*^15
 cl[[1]] deltaphi E^ (zcalc / attn) fthermal
 horizonfactordip lrock neutronmufrn pfast spallationfactor -
5.65622678464828432`*^15 deltaphi E^ (zcalc / attn + zcalc /
      lrock) fthermal horizonfactordip k2o[[1]]
 lrock nthermalzcorrection pfast spallationfactor +
5.65622678464828432`*^15 deltaphi E^ (zcalc / attn + zcalc /
      lrock) fthermal horizonfactordip k2o[[1]] lrock
 neutronmufrn nthermalzcorrection pfast spallationfactor -
6.18982673067167876`*^15 attn cl[[1]] E^ (zcalc /
     lrock) horizonfactordip pfast phistar spallationfactor +
6.18982673067167876`*^15 attn cl[[1]] E^ (zcalc / lrock)
 horizonfactordip neutronmufrn pfast phistar spallationfactor -
5.65622678464828432`*^15 attn E^ (zcalc / attn + zcalc / lrock)
 horizonfactordip k2o[[1]] nthermalzcorrection pfast phistar
 spallationfactor + 5.65622678464828432`*^15 attn E^ (zcalc /
      attn + zcalc / lrock) horizonfactordip k2o[[1]] neutronmufrn
 nthermalzcorrection pfast phistar spallationfactor)) /
(2 √(-4.41228530917291195`*^22 attn cosmocl36 density^2 E^ (zcalc /
      attn + zcalc / lrock) lamda
 lrock (1.10307132729322798`*^22 cosmocl36 E^ (zcalc /
        attn + zcalc /
        lrock) lamda - 1.10307132729322798`*^22 E^ (zcalc /
        attn + zcalc / lrock) horizonfactordip pcaspall -
   6.18982673067167876`*^15 cl[[1]] deltaphi E^ (zcalc /
       attn) fthermal horizonfactordip muonfactor neutronmufrn
    pfast - 5.65622678464828432`*^15 deltaphi E^ (zcalc /
       attn + zcalc / lrock) fthermal horizonfactordip k2o[[1]]
    muonfactor neutronmufrn nthermalzcorrection
    pfast - 6.18982673067167876`*^15 cl[[1]] E^ (zcalc /
       lrock) horizonfactordip muonfactor neutronmufrn
    pfast phistar - 5.65622678464828432`*^15 E^ (zcalc /
       attn + zcalc / lrock) horizonfactordip k2o[[1]]
    muonfactor neutronmufrn nthermalzcorrection
    pfast phistar - 1.10307132729322798`*^22 E^ (zcalc /
       attn + zcalc / lrock) horizonfactordip pkspall -
   6.18982673067167876`*^15 cl[[1]] deltaphi E^ (zcalc /
       attn) fthermal horizonfactordip pfast spallationfactor +
   6.18982673067167876`*^15 cl[[1]] deltaphi E^ (zcalc /
       attn) fthermal
    horizonfactordip neutronmufrn pfast spallationfactor -
   5.65622678464828432`*^15 deltaphi E^ (zcalc /
       attn + zcalc / lrock) fthermal horizonfactordip k2o[[1]]
    nthermalzcorrection pfast spallationfactor +
```

```
5.65622678464828432`*^15 deltaphi E^ (zcalc /
      attn + zcalc / lrock) fthermal horizonfactordip k2o[[1]]
 neutronmufrn nthermalzcorrection pfast spallationfactor -
6.18982673067167876`*^15 cl[[1]] E^ (zcalc /
     lrock) horizonfactordip pfast phistar spallationfactor +
6.18982673067167876`*^15 cl[[1]] E^ (zcalc /
     lrock) horizonfactordip neutronmufrn pfast phistar
 spallationfactor - 5.65622678464828432`*^15 E^ (zcalc /
      attn + zcalc / lrock) horizonfactordip
 k2o[[1]] nthermalzcorrection pfast phistar
 spallationfactor + 5.65622678464828432`*^15 E^ (zcalc /
      attn + zcalc / lrock) horizonfactordip k2o[[1]]
 neutronmufrn nthermalzcorrection pfast phistar
 spallationfactor) + density^2 (1.10307132729322798`*^22
  attn cosmocl36 E^ (zcalc / attn +
      zcalc / lrock)
  lamda + 1.10307132729322798`*^22 cosmocl36 E^ (zcalc / attn +
      zcalc / lrock) lamda
  lrock - 1.10307132729322798`*^22 attn E^ (zcalc / attn +
      zcalc / lrock) horizonfactordip pcaspall -
 6.18982673067167876`*^15 cl[[1]] deltaphi E^ (zcalc /
      attn) fthermal
  horizonfactordip lrock muonfactor neutronmufrn
  pfast - 5.65622678464828432`*^15 deltaphi E^ (zcalc / attn +
      zcalc / lrock) fthermal horizonfactordip k2o[[1]]
  lrock muonfactor neutronmufrn nthermalzcorrection
  pfast - 6.18982673067167876`*^15 attn cl[[1]] E^ (zcalc /
      lrock) horizonfactordip muonfactor neutronmufrn pfast
  phistar - 5.65622678464828432`*^15 attn E^ (zcalc / attn +
      zcalc / lrock) horizonfactordip k2o[[1]]
  muonfactor neutronmufrn nthermalzcorrection pfast
  phistar - 1.10307132729322798`*^22 attn E^ (zcalc / attn +
      zcalc / lrock) horizonfactordip pkspall -
 6.18982673067167876`*^15 cl[[1]] deltaphi E^ (zcalc /
      attn) fthermal
  horizonfactordip lrock pfast spallationfactor +
 6.18982673067167876`*^15 cl[[1]] deltaphi E^ (zcalc /
      attn) fthermal horizonfactordip
  lrock neutronmufrn pfast spallationfactor -
 5.65622678464828432`*^15 deltaphi E^ (zcalc / attn +
      zcalc / lrock) fthermal horizonfactordip k2o[[1]]
  lrock nthermalzcorrection pfast spallationfactor +
 5.65622678464828432`*^15 deltaphi E^ (zcalc / attn +
      zcalc / lrock) fthermal horizonfactordip k2o[[1]] lrock
  neutronmufrn nthermalzcorrection pfast spallationfactor -
 6.18982673067167876`*^15 attn cl[[1]] E^ (zcalc /
      lrock) horizonfactordip pfast phistar spallationfactor +
 6.18982673067167876`*^15 attn cl[[1]] E^ (zcalc /
      lrock) horizonfactordip
  neutronmufrn pfast phistar spallationfactor -
 5.65622678464828432`*^15 attn E^ (zcalc / attn +
      zcalc / lrock) horizonfactordip k2o[[1]]
  nthermalzcorrection pfast phistar spallationfactor +
 5.65622678464828432`*^15 attn E^ (zcalc / attn +
      zcalc / lrock) horizonfactordip k2o[[1]] neutronmufrn
```

```
nthermalzcorrection pfast phistar spallationfactor) ^2)))) *
 phistarstddvn) ^2 +
(1 / (cosmocl36 density^2) (4.53279844764821504`*^-23
    E^(-zcalc / attn - zcalc / lrock) (-1.` density (-6.18982673067167876`*^15
       cl[[1]] deltaphi E^(zcalc / attn) horizonfactordip lrock muonfactor
       neutronmufrn pfast - 5.65622678464828432`*^15 deltaphi E^(zcalc /
          attn + zcalc / lrock) horizonfactordip k2o[[1]] lrock muonfactor
       neutronmufrn nthermalzcorrection pfast - 6.18982673067167876`*^15
       cl[[1]] deltaphi E^(zcalc / attn) horizonfactordip lrock pfast
       spallationfactor + 6.18982673067167876`*^15 cl[[1]] deltaphi
       E^(zcalc / attn) horizonfactordip lrock neutronmufrn
       pfast spallationfactor - 5.65622678464828432`*^15
       deltaphi E^(zcalc / attn + zcalc / lrock) horizonfactordip
       k2o[[1]] lrock nthermalzcorrection pfast spallationfactor +
      5.65622678464828432`*^15 deltaphi E^(zcalc / attn + zcalc / lrock)
       horizonfactordip k2o[[1]] lrock neutronmufrn nthermalzcorrection
       pfast spallationfactor) + (-4.41228530917291195`*^22 attn
       cosmocl36 density^2 E^(zcalc / attn + zcalc / lrock) lamda lrock
       (-6.18982673067167876`*^15 cl[[1]] deltaphi E^(zcalc /
          attn) horizonfactordip muonfactor neutronmufrn pfast -
        5.65622678464828432`*^15 deltaphi E^(zcalc / attn + zcalc /
             lrock) horizonfactordip k2o[[1]] muonfactor neutronmufrn
         nthermalzcorrection pfast - 6.18982673067167876`*^15 cl[[1]]
         deltaphi E^(zcalc / attn) horizonfactordip pfast
         spallationfactor + 6.18982673067167876`*^15 cl[[1]] deltaphi E^
          (zcalc / attn) horizonfactordip neutronmufrn pfast
         spallationfactor - 5.65622678464828432`*^15 deltaphi E^(zcalc /
             attn + zcalc / lrock) horizonfactordip
         k2o[[1]] nthermalzcorrection pfast spallationfactor +
        5.65622678464828432`*^15 deltaphi E^(zcalc / attn + zcalc /
             lrock) horizonfactordip k2o[[1]] neutronmufrn
         nthermalzcorrection pfast spallationfactor) +
      2 density^2 (-6.18982673067167876`*^15 cl[[1]] deltaphi E^(zcalc /
          attn) horizonfactordip lrock muonfactor neutronmufrn
         pfast - 5.65622678464828432`*^15 deltaphi E^(zcalc /
             attn + zcalc / lrock) horizonfactordip k2o[[1]]
         lrock muonfactor neutronmufrn nthermalzcorrection
         pfast - 6.18982673067167876`*^15 cl[[1]] deltaphi E^(zcalc /
            attn) horizonfactordip lrock pfast spallationfactor +
        6.18982673067167876`*^15 cl[[1]] deltaphi E^(zcalc /
            attn) horizonfactordip lrock neutronmufrn pfast
         spallationfactor - 5.65622678464828432`*^15 deltaphi E^(zcalc /
             attn + zcalc / lrock)
         horizonfactordip k2o[[1]] lrock nthermalzcorrection pfast
         spallationfactor + 5.65622678464828432`*^15 deltaphi E^(zcalc /
             attn + zcalc / lrock) horizonfactordip k2o[[1]] lrock
         neutronmufrn nthermalzcorrection pfast spallationfactor)
       (1.10307132729322798`*^22 attn cosmocl36 E^(zcalc / attn + zcalc /
             lrock) lamda + 1.10307132729322798`*^22 cosmocl36 E^(zcalc /
             attn + zcalc / lrock) lamda lrock -
        1.10307132729322798`*^22 attn E^(zcalc / attn + zcalc /
             lrock) horizonfactordip pcaspall - 6.18982673067167876`*^15
         cl[[1]] deltaphi E^(zcalc / attn) fthermal
         horizonfactordip lrock muonfactor neutronmufrn pfast -
        5.65622678464828432`*^15 deltaphi E^(zcalc / attn + zcalc /
             lrock) fthermal horizonfactordip k2o[[1]] lrock
         muonfactor neutronmufrn nthermalzcorrection pfast -
        6.18982673067167876`*^15 attn cl[[1]] E^(zcalc / lrock)
         horizonfactordip muonfactor neutronmufrn pfast phistar -
        5.65622678464828432`*^15 attn E^(zcalc / attn + zcalc /
             lrock) horizonfactordip k2o[[1]] muonfactor
         neutronmufrn nthermalzcorrection pfast phistar -
        1.10307132729322798`*^22 attn E^(zcalc / attn + zcalc / lrock)
         horizonfactordip pkspall - 6.18982673067167876`*^15 cl[[1]]
         deltaphi E^(zcalc / attn) fthermal horizonfactordip
         lrock pfast spallationfactor + 6.18982673067167876`*^15
         cl[[1]] deltaphi E^(zcalc / attn) fthermal
         horizonfactordip lrock neutronmufrn pfast spallationfactor -
        5.65622678464828432`*^15 deltaphi E^(zcalc / attn + zcalc /
             lrock) fthermal horizonfactordip k2o[[1]]
         lrock nthermalzcorrection pfast spallationfactor +
        5.65622678464828432`*^15 deltaphi E^(zcalc / attn + zcalc /
             lrock) fthermal horizonfactordip k2o[[1]] lrock
         neutronmufrn nthermalzcorrection pfast spallationfactor -
        6.18982673067167876`*^15 attn cl[[1]] E^(zcalc /
            lrock) horizonfactordip pfast phistar spallationfactor +
        6.18982673067167876`*^15 attn cl[[1]] E^(zcalc / lrock)
         horizonfactordip neutronmufrn pfast phistar spallationfactor -
        5.65622678464828432`*^15 attn E^(zcalc / attn + zcalc / lrock)
         horizonfactordip k2o[[1]] nthermalzcorrection pfast phistar
         spallationfactor + 5.65622678464828432`*^15 attn E^(zcalc /
             attn + zcalc / lrock) horizonfactordip k2o[[1]] neutronmufrn
         nthermalzcorrection pfast phistar spallationfactor)) /
   (2 √(-4.41228530917291195`*^22 attn cosmocl36 density^2 E^(zcalc /
             attn + zcalc / lrock) lamda
         lrock (1.10307132729322798`*^22 cosmocl36 E^(zcalc /
                attn + zcalc /
                lrock) lamda - 1.10307132729322798`*^22 E^(zcalc /
                attn + zcalc / lrock) horizonfactordip pcaspall -
           6.18982673067167876`*^15 cl[[1]] deltaphi E^(zcalc /
               attn) fthermal horizonfactordip muonfactor neutronmufrn
            pfast - 5.65622678464828432`*^15 deltaphi E^(zcalc /
                attn + zcalc / lrock) fthermal horizonfactordip k2o[[1]]
            muonfactor neutronmufrn nthermalzcorrection
            pfast - 6.18982673067167876`*^15 cl[[1]] E^(zcalc /
               lrock) horizonfactordip muonfactor neutronmufrn
            pfast phistar - 5.65622678464828432`*^15 E^(zcalc /
                attn + zcalc / lrock) horizonfactordip k2o[[1]]
            muonfactor neutronmufrn nthermalzcorrection
            pfast phistar - 1.10307132729322798`*^22 E^(zcalc /
                attn + zcalc / lrock) horizonfactordip pkspall -
           6.18982673067167876`*^15 cl[[1]] deltaphi E^(zcalc /
               attn) fthermal horizonfactordip pfast spallationfactor +
           6.18982673067167876`*^15 cl[[1]] deltaphi E^(zcalc /
               attn) fthermal
            horizonfactordip neutronmufrn pfast spallationfactor -
           5.65622678464828432`*^15 deltaphi E^(zcalc /
                attn + zcalc / lrock) fthermal horizonfactordip k2o[[1]]
            nthermalzcorrection pfast spallationfactor +
           5.65622678464828432`*^15 deltaphi E^(zcalc /
```

```
    attn + zcalc / lrock) fthermal horizonfactordip k2o[[1]]
 neutronmufrn nthermalzcorrection pfast spallationfactor -
6.18982673067167876`*^15 cl[[1]] E^(zcalc /
    lrock) horizonfactordip pfast phistar spallationfactor +
6.18982673067167876`*^15 cl[[1]] E^(zcalc /
    lrock) horizonfactordip neutronmufrn pfast phistar
 spallationfactor - 5.65622678464828432`*^15 E^(zcalc /
    attn + zcalc / lrock) horizonfactordip
 k2o[[1]] nthermalzcorrection pfast phistar
 spallationfactor + 5.65622678464828432`*^15 E^(zcalc /
    attn + zcalc / lrock) horizonfactordip k2o[[1]]
 neutronmufrn nthermalzcorrection pfast phistar
 spallationfactor) + density^2 (1.10307132729322798`*^22
  attn cosmocl36 E^(zcalc / attn +
    zcalc / lrock)
  lamda + 1.10307132729322798`*^22 cosmocl36 E^(zcalc / attn +
    zcalc / lrock) lamda
  lrock - 1.10307132729322798`*^22 attn E^(zcalc / attn +
    zcalc / lrock) horizonfactordip pcaspall -
6.18982673067167876`*^15 cl[[1]] deltaphi E^(zcalc /
    attn) fthermal
  horizonfactordip lrock muonfactor neutronmufrn
  pfast - 5.65622678464828432`*^15 deltaphi E^(zcalc / attn +
    zcalc / lrock) fthermal horizonfactordip k2o[[1]]
  lrock muonfactor neutronmufrn nthermalzcorrection
  pfast - 6.18982673067167876`*^15 attn cl[[1]] E^(zcalc /
    lrock) horizonfactordip muonfactor neutronmufrn pfast
  phistar - 5.65622678464828432`*^15 attn E^(zcalc / attn +
    zcalc / lrock) horizonfactordip k2o[[1]]
  muonfactor neutronmufrn nthermalzcorrection pfast
  phistar - 1.10307132729322798`*^22 attn E^(zcalc / attn +
    zcalc / lrock) horizonfactordip pkspall -
6.18982673067167876`*^15 cl[[1]] deltaphi E^(zcalc /
    attn) fthermal
  horizonfactordip lrock pfast spallationfactor +
6.18982673067167876`*^15 cl[[1]] deltaphi E^(zcalc /
    attn) fthermal horizonfactordip
  lrock neutronmufrn pfast spallationfactor -
5.65622678464828432`*^15 deltaphi E^(zcalc / attn +
    zcalc / lrock) fthermal horizonfactordip k2o [[1]]
  lrock nthermalzcorrection pfast spallationfactor +
5.65622678464828432`*^15 deltaphi E^(zcalc / attn +
    zcalc / lrock) fthermal horizonfactordip k2o [[1]] lrock
  neutronmufrn nthermalzcorrection pfast spallationfactor -
6.18982673067167876`*^15 attn cl[[1]] E^(zcalc /
    lrock) horizonfactordip pfast phistar spallationfactor +
6.18982673067167876`*^15 attn cl[[1]] E^(zcalc /
    lrock) horizonfactordip
  neutronmufrn pfast phistar spallationfactor -
5.65622678464828432`*^15 attn E^(zcalc / attn +
    zcalc / lrock) horizonfactordip k2o[[1]]
  nthermalzcorrection pfast phistar spallationfactor +
5.65622678464828432`*^15 attn E^(zcalc / attn +
    zcalc / lrock) horizonfactordip k2o[[1]] neutronmufrn
  nthermalzcorrection pfast phistar spallationfactor)^2))))*
    fthermalstddvn)^2 +
 (1 / (cosmocl36 density^2) (4.53279844764821504`*^-23
    E^(-zcalc / attn - zcalc / lrock) (-1.` density (-6.18982673067167876`*^15
        cl[[1]] E^(zcalc / attn) fthermal horizonfactordip lrock muonfactor
        neutronmufrn pfast - 5.65622678464828432`*^15 E^(zcalc /
          attn + zcalc / lrock) fthermal horizonfactordip k2o[[1]]
        lrock muonfactor neutronmufrn nthermalzcorrection pfast -
       6.18982673067167876`*^15 cl[[1]] E^(zcalc / attn)
        fthermal horizonfactordip lrock pfast spallationfactor +
       6.18982673067167876`*^15 cl[[1]] E^(zcalc / attn) fthermal
        horizonfactordip lrock neutronmufrn pfast spallationfactor -
       5.65622678464828432`*^15 E^(zcalc / attn + zcalc / lrock) fthermal
        horizonfactordip k2o[[1]] lrock nthermalzcorrection pfast
        spallationfactor + 5.65622678464828432`*^15 E^(zcalc / attn + zcalc /
          lrock) fthermal horizonfactordip k2o[[1]] lrock
        neutronmufrn nthermalzcorrection pfast spallationfactor) +
      (-4.41228530917291195`*^22 attn cosmocl36 density^2 E^(zcalc / attn +
          zcalc / lrock) lamda lrock (-6.18982673067167876`*^15 cl[[1]] E^
           (zcalc / attn) fthermal horizonfactordip muonfactor
          neutronmufrn pfast - 5.65622678464828432`*^15 E^(zcalc /
            attn + zcalc / lrock) fthermal horizonfactordip
          k2o[[1]] muonfactor neutronmufrn nthermalzcorrection
          pfast - 6.18982673067167876`*^15 cl[[1]] E^(zcalc /
            attn) fthermal horizonfactordip pfast spallationfactor +
         6.18982673067167876`*^15 cl[[1]] E^(zcalc / attn) fthermal
          horizonfactordip neutronmufrn pfast spallationfactor -
         5.65622678464828432`*^15 E^(zcalc / attn + zcalc / lrock)
          fthermal horizonfactordip k2o[[1]] nthermalzcorrection pfast
          spallationfactor + 5.65622678464828432`*^15 E^(zcalc / attn +
            zcalc / lrock) fthermal horizonfactordip k2o[[1]] neutronmufrn
          nthermalzcorrection pfast spallationfactor) + 2 density^2
        (-6.18982673067167876`*^15 cl[[1]] E^(zcalc / attn) fthermal
          horizonfactordip lrock muonfactor neutronmufrn pfast -
         5.65622678464828432`*^15 E^(zcalc / attn + zcalc / lrock)
          fthermal horizonfactordip k2o[[1]] lrock muonfactor neutronmufrn
          nthermalzcorrection pfast - 6.18982673067167876`*^15 cl[[1]] E^
           (zcalc / attn) fthermal horizonfactordip lrock pfast
          spallationfactor + 6.18982673067167876`*^15 cl[[1]] E^(zcalc /
            attn) fthermal horizonfactordip lrock neutronmufrn pfast
          spallationfactor - 5.65622678464828432`*^15 E^(zcalc /
            attn + zcalc / lrock) fthermal horizonfactordip k2o[[1]]
          lrock nthermalzcorrection pfast spallationfactor +
         5.65622678464828432`*^15 E^(zcalc / attn + zcalc /
            lrock) fthermal horizonfactordip k2o[[1]] lrock
          neutronmufrn nthermalzcorrection pfast spallationfactor)
        (1.10307132729322798`*^22 attn cosmocl36 E^(zcalc / attn + zcalc /
            lrock) lamda + 1.10307132729322798`*^22 cosmocl36 E^(zcalc /
            attn + zcalc / lrock) lamda lrock -
         1.10307132729322798`*^22 attn E^(zcalc / attn + zcalc /
            lrock) horizonfactordip pcaspall - 6.18982673067167876`*^15
          cl[[1]] deltaphi E^(zcalc / attn) fthermal
          horizonfactordip lrock muonfactor neutronmufrn pfast -
         5.65622678464828432`*^15 deltaphi E^(zcalc / attn + zcalc /
            lrock) fthermal horizonfactordip k2o[[1]] lrock
          muonfactor neutronmufrn nthermalzcorrection pfast -
```

```
6.18982673067167876`*^15 attn cl[[1]] E^ (zcalc / lrock)
 horizonfactordip muonfactor neutronmufrn pfast phistar -
5.65622678464828432`*^15 attn E^ (zcalc / attn + zcalc /
      lrock) horizonfactordip k2o[[1]] muonfactor
 neutronmufrn nthermalzcorrection pfast phistar -
1.10307132729322798`*^22 attn E^ (zcalc / attn + zcalc / lrock)
 horizonfactordip pkspall - 6.18982673067167876`*^15 cl[[1]]
 deltaphi E^ (zcalc / attn) fthermal horizonfactordip
 lrock pfast spallationfactor + 6.18982673067167876`*^15
 cl[[1]] deltaphi E^ (zcalc / attn) fthermal
 horizonfactordip lrock neutronmufrn pfast spallationfactor -
5.65622678464828432`*^15 deltaphi E^ (zcalc / attn + zcalc /
      lrock) fthermal horizonfactordip k2o[[1]]
 lrock nthermalzcorrection pfast spallationfactor +
5.65622678464828432`*^15 deltaphi E^ (zcalc / attn + zcalc /
      lrock) fthermal horizonfactordip k2o[[1]] lrock
 neutronmufrn nthermalzcorrection pfast spallationfactor -
6.18982673067167876`*^15 attn cl[[1]] E^ (zcalc /
     lrock) horizonfactordip pfast phistar spallationfactor +
6.18982673067167876`*^15 attn cl[[1]] E^ (zcalc / lrock)
 horizonfactordip neutronmufrn pfast phistar spallationfactor -
5.65622678464828432`*^15 attn E^ (zcalc / attn + zcalc / lrock)
 horizonfactordip k2o[[1]] nthermalzcorrection pfast phistar
 spallationfactor + 5.65622678464828432`*^15 attn E^ (zcalc /
      attn + zcalc / lrock) horizonfactordip k2o[[1]] neutronmufrn
 nthermalzcorrection pfast phistar spallationfactor)) /
(2 √(-4.41228530917291195`*^22 attn cosmocl36 density^2 E^ (zcalc /
        attn + zcalc / lrock) lamda
 lrock (1.10307132729322798`*^22 cosmocl36 E^ (zcalc /
          attn + zcalc /
          lrock) lamda - 1.10307132729322798`*^22 E^ (zcalc /
          attn + zcalc / lrock) horizonfactordip pcaspall -
    6.18982673067167876`*^15 cl[[1]] deltaphi E^ (zcalc /
       attn) fthermal horizonfactordip muonfactor neutronmufrn
     pfast - 5.65622678464828432`*^15 deltaphi E^ (zcalc /
        attn + zcalc / lrock) fthermal horizonfactordip k2o[[1]]
     muonfactor neutronmufrn nthermalzcorrection
     pfast - 6.18982673067167876`*^15 cl[[1]] E^ (zcalc /
        lrock) horizonfactordip muonfactor neutronmufrn
     pfast phistar - 5.65622678464828432`*^15 E^ (zcalc /
        attn + zcalc / lrock) horizonfactordip k2o[[1]]
     muonfactor neutronmufrn nthermalzcorrection
     pfast phistar - 1.10307132729322798`*^22 E^ (zcalc /
        attn + zcalc / lrock) horizonfactordip pkspall -
    6.18982673067167876`*^15 cl[[1]] deltaphi E^ (zcalc /
       attn) fthermal horizonfactordip pfast spallationfactor +
    6.18982673067167876`*^15 cl[[1]] deltaphi E^ (zcalc /
       attn) fthermal
     horizonfactordip neutronmufrn pfast spallationfactor -
    5.65622678464828432`*^15 deltaphi E^ (zcalc /
        attn + zcalc / lrock) fthermal horizonfactordip k2o[[1]]
     nthermalzcorrection pfast spallationfactor +
    5.65622678464828432`*^15 deltaphi E^ (zcalc /
        attn + zcalc / lrock) fthermal horizonfactordip k2o[[1]]
     neutronmufrn nthermalzcorrection pfast spallationfactor -
6.18982673067167876`*^15 cl[[1]] E^ (zcalc /
     lrock) horizonfactordip pfast phistar spallationfactor +
6.18982673067167876`*^15 cl[[1]] E^ (zcalc /
     lrock) horizonfactordip neutronmufrn pfast phistar
 spallationfactor - 5.65622678464828432`*^15 E^ (zcalc /
     attn + zcalc / lrock) horizonfactordip
 k2o[[1]] nthermalzcorrection pfast phistar
 spallationfactor + 5.65622678464828432`*^15 E^ (zcalc /
     attn + zcalc / lrock) horizonfactordip k2o[[1]]
 neutronmufrn nthermalzcorrection pfast phistar
 spallationfactor) + density^2 (1.10307132729322798`*^22
  attn cosmocl36 E^ (zcalc / attn +
     zcalc / lrock)
  lamda + 1.10307132729322798`*^22 cosmocl36 E^ (zcalc / attn +
     zcalc / lrock) lamda
  lrock - 1.10307132729322798`*^22 attn E^ (zcalc / attn +
     zcalc / lrock) horizonfactordip pcaspall -
 6.18982673067167876`*^15 cl[[1]] deltaphi E^ (zcalc /
     attn) fthermal
  horizonfactordip lrock muonfactor neutronmufrn
  pfast - 5.65622678464828432`*^15 deltaphi E^ (zcalc / attn +
     zcalc / lrock) fthermal horizonfactordip k2o[[1]]
  lrock muonfactor neutronmufrn nthermalzcorrection
  pfast - 6.18982673067167876`*^15 attn cl[[1]] E^ (zcalc /
     lrock) horizonfactordip muonfactor neutronmufrn pfast
  phistar - 5.65622678464828432`*^15 attn E^ (zcalc / attn +
     zcalc / lrock) horizonfactordip k2o[[1]]
  muonfactor neutronmufrn nthermalzcorrection pfast
  phistar - 1.10307132729322798`*^22 attn E^ (zcalc / attn +
     zcalc / lrock) horizonfactordip pkspall -
 6.18982673067167876`*^15 cl[[1]] deltaphi E^ (zcalc /
     attn) fthermal
  horizonfactordip lrock pfast spallationfactor +
 6.18982673067167876`*^15 cl[[1]] deltaphi E^ (zcalc /
     attn) fthermal horizonfactordip
  lrock neutronmufrn pfast spallationfactor -
 5.65622678464828432`*^15 deltaphi E^ (zcalc / attn +
     zcalc / lrock) fthermal horizonfactordip k2o[[1]]
  lrock nthermalzcorrection pfast spallationfactor +
 5.65622678464828432`*^15 deltaphi E^ (zcalc / attn +
     zcalc / lrock) fthermal horizonfactordip k2o[[1]] lrock
  neutronmufrn nthermalzcorrection pfast spallationfactor -
 6.18982673067167876`*^15 attn cl[[1]] E^ (zcalc /
     lrock) horizonfactordip pfast phistar spallationfactor +
 6.18982673067167876`*^15 attn cl[[1]] E^ (zcalc /
     lrock) horizonfactordip
  neutronmufrn pfast phistar spallationfactor -
 5.65622678464828432`*^15 attn E^ (zcalc / attn +
     zcalc / lrock) horizonfactordip k2o[[1]]
  nthermalzcorrection pfast phistar spallationfactor +
 5.65622678464828432`*^15 attn E^ (zcalc / attn +
     zcalc / lrock) horizonfactordip k2o[[1]] neutronmufrn
  nthermalzcorrection pfast phistar spallationfactor) ^2)))) *
   deltaphistddvn) ^2 +
(1 / (cosmocl36 density^2)
```

```
(4.53279844764821504`*^-23 E^(-zcalc/attn - zcalc/lrock)
  (-1.` density (1.10307132729322798`*^22 attn E^(zcalc/attn + zcalc/
        lrock) lamda + 1.10307132729322798`*^22 E^(zcalc/attn + zcalc/
        lrock) lamda lrock) + (-4.86706541238577372`*^44
      attn cosmocl36 density^2 E^((2 zcalc)/attn + (2
          zcalc)/lrock) lamda^2 lrock - 4.41228530917291195`*^22 attn
      density^2 E^(zcalc/attn + zcalc/lrock) lamda lrock
      (1.10307132729322798`*^22 cosmocl36 E^(zcalc/attn + zcalc/
          lrock) lamda - 1.10307132729322798`*^22 E^(zcalc/
          attn + zcalc/lrock) horizonfactordip
        pcaspall - 6.18982673067167876`*^15 cl[[1]] deltaphi E^(zcalc/
          attn) fthermal horizonfactordip muonfactor neutronmufrn
        pfast - 5.65622678464828432`*^15 deltaphi E^(zcalc/
          attn + zcalc/lrock) fthermal horizonfactordip
        k2o[[1]] muonfactor neutronmufrn nthermalzcorrection
        pfast - 6.18982673067167876`*^15 cl[[1]] E^(zcalc/
          lrock) horizonfactordip muonfactor neutronmufrn
        pfast phistar - 5.65622678464828432`*^15 E^(zcalc/
          attn + zcalc/lrock) horizonfactordip
        k2o[[1]] muonfactor neutronmufrn nthermalzcorrection
        pfast phistar - 1.10307132729322798`*^22 E^(zcalc/
          attn + zcalc/lrock) horizonfactordip
        pkspall - 6.18982673067167876`*^15 cl[[1]] deltaphi E^(zcalc/
          attn) fthermal horizonfactordip pfast spallationfactor +
       6.18982673067167876`*^15 cl[[1]] deltaphi E^(zcalc/
          attn) fthermal horizonfactordip neutronmufrn pfast
        spallationfactor - 5.65622678464828432`*^15 deltaphi E^(zcalc/
          attn + zcalc/lrock) fthermal
        horizonfactordip k2o[[1]] nthermalzcorrection pfast
        spallationfactor + 5.65622678464828432`*^15 deltaphi E^(zcalc/
          attn + zcalc/lrock) fthermal horizonfactordip
        k2o[[1]] neutronmufrn nthermalzcorrection pfast
        spallationfactor - 6.18982673067167876`*^15 cl[[1]] E^(zcalc/
          lrock) horizonfactordip pfast phistar spallationfactor +
       6.18982673067167876`*^15 cl[[1]] E^(zcalc/lrock)
        horizonfactordip neutronmufrn pfast phistar spallationfactor -
       5.65622678464828432`*^15 E^(zcalc/attn + zcalc/
          lrock) horizonfactordip k2o[[1]] nthermalzcorrection pfast
        phistar spallationfactor + 5.65622678464828432`*^15 E^(zcalc/
          attn + zcalc/lrock) horizonfactordip k2o[[1]] neutronmufrn
        nthermalzcorrection pfast phistar spallationfactor) + 2 density^
      2 (1.10307132729322798`*^22 attn E^(zcalc/attn + zcalc/
          lrock) lamda + 1.10307132729322798`*^22 E^(zcalc/
          attn + zcalc/lrock) lamda lrock) (1.10307132729322798`*^22
        attn cosmocl36 E^(zcalc/attn + zcalc/
          lrock) lamda + 1.10307132729322798`*^22 cosmocl36 E^(zcalc/
          attn + zcalc/lrock)
        lamda lrock - 1.10307132729322798`*^22 attn E^(zcalc/
          attn + zcalc/lrock) horizonfactordip pcaspall -
       6.18982673067167876`*^15 cl[[1]] deltaphi E^(zcalc/attn)
        fthermal horizonfactordip lrock muonfactor neutronmufrn pfast -
       5.65622678464828432`*^15 deltaphi E^(zcalc/attn + zcalc/
          lrock) fthermal horizonfactordip k2o[[1]]
        lrock muonfactor neutronmufrn nthermalzcorrection
        pfast - 6.18982673067167876`*^15 attn cl[[1]] E^(zcalc/
          lrock) horizonfactordip muonfactor neutronmufrn pfast
        phistar - 5.65622678464828432`*^15 attn E^(zcalc/
          attn + zcalc/lrock) horizonfactordip k2o[[1]]
        muonfactor neutronmufrn nthermalzcorrection pfast
        phistar - 1.10307132729322798`*^22 attn E^(zcalc/attn + zcalc/
          lrock) horizonfactordip pkspall - 6.18982673067167876`*^15
        cl[[1]] deltaphi E^(zcalc/attn) fthermal
        horizonfactordip lrock pfast spallationfactor +
       6.18982673067167876`*^15 cl[[1]] deltaphi E^(zcalc/
          attn) fthermal horizonfactordip lrock neutronmufrn pfast
        spallationfactor - 5.65622678464828432`*^15 deltaphi E^(zcalc/
          attn + zcalc/lrock) fthermal horizonfactordip k2o[[1]]
        lrock nthermalzcorrection pfast spallationfactor +
       5.65622678464828432`*^15 deltaphi E^(zcalc/attn + zcalc/
          lrock) fthermal horizonfactordip k2o[[1]] lrock
        neutronmufrn nthermalzcorrection pfast spallationfactor -
       6.18982673067167876`*^15 attn cl[[1]] E^(zcalc/
          lrock) horizonfactordip pfast phistar spallationfactor +
       6.18982673067167876`*^15 attn cl[[1]] E^(zcalc/
          lrock) horizonfactordip neutronmufrn pfast phistar
        spallationfactor - 5.65622678464828432`*^15 attn E^(zcalc/
          attn + zcalc/lrock) horizonfactordip k2o[[1]]
        nthermalzcorrection pfast phistar spallationfactor +
       5.65622678464828432`*^15 attn E^(zcalc/attn + zcalc/
          lrock) horizonfactordip k2o[[1]] neutronmufrn
        nthermalzcorrection pfast phistar spallationfactor))/
  (2 √(-4.41228530917291195`*^22 attn cosmocl36 density^2 E^(zcalc/
          attn + zcalc/lrock) lamda lrock (1.10307132729322798`*^22
        cosmocl36 E^(zcalc/attn +
            zcalc/lrock)
          lamda - 1.10307132729322798`*^22 E^(zcalc/attn +
            zcalc/lrock) horizonfactordip pcaspall -
         6.18982673067167876`*^15 cl[[1]] deltaphi E^(zcalc/
            attn) fthermal horizonfactordip muonfactor neutronmufrn
          pfast - 5.65622678464828432`*^15 deltaphi E^(zcalc/attn +
            zcalc/lrock) fthermal horizonfactordip k2o[[1]]
          muonfactor neutronmufrn nthermalzcorrection
          pfast - 6.18982673067167876`*^15 cl[[1]] E^(zcalc/
            lrock) horizonfactordip muonfactor neutronmufrn pfast
          phistar - 5.65622678464828432`*^15 E^(zcalc/attn +
            zcalc/lrock) horizonfactordip k2o[[1]]
          muonfactor neutronmufrn nthermalzcorrection pfast
          phistar - 1.10307132729322798`*^22 E^(zcalc/attn +
            zcalc/lrock) horizonfactordip pkspall -
         6.18982673067167876`*^15 cl[[1]] deltaphi E^(zcalc/
            attn) fthermal horizonfactordip pfast spallationfactor +
         6.18982673067167876`*^15 cl[[1]] deltaphi E^(zcalc/
            attn) fthermal
          horizonfactordip neutronmufrn pfast spallationfactor -
         5.65622678464828432`*^15 deltaphi E^(zcalc/attn +
            zcalc/lrock) fthermal horizonfactordip k2o[[1]]
          nthermalzcorrection pfast spallationfactor +
         5.65622678464828432`*^15 deltaphi E^(zcalc/attn +
            zcalc/lrock) fthermal horizonfactordip k2o[[1]]
          neutronmufrn nthermalzcorrection pfast spallationfactor -
```

```
6.18982673067167876`*^15 cl[[1]] E^(zcalc/
    lrock) horizonfactordip pfast phistar spallationfactor +
6.18982673067167876`*^15 cl[[1]] E^(zcalc/
    lrock) horizonfactordip neutronmufrn pfast phistar
  spallationfactor - 5.65622678464828432`*^15 E^(zcalc/attn +
    zcalc/lrock) horizonfactordip
  k2o[[1]] nthermalzcorrection pfast phistar
  spallationfactor + 5.65622678464828432`*^15 E^(zcalc/attn +
    zcalc/lrock) horizonfactordip k2o[[1]]
  neutronmufrn nthermalzcorrection pfast phistar
  spallationfactor) + density^2 (1.10307132729322798`*^22
   attn cosmocl36 E^(zcalc/attn + zcalc/lrock)
   lamda + 1.10307132729322798`*^22 cosmocl36 E^
    (zcalc/attn + zcalc/lrock)
   lamda lrock - 1.10307132729322798`*^22 attn E^
    (zcalc/attn + zcalc/lrock) horizonfactordip pcaspall -
  6.18982673067167876`*^15 cl[[1]] deltaphi E^(zcalc/attn)
   fthermal horizonfactordip lrock muonfactor neutronmufrn
   pfast - 5.65622678464828432`*^15 deltaphi E^
    (zcalc/attn + zcalc/lrock) fthermal horizonfactordip
   k2o[[1]] lrock muonfactor neutronmufrn nthermalzcorrection
   pfast - 6.18982673067167876`*^15 attn cl[[1]] E^
    (zcalc/lrock) horizonfactordip muonfactor neutronmufrn
   pfast phistar - 5.65622678464828432`*^15 attn E^
    (zcalc/attn + zcalc/lrock) horizonfactordip k2o[[1]]
   muonfactor neutronmufrn nthermalzcorrection
   pfast phistar - 1.10307132729322798`*^22 attn E^
    (zcalc/attn + zcalc/lrock) horizonfactordip pkspall -
  6.18982673067167876`*^15 cl[[1]] deltaphi E^(zcalc/attn)
   fthermal horizonfactordip lrock pfast spallationfactor +
  6.18982673067167876`*^15 cl[[1]] deltaphi E^(zcalc/attn)
   fthermal horizonfactordip lrock neutronmufrn pfast
   spallationfactor - 5.65622678464828432`*^15 deltaphi E^
    (zcalc/attn + zcalc/lrock) fthermal horizonfactordip
   k2o[[1]] lrock nthermalzcorrection pfast
   spallationfactor + 5.65622678464828432`*^15 deltaphi E^
    (zcalc/attn + zcalc/lrock) fthermal horizonfactordip
   k2o[[1]] lrock neutronmufrn nthermalzcorrection pfast
   spallationfactor - 6.18982673067167876`*^15 attn cl[[1]] E^
    (zcalc/lrock) horizonfactordip pfast phistar
   spallationfactor + 6.18982673067167876`*^15 attn cl[[1]] E^
    (zcalc/lrock) horizonfactordip neutronmufrn pfast
   phistar spallationfactor - 5.65622678464828432`*^15 attn E^
    (zcalc/attn + zcalc/lrock) horizonfactordip
   k2o[[1]] nthermalzcorrection pfast phistar
   spallationfactor + 5.65622678464828432`*^15 attn E^
    (zcalc/attn + zcalc/lrock) horizonfactordip
   k2o[[1]] neutronmufrn nthermalzcorrection
   pfast phistar spallationfactor)^2))) -
1/(cosmocl36^2 density^2) (4.53279844764821504`*^-23
  E^(-zcalc/attn - zcalc/lrock) (-1.` density (1.10307132729322798`*^22
      attn cosmocl36 E^(zcalc/attn + zcalc/lrock) lamda +
    1.10307132729322798`*^22 cosmocl36 E^(zcalc/attn + zcalc/lrock)
     lamda lrock - 1.10307132729322798`*^22 attn E^(zcalc/attn + zcalc/
         lrock) horizonfactordip pcaspall - 6.18982673067167876`*^15
```

```
   cl[[1]] deltaphi E^(zcalc/attn) fthermal horizonfactordip lrock
   muonfactor neutronmufrn pfast - 5.65622678464828432`*^15 deltaphi
   E^(zcalc/attn + zcalc/lrock) fthermal horizonfactordip
   k2o[[1]] lrock muonfactor neutronmufrn nthermalzcorrection pfast -
  6.18982673067167876`*^15 attn cl[[1]] E^(zcalc/
      lrock) horizonfactordip muonfactor neutronmufrn pfast phistar -
  5.65622678464828432`*^15 attn E^(zcalc/attn + zcalc/
       lrock) horizonfactordip k2o[[1]] muonfactor neutronmufrn
   nthermalzcorrection pfast phistar - 1.10307132729322798`*^22 attn
   E^(zcalc/attn + zcalc/lrock) horizonfactordip pkspall -
  6.18982673067167876`*^15 cl[[1]] deltaphi E^(zcalc/
      attn) fthermal horizonfactordip lrock pfast spallationfactor +
  6.18982673067167876`*^15 cl[[1]] deltaphi E^(zcalc/attn) fthermal
   horizonfactordip lrock neutronmufrn pfast spallationfactor -
  5.65622678464828432`*^15 deltaphi E^(zcalc/attn + zcalc/lrock)
   fthermal horizonfactordip k2o[[1]] lrock nthermalzcorrection pfast
   spallationfactor + 5.65622678464828432`*^15 deltaphi E^(zcalc/
       attn + zcalc/lrock) fthermal horizonfactordip k2o[[1]] lrock
   neutronmufrn nthermalzcorrection pfast spallationfactor -
  6.18982673067167876`*^15 attn cl[[1]] E^(zcalc/
      lrock) horizonfactordip pfast phistar spallationfactor +
  6.18982673067167876`*^15 attn cl[[1]] E^(zcalc/lrock)
   horizonfactordip neutronmufrn pfast phistar spallationfactor -
  5.65622678464828432`*^15 attn E^(zcalc/attn + zcalc/lrock)
   horizonfactordip k2o[[1]] nthermalzcorrection pfast phistar
   spallationfactor + 5.65622678464828432`*^15 attn E^(zcalc/
       attn + zcalc/lrock) horizonfactordip k2o[[1]] neutronmufrn
   nthermalzcorrection pfast phistar spallationfactor) +
√(-4.41228530917291195`*^22 attn cosmocl36 density^2 E^(zcalc/
       attn + zcalc/lrock) lamda lrock
    (1.10307132729322798`*^22 cosmocl36 E^(zcalc/attn + zcalc/
          lrock) lamda - 1.10307132729322798`*^22 E^(zcalc/
          attn + zcalc/lrock) horizonfactordip
      pcaspall - 6.18982673067167876`*^15 cl[[1]] deltaphi E^(zcalc/
         attn) fthermal horizonfactordip muonfactor neutronmufrn
      pfast - 5.65622678464828432`*^15 deltaphi E^(zcalc/
          attn + zcalc/lrock) fthermal horizonfactordip
      k2o[[1]] muonfactor neutronmufrn nthermalzcorrection
      pfast - 6.18982673067167876`*^15 cl[[1]] E^(zcalc/
         lrock) horizonfactordip muonfactor neutronmufrn
      pfast phistar - 5.65622678464828432`*^15 E^(zcalc/
          attn + zcalc/lrock) horizonfactordip
      k2o[[1]] muonfactor neutronmufrn nthermalzcorrection
      pfast phistar - 1.10307132729322798`*^22 E^(zcalc/
          attn + zcalc/lrock) horizonfactordip
      pkspall - 6.18982673067167876`*^15 cl[[1]] deltaphi E^(zcalc/
         attn) fthermal horizonfactordip pfast spallationfactor +
    6.18982673067167876`*^15 cl[[1]] deltaphi E^(zcalc/
         attn) fthermal horizonfactordip neutronmufrn pfast
      spallationfactor - 5.65622678464828432`*^15 deltaphi E^(zcalc/
          attn + zcalc/lrock) fthermal
      horizonfactordip k2o[[1]] nthermalzcorrection pfast
      spallationfactor + 5.65622678464828432`*^15 deltaphi E^(zcalc/
          attn + zcalc/lrock) fthermal horizonfactordip
      k2o[[1]] neutronmufrn nthermalzcorrection pfast
```

```
spallationfactor - 6.18982673067167876`*^15 cl[[1]] E^(zcalc /
      lrock) horizonfactordip pfast phistar spallationfactor +
   6.18982673067167876`*^15 cl[[1]] E^(zcalc / lrock)
    horizonfactordip neutronmufrn pfast phistar spallationfactor -
   5.65622678464828432`*^15 E^(zcalc / attn + zcalc /
        lrock) horizonfactordip k2o[[1]] nthermalzcorrection pfast
    phistar spallationfactor + 5.65622678464828432`*^15 E^(zcalc /
        attn + zcalc / lrock) horizonfactordip k2o[[1]] neutronmufrn
    nthermalzcorrection pfast phistar spallationfactor) +
 density^2 (1.10307132729322798`*^22 attn cosmocl36 E^(zcalc /
        attn + zcalc / lrock)
    lamda + 1.10307132729322798`*^22 cosmocl36 E^(zcalc /
        attn + zcalc / lrock) lamda
    lrock - 1.10307132729322798`*^22 attn E^(zcalc /
        attn + zcalc / lrock) horizonfactordip pcaspall -
   6.18982673067167876`*^15 cl[[1]] deltaphi E^(zcalc / attn)
    fthermal horizonfactordip lrock muonfactor neutronmufrn
    pfast - 5.65622678464828432`*^15 deltaphi E^(zcalc /
        attn + zcalc / lrock) fthermal horizonfactordip k2o[[1]]
    lrock muonfactor neutronmufrn nthermalzcorrection
    pfast - 6.18982673067167876`*^15 attn cl[[1]] E^(zcalc /
      lrock) horizonfactordip muonfactor neutronmufrn pfast
    phistar - 5.65622678464828432`*^15 attn E^(zcalc /
        attn + zcalc / lrock) horizonfactordip k2o[[1]]
    muonfactor neutronmufrn nthermalzcorrection pfast
    phistar - 1.10307132729322798`*^22 attn E^(zcalc /
        attn + zcalc / lrock) horizonfactordip pkspall -
   6.18982673067167876`*^15 cl[[1]] deltaphi E^(zcalc / attn)
    fthermal horizonfactordip lrock pfast spallationfactor +
   6.18982673067167876`*^15 cl[[1]] deltaphi E^(zcalc /
      attn) fthermal horizonfactordip
    lrock neutronmufrn pfast spallationfactor -
   5.65622678464828432`*^15 deltaphi E^(zcalc /
        attn + zcalc / lrock) fthermal horizonfactordip k2o[[1]]
    lrock nthermalzcorrection pfast spallationfactor +
   5.65622678464828432`*^15 deltaphi E^(zcalc /
        attn + zcalc / lrock)
    fthermal horizonfactordip k2o[[1]] lrock neutronmufrn
    nthermalzcorrection pfast spallationfactor -
   6.18982673067167876`*^15 attn cl[[1]] E^(zcalc /
      lrock) horizonfactordip pfast phistar spallationfactor +
   6.18982673067167876`*^15 attn cl[[1]] E^(zcalc /
      lrock) horizonfactordip neutronmufrn pfast phistar
    spallationfactor - 5.65622678464828432`*^15 attn E^(zcalc /
        attn + zcalc / lrock) horizonfactordip
    k2o[[1]] nthermalzcorrection pfast phistar
    spallationfactor + 5.65622678464828432`*^15 attn E^(zcalc /
        attn + zcalc / lrock) horizonfactordip
    k2o[[1]] neutronmufrn nthermalzcorrection pfast
    phistar spallationfactor)^2))) * cosmocl36stddvn)^
2 +
(1 / (cosmocl36 density^2) (4.53279844764821504`*^-23
   E^(-zcalc / attn - zcalc / lrock) (-1.` density (-5.65622678464828432`*^15
      deltaphi E^(zcalc / attn + zcalc / lrock) fthermal horizonfactordip
      lrock muonfactor neutronmufrn nthermalzcorrection pfast -
5.65622678464828432`*^15 attn E^(zcalc / attn + zcalc / lrock)
 horizonfactordip muonfactor neutronmufrn nthermalzcorrection pfast
 phistar - 5.65622678464828432`*^15 deltaphi E^(zcalc / attn + zcalc /
      lrock) fthermal horizonfactordip lrock nthermalzcorrection
 pfast spallationfactor + 5.65622678464828432`*^15 deltaphi
 E^(zcalc / attn + zcalc / lrock) fthermal horizonfactordip lrock
 neutronmufrn nthermalzcorrection pfast spallationfactor -
5.65622678464828432`*^15 attn E^(zcalc / attn + zcalc /
      lrock) horizonfactordip nthermalzcorrection pfast phistar
 spallationfactor + 5.65622678464828432`*^15 attn E^(zcalc / attn +
    zcalc / lrock) horizonfactordip neutronmufrn nthermalzcorrection
 pfast phistar spallationfactor) + (-4.41228530917291195`*^22 attn
 cosmocl36 density^2 E^(zcalc / attn + zcalc / lrock) lamda lrock
 (-5.65622678464828432`*^15 deltaphi E^(zcalc / attn + zcalc /
        lrock) fthermal horizonfactordip muonfactor neutronmufrn
    nthermalzcorrection pfast - 5.65622678464828432`*^15 E^(zcalc /
        attn + zcalc / lrock) horizonfactordip muonfactor
    neutronmufrn nthermalzcorrection pfast phistar -
   5.65622678464828432`*^15 deltaphi E^(zcalc / attn + zcalc /
        lrock) fthermal horizonfactordip nthermalzcorrection pfast
    spallationfactor + 5.65622678464828432`*^15 deltaphi E^(zcalc /
        attn + zcalc / lrock) fthermal horizonfactordip
    neutronmufrn nthermalzcorrection pfast spallationfactor -
   5.65622678464828432`*^15 E^(zcalc / attn + zcalc /
        lrock) horizonfactordip nthermalzcorrection pfast phistar
    spallationfactor + 5.65622678464828432`*^15 E^(zcalc /
        attn + zcalc / lrock) horizonfactordip neutronmufrn
    nthermalzcorrection pfast phistar spallationfactor) +
2 density^2 (-5.65622678464828432`*^15 deltaphi E^(zcalc /
        attn + zcalc / lrock) fthermal horizonfactordip lrock
    muonfactor neutronmufrn nthermalzcorrection pfast -
   5.65622678464828432`*^15 attn E^(zcalc / attn + zcalc / lrock)
    horizonfactordip muonfactor neutronmufrn nthermalzcorrection
    pfast phistar - 5.65622678464828432`*^15 deltaphi E^(zcalc /
        attn + zcalc / lrock) fthermal
    horizonfactordip lrock nthermalzcorrection pfast
    spallationfactor + 5.65622678464828432`*^15 deltaphi E^(zcalc /
        attn + zcalc / lrock) fthermal horizonfactordip lrock
    neutronmufrn nthermalzcorrection pfast spallationfactor -
   5.65622678464828432`*^15 attn E^(zcalc / attn + zcalc /
        lrock) horizonfactordip nthermalzcorrection pfast phistar
    spallationfactor + 5.65622678464828432`*^15 attn E^(zcalc /
        attn + zcalc / lrock) horizonfactordip neutronmufrn
    nthermalzcorrection pfast phistar spallationfactor)
 (1.10307132729322798`*^22 attn cosmocl36 E^(zcalc / attn + zcalc /
        lrock) lamda + 1.10307132729322798`*^22 cosmocl36 E^(zcalc /
        attn + zcalc / lrock) lamda lrock -
   1.10307132729322798`*^22 attn E^(zcalc / attn + zcalc /
        lrock) horizonfactordip pcaspall - 6.18982673067167876`*^15
    cl[[1]] deltaphi E^(zcalc / attn) fthermal
    horizonfactordip lrock muonfactor neutronmufrn pfast -
   5.65622678464828432`*^15 deltaphi E^(zcalc / attn + zcalc /
        lrock) fthermal horizonfactordip k2o[[1]] lrock
    muonfactor neutronmufrn nthermalzcorrection pfast -
   6.18982673067167876`*^15 attn cl[[1]] E^(zcalc / lrock)
```

```
horizonfactordip muonfactor neutronmufrn pfast phistar -
5.65622678464828432`*^15 attn E^ (zcalc / attn + zcalc /
    lrock) horizonfactordip k2o[[1]] muonfactor
 neutronmufrn nthermalzcorrection pfast phistar -
1.10307132729322798`*^22 attn E^ (zcalc / attn + zcalc / lrock)
 horizonfactordip pkspall - 6.18982673067167876`*^15 cl[[1]]
 deltaphi E^ (zcalc / attn) fthermal horizonfactordip
 lrock pfast spallationfactor + 6.18982673067167876`*^15
 cl[[1]] deltaphi E^ (zcalc / attn) fthermal
 horizonfactordip lrock neutronmufrn pfast spallationfactor -
5.65622678464828432`*^15 deltaphi E^ (zcalc / attn + zcalc /
    lrock) fthermal horizonfactordip k2o[[1]]
 lrock nthermalzcorrection pfast spallationfactor +
5.65622678464828432`*^15 deltaphi E^ (zcalc / attn + zcalc /
    lrock) fthermal horizonfactordip k2o[[1]] lrock
 neutronmufrn nthermalzcorrection pfast spallationfactor -
6.18982673067167876`*^15 attn cl[[1]] E^ (zcalc /
    lrock) horizonfactordip pfast phistar spallationfactor +
6.18982673067167876`*^15 attn cl[[1]] E^ (zcalc / lrock)
 horizonfactordip neutronmufrn pfast phistar spallationfactor -
5.65622678464828432`*^15 attn E^ (zcalc / attn + zcalc / lrock)
 horizonfactordip k2o[[1]] nthermalzcorrection pfast phistar
 spallationfactor + 5.65622678464828432`*^15 attn E^ (zcalc /
    attn + zcalc / lrock) horizonfactordip k2o[[1]] neutronmufrn
 nthermalzcorrection pfast phistar spallationfactor)) /
(2 √(-4.41228530917291195`*^22 attn cosmocl36 density^2 E^ (zcalc /
    attn + zcalc / lrock) lamda
 lrock (1.10307132729322798`*^22 cosmocl36 E^ (zcalc /
       attn + zcalc /
       lrock) lamda - 1.10307132729322798`*^22 E^ (zcalc /
       attn + zcalc / lrock) horizonfactordip pcaspall -
   6.18982673067167876`*^15 cl[[1]] deltaphi E^ (zcalc /
      attn) fthermal horizonfactordip muonfactor neutronmufrn
    pfast - 5.65622678464828432`*^15 deltaphi E^ (zcalc /
       attn + zcalc / lrock) fthermal horizonfactordip k2o[[1]]
    muonfactor neutronmufrn nthermalzcorrection
    pfast - 6.18982673067167876`*^15 cl[[1]] E^ (zcalc /
      lrock) horizonfactordip muonfactor neutronmufrn
    pfast phistar - 5.65622678464828432`*^15 E^ (zcalc /
       attn + zcalc / lrock) horizonfactordip k2o[[1]]
    muonfactor neutronmufrn nthermalzcorrection
    pfast phistar - 1.10307132729322798`*^22 E^ (zcalc /
       attn + zcalc / lrock) horizonfactordip pkspall -
   6.18982673067167876`*^15 cl[[1]] deltaphi E^ (zcalc /
      attn) fthermal horizonfactordip pfast spallationfactor +
   6.18982673067167876`*^15 cl[[1]] deltaphi E^ (zcalc /
      attn) fthermal
    horizonfactordip neutronmufrn pfast spallationfactor -
   5.65622678464828432`*^15 deltaphi E^ (zcalc /
       attn + zcalc / lrock) fthermal horizonfactordip k2o[[1]]
    nthermalzcorrection pfast spallationfactor +
   5.65622678464828432`*^15 deltaphi E^ (zcalc /
       attn + zcalc / lrock) fthermal horizonfactordip k2o[[1]]
    neutronmufrn nthermalzcorrection pfast spallationfactor -
   6.18982673067167876`*^15 cl[[1]] E^ (zcalc /
       lrock) horizonfactordip pfast phistar spallationfactor +
  6.18982673067167876`*^15 cl[[1]] E^ (zcalc /
       lrock) horizonfactordip neutronmufrn pfast phistar
    spallationfactor - 5.65622678464828432`*^15 E^ (zcalc /
       attn + zcalc / lrock) horizonfactordip
    k2o[[1]] nthermalzcorrection pfast phistar
    spallationfactor + 5.65622678464828432`*^15 E^ (zcalc /
       attn + zcalc / lrock) horizonfactordip k2o[[1]]
    neutronmufrn nthermalzcorrection pfast phistar
    spallationfactor) + density^2 (1.10307132729322798`*^22
     attn cosmocl36 E^ (zcalc / attn +
        zcalc / lrock)
     lamda + 1.10307132729322798`*^22 cosmocl36 E^ (zcalc / attn +
        zcalc / lrock) lamda
     lrock - 1.10307132729322798`*^22 attn E^ (zcalc / attn +
        zcalc / lrock) horizonfactordip pcaspall -
    6.18982673067167876`*^15 cl[[1]] deltaphi E^ (zcalc /
        attn) fthermal
     horizonfactordip lrock muonfactor neutronmufrn
     pfast - 5.65622678464828432`*^15 deltaphi E^ (zcalc / attn +
        zcalc / lrock) fthermal horizonfactordip k2o[[1]]
     lrock muonfactor neutronmufrn nthermalzcorrection
     pfast - 6.18982673067167876`*^15 attn cl[[1]] E^ (zcalc /
        lrock) horizonfactordip muonfactor neutronmufrn pfast
     phistar - 5.65622678464828432`*^15 attn E^ (zcalc / attn +
        zcalc / lrock) horizonfactordip k2o[[1]]
     muonfactor neutronmufrn nthermalzcorrection pfast
     phistar - 1.10307132729322798`*^22 attn E^ (zcalc / attn +
        zcalc / lrock) horizonfactordip pkspall -
    6.18982673067167876`*^15 cl[[1]] deltaphi E^ (zcalc /
        attn) fthermal
     horizonfactordip lrock pfast spallationfactor +
    6.18982673067167876`*^15 cl[[1]] deltaphi E^ (zcalc /
        attn) fthermal horizonfactordip
     lrock neutronmufrn pfast spallationfactor -
    5.65622678464828432`*^15 deltaphi E^ (zcalc / attn +
        zcalc / lrock) fthermal horizonfactordip k2o [[1]]
     lrock nthermalzcorrection pfast spallationfactor +
    5.65622678464828432`*^15 deltaphi E^ (zcalc / attn +
        zcalc / lrock) fthermal horizonfactordip k2o [[1]] lrock
     neutronmufrn nthermalzcorrection pfast spallationfactor -
    6.18982673067167876`*^15 attn cl[[1]] E^ (zcalc /
        lrock) horizonfactordip pfast phistar spallationfactor +
    6.18982673067167876`*^15 attn cl[[1]] E^ (zcalc /
        lrock) horizonfactordip
     neutronmufrn pfast phistar spallationfactor -
    5.65622678464828432`*^15 attn E^ (zcalc / attn +
        zcalc / lrock) horizonfactordip k2o[[1]]
     nthermalzcorrection pfast phistar spallationfactor +
    5.65622678464828432`*^15 attn E^ (zcalc / attn +
        zcalc / lrock) horizonfactordip
     k2o[[1]] neutronmufrn nthermalzcorrection pfast
     phistar spallationfactor)^2)))) * k2o[[2]])^2 +
(1 / (cosmocl36 density^2) (4.53279844764821504`*^-23
    E^ (-zcalc / attn - zcalc / lrock) (-1.` density (1.10307132729322798`*^22
```

```
attn cosmocl36 E^(zcalc / attn + zcalc / lrock) +
1.10307132729322798`*^22 cosmocl36 E^(zcalc / attn + zcalc /
    lrock) lrock) + (-4.86706541238577372`*^44 attn
 cosmocl36^2 density^2 E^((2 zcalc) / attn + (2 zcalc) / lrock)
 lamda lrock - 4.41228530917291195`*^22 attn cosmocl36 density^2
 E^(zcalc / attn + zcalc / lrock) lrock (1.10307132729322798`*^22
    cosmocl36 E^(zcalc / attn + zcalc / lrock)
    lamda - 1.10307132729322798`*^22 E^(zcalc / attn + zcalc / lrock)
    horizonfactordip pcaspall - 6.18982673067167876`*^15 cl[[1]]
    deltaphi E^(zcalc / attn) fthermal horizonfactordip
    muonfactor neutronmufrn pfast - 5.65622678464828432`*^15
    deltaphi E^(zcalc / attn + zcalc / lrock)
    fthermal horizonfactordip k2o[[1]] muonfactor neutronmufrn
    nthermalzcorrection pfast - 6.18982673067167876`*^15 cl[[1]] E^
     (zcalc / lrock) horizonfactordip muonfactor
    neutronmufrn pfast phistar - 5.65622678464828432`*^15 E^(zcalc /
        attn + zcalc / lrock) horizonfactordip k2o[[1]] muonfactor
    neutronmufrn nthermalzcorrection pfast phistar -
   1.10307132729322798`*^22 E^(zcalc / attn + zcalc / lrock)
    horizonfactordip pkspall - 6.18982673067167876`*^15 cl[[1]]
    deltaphi E^(zcalc / attn) fthermal horizonfactordip
    pfast spallationfactor + 6.18982673067167876`*^15 cl[[1]]
    deltaphi E^(zcalc / attn) fthermal horizonfactordip
    neutronmufrn pfast spallationfactor - 5.65622678464828432`*^15
    deltaphi E^(zcalc / attn + zcalc / lrock)
    fthermal horizonfactordip k2o[[1]] nthermalzcorrection pfast
    spallationfactor + 5.65622678464828432`*^15 deltaphi E^(zcalc /
        attn + zcalc / lrock) fthermal horizonfactordip
    k2o[[1]] neutronmufrn nthermalzcorrection pfast
    spallationfactor - 6.18982673067167876`*^15 cl[[1]] E^(zcalc /
       lrock) horizonfactordip pfast phistar spallationfactor +
   6.18982673067167876`*^15 cl[[1]] E^(zcalc / lrock)
    horizonfactordip neutronmufrn pfast phistar spallationfactor -
   5.65622678464828432`*^15 E^(zcalc / attn + zcalc / lrock)
    horizonfactordip k2o[[1]] nthermalzcorrection pfast phistar
    spallationfactor + 5.65622678464828432`*^15 E^(zcalc /
        attn + zcalc / lrock) horizonfactordip k2o[[1]] neutronmufrn
    nthermalzcorrection pfast phistar spallationfactor) + 2 density^
  2 (1.10307132729322798`*^22 attn cosmocl36 E^(zcalc / attn + zcalc /
        lrock) + 1.10307132729322798`*^22 cosmocl36 E^(zcalc /
        attn + zcalc / lrock) lrock)
 (1.10307132729322798`*^22 attn cosmocl36 E^(zcalc / attn + zcalc /
        lrock) lamda + 1.10307132729322798`*^22 cosmocl36 E^(zcalc /
        attn + zcalc / lrock) lamda lrock -
   1.10307132729322798`*^22 attn E^(zcalc / attn + zcalc /
        lrock) horizonfactordip pcaspall - 6.18982673067167876`*^15
     cl[[1]] deltaphi E^(zcalc / attn) fthermal
    horizonfactordip lrock muonfactor neutronmufrn pfast -
   5.65622678464828432`*^15 deltaphi E^(zcalc / attn + zcalc /
        lrock) fthermal horizonfactordip k2o[[1]] lrock
    muonfactor neutronmufrn nthermalzcorrection pfast -
   6.18982673067167876`*^15 attn cl[[1]] E^(zcalc / lrock)
    horizonfactordip muonfactor neutronmufrn pfast phistar -
   5.65622678464828432`*^15 attn E^(zcalc / attn + zcalc /
        lrock) horizonfactordip k2o[[1]] muonfactor
    neutronmufrn nthermalzcorrection pfast phistar -
  1.10307132729322798`*^22 attn E^(zcalc / attn + zcalc / lrock)
   horizonfactordip pkspall - 6.18982673067167876`*^15 cl[[1]]
   deltaphi E^(zcalc / attn) fthermal horizonfactordip
   lrock pfast spallationfactor + 6.18982673067167876`*^15
   cl[[1]] deltaphi E^(zcalc / attn) fthermal
   horizonfactordip lrock neutronmufrn pfast spallationfactor -
  5.65622678464828432`*^15 deltaphi E^(zcalc / attn + zcalc /
       lrock) fthermal horizonfactordip k2o[[1]]
   lrock nthermalzcorrection pfast spallationfactor +
  5.65622678464828432`*^15 deltaphi E^(zcalc / attn + zcalc /
       lrock) fthermal horizonfactordip k2o[[1]] lrock
   neutronmufrn nthermalzcorrection pfast spallationfactor -
  6.18982673067167876`*^15 attn cl[[1]] E^(zcalc /
      lrock) horizonfactordip pfast phistar spallationfactor +
  6.18982673067167876`*^15 attn cl[[1]] E^(zcalc / lrock)
   horizonfactordip neutronmufrn pfast phistar spallationfactor -
  5.65622678464828432`*^15 attn E^(zcalc / attn + zcalc / lrock)
   horizonfactordip k2o[[1]] nthermalzcorrection pfast phistar
   spallationfactor + 5.65622678464828432`*^15 attn E^(zcalc /
       attn + zcalc / lrock) horizonfactordip k2o[[1]] neutronmufrn
   nthermalzcorrection pfast phistar spallationfactor)) /
(2 √(-4.41228530917291195`*^22 attn cosmocl36 density^2 E^(zcalc /
       attn + zcalc / lrock) lamda
   lrock (1.10307132729322798`*^22 cosmocl36 E^(zcalc /
         attn + zcalc /
         lrock) lamda - 1.10307132729322798`*^22 E^(zcalc /
         attn + zcalc / lrock) horizonfactordip pcaspall -
     6.18982673067167876`*^15 cl[[1]] deltaphi E^(zcalc /
        attn) fthermal horizonfactordip muonfactor neutronmufrn
     pfast - 5.65622678464828432`*^15 deltaphi E^(zcalc /
         attn + zcalc / lrock) fthermal horizonfactordip k2o[[1]]
     muonfactor neutronmufrn nthermalzcorrection
     pfast - 6.18982673067167876`*^15 cl[[1]] E^(zcalc /
        lrock) horizonfactordip muonfactor neutronmufrn
     pfast phistar - 5.65622678464828432`*^15 E^(zcalc /
         attn + zcalc / lrock) horizonfactordip k2o[[1]]
     muonfactor neutronmufrn nthermalzcorrection
     pfast phistar - 1.10307132729322798`*^22 E^(zcalc /
         attn + zcalc / lrock) horizonfactordip pkspall -
     6.18982673067167876`*^15 cl[[1]] deltaphi E^(zcalc /
        attn) fthermal horizonfactordip pfast spallationfactor +
     6.18982673067167876`*^15 cl[[1]] deltaphi E^(zcalc /
        attn) fthermal
     horizonfactordip neutronmufrn pfast spallationfactor -
     5.65622678464828432`*^15 deltaphi E^(zcalc /
         attn + zcalc / lrock) fthermal horizonfactordip k2o[[1]]
     nthermalzcorrection pfast spallationfactor +
     5.65622678464828432`*^15 deltaphi E^(zcalc /
         attn + zcalc / lrock) fthermal horizonfactordip k2o[[1]]
     neutronmufrn nthermalzcorrection pfast spallationfactor -
     6.18982673067167876`*^15 cl[[1]] E^(zcalc /
        lrock) horizonfactordip pfast phistar spallationfactor +
     6.18982673067167876`*^15 cl[[1]] E^(zcalc /
        lrock) horizonfactordip neutronmufrn pfast phistar
```

```
spallationfactor - 5.65622678464828432`*^15 E^(zcalc /
    attn + zcalc / lrock) horizonfactordip
k2o[[1]] nthermalzcorrection pfast phistar
spallationfactor + 5.65622678464828432`*^15 E^(zcalc /
    attn + zcalc / lrock) horizonfactordip k2o[[1]]
neutronmufrn nthermalzcorrection pfast phistar
spallationfactor) + density^2 (1.10307132729322798`*^22
 attn cosmocl36 E^(zcalc / attn +
    zcalc / lrock)
 lamda + 1.10307132729322798`*^22 cosmocl36 E^(zcalc / attn +
    zcalc / lrock) lamda
 lrock - 1.10307132729322798`*^22 attn E^(zcalc / attn +
    zcalc / lrock) horizonfactordip pcaspall -
6.18982673067167876`*^15 cl[[1]] deltaphi E^(zcalc /
    attn) fthermal
 horizonfactordip lrock muonfactor neutronmufrn
 pfast - 5.65622678464828432`*^15 deltaphi E^(zcalc / attn +
    zcalc / lrock) fthermal horizonfactordip k2o[[1]]
 lrock muonfactor neutronmufrn nthermalzcorrection
 pfast - 6.18982673067167876`*^15 attn cl[[1]] E^(zcalc /
    lrock) horizonfactordip muonfactor neutronmufrn pfast
 phistar - 5.65622678464828432`*^15 attn E^(zcalc / attn +
    zcalc / lrock) horizonfactordip k2o[[1]]
 muonfactor neutronmufrn nthermalzcorrection pfast
 phistar - 1.10307132729322798`*^22 attn E^(zcalc / attn +
    zcalc / lrock) horizonfactordip pkspall -
6.18982673067167876`*^15 cl[[1]] deltaphi E^(zcalc /
    attn) fthermal
 horizonfactordip lrock pfast spallationfactor +
6.18982673067167876`*^15 cl[[1]] deltaphi E^(zcalc /
    attn) fthermal horizonfactordip
 lrock neutronmufrn pfast spallationfactor -
5.65622678464828432`*^15 deltaphi E^(zcalc / attn +
    zcalc / lrock) fthermal horizonfactordip k2o[[1]]
 lrock nthermalzcorrection pfast spallationfactor +
5.65622678464828432`*^15 deltaphi E^(zcalc / attn +
    zcalc / lrock) fthermal horizonfactordip k2o[[1]] lrock
 neutronmufrn nthermalzcorrection pfast spallationfactor -
6.18982673067167876`*^15 attn cl[[1]] E^(zcalc /
    lrock) horizonfactordip pfast phistar spallationfactor +
6.18982673067167876`*^15 attn cl[[1]] E^(zcalc /
    lrock) horizonfactordip
 neutronmufrn pfast phistar spallationfactor -
5.65622678464828432`*^15 attn E^(zcalc / attn +
    zcalc / lrock) horizonfactordip k2o[[1]]
 nthermalzcorrection pfast phistar spallationfactor +
5.65622678464828432`*^15 attn E^(zcalc / attn +
    zcalc / lrock) horizonfactordip k2o[[1]] neutronmufrn
 nthermalzcorrection pfast phistar spallationfactor)^2))))*
  (0.05*lamda))^2 +
(1 / (attn^2 cosmocl36 density^2) (4.53279844764821504`*^-23
    E^(-zcalc / attn - zcalc / lrock) (-1.` density (1.10307132729322798`*^22
        attn cosmocl36 E^(zcalc / attn + zcalc / lrock) lamda +
      1.10307132729322798`*^22 cosmocl36 E^(zcalc / attn + zcalc / lrock)
       lamda lrock - 1.10307132729322798`*^22 attn E^(zcalc / attn + zcalc /
    lrock) horizonfactordip pcaspall - 6.18982673067167876`*^15
 cl[[1]] deltaphi E^(zcalc / attn) fthermal horizonfactordip lrock
 muonfactor neutronmufrn pfast - 5.65622678464828432`*^15 deltaphi
 E^(zcalc / attn + zcalc / lrock) fthermal horizonfactordip
 k2o[[1]] lrock muonfactor neutronmufrn nthermalzcorrection pfast -
6.18982673067167876`*^15 attn cl[[1]] E^(zcalc /
    lrock) horizonfactordip muonfactor neutronmufrn pfast phistar -
5.65622678464828432`*^15 attn E^(zcalc / attn + zcalc /
    lrock) horizonfactordip k2o[[1]] muonfactor neutronmufrn
 nthermalzcorrection pfast phistar - 1.10307132729322798`*^22 attn
 E^(zcalc / attn + zcalc / lrock) horizonfactordip pkspall -
6.18982673067167876`*^15 cl[[1]] deltaphi E^(zcalc /
    attn) fthermal horizonfactordip lrock pfast spallationfactor +
6.18982673067167876`*^15 cl[[1]] deltaphi E^(zcalc / attn) fthermal
 horizonfactordip lrock neutronmufrn pfast spallationfactor -
5.65622678464828432`*^15 deltaphi E^(zcalc / attn + zcalc / lrock)
 fthermal horizonfactordip k2o[[1]] lrock nthermalzcorrection pfast
 spallationfactor + 5.65622678464828432`*^15 deltaphi E^(zcalc /
    attn + zcalc / lrock) fthermal horizonfactordip k2o[[1]] lrock
 neutronmufrn nthermalzcorrection pfast spallationfactor -
6.18982673067167876`*^15 attn cl[[1]] E^(zcalc /
    lrock) horizonfactordip pfast phistar spallationfactor +
6.18982673067167876`*^15 attn cl[[1]] E^(zcalc / lrock)
 horizonfactordip neutronmufrn pfast phistar spallationfactor -
5.65622678464828432`*^15 attn E^(zcalc / attn + zcalc / lrock)
 horizonfactordip k2o[[1]] nthermalzcorrection pfast phistar
 spallationfactor + 5.65622678464828432`*^15 attn E^(zcalc /
    attn + zcalc / lrock) horizonfactordip k2o[[1]] neutronmufrn
 nthermalzcorrection pfast phistar spallationfactor) +
√(-4.41228530917291195`*^22 attn cosmocl36 density^2 E^(zcalc /
    attn + zcalc / lrock) lamda lrock
 (1.10307132729322798`*^22 cosmocl36 E^(zcalc / attn + zcalc /
        lrock) lamda - 1.10307132729322798`*^22 E^(zcalc /
        attn + zcalc / lrock) horizonfactordip
    pcaspall - 6.18982673067167876`*^15 cl[[1]] deltaphi E^(zcalc /
       attn) fthermal horizonfactordip muonfactor neutronmufrn
    pfast - 5.65622678464828432`*^15 deltaphi E^(zcalc /
       attn + zcalc / lrock) fthermal horizonfactordip
    k2o[[1]] muonfactor neutronmufrn nthermalzcorrection
    pfast - 6.18982673067167876`*^15 cl[[1]] E^(zcalc /
       lrock) horizonfactordip muonfactor neutronmufrn
    pfast phistar - 5.65622678464828432`*^15 E^(zcalc /
       attn + zcalc / lrock) horizonfactordip
    k2o[[1]] muonfactor neutronmufrn nthermalzcorrection
    pfast phistar - 1.10307132729322798`*^22 E^(zcalc /
       attn + zcalc / lrock) horizonfactordip
    pkspall - 6.18982673067167876`*^15 cl[[1]] deltaphi E^(zcalc /
       attn) fthermal horizonfactordip pfast spallationfactor +
  6.18982673067167876`*^15 cl[[1]] deltaphi E^(zcalc /
       attn) fthermal horizonfactordip neutronmufrn pfast
    spallationfactor - 5.65622678464828432`*^15 deltaphi E^(zcalc /
       attn + zcalc / lrock) fthermal
    horizonfactordip k2o[[1]] nthermalzcorrection pfast
    spallationfactor + 5.65622678464828432`*^15 deltaphi E^(zcalc /
       attn + zcalc / lrock) fthermal horizonfactordip
```

```
k2o[[1]] neutronmufrn nthermalzcorrection pfast
 spallationfactor - 6.18982673067167876`*^15 cl[[1]] E^ (zcalc /
    lrock) horizonfactordip pfast phistar spallationfactor +
 6.18982673067167876`*^15 cl[[1]] E^ (zcalc / lrock)
 horizonfactordip neutronmufrn pfast phistar spallationfactor -
 5.65622678464828432`*^15 E^ (zcalc / attn + zcalc /
      lrock) horizonfactordip k2o[[1]] nthermalzcorrection pfast
 phistar spallationfactor + 5.65622678464828432`*^15 E^ (zcalc /
      attn + zcalc / lrock) horizonfactordip k2o[[1]] neutronmufrn
 nthermalzcorrection pfast phistar spallationfactor) +
density^2 (1.10307132729322798`*^22 attn cosmocl36 E^ (zcalc /
      attn + zcalc / lrock)
 lamda + 1.10307132729322798`*^22 cosmocl36 E^ (zcalc /
      attn + zcalc / lrock) lamda
 lrock - 1.10307132729322798`*^22 attn E^ (zcalc /
      attn + zcalc / lrock) horizonfactordip pcaspall -
 6.18982673067167876`*^15 cl[[1]] deltaphi E^ (zcalc / attn)
 fthermal horizonfactordip lrock muonfactor neutronmufrn
 pfast - 5.65622678464828432`*^15 deltaphi E^ (zcalc /
      attn + zcalc / lrock) fthermal horizonfactordip k2o[[1]]
 lrock muonfactor neutronmufrn nthermalzcorrection
 pfast - 6.18982673067167876`*^15 attn cl[[1]] E^ (zcalc /
    lrock) horizonfactordip muonfactor neutronmufrn pfast
 phistar - 5.65622678464828432`*^15 attn E^ (zcalc /
      attn + zcalc / lrock) horizonfactordip k2o[[1]]
 muonfactor neutronmufrn nthermalzcorrection pfast
 phistar - 1.10307132729322798`*^22 attn E^ (zcalc /
      attn + zcalc / lrock) horizonfactordip pkspall -
 6.18982673067167876`*^15 cl[[1]] deltaphi E^ (zcalc / attn)
 fthermal horizonfactordip lrock pfast spallationfactor +
 6.18982673067167876`*^15 cl[[1]] deltaphi E^ (zcalc /
    attn) fthermal horizonfactordip
 lrock neutronmufrn pfast spallationfactor -
 5.65622678464828432`*^15 deltaphi E^ (zcalc /
      attn + zcalc / lrock) fthermal horizonfactordip k2o[[1]]
 lrock nthermalzcorrection pfast spallationfactor +
 5.65622678464828432`*^15 deltaphi E^ (zcalc /
      attn + zcalc / lrock)
 fthermal horizonfactordip k2o[[1]] lrock neutronmufrn
 nthermalzcorrection pfast spallationfactor -
 6.18982673067167876`*^15 attn cl[[1]] E^ (zcalc /
    lrock) horizonfactordip pfast phistar spallationfactor +
 6.18982673067167876`*^15 attn cl[[1]] E^ (zcalc /
    lrock) horizonfactordip neutronmufrn pfast phistar
 spallationfactor - 5.65622678464828432`*^15 attn E^ (zcalc /
      attn + zcalc / lrock) horizonfactordip
 k2o[[1]] nthermalzcorrection pfast phistar
 spallationfactor + 5.65622678464828432`*^15 attn E^ (zcalc /
      attn + zcalc / lrock) horizonfactordip
 k2o[[1]] neutronmufrn nthermalzcorrection
 pfast phistar spallationfactor) ^2)) zcalc) +
1 / (cosmocl36 density^2) (4.53279844764821504`*^-23
   E^ (-zcalc / attn - zcalc / lrock) (-1.` density (1.10307132729322798`*^22
        cosmocl36 E^ (zcalc / attn + zcalc / lrock) lamda -
      1.10307132729322798`*^22 E^ (zcalc / attn + zcalc / lrock)
```

```
horizonfactordip pcaspall - 6.18982673067167876`*^15 cl[[1]] E^
  (zcalc / lrock) horizonfactordip muonfactor neutronmufrn pfast
 phistar - 5.65622678464828432`*^15 E^ (zcalc / attn + zcalc /
      lrock) horizonfactordip k2o[[1]] muonfactor neutronmufrn
 nthermalzcorrection pfast phistar - 1.10307132729322798`*^22 E^
  (zcalc / attn + zcalc / lrock) horizonfactordip pkspall -
6.18982673067167876`*^15 cl[[1]] E^ (zcalc / lrock) horizonfactordip
 pfast phistar spallationfactor + 6.18982673067167876`*^15 cl[[1]]
 E^ (zcalc / lrock) horizonfactordip neutronmufrn pfast phistar
 spallationfactor - 5.65622678464828432`*^15 E^ (zcalc / attn +
    zcalc / lrock) horizonfactordip k2o[[1]] nthermalzcorrection
 pfast phistar spallationfactor + 5.65622678464828432`*^15 E^
  (zcalc / attn + zcalc / lrock) horizonfactordip k2o[[1]]
 neutronmufrn nthermalzcorrection pfast phistar spallationfactor -
(1.10307132729322798`*^22 cosmocl36 E^ (zcalc / attn + zcalc / lrock)
    lamda zcalc) / attn - 1 / attn^2 (1.10307132729322798`*^22
    cosmocl36 E^ (zcalc / attn + zcalc / lrock)
    lamda lrock zcalc) + 1 / attn (1.10307132729322798`*^22 E^ (zcalc /
        attn + zcalc / lrock) horizonfactordip pcaspall zcalc) +
1 / attn^2 (6.18982673067167876`*^15 cl[[1]] deltaphi E^ (zcalc /
      attn) fthermal horizonfactordip
    lrock muonfactor neutronmufrn pfast zcalc) + 1 / attn^
    2 (5.65622678464828432`*^15 deltaphi E^ (zcalc / attn + zcalc /
        lrock) fthermal horizonfactordip k2o[[1]] lrock muonfactor
    neutronmufrn nthermalzcorrection pfast zcalc) +
1 / attn (5.65622678464828432`*^15 E^ (zcalc / attn + zcalc /
        lrock) horizonfactordip k2o[[1]] muonfactor
    neutronmufrn nthermalzcorrection pfast phistar zcalc) +
1 / attn (1.10307132729322798`*^22 E^ (zcalc / attn + zcalc /
        lrock) horizonfactordip pkspall zcalc) + 1 / attn^
    2 (6.18982673067167876`*^15 cl[[1]] deltaphi E^ (zcalc / attn)
    fthermal horizonfactordip lrock pfast spallationfactor zcalc) -
1 / attn^2 (6.18982673067167876`*^15 cl[[1]] deltaphi E^ (zcalc /
      attn) fthermal horizonfactordip lrock
    neutronmufrn pfast spallationfactor zcalc) + 1 / attn^
    2 (5.65622678464828432`*^15 deltaphi E^ (zcalc / attn + zcalc /
        lrock) fthermal horizonfactordip k2o[[1]] lrock
    nthermalzcorrection pfast spallationfactor zcalc) - 1 / attn^
    2 (5.65622678464828432`*^15 deltaphi E^ (zcalc / attn + zcalc /
        lrock) fthermal horizonfactordip k2o[[1]] lrock
    neutronmufrn nthermalzcorrection pfast spallationfactor
    zcalc) + 1 / attn (5.65622678464828432`*^15 E^ (zcalc /
        attn + zcalc / lrock) horizonfactordip k2o[[1]]
    nthermalzcorrection pfast phistar spallationfactor zcalc) -
1 / attn (5.65622678464828432`*^15 E^ (zcalc / attn + zcalc /
        lrock) horizonfactordip k2o[[1]] neutronmufrn
    nthermalzcorrection pfast phistar spallationfactor zcalc)) +
(-4.41228530917291195`*^22 cosmocl36 density^2 E^ (zcalc /
      attn + zcalc / lrock) lamda lrock
  (1.10307132729322798`*^22 cosmocl36 E^ (zcalc / attn + zcalc /
        lrock) lamda - 1.10307132729322798`*^22 E^ (zcalc /
        attn + zcalc / lrock) horizonfactordip
    pcaspall - 6.18982673067167876`*^15 cl[[1]] deltaphi E^ (zcalc /
      attn) fthermal horizonfactordip muonfactor neutronmufrn
    pfast - 5.65622678464828432`*^15 deltaphi E^ (zcalc /
```

```
attn + zcalc / lrock) fthermal horizonfactordip
k2o[[1]] muonfactor neutronmufrn nthermalzcorrection
pfast - 6.18982673067167876`*^15 cl[[1]] E^ (zcalc /
lrock) horizonfactordip muonfactor neutronmufrn
pfast phistar - 5.65622678464828432`*^15 E^ (zcalc /
attn + zcalc / lrock) horizonfactordip
k2o[[1]] muonfactor neutronmufrn nthermalzcorrection
pfast phistar - 1.10307132729322798`*^22 E^ (zcalc /
attn + zcalc / lrock) horizonfactordip
pkspall - 6.18982673067167876`*^15 cl[[1]] deltaphi E^ (zcalc /
attn) fthermal horizonfactordip pfast spallationfactor +
6.18982673067167876`*^15 cl[[1]] deltaphi E^ (zcalc /
attn) fthermal horizonfactordip neutronmufrn pfast
spallationfactor - 5.65622678464828432`*^15 deltaphi E^ (zcalc /
attn + zcalc / lrock) fthermal
horizonfactordip k2o[[1]] nthermalzcorrection pfast
spallationfactor + 5.65622678464828432`*^15 deltaphi E^ (zcalc /
attn + zcalc / lrock) fthermal horizonfactordip
k2o[[1]] neutronmufrn nthermalzcorrection pfast
spallationfactor - 6.18982673067167876`*^15 cl[[1]] E^ (zcalc /
lrock) horizonfactordip pfast phistar spallationfactor +
6.18982673067167876`*^15 cl[[1]] E^ (zcalc / lrock)
horizonfactordip neutronmufrn pfast phistar spallationfactor -
5.65622678464828432`*^15 E^ (zcalc / attn + zcalc /
lrock) horizonfactordip k2o[[1]] nthermalzcorrection pfast
phistar spallationfactor + 5.65622678464828432`*^15 E^ (zcalc /
attn + zcalc / lrock) horizonfactordip k2o[[1]] neutronmufrn
nthermalzcorrection pfast phistar spallationfactor) + 1 / attn
(4.41228530917291195`*^22 cosmocl36 density^2 E^ (zcalc /
attn + zcalc / lrock) lamda
lrock (1.10307132729322798`*^22 cosmocl36 E^ (zcalc /
attn + zcalc /
lrock) lamda - 1.10307132729322798`*^22 E^ (zcalc /
attn + zcalc / lrock) horizonfactordip pcaspall -
6.18982673067167876`*^15 cl[[1]] deltaphi E^ (zcalc /
attn) fthermal horizonfactordip muonfactor neutronmufrn
pfast - 5.65622678464828432`*^15 deltaphi E^ (zcalc /
attn + zcalc / lrock) fthermal horizonfactordip k2o[[1]]
muonfactor neutronmufrn nthermalzcorrection
pfast - 6.18982673067167876`*^15 cl[[1]] E^ (zcalc /
lrock) horizonfactordip muonfactor neutronmufrn
pfast phistar - 5.65622678464828432`*^15 E^ (zcalc /
attn + zcalc / lrock) horizonfactordip k2o[[1]]
muonfactor neutronmufrn nthermalzcorrection
pfast phistar - 1.10307132729322798`*^22 E^ (zcalc /
attn + zcalc / lrock) horizonfactordip pkspall -
6.18982673067167876`*^15 cl[[1]] deltaphi E^ (zcalc /
attn) fthermal horizonfactordip pfast spallationfactor +
6.18982673067167876`*^15 cl[[1]] deltaphi E^ (zcalc /
attn) fthermal
horizonfactordip neutronmufrn pfast spallationfactor -
5.65622678464828432`*^15 deltaphi E^ (zcalc /
attn + zcalc / lrock) fthermal horizonfactordip k2o[[1]]
nthermalzcorrection pfast spallationfactor +
5.65622678464828432`*^15 deltaphi E^ (zcalc /
attn + zcalc / lrock) fthermal horizonfactordip k2o[[1]]
neutronmufrn nthermalzcorrection pfast spallationfactor -
6.18982673067167876`*^15 cl[[1]] E^ (zcalc /
lrock) horizonfactordip pfast phistar spallationfactor +
6.18982673067167876`*^15 cl[[1]] E^ (zcalc /
lrock) horizonfactordip neutronmufrn pfast phistar
spallationfactor - 5.65622678464828432`*^15 E^ (zcalc /
attn + zcalc / lrock) horizonfactordip
k2o[[1]] nthermalzcorrection pfast phistar
spallationfactor + 5.65622678464828432`*^15 E^ (zcalc /
attn + zcalc / lrock) horizonfactordip k2o[[1]]
neutronmufrn nthermalzcorrection pfast phistar
spallationfactor) zcalc) - 4.41228530917291195`*^22
attn cosmocl36 density^2 E^ (zcalc / attn + zcalc /
lrock) lamda lrock (- (1.10307132729322798`*^22
cosmocl36 E^ (zcalc / attn +
zcalc / lrock) lamda zcalc) / attn^
2 + 1 / attn^2 (1.10307132729322798`*^22 E^ (zcalc /
attn + zcalc / lrock) horizonfactordip pcaspall zcalc) + 1 /
attn^2 (6.18982673067167876`*^15 cl[[1]] deltaphi E^ (zcalc /
attn) fthermal horizonfactordip
muonfactor neutronmufrn pfast zcalc) + 1 / attn^
2 (5.65622678464828432`*^15 deltaphi E^ (zcalc /
attn + zcalc / lrock) fthermal horizonfactordip k2o[[1]]
muonfactor neutronmufrn nthermalzcorrection pfast
zcalc) + 1 / attn^2 (5.65622678464828432`*^15 E^ (zcalc /
attn + zcalc / lrock) horizonfactordip k2o [[1]] muonfactor
neutronmufrn nthermalzcorrection pfast phistar
zcalc) + 1 / attn^2 (1.10307132729322798`*^22 E^ (zcalc /
attn + zcalc / lrock) horizonfactordip pkspall zcalc) + 1 /
attn^2 (6.18982673067167876`*^15 cl[[1]] deltaphi E^ (zcalc /
attn) fthermal
horizonfactordip pfast spallationfactor zcalc) - 1 / attn^
2 (6.18982673067167876`*^15 cl[[1]] deltaphi E^ (zcalc /
attn) fthermal horizonfactordip
neutronmufrn pfast spallationfactor zcalc) + 1 / attn^
2 (5.65622678464828432`*^15 deltaphi E^ (zcalc /
attn + zcalc / lrock) fthermal horizonfactordip k2o[[1]]
nthermalzcorrection pfast spallationfactor zcalc) - 1 / attn^
2 (5.65622678464828432`*^15 deltaphi E^ (zcalc /
attn + zcalc / lrock) fthermal horizonfactordip k2o[[1]]
neutronmufrn nthermalzcorrection pfast spallationfactor
zcalc) + 1 / attn^2 (5.65622678464828432`*^15 E^ (zcalc /
attn + zcalc / lrock) horizonfactordip k2o[[1]]
nthermalzcorrection pfast phistar spallationfactor
zcalc) - 1 / attn^2 (5.65622678464828432`*^15 E^ (zcalc /
attn + zcalc / lrock) horizonfactordip
k2o [[1]] neutronmufrn nthermalzcorrection
pfast phistar spallationfactor zcalc)) +
2 density^2 (1.10307132729322798`*^22 attn cosmocl36 E^ (zcalc /
attn + zcalc /
lrock) lamda + 1.10307132729322798`*^22 cosmocl36 E^ (zcalc /
attn + zcalc / lrock)
lamda lrock - 1.10307132729322798`*^22 attn E^ (zcalc /
attn + zcalc / lrock) horizonfactordip pcaspall -
```

```
6.18982673067167876`*^15 cl[[1]] deltaphi E^ (zcalc / attn)
 fthermal horizonfactordip lrock muonfactor neutronmufrn pfast -
5.65622678464828432`*^15 deltaphi E^ (zcalc / attn + zcalc /
      lrock) fthermal horizonfactordip k2o[[1]]
 lrock muonfactor neutronmufrn nthermalzcorrection
 pfast - 6.18982673067167876`*^15 attn cl[[1]] E^ (zcalc /
     lrock) horizonfactordip muonfactor neutronmufrn pfast
 phistar - 5.65622678464828432`*^15 attn E^ (zcalc /
      attn + zcalc / lrock) horizonfactordip k2o[[1]]
 muonfactor neutronmufrn nthermalzcorrection pfast
 phistar - 1.10307132729322798`*^22 attn E^ (zcalc / attn + zcalc /
      lrock) horizonfactordip pkspall - 6.18982673067167876`*^15
 cl[[1]] deltaphi E^ (zcalc / attn) fthermal
 horizonfactordip lrock pfast spallationfactor +
6.18982673067167876`*^15 cl[[1]] deltaphi E^ (zcalc /
     attn) fthermal horizonfactordip lrock neutronmufrn pfast
 spallationfactor - 5.65622678464828432`*^15 deltaphi E^ (zcalc /
      attn + zcalc / lrock) fthermal horizonfactordip k2o[[1]]
 lrock nthermalzcorrection pfast spallationfactor +
5.65622678464828432`*^15 deltaphi E^ (zcalc / attn + zcalc /
      lrock) fthermal horizonfactordip k2o[[1]] lrock
 neutronmufrn nthermalzcorrection pfast spallationfactor -
6.18982673067167876`*^15 attn cl[[1]] E^ (zcalc /
     lrock) horizonfactordip pfast phistar spallationfactor +
6.18982673067167876`*^15 attn cl[[1]] E^ (zcalc /
     lrock) horizonfactordip neutronmufrn pfast phistar
 spallationfactor - 5.65622678464828432`*^15 attn E^ (zcalc /
      attn + zcalc / lrock) horizonfactordip k2o[[1]]
 nthermalzcorrection pfast phistar spallationfactor +
5.65622678464828432`*^15 attn E^ (zcalc / attn + zcalc /
      lrock) horizonfactordip k2o[[1]] neutronmufrn
 nthermalzcorrection pfast phistar spallationfactor)
(1.10307132729322798`*^22 cosmocl36 E^ (zcalc / attn + zcalc /
      lrock) lamda - 1.10307132729322798`*^22 E^ (zcalc /
      attn + zcalc / lrock) horizonfactordip
 pcaspall - 6.18982673067167876`*^15 cl[[1]] E^ (zcalc /
     lrock) horizonfactordip muonfactor neutronmufrn
 pfast phistar - 5.65622678464828432`*^15 E^ (zcalc /
      attn + zcalc / lrock) horizonfactordip k2o[[1]]
 muonfactor neutronmufrn nthermalzcorrection pfast
 phistar - 1.10307132729322798`*^22 E^ (zcalc / attn + zcalc /
      lrock) horizonfactordip pkspall - 6.18982673067167876`*^15
 cl[[1]] E^ (zcalc / lrock) horizonfactordip
 pfast phistar spallationfactor + 6.18982673067167876`*^15
 cl[[1]] E^ (zcalc / lrock) horizonfactordip
 neutronmufrn pfast phistar spallationfactor -
5.65622678464828432`*^15 E^ (zcalc / attn + zcalc /
      lrock) horizonfactordip k2o[[1]] nthermalzcorrection pfast
 phistar spallationfactor + 5.65622678464828432`*^15 E^ (zcalc /
      attn + zcalc / lrock) horizonfactordip k2o[[1]] neutronmufrn
 nthermalzcorrection pfast phistar spallationfactor -
(1.10307132729322798`*^22 cosmocl36 E^ (zcalc /
       attn + zcalc / lrock) lamda zcalc) / attn - 1 / attn^
   2 (1.10307132729322798`*^22 cosmocl36 E^ (zcalc /
       attn + zcalc / lrock) lamda lrock
```

```
 zcalc) + 1 / attn (1.10307132729322798`*^22 E^ (zcalc /
      attn + zcalc / lrock) horizonfactordip pcaspall zcalc) + 1 /
 attn^2 (6.18982673067167876`*^15 cl[[1]] deltaphi E^ (zcalc /
     attn) fthermal horizonfactordip lrock
 muonfactor neutronmufrn pfast zcalc) + 1 / attn^
 2 (5.65622678464828432`*^15 deltaphi E^ (zcalc /
      attn + zcalc / lrock) fthermal horizonfactordip k2o[[1]]
 lrock muonfactor neutronmufrn nthermalzcorrection pfast
 zcalc) + 1 / attn (5.65622678464828432`*^15 E^ (zcalc /
      attn + zcalc / lrock) horizonfactordip k2o[[1]] muonfactor
 neutronmufrn nthermalzcorrection pfast phistar
 zcalc) + 1 / attn (1.10307132729322798`*^22 E^ (zcalc /
      attn + zcalc / lrock) horizonfactordip pkspall zcalc) + 1 /
 attn^2 (6.18982673067167876`*^15 cl[[1]] deltaphi E^ (zcalc /
     attn) fthermal horizonfactordip
 lrock pfast spallationfactor zcalc) - 1 / attn^
 2 (6.18982673067167876`*^15 cl[[1]] deltaphi E^ (zcalc /
     attn) fthermal horizonfactordip lrock
 neutronmufrn pfast spallationfactor zcalc) + 1 / attn^
 2 (5.65622678464828432`*^15 deltaphi E^ (zcalc /
      attn + zcalc / lrock) fthermal horizonfactordip k2o[[1]]
 lrock nthermalzcorrection pfast spallationfactor zcalc) - 1 /
 attn^2 (5.65622678464828432`*^15 deltaphi E^ (zcalc /
      attn + zcalc / lrock) fthermal
 horizonfactordip k2o[[1]] lrock neutronmufrn
 nthermalzcorrection pfast spallationfactor
 zcalc) + 1 / attn (5.65622678464828432`*^15 E^ (zcalc /
      attn + zcalc / lrock) horizonfactordip k2o [[1]]
 nthermalzcorrection pfast phistar spallationfactor
 zcalc) - 1 / attn (5.65622678464828432`*^15 E^ (zcalc /
      attn + zcalc / lrock) horizonfactordip k2o[[1]]
 neutronmufrn nthermalzcorrection pfast phistar
 spallationfactor zcalc))) / (2 √(-4.41228530917291195`*^22
attn cosmocl36 density^2 E^ (zcalc / attn + zcalc /
     lrock) lamda lrock (1.10307132729322798`*^22
   cosmocl36 E^ (zcalc / attn +
      zcalc / lrock)
   lamda - 1.10307132729322798`*^22 E^ (zcalc / attn +
      zcalc / lrock) horizonfactordip pcaspall -
 6.18982673067167876`*^15 cl[[1]] deltaphi E^ (zcalc /
      attn) fthermal horizonfactordip muonfactor neutronmufrn
  pfast - 5.65622678464828432`*^15 deltaphi E^ (zcalc / attn +
      zcalc / lrock) fthermal horizonfactordip k2o[[1]]
   muonfactor neutronmufrn nthermalzcorrection
   pfast - 6.18982673067167876`*^15 cl[[1]] E^ (zcalc /
      lrock) horizonfactordip muonfactor neutronmufrn pfast
   phistar - 5.65622678464828432`*^15 E^ (zcalc / attn +
      zcalc / lrock) horizonfactordip k2o[[1]]
   muonfactor neutronmufrn nthermalzcorrection pfast
   phistar - 1.10307132729322798`*^22 E^ (zcalc / attn +
      zcalc / lrock) horizonfactordip pkspall -
 6.18982673067167876`*^15 cl[[1]] deltaphi E^ (zcalc /
      attn) fthermal horizonfactordip pfast spallationfactor +
 6.18982673067167876`*^15 cl[[1]] deltaphi E^ (zcalc /
      attn) fthermal
```

```
horizonfactordip neutronmufrn pfast spallationfactor -
5.65622678464828432`*^15 deltaphi E^(zcalc / attn +
    zcalc / lrock) fthermal horizonfactordip k2o[[1]]
 nthermalzcorrection pfast spallationfactor +
5.65622678464828432`*^15 deltaphi E^(zcalc / attn +
    zcalc / lrock) fthermal horizonfactordip k2o[[1]]
 neutronmufrn nthermalzcorrection pfast spallationfactor -
6.18982673067167876`*^15 cl[[1]] E^(zcalc /
    lrock) horizonfactordip pfast phistar spallationfactor +
6.18982673067167876`*^15 cl[[1]] E^(zcalc /
    lrock) horizonfactordip neutronmufrn pfast phistar
 spallationfactor - 5.65622678464828432`*^15 E^(zcalc / attn +
    zcalc / lrock) horizonfactordip
 k2o[[1]] nthermalzcorrection pfast phistar
 spallationfactor + 5.65622678464828432`*^15 E^(zcalc / attn +
    zcalc / lrock) horizonfactordip k2o[[1]]
 neutronmufrn nthermalzcorrection pfast phistar
 spallationfactor) + density^2 (1.10307132729322798`*^22
  attn cosmocl36 E^(zcalc / attn + zcalc / lrock)
  lamda + 1.10307132729322798`*^22 cosmocl36 E^
   (zcalc / attn + zcalc / lrock)
  lamda lrock - 1.10307132729322798`*^22 attn E^
   (zcalc / attn + zcalc / lrock) horizonfactordip pcaspall -
6.18982673067167876`*^15 cl[[1]] deltaphi E^(zcalc / attn)
  fthermal horizonfactordip lrock muonfactor neutronmufrn
  pfast - 5.65622678464828432`*^15 deltaphi E^
   (zcalc / attn + zcalc / lrock) fthermal horizonfactordip
  k2o[[1]] lrock muonfactor neutronmufrn nthermalzcorrection
  pfast - 6.18982673067167876`*^15 attn cl[[1]] E^
   (zcalc / lrock) horizonfactordip muonfactor neutronmufrn
  pfast phistar - 5.65622678464828432`*^15 attn E^
   (zcalc / attn + zcalc / lrock) horizonfactordip k2o[[1]]
  muonfactor neutronmufrn nthermalzcorrection
  pfast phistar - 1.10307132729322798`*^22 attn E^
   (zcalc / attn + zcalc / lrock) horizonfactordip pkspall -
6.18982673067167876`*^15 cl[[1]] deltaphi E^(zcalc / attn)
  fthermal horizonfactordip lrock pfast spallationfactor +
6.18982673067167876`*^15 cl[[1]] deltaphi E^(zcalc / attn)
  fthermal horizonfactordip lrock neutronmufrn pfast
  spallationfactor - 5.65622678464828432`*^15 deltaphi E^
   (zcalc / attn + zcalc / lrock) fthermal horizonfactordip
  k2o[[1]] lrock nthermalzcorrection pfast
  spallationfactor + 5.65622678464828432`*^15 deltaphi E^
   (zcalc / attn + zcalc / lrock) fthermal horizonfactordip
  k2o[[1]] lrock neutronmufrn nthermalzcorrection pfast
  spallationfactor - 6.18982673067167876`*^15 attn cl[[1]] E^
   (zcalc / lrock) horizonfactordip pfast phistar
  spallationfactor + 6.18982673067167876`*^15 attn cl[[1]] E^
   (zcalc / lrock) horizonfactordip neutronmufrn pfast
  phistar spallationfactor - 5.65622678464828432`*^15 attn E^
   (zcalc / attn + zcalc / lrock) horizonfactordip
  k2o[[1]] nthermalzcorrection pfast phistar
  spallationfactor + 5.65622678464828432`*^15 attn E^
   (zcalc / attn + zcalc / lrock) horizonfactordip k2o[[1]]
  neutronmufrn nthermalzcorrection pfast phistar
                                    spallationfactor) ^2)))) * (0.10 * attn)) ^2) ^
    0.5) +
  (evalue * (pcamustddvn + pkmustddvn + pnmuoncl35stddvn + pnmuonk39stddvn) / ptotal);
```

■ Cl-36 Results

```
StringForm[
"`` :
[Cl-36] = `` +/- ``atom/g\n
: Cosmogenic Cl-36 = `` +/- ``atom/g\n
: N-produced background = `` +/- ``atom/g\n",
samplename,
ScientificForm[N[cl36concentration, 4]], ScientificForm[N[cl36concentrationstddvn,
3]],
ScientificForm[N[cosmocl36, 4]], ScientificForm[N[cosmocl36stddvn, 3]],
ScientificForm[N[cl36bckgd, 3]], ScientificForm[N[cl36bckgdstddvn, 2]]]
```

```
N5/97 - CN0597 : [Cl-36] = 2.011×10^5 +/- 1.7×10^4atom/g
 : Cosmogenic Cl-36 = 2.011×10^5 +/- 1.7×10^4atom/g
 : N-produced background = 7.86×10^1 +/- 1.2×10^1atom/g
```

■ Neutron capture results

```
StringForm[
"\t\tFraction stopped by Cl35 = `` +/- ``\n
K39(n,alpha)Cl36 fraction = `` +/- ``\n
Fraction stopped by major elts = ``\n
Fraction stopped by trace elts = ``\n
X-section = `` +/- ``cm^2/g\n
Mean Free Path = `` +/- ``g/cm^2\n
Major absorber is ``\n
Background n prod'n from U and Th = `` +/- ``n/g/a\n",

N[cl35capturefrn, 4], N[cl35capturefrnstddvn, 4], N[k39capturefrn, 3],
N[k39capturefrnstddvn, 3], N[stopping[[1]], 4], N[stopping[[2]], 4],
N[sigmathermalrock, 4], N[sigmathermalrockstddvn, 3], N[sigmathermalrock^-1, 4],
N[sigmathermalrockstddvn sigmathermalrock^-2, 2], maxabsorber, N[bckgdneutrons, 3],
N[bckgdneutronsstddvn, 2]]
```

```
 Fraction stopped by Cl35 = 0.000154211960050401941` +/- 0.000018196107665879392`
K39(n,alpha)Cl36 fraction = 0.000076261489770527930 4` +/- 1.07832281547951946`*^-6
Fraction stopped by major elts = 0.847109043971459385`
Fraction stopped by trace elts = 0.152809056028540543`
X-section = 0.00618594081517553284` +/- 0.00005594318066875009 87`cm^2/g
Mean Free Path = 161.656897451519521` +/- 1.46196048276018668`g/cm^2
Major absorber is Iron
Background
 n prod'n from U and Th = 1.17439224999999991` +/- 0.106156747550190999`n/g/a
```

■ Production Rate Results

```
StringForm["
\t\tThermal n Cl35 capture (excluding muon contribution) = `` +/- ``atom/g/a\n
Thermal n Cl35 capture from muon contribution = `` +/- ``atom/g/a\n
Total thermal n Cl35 capture = `` +/- ``atom/g/a\n
Epith. n Cl35 capture = `` +/- ``atom/g/a\n
Ca spallation rate = `` +/- ``atom/g/a\n
Ca (mu, alpha) = `` +/- ``atom/g/a\n
K spallation rate = `` +/- ``atom/g/a\n
K (mu, alpha) = `` +/- ``atom/g/a\n
K-39(n, alpha)Cl-36 excluding muon rate = `` +/- ``atom/g/a\n
K-39(n, alpha)Cl-36 from muon rate = `` +/- ``atom/g/a\n
Total K-39(n, alpha)Cl-36 rate = `` +/- ``atom/g/a\n
P_Ca = `` ± `` atom/g/a\n
P_K = `` ± `` atom/g/a\n
P_35Cl(n,γ)36Cl = `` ± ``\n\n
Total production = `` +/- ``atom/g/a\n",

N[pnthermal, 4], N[pnthermalstddvn, 3],
N[pnmuoncl35, 4], N[pnmuoncl35stddvn, 3],
N[pneutronscl35total, 4], N[pneutronscl35totalstddvn, 3],
N[pnepithermal, 4], N[pnepithermalstddvn, 3],
N[pcaspallx, 4], N[pcaspallxstddvn, 3],
N[pcamu, 4], N[pcamustddvn, 3],
N[pkspallx, 4], N[pkspallxstddvn, 3],
N[pkmu, 4], N[pkmustddvn, 3],
N[p39, 4], N[p39stddvn, 3],
N[pnmuonk39, 4], N[pnmuonk39stddvn, 3],
N[pneutronsk39total, 4], N[pneutronsk39totalstddvn, 3],
N[horizonfactordip * pcaspall + pcaperstoppedmuon * slopestop[zcalc], 4],
 N[horizonfactordip * pcaspall ((pcaspallstddvn / pcaspall) ^2 + (0.10) ^2) ^0.5, 3],
N[horizonfactordip * pkspall + pkperstoppedmuon * slopestop[zcalc], 4],
 N[horizonfactordip * pkspall ((pkspallstddvn / pkspall) ^2 + (0.10) ^2) ^0.5, 3],
N[pneutronscl35total, 4], N[pneutronscl35totalstddvn, 3],
N[ptotal, 4], N[ptotalstddvn, 3]]
```

```
  Thermal n Cl35 capture (excluding muon
 contribution) = 0.110440130973677819` +/- 0.025985190988734077`atom/g/a
Thermal n Cl35 capture from muon contribution =
 0.0174684114302705362` +/- 0.0072850316553487015 6`atom/g/a
  Total
 thermal n Cl35 capture = 0.127908542403948355` +/- 0.0269870679574573113`atom/g/a
Epith. n Cl35 capture = 0.0200621556978077997` +/- 0.00467741830756028864`atom/g/a
Ca spallation rate = 8.75973791616711849` +/- 1.75196943870881227`atom/g/a
Ca (mu, alpha) = 0.563630587865690113` +/- 0.225452235146276036`atom/g/a
K spallation rate = 3.28042735275649022` +/- 0.657053691423618779`atom/g/a
K (mu, alpha) = 0.0497467739461904034` +/- 0.0198987095784761649`atom/g/a
K-39(n, alpha)Cl-36 excluding muon
 rate = 0.0546152770235990736` +/- 0.0111444052609586585`atom/g/a
K-39(n, alpha)Cl-36 from muon
 rate = 0.00863854579866276495` +/- 0.00345757657102160287`atom/g/a
   Total K-39(n, alpha)Cl-36
 rate = 0.0632538228222618315` +/- 0.0116684448134685259`atom/g/a
P_Ca = 9.3234125796333469` ± 1.95875649271904865` atom/g/a
P_K = 3.33017801687291559` ± 0.734391986326466827` atom/g/a
P_35Cl(n,γ)36Cl = 0.127908542403948355` ± 0.0269870679574573113`

Total production = 12.8647671516595085` +/- 1.88500065497117113`atom/g/a
```

■ Correction Factors

```
If[Apply[Plus, shielding][[1]] == 360,
StringForm["
\t\tAltitude/Latitude scaling (spallation) = ``\n
Altitude/Latitude scaling (muons) = ``\n
Fraction of 2Pi flux = ``\n
Free face shielding correction for spallogenic reactions = ``\n
Total reduction in 2Pi surface rate due to slope and topography = ``\n
Dipping surface correction for muon reactions = ``\n
Effective attenuation length for spallation = ``\n
Depth/thickness correction (spallation) = ``\n
Depth/thickness correction (thermal n) = ``\n
Depth/thickness correction (epithermal n) = ``\n",

spallationfactor, muonfactor, horizonfactor, hzncorrn[dip], horizonfactordip,
muonhzncorrn[dip], If[dip == 0, 160, NumberForm[attn, 4]], depthfactor,
nthermalzcorrection, nepizcorrection],

StringForm["!!Danger !!Danger, horizon sectors don't add up to 360 degrees. Try
again stupid"]]
```

```
   Altitude/Latitude scaling (spallation) = 5.09938723756235834`
 Altitude/Latitude scaling (muons) = 2.52619943410068525`
 Fraction of 2Pi flux = 0.999921806667219748`
 Free face shielding correction for spallogenic reactions = 0.530772736000000122`
 Total
  reduction in 2Pi surface rate due to slope and topography = 0.530731233110823374`
 Dipping surface correction for muon reactions = 0.525350040000000007`
 Effective attenuation length for spallation = 95.99
 Depth/thickness correction (spallation) = 0.927815479147153965`
 Depth/thickness correction (thermal n) = 1.32536001481881293`
 Depth/thickness correction (epithermal n) = 1.0132161336809049`
```

■ Denudation Rate

```
StringForm[" Dip = ```°\n
Error calculated using iteration only = ``m/Ma\n
Perpendicular denudation rate =  `` ± `` m/Ma\n",

dip, NumberForm[deltaevalueiterative,6], NumberForm[evalue, 6],
NumberForm[deltaevalue, 6]]
```

```
 Dip = 88°
 Error calculated using iteration only = 2.53562m/Ma
 Perpendicular denudation rate =  22.9523 ± 4.41427 m/Ma
```

■ Calibration used for the calculation

```
StringForm[

"Calculation assumes surface prod'n rates (at sea-level and high latitude)as
follows:\n

Fast n prod'n rate in air = `` +/- ``n/g/a\n
P Ca spallation = `` +/- ``aton/gCa/a\n
P K spallation = `` +/- ``atom/gK/a\n
P Ca-40(mu-,alpha) = `` +/- ``atom/gCa/a\n
P K(mu-,p2n) = `` +/- ``atom/gk/a\n
These can be adjusted in the 'Input data' cell at the top of the worksheet if
required.", N[pfast, 4], N[pfaststddvn, 3], N[139.92 caspall, 3], N[139.92
caspallstddvn, 3], N[120.46 kspall, 4], N[120.46 kspallstddvn, 3], N[139.92 camu,
3], N[139.92 camustddvn, 2], N[120.46 kmu, 3], N[120.46 kmustddvn, 2]]
```

```
Calculation assumes
  surface prod'n rates (at sea-level and high latitude)as follows:
  Fast n prod'n rate in air = 586.000000000000031` +/- 117.200000000000015`n/g/a
 P Ca spallation = 48.7621199999999888` +/- 9.75242399999999953`aton/gCa/a
 P K spallation = 171.053199999999989` +/- 34.2106399999999988`atom/gK/a
 P Ca-40(mu-,alpha) = 5.29737119999999883` +/- 1.05919439999999998`atom/gCa/a
 P K(mu-,p2n) = 8.99836200000000019` +/- 1.99963599999999992`atom/gk/a
 These
  can be adjusted in the 'Input data' cell at the top of the worksheet if required.
```

Appendix 9

Fleming, A., Summerfield, M.A., Stone, J.O., Fifield, L.K., and Cresswell, R.G., 1999. Denudation rates for the southern Drakensberg escarpment, SE Africa, derived from *in-situ*-produced cosmogenic ^{36}Cl: initial results. *Journal of the Geological Society, London*. **156**, 209-212.

Journal of the Geological Society, London, Vol. **156,** 1999, pp. 209–212. Printed in Great Britain

SPECIAL

Denudation rates for the southern Drakensberg escarpment, SE Africa, derived from *in-situ*-produced cosmogenic ^{36}Cl: initial results

A. FLEMING[1], M. A. SUMMERFIELD[1], J. O. STONE[2], L. K. FIFIELD[3] & R. G. CRESSWELL[3]

[1]*Department of Geography, University of Edinburgh, Edinburgh EH9 8XP, UK (e-mail: af@geo.ed.ac.uk)*
[2]*Research School of Earth Sciences, Australian National University, Canberra, ACT 0200, Australia*
[3]*Department of Nuclear Physics, Research School of Physical Sciences and Engineering, Australian National University, Canberra, ACT 0200, Australia*

Cosmogenic ^{36}Cl concentrations in basalt samples from the Drakensberg escarpment on the SE African passive margin give quantitative estimates of denudation and scarp retreat rates. Over the 10^4–10^6 year timespan addressed by these data, the calculated escarpment retreat rate has been 50–95 m Ma^{-1} and the average summit denudation rate 6 m Ma^{-1}. The scarp retreat rate is an order of magnitude less than previously suggested. The rate of summit lowering is sufficient to prevent the long-term intact survival of erosion cycle surfaces formed in the Mesozoic that were previously inferred for this region.

Keywords: SE Africa, cosmogenic isotopes, denudation, landscapes, scarps.

High-elevation passive margins, comprising elevated terrain flanked by ocean-facing escarpments, are fundamental morphological features on a global scale, and their development reflects the long-term interaction of tectonic and surface geomorphic processes following supercontinent fragmentation (Gilchrist & Summerfield 1994). Acknowledgment of the importance of passive margin landscapes to an understanding of tectonic processes associated with rifting and continental break-up has recently prompted a number of attempts to model their morphological evolution (Beaumont *et al.* 1998). Such numerical modelling studies, however, are currently poorly constrained due to a lack of empirical data on long-term rates of denudation and landscape change (van der Beek & Braun 1998).

Analysis of *in-situ*-produced cosmogenic isotopes affords unique insights into the exposure history of the Earth's surface. For erosional environments the isotopic concentrations measured can yield mean denudation rates applicable to the past 10^3–10^6 years (Lal 1991). Here we report direct quantitative estimates of long-term escarpment retreat and summit denudation rates for sites in the southern section of the Drakensberg on the SE African passive margin, derived from measurements of *in-situ*-produced cosmogenic ^{36}Cl.

Drakensberg escarpment. The Drakensberg area of SE Africa is widely regarded as the 'type' high-elevation passive margin landscape following the early work of King (1944), and it has subsequently played a key role in the development of theories of long-term, large-scale landscape evolution. The Drakensberg (Fig. 1) forms the most dramatic section (up to 1000 m of relief) of the Great Escarpment that lies *c.* 100–200 km inland of the coast of southern Africa. It separates a dissected coastal zone from the elevated terrain of the Lesotho Highlands which reaches a maximum elevation of 3482 m at Thabana–Ntlenyana (Fig. 1). The highest terrain (>2000 m, Fig. 1) corresponds to the major remnant of the early Jurassic Karoo flood basalt province (Cox 1988; Duncan *et al.* 1997), and the southern sector of the Drakensberg escarpment forms the eroded coastal side of the basalt pile. Existing geomorphological models of the development of this landscape lack adequate geochronological control and rely heavily on the allocation of 'ages' to land surfaces based on the characteristics of associated weathering deposits and the correlation of erosion surface remnants (see Partridge & Maud 1987 for a review). Central to these interpretations of landscape evolution is the idea that the present Drakensberg escarpment originated at the Indian Ocean continental margin at the time of the shearing away of the Falkland Plateau *c.* 130 Ma ago, and this implies a mean escarpment retreat rate of *c.* 1–1.5 km Ma^{-1} since that time.

Sampling and methods. *In-situ* cosmogenic isotopes are produced by the interaction of highly energetic cosmic-ray-derived particles with nuclei in minerals at the earth's surface (see, for example, Cerling & Craig 1994 for a review). For radionuclides the cosmogenic isotopic abundance is determined by the rate of radioactive decay, and by the dwell time of rock within the cosmic ray attenuation zone which extends 1–2 m below the ground surface for the dominant spallation reactions. This dwell time reflects the rate of removal of rock from the surface and can therefore be used to estimate the rate of denudation. It has been shown (e.g. Lal 1991), that in the case of spallogenic

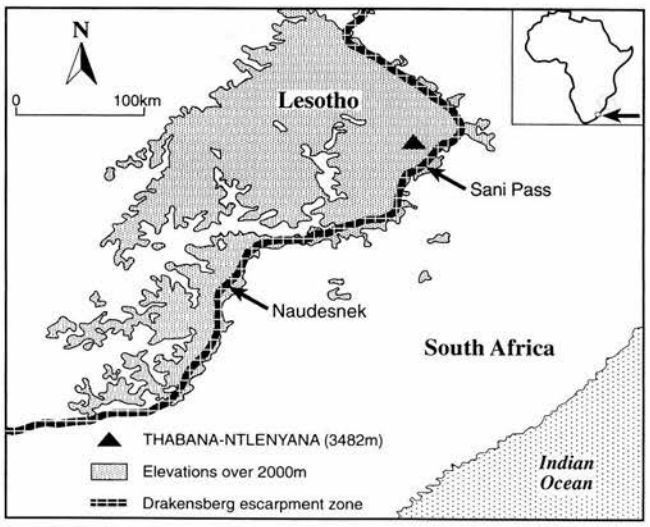

Fig. 1. Location map showing the sample sites at Naudesnek and Sani Pass, in relation to the Drakensberg escarpment, SE Africa.

reactions, where the production rate declines exponentially with depth, the denudation rate, ε, for a bedrock surface eroding at a constant rate, is given by the equation:

$$\varepsilon = \frac{\Lambda}{\rho}\left(\frac{P}{N} - \lambda\right) \quad (1)$$

where, Λ is the absorption mean free path for nuclear interacting particles in the target rock (g cm^{-2}), ρ is the mean rock density (g cm^{-3}), P is the site specific production rate for the cosmogenic nuclide (atoms g (element)$^{-1}$ a^{-1}), N is the measured nuclide concentration (atoms g (element)$^{-1}$), and λ is the decay constant (a^{-1}). More complex equations similar to (1) exist for cosmogenic ^{36}Cl, which is produced in part by neutron and muon reactions with non-exponential production profiles (Liu *et al.* 1994; Stone *et al.* 1998).

Samples of basalt were collected from free faces and summit bedrock exposures at two separate locations (Sani Pass and Naudesnek) on the southern Drakensberg escarpment (Fig. 1). Of the Sani Pass samples, S1/95 is from an extensive area of low relief (Sani Flats) at the highest point on the top of the escarpment, while S2/95 is from the free face of the main escarpment. At Naudesnek, two samples were collected from the escarpment summit, one 500 m inland of the escarpment edge (N1/95) and one from a high summit on the escarpment edge flanked by a narrow buttress ridge extending out from the main escarpment face (N2/95). A third sample (N3/95) was collected from a flat section of this buttress ridge (i.e. seaward of the escarpment) and a fourth (N4/95) from the free face. Summit samples were taken from outcrops standing *c.* 0.5–1 m proud of the surrounding thin soil mantled surface. Free face samples were collected from accessible cliffs 15–30 m below the escarpment crest. Positional details were obtained by GPS and digital altimeter. Topographic shielding and details of the geomorphological setting were recorded in the field.

The most appropriate cosmogenic nuclide for the basalt lithology of the Drakensberg is ^{36}Cl ($t_{1/2} \approx 0.3$ Ma). In Cl-poor basalt samples such as these, ^{36}Cl is principally produced by spallation reactions involving Ca and K, with minor contributions from neutron activation of ^{35}Cl and muon reactions with Ca and K. Chlorine was chemically extracted from leached whole-rock basalt using the methods described by Stone *et al.* (1996). Chlorine-36 was measured using the 14-UD pelletron accelerator mass spectrometer (AMS) at the Australian National University (Fifield *et al.* 1994). Chlorine concentrations were determined by isotope dilution with ^{37}Cl on subsamples of the same leached rock prepared for AMS analysis. In order to calculate the effects of bulk sample chemistry on ^{36}Cl production, concentrations of major elements and neutron-absorbing trace elements were determined by X-ray fluorescence and inductively coupled plasma mass spectrometry.

Cosmogenic isotope production rates vary with altitude and latitude (Cerling & Craig 1994) and hence overall production rates for the Drakensberg samples were obtained by scaling spallation, neutron capture and muon capture calibrated production rates (Table 1) to the sampling site locations using the methods given by Lal (1991) and Stone *et al.* (1998). For flat-lying samples, denudation rates were calculated using equations analogous to (1) above, but incorporating the effect of ^{36}Cl production by neutrons (Liu *et al.* 1994) and by muons, which penetrate beyond the attenuation depth of spallogenic production (Stone *et al.* 1998). At the two free face sites (S2/95 & N4/95), very few boulders (all less than 0.5 m thick) were identified on the well vegetated talus slopes or, where natural exposures permitted, within the colluvium. This suggests that, at these sites, the faces retreat by the regular spalling of thin sheets or individual grains and/or the periodic loss of blocks less than 0.5 m thick. Therefore for these steeply dipping surfaces, maximum back-wearing rates were calculated with two models, assuming (i) steady erosion, or (ii) intermittent shedding of 0.5 m blocks. In both models allowance was made for obstruction of the incident cosmic ray flux by the cliff and reduction of the effective cosmic ray attenuation length perpendicular to the steep face, which receives most of the incoming radiation at grazing angles. These effects were addressed assuming that the radiation responsible for spallogenic production has a $\cos^{2.3}(\theta)$ zenith angle distribution and is absorbed with a 1/e absorption length of *c.* 210 g cm^{-2} (approximately 70 cm in basalt) (Dunne *et al.* 1998; Nishiizumi *et al.* 1989). These assumptions reproduce the observed vertical attenuation length of *c.* 160 g cm^{-2} (approximately 55 cm in basalt) for spallogenic production beneath a flat lying 2π surface (e.g. Brown *et al.* 1992), although they greatly oversimplify cosmic ray propagation by secondary reactions below ground. Analogous trigonometric corrections to the sub-surface neutron and muon capture rates for the cliff samples were derived from the production models of Liu *et al.* (1994) and Stone *et al.* (1998).

Results. Analytical data and the resulting estimated denudation rates, ε, are given in Table 1. Summit denudation rates range between 1.4 m Ma^{-1} and 10 m Ma^{-1}. Averaging these yields a medium-term mean denudation rate of 6 m Ma^{-1}. The ridge-top denudation rate seaward of the escarpment (N3/95) is higher at 27 m Ma^{-1}. If the free face of the escarpment is assumed to retreat gradually, by spalling of fragments thinner than the attenuation length for ^{36}Cl production (*c.* 30–35 cm perpendicular to the cliff face), erosion rates of 48 ± 6 m Ma^{-1} and 62 ± 7 m Ma^{-1} are calculated for S2/95 (76° dip) and N4/95 (82° dip) respectively. These convert to escarpment back-wearing rates of 49 and 63 m Ma^{-1}. However, if escarpment retreat occurs by shedding of blocks similar to, or thicker than, the attenuation length for ^{36}Cl production, our results should be interpreted as exposure ages, indicating the time between rockfall events. For the typical 0.5 m thick block, the interval between shedding events would be calculated to be greater than 6.2 ± 0.8 ka and 5.3 ± 0.6 ka at Sani Pass and Naudesnek, respectively. These ages provide maximum limits to the back-wearing rate of 83 m Ma^{-1} and 95 m Ma^{-1}. Taking the timescale represented by these estimates as the time to erode one attenuation length for ^{36}Cl production, our measurements average denudation over the past 7–10 ka (for the free-face samples) to 400 ka for the most slowly eroding summit sample.

As expected, there is a significant contrast between escarpment and summit denudation rates at both sites, although the escarpment retreat rates are only 2–3 times higher than the denudation rate of the flat-lying ridgecrest (N3/95). The cause of the variability observed between the summit rates is unclear, but may be related to local variability in slope, drainage conditions and erodibility of the substrate. In comparison, the effective back-wearing rates calculated for the escarpment are surprisingly similar at the two sites, though the two areas sampled are 175 km apart.

Discussion. Although there are no other direct measurements of mean denudation rates for the past *c.* 10^4–10^5 a for the Drakensberg, the rates derived from cosmogenic isotope analysis reported here can be compared with existing longer term estimates of depths of denudation for the basalt pile forming the escarpment rim and the Lesotho Highlands. For instance, zeolite zonation studies indicate that 200–400 m has been eroded from the top of the present Drakensberg basalt sequence since its formation (Dunlevey *et al.* 1993). Using the ^{40}Ar–^{39}Ar age of 183 ± 1 Ma for the Karoo igneous event (Duncan *et al.* 1997) gives a mean denudation rate of *c.* 1–3 m Ma^{-1} for the top of the pile, assuming no post-eruptive sediment accumulation. This rate, if extrapolated (based on the present-day thickness of the basalt at the sample sites and a generally flat-lying post-eruptive topography (Marsh *et al.* 1997)), corresponds to *c.* 4–6 m Ma^{-1} at the sampling sites. In northern Lesotho the shallow exposure of the Letseng-la-Terae kimberlite pipe has been used to infer the removal of *c.* 300 m of section since its eruption *c.* 90 Ma ago (Hawthorne 1975),

Table 1. *^{36}Cl results for samples from the southern Drakensberg, southern Africa*

Sample	Latitude (S)	Elevation (m)	Thickness (g cm^{-2})	[Ca] (wt%)	[K] (wt%)	[Cl] μg g^{-1}	$s_{35}n_{35}/S$*	[^{36}Cl]$_{cosmogenic}$† (10^6 atom g^{-1})	P_{Ca}‡ (atom g^{-1} a^{-1})	P_K‡ (atom g^{-1} a^{-1})	P_{35Cl}‡ (atom g^{-1} a^{-1})	ε§ (m Ma^{-1})
Flat lying samples												
S1/95 Sani Pass	29°35′	2884	15.9	6.55	0.95	10.1 ± 0.2	0.00082	2.46 ± 0.13	20.03 ± 0.68	9.84 ± 0.84	1.93 ± 0.25	6.7 ± 0.5
N1/95 Naudesnek	30°47′	2728	11.6	6.58	0.79	10.3 ± 0.4	0.00090	1.61 ± 0.05	19.05 ± 0.65	7.68 ± 0.66	1.80 ± 0.24	10.0 ± 0.5
N2/95 Naudesnek	30°45′	2641	10.2	6.70	0.32	14.7 ± 0.4	0.00120	5.43 ± 0.10	18.58 ± 0.63	2.93 ± 0.29	2.48 ± 0.32	1.4 ± 0.1
N3/95 Naudesnek	30°45′	2572	8.7	7.91	0.64	9.9 ± 0.3	0.00086	0.66 ± 0.03	21.06 ± 0.71	5.69 ± 0.50	1.54 ± 0.20	26.9 ± 1.7
Free face samples												
S2/95 Sani Pass	29°35′	2824	10.2	6.10	0.51	8.0 ± 0.2	0.00064	0.148 ± 0.017	12.27 ± 1.23	3.49 ± 0.46	0.73 ± 0.11	47.8 ± 6.3
N4/95 Naudesnek	30°45′	2550	11.6	6.97	0.73	13.8 ± 0.4	0.00121	0.106 ± 0.009	10.99 ± 1.11	3.89 ± 0.50	1.01 ± 0.16	62.3 ± 6.8

*Fraction of thermal neutrons captured by ^{35}Cl.
†Cosmogenic ^{36}Cl, corrected for contribution of radiogenic ^{36}Cl derived from U-fission and (α, n) neutrons.
‡Scaled production rate, total of spallogenic and muon-initiated reactions, corrected for sample composition, latitude, elevation, sample thickness and shielding geometry.
§Erosion rate perpendicular to surface, assuming gradual, continuous erosion. For scarp face sample with dip β, back-wearing rate is ε/sinβ, hence 49.3 m Ma^{-1} for S2/95 and 63 m Ma^{-1} for N4/95.
^{36}Cl production rates from Ca, K and ^{35}Cl are based on calibrated production measurements as follows: Ca spallation, 48.8 ± 1.7 atoms g(Ca)$^{-1}$ a^{-1} (Stone *et al.* 1996); K spallation, 171 ± 15 atoms g(K)$^{-1}$ a^{-1} (Evans *et al.* 1997); muon capture by Ca, 5.3 ± 0.53 atoms g(Ca)$^{-1}$ a^{-1} (Stone *et al.* 1998); and muon capture by K, 9 ± 2 atoms g(K)$^{-1}$ a^{-1} (as assumed by Evans *et al.* 1997; this reaction has not been independently calibrated). Production of spallogenic secondary neutrons and capture by ^{35}Cl vary with sample composition and were calculated using the model of Liu *et al.* (1994), with $P_f(0) = 586 \pm 40$ n (g air)$^{-1}$ a^{-1} (Phillips *et al.* 1996). Production of ^{36}Cl by muon-initiated neutron reactions was determined as described by Stone *et al.* (1998), using reaction parameters given by Charalambus (1971).

and this indicates a mean denudation rate of *c.* 3 m Ma^{-1}. This mean figure, adjusted to reflect the thickness of the basalt presently found at our sites, yields a rate for the sampling sites since the mid-Cretaceous of *c.* 6–8 m Ma^{-1}. Although an extensive apatite fission-track thermochronology dataset exists for southern Africa which provides information on long-term regional scale denudation (Brown 1992), no data are available for the area of the basalt outcrop. However, extrapolation of depths of denudation estimated from apatite fission track analysis data from borehole samples located on both the coastal and inland flanks of the Lesotho Highlands can been used to infer *c.* 500–1000 m of crustal stripping since the Karoo igneous event if an originally low relief summit is assumed for the basalt pile. This yields a mean denudation rate of 3–6 m Ma^{-1}.

King (1944) argued that remnants of an erosion surface formed before the break-up of Gondwana were preserved at the highest elevations in the Drakensberg and Lesotho Highlands. However, it is not clear in King's cyclic scheme of landscape development whether he meant that landsurface remnants could survive without any alteration, or whether he envisaged that, although subject to some denudation, they retained their original minimal local relief. Our cosmogenic ^{36}Cl isotope data confirm that denudation has been occurring actively over the past 10^5–10^6 a on the summit of the Drakensberg escarpment and, by inference, the Lesotho Highlands, and that if similar rates apply over longer time scales, unmodified Gondwana erosion surface remnants cannot have survived. More generally, if the rates of summit denudation reported here are more widely characteristic of bedrock outcrops on low relief surfaces (a point we are addressing by additional sampling) then our findings have important implications for denudation chronologies which assume that erosion surfaces are preserved unaltered over geological time scales.

If extrapolated back in time, retreat of the Drakensberg escarpment at the mean rate estimated here of *c.* 70 m Ma^{-1} would have limited the total escarpment retreat to less than 10 km since break-up along the SE African margin *c.* 135 Ma ago. This is more than an order of magnitude less than the mean rate of retreat that would be required for the escarpment to have moved to its present position from an original location at, or near, the present-day coastline. This conclusion does not preclude the formation of the Drakensberg escarpment being a direct consequence of the continental break-up event; rather our initial results suggest that long-standing views about the mode of post-Gondwana landscape evolution along the SE African continental margin require re-examination. Current conceptual models envisage an immediate post-break-up landscape with a major escarpment and drainage divide close to the continental edge, with subsequent landscape development being characterized by their progressive retreat inland. However, there is no direct evidence of the drainage pattern immediately after break-up, and it is possible that a major drainage divide existed some distance inland. If this is the case, any escarpment created along the coast at the time of break-up would rapidly have been destroyed by fluvial incision. The present escarpment would have originally grown vertically through differential denudation as a feature pinned at the seaward flank of the drainage divide, with subsequent inland retreat of only a few kilometres. Modelling studies also suggest that escarpment retreat is favoured where an escarpment coincides with a drainage divide and where continuous back-tilting of the escarpment zone, due to the flexural isostatic

response to denudational unloading, helps to maintain the escarpment summit as a drainage divide (Beaumont *et al.* 1998).

Conclusions. The cosmogenic isotope data reported here indicate that (1) the rate of retreat of the Drakensberg escarpment, for at least the past *c.* 10^4 a, is an order of magnitude lower than previously thought; (2) rates of escarpment summit denudation are an order of magnitude less than rates of escarpment retreat; and (3) rates of summit denudation, though low, are sufficient to prevent the preservation intact of erosion surfaces over geological time. Although our data are too limited to allow firm conclusions to be drawn, we have demonstrated that cosmogenic isotope analysis has considerable potential as a means of addressing long-standing questions of landscape evolution given an appropriate sampling strategy which targets key landscape elements from which broader inferences can be drawn.

This work was supported by NERC grant GR9/01730 to M.A.S. Some of the sample analysis was undertaken while A.F. was a School Visitor at RSES, ANU. A.F. acknowledges the financial support of the Department of Geography, Edinburgh University. We thank H. Cockburn for assistance with sample collection, D. James for XRF analysis, M. McCartney for ICP-MS results and K. Gallagher and M. Widdowson for providing valuable comments on an earlier version of this manuscript.

References

Beaumont, C., Kooi, H. & Willett, S. 1998. Coupled tectonic-surface process models with applications to rifted margins and collisional orogens. *In*: Summerfield, M.A. (ed.) *Geomorphology and Global Tectonics*. Wiley, London, in press.

Brown, E.T., Brook, E.J., Raisbeck, G.M., Yiou, F.M. & Kurz, M.D. 1992. Effective attenuation lengths of cosmic rays producing ^{10}Be and ^{26}Al in quartz: Implications for exposure age dating. *Geophysical Research Letters*, **19**, 369–372.

Brown, R.W. 1992. *A fission track thermochronology study of the tectonic and geomorphic development of the sub-aerial continental margins of southern Africa*. PhD thesis, La Trobe University, Bundoora, Australia.

Cerling, T.E. & Craig, H. 1994. Geomorphology and *in-situ* cosmogenic isotopes. *Annual Review of Earth and Planetary Science*, **22**, 273–317.

Charalambus, S. 1971. Nuclear transmutations by negative stopped muons and the activity induced by cosmic-ray muons. *Nuclear Physics*, **A166**, 145–161.

Cox, K.G. 1988. The Karoo Province. *In*: Macdougall, J. (ed.) *Continental Flood Basalts*. Kluwer, Dordrecht, 239–271.

Duncan, R.A., Hooper, P.R., Rehacek, J., Marsh, J.S. & Duncan, A.R. 1997. The timing and duration of the Karoo igneous event, southern Gondwana. *Journal of Geophysical Research*, **102**, 18 127–18 138.

Dunlevey, J.N., Ramluckan, V.R. & Mitchell, A.A. 1993. Secondary mineral zonation in the Drakensberg Basalt Formation, South Africa. *South African Journal of Geology*, **96**, 216–220.

Dunne, A., Elmore, D. & Muzikar, P. 1998. Scaling of cosmogenic nuclide production rates for geometric shielding and attenuation at depth on sloped surfaces. *Geomorphology*, in press.

Evans, J.M., Stone, J.O.H., Fifield, L.K. & Cresswell, R.G. 1997. Cosmogenic chlorine-36 production in K-feldspar. *Nuclear Instruments and Methods*, **123**, 334–340.

Fifield, L.K., Allan, G.L., Stone, J. & Ophel, T.R. 1994. The ANU AMS system and research program. *Nuclear Instruments and Methods*, **B92**, 85–89.

Gilchrist, A.R. & Summerfield, M.A. 1994. Tectonic models of passive margin evolution and their implications for theories of long-term landscape development. *In*: Kirkby, M.J. (ed.) *Process models and theoretical geomorphology*. Wiley, London, 55–84.

Hawthorne, J.B. 1975. Model of a kimberlite pipe. *In*: Ahrens, L.H., Dawson, J.B., Duncan, A.R. & Erlank, A.J. (eds) *Physics and Chemistry of the Earth*. Pergamon, Oxford, 1–15.

King, L.C. 1944. Geomorphology of the Natal Drakensberg. *Transactions of the Geological Society of South Africa*, **47**, 255–282.

Lal, D. 1991. Cosmic ray labeling of erosion surfaces: in situ nuclide production rates and erosion models. *Earth and Planetary Science Letters*, **104**, 424–439.

Liu, B., Phillips, F.M., Fabryka-martin, J.T., Fowler, M.M. & Stone, W.D. 1994. Cosmogenic ^{36}Cl accumulation in unstable landforms 1. Effects of the thermal neutron distribution. *Water Resources Research*, **30**, 3115–3125.

Marsh, J.S., Hooper, P.R., Rehacek, J., Duncan, R.A. & Duncan, A.R. 1997. Stratigraphy and Age of Karoo Basalts of Lesotho and Implications for Correlations Within the Karoo Igneous Province. *In*: Mahoney, J.J. & Coffin, M.F. (eds) *Large Igneous Provinces: Continental, Oceanic, and Planetary Flood Volcanism*. AGU Geophysical Monographs, **100**, 247–272.

Nishiizumi, K., Winterer, E.L., Kohl, C.P., Klein, J., Middleton, R., Lal, D. & Arnold, J.R. 1989. Cosmic ray production rates of ^{10}Be and ^{26}Al in quartz from glacially polished rocks. *Journal of Geophysical Research*, **94**, 17 907–17 915.

Partridge, T.C. & Maud, R.R. 1987. Geomorphic evolution of southern Africa since the Mesozoic. *South African Journal of Geology*, **90**, 179–208.

Phillips, F.M., Zreda, M.G., Flinsch, M.R., Elmore, D. & Sharma, P. 1996. A reevaluation of the cosmogenic ^{36}Cl production rates in terrestrial rocks. *Geophysical Research Letters*, **23**, 949–951.

Stone, J.O., Allan, G.L., Fifield, L.K. & Cresswell, R.G. 1996. Cosmogenic chlorine-36 from calcium spallation. *Geochimica et Cosmochimica Acta*, **60**, 679–692.

——, Evans, J.M., Fifield, L.K., Allan, G.L. & Cresswell, R.G. 1998. Cosmogenic chlorine-36 production in calcite by muons. *Geochimica et Cosmochimica Acta*, **62**, 433–454.

van der Beek, P. & Braun, J. 1998. Numerical modelling of landscape evolution on geological time-scales: a parameter analysis and comparison with the south-eastern highlands of Australia. *Basin Research*, **10**, 49–68.

Received 19 August 1998; revised typescript accepted 30 October 1998.